

Dynamic of Civil Engineering and Transport Structures and Wind Engineering

Edited by
Kamila Kotrasova and Jozef Melcer



TRANS TECH PUBLICATIONS

@SeismicIsolation

Dynamic of Civil Engineering and Transport Structures and Wind Engineering

Edited by
Kamila Kotrasova
Jozef Melcer

Dynamic of Civil Engineering and Transport Structures and Wind Engineering

Selected, peer reviewed papers from the
6th International Scientific Conference on
Dynamic of Civil Engineering and Transport Structures
and Wind Engineering
(DYN-WIND 2014),
May 25-29, 2014, Donovaly, Slovak Republic

Edited by

Kamila Kotrasova and Jozef Melcer



Copyright © 2014 Trans Tech Publications Ltd, Switzerland

All rights reserved. No part of the contents of this publication may be reproduced or transmitted in any form or by any means without the written permission of the publisher.

Trans Tech Publications Ltd
Churerstrasse 20
CH-8808 Pfäffikon
Switzerland
<http://www.ttp.net>

Volume 617 of
Applied Mechanics and Materials
ISSN print 1660-9336
ISSN cd 1660-9336
ISSN web 1662-7482

Full text available online at <http://www.scientific.net>

Distributed worldwide by

Trans Tech Publications Ltd
Churerstrasse 20
CH-8808 Pfäffikon
Switzerland

Fax: +41 (44) 922 10 33
e-mail: sales@ttp.net

and in the Americas by

Trans Tech Publications Inc.
PO Box 699, May Street
Enfield, NH 03748
USA

Phone: +1 (603) 632-7377
Fax: +1 (603) 632-5611
e-mail: sales-usa@ttp.net

PREFACE

Ladies and Gentleman, dear Readers,

the publication summarizes conference papers from the 6th international scientific conference on Dynamic of Civil Engineering and Transport Structures and Wind Engineering (DYN-WIND 2014). The conference was held from the 25th to 29th of May 2014 at Donovaly in Slovak Republic. The conference was organized by University of Žilina, Faculty of Civil Engineering, Department of Structural Mechanics, Slovak Scientific - Technical Transport Society in Zvolen, Doprastav, a.s. Bratislava.

In the submitted publication, which is divided into two chapters, are summarized selected conference papers from researchers of eminent slovak-czech-polish-russian-ukrainian and other educational universities, research institutes and industrial practice.

The publication includes following issues

- Effects of transport means on structures and environment
- Quasi-static and dynamic problems of roads, pavements and railroad tracks, bridges, incline and ground solids stability, buildings and other civil engineering and transport structures
- Problems of fatigue, life-time and reliability of structural materials and constructions
- Numerical and experimental methods and computer simulations
- Mathematical applications
- Earthquake engineering
- Transport noise and environment
- Wind characteristics
- Wind loads on building and structures and their aero-elastic response
- Experimental methods, wind tunnels, field and full-scale measurements
- Industrial and architectonical aerodynamics, cross wind on transport means and other problems
- Computational methods in wind engineering
- Risk and social impact

Kamila Kotrasová and Jozef Melcer
issue editors

Scientific Guarantor

Prof. Ing. Jozef Melcer, DrSc. - University of Žilina

Organizing Guarantors

Alžbeta Švidraňová - University of Žilina

doc. Ing. Daniela Kuchárová, PhD. - University of Žilina

doc. Ing. Gabriela Lajčáková, PhD. - University of Žilina

Ing. Miroslav Vítazka - Slovak Railways Zvolen

Ing. Oliver Čvirik – Doprastav, a.s. Bratislava

International Scientific Committee

Argalášová, L.	Slovak Republic	Partov, D.	Bulgaria
Beniač, M.	Slovak Republic	Pazdera, L.	Czech Republic
Benin, A.V.	Russia	Petinov, S.V.	Russia
Bielek, M.	Slovak Republic	Petrangeli, M. P.	Italy
Bogdanova, G.	Russia	Pirner, M.	Czech Republic
Čajka, R.	Czech Republic	Polach, P.	Czech Republic
Jendželovský, N.	Slovak Republic	Polák, M.	Czech Republic
Keršner, Z.	Czech Republic	Petkova, R.	Bulgaria
Kormaníková, E.	Slovak Republic	Ravinger, J.	Slovak Republic
Kotrasová, K.	Slovak Republic	Smutný, J.	Czech Republic
Králik, J.	Slovak Republic	Szava, I.	Rumania
Krejsa, M.	Czech Republic	Temirbekov, Y.	Kazakhstan
Lalin, V.V.	Russia	Tesár, A.	Slovak Republic
Máca, J.	Czech Republic	Vatin, N.I.	Russia
Makovička, D.	Czech Republic	Vatulia G.	Ukraine
Melcer, J.	Slovak Republic	Zamorowski J.	Poland
Menšík, F.	Czech Republic	Zolotov, M.	Ukraine
Michalcová, V.	Czech Republic	Žmindák, M.	Slovak Republic

Table of Contents

Preface and Committee

Chapter 1: Dynamics of Civil Engineering and Transport Structures

Experimental Modal Analysis of the Footbridge across Vltava River in Prague Damaged by Flood in June 2013	
M. Polák, T. Plachý and J. Máca	3
Human-Induced Vertical Vibration of the Footbridge across Opatovicka Street	
V. Šána and M. Polák	7
Long-Term Monitoring of a Composite Steel-Concrete Bridge on the Prague Ring Road	
P. Tej, J. Král, A. Tejová and J. Marková	13
Dynamic Deflection of a Bridge versus Speed of Vehicle Motion	
E. Daniel	19
Moving Load Effect of a Truck on Concrete Pavements	
G. Lajčáková	24
Dynamic Load of Vehicle on Asphalt Pavement	
J. Melcer	29
Applications of Integral Transforms in Solving Problems of Dynamic Interaction in the Vehicle-Roadway System	
D. Stachová	34
The Comparison between the Applications of Different Types of Boundary Conditions that are Used in the Dynamic Simulation of the Tests of Pavements	
J. Kortiš and N. Rapanová	40
The Stress Analysis of the Industrial Fiber-Reinforced Concrete Slab on Elastic Subgrade Loaded by the Operational Loading	
J. Kortiš	46
Natural Frequencies of Railway Slab on Winkler Foundation	
D. Kuchárová	50
Influence of Construction of Railway Superstructure on Railway Quality	
L. Ižvolt, J. Ižvoltová and J. Šestáková	54
Utilization of Multibody Simulations at the Verification of the Stabilizer Bar of the Trolleybus	
P. Polach	60
Dynamic Time-History Response of Cylindrical Tank Considering Fluid - Structure Interaction due to Earthquake	
K. Kotrasová, I. Grajciar and E. Kormaníková	66
Engineering Approach of Seismic Analysis of Piling Quay Walls Subject to Redistribution of Lateral Earth Pressure	
V. Zhdanirov and V. Korovkin	70
Safety of Nuclear Power Plants against the Aircraft Attack	
J. Králik	76
Failure Probability of NPP Communication Bridge under the Extreme Loads	
J. Králik and J. Králik	81
Structure Analysis Loaded by Interior Blast Effect	
D. Makovička and D. Makovička	86
Single Degree of Freedom Analysis of Steel Beams under Blast Loading	
L. Figuli and D. Papán	92
Impact Resistance of Thin-Walled Shell Structures	
S. Reháček, P. Huňka, D. Čítek, J. Kolísko and I. Šimůnek	96
Impact Loading of Concrete Slabs	
N. Jendželovský and K. Vráblová	100
Analysis of High Velocity Impact on Composite Structures	
M. Žmindák, Z. Pelagić and M. Bvoc	104

Environmental Noise and Annoyance in the Urban Area at Different Time Intervals	
L. Argalášová, J. Jurkovičová, L. Ševčíková, Z. Štefániková, K. Hirošová, J. Babjaková, A. Kánovicsová and A. Filová	110
3D Traffic Noise Simulation	
T. Melova, M. Kolousek and T. Priscak	116
Monitoring of Tram Traffic Noise in the Small Curve Radius	
E. Panulinová and S. Harabinová	120
The Efficiency of Dynamic Relaxation Methods in Static Analysis of Cable-Membrane Structures	
M. Hüttner, J. Máca and P. Fajman	124
Form-Finding of Membrane Structures and Necessary Stabilization of this Process	
R. Lang, I. Němec and I. Ševčík	130
Vibrations in the Assessment of Construction State	
B. Žóltowski and M. Žóltowski	136
Assessment State of Masonry Components Degradation	
M. Žóltowski	142
Numerical Modeling of Cylindrical Tank and Compare with Experiment	
N. Jendželovský and L. Baláz	148
Non-Destructive Tracking of Structural Changes of Concrete Mixtures during Thermal Stress	
I. Kusák, M. Luňák and Z. Chobola	152
Fatigue of Steel Specimens at Low Temperatures	
A. Tesár and M. Sedlár	156
Dynamic Heat Transfer through the External Wall of a Timber Structure	
I. Skotnicová, L. Lausová and J. Brožovský	162
Carrying Capacity Definition of Steel-Concrete Beams with External Reinforcement under the Fire Impact	
G. Vatulia, Y. Orel and M. Kovalov	167
Mathematical Modelling of Thin-Walled Cold-Rolled Cross-Section	
J. Flodr, M. Krejsa, D. Mikolášek, O. Sucharda and L. Žídek	171
Experimental Study of Torsion of Guyed Mast Shaft	
S. Urushadze, M. Pirner and O. Fischer	175
New Results in Dynamics Stability Problems of Elastic Rods	
V.V. Lalin and D.A. Kushova	181
Fatigue Damage Accumulation under the Complex Varying Loading	
B. Melnikov and A. Semenov	187
Probability and Sensitivity Analysis of Plate	
K. Tvrdá	193
Strain-Life Approach: Application for Fatigue Design of Ship Superstructure Critical Detail	
S. Petinov	197
Simulating Couette Flow Using the Meshless Local Petrov-Galerkin Method	
J. Mužík	203
A 2-D Meshless Model for Soil Subsurface Settlement	
J. Mužík	209
Experimental Study and Mathematical Modeling of Bond of Different Types Winding Glass-Plastic Reinforcement with Concrete	
A.V. Benin, G. Bogdanova and S. Semenov	215
Fatigue Assessment of Concrete Members Strengthened by FRP Materials	
A. Čavojcová and M. Moravčík	221
Investigation of the Bond Behavior of UHPC	
D. Čítek, P. Huňka, S. Řeháček and J. Kolísko	225
Damage Detection and Localization on Cement Specimens	
T. Plachý, J. Okénka, P. Tesárek and M. Polák	229
Two Examples of the Use of FRP Reinforcement to Strengthen Structures	
L. Podolka	233
Effect of Cement Dosage on Selected Mechanical Fracture Parameters of Concretes	
H. Šimonová, I. Havlíková, P. Daněk, D. Lehký, B. Kucharczyková and Z. Keršner	239

The Effect of the Carbon Nanotubes on the Mechanical Fracture Properties of Alkali Activated Slag Mortars

L. Topolář, H. Šimonová, P. Rovnaník and P. Schmid

243

Finite Element Analysis of Damage Modeling of Fiber Reinforced Laminate Plate

E. Kormaníková and K. Kotrasová

247

Chapter 2: Wind Engineering**Analysis of Structures Having an Irregular Cross-Section Subjected to a Wind Load**

N. Jendželovský

253

Influence of Walls and Ceiling on a Wind Flow in BLWT Tunnel

O. Hubová, L. Konečná and P. Lobotka

257

Response of Layered Plates to Effects of Wind

P. Marton

263

Response of Masts of Power Lines to the Blast Effects of Wind

P. Marton

269

Numerical and Experimental Investigations of Air Flow Turbulence Characteristics in the Wind Tunnel Contraction

V. Michalcová, S. Kuznětsov, J. Brožovský and S. Pospíšil

275

Wind Tunnel Study of Vortex Shedding behind Cooling Tower Models

P. Michálek and D. Zacho

280

Analysis of Stochastic Resonance Phenomenon in Wind Induced Vibration of a Girder

S. Pospíšil and J. Náprstek

285

Numerical Estimation of Aerodynamic Characteristics of Footbridge Deck

R. Šoltýs and M. Tomko

291

The Effect of the Crosswinds on the Stability of the Moving Vehicles

T. Skrúcaný and J. Gnap

296

Estimation of Wind Energy Potential of the Territory

V. Badenko and N. Arefiev

302

Wind Power Market Development Initiative

X.M. Rakova

307

CHAPTER 1:

Dynamics of Civil Engineering and Transport Structures

Experimental Modal Analysis of the Footbridge across Vltava River in Prague Damaged by Flood in June 2013

POLÁK Michal^{1,a*}, PLACHÝ Tomáš^{1,b} and MÁCA Jiří^{1,c}

¹Department of Mechanics, Faculty of Civil Engineering, Czech Technical University in Prague,
Thákurova 7, CZ – 166 29, Prague, Czech Republic

^apolak@fsv.cvut.cz, ^bplachy@fsv.cvut.cz, ^cmaca@fsv.cvut.cz

Keywords: damage, flood, footbridge, experimental modal analysis, natural frequencies, natural modes

Abstract. The investigated footbridge across Vltava River in Prague was built in 1984. Almost the entire footbridge structure was overflowed by the extreme flood in August 2002 and the substantial part of the footbridge deck was overflowed afterwards by the great flood in June 2013 again. A significant damage on the footbridge deck was found out by a visual inspection of the load-bearing structure of the footbridge after the second flood. The basic objective of the performed experimental modal analysis was the initial experimental reliability verification of the obviously damaged footbridge structure. The measured natural frequencies and modes were compared with results of the several dynamic tests which were performed regularly during the lifetime of the footbridge. The localization of potential invisible damages was carried out. The recommendations for the range and the arrangement of the static load test, which was performed afterwards for fundamental reliability assessment of a footbridge structure, were made on the basis of the evaluated results of the experimental modal analysis.

Introduction

In the last two decades, the whole territory of the Czech Republic has been hit by a series of great floods, in which many bridges have been damaged significantly. The important question was solved in many cases whether the bridge structure has to be demolished or under which operating conditions the bridge operation is acceptable.

The investigated footbridge across Vltava River in Prague was built in 1984. The footbridge has been a very important way for pedestrians and cyclists from its commissioning because the nearest possible river crossing has been at a distance of about 2 km therefore the eventual closure of the footbridge always has been not only technical but also “political” problem.

The five hundred year flood hit Prague in August 2002 almost the entire footbridge structure was overflowed by this extreme flood. The parts of the footbridge upon the central pillars remained above the water level only. However no damage was found out on the footbridge load-bearing structure subsequently.

The substantial part of the footbridge deck was overflowed afterwards by the fifty year flood in June 2013 again and a large object floating down the river crashed into the footbridge deck, afterward a significant damage on the footbridge deck was found out by a visual inspection of the footbridge load-bearing structure after the end of the flood. It was determined immediately to investigate experimentally the footbridge structure more in detail. It was decided to realize an experimental modal analysis and a static load test on the footbridge.

The basic objective of the performed experimental modal analysis was the primary experimental reliability verification of the evidently damaged footbridge structure. The basic goal was divided to the several partial goals:

- Determination of the important natural frequencies and mode shapes.

b) Comparison of the measured characteristics of the natural vibration with the characteristics measured by three dynamic tests which were performed regularly during the lifetime of the footbridge in 1984, in September 1997 [1] and in November 2010 [2].

c) Damage detection and localization of the footbridge [3].

d) The data obtaining for determination of the range and arrangement of the static load test. The static load test had to check the load carrying capacity more deeply.

Authors solved a very similar problem in 2010 [4]. The footbridge across Bečva River, which had the same structural system practically, was damaged by the great flood in May 2010.

Description of the Investigated Footbridge

The footbridge is made from the prestressed concrete. The bearing structure is the prestressed suspension deck with three spans 85.5 m, 96.0 m and 67.5 m (Fig. 1). The prestressed deck is composed from precast segments DS – L and DS – Lv made from concrete B500 and from the monolithic saddle designed upon both of two intermediate piers. The dimensions of segments are 3.8×0.3×3.0 m. The concrete hinge joints were made in the lower part of the piers.



Fig. 1 The overview on the investigated footbridge (left) and the view of the damage (right), which was found out on the footbridge deck by a visual inspection after the end of the flood.

Description of the Experimental Modal Analysis Arrangement

Random wind excitation and the ambient vibration technique were used for determination of fundamental natural frequencies and modes of the footbridge. The footbridge vibration was measured by three seismic piezoelectric accelerometers Type 8344 Brüel&Kjaer. The measurement system Pulse and Front-end 3050-B-040 Brüel&Kjaer were used for data acquisition and data analysis. The response of the footbridge to wind excitation was measured in vertical direction in a chosen net of points (48 points – 24 cross sections and 2 points in each one) on the upper face of the footbridge deck. Two sensors were placed in the points of the net successively during the experiment. Third sensor was located throughout the experiment in the reference point, which was situated about one quarter of the central span of the footbridge.

The Results of the Experiment

The 11 natural frequencies were evaluated in the frequency range 0.4 to 3.0 Hz during the experimental modal analysis of the investigated footbridge. The mode shapes corresponding to the natural frequencies were evaluated too. The comparison of the chosen natural frequencies with corresponding ones measured by the dynamic tests performed in 1984, 1997 and 2010 is mentioned in Table 1. The selected measured mode shapes are compared in Fig. 2, Fig. 3 and Fig. 4.

Table 1 The comparison of the selected evaluated natural frequencies of the footbridge with ones measured by the dynamic tests performed in September 1997 [1] and in November 2010 [2].

Measured natural frequencies in 2013			Measured natural frequencies in 2010 [2]			Measured natural frequencies in 1997 [1]			Deviation between frequencies from 2010 and 2013	
No.	$f_{(j)}$	Expanded uncertainty $U_{k=2}$	No.	$f_{(j)}$	Expanded uncertainty $U_{k=2}$	No.	$f_{(j)}$	[Hz]	$\Delta_{(j)}$	[%]
(j)	[Hz]	[Hz]	(j)	[Hz]	[Hz]	(j)	[Hz]			
(1)	0.47	+/- 0.02	(1)	0.51	+/- 0.02	(1)	0.525		-8.3	+/- 5.3
(2)	0.63	+/- 0.02	(2)	0.66	+/- 0.02	(2)	0.650		-5.2	+/- 4.2
(3)	-	-	(3)	0.92	+/- 0.02	(3)	0.925			
(4)	0.97	+/- 0.02	(4)	1.04	+/- 0.02	-	-		-6.7	+/- 2.6

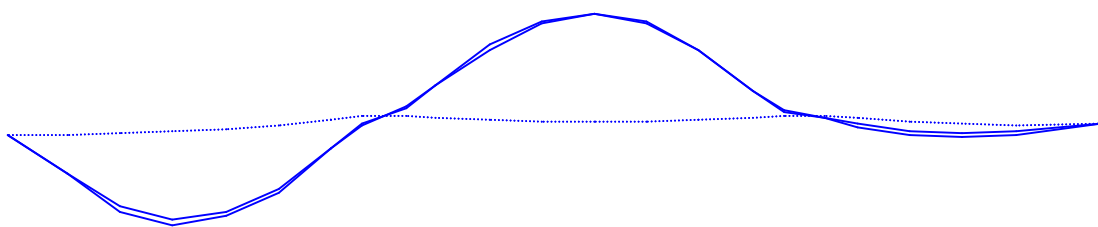


Fig. 2 The comparison of the 1st natural mode shapes of the footbridge measured in 1997 and 2010.

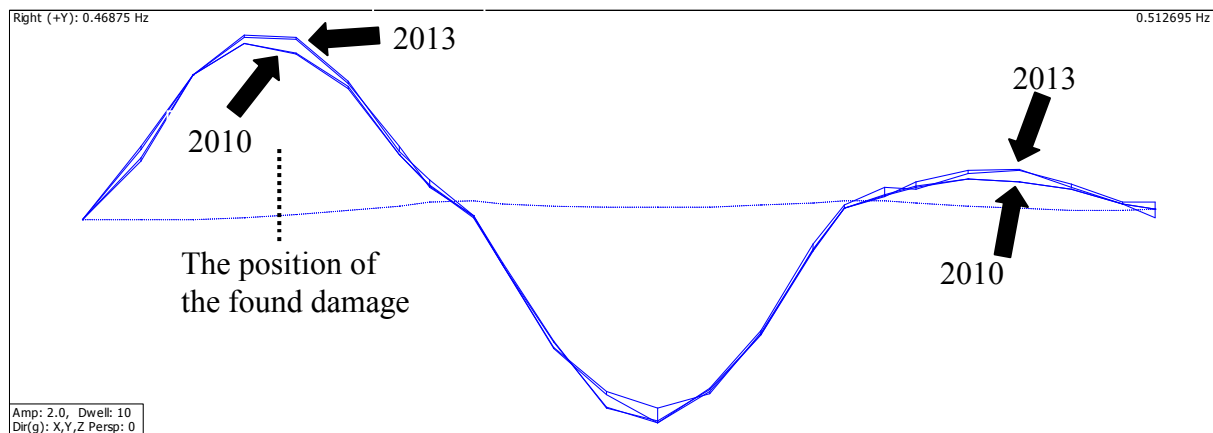


Fig. 3 The comparison of the 1st natural mode shapes of the footbridge measured in 2010 and 2013.

Summary

The results of the experimental modal analysis performed on the footbridge after the flood in the June 2013 were compared with the results of three dynamic tests which were performed regularly during the lifetime of the footbridge [1,2] especially the fundamental natural modes determined in November 2010 [2] were used.

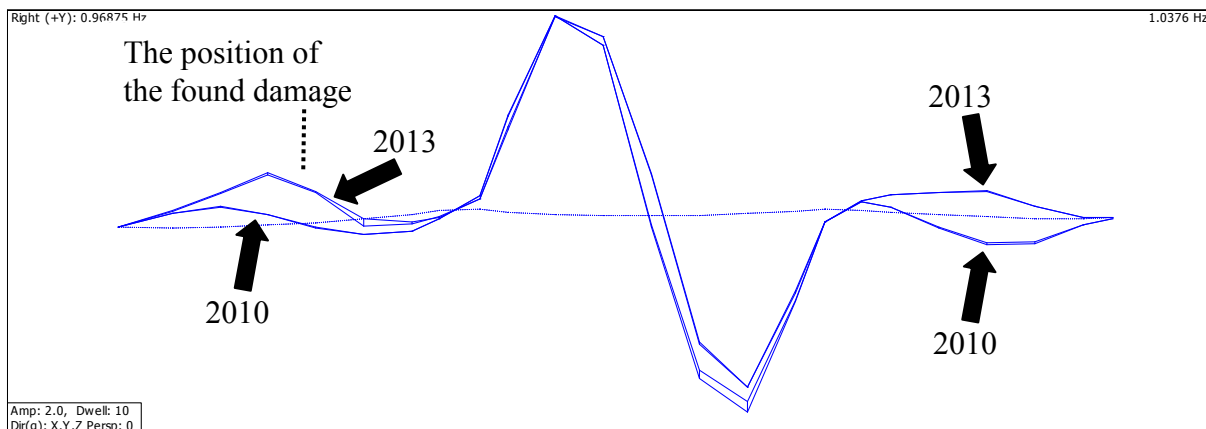


Fig. 4 The comparison of the 4th natural mode shapes of the footbridge measured in 2010 and 2013.

All compared frequencies decreased between November 2010 and June 2013 (some examples are shown in Table 1). It was caused evidently by the deterioration of the structural condition of the footbridge.

The similarity of the natural mode shapes measured in 2010 and in 1997 was high (see Fig. 2). On the other hand, some differences were found out between the natural mode shapes from 2013 and 2010 (see Fig. 3 and Fig. 4). Based on the detailed comparison of the natural mode shapes, several areas were determined, where the dynamic behaviour of the footbridge was changed evidently (see Fig. 3 and Fig. 4) and where some hidden fault could be at these places. The damage shown in Fig. 1, which was found before the start of the modal analysis, was located in one of these areas. It was recommended to investigate these areas in more detail especially during the static load test.

Acknowledgements

This work has been supported by the Technology Agency of the Czech Republic – Competence Centers under No. TE01020168 Centre for Effective and Sustainable Transport Infrastructure.

References

- [1] M. Pirner, O. Fischer, Studijní dynamická zkouška lávky v Praze – Troji (in Czech) (Experimental Dynamic Study of a Footbridge in Prague - Troja) – expert report, Institute of Theoretical and Applied Mechanics Academy of Sciences of Czech Republic, Prague, 1997.
- [2] M. Polák, T. Plachý, Dynamická zatěžovací zkouška stávající lávky pro pěší přes řeku Vltavu v Praze – Troji (in Czech) (Dynamic Load Test of an Existing Footbridge across Vltava River in Prague - Troja) – expert report, Czech Technical University in Prague Faculty of Civil Engineering, Prague, 2010.
- [3] T. Plachý, M. Polák, Damage detection and localisation on reinforced concrete slabs based on modal analysis, in: L. Collini (Ed.), 22nd Danubia-Adria Symposium on Experimental Methods in Solid Mechanics, DAS 2005, University of Parma / Ingegneria Industriale, Parma, 2005, pp. 247-248.
- [4] T. Plachý, M. Polák, Experimental Modal Analysis of the Footbridge across Bečva River in Přerov, in: M. Růžička, K. Doubrava, Z. Horák (Eds.), Proceedings of the 50th Annual Conference on Experimental Stress Analysis (EAN 2012), Czech Technical University in Prague Faculty of Mechanical Engineering, Prague, 2012, pp. 327 - 332.

Human-Induced Vertical Vibration of the Footbridge across Opatovicka Street

ŠÁNA Vladimír^{1,a*} and POLÁK Michal^{1,b}

¹Department of Mechanics, Faculty of Civil Engineering, Czech Technical University in Prague,
Thákurova 7, CZ 166 29 Prague, Czech Republic

^avladimir.sana@fsv.cvut.cz, ^bpolak@fsv.cvut.cz

Keywords: forced vibration, human – structure interaction, human – induced vibration, vandalism, ordinary pedestrian traffic, Monte Carlo simulation

Abstract. The presented article is focused on a theoretical dynamic analysis of the footbridge across the Opatovicka street in Prague, which acts as a simply supported beam. The structure was loaded by an ordinary pedestrian traffic, synchronous runners and vandals. The ordinary traffic was simulated by the Monte Carlo method as a stream of moving periodic forces with stochastic parameters. The synchronous runners and vandals were modeled as a combination of biomechanical models of human body, which influenced the structure vibration only passively, and driving forces, which loaded the structure in the contact points between the human body models and the structure. The driving force was the time – dependent function based on decomposition to the Fourier's Series and periodic triangle function. The obtained theoretical results are compared with experimental data.

Introduction

Mathematical description of the dynamic loading of structures, caused by a human walking, is quite complex process, which is mostly simplified by a deterministic loading model, also called the DLF (Dynamic Loading Factor) approach [2,3]. This model has been derived from the theory of Fourier's Series and could be expressed by the Eq. 4. The computed response of the structure loaded as a combination of the DLF model and biomechanical models of vandals and runners is described in this paper. The response caused by an ordinary pedestrian traffic was determined too.

Solved Structure

The footbridge chosen for the theoretical and experimental dynamic analysis is located in Prague across Opatovicka Street. It is a slab-on-girder bridge. The load-bearing structure consists of 6 steel girders and a reinforced concrete deck. The shape of the steel girders is box section with height $h = 520$ mm. Horizontal axial distance of steel beams is $b = 1100$ mm. The structure acts as a simply supported beam with the length of a span $L = 25.1$ m.

Theoretical Modal Analysis

Two models of investigated structure were created for a theoretical modal analysis, 3D solid model – ADINA and 2D beam model MATLAB, which has been used for the forced vibration as well. The problem of natural vibration is described by the equation

$$[\mathbf{M}]\{\ddot{\mathbf{w}}(t)\} + [\mathbf{K}]\{\mathbf{w}(t)\} = \{\mathbf{0}\} \quad (1)$$

where $[\mathbf{M}]$ denotes the mass matrix of the structure, $[\mathbf{K}]$ is the stiffness matrix, $\{\ddot{\mathbf{w}}(t)\}$ $\{\mathbf{w}(t)\}$ are the column vectors of acceleration and deflection respectively and $\{\mathbf{0}\}$ is the zero column vector. The computed natural frequencies are summarized in Table 1. Note that in the case of the 2D beam model the natural frequencies were computed via the Inverse Iteration Method. The Subspace

Iteration Method was implemented for the 3D model in the ADINA software. The 3D model was created for estimation of torsional natural modes of vibration, which are not calculable with using a 2D beam model.

Table 1 The computed natural frequencies.

	$f_{(1)}$ [Hz]	$f_{(2)}$ [Hz]	$f_{(3)}$ [Hz]	$f_{(4)}$ [Hz]
ADINA 3D model	2.47	5.13	9.74	13.18
2D beam model MATLAB	2.14	x	8.56	x

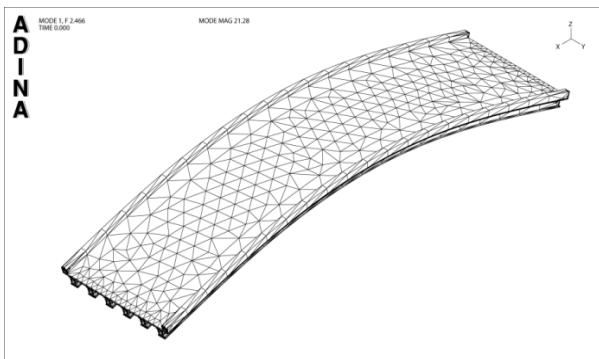


Fig. 1 The first natural mode $f_{(1)}= 2.47$ Hz computed on the 3D model.

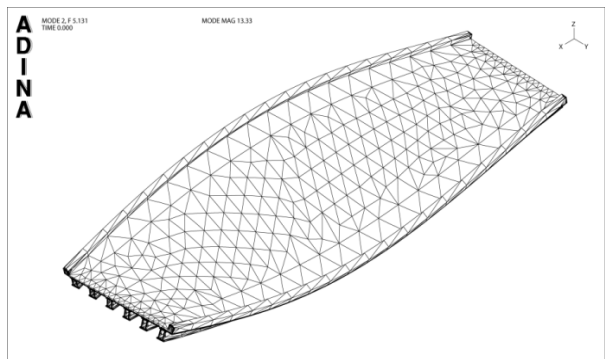


Fig. 2 The second natural mode $f_{(2)}= 5.13$ Hz computed on the 3D model.

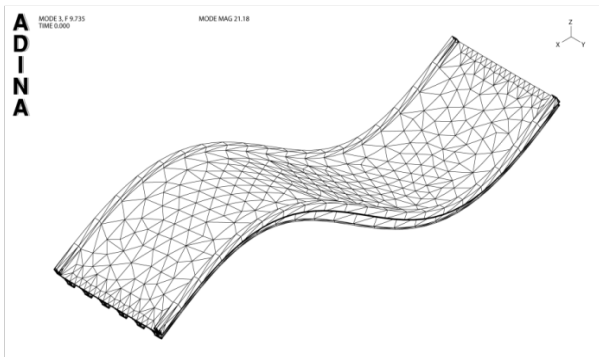


Fig. 3 The third natural mode $f_{(3)}= 9.74$ Hz computed on the 3D model.

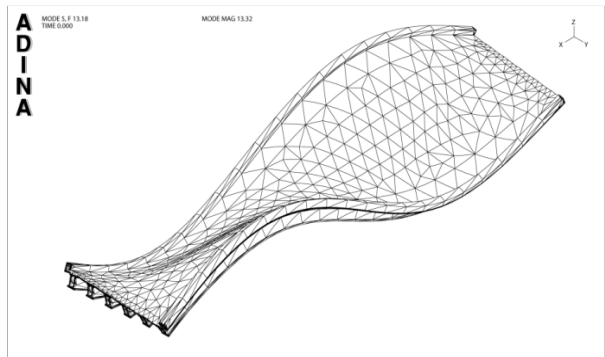


Fig. 4 The fourth natural mode $f_{(4)}= 13.18$ Hz computed on the 3D model.

Modeling of Acting Pedestrians and Vandals – Forced Vibration

The 2D beam model was used for a study of the forced vibration. The bending stiffness and continuously distributed mass of the model were taken from the static design with values $EI_y = 3.83 \times 10^9$ Nm² and $\mu = 5300$ kg. The forced vibration of 2D model, discretized into N nodes with N degrees of freedom, is defined by the equation

$$[\mathbf{M}]\{\ddot{\mathbf{w}}(t)\} + [\mathbf{C}]\{\dot{\mathbf{w}}(t)\} + [\mathbf{K}]\{\mathbf{w}(t)\} = \{\mathbf{P}(t)\} \quad (2)$$

Note that only vertical parts of deflection in the beam nodes were considered in the present study. The meaning of symbols in the Eq. 2 is following, $[\mathbf{M}]$ is the mass matrix, $[\mathbf{K}]$ is the stiffness

matrix, $[\mathbf{C}]$ is the damping matrix (Rayleigh's damping model was used), $\{\ddot{\mathbf{w}}(t)\}\{\dot{\mathbf{w}}(t)\}\{\mathbf{w}(t)\}$ are column vectors of acceleration, velocity and deflection, $\{\mathbf{P}(t)\}$ is the force column vector. The initial conditions for the system of differential Eq. 2 were based on the assumption that the beam is inactive at the beginning of the numerical analysis ($\{\ddot{\mathbf{w}}(t)\}, \{\dot{\mathbf{w}}(t)\}, \{\mathbf{w}(t)\}|_{t=0} = \{\mathbf{0}\}$).

Dynamic loading of the solved footbridge, which is presented in this paper, could be divided into three groups, which are presented in this paper. Firstly the generator of pedestrians with stochastic parameters based on the Monte Carlo method was created. This approach is able to simulate an ordinary pedestrian traffic across this structure. In this case a pedestrian was modeled as a periodic force moving across the structure with constant velocity v_p . The moving periodic force is described by the formula

$$P(t) = m_p g (1 + \alpha_i \sin(2\pi f_p t)) \quad (3)$$

where α_i is the dynamic factor, m_p is the mass of a pedestrian, g is the gravitational acceleration and f_p is the pacing frequency. The scheme of the algorithm for generation of pedestrians with stochastic parameters is symbolized in Fig. 6. A finite time T was considered, when a new pedestrian could come on the footbridge deck. It is decided in the first step of the algorithm if a new pedestrian will come or not. Further there is generated quantity of pedestrians n and parameters of each pedestrian such as body weight m_{pi} and velocity v_{pi} . The conversion from the pedestrian velocity to the pacing frequency is based on experimentally observed phenomenological aspects of human walking process $v_p \approx 0.9f_p$. All of the stochastic parameters were generated with the uniform distribution of probability $n \in \langle 1; 15 \rangle$, $m_p \in \langle 60; 85 \rangle$ kg and $v_p \in \langle 1.3; 2 \rangle$ ms⁻¹.

Next a dynamic loading of synchronous runners and vandals was investigated. The runner and vandal bodies were modeled via biomechanical models (see Fig. 5), which influenced the footbridge vibration only passively. The DLF model was used for active effect of synchronous runners. It is defined by

$$P(t) = m_p g \left(1 + \sum_{i=1}^3 \alpha_i \sin(2\pi f_p t) \right) \quad (4)$$

where m_p is the body weight of runners, g is the gravitational acceleration, α_i is the dynamic factor and f_p is the pacing frequency. It was found out that the most accordance between experiment and results obtained from the DLF approach was achieved with using the Bachmann's model [1,2]. Therefore only this model was used for excitation of the footbridge with the biomechanical models.

The driving force by Eq. 4 was used for stationary excitation of the footbridge midpoint and it was located to the contact between biomechanical models of runners and the structure (see Fig. 5). Numerical parameters of the used biomechanical models are summarized in the Table 2.

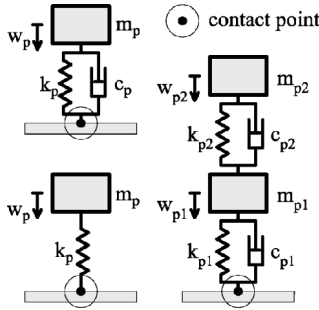


Fig. 5 The scheme of the used biomechanical models of passive pedestrian – SDOF damped and undamped, 2DOF damped model.

Table 2 The parameters of the used biomechanical models, taken from [6].

DOF	model	m_{p1} [kg]	m_{p2} [kg]	k_{p1} [kN/m]	k_{p2} [kN/m]	c_{p1} [kNs/m]	c_{p2} [kNs/m]
2-DOF	<i>ISO 1981</i>	13	62	80	62	0.93	1.46
	<i>Farah (1977)</i>	7.3	74.4	15.4	149.2	0.086	2.85
SDOF – undamped	<i>Lenzing(1988)</i>	76	-	50	-	-	-
	<i>Hothan(1999)</i>	80	-	113.7	-	-	-
	<i>Williams et al. (1999)</i>	75	-	66	-	-	-
SDOF – damped	<i>Brownjohn(1999)</i>	80	-	82	-	1.946	-

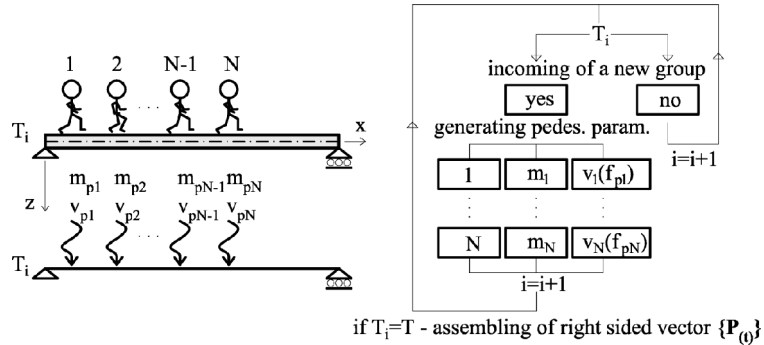


Fig. 6 The scheme of the algorithm for generation of the ordinary pedestrian traffic.

The dynamic influence of the vandals was considered as a periodic force in form of a triangle function in the dynamic study described in this paper. The other possibilities of expressing of dynamic loading due to vandalism are presented in [1,2]. The time equation of time behaviour of the triangle function is defined by

$$P(t) = \begin{cases} k_p G(2t/t_p) & \text{if } t \leq t_p/2 \\ k_p G[1 - 2(t - t_p/2)/t_p] & \text{if } t_p/2 < t \leq t_p \\ 0 & \text{if } t_p < t \leq T_p \end{cases} \quad (5)$$

where G is the total gravitational force of jumping vandals, f_p is the frequency of jumping, t_p is the time of contact between the structure and vandals, k_p is the dynamic increment, which is dependent on the frequency of jumping and the contact time. It is defined as

$$k_p = 2f_p t_p . \quad (6)$$

Note that the vandals were jumping in the midpoint of the structure span with the pacing frequency equal to the first natural bending frequency of the 2D beam model (see Table. 1). Numerical solution of the Eq. 2 was executed via the Newmark's integration method.

Results

The obtained numerical results from the theoretical analysis and the experimental results are summarized and visualized in the Fig. 7 – Fig. 10.

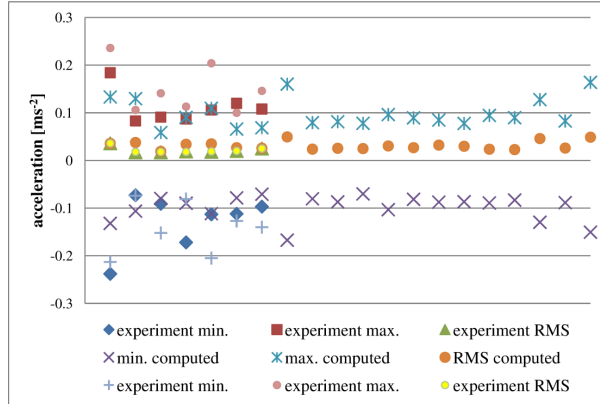


Fig. 7 The comparison of measured and computed values of acceleration in the structure midpoint – ordinary pedestrian traffic.

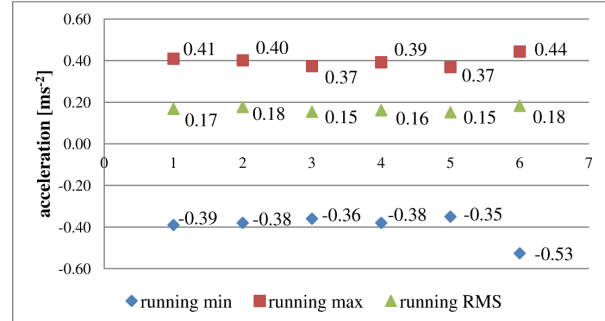


Fig. 8 The comparison of computed acceleration in the structure midpoint – biomechanical models of synchronous runners.

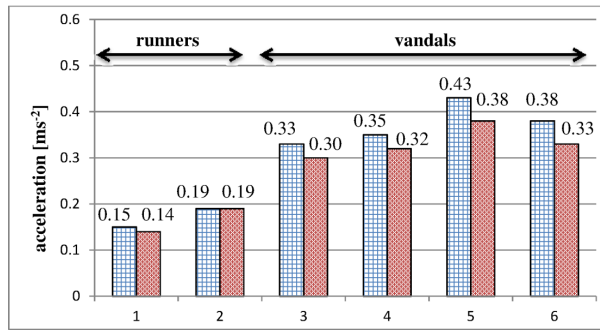


Fig. 9 Measured RMS values of acceleration in the structure midpoint – runners and vandals.

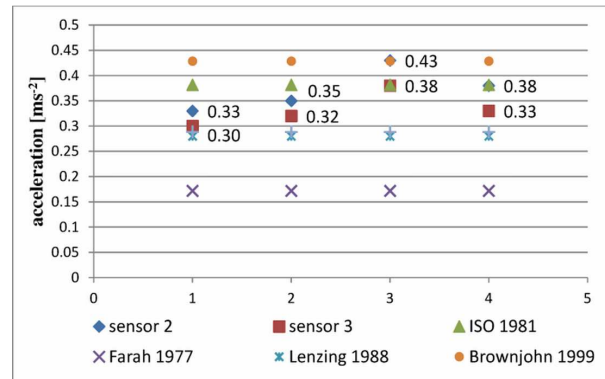


Fig. 10 The comparison of measured and computed values of acceleration in the structure midpoint – vandals.

The measured and computed results of ordinary pedestrian traffic are summarized in the Fig. 7. The generator of stochastic pedestrians shown in Fig. 6 was used for the ordinary pedestrian traffic simulation. Twenty of realizations are shown in Fig. 7. The Fig. 8 compares the obtained theoretical data of synchronous biomechanical models. The meaning of the numbering in Fig. 8 is following: 1. ISO model, 2. Farah's model, 3. Lenzing's model, 4. Hothan's model, 5. Williams' model, 6.Brownjohn's model, see [4]. The measured RMS values of the footbridge midpoint are presented in the Fig. 9. The last Fig. 10 represents computed structure response to vandals, which have been modeled with using of the biomechanical models.

Conclusion

In this paper were presented the results of the theoretical dynamic analysis of the footbridge loaded by an ordinary traffic of pedestrians, synchronous runners who have ran with pacing frequency f_p equal to the first natural bending frequency of the structure and vandals who jumped with the same frequency in the footbridge midpoint. Ordinary pedestrian traffic was modeled as stochastic stream of pedestrians with random parameters m_p and v_p . The dynamic effect of synchronous runners was modeled via the DLF approach (*Bachmann's* loading model). The body properties of runners were considered as biomechanical models (SDOF, 2DOF). The footbridge was excited by periodic force (DLF) in the contact point between the biomechanical models and the structure.

The footbridge excitation via the triangle force function (see Eq. 5) was used in the case of dynamic vandal effects. The group of vandals was also modeled with using the biomechanical models.

The Fig. 7 shows that the generator of stochastic pedestrians provides the results which are in a good accordance with experimentally obtained results.

It is obvious from the Fig. 8 – Fig. 9 that all of the biomechanical models presented in this paper are usable for modeling of acting pedestrians. The best accordance with experiment is achieved by using of the ISO 1981 2DOF biomechanical model (see Fig. 10).

Acknowledgements

This work has been supported by the Technology Agency of the Czech Republic – Competence Centers under No. TE01020168 Centre for Effective and Sustainable Transport Infrastructure (CESTI).

References

- [1] H. Bachmann, W. Ammann, *Vibrations in Structures Induced by Man and Machine*, Zürich, Switzerland, 1987.
- [2] H. Bachmann, W. Ammann, et al., *Vibration Problems in Structures, Practical Guideline*, Zürich, Switzerland, 1995.
- [3] S. Živanović, A. Pavić, P. Reynolds, Vibration Serviceability of footbridges under human – induced excitation: a literature review, *Sound and Vibration*. 279 (2005) 1-74.
- [4] R. Sachse, A. Pavić, P. Reynolds, *Human-Structure Dynamic Interaction in Civil Engineering Dynamics. A Literature Review*, University of Sheffield, UK.
- [5] V. Šána, M. Polák, *Dynamická analýza lávky pro pěší přes ulici Opatovická*, 11th International Conference on New Trends in Statics and Dynamics of Building Conference Proceedings, Bratislava, Slovak University of Technology in Bratislava, pp. 205-208, 2013, (in Czech).
- [6] E. Fanfulová, *Experimental Analysis of Dynamic Response of Footbridges*, Bachelor thesis, 2013, in Czech.
- [7] J. Máca, M. Valášek, *Interaction of Human Gait and Footbridges*, Proceedings of the 8th International Conference on Structural Dynamics Eurodyn 2011, pp. 1083 – 1089, Katholieke Universiteit, Leuven, 2011.
- [8] J. Máca, M. Valášek, *Dynamic interaction of pedestrians and footbridges*, Proceedings of the 12th International Conference on Civil, Structural and Environmental Engineering Computing, pp.1–11, Madeira, Portugal, 2009.

Long-Term Monitoring of a Composite Steel-Concrete Bridge on the Prague Ring Road

TEJ Petr^{1, a*}, KRÁL Jaromír^{1,b},
TEJOVÁ Alena^{1,c} and MARKOVÁ Jana^{1,d}

¹CTU in Prague, Klokner Institute, Šolínova 7, Czech Republic

^apetr.tej@klok.cvut.cz, ^bjaromir.kral@klok.cvut.cz,

^calena.tejova@klok.cvut.cz, ^djana.markova@klok.cvut.cz

Keywords: composite steel-concrete bridge, long-term traffic monitoring

Abstract. The composite steel-concrete bridge across the “Slavičí údolí” on the Prague ring exposed to extreme traffic is selected for present traffic flow monitoring. The response of the bridge to the traffic loads is monitored using strain gauges. The record of voltage is converted to the amount of relative deformation, respectively stress in the bottom flange of steel I beam of the bridge. In parallel with the measurements, the computer slab - wall model based on finite element method is developed. The computer model is used for comparison of calculated and measured stresses and deflections in the flanges and to determine the natural frequencies of the examined bridge structure. Calibrated measurements are used for three-year monitoring of the effects of road traffic on bridge facilitating national decision in the National Annex to EN 1991-2.

Introduction

After two years of application of Eurocodes as exclusive standards for the design of bridges in the Czech Republic, the Nationally Determined Parameters (NDPs) of the traffic load models LM1 and LM3 for road bridges are analysed and recalibrated (Markova et al. 2013). The intensity and effect of actual traffic has been monitored on two selected Bohemian highway bridges. The first bridge was a prestressed concrete highway bridge with periods of monitoring (2005-2006) and (2011 - till now), the second composite steel-concrete bridge was monitored from 2011 till 2013. Selected results of theoretical analysis and monitoring of traffic loads on the composite bridge are presented.

Experimental Results

A Road Bridge. The purpose of the experimental part was the long-term monitoring response of the composite steel-concrete girder bridge to heavy traffic. A three span continuous bridge (16 m, 25 m, 16 m) across the „Slavičí údolí“ is chosen for monitoring (refer with: Fig. 1). The bridge has a three lane road and a highway shoulder. It is located on the Prague ring between the exit of the Lochkov tunnel and the Lochkov bridge.



Fig. 1 The bridge across “Slavičí údolí” on the Prague ring

Bridge Monitoring. The bridge response is monitored by strain gauges. They are installed on the bottom flanges of four steel girders (N5, N6, N7 and N8, marked from the left side of the bridge) under traffic lanes in the middle of the abutment span and in one girder under slow lane (N17) in the middle span. A computer equipped with A/D converter is installed under bridge superstructure as a control unit. The control programme performs measurements and preliminary assessments. A twelve minutes test cycle consists of 11 minutes long records of the bridge response and one minute interval, being reserved for the preliminary analysis of the records and measured data on a computer disk. Obtained data are periodically transferred by GSM to the Klokner Institute for the follow-up analysis. Presented data of 235 days were recorded in the period from 01/2013 to 11/2013.

Results of Measurements. Basic outputs of the monitoring consist of the time histories of axial stresses at bottom flanges of girders. An example is illustrated in Fig. 2. The attention is concentrated on passage of heavy truck or articulated truck with total weight greater than 100 kN. Time of the passage, the traffic lane and the maximum axial stress value are assigned to each vehicle. Numbers of vehicles are corrected with respect to the test cycle. Representative results of the follow-up statistical processing are:

- Total number of heavy vehicles passing over each traffic lane within the period of monitoring is presented in the Table 1.

Table 1 Relative and absolute number of heavy vehicles

Number of vehicles	Left (fast) lane (N5)	Middle (fast) lane (N6)	Right (slow) lane (N7)	Highway shoulder (N8)	Total number
Corrected	941	52215	941915	2974	998045
Percentage [%]	0.09	5.23	94.38	0.30	100.00

- An averaged number of vehicles passing across the bridge in individual days of the week is presented in the Table 2.

Table 2 Average number of heavy vehicles (33 weeks average)

Day	Monday	Tuesday	Wednesday	Thursday	Friday	Saturday	Sunday
Number of vehicles	5908	5313	4888	4729	3900	1664	1499

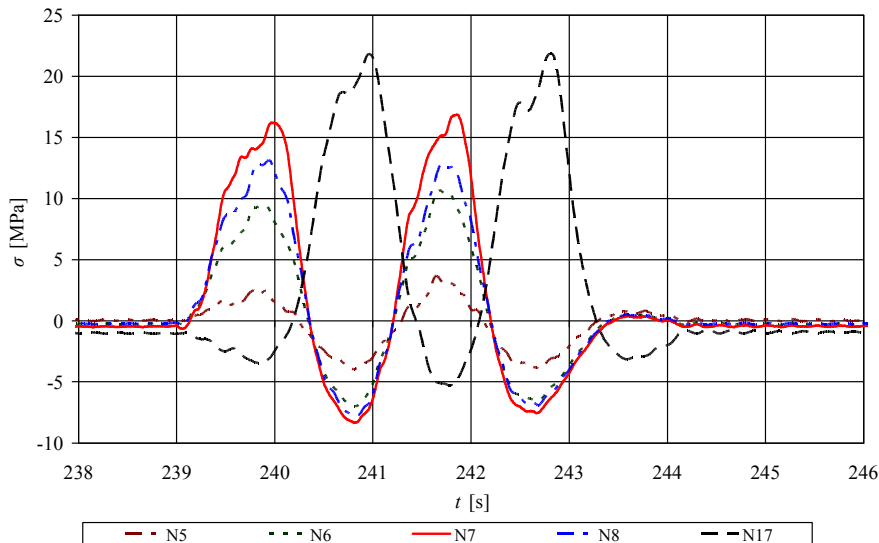


Fig. 2 Time history of the axial stresses in bottom flanges of girders during the passage of the vehicles (an example; part of the record)

- The frequency diagram of the averaged number of trucks classified according to maximal axial stresses and regarding days of the week is shown on Fig. 3.
- The bridge response was calibrated by the passing of a truck with known weight. The weight of equivalent vehicle (i.e. the vehicle with similar configuration of axles) could be assigned to the each axial stress value. Frequency diagrams of the number of vehicles classified according to equivalent weight have been developed as they are more suitable for interpretation the traffic intensity. The frequency diagram of the total number of vehicles in the slow lane above girder N7 is shown in Fig. 4.

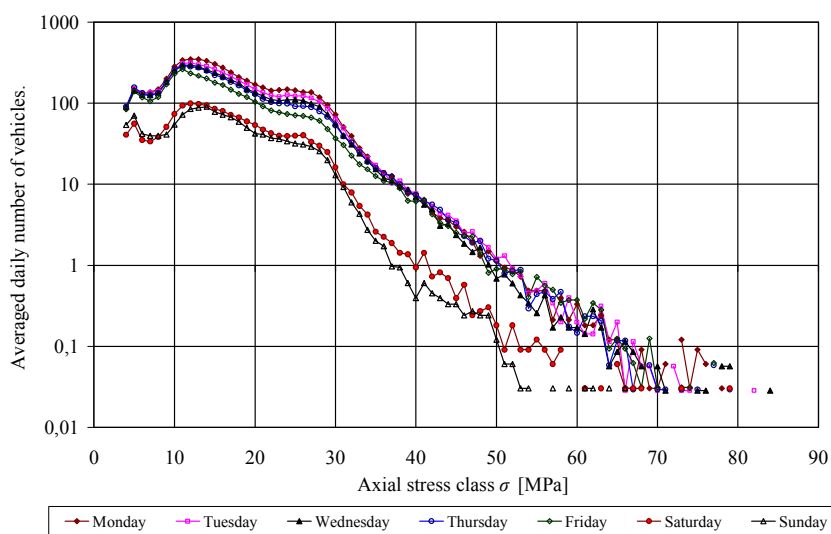


Fig. 3 Daily frequency diagram of the number of vehicles classified according to maximal axial stresses

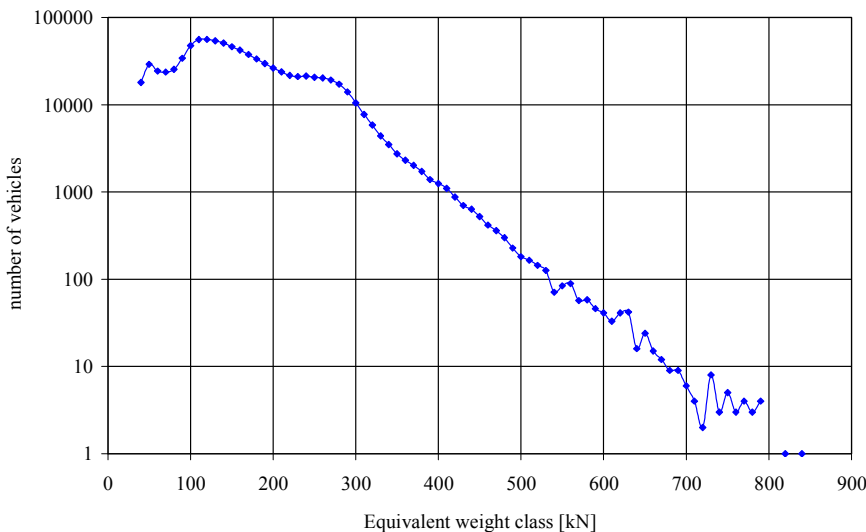


Fig. 4 Total frequency diagram of the number of vehicles classified according to equivalent weight

Computer Analysis

Computer slab-wall model of composite steel-concrete bridge is created in a 3D environment of the software SCIA Engineer. The model is meshed by hexahedron elements of a size of 0.02 m. Material characteristic of bridge are concrete C 35/45 and steel S 355. The thickness of bridge slab is 350 mm and steel load-bearing structure consists of:

- Longitudinal beams of the I cross-section (N5 – N8), web of the thickness of 20 mm and height of 1045 mm, upper flange of the thickness of 20 mm and width of 250 mm, lower flange of the thickness of 30 mm and width of 400 mm,
- Transverse beams of the I cross-section of the end abutments, web of the thickness of 15 mm and height of 560 mm, upper flange of the thickness of 20 mm and width of 300 mm, lower flange of the thickness of 20 mm and width of 300 mm,
- Transverse beams of the I cross-section of the middle supports, web of the thickness of 20 mm and height of 1045 mm, upper flange of the thickness of 20 mm and width of 300 mm, lower flange of the thickness of 30 mm width of 550 mm.

The total weight of the bridge superstructure is 8397.8 kN.

The selected results of theoretical analysis are illustrated in Figs. 5 and 6. Deflection caused by a heavy truck TATRA 815 in the middle of the beam N7 is modelled by ten point forces $F = 26.75$ kN, see Fig. 5. The maximum value of deflection on the lower flange of the beam N7 is - 2 mm.

The distribution of the stresses caused by a heavy truck TATRA 815 is shown in Fig. 6. The maximum value of the stress in the lower flange of the beam N7 is 19.3 MPa.

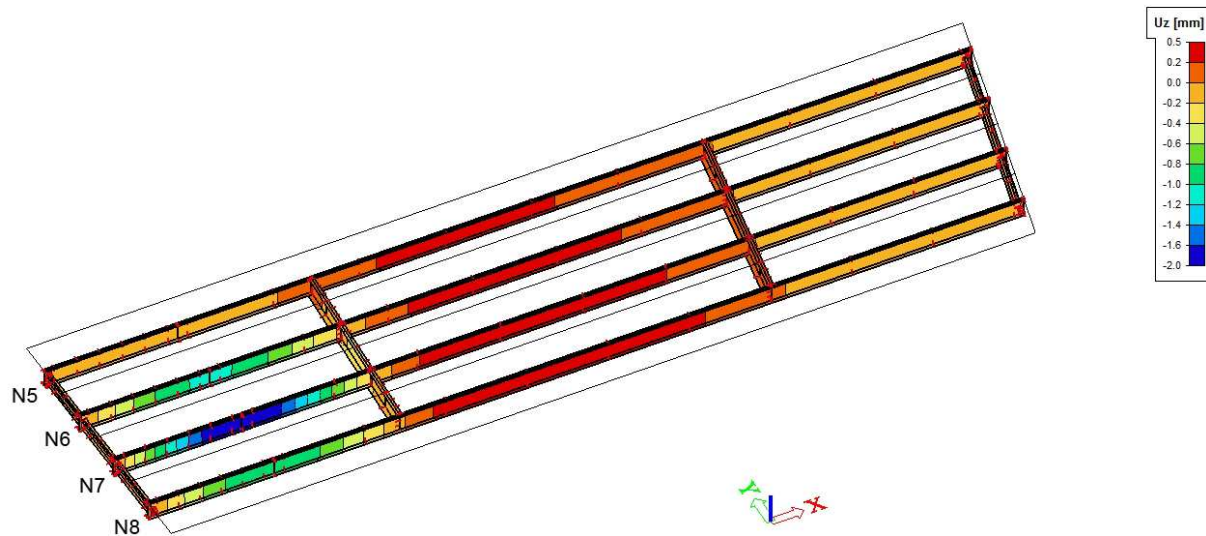


Fig. 5 Deflection caused by a heavy truck TATRA 815 in the middle of the beam N7. Vehicle load in the calculation is modelled by ten point forces $F = 26.75 \text{ kN}$, acting in locations of tires of the truck. The maximum value of deflection on the lower flange of the beam N7 is - 2 mm

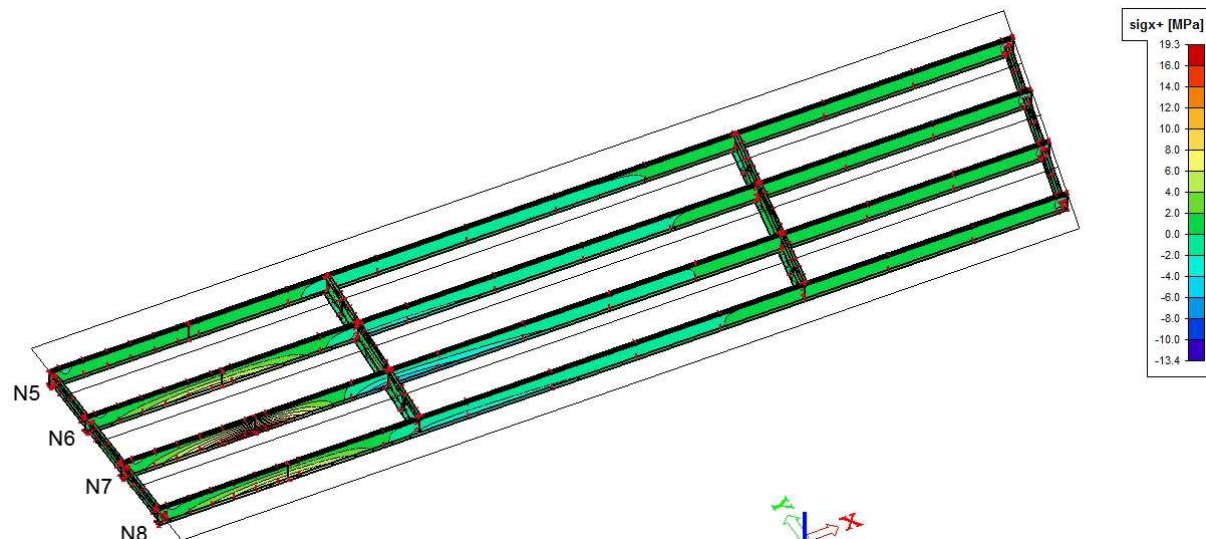


Fig. 6 The distribution of the stress caused by a heavy truck TATRA 815. The maximum value of the stress in the lower flange of the beam N7 is 19.3 MPa

Theoretical results are compared with experimental data from the axial stresses calibrated by means of the passing of a heavy truck TATRA 815 with the known mass and configuration of its axles. The maximal values of the calculated and measured axial stresses in bottom flanges of the bridge girders N5 to N8 are given in Table 3.

Table 3 Maximal values of calculated and measured axial stresses in bottom flanges of the girders in the abutment span of the bridge

Girder	Measurements		Calculations	
	[MPa]	[%]	[MPa]	[%]
N5	3.02	14.1	1.3	6.74
N6	11.5	53.5	7.4	38.3
N7	21.5	100	19.3	100
N8	14.9	69.4	8.0	41.5

Damped vibrations of the unloaded bridge are observed on the time records of axial stresses after passage of the same heavy truck. Amplitudes of vibration are small and frequency is about 4.1 Hz, see end of diagram in Figure 2. A frequency analysis of the time records is performed. The natural frequency about 4.125 Hz is determined by application of transfer and coherence functions. Higher natural frequencies are not analysed because of the small number and inappropriate configuration of the points of measurement for this purpose.

Concluding Remarks

Results of theoretical analyses of the effects of known a heavy truck TATRA 815 on bridge superstructure and experimental measurements of bridge response are in a good agreement. Calibrated measurements have facilitated to analyse of effects of actual three year traffic in Prague ring.

On the basis of measurements and theoretical analyses, the new sets of adjustment factors for the Load model LM1 and two types of special heavy vehicles (1800/200, 3000/240) of the Load Model LM3 are proposed for the Amendment of the National Annex to EN 1991-2. It is assumed that application of the recalibrated traffic models for bridge design will facilitate the transport of heavy industrial devices and could also serve for military and other special purposes.

In case that the monitoring, recalibration and new selection of NDPs for models LM1 and LM3 is not nationally developed, the new bridges designed according to Eurocodes could not meet requirements of current traffic and might be significantly deteriorating.

Acknowledgements

The study has been conducted in the framework of the research project VG20122015089 Safety Assessment of Transportation Structures supported by the Ministry of the Interior of the Czech Republic.

References

- [1] R. Cantieni, Dynamic Behaviour of Highway Bridges Under the Passage of Heavy Vehicles, EMPA, Report No. 220, Dübendorf, 1992.
- [2] J. Král, Monitoring Response of a Highway Concrete Bridge to the Effects of Thermal Actions and Heavy Traffic, Experimental Stress Analysis, EAN 2010, Velké Losiny.
- [3] J. Markova et al., Probabilistic Assessment of Traffic Loads on Bridges. R.D.J.M. Steenbergen, P.H.A.J.M. van Gelder, S. Miraglia, A.C.W.M. Vrouwenvelder (eds.) Proceedings of the European Safety and Reliability Conference ESREL 2013, Amsterdam, 29 September – 2 October, 2013, Leiden: Balkema/CRC Press, pp. 2613-2618.

Dynamic Deflection of a Bridge versus Speed of Vehicle Motion

DANIEL L'uboš^{1, a *}

¹University of Žilina, Department of Structural Mechanics, Univerzitná 8215/1, 010 26 Žilina,
Slovak Republic

^alubos.daniel@fstav.uniza.sk

Keywords: ANSYS, dynamic analysis, vehicle model, bridge model, vibration, numerical analysis

Abstract. The vehicle-bridge interaction (VBI) is the actual problem solved on many work places. The mid-span deflection of a bridge versus speed of vehicle motion is interesting from a practical point of view. The numerical methods based on Finite Element Method (FEM) are mainly applied for the solution. The task of VBI described in the submitted article is solved using commercial software ANSYS. The 2D spring model of vehicle is modeled as combination of mass, spring and beam elements. The mid-range bridge is modeled as simple beam created from beam elements.

Introduction

The investigation of the vehicle-bridge interaction (VBI) was induced by the collapse of the Chester railway bridge in UK in 1847. It was the first case of collapse of the railway bridge in the history. The important work by Frýba [4] provided extensive literature review on VBI. At that time, the problem of VBI was solved by analytic solution of differential or integral equations. Numerical methods based on the Finite Element Method (FEM) have mostly been used since computers started. In the article a numerical model of the vehicle and a numerical model of the bridge are created using the ANSYS software [1,5].

The vehicle moved on the bridge belongs among non-stationary dynamic action, which is described by the following differential equation [6]

$$[\mathbf{M}] \cdot \{\ddot{\mathbf{u}}(t)\} + [\mathbf{C}] \cdot \{\dot{\mathbf{u}}(t)\} + [\mathbf{K}] \cdot \{\mathbf{u}(t)\} = \{\mathbf{F}(t)\}. \quad (1)$$

Where $[\mathbf{M}]$, $[\mathbf{C}]$ and $[\mathbf{K}]$ are mass, damping and stiffness matrices, respectively, describing the spatial properties of the system. FEM is often used to solve the previous equation. Program ANSYS offers many techniques for that purpose. It was decided to use Newmark's method that is widely used to do dynamic numerical simulations. This method is also called implicit because the solution at time $t + \Delta t$ is not explicitly determined by the state at time t . The relations between displacement, velocity and acceleration are governed by the following equations [6]:

$$\begin{aligned} \{\dot{\mathbf{u}}_{t+\Delta t}\} &= \{\dot{\mathbf{u}}_t\} + [(1 - \delta) \cdot \{\ddot{\mathbf{u}}_t\} + \delta \cdot \{\ddot{\mathbf{u}}_{t+\Delta t}\}] \cdot \Delta t, \\ \{\mathbf{u}_{t+\Delta t}\} &= \{\mathbf{u}_t\} + \{\dot{\mathbf{u}}_t \cdot \Delta t\} + \left[\left(\frac{1}{2} - \alpha \right) \cdot \{\ddot{\mathbf{u}}_t\} + \alpha \{\ddot{\mathbf{u}}_{t+\Delta t}\} \right] \cdot \Delta t^2. \end{aligned} \quad (2)$$

As a result, the time is also discredited and the solution is given in a form of the functional values for all defined geometrical points in every time step. The different value for the time step affects the quality of the obtained results. It is very important to choose the right value of the time step.

Interaction between vehicle and bridge is created using contact "node to surface". Elements are used in the contact pair of the Conta175 type (contact elements on the vehicle) and Targe169 (contact elements on the bridge). The arrangement of contact elements is shown in Fig. 1.

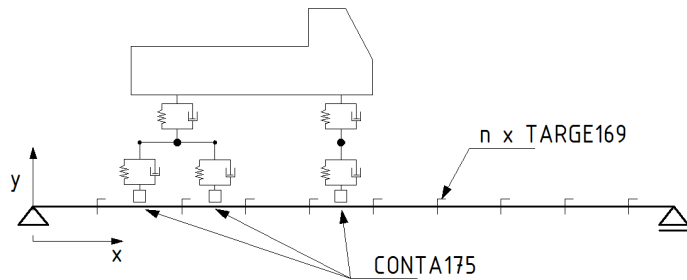


Fig. 1 The arrangement of contact elements

Numerical Model of Vehicle

Important part of the simulation is the choice of the right model of vehicle, which is represented with appropriate mathematical formulation [2]. The „fourth-part model“ or the „half-part model“ [3] are usually preferred in 2D analysis. The half-part model (Fig. 2) is used as combination of mass (mass21), spring (combin14) and beam (beam3) elements for the purpose of the work. The main characteristic of the discrete model can be defined by three diagonal matrices. They contain the mass, stiffness and damping characteristics.

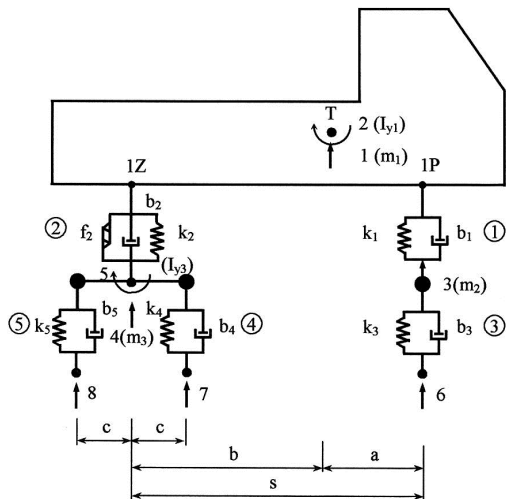


Fig. 2 The half-part model of vehicle

Diagonal mass matrix

$$\{\mathbf{m}\}_D = \{m_1, I_{y1}, m_2, m_3, I_{y3}\}_D = \{17400, 62298, 910, 2140, 932\}_D \quad [\text{kg, kg.m}^2]$$

Diagonal stiffness matrix

$$\{\mathbf{k}_i\}_D = \{k_1, k_2, k_3, k_4, k_5\}_D = \{247686, 1869724, 3242424, 5095000, 5095000\}_D \quad [\text{N/m}]$$

Diagonal damping matrix

$$\{\mathbf{b}_i\}_D = \{b_1, b_2, b_3, b_4, b_5\}_D = \{19228, 260197, 2746, 5494, 5494\}_D \quad [\text{kg/s}]$$

Discrete models of the vehicle with finite degrees of freedom make solution easier from the mathematical point of view. This assumption changes partial differential equations to the ordinary differential equations. The article describes the way how to create the right numerical model of the vehicle and also how to create interaction with numerical model of the bridge by using the software ANSYS [1,5].

Numerical Model of the Bridge

The subject of the analysis is real construction of the road bridge situated between two villages Varín and Mojš in the Slovak Republic. The whole length of the bridge is 87 m, which is divided

into three parts. Each part acts independently as a simple-supported beam. The main girders are prefabricated prestressed concrete structures with the length 29 m. The cross-section of the bridge contains eight girders with the mutual distance 1.44 – 1.45 m (Fig. 3).

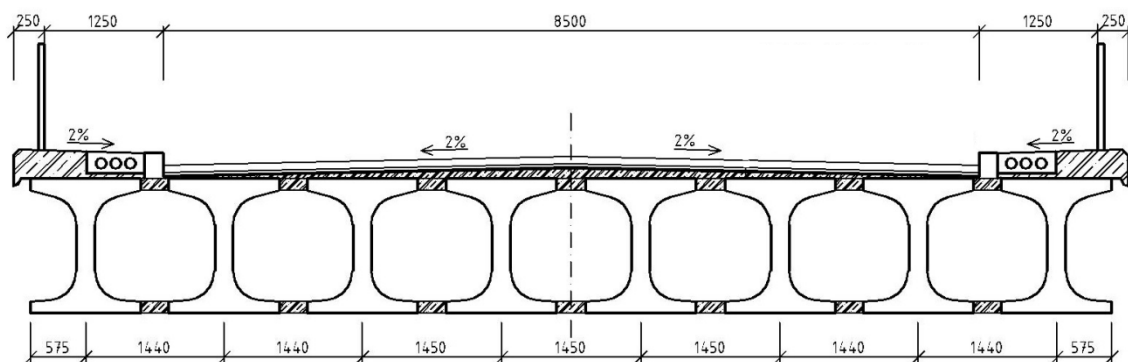


Fig. 3 The cross-section of the bridge

The analysis is focused on the middle span of the bridge that is modelled using BEAM188 beam elements. The boundary conditions are similar to a simple-supported beam. The Young's modulus is 3.85×10^{10} N/m² and the weight intensity is 19680 kg/m. Both values are defined in accordance with dynamic characteristics of the real bridge structure. The surfaces are defined before and after the model of the bridge. Their purpose is to start and finish the movement of the vehicle. Thanks to this, the vehicle moves over the bridge at a constant speed. The model used in the simulation is shown in Fig. 4.

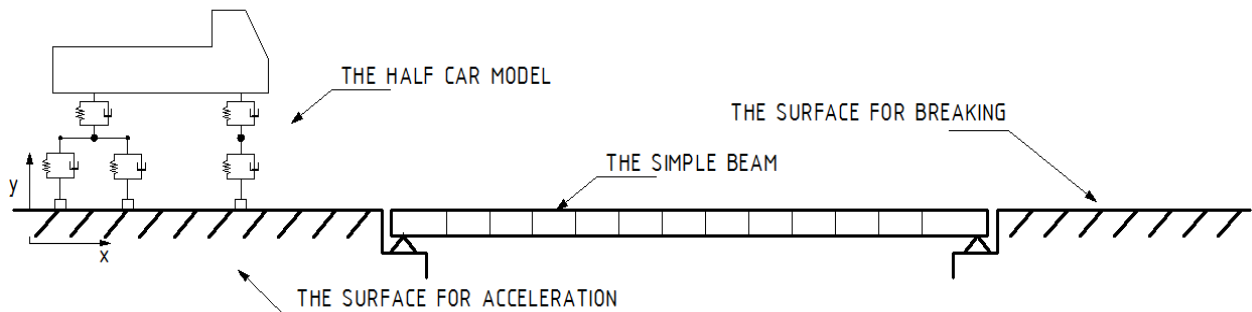


Fig. 4 Schema of used model in simulation

Analysis of the Results

The analysis of VBI is focused on influence of the moving vehicle on the bridge construction. Dynamic coefficient of construction is very important factor for assessment of construction. Dynamic coefficient is a ratio of maximum dynamic deflection to the static deflection. The simply-supported beam was used as a model of the bridge in the calculation. The deflection of the node in mid-span of the bridge was monitored only. The relation between speed of the vehicle and the deflection in mid-span of the bridge was examined. The function of this relation is shown in Fig. 5.

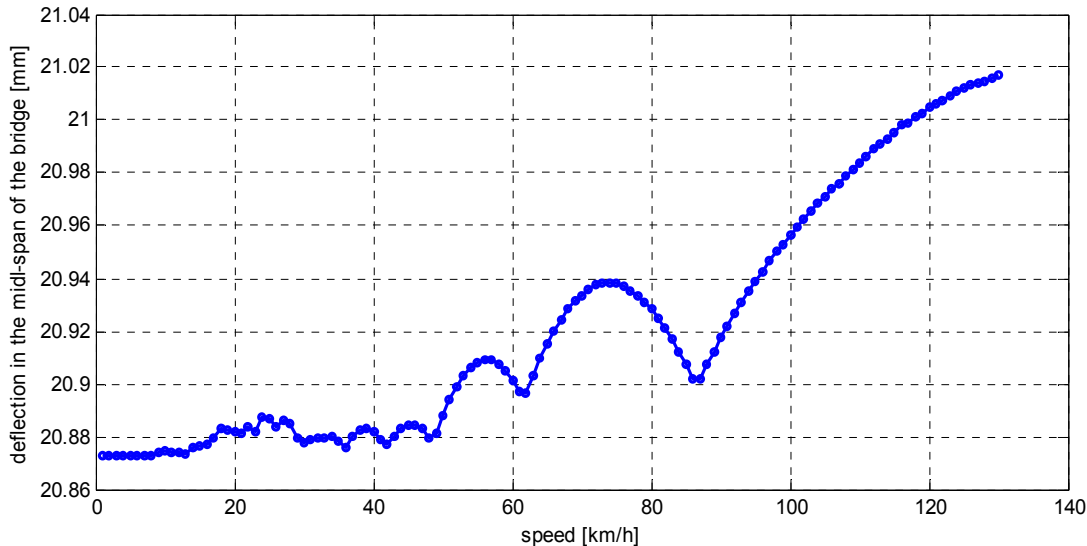


Fig. 5 Deflection of the bridge versus speed of the vehicle

The function in Fig. 5 is not a smooth curve. The curve tends to increase and contains a lot of local maximums and tips. This function often rises independently on ratio of natural frequency of vehicle and bridge. However, the cases presented in the article [6] show that the function can decrease, too. The character of this function is closely associated with discontinuous course of function that describes relation between the speed and position of the vehicle on the bridge, when maximum deflection in mid-span of the bridge arises (Fig. 6).

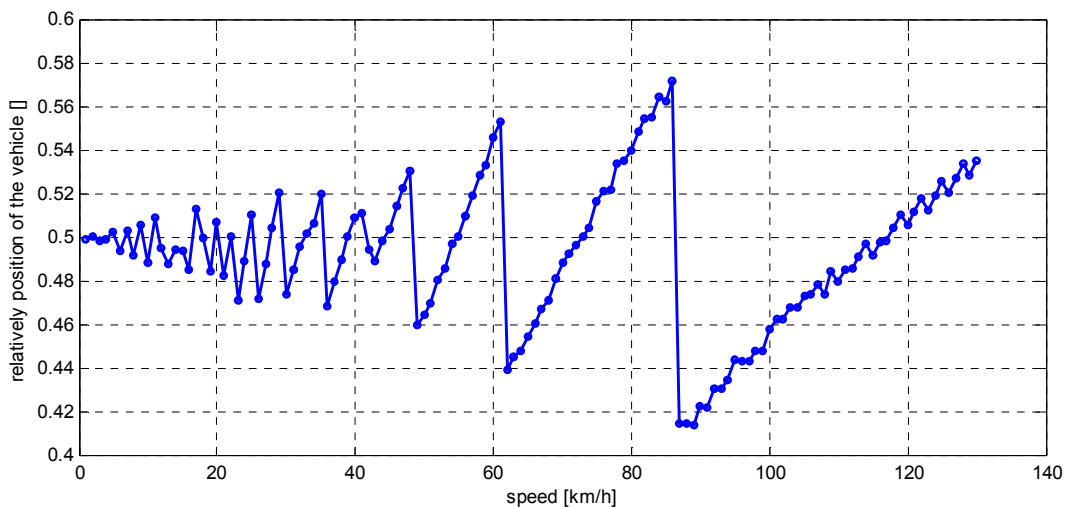


Fig. 6 Relative position of the vehicle when is max deflection in mid-span of the bridge

The position of the vehicle is given by relative position, which defines the ratio of position of the vehicle on the bridge to length of the bridge. The position of tips in function from Fig. 5 corresponds with the point of discontinuity in function from Fig. 6. It means that the maxim value of deflection in the mid-span of the bridge does not arise for the same position of the vehicle on the bridge.

Summary

Despite the fact that the investigation of the problem in vehicle-bridge interaction has begun in the 19th century it is the topical problem at many work places. Nowadays the methods based on Finite Element Methods (FEM) are mostly used for solution of these problems. This article describes the numerical solution of moving of the vehicle along the bridge using the ANSYS FEM software. The numerical solution shows the relation between maximum deflection in mid-span of the bridge and position of the vehicle on the bridge. The article also describes the way of using the commercial software for simulation of VBI problem.

Acknowledgements

This contribution is the result of the research supported by GA MŠVVaŠ SR VEGA, grant No. 1/0259/12.

References

- [1] ANSYS, Inc. ANSYS 8.0 Documentation.
- [2] L. Daniel, Interaction in the system vehicle-bridge, ŠVOČ, SvF, University of Žilina, Žilina, 2012.
- [3] J. Melcer, Dynamic calculations of highway bridges. EDIS, University of Žilina, Žilina, 1997.
- [4] L. Frýba, Vibration of Solids and Structures Under Moving Loads. ACADEMIA, Prague, Nordhoff International Publishing, Groningen, 1972.
- [5] E.H. Dill, The Finite Element Method for Mechanics of Solids with ANSYS Applications, CRC Press, 2012, pp. 446-456.
- [6] J. Melcer, Dynamic coefficients of a bridge versus speed of vehicle motion. Civil and Environmental Engineering, No.2, EDIS, University of Žilina, 2009.
- [7] Jimin He, Zhi-Fang Fu, Modal Analysis, Butterworth-Heinemann, 2001.

Moving Load Effect of a Truck on Concrete Pavements

LAJČÁKOVÁ Gabriela^{1, a*}

¹University of Zilina, Univerzitna 1, 010 26 Zilina, Slovak Republic

^agabriela.lajcakova@fstav.uniza.sk

Keywords: moving load, concrete pavements, numerical solution, vehicle computing models

Abstract. Pavements represent the transport structures subjected to dynamic effect of moving vehicles. The real transport load is needed for the assessment of pavements. Such data can be obtained by numerical or experimental way. Various computing models can be used for the analysis of concrete pavements. Some possibilities are presented in this contribution.

Introduction

The road structure is the typical transport structure exposed to the dynamic effects of moving vehicles. At the present time the pavements are also utilized in the form of concrete slabs. It is necessary to know the dynamic response of the slab structure on the effect of moving vehicles [1,2]. The analysis can be carried out by experimental or by numerical way. Numerical approach demands to pay attention to the proposal of the computing models of vehicle and the computing models of the road concrete slab. The submitted paper compares the results obtained for space and plane computing models of vehicle moving along concrete pavement.

Computing Model of Concrete Slab

The computing model of the concrete pavement is based on the Kirchhoff theory of the thin slabs on elastic foundation [3]

$$D \left(\frac{\partial^4 w}{\partial x^4} + 2 \frac{\partial^4 w}{\partial x^2 \partial y^2} + \frac{\partial^4 w}{\partial y^4} \right) + Kw + \mu \frac{\partial^2 w}{\partial t^2} + 2\mu\omega_b \frac{\partial w}{\partial t} = p(x, y, t). \quad (1)$$

The desired function $w(x, y, t)$ describing the slab vertical deflections will be expressed as the product of two functions

$$w(x, y, t) = w_0(x, y) q(t). \quad (2)$$

The function $w_0(x, y)$ stands for the known function and it is dependent on the coordinates x, y only and the function $q(t)$ stands for the unknown function and it is dependent on the time t . The function $q(t)$ has the meaning of generalized Lagrange coordinate. The assumption about the form of the function $w_0(x, y)$ was introduced as.

$$w_0(x, y) = \frac{1}{4} \left(1 - \cos \frac{2\pi x}{l_x} \right) \left(1 - \cos \frac{2\pi y}{l_y} \right). \quad (3)$$

The meaning of remaining symbols is as follows: D slab stiffness [Nm^2/m], K modulus of foundation [Nm^{-3}], μ mass intensity [kgm^{-2}], ω_b angular frequency of damping [rad/s], $p(x, y, t)$ is the intensity of the dynamic load. In the case of moving vehicles the discrete load due to the tire forces $F_j(t)$ must be transformed on continuous load by the procedure proposed by Dirac [3]

$$p(x, y, t) = \sum_j \varepsilon_j F_j(t) \delta(x - x_j) \delta(y - y_j), \quad (4)$$

$$p(x, y, t) = \sum_j \sum_{m=1}^{\infty} \sum_{n=1}^{\infty} p_{mn,j}(t) \frac{1}{4} \left(1 - \cos \frac{m2\pi x}{l_x} \right) \left(1 - \cos \frac{n2\pi y}{l_y} \right), \quad (5)$$

where

$$\begin{aligned} p_{mn,j}(t) &= \frac{2}{l_x} \frac{2}{l_y} \int_0^{l_x} \int_0^{l_y} \varepsilon_j F_j(t) \delta(x - x_j) \delta(y - y_j) \frac{1}{4} \left(1 - \cos \frac{m2\pi x}{l_x} \right) \left(1 - \cos \frac{n2\pi y}{l_y} \right) dx dy = \\ &= \varepsilon_j F_j(t) \frac{4}{l_x l_y} \frac{1}{4} \left(1 - \cos \frac{m2\pi x_j}{l_x} \right) \left(1 - \cos \frac{n2\pi y_j}{l_y} \right). \end{aligned} \quad (6)$$

Then

$$\begin{aligned} p(x, y, t) &= \sum_j \sum_{m=1}^{\infty} \sum_{n=1}^{\infty} \varepsilon_j F_j(t) \frac{1}{l_x l_y} \left(1 - \cos \frac{m2\pi x_j}{l_x} \right) \left(1 - \cos \frac{n2\pi y_j}{l_y} \right) \\ &\quad \cdot \frac{1}{4} \left(1 - \cos \frac{m2\pi x}{l_x} \right) \left(1 - \cos \frac{n2\pi y}{l_y} \right). \end{aligned} \quad (7)$$

Regarding to the convergence of the series in Eq. 7 we can take in to account the 1st member of the series only. Then the Eq. 7 can be rewritten as

$$p(x, y, t) = \sum_j \varepsilon_j F_j(t) \frac{1}{4l_x l_y} \left(1 - \cos \frac{2\pi x_j}{l_x} \right) \left(1 - \cos \frac{2\pi y_j}{l_y} \right) \left(1 - \cos \frac{2\pi x}{l_x} \right) \left(1 - \cos \frac{2\pi y}{l_y} \right). \quad (8)$$

For the space truck computing model

$$F_j(t) = -G_j + k_j d_j(t) + b_j \dot{d}_j(t), \quad (9)$$

where G_j is the gravity force of j -th axis, k_j and b_j stiffness and damping of the j -th tire and $d_j(t)$ is the tire deformation. Derivation with respect to the time t is denoted by the dot over the symbol.

Substituting the assumption Eq. 2 and Eq. 3 into Eq. 1 the left side of the Eq. 1 will change into

$$\begin{aligned} &\ddot{q}(t) \left[\frac{1}{4} \mu \left(1 - \cos \frac{2\pi x}{l_x} \right) \left(1 - \cos \frac{2\pi y}{l_y} \right) \right] + \dot{q}(t) \left[\frac{1}{4} 2\mu\omega_b \left(1 - \cos \frac{2\pi x}{l_x} \right) \left(1 - \cos \frac{2\pi y}{l_y} \right) \right] + \\ &+ q(t) \frac{1}{4} \left[-D \left(\frac{2\pi}{l_x} \right)^4 \cos \frac{2\pi x}{l_x} \left(1 - \cos \frac{2\pi y}{l_y} \right) + 2D \left(\frac{2\pi}{l_x} \right)^2 \left(\frac{2\pi}{l_y} \right)^2 \cos \frac{2\pi x}{l_x} \cos \frac{2\pi y}{l_y} - \right. \\ &\left. - D \left(\frac{2\pi}{l_y} \right)^4 \left(1 - \cos \frac{2\pi x}{l_x} \right) \cos \frac{2\pi y}{l_y} + K \left(1 - \cos \frac{2\pi x}{l_x} \right) \left(1 - \cos \frac{2\pi y}{l_y} \right) \right] = p(x, y, t). \end{aligned} \quad (10)$$

When we study the deflections at one point of the slab only, for example in the middle of the slab, than $x = l_x/2$ and $y = l_y/2$ and the Eq. 1 comes by the final form

$$\ddot{q}(t) \mu + \dot{q}(t) 2\mu\omega_b + q(t) \frac{D}{2} \left[\left(\frac{2\pi}{l_x} \right)^4 + \left(\frac{2\pi}{l_x} \right)^2 \left(\frac{2\pi}{l_y} \right)^2 + \left(\frac{2\pi}{l_y} \right)^4 + 2 \frac{K}{D} \right] =$$

$$= \sum_j \varepsilon_j F_j(t) \frac{1}{l_x l_y} \left(1 - \cos \frac{2\pi x_j}{l_x} \right) \left(1 - \cos \frac{2\pi y_j}{l_y} \right). \quad (11)$$

Computing Models of Vehicle

Generally the two or three dimensional computing model of vehicle can be adopted. For the purpose of this paper the space and plane computing models of the truck TATRA were adopted, Fig. 1.

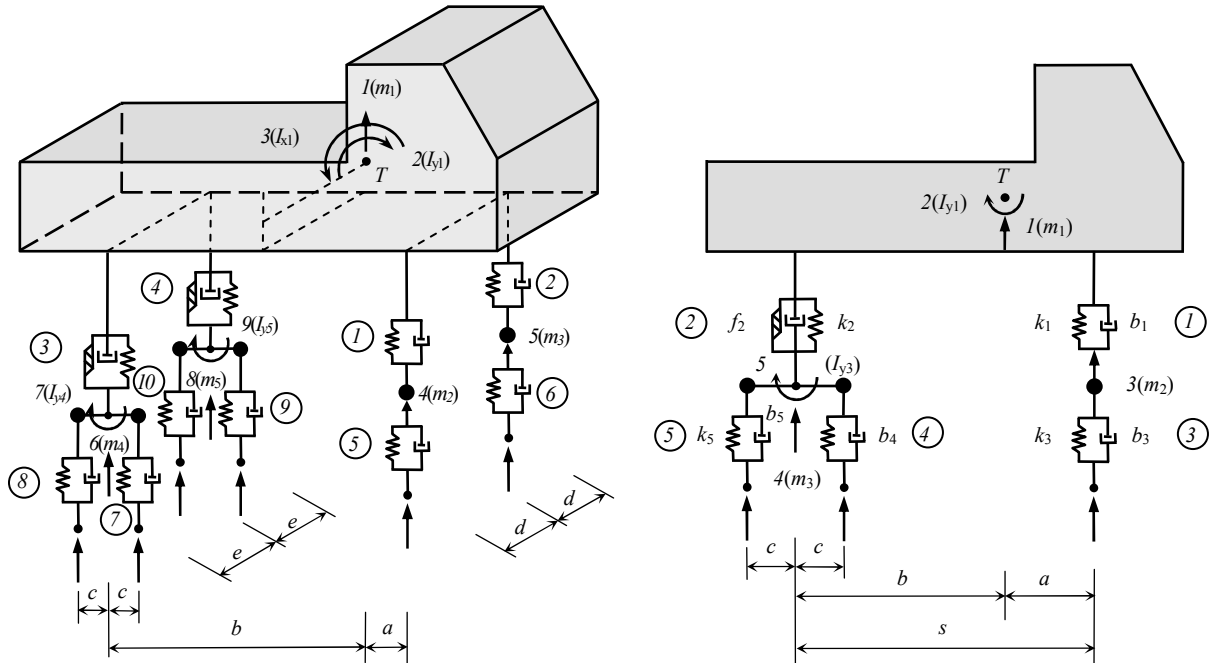


Fig. 1 Space and plane computing models of vehicle TATRA

The space computing model of the truck has 15 degrees of freedom – 9 mass and 6 mass-less and plane computing model 8 degrees of freedom – 5 mass and 3 mass-less. The mass-less degrees of freedom correspond to the vertical movements of the contact points of the model with the surface of the roadway. The vibration of the mass objects of the models is described by the functions of time $r_i(t)$. The mass-less degrees of freedom are associated with the tire forces $F_j(t)$ acting at the contact points. The equations of motions are derived in the form of ordinary differential equations.

Numerical Solution

For the purpose of numerical analysis the following slab construction was considered:

- | | |
|---|---|
| 1. CS – concrete slab, | $h_1 = 240$ mm, $E_1 = 37\ 500$ MPa, $\nu_1 = 0.20$ |
| 2. CA II – coating aggregate, quality class II, | $h_2 = 40$ mm, $E_2 = 4\ 500$ MPa, $\nu_2 = 0.21$ |
| 3. SC I – soil cement, quality class I, | $h_3 = 200$ mm, $E_3 = 2\ 000$ MPa, $\nu_3 = 0.23$ |
| 4. PC – protective coat, gravel sand, | $h_4 = 250$ mm, $E_4 = 120$ MPa, $\nu_4 = 0.35$ |
| 5. SS – sub-soil, | $h_5 = \infty$ mm, $E_5 = 30$ MPa, $\nu_5 = 0.35$ |

The 1st layer of the computing model is the concrete slab of the thickness $h = 240$ mm, the length $l_x = 6.8$ m, the width $l_y = 4.9$ m, modulus of elasticity $E = 37\ 500$ MPa, Poisson ratio $\nu = 0.20$. The mass intensity of the slab $\mu = \rho h = 2500 \times 0.24 = 600.0$ kg/m. The damping circular frequency is taken as $\omega_b = 0.1$ rad/s. The layers 2 – 5 are taken into calculation as Winkler elastic foundation. The modulus of compressibility $K = 171.8$ MNm⁻³ was obtained as the result of numerical loading test of the layered half-space, using the program LAYMED [4].

The vehicle motion along the slab structure was numerically simulated. The space (3D) and plane (2D) computing models of vehicle were used. The value of mid span deflection and the values of

tire forces for space and plane computing models of vehicle were mutually compared, Figs. 2 – 5. The mutual comparison of extreme monitored values is done in the Table 1.

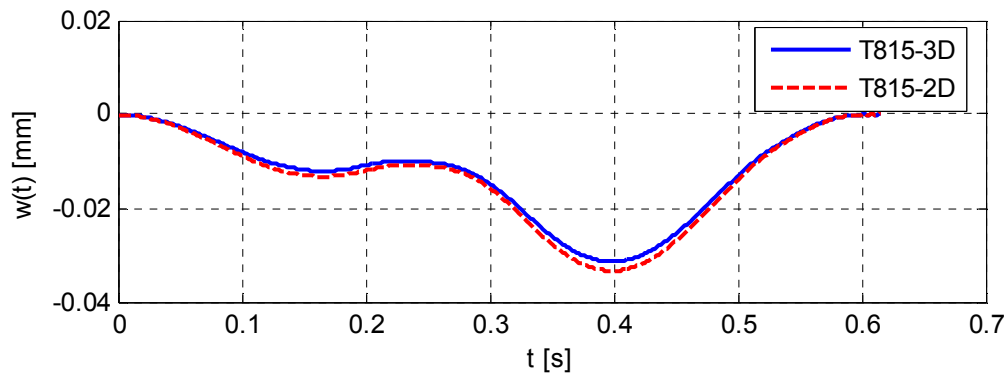


Fig. 2 Mid span slab deflection w for 3D and 2D computing models of vehicle

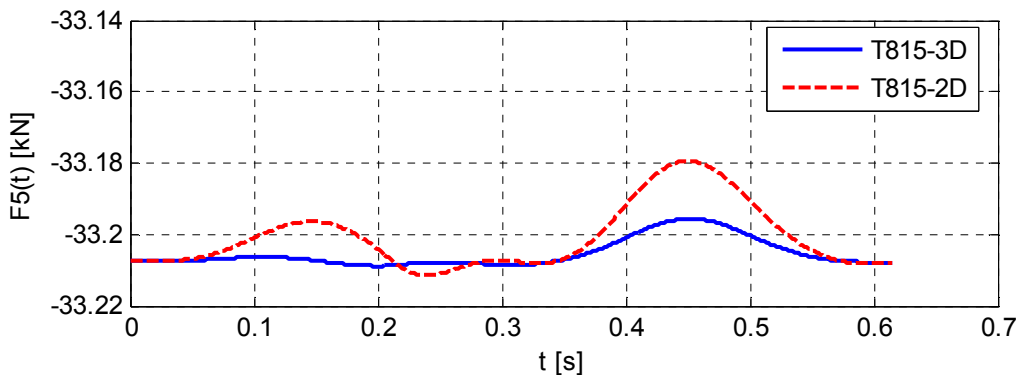


Fig. 3 Tire force $F_5(t)$ for 3D and 2D computing models of vehicle

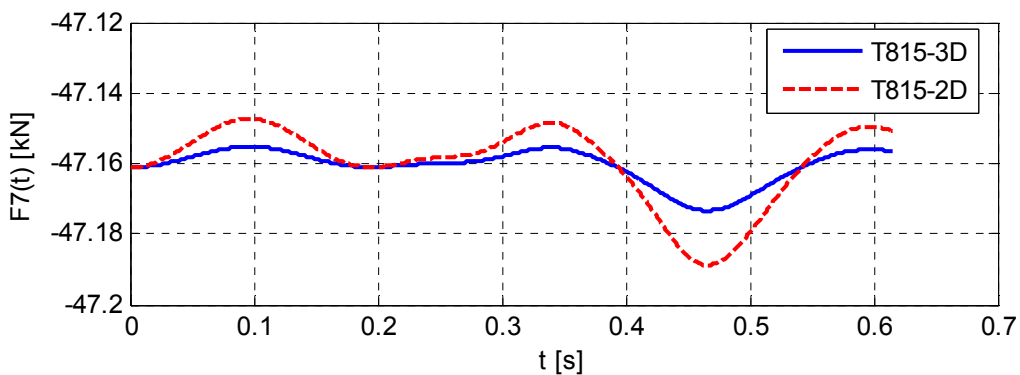


Fig. 4 Tire force $F_7(t)$ for 3D and 2D computing models of vehicle

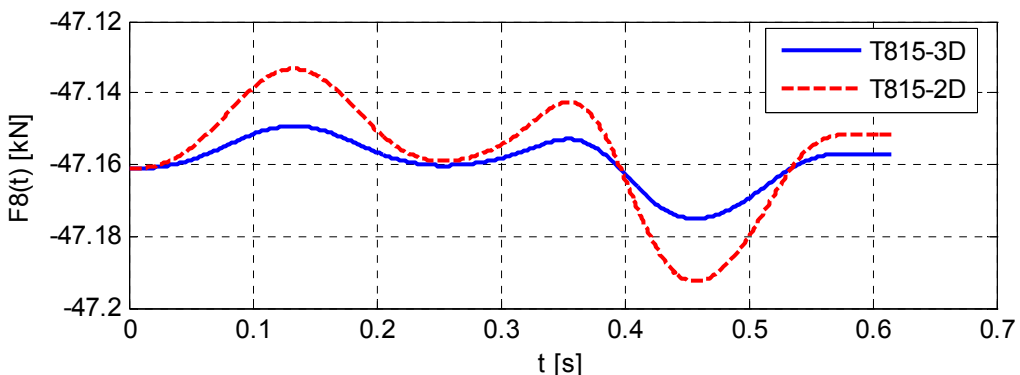


Fig. 5 Tire force $F_8(t)$ for 3D and 2D computing models of vehicle

Table 1 Mutual comparison of extreme monitored values

	plane model (2D)	space model (3D)	$\Delta = 2D - 3D$	Δ in % 3D
w_{\max} [mm]	0.033341	0.031358	0.001983	6.3237
t_{\max} [s]	0.400472	0.400484	-0.000012	-0.0029
$F_{5,\max}$ [kN]	33.211452	33.208852	0.002600	0.0078
$t_{5,\max}$ [s]	0.241302	0.199790	0.041512	20.7778
$F_{5,\min}$ [kN]	33.179335	33.195554	-0.016219	-0.0488
$t_{5,\min}$ [s]	0.451099	0.451994	-0.000895	-0.1980
$F_{7,\max}$ [kN]	47.188800	47.173398	0.015482	0.0328
$t_{7,\max}$ [s]	0.467326	0.467257	0.000069	0.0147
$F_{7,\min}$ [kN]	47.147477	47.155338	-0.007861	-0.0166
$t_{7,\min}$ [s]	0.096664	0.096889	-0.000225	-0.2322
$F_{8,\max}$ [kN]	47.192669	47.175138	0.017531	0.0371
$t_{8,\max}$ [s]	0.455923	0.455942	-0.000019	-0.0041
$F_{8,\min}$ [kN]	47.133319	47.149278	-0.015959	-0.0338
$t_{8,\min}$ [s]	0.133517	0.133814	-0.000297	-0.2219

Summary

Moving load effect on concrete pavements can be simulated by numerical way. Various computing models of pavement and vehicles can be adopted. The simplified slab pavement model is introduced in this paper. The obtained results for space (3D) and plane (2D) computing models of vehicle are mutually compared. The values of mid span slab deflection for the space (3D) vehicle computing model are slightly smaller than the mid span slab deflection for the plane (2D) vehicle computing model. The maximum difference is 0.001983 mm. From the point of view of practical engineering activities the results are practically the same. Similar consideration can also be done in relation to the tire forces. On the basis of results introduced in the Table 1 we can say that plane (2D) vehicle computing model will be satisfactory for the solution of many engineering tasks.

Acknowledgements

This contribution is the result of the research supported by the Grant National Agency VEGA, project G1/0259/12.

References

- [1] G. Martinček, Dynamics of Pavement Structures. E & FN Spon and Ister Science Press, London/Bratislava, 1994.
- [2] B.T. Kulakowski, J.F. Gardner, S.J. Lowen, Dynamic Modeling and Control of Engineering Systems. The 3rd edition, Cambridge University Press, New York, 2009.
- [3] L. Frýba, Vibration of Solids and Structures under Moving Loads. ACADEMIA, Praha, Noordhoff International Publishing, Groningen, 1972.
- [4] B. Novotny, A. Hanuska, Theory of layered half-space (in Slovak), VEDA, SAV, Bratislava, 1983.

Dynamic Load of Vehicle on Asphalt Pavement

MELCER Jozef^{1,a*}

¹University of Zilina, Univerzitna 1, 010 26 Zilina, Slovak Republic

^ajozef.melcer@fstav.uniza.sk

Keywords: dynamic load, asphalt pavement, vehicle, computing model, road unevenness, numerical solution

Abstract. Asphalt pavements are the transport structures subjected to dynamic effect of moving vehicles. Many effects influence the real values of vehicle tire forces. Road unevenness represents the most important factor influencing the magnitudes of tire forces. Such data can be obtained by numerical or experimental way. The paper deals with the numerical simulation of moving load effect on asphalt pavements and with numerical simulation of tire forces in relation to the road unevenness.

Introduction

The roads are the transport structures subjected to direct dynamic effect of moving vehicles. Road unevenness pavement deflections and tire unevenness represent the sources of kinematical excitation of vehicle. The dimension of road unevenness is the higher order than pavement deflections or tire unevenness. So it is fully legitimate to take into account the road unevenness only as the source of kinematical excitation of vehicle. The knowledge of the real load acting on the roads, its variability in time and frequency composition, is needed for the solution of many engineering tasks as design, fatigue, lifetime, reliability, maintenance, structure development, micro-tremor, etc [1,2,3,4]. The task can be solved by experimental or by numerical way. But the most effective way is the combination of the both mentioned advances. The process of numerical simulation requires creation the computing models of vehicles, the computing models of the roads and to pay attention to the numerical solution of equations of motion and to analyse the obtained results in time or in frequency domain.

Track Computing Model

For the purpose of this contribution the quarter computing model of the TATRA 815 truck is adopted, Fig. 1. The computing model of the truck has 3 degrees of freedom – 2 mass and 1 massless. The mass-less degree of freedom corresponds to the vertical movements of the contact points of the model with the surface of the roadway. The vibrations of the mass objects of the model are described by the 2 functions of time $r_i(t)$, ($i = 1, 2$). The massless degree of freedom is coupled by the tire force $F(t)$ acting at the contact point. The equations of motions and the expressions for tire forcers have the following form:

$$\begin{aligned}\ddot{r}_1(t) &= \{-k_1[r_1(t) - r_2(t)] - b_1[\dot{r}_1(t) - \dot{r}_2(t)]\}/m_1, \\ \ddot{r}_2(t) &= \{+k_1[r_1(t) - r_2(t)] - k_2[r_2(t) - h(t)] + b_1[\dot{r}_1(t) - \dot{r}_2(t)]\}/m_2,\end{aligned}\quad (1)$$

$$F(t) = -G + k_2[r_2(t) - h(t)]. \quad (2)$$

G is the gravity force acting at the contact point and h represents the road unevenness. The meaning of the other symbols is clear from Fig. 1.

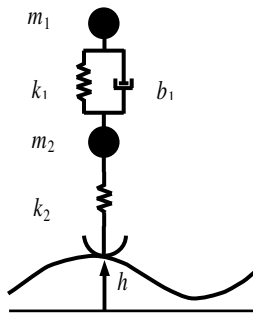


Fig. 1 Quarter computing model of vehicle

Pavement Computing Model

The plane computing model of an asphalt pavement is based on theory of endless beam resting on Winkler elastic foundation [5]

$$EI \frac{\partial^4 v(x,t)}{\partial x^4} + \mu \frac{\partial^2 v(x,t)}{\partial t^2} + 2\mu\omega_b \frac{\partial v(x,t)}{\partial t} + kv(x,t) = p(x,t). \quad (3)$$

The wanted function $v(x,t)$ describing the beam vertical deflections will be expressed as the product of two functions

$$v(x,t) = v_0(x)q(t). \quad (4)$$

The function $v_0(x)$ figures as known function and it is dependent on the coordinate x only and the function $q(t)$ figures as unknown function and it is dependent on the time t . The function $q(t)$ has the meaning of generalized Lagrange coordinate. With respect to the goal of the solution and with respect to the results of experimental tests the assumption of the shape of the function $v_0(x)$ was adopted as

$$v_0(x) = \frac{1}{2} \left(1 - \cos \frac{2\pi x}{l} \right). \quad (5)$$

The meanings of the other symbol are as follows: E modulus of elasticity [Nm^{-2}], I cross section moment of inertia [m^4], μ mass intensity [kgm^{-1}], ω_b damping circular frequency [rad/s], k modulus of foundation [Nm^{-2}], $p(x,t)$ represents the continuous load in [Nm^{-1}], l the length of the beam on which the deformation due to truck load occurs. With respect to the assumption (Eq. 5) for plane computing model of the truck and for $x = l/2$ the Eq. 3 can be rewritten to the form

$$\ddot{q}(t)\mu + \dot{q}(t)2\mu\omega_b + q(t) \left[k + \frac{1}{2} EI \left(\frac{2\pi}{l} \right)^4 \right] = F_l(t) \frac{1}{l} \left(1 - \cos \frac{2\pi x_l}{l} \right). \quad (6)$$

Road Surface Unevenness

The rigid pavement with random road profile is assumed for the purpose of numerical solution. The random road profile $h(x)$ is assumed as stationary ergodic function with zero mean value and normal distribution. The properties of the road profile are described by Power Spectral Density function (PSD) in the form

$$S_h(\Omega) = S_h(\Omega_0) \left(\frac{\Omega}{\Omega_0} \right)^{-k}, \quad (7)$$

where Ω in [rad/m] denotes the wave number, $\Omega_0 = 1$ rad/m is the reference wave number and the waviness $k = 2$. According to the international directive ISO 8608 [6], typical road profiles can be grouped into classes from A to E. Each class is simply defined by its reference value $S_h(\Omega_0)$. A random profile of a single track can be approximated as

$$h(x) = \sum_i^N \sqrt{2S(\Omega_i)\Delta\Omega} \cos(\Omega_i x + \varphi_i), \quad (8)$$

where φ_i is the uniformly distributed phase angle and x the length coordinate.

Numerical Solution

For the purpose of numerical analysis the pavement construction by Fig. 2 was considered. The upper 3 layers of the pavement construction are considered to the beam with the height $h = h_1 + h_2 + h_3 = 40 + 50 + 50 = 140$ mm = 0.14 m and the width $b = 1.0$ m. For these 3 layers the equivalent modulus of elasticity and moment of inertia of the cross section were calculated: $E = 4800$ MPa, $I = 2.2866 \times 10^{-4}$ m⁴. In Fig. 2 ν represents the Poisson ratio.

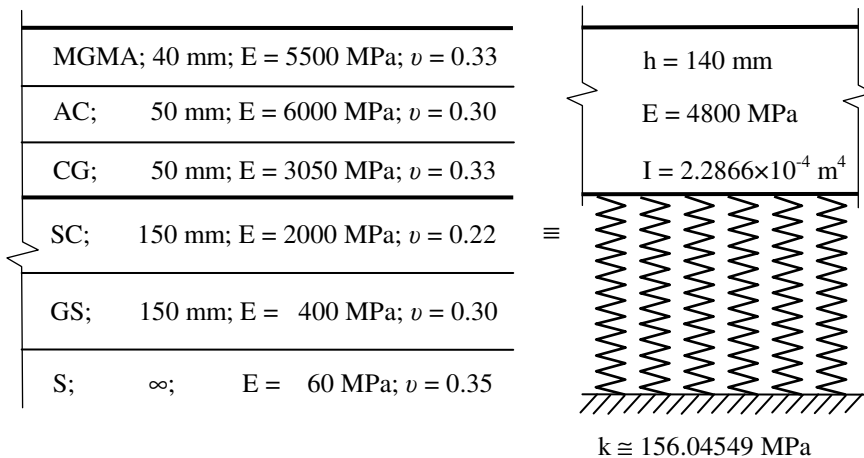


Fig. 2 Pavement computing model, MGMA – medium grained mastic asphalt, AC – asphalt concrete, CG – coated gravel, SC – soil cement, GS – gravel sand, S – subgrade

The layers, No. 4 – 6, are taken into calculation as Winkler elastic foundation. The modulus of compressibility $K = 156.04549$ MNm⁻³ was calculated using the LAYMED program [7]. The modulus of compressibility used at the beam computing model respects the beam width b , $k = Kb = 156.04549$ MNm⁻³ × 1.0 m = 156.04549 MPa. The mass intensity of the beam $\mu = \rho bh = 2200 \times 1.0 \times 0.14 \cong 310.0$ kg/m. The damping circular frequency is taken as $\omega_b = 0.1$ rad/s.

Numerical data of vehicle quarter model are: $k_1 = 143\ 716.5$ N/m, $k_2 = 1\ 275\ 300.0$ N/m, $b_1 = 9\ 614.0$ kg/s, $m_1 = 2\ 930.072$ kg, $m_2 = 455.0$ kg.

Road unevenness, pavement flexibility and tire unevenness represent the sources of kinematical excitation of vehicle. The dimension of road unevenness is the higher order than pavement deflection or tire unevenness. So it is fully legitimate to take into account the road unevenness as the source of kinematical excitation of vehicle only. To prove this declaration two computations were realized, one with flexible pavement and one with inflexible pavement. The random road profile h on the basis of known power spectral density for the value $S_h(\Omega_0) = 4 \times 10^{-6}$ [m²/(rad/m)], category B, was generated [6]. Extreme values: $h_{\max} = 8.4610$ mm, $h_{\min} = -0.0298$ mm, $\Delta h = h_{\max} - h_{\min} = 8.4908$ mm. The road profile was generated with the step 0.01 m for a given wavelength from $L = 0.3$ m to $L = 90$ m, Fig. 3. The numerical simulation of vehicle motion along the flexible pavement with random road profile was performed. The time history of pavement deflection at

monitored point and time history of contact force is plot in Fig. 4 and Fig. 5. Extreme values of tire force: $F_{\max} = -37.2587 \text{ kN}$, $F_{\min} = -28.7812 \text{ kN}$, $\Delta F = |F_{\max}| - |F_{\min}| = 8.4775 \text{ kN}$.

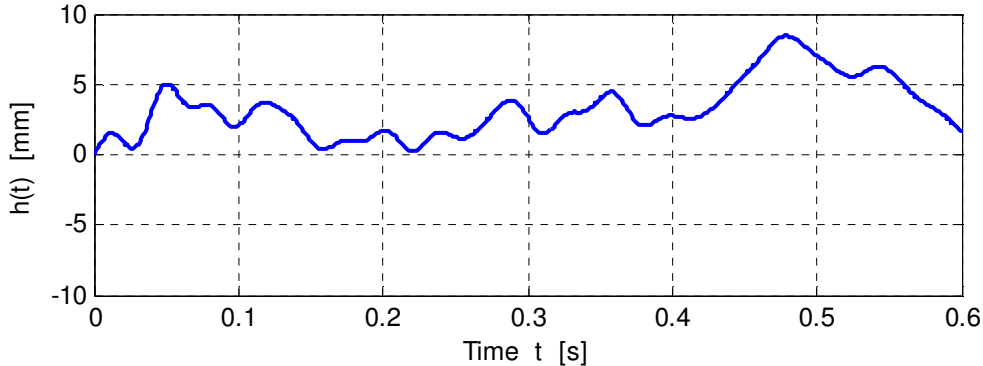


Fig. 3 Random road profile for $S_h(\Omega_0) = 4 \times 10^{-6} [\text{m}^2/(\text{rad}/\text{m})]$

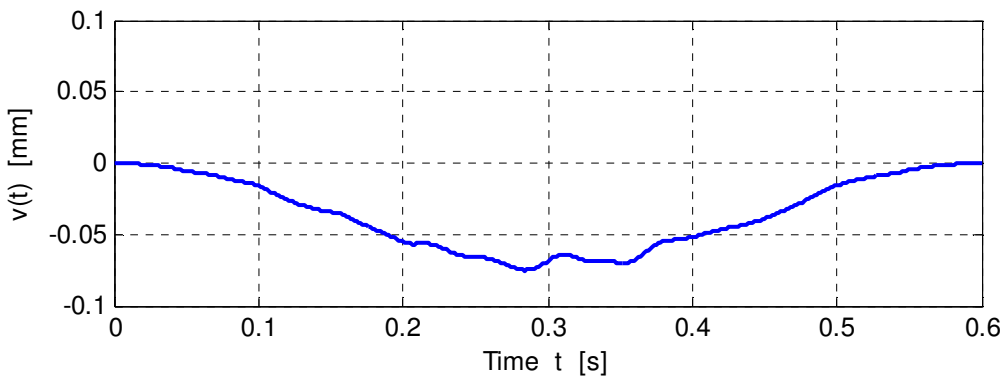


Fig. 4 Time history of pavement deflection at monitored point, $S_h(\Omega_0) = 4 \times 10^{-6} [\text{m}^2/(\text{rad}/\text{m})]$, speed $V = 36 \text{ km/h}$, $v_{\max} = 0.0749 \text{ mm}$

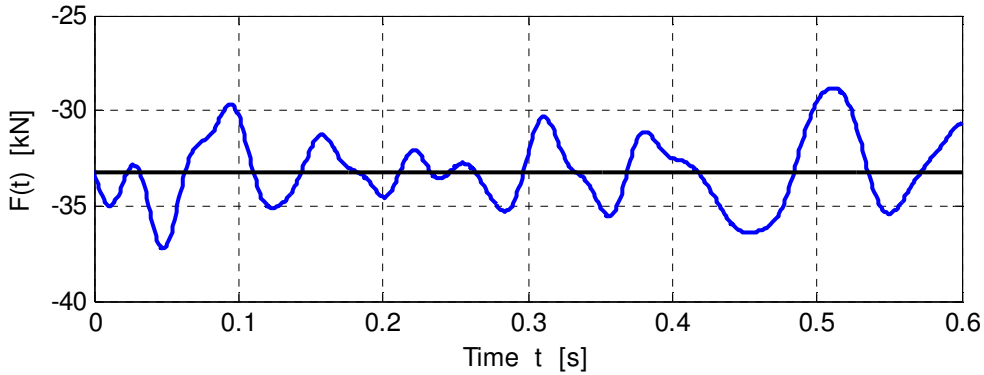


Fig. 5 Time history of contact force, flexible pavement, $S_h(\Omega_0) = 4 \times 10^{-6} [\text{m}^2/(\text{rad}/\text{m})]$, speed $V = 36 \text{ km/h}$, $F_{\max} = -37.2587 \text{ kN}$, $F_{\min} = -28.7812 \text{ kN}$

The numerical simulation of vehicle motion along the inflexible pavement with random road profile by Fig. 3 was performed in the second step. The time history of pavement deflection at monitored point in this case will be zero and time history of contact force is plot in Fig. 6. Extreme values of tire force: $F_{\max} = -37.2713 \text{ kN}$, $F_{\min} = -28.7887 \text{ kN}$, $\Delta F = |F_{\max}| - |F_{\min}| = 8.4826 \text{ kN}$.

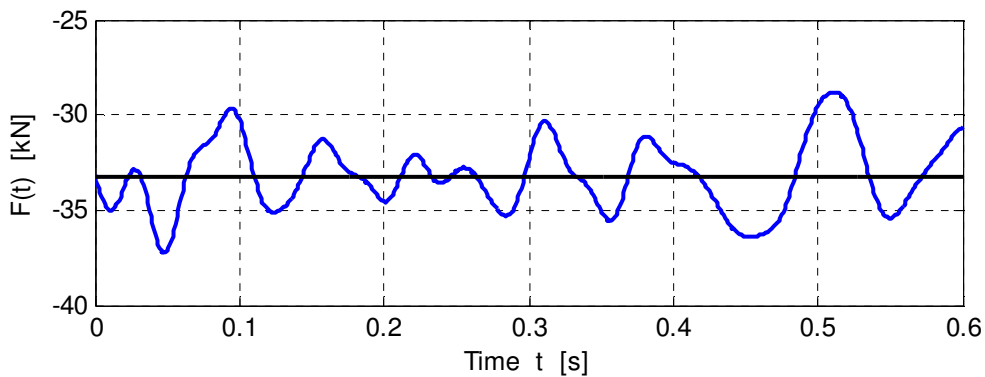


Fig. 6 Time history of contact force, inflexible pavement, $S_h(\Omega_0) = 4 \times 10^{-6} [\text{m}^2/(\text{rad}/\text{m})]$, speed $V = 36 \text{ km/h}$, $F_{\max} = -37.2713 \text{ kN}$, $F_{\min} = -28.7887 \text{ kN}$

Summary

Moving load effect on asphalt pavements can be analyzed by numerical or by experimental way. Road unevenness represents the main source of kinematical excitation of vehicle. The influence of pavement flexibility on the kinematic excitation of vehicle can be neglected. The results of numerical simulation confirm that the pavement flexibility can be neglected within the process of numerical simulation of contact forces and only the road unevenness can be regarded as the source of kinematical excitation of vehicle.

Acknowledgements

This work was supported by the Grant National Agency VEGA, project G1/0259/12.

References

- [1] E. Panulinová, Influence of roar unevenness on the level of noise induced by road transport (in Slovak), *Silniční obzor*, Praha. 62 (2001), 11/12, 275 – 279.
- [2] K. Kotrasová, E. Kormaníková, Seismic design of liquid storage tank made from composite material, *World Journal of Engineering*. 5 (2008), 3, 445-446.
- [3] O. Ivánková, Seismic effect on tall building construction systems (in Slovak), International Conference, *Vývoj a aplikace MKP systémů pro analýzu stavebních konstrukcí*, VÚT Brno, 2003, pp.17.1 – 17.6.
- [4] G. Lajčáková, Interaction in the system vehicle – roadway, 2nd International Conference: New Trends in Statics and Dynamics of Buildings, STU Bratislava. October 16 – 17, 2003, pp.27-30.
- [5] L. Frýba, *Vibration of Solids and Structures under Moving Loads*. ACADEMIA, Praha, Noordhoff International Publishing, Groningen, 1972.
- [6] ISO 8608, Mechanical vibration – road surface profiles – reporting of measured data. International Standard (ISO), 1995.
- [7] B. Novotny, A. Hanuska, Theory of Layered Half-Space (in Slovak), VEDA, SAV, Bratislava, 1983.

Applications of Integral Transforms in Solving Problems of Dynamic Interaction in the Vehicle-Roadway System

STACHOVÁ Darina^{1,a*}

¹Department of Mathematics, Faculty of Humanities, University of Zilina,

Univerzitna 1, SK-010 26 Zilina, Slovak Republic

^adarina.stachova@fhv.uniza.sk

Keywords: Fourier transform, time series, frequency representation

Abstract. Fourier transform is an important tool in a number of scientific fields. Its advantages, disadvantages and subtleties have been examined many times by dozens of mathematicians, physicists and engineers. In this contribution we try to summarize important aspects of this transform and discuss variety of its uses in contemporary science with emphasis on demonstrating connections to dynamic interactions in the vehicle-roadway system.

Introduction

Empirical measurements in various domains – economical, technical, or other – are often turned into time series. Based on this it is possible to perform analysis, which in turn allows us to better understand the dynamics of the factors involved. To this end, we use the Fourier transform. Being discovered at the turn of the 19th century, the theory of the Fourier transform is currently used in signal processing such as in image sharpening, noise filtering, etc. For us the relevant application is in the theory of dynamic interaction in the vehicle-roadway system.

The basis of the Fourier transform is the so-called Fourier mapping, i.e., the transformation of one function to another, from properties of which we can obtain information about the original function. Fourier transform expresses a time-dependent signal using harmonic signals, i.e., the sine and cosine functions, in general functions of complex exponentials. It is used to transform signals from the time domain to the frequency domain. A signal can be continuous or discrete. See Fig. 1 for a depiction of the correspondence between the time-based and frequency-based representation:

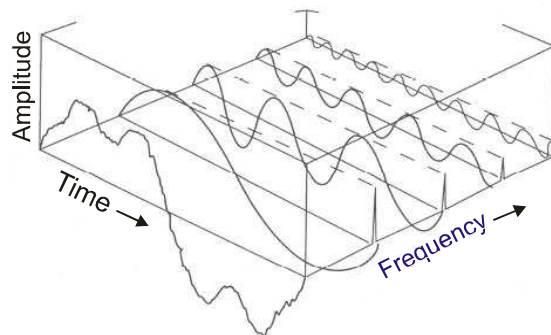


Fig. 1 Amplitude-frequency diagram

Fourier integral

A generalization of the Fourier series that permits in some applications a more appropriate expression of a non-periodical function defined almost everywhere in R is the Fourier integral.

Theorem 1: Let $f: R \rightarrow R$ be a function that

- is piece-wise continuous on R along with its derivative f' ,
- is absolutely integrable on R , i.e. $\int_{-\infty}^{\infty} |f(t)| dt$ converges.

Then all $t \in R$ satisfy $\tilde{f}(t) = \frac{1}{\pi} \int_0^\infty d\omega \int_{-\infty}^\infty f(s) \cos \omega(t-s) ds$, (1)

where $\tilde{f}(t) = \frac{1}{2} \left[\lim_{s \rightarrow t+} f(s) + \lim_{s \rightarrow t-} f(s) \right]$.

Note 1: From the claim of Theorem 1, it follows that the values of the double integral on the right-hand side of (Eq. 1) is equal to $f(t)$ for each $t \in R$ in which f is continuous and is equal to the arithmetic mean of the left- and right- limits of this function in each point of discontinuity, provided the conditions a) and b) of this claim hold.

Note 2: Using the fact that $\forall t \in R, \forall s \in R$ and $\forall \omega \in \langle 0; \infty \rangle$ we have

$$\cos \omega(t-s) = \cos \omega t \cos \omega s + \sin \omega t \sin \omega s,$$

we can rewrite (Eq. 1) in the form $\tilde{f}(t) = \int_0^\infty [a(\omega) \cos \omega t + b(\omega) \sin \omega t] d\omega$, (2)

where $a(\omega) = \frac{1}{\pi} \int_{-\infty}^\infty f(s) \cos \omega s ds$, $b(\omega) = \frac{1}{\pi} \int_{-\infty}^\infty f(s) \sin \omega s ds$, $\omega \in \langle 0; \infty \rangle$ (3)

Definition 1: The right-hand side of (Eq. 1) is called the *double Fourier integral* of $f: R \rightarrow R$. The right-hand side of (Eq. 2) is the *single Fourier integral* of f .

Note 3: It is not difficult to see that the single Fourier integral (Eq. 2) is a generalization of the double Fourier integral and the functions $a: \langle 0; \infty \rangle \rightarrow R$, $b: \langle 0; \infty \rangle \rightarrow R$ defined by (Eq. 3) are a generalization of the standard Fourier coefficients of a periodic function. Moreover, it is clear that if $f: R \rightarrow R$ is an even function, then $b(\omega)=0$, $a(\omega)=\frac{2}{\pi} \int_0^\infty f(s) \cos \omega s ds$ and we have $\tilde{f}(t)=\int_0^\infty a(\omega) \cos \omega t d\omega = \frac{2}{\pi} \int_0^\infty d\omega \int_0^\infty f(s) \cos \omega s \cos \omega t ds$. Similarly, if f is odd, we have: $a(\omega)=0$, $b(\omega)=\frac{2}{\pi} \int_0^\infty f(s) \sin \omega s ds$ and we have $\tilde{f}(t)=\int_0^\infty b(\omega) \sin \omega t d\omega = \frac{2}{\pi} \int_0^\infty d\omega \int_0^\infty f(s) \sin \omega s \sin \omega t ds$.

Note 4: Using the well-known Euler's formula for exponential and goniometric functions: $\cos \omega t = \frac{1}{2} (e^{i\omega t} + e^{-i\omega t})$, $\sin \omega t = \frac{1}{2i} (e^{i\omega t} - e^{-i\omega t})$ in the single Fourier integral (Eq. 2), we obtain $\forall t \in R$:

$$\tilde{f}(t) = \int_0^\infty \left[\frac{a(\omega) - ib(\omega)}{2} e^{i\omega t} + \frac{a(\omega) + ib(\omega)}{2} e^{-i\omega t} \right] d\omega.$$

By letting $\frac{a(\omega) - ib(\omega)}{2} = c(\omega)$, $\frac{a(\omega) + ib(\omega)}{2} = c(-\omega) = \overline{c(\omega)}$ for $\omega \in \langle 0; \infty \rangle$, we have for all $t \in R$:

$$\tilde{f}(t) = \int_{-\infty}^\infty c(\omega) e^{i\omega t} d\omega, \quad (4)$$

where $c(\omega) = \frac{1}{2} [a(\omega) - ib(\omega)] = \frac{1}{2\pi} \int_{-\infty}^\infty f(s) e^{-i\omega s} ds$ for all $\omega \in R$. (5)

Definition 2: The right-hand side of (Eq. 4), where $c: R \rightarrow C$ is defined by (Eq. 5) is called the *Fourier integral* of $f: R \rightarrow R$ in a *complex form*.

Fourier transform

Definition 3: Let $f: R \rightarrow R$ along with its derivative f' be piece-wise continuous on R , and let f be absolutely integrable on R . Then we call f the *source of Fourier transform*. Let the set of such functions $f: R \rightarrow R$ be denoted by D_F . Then the function $F: i\omega \rightarrow F(f(t))$, where

$$F(f(t)) = F(i\omega) = \int_{-\infty}^\infty f(t) e^{-i\omega t} dt, \quad (6)$$

where $\omega \in (-\infty; \infty)$ and $i = \sqrt{-1}$ is called the *Fourier image* of f and the mapping F from the set of functions D_F defined by (Eq. 6) is called the *forward Fourier transform*.

Theorem 2: If $f \in D_F$, then there exists a Fourier image $F(i\omega)$ of f defined by (Eq.6), which satisfies

$$\tilde{f}(t) = \frac{1}{2\pi} \int_{-\infty}^{\infty} F(i\omega) e^{i\omega t} d\omega, \quad (7)$$

where $\tilde{f}(t) = \frac{1}{2} \left[\lim_{s \rightarrow t+} f(s) + \lim_{s \rightarrow t-} f(s) \right]$ for all $t \in R$.

Definition 4: The mapping $F^{-1}(D_F)$ defined by (Eq. 7) is called the *inverse Fourier transform*, i.e.,

$$F^{-1}(F(i\omega)) = \tilde{f}(t) = \frac{1}{2\pi} \int_{-\infty}^{\infty} F(i\omega) e^{i\omega t} d\omega, \quad t \in R.$$

Note 5: The Fourier image $F(i\omega)$ is in the technical literature often called the *spectral characteristic* of f . Its magnitude $F(\omega) = |F(i\omega)|$ is the *amplitude characteristic* (*amplitude spectrum*) of f , function $\alpha(\omega) = -\text{Arg } F(i\omega)$, $\omega \in (-\infty; \infty)$ is called the *phase characteristic* (*phase spectrum*) of f and the function $P(\omega) = |F(i\omega)|^2$ *power characteristic* (*power spectrum*) of f . Hence, for all $\omega \in R$

$$F(i\omega) = F(\omega) e^{-i\alpha(\omega)} = A(\omega) - iB(\omega), \text{ where } A(\omega) = \int_{-\infty}^{\infty} f(t) \cos \omega t dt, B(\omega) = \int_{-\infty}^{\infty} f(t) \sin \omega t dt.$$

From this it follows that $F(\omega) = \sqrt{A^2(\omega) + B^2(\omega)}$, $\alpha(\omega) = \arctan [B(\omega)/A(\omega)]$, which means that the amplitude function $F(\omega)$ is an even function and the phase function $\alpha(\omega)$ is an odd function of the independent variable (frequency) ω .

Use of Fourier transform in solving representative problems

Recall that according to the Euler's formula we can write $e^{i\omega t} = \cos \omega t - i \sin \omega t$.

Example 1: Find the Fourier image of the following functions:

- a) $f(t): R \rightarrow R$, $f(t) = e^{-a|t|}$, $a \in R^+$;
- b) $f(t): R \rightarrow R$, $f(t) = e^{-t^2}$,
- c) $f(t): R \rightarrow R$, $f(t) = 0$ for $t \in (-\infty; 0) \cup (a; \infty)$, $f(t) = \sin bt$ for $t \in (0; a)$.

Solution: a) From equations (Eq. 4) and (Eq. 5) it follows that

$$\begin{aligned} c(\omega) &= \frac{1}{2\pi} \int_{-\infty}^{\infty} e^{-a|s|} e^{-i\omega s} ds = \frac{1}{2\pi} \left(\int_{-\infty}^0 e^{(a-i\omega)s} ds + \int_0^{\infty} e^{-(a+i\omega)s} ds \right) = \frac{1}{2\pi} \left[\frac{e^{(a-i\omega)s}}{a-i\omega} \right]_0^{\infty} - \frac{1}{2\pi} \left[\frac{e^{-(a+i\omega)s}}{a+i\omega} \right]_0^{\infty} = \\ &= \frac{1}{2\pi} \left(\frac{1}{a-i\omega} + \frac{1}{a+i\omega} \right) = \frac{1}{\pi} \frac{1}{a+\omega^2}, \text{ i.e., } \tilde{f}(t) = f(t) = \frac{1}{\pi} \int_{-\infty}^{\infty} \frac{e^{i\omega t}}{a+\omega^2} d\omega. \end{aligned}$$

Therefore the Fourier image of $e^{-a|t|}$ is $F(e^{-a|t|}) = \frac{1}{a} \cdot \frac{2}{1 + \left(\frac{\omega}{a}\right)^2} = \frac{2}{a^2 + \omega^2}$.

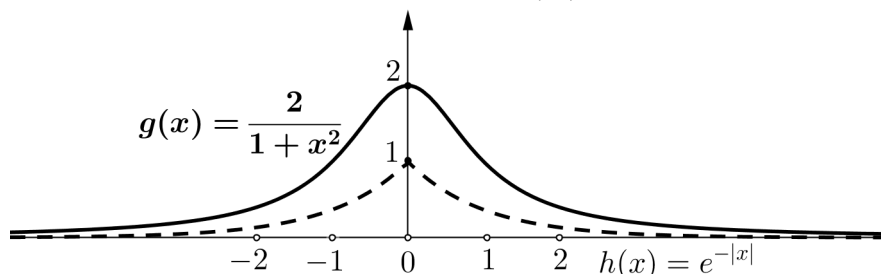


Fig. 2 Comparing a graph of a function with its Fourier image

b) By Definition 3 we have $F(e^{-t^2}) = \int_{-\infty}^{\infty} e^{-i\omega t - t^2} dt = e^{-\frac{\omega^2}{4}} \int_{-\infty}^{\infty} e^{-\left(t + \frac{i\omega}{2}\right)^2} dt = |t + \frac{i\omega}{2}| = z, dt = dz, z_1 = -\infty,$

$$z_2 = \infty | = e^{-\frac{\omega^2}{4}} \int_{-\infty}^{\infty} e^{-z^2} dz = \sqrt{\pi} e^{-\frac{\omega^2}{4}}, \text{ since the Poisson integral is } \int_{-\infty}^{\infty} e^{-z^2} dz = \sqrt{\pi}.$$

$$\begin{aligned} c) \text{ From (Eq. 6) it follows that } F(f(t)) &= \int_{-\infty}^{\infty} f(t) e^{-i\omega t} dt = \int_0^a \sin bt e^{-i\omega t} dt = \int_0^a \frac{e^{ibt} - e^{-ibt}}{2i} e^{-i\omega t} dt = \\ &= \frac{1}{2i} \int_0^a (e^{i(b-\omega)t} - e^{-i(b+\omega)t}) dt = \frac{1}{2i} \left[\frac{e^{i(b-\omega)t}}{i(b-\omega)} + \frac{e^{-i(b+\omega)t}}{i(b+\omega)} \right]_0^a = \\ &= \frac{1}{2i} \left(\frac{e^{i(b-\omega)a}}{i(b-\omega)} + \frac{e^{-i(b+\omega)a}}{i(b+\omega)} - \frac{1}{i(b-\omega)} - \frac{1}{i(b+\omega)} \right) = \frac{b - e^{-i\omega a} (b \cos ab + i\omega \sin ab)}{b^2 - \omega^2}. \end{aligned}$$

Fourier transform has a wide variety of uses; we have already shown some of them for illustration. Fourier transform is also used to solve differential equations. The key idea is that the Fourier transform transforms the operation of taking derivatives into multiplication of the image by the independent variable. If we perform the Fourier transform using all independent variables we obtain as image a solution of the equation with no derivatives. When we solve it, it suffices to find the Fourier preimage which usually is the most difficult part. Unfortunately, it can also happen that the solution has no preimage. Then this method does not work. However, we may perform the Fourier transform using only some independent variables. This yields a differential equation with fewer variables and with parameters, which might be easier to solve than the original equation; nonetheless the ultimate difficulty may still be in finding the preimage.

Example 2: Using the Fourier transform find a solution of the differential equation satisfying the following conditions:

$$a) y'(t) + k y(t) = a e^{-|t|}, \text{ where } k \in R^+ - \{1\}, b \in R, t \in R, \lim_{t \rightarrow -\infty} y(t) = \lim_{t \rightarrow \infty} y(t) = 0,$$

$$b) y''(t) + 3y'(t) + 2 y(t) = e^{-|t|}, t \in R, \lim_{t \rightarrow -\infty} y(t) = \lim_{t \rightarrow \infty} y(t) = 0.$$

Note 6: Fourier transform can also be used for solving ordinary linear differential equations with constant coefficients assuming that the solution of such equation along with its derivatives of order up to the order of the equation has properties from Definition 3.

Solution: Let $y, y', y'' \in D_F$ and write $F(y(t)) = Y(i\omega)$. Then $F(y'(t)) = i\omega Y(i\omega)$, $F(y''(t)) = -\omega^2 Y(i\omega)$.

$$a) \text{ Since } F(a e^{-|t|}) = a \frac{2}{1 + \omega^2}, \text{ we have } y(t) = \frac{1}{2\pi} \int_{-\infty}^{\infty} Y(i\omega) e^{i\omega t} dt = \frac{a}{\pi} \int_{-\infty}^{\infty} \frac{1}{1 + \omega^2} e^{i\omega t} dt.$$

$$\text{Thus } y(t) = \frac{ae^t}{k+1} \text{ for } t \in (-\infty; 0), y(t) = a \left(\frac{e^{-t}}{k-1} - 2 \frac{e^{-kt}}{k^2-1} \right) \text{ for } t \in (0; \infty).$$

$$b) \text{ Since } F(e^{-|t|}) = \frac{2}{1 + \omega^2}, \text{ it follows that } y(t) = \frac{1}{2\pi} \int_{-\infty}^{\infty} Y(i\omega) e^{i\omega t} dt = \frac{1}{\pi} \int_{-\infty}^{\infty} \frac{1}{1 + \omega^2} e^{i\omega t} dt.$$

$$\text{Hence } y(t) = \frac{1}{6} e^t \text{ for } t \in (-\infty; 0), y(0) = \frac{1}{6}, \text{ and } y(t) = \frac{2t-1}{2} e^{-t} + \frac{2}{3} e^{-2t} \text{ for } t \in (0; \infty).$$

Example 3: Some situations require specifying the problem using a diagram. Here the subject of analysis is the so-called *quarter model* of a vehicle shown in Fig. 3a. This computational model represents one half of one axle of a vehicle. Unevenness of the road surface is the main source of kinematic excitation of the vehicle. The vehicle's response to this excitation can be found numerically in both the time and frequency domain. In the time domain we are mainly interested in

time evolution of contact forces and in the frequency domain in the power spectral densities of power forces in relation to the power spectral densities of the unevenness of the road [1].

As an example, we use numerical characteristics of the vehicle Tatra model T148.

Weight parameters of the model:

$$m_1 = 2930 \text{ kg} \quad m_2 = 455 \text{ kg}$$

Rigidity constants of the coupling:

$$k_1 = 143\,716.5 \text{ Nm}^{-1} \quad k_2 = 1275\,300.0 \text{ Nm}^{-1}$$

Damping coefficients:

$$b_1 = 9\,614.0 \text{ kg s}^{-1}$$

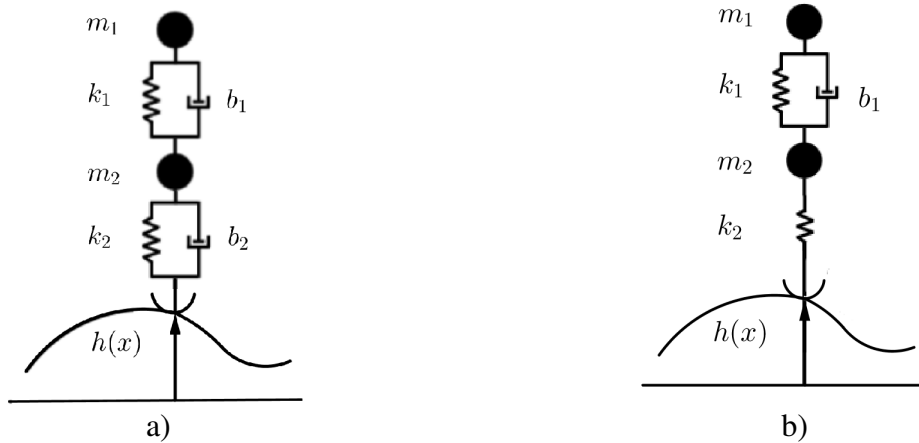


Fig. 3 Quarter model of a vehicle

Note 7: Inherent part of the process of solving the problem is the formulation of simplified models of the vehicle, their mathematical description, and determination of the vehicle's response in the time domain. Computational models of vehicles can have varied complexity depending on the nature of problem to be solved. Oftentimes the so-called quarter- or half models are used; these models model motion and effects of a quarter or half of the vehicle. Nowadays, however, it is not uncommon to use spatial models of vehicles.

The law of conservation of mechanical energy is a special case of the conservation of energy law, which applies to all types of energy. In the case of dissipative forces such as frictional forces, part of the mechanical energy is converted to heat, but the total amount of energy remains the same.

Solution: Applying a general procedure [2] to the model from Fig. 3a, we obtain equations of motion of the modeled vehicle. With that we also obtain expressions describing interaction forces at the point of contact of the vehicle's axle with the road surface.

$$\begin{aligned} \ddot{r}_1(t)m_1 &= \{-k_1[r_1(t) - r_2(t)] - b_1[\dot{r}_1(t) - \dot{r}_2(t)]\}, \\ \ddot{r}_2(t)m_2 &= \{+k_1[r_1(t) - r_2(t)] - k_2[r_2(t) - h(t)] + b_1[\dot{r}_1(t) - \dot{r}_2(t)] - b_2[\dot{r}_2(t) - \dot{h}(t)]\}. \end{aligned} \quad (8)$$

Using the principle of equal action and reaction, we derive the following:

$$\begin{aligned} F(t) &= -F_{RV}(t) = -G_2 + k_2[r_2(t) - h(t)] + b_2[\dot{r}_2(t) - \dot{h}(t)] = F_{st} + F_{dyn}(t), \\ \text{i.e., } F_{st} &= -G_2 \text{ and } F_{dyn}(t) = k_2[r_2(t) - h(t)] + b_2[\dot{r}_2(t) - \dot{h}(t)]. \end{aligned} \quad (9)$$

We rearrange the equations (Eq. 8) as follows:

$$\begin{aligned} m_1 \ddot{r}_1(t) + b_1 \dot{r}_1(t) - b_1 \dot{r}_2(t) + k_1 r_1(t) - k_1 r_2(t) &= 0, \\ m_2 \ddot{r}_2(t) - b_1 \dot{r}_1(t) + b_1 \dot{r}_2(t) + b_2 \dot{r}_2(t) - b_2 \dot{h}(t) - k_1 r_1(t) + k_1 r_2(t) - k_2 h(t) &= 0, \\ F_{dyn}(t) &= b_2 \dot{r}_2(t) - b_2 \dot{h}(t) + k_2 r_2(t) - k_2 h(t). \end{aligned} \quad (10)$$

Function $f(t)$ and its time derivative will be then transformed to

$$a f(t) \rightarrow a F(\omega),$$

$$\dot{f}(t) \text{ for } f(\pm\infty) = 0 \rightarrow i\omega F(\omega),$$

$$\ddot{f}(t) \text{ for } f(\pm\infty) = \dot{f}(\pm\infty) = 0 \rightarrow -\omega^2 F(\omega).$$

The complex Fourier transform of (Eq. 10) after rearranging has the following form:

$$\begin{aligned}\bar{r}_1 & [-m_1 \omega^2 + i b_1 \omega + k_1] + \bar{r}_2 [-i b_1 \omega - k_1] = 0, \\ \bar{r}_1 & [-i b_1 \omega - k_1] + \bar{r}_2 [-m_2 \omega^2 + i b_1 \omega + i b_2 \omega + k_1 + k_2] + [-i b_2 \omega - k_2] = 0, \\ \bar{F}_{dyn} & = \bar{r}_2 [i b_2 \omega + k_2] + [-i b_2 \omega - k_2].\end{aligned}\quad (11)$$

The first two equations of (Eq. 11) can be written as $[a] \cdot \{\bar{r}\} = \{PS\}$ or in the matrix form as

$$\begin{pmatrix} a_{11} & a_{12} \\ a_{21} & a_{22} \end{pmatrix} \cdot \begin{Bmatrix} \bar{r}_1 \\ \bar{r}_2 \end{Bmatrix} = \begin{Bmatrix} PS_1 \\ PS_2 \end{Bmatrix}. \quad (12)$$

A solution is then found using the Cramer's rule, i.e.,

$$\bar{r}_1 = \frac{D_1}{D}, \quad \bar{r}_2 = \frac{D_2}{D}, \quad (13)$$

where $D = a_{11} a_{22} - a_{12} a_{21}$, $D_1 = PS_1 a_{22} - PS_2 a_{12}$, $D_2 = a_{11} PS_2 - PS_1 a_{21}$.

If we then consider that in the Fourier transform the parameter ω represents the angular frequency in $\left[\frac{rad}{s}\right]$, then the coefficients a_{ij} in (Eq. 12) have the following form:

$$\begin{aligned}a_{11} &= (k_1 - m_1 \omega^2) + i b_1 \omega, \quad a_{12} = k_1 + i(-b_1 \omega), \quad PS_1 = 0 + i \cdot 0, \quad a_{21} = k_1 + i(-b_1 \omega), \\ a_{22} &= (k_1 + k_2 - m_2 \omega^2) + i(b_1 + b_2) \omega, \quad PS_2 = k_2 + i b_2 \omega.\end{aligned}$$

The expression (Eq. 13) is calculated numerically for chosen values of ω in the selected frequency band. In this solution we ignore the damping of the tire, i.e. $b_2 = 0$ [kg s^{-1}]. The solution thus applies to the simplified model shown in Fig. 3b. Since $b_2 = 0$, we have $\bar{F}_{dyn} = k_2 (\bar{r}_2 - 1)$.

Conclusion

Why do we use transformations? For various reasons, for instance:

- Transformations allow transforming a complicated problem to a potentially simpler one.
- The problem can be then solved in the transform domain.
- Using the inverse transform we obtain solutions in the original domain.
- Fourier transform is appropriate for periodical signals.
 - It allows uniquely transforming a signal from/to time representation $f(t)$ to/from frequency representation $F(i\omega)$.
 - It allows analyzing the frequency content (spectrum) of a signal (for instance in non-invasive methods – material diagnostics or magnetic resonance).

The basis of every experimental science is measurement, since it is the only tool to quantitatively describe properties of real-world physical processes. Solution of dynamic problems can be realized both in the time and the frequency domain. Both forms have their advantages, complement one another and represent two different facets of the same physical phenomenon.

Acknowledgement

This work was produced as part of the project VEGA SR 1/0259/12.

References

- [1] J. Melcer, G. Lajčáková, Application of program system Matlab for the solution of structural dynamic problems (in Slovak), Zilina, ZU v Ziline EDIS, 2011.
- [2] J. Melcer, The use of Fourier and Laplace transform on the solution of vehicle-roadway interaction problems. Civil and environmental engineering, 8 (2012) 145-155.
- [3] J. Moravčík, Mathematics 5, Integral transforms (in Slovak), Zilina, ZU v Ziline EDIS, 2000.

The Comparison between the Applications of Different Types of Boundary Conditions that are Used in the Dynamic Simulation of the Tests of Pavements

KORTIŠ Ján^{1, a *} and RAPANOVÁ Nina^{2, b}

¹Department of Structural Mechanics, Faculty of Civil Engineering, University of Zilina,
Univerzitná 8215/1, 010 26 Žilina, Slovak Republic

²Department of Highway Engineering, Faculty of Civil Engineering, University of Zilina,
Univerzitná 8215/1, 010 26 Žilina, Slovak Republic

^ajan.kortis@fstav.uniza.sk, ^bnina.rapanova@fstav.uniza.sk

Keywords: elastic subgrade, dynamic analysis, computer model, FWD Dynatest

Abstract. Many new modern gadgets, which can measure very fast changes of the displacement, have been developed for the last years. Consequently the new modern dynamic diagnostic methods are widely put into service. One of them is FWD Dynatest, which measures displacements on the surface of the pavement while it is loaded by force impulse. This article describes dynamic numerical simulation of pavement loaded by force impulse.

Introduction

Pavements have been damaging during the service life so knowing their current state is valuable and offers important information to choose the right technique to repair the damage caused by vehicles traveling on it. The loading by force impulse is one of the diagnostic techniques. The numerical model was done to evaluate the results of the impulse force. It is focused on the influence of dimensions of the modeled area and boundary conditions on the quality of the results. The dynamic analysis gives correct results of the solution if the requirements for correct boundary conditions are fulfilled. For that reason a comparison is done between different kind of boundary conditions and dimensions of modeled area. There are two possibilities to define the boundary conditions that do not influence the results.

The Possibilities to Define Boundary Conditions

The first option is to create an area where the distance from the loaded point to the boundary of the area is longer than the distance that waves can travel during the time of the solution. Despite the fact that this is very easy to do, it is not used very often. It is suggested to apply it only if the time of the solution is very short, so the boundary conditions do not influence the results. The second choice is to prescribe the boundary conditions which do not allow the waves spread in the elastic material to bounce and influence the results of the solution. Thanks to this the modeled area could be smaller. However, it is sometimes difficult to define the right characteristics for the elements used at the edge of the area. The viscous damping elements are used for this purpose. These are spring elements which are showed in the Fig. 1. They have zero stiffness and the damping characteristics are prescribed by the equations.

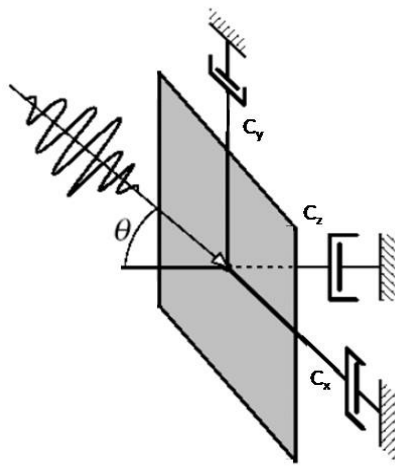


Fig. 1 The damping characteristics of elements oriented according to the boundary surface

$$c_z = \int_S a \rho v_p dS , \quad (1)$$

$$c_y = c_x = \int_S b \rho v_s dS . \quad (2)$$

The damping value c_z is used to stop bounding of the longitudinal waves. The c_x and c_y are supposed to stop bounding of the shear waves. The previous equations show that the damping of the elements depends on the velocity of waves spread in the elastic material, density of the material, and on the size of the boundary area for which the damping element is used. There are also used a and b constants to better adjust the damping values for the particular model. Values of velocity for longitudinal and shear waves are expressed by the next equations

$$v_p = \sqrt{\frac{(1-\nu)E}{(1-2\nu)(1+\nu)\rho}} , \quad (3)$$

$$v_s = \sqrt{\frac{E}{2(1+\nu)\rho}} . \quad (4)$$

Finding the right values of the damping characteristics could be difficult and depend highly on the experience. The restriction is prescribed for the angle between the axis perpendicular to the surface at the boundary of the modeled area and the direction in which the wave spreads. On the other hand, the solution could be time efficient and it can be done by using common computer.

The Description of the Numerical Model

The calculation model was created in the software Adina, using finite element method (FEM). It represents the composition of the structural layers of the pavement on subgrade. Material characteristics of the construction layers of pavement and individual thicknesses are similar to the pavement commonly used. Boundary conditions depend on the type of calculation model. Zero displacement at the edges of calculation model was prescribed for model where is assumed that the length of the model is sufficient. For the model with the viscous damping elements the boundary conditions are replaced by spring elements with defined damping characteristics.

The load is characterized by a pressure applied on the load plate differing in dependence on the power impulse. Positions of the points in which the results are analyzed (their distance from the axis of the load) are equal to the location of points for road surface deflection measurement. Measurement was carried out by diagnostic device FWD Dynatest.

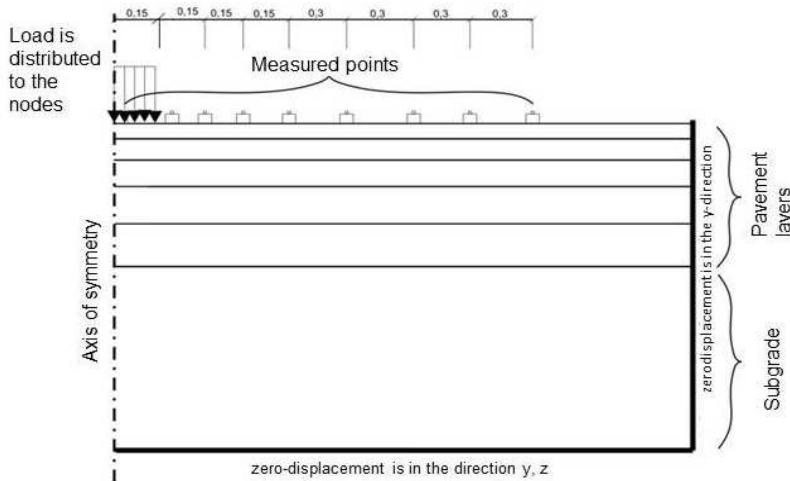


Fig. 2 Scheme of road's 2D solid model with nodes where z -displacements were evaluated

Comparison of the Results

The results of the numerical simulation are compared what gives possibility to evaluate the differences between the various boundary conditions. Displacements in the observed points changed during the time what was influenced by the boundary conditions. Three different numerical models of the same pavement were solved. The changes were done only in the length of the model and the application of the boundary conditions.

Firstly, the model with the length 3 meter and zero displacement at the boundary was done. The results are showed in the Fig. 3. We can see that the displacements in the points that are closer to the boundary are influenced by the wave bounded back to the center of the model.

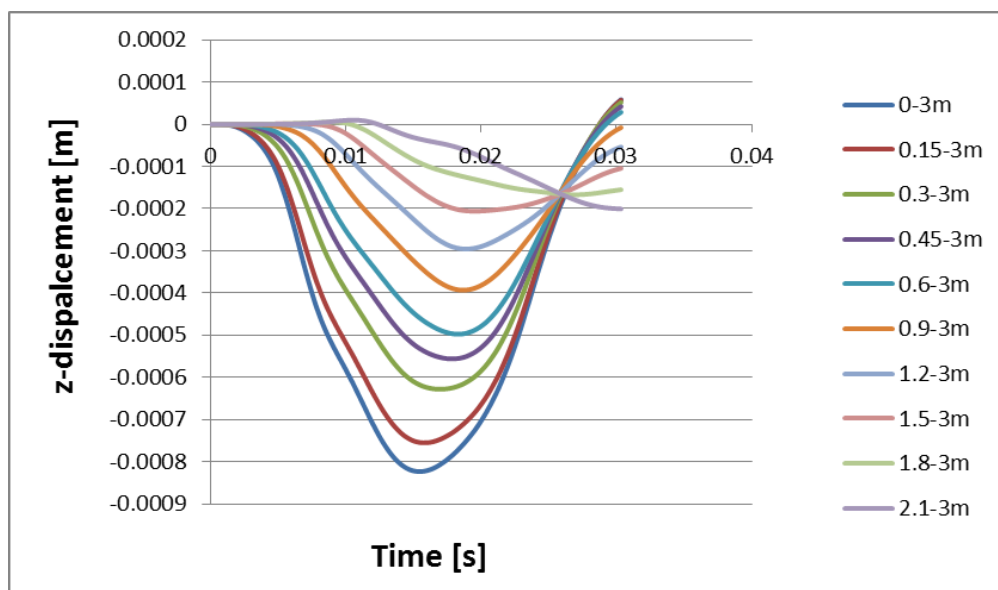


Fig. 3 Results of the model with the length 3 m and zero displacement in the x direction at the boundary

The second model was 10 meter long what changed the shape of the curve describe the time-history of displacements. But the shapes of the curves for the points closer to the center are very similar to results from the previous 3 meter long model. So we could say that these places are not influenced by the bounded waves in the previous model.

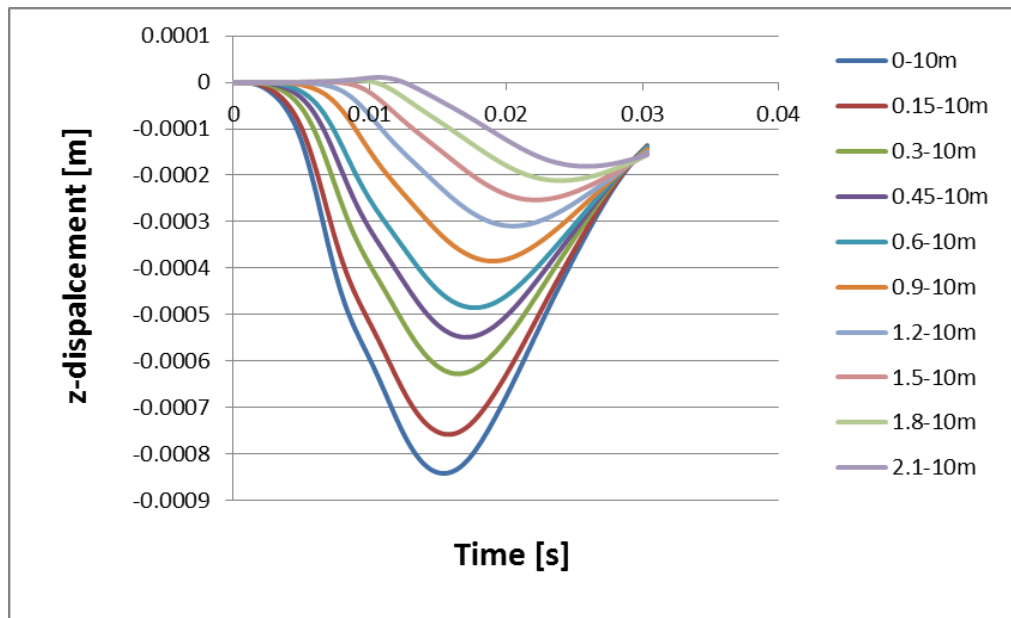


Fig. 4 Results of the model with the length 10 m and zero displacement in the x direction at the boundary

The last model was only 3 meter long which has viscous damping elements with the damping characteristics. They depend on the used material characteristics at the boundary of the modeled area. The displacements have comparable values to the results of the 10 m long model with common boundary conditions. It only changed in the last observed point which is influenced by the bounded wave. It means that also by using these kinds of boundary conditions it is impossible to stop the bounding of the waves definitely. Despite the fact that a little part of the energy is bounding back, it improves the results.

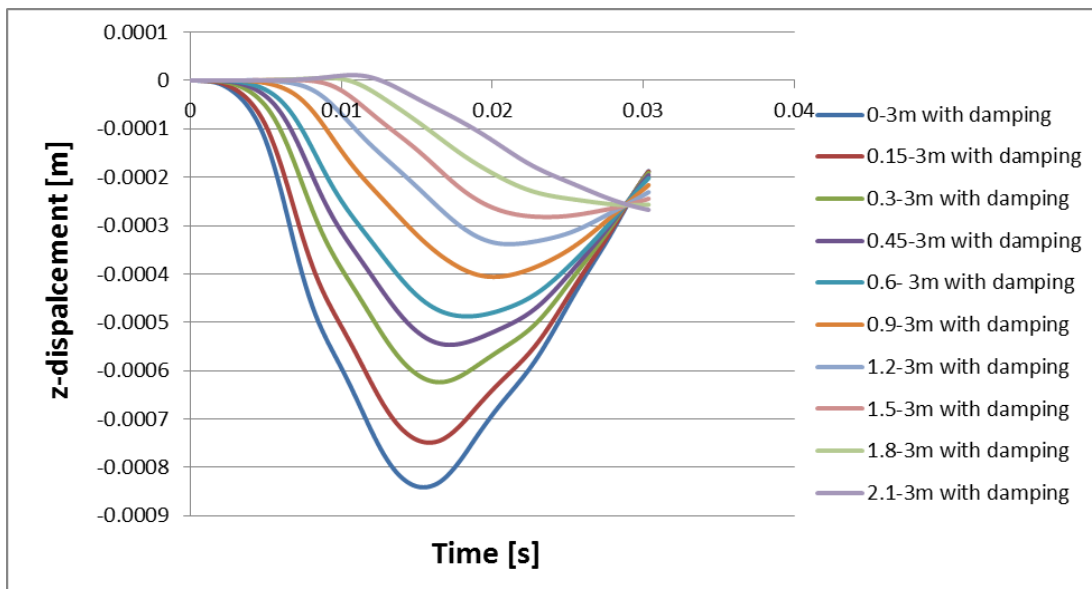


Fig. 5 Results of the model with the length 3 m and damping elements at the boundary

In the last picture there are compared the maximal values of displacement in the observed points for all three models. It seems that the first seven points have the same or very similar values but the next three points are different. In the first model with 3 meter long and common boundary conditions has the displacement in the last point bigger than the previous point. That is the result of the bounded waves. In the last model with damping elements is the same situation but the differences between these both points are not so big.

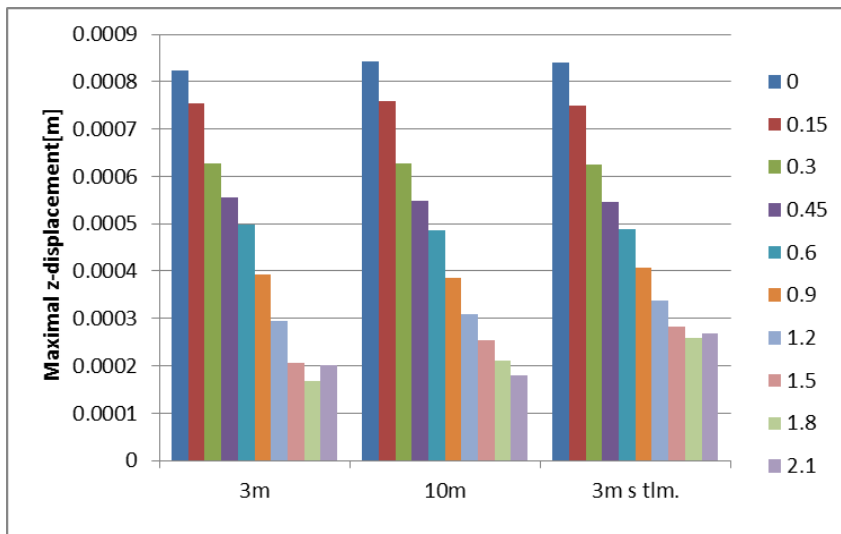


Fig. 6 Comparison of the maximal displacement for all three models

Conclusions

Preparing an effective numerical model which can describe the real conditions of the structure is very difficult or impossible. It is suitable to concentrate on the parts of model which could really spoil the results. Some of these parts are boundary conditions especially if the dynamic solution is done and the spreading of waves is the main goal of the solution. In this reason we have some possibilities like applying of viscous damping elements or create an extensive area where is not possible for waves to reach the end of this area. The comparison of models with different length and applied special boundary conditions was done. The result is that by applying special boundary condition it is possible to diminish the space of the model. The result for model 10 m long and 3m long with damping is very similar. However, there are small differences in the results especially for the points very close to the boarders of the model. To sum up, both have advantages or disadvantages what is clear from this article. One of the crucial parameter for the right choice is the time during which the solution would be done. In the case where only a short time solution is needed the application of an extensive area is recommended because of no influence of the boundary conditions on the results. But it is not possible for the case when the time of the solution is longer and the wave are bounded from the edge of the model. There is recommended to use viscous damping elements.

Acknowledgements

This contribution is the result of the research supported by GA MŠVVaŠ SR VEGA, grant num. 1/0259/12.

References

- [1] Adina Theory and modeling guide, ADINA 9.0.2, 2014
- [2] M. Decký, et all., Designing and budgeting of asphalt pavements, EDIS ŽU Žilina, 2010.
- [3] E.H. Dill, The Finite Element Method for Mechanics of Solids with ANSYS Applications, Taylor&Francis Group, 2012.
- [4] Yuanqiang Gai, Zhigang Cao, Honglei Sun, Changjie Xu. Dynamic response of pavements on poroelastic half-space soil medium to a moving traffic load, Computers and Geotechnics. 36 (2009) 52-60.
- [5] TP 3/2009, Design of flexible and semi-rigid pavements, Ministry of Transport, Posts and Telecommunications, Department of Road Transport and Roads, (In Slovak).

The Stress Analysis of the Industrial Fiber-Reinforced Concrete Slab on Elastic Subgrade Loaded by the Operational Loading

KORTIŠ Ján^{1, a *}

¹Department of Structural Mechanics, Faculty of Civil Engineering, University of Žilina,
Univerzitna 8215/1, 010 26 Žilina, Slovak Republic

^ajan.kortis@fstav.uniza.sk

Keywords: concrete slab, elastic subgrade, stress analysis, computer model

Abstract. Floors which are used for factory building are usually located in an environment where are expected to be used heavy vehicles and also heavy supplies stored on the floor. What means that these structures have to be designed to withstand the action of the forces. For that reason it is useful to do a numerical simulation followed by stress analysis and evaluation of results. The parametric study was done to compare the influence of different thickness and different characteristics of the subgrade on the values of stress in a concrete slab. It was loaded by forklifts and structures used for storage of material and products.

Introduction

The design of all structures has to meet two main goals. The first one is that the structure should be suitable for owners or someone who will use it for designed purposes. The second is a right proportion between the price and the design of the structure. While the purpose of the structure is well known at the beginning, the proportion between the design and the appropriate price is difficult to define. There are many factors which influence the final price such as selected materials or dimensions of the structure [1]. The right dimensions of the structure as well as using of appropriate material depend also on the certainty of engineers [2]. It means that well experienced engineers who have a lot of information about the real application can find better solution mainly if complicated circumstances are present.

The complex way for designing of structure should be used in these cases. But the computer models, which are useful and can help to optimize the design of the structure, need a lot of time and powerful computers for solutions of complex numerical models [3,4]. This is possible to do only for research but practical application has to be more effective and faster. For this reason, it is possible to do only a few complex numerical simulations. The rest of the optimization can be derived from them. This approach shows the influence of thickness of the slab and subgrade stiffness on the displacement and stress.

Model Description

The model is based on a real structure of the fiber-reinforced slab. It is divided into parts which are 6 m long and 6 m wide and each part acts independently. The designed loading was higher than the operational loading. The difference between loading for design and loading that is determined for real service is usually accepted because we have for many cases only poor information about the real physical characteristics of the structure. As a result it is needed to have higher carrying capacity to assure that there will not appear any failures. For that reason it was done another analysis to find out if the smaller thickness of the slab and the low stiffness of the subgrade could lead to a damage of the slab during the real service. The loading was defined as a pressure on a surface size of which is similar to the contact surface between the wheel and the slab. The value of pressure and relative distances between loading surfaces define one of the heaviest forklifts that could be used in the building with the fiber-reinforced slab.

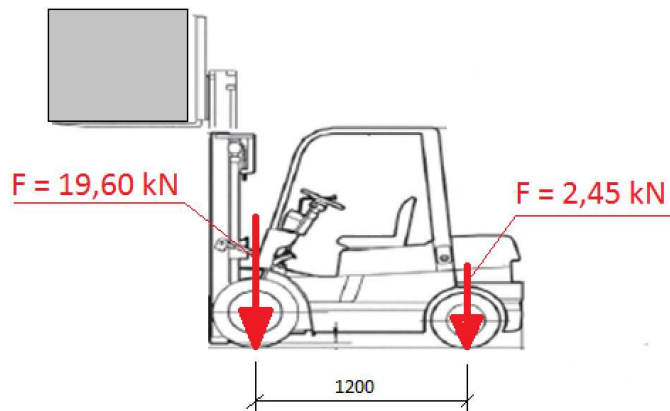


Fig. 1 The scheme of loaded forklift with defined forces for each wheel

The position of loading was changed during the time what simulates the movement of the loading vehicle. The inertial forces were also included, but their influence was very small. So we assume that the results are similar to the static analysis so the static loading was used for the following analysis. The response of the slab was analyzed by using maximum values of z -displacement and maximum values of effective stress. The position at the edge of the slab was identified as the most unfavorable. For that reason, the other results were obtained only for this position of the forklift.

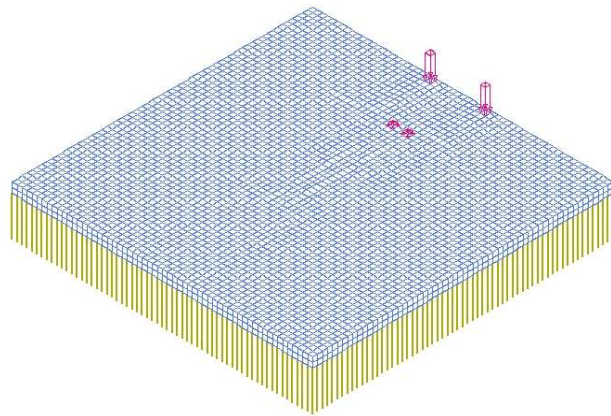


Fig. 2 The position of the forklift at the edge of the slab

Evaluation of Results

The z -displacements as well as values of effective stress depend mainly on the thickness of the slab and the stiffness of the subgrade. A parametric study, that was done, is based on the changing of mentioned parameters. The distribution of z -displacements is approximately the same for all cases, therefore it is easier and more effective to compare the influence only by comparison of the maximum values. It is the same for the values of effective stress.

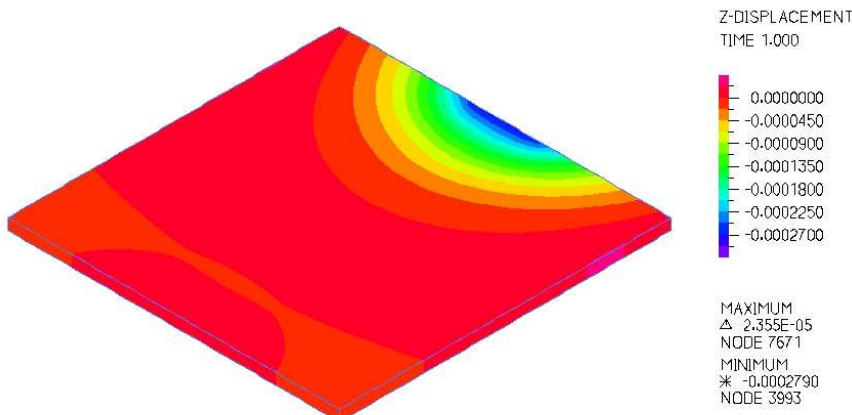


Fig. 3 The distribution of z -displacement

The comparison between the observed values showed the relation. The small inaccuracies especially for effective stress are caused by changing of the mesh density. It can be seen in the next Table 1 where the effective stress for thickness 0.12 m is lower than for the thickness 0.10. It is the result of different thickness of the slab. It also means that it is not valuable to do a solution with small steps between the values but for this case it is useful to do the solution only for the first and the last value.

Table 1 The maximum values of effective stress and z -displacement for model with different thickness and different modulus of subsoil reaction.

The modulus of subsoil reaction is 80 MPa			The thickness of the slab is 0.16 m		
Thickness of the slab [m]	Maximum values of the effective stress [MPa]	Maximum values of the z -displacement [mm]	Modulus of subsoil reaction [MPa]	Maximum values of the effective stress [MPa]	Maximum values of the z -displacement [mm]
0.10	2.87	0.515	40	3.28	0.552
0.12	2.20	0.440	60	2.68	0.423
0.14	2.37	0.425	80	2.32	0.341
0.16	2.32	0.341	100	2.06	0.292
0.18	2.15	0.307	120	1.87	0.257
0.20	2.02	0.279	140	1.72	0.231

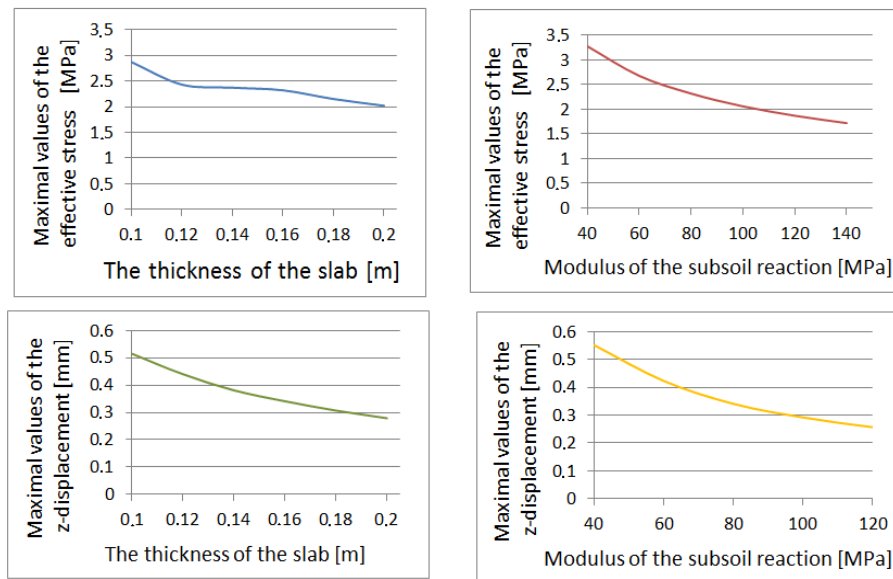


Fig. 4 Functions that show the maximum values of z -displacement and effective stress for different input data

Conclusions

The results of analysis show us that it is able to obtain results with good quality by using a simple numerical model. However, it is important to know what is possible to neglect and what is important to insert into the model to obtain results with good quality. For the case it seems that the inertial forces can be neglected if the smooth surface of the slab is there. There were the same results for dynamic and static analysis. It is also not important to do solution for many different physical characteristics of the model. There is needed to know only the results for the smallest and the largest input dimensions or other physical characteristics. Thanks this, the range was obtained and results were available for other input data. Then for better results the solution was done only for the conditions that were more valuable. To sum up, it is more useful way for practical tasks and it is also faster. There is also possibility to write a short program for leading of this procedure.

Acknowledgements

This contribution is the result of the research supported by GA MŠVVaŠ SR VEGA, grant № 1/0259/12.

References

- [1] O. Sucharda, J. Brožovský, Failure and Plasticity Conditions of Concrete in the Finite Element Analysis. *Applied Mechanics and Materials*. 367 (2013) 165-168.
- [2] Adina Theory and Modeling Guide.
- [3] A.M. Alani, D. Beckett, Mechanical Properties of a Large Scale Synthetic Fibre Reinforced Concrete Ground Slab, *Construction and Building Materials*. 41 (2013) 335-344.
- [4] E.H. Dill, *The Finite Element Method for Mechanics of Solids with ANSYS Applications*, Taylor&Francis Group, 2012.

Natural Frequencies of Railway Slab on Winkler Foundation

KUCHÁROVÁ Daniela^{1, a*}

¹University of Zilina, Univerzitna 1, 010 26 Zilina, Slovak Republic

^adaniela.kucharova@fstav.uniza.sk

Keywords: natural frequencies, railway slabs, Winkler foundation, numerical solution, approximation relations

Abstract. Natural frequencies and natural modes represent the basic dynamic characteristics of all dynamic systems. They define the dynamic individuality of dynamic system. It is useful to know approximate relations giving the results with adequate accuracy. The analysis of plates in contact with elastic foundation is the part of structural dynamic which demands hard numerical solutions. The submitted paper presents approximate relations enabling with satisfactory accuracy to carry out the assessment of natural frequencies of the slabs on elastic foundation at variable subgrade stiffness.

Slab on Winkler Foundation

Equation of motion of the thin slab on Winkler elastic foundation can be written in the following form

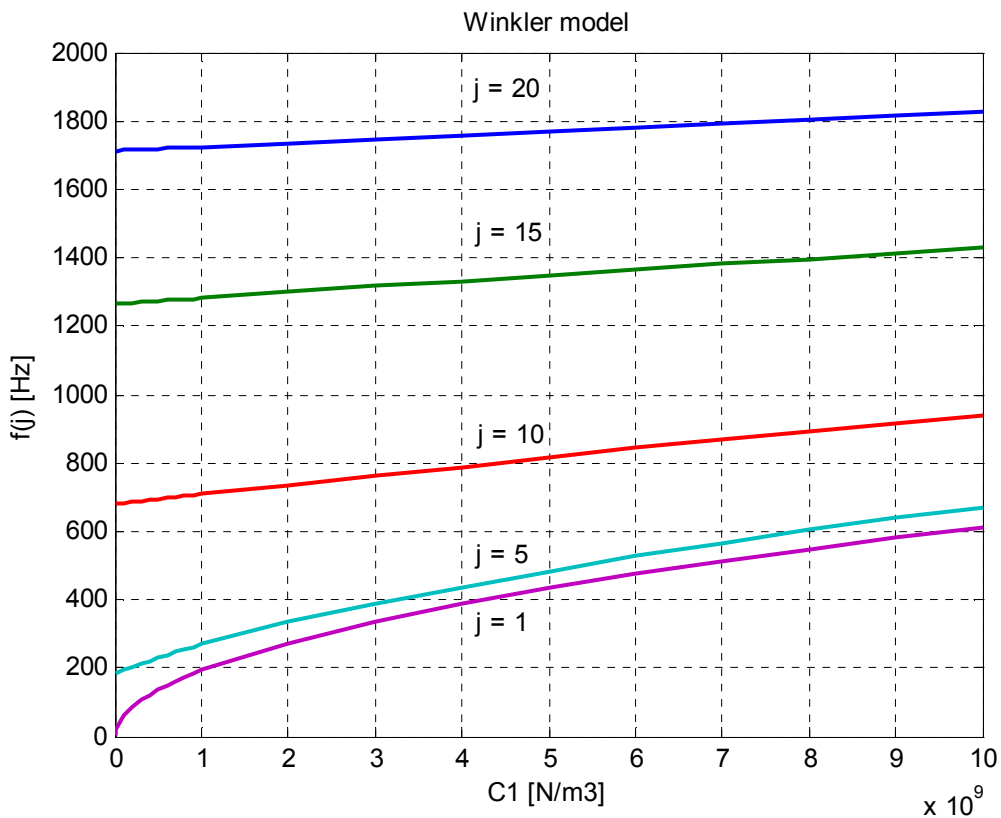
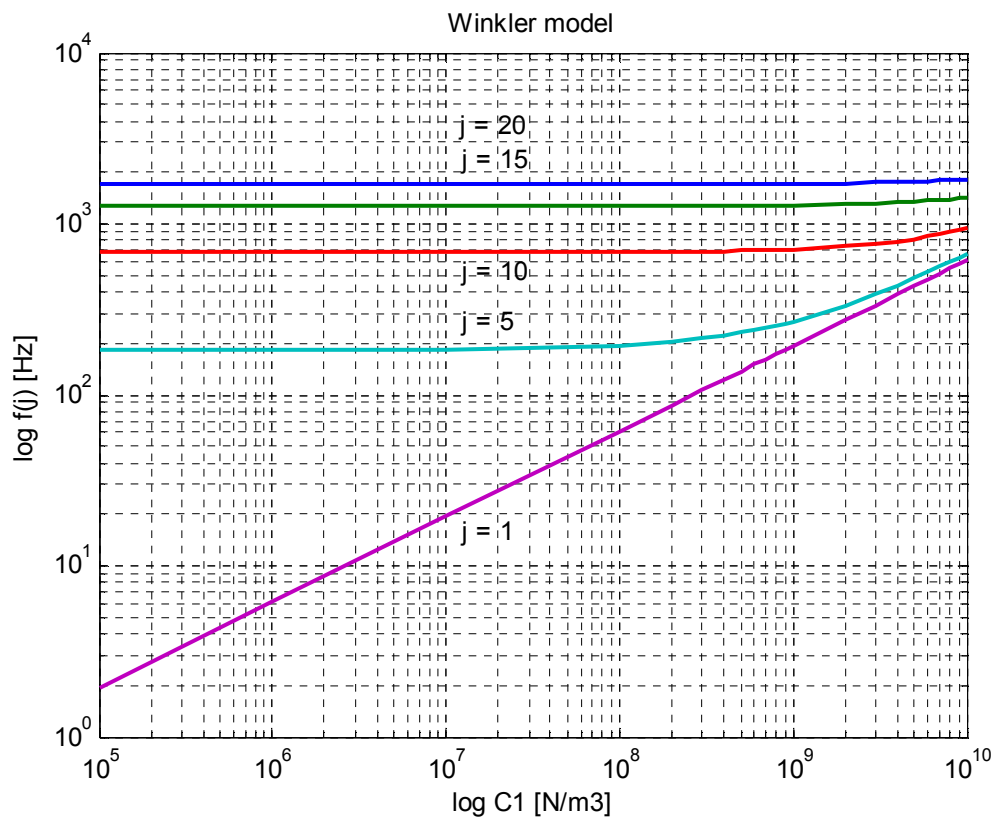
$$\mu \frac{\partial^2 w(x,y,t)}{\partial t^2} + D \nabla^4 w(x,y,t) + C_1 w(x,y,t) = p(x,y,t). \quad (1)$$

$w(x,y,t)$ represents the displacement of the point (x,y) of the slab middle surface in time t . D is slab stiffness and μ the planar mass density. There is no external load in the case of natural vibration so the term $p(x,y,t) = 0$. Eq. 1 has homogenous form. The best way of solving this equation at the present time is the solution on variation principle by the use of finite element method [1,2,3].

The subject of solution is a concrete slab on Winkler foundation. The slab dimension is $1\ 210 \times 2\ 300$ mm. Following dimensions $1\ 216 \times 2\ 280$ mm are taken into consideration because of the meshing of the slab. It was covered by the mesh of square finite elements with the dimensions 76×76 mm. The slab thickness h is 200 mm. The four node finite elements with nodes in corners are used. The solved area is covered by the mesh of $16 \times 30 = 480$ elements with 527 nodes. The material modulus of elasticity $E = 3.6 \times 10^{10}$ Nm $^{-2}$, Poisson ratio $\nu = 0.15$, mass density $\rho = 2\ 600$ kgm $^{-3}$, planar mass density $\mu = \rho h = 2\ 600 \times 0.20 = 520$ kgm $^{-2}$.

The object of the presented paper is to follow the influence of subgrade parameters on the natural frequencies of railway concrete slab. The subgrade stiffness stated by coefficient C_1 [N/m 3] in interval from 1.0×10^5 N/m 3 to 1.0×10^{10} N/m 3 was changed. The calculation was carried out for 22 values of coefficient C_1 . The results in graphical form are shown in the Fig. 1. In this figure, the dependences of $f_{(j)}$ on C_1 for $j = 1, 5, 10, 15, 20$ are presented.

The interesting dependence is obtained in the case of logarithmic scaling of axes X and Y as it is shown on the Fig. 2. The picture of functional dependence $f_{(1)}$ versus C_1 is the straight line.

Fig. 1 Natural frequencies $f_{(j)}$ versus C_1 , Winkler foundationFig. 2 Natural frequencies $f_{(j)}$ versus C_1 , logarithm scale, Winkler foundation

Derivation of Approximation Relations

It was found that similar relation as $f_{(1)}$ versus C_1 has the inverse function to the function

$$X = a \cdot Y^2 + c, \quad (2)$$

that is

$$Y = \sqrt{(X - c) / a}. \quad (3)$$

When we know the coordinates of two points in functional dependence $f_{(1)}(C_1)$, for example

$$\begin{aligned} X_1 = C_1 &= 1.0 \times 10^5 & Y_1 = f_{(1)} &= 1.940, \\ X_2 = C_1 &= 1.0 \times 10^{10} & Y_2 = f_{(1)} &= 612.1, \end{aligned}$$

we can calculate the unknown coefficients a, c in Eq. 2 respectively Eq. 3 from the solution of the system of two equations. We obtain these equations by putting the coordinates of these two points into Eq. 2.

$$\begin{aligned} 1.0 \times 10^5 &= a \times 1.940^2 + c \times 1, \\ 1.0 \times 10^{10} &= a \times 612.1^2 + c \times 1. \end{aligned} \quad (4)$$

The system (Eq. 4) in matrix form

$$[\mathbf{a}] \cdot \{\mathbf{n}\} = \{\mathbf{p}\}, \quad (5)$$

where $[\mathbf{a}]$ is matrix of coefficients

$$[\mathbf{a}] = \begin{bmatrix} 1.940^2 & 1.0 \\ 612.1^2 & 1.0 \end{bmatrix}, \quad (6)$$

$\{\mathbf{n}\}$ is the vector of unknown coefficients

$$\{\mathbf{n}\} = [a, c]^T \quad (7)$$

and $\{\mathbf{p}\}$ is the right hand side vector

$$\{\mathbf{p}\} = [1.0 \times 10^5; 1.0 \times 10^{10}]^T. \quad (8)$$

The solution of Eq. 5 can be written as

$$\{\mathbf{n}\} = [\mathbf{b}] \{\mathbf{p}\}, \quad (9)$$

where $[\mathbf{b}]$ is inverse matrix to matrix $[\mathbf{a}]$. Coefficients a, c have the following values

$$a = 2.66904109499185 \times 10^4, \quad c = -0.04520306511132 \times 10^4. \quad (10)$$

Approximation function has the form

$$Y = \sqrt{(X + 452.0306511132) / 266904109499185} \quad (11)$$

Summary

For the solution of this task and for displaying of obtained results the short program in MATLAB was created. The comparison of actual results with the results obtained by the approximation function (Eq. 11) is done in the Table 1. The obtained results shown that the maximal deviation between actual results and results obtained on the approximation function (Eq. 11) are less than 0.5 Hz. It is in percentage less than 0.24 % of actual value. The values obtained from the approximation function (Eq. 11) are less than actual value. The advantage of the knowledge of approximation function is that the value of the 1st natural frequency $f_{(1)}$ [Hz] versus C_1 [N/m³] need not be calculated by the Finite Element Method. It can be obtained very quickly and correctly by putting C_1 [N/m³] in stead of x in to the function (Eq. 11).

Table 1 Comparison of actual result with results obtained by approximation function

$X (C_1)$	$Y_{\text{act}} (f_{(1)})$	$Y_{\text{aprox}} (f_{(1)})$	deviation in %	$X (C_1)$	$Y_{\text{act}} (f_{(1)})$	$Y_{\text{aprox}} (f_{(1)})$	deviation in %
1.0×10^5	1.940	1.940	0.00	9.0×10^8	184.0	183.6	-0.21
1.0×10^6	6.134	6.122	-0.19	1.0×10^9	193.9	193.6	-0.15
1.0×10^7	19.40	19.36	-0.20	2.0×10^9	274.2	273.7	-0.18
1.0×10^8	61.34	61.21	-0.21	3.0×10^9	335.8	335.3	-0.14
2.0×10^8	86.75	86.56	-0.21	4.0×10^9	387.6	387.1	-0.12
3.0×10^8	106.2	106.0	-0.18	5.0×10^9	433.3	432.8	-0.11
4.0×10^8	122.7	122.4	-0.24	6.0×10^9	474.5	474.1	-0.08
5.0×10^8	137.2	136.9	-0.21	7.0×10^9	512.5	512.1	-0.07
6.0×10^8	150.2	149.9	-0.19	8.0×10^9	547.7	547.5	-0.03
7.0×10^8	162.3	161.9	-0.24	9.0×10^9	580.8	580.7	-0.01
8.0×10^8	173.5	173.1	-0.23	1.0×10^{10}	612.1	612.1	0.00

Acknowledgements

This contribution is the result of the research supported by the Grant National Agency VEGA, project G1/0259/12.

This contribution was created thanks to the support of Operational Programme Education for the Project „Support of the quality of education and research in the domain of transport serves as an engine of the economy“ (ITMS: 26110230076), which is co-financed from the sources of European Social Fund.

References

- [1] I. Němec, et al, Finite element analysis of structures, principles and praxis. Shaker Verlag, Aachen, 2010.
- [2] J. Králik, Program MEP2DO. Solution of elasto - plastic Mindlin plates by FEM on Winkler-Pasternak foundation (in Slovak). Pogramy MKP a MHR v ČSFR IV, 1991.
- [3] D. Kuchárová, Natural frequencies of railway plates (in Slovak). Zborník z konf. s medz. účasťou Staticko - konštrukčné a stavebno - fyzikálne problémy stavebných konštrukcií, T. Lomnica, hotel Urán, 22.-24.11.2000, IKC Košice, (2000), pp.108-112.

Influence of Construction of Railway Superstructure on Railway Quality

IŽVOLT Libor^{1, a}, IŽVOLTOVÁ Jana^{2, b} and ŠESTÁKOVÁ Janka^{1, c*}

¹University of Žilina, Faculty of Civil Engineering, Department of Railway Engineering,
Univerzitná 8215/1, SK-010 26 Žilina, Slovak Republic

²University of Žilina, Faculty of Civil Engineering, Department of Geodesy,
Univerzitná 8215/1, SK-010 26 Žilina, Slovak Republic

^alibor.izvolt@fstav.uniza.sk, ^bjana.izvoltova@fstav.uniza.sk, ^cjanka.sestakova@fstav.uniza.sk

Keywords: railway track, geometric location of the track, diagnostics

Introduction

Present railway operation has confirmed that the classic structure of the railway superstructure is capable to ensure operational capability of standard railway tracks for a relatively long period of time (railways tracks up to speed 160 kmh^{-1}). Such a railway track means a classic structure of the railway superstructure, where track removal is based on ballast. In case of high operating and axle loading, increasing speed and requirements for safety of operation, which are associated with high requirements on the track geometry, it appears that such a structure has its operational (in terms of guaranteeing the long-term safety and reliability of the railway track) and economic (in terms of the cost of maintenance of railway track) limits. "Floating" placement of the track removal during each passage of a rail vehicle, or train leads to the growth of dynamic horizontal and vertical forces that cause gradual degradation of track geometry, what subsequently leads to restless journey of moving rail vehicles. Elimination of imperfections in track geometry - the quality of the railway track - forces the operators to remove such imperfections of railway track in time and financially consuming maintenance work in certain periods. However, it is sufficient if only the weakest element of classic railway superstructure is replaced in the railway, and it is the track ballast using other more appropriate component representing no elastic and plastic behaviour. The structure is such replacement, in which the track removal is concreted (monolithic structure) or stored on concrete or asphalt bearing layer (layered structure), namely structural design, which is referred to as unconventional railway superstructure. The structure of railway superstructure is characterized by cross sleepers used in a modified shape or they are not part of it at all. Currently, thus conceived railway track is referred to as a slab track (hereinafter referred to as the "ST"), which requires flexibility of the railway superstructure for the system of the wheel/rail secured using elastic elements disposed between the rail and the sleeper and/or under the sleeper. In general, the structure of ST has been currently applied mainly to high-speed track and the tracks that have high operational load, where the cost of maintaining the track with the classic structure of the railway superstructure strongly grows. At the same time, however, this structure also promotes in the upgraded sections of the standard tracks (track speed to 160 kmh^{-1}), especially in track sections conducted in tunnels, as there are located the required properties of the ballast that do not demonstrate subsidence. The subgrade without a drop also offers for application of the ST structure bridges, and therefore, the application of this structure is also possible in these track sections.

Characteristics of the Test Section with the Unconventional Structure of Railway Superstructure

In connection with the modernization of the V. trans-European corridor Venezia - Trieste/Koper - Ljubljana - Budapest - Čop - Lvov, with the branch Va passing through the territory of the Slovak Republic in the area of Bratislava - Žilina - Košice - Čierna nad Tisou - Čop, under the construction of Railways of the Slovak Republic, Modernisation of railway track Nové Mesto nad Váhom - Púchov, km 100.500 – 159.100, object 24-32-01 Nové Mesto nad Váhom - Trenčianske Bohuslavice, proposed by project contractor (BIMING Consult, a. s.) and the client (Railways of

the Slovak Republic) was approved the ST structure of type RHEDA 2000®. After analyzing alternative solutions of the track conduction around Turecký vrch in the current railway track and a new route - tunnel variant - the builder decided for tunnel variant.

Railway tunnel Turecký vrch, which is part of the track section, is the first tunnel in Slovakia, which is designed and implemented according to technical specifications for interoperability for conventional tracks. The total length of the tunnel Turecký vrch in the axis is 1 775 m. Tunnel tube of the section mined has a length of 1 738.5 m and is followed by excavated sections of the south portal of length 25 m and the northern portal in the length of 10 m. Double track in the tunnel is designed for the speed of 200 kmh⁻¹ with reverse curves with a radius of 2 000 meters.

Due to the complex directional conditions and bridge buildings localized directly behind the north portal, the structure of ST is established not only in the tunnel, but it practically continues to railway station Trenčianske Bohuslavice on the north side of the tunnel. The total length of the ST structure built is up to 4 480 m of track. Due to the diversity of subgrade toughness (tunnel bottom, bridge and railway subgrade substructure), the system of the ST structure is modified, which is reflected in the thickness of the concrete structure and also in the reinforcements.

The structure of ST of RHEDA 2000® system is composed of its own monolithic ST structure, which in the present, track section is divided into 3 basic types:

- in the tunnel: monolithic reinforced concrete board of variable thickness (according to track elevation) - concrete of class C 35/45 with the two-block sleepers concreted, lying on the concrete bottom of the tunnel tube (in the place at the portals anchored to the underlying board of tunnel bottom),
- on soil formation: monolithic reinforced concrete board of constant thickness of 240 mm - concrete of class C 35/45 with the two-block sleepers concreted (also called TCL), lying on a monolithic board of plain concrete of class C 12/15 of constant thickness of 300 mm (also called HBL). Track elevation in the curves consists of an inclined track subgrade. There is the TLC board anchored to the HBL board in the place between the northern portal of the tunnel and the bridge over the stream Bošáčka.
- on bridges: monolithic reinforced concrete board of variable thickness (according to track elevation) - concrete of class C 35/45 with the two-block sleepers concreted, lying on the separation layer Styrodur+ foil on the structure of the bridge.

The critical place of the ST structure is its completion and transition to the classic structure of the railway superstructure. In terms of dynamic effects it is a place with a change in toughness and thus there was paid a special attention. There was used a new type of transition area using standard components of the railway superstructure, while without the need for stabilization of the railway superstructure within the transition area using sticking.

In view of the required quality characteristics and the lifetime declared the structure of ST, including its transition areas and adjacent sections with the classic structure of the railway superstructure, is monitored at regular intervals. Input measurements were performed always just before submission of the track into operation and subsequently implemented a six-month period (every spring and autumn of the year concerned). Monitoring is implemented by the Department of Railway Engineering and Track Management in cooperation with the Department of Surveying of Faculty of Civil Engineering of University of Žilina, in cooperation with the manager of railway infrastructure - Railways of the Slovak Republic (ŽSR) and its Research and Development Institute (VVÚŽ). Monitoring on both tunnel portals of Turecký vrch is focused on a complex diagnosis of the relative geometrical parameters of the track of the ST in the tunnel (length of 100 m) behind the portal, in the area of transition sections of the structure and in the classic structure of the railway superstructure (length of 100 m).

Preliminary Results of Monitoring of Track Geometry Quality - a Complex Diagnosis of the Relative Track Geometry

Diagnosis of relative track geometry has been implemented three times so far: in the track no. 1, section no. 1 (km 102.360 000 - km 102.535 000) and section no. 2 (km 104.200 000 - km 104.840 000) 03.10.2012 (measurement before putting sections into operation /MSO/), 09.04.2013 (first operational measurement /PO1/) and 08.10.2013 (second operational measurement /PO2/) and in the track No. 2, section No. 1 and section No. 2 10.07.2012 (MSO), 22.04.2013 (PO1) and 22.10.2013 (PO2).

Within the diagnosis of relative track geometry, which is implemented continuously using measuring device (measuring trolley KRABTM- Light), based on primarily measured values there are detected the following parameters: track gauge RK (mm), change of gauge ZR (mm/m), track elevation PK (mm), twist track, rated above the respective base ZK (mm/m), longitudinal vertical position of left and right rail VL, VP (mm), directional position of the left and right rail SL, SP (mm). Within the control of the diagnosis, which is implemented by spot (manual gauge ROBEL), there are observed deviation of the track gauge (mm) and track elevation (mm).

Diagnosing the section monitored in 2012 was carried out before putting the tracks no. 1 and 2 in operation. The impact of correction performance (grinding rails, horizontal and vertical adjustment of the track), implemented under maintenance operation of the manager between measurements in 2012 and 2013 were not considered in the evaluation of the relative track geometry.

The development of quality is shown in Table 1. Considering the detection of operational deviations the quality of direct section, or section in transition curve and arc is specifically evaluated according to [1]. Local errors of parameters measured are calculated separately for the section with the classic structure of the railway superstructure (CS), for the transition area and the section with a slab track (ST).

The Comparison of Measurements before Putting Experimental Section into Operation, the First Operational Measurement and the Second Operational Measurement

The difference of values of deviations of track gauge found in PO1 and MSO is in the interval from 1.27 mm in the track No. 2, section No. 1 to -0.74 mm in the track No. 1 section No. 2. The difference of values of deviations of track gauge in PO2 and MSO is in the interval from 1.67 mm in the track No. 2, section No. 2 to -2.57 mm in the track No. 2 section No. 2. The difference of values of deviations of track gauge in PO2 and PO1 ranges (excluding the section No. 2 in the track No. 2) at an average interval of about 0.3 mm. Higher values are found in all three subsections of the section No. 2 in track No. 2: in the section of the structure with a slab track, in the transition area and in the section with the structure of the track ballast. The values are in the interval from 0.92 mm in the track No. 2, section No. 2 to -3.05 mm in the track No. 2 section No. 2.

The difference of values of track elevation found in PO1 and MSO is in the interval from 3.36 mm in the track No. 1, section No. 2 to -5.27 mm in the track No. 2 section No. 2. The difference of values of track elevation found in PO2 and MSO is in the interval from 4.35 mm in the track No. 2, section No. 2 to -5.19 mm in the track No. 1 section No. 1. The difference of values of track elevation measured in PO1 and PO2 ranges at an average interval of about 1 mm. Higher values of track elevation differences occur in all three subsections of individual sections: the section with the structure of a slab track, and in the transition area in the section with the structure of the track ballast. The values are in the interval from 3.51 mm in the track No. 2, section no. 2 to -1.50 mm in the track No. 1 section No. 1.

Table 1 Quality of sections – relative track geometry

Stationing (km)	Railway superstructure	Directional conditions	MSO (03.10.2012)			PO1 (09.04.2013)			PO2 (08.10.2013)		
			Local errors	MQ	NQ	NQ _{max}	Local errors	MQ	NQ	NQ _{max}	Local errors
102.360000	CS sect. 1, No 1 Transition area sect. 1, No 1 ST sect. 1, No 1 102.535000	Direct section Transition curve and curve	9	1.15 1.55 2.3 0	0 0 0 0	0 0 0 0	1.66 2.12 3.6 2.87	0 0 0 1.59	0 0 0 0	1.19 2.10 3.6 2.19	1.18
102.460500			0								
102.480500			0								
102.487250			0								
102.535000			0								
104.200000	ST sect. 2, No 1 Transition area sect. 2, No 1 CS sect. 2, No 1 104.840000	Transition curve and curve Direct section	0	0.65 1.21 2.3 1	0 0 0 0	0 0 0 0	2.16 1.07 3.6 0.75	0 0 0 1.24	0 0 0 0	2.23 1.04 3.6 0.93	1.50
104.716000			0								
104.720000			0								
104.740000			0								
104.840000			1								
102.360000	CS sect. 1, No 2 Transition area sect. 1, No 2 ST sect. 1, No 2 102.535000	Direct section Transition curve and curve	10	0.92 1.38 2.3 0	0 0 0 0	0 0 0 0	1.05 1.53 3.6 2.30	0 0 0 1.29	0 0 0 0	0.81 1.55 3.6 2.93	1.51
102.460500			1								
102.480500			0								
102.487250			0								
102.535000			0								
104.200000	ST sect. 2, No 2 Transition area sect. 2, No 2 CS sect. 2, No 2 104.840000	Transition curve and curve Direct section	2	0.71 1.31 2.3 6	0 0 0 0	0 0 0 0	2.35 1.19 3.6 0.90	0 0 0 0	0 0 0 0	2.35 1.14 3.6 0.70	1.51 3.6 1.46 1.46
104.716000			2								
104.720000			0								
104.740000			0								
104.840000			6								

Geodetic Specialization of a Slab Track

Geodetic measurements were part of geometrical quality control of slab track, whose task was to monitor the spatial position of the track and its geometry, namely the control of directional conditions of the track and track gradient. An important part of the measurements was investigating the stability of a solid board structure of a slab track in defined sections of the route. Geodetic measurements were performed in the same track sections and in the same time periods as relative measurements, where there was separately determined the position and height of both tracks, based on the right railway belt towards stationing. Position measurements were made by universal stations TRIMBLE S8, TRIMBLE VX, with an accuracy of ± 0.3 mgon and $1 + 1$ ppm, or $1 + 2$ ppm and vertical measurements by levelling device LEICA NA 3003 with an accuracy of 0.40 mm. An essential part of control measurements was to check position and vertical stability of reference system stabilized around measured section, thus defined its accuracy. Position stability of the reference points are determined from the deviations of coordinates obtained by coordinate transformation in stage measurement at basic measurement procedure referred to in [8]. The critical value follows from the test of positional change measured and was set at twice the mean value of standard deviations observed in individual stage measurements:

$$|e_{\max}| > 2\bar{m}_T, \quad m_{Ti} = \sqrt{m_{xi}^2 + m_{yi}^2}. \quad (1)$$

When determining the positional accuracy of the measurements it was based on the value of fundamental coordinate deviation of the reference system $\bar{m}_{xy} \leq 0.015$ m so the control accuracy of measurement, according to Eq. 1 should not exceed the value $2\bar{m}_T = 0.030$ m. The elevation stability of the reference system was assessed by the method of Marčák and Kubaček [3], where the determination of the vertical remoteness of reference point from the reference line there was determined critical value as twice the standard deviation of elevation:

$$\begin{aligned} |e_{\max}| &> 2m_h, \quad m_h = m_0 \sqrt{L}, \\ m_0 &= 0,5 \sqrt{\frac{1}{n_R} \sum \frac{\rho^2}{R}} \end{aligned} \quad (2)$$

We have achieved the values of standard deviations in the section 1 and 2 $m_{h,juh} = 0.44$ mm and $m_{h,sever} = 0.37$ mm so the differences in elevations greater than twice of these values can be considered as vertical shifts, to the exclusion of remote measurements. The result of geodetic measurement are the gradient conditions of both track routes defined in the national reference system, directional conditions of the route, elevation of track belts and position and vertical changes of the route and solid board structure, obtained in the individual stage measurements. When determining the positional change of the route we were based on the comparison of stage position measurements of points of the track with realized directional conditions of the route found in after-use measurements, based on given values of arch radius parameters, transition parameters and the length of direct sections of track. There was tested transverse shift of point route on the positional change from its defined position, which should not exceed twice the critical value, resulting from the accumulation of secondary law of errors:

$$|q| \leq 2 \sqrt{m_s^2 + s^2 m_\omega^2 + \bar{m}_T^2}. \quad (3)$$

During the test of positional change of detailed point the greatest impact has the mean value of standard deviation Eq. 1, obtained in measurements in reference system in the individual stage measurements, because the values of precision measuring lengths m_s and angles m_ω in comparison with it, they have negligible value. From the calculated transverse shifts we can say that there has not been detected positional change of track belt points fitted with a solid board structure. The

average value of the transverse deviation of track belt point from defined position was 0.009 m. Vertical stability of both tracks in these sections was determined with respect to a line graders translated by reference system. In order to define the vertical shifts, we have set tolerance limits, according to Eq. 2, at twice the value of the standard deviation from the mean elevation. The elevation change of track mounted on a board structure has not been confirmed. There was detected decline of track No. 1 on standard railway structure in section 1 (km 102.360 – 102.485) compared with basic measurements by an average of -3.06 mm and the track No. 2 of -1.85 mm. There was recorded the expected change in the height of track route in section 2 in the standard structure in km 104.705 -104.820 on the track No. 1 of an average value -2.68 mm and track No. 2 of an average value -2.10 mm.

Conclusions

The results of continuous diagnostics of relative track geometry during the operation do not represent local errors of parameters in any of the sections diagnosed. The total numbers of quality (NQ) in the sections diagnosed slightly improved within the second operational measurement in 4 of the 8 subsections compared to the first operational measurement (maximum improvement is from 1.59 to 1.18) and slightly worsened in the other 4 subsections (maximum from 1.24 to 1.50). From the geodetic point of view, positional shifts of railway track mounted on a solid board structure have not been confirmed. Vertical shifts of railway track mounted on a solid board have not been shown and are within the measurement accuracy. There has been recorded decline in both tracks in the sections of the standard mounting of tracks.

Summary

The paper discusses the current results of monitoring of absolute track geometry on the classic and unconventional structure of the railway superstructure, including transitional areas using continuous device (measuring trolley KRAB™- Light) and geodetic methods (terrestrial measurements, precise levelling). Measurements are carried out at regular intervals in experimental section, which is part of a modernized track with a view to assessing the quality of track geometry.

Acknowledgements

There are presented partial results of solutions of grant VEGA 1/0597/14 "Analysis of measurement methods of unconventional railway from the point of view of accuracy and reliability" in the paper.

References

- [1] ŽSR SR 103-8 (S) General requirement on design, building, rebuilding, maintenance and acceptance of building, rebuilding and maintenance works on the slab track construction, Railways of the Slovak Republic, Bratislava, 2012.
- [2] D. Cebecauer, L. Bitterer, J. Štubňa, S. Hodas, Engineering surveys in transport building, University of Zilina, Zilina, 1998, 216 p.
- [3] P. Marčák, L. Kubáček, The Problem of System of Height Reference in Determining the Setting of Foundations and Buildings, Studia geophysica et geodaetica. 18 (1974) 33-46.
- [4] STN 73 0275 Accuracy of the geometrical parameters in construction. Supervisory measurement of line building objects, SÚTN, Bratislava, 1985 (alteration 1991).

Utilization of Multibody Simulations at the Verification of the Stabilizer Bar of the Trolleybus

POLACH Pavel^{1,a}

¹Výzkumný a zkušební ústav Plzeň s.r.o., Section of Materials and Mechanical Engineering Research, Tylova 1581/46, 301 00 Plzeň, Czech Republic

^apolach@vzuplzen.cz

Keywords: trolleybus, multibody model, dynamics, stabilizer bar, constructional design

Abstract. ŠKODA VÝZKUM s.r.o. (now Výzkumný a zkušební ústav Plzeň s.r.o.) cooperated on the development of the NEOPLAN DMA low-floor articulated trolleybus indented for the City of Boston. Multibody models and finite element models of the trolleybus were utilized in the stage of the vehicle design. The effect of using the rear section stabilizer on driving properties of the trolleybus was investigated utilizing the multibody simulations among others.

Introduction

Optimum dynamic properties of a vehicle intended for public transport can usually be achieved in dependence on its structural design by the proper choice of the suspension elements. The design must be the compromise of requirements for the vehicle behaviour during driving manoeuvres, for riding comfort and for the vehicle body and the chassis parts lifetime when driving on an uneven road surface, and for the passenger safety (e.g. [1]).



Fig. 1 The NEOPLAN DMA low-floor articulated trolleybus

The assessment of vehicle's dynamic properties is related to three essential motions: longitudinal motion (driving and braking), lateral motion (guidance and steering) and vertical motion (suspension and damping) [2]. Driving on an uneven road surface can reveal many facts about the vehicle vertical dynamical properties and about the suitability of the used suspension elements of axles. Start, braking and driving manoeuvres can give significant information about vehicle driving properties and handlings in the field of the horizontal dynamics.

In 2003 Neoplan USA Corporation, the American producer of buses and trolleybuses, started to develop the NEOPLAN DMA low-floor articulated trolleybus intended for the Boston city (see Fig. 1). ŠKODA VÝZKUM s.r.o. (now Výzkumný a zkušební ústav Plzeň s.r.o.) cooperated on the development of the trolleybus. Multibody models and finite element (FE) models of the trolleybus were utilized in the stage of the trolleybus design. The multibody models of the trolleybus (empty and fully loaded) were created in the *alaska* simulation tool [3].

The effect of using the rear section stabilizer on the driving properties of the trolleybus was investigated besides utilizing the multibody simulations among others. Severe double lane-change manoeuvres (according to ISO 3888-1) and selected (more demanding) documented test drives with the ŠKODA 22 Tr low-floor articulated trolleybus focused on the driving stability evaluation (on the basis of these test drives the suitability of the constructional design of the stabilizer bar of the rear section of this trolleybus was confirmed) were simulated with the multibody models of both empty and fully loaded trolleybus [4]. Simulations were carried out with the multibody models without the stabilizer bar and with two considered variants of the construction design of the rear section stabilizer bar. Results of simulations were used for the evaluation of the stabilizer bar construction design effect on the improvements in the driving stability of the trolleybus.

Multibody Models of the Articulated Trolleybus

In order to obtain a tool for dynamic analysis (e.g. [5,6]) multibody models of an empty (21 tons weight) and a fully loaded (31 tons weight) NEOPLAN DMA low-floor articulated trolleybus were created [7,8] (Fig. 2). As it has been already mentioned, the multibody models were created in the *alaska* 2.3 simulation tool [3].

Multibody models of the NEOPLAN DMA trolleybus are formed by 54 rigid bodies mutually coupled by 63 kinematic joints. The number of degrees of freedom of multibody models in kinematic joints is 164. The multibody models description and kinematic scheme of the multibody model are given in [7,8].

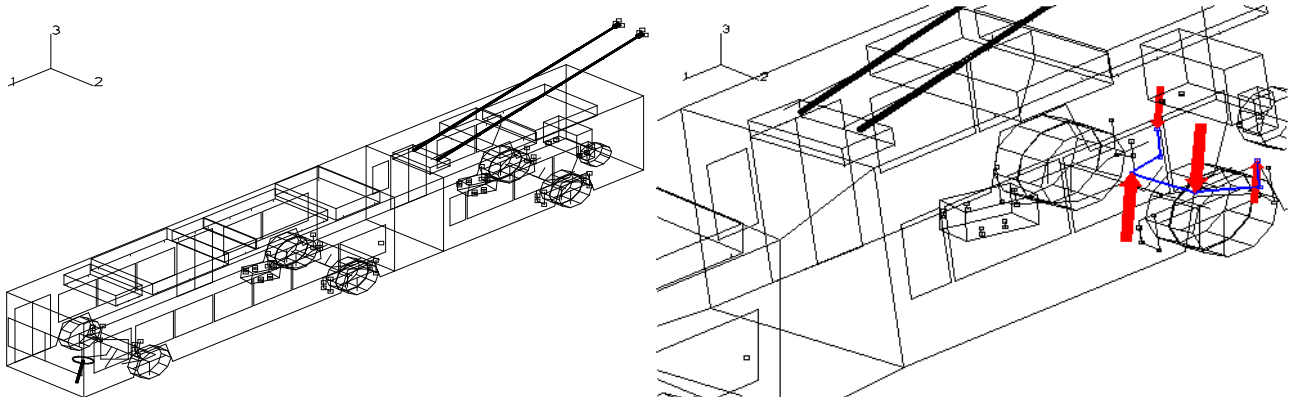


Fig. 2 Simple visualization of the NEOPLAN DMA trolleybus multibody model and visualization of the stabilizer bar detail (points of external force action) in the *alaska* 2.3 simulation tool

The rigid bodies correspond to the trolleybus individual structural parts and are defined by mass, centre of gravity coordinates and mass moments of inertia. Air springs and hydraulic shock absorbers in axles' suspension and bushings in the places of mounting certain trolleybus structural parts are modelled by connecting the corresponding bodies by nonlinear spring-damper elements. The stationary tire model is used to describe the directional properties of the tires.

In the multibody models of the NEOPLAN DMA articulated trolleybus the rear section stabilizer bar is not considered to be an individual rigid body, its function is modelled by the external forces acting on the rear section chassis frame and the rear axle. The forces acting against the rear section roll angle and their points of action are in the positions of mounting the stabilizer bar to the rear section chassis frame and the rear axle (see Fig. 2). A linear dependence is considered between the magnitudes of the forces and the stabilizer bar deformations. Magnitudes of the forces are

dependent only on the rear section roll angle, vertical displacements between the rear section chassis frame and the rear axle do not influence their magnitudes at all (this fact is given by the used structural design of the stabilizer bar) [7].

Generally, the aim of the simulations with the multibody models of the NEOPLAN DMA low-floor articulated trolleybus is the determination of time histories or FFT results of time histories of monitored kinematic and dynamic quantities in the course of the chosen operational situation.

Simulation of a Severe Double Lane-change Manoeuvre

Fifteen sets of test drives [4] were simulated with the multibody models of the empty and the fully loaded trolleybus: ten times the severe double lane-change manoeuvre according to ISO 3888-1 and five times selected documented test drives with the ŠKODA 22 Tr low-floor articulated trolleybus. In this paper results of the simulations of the severe double lane-change manoeuvre according to ISO 3888-1 with the trolleybus at speed 50 km/h are presented.

The severe double lane-change manoeuvre according to ISO 3888-1 is a widespread testing method for a subjective evaluation of the dynamic properties of the road vehicles. The scheme of the test track, which must be run through, is in Fig. 3. The overall track length in case of the double lane-change manoeuvre according to ISO 3888-1 is 125 m, the individual track sections width is dependent on the vehicle width.

Two variants of the construction design of the rear section stabilizer differ in the diameter of the steel rods of the circle section used for its production (42 mm or 45 mm), construction design itself and the place of mounting to the rear section and the rear axle are identical. Maximum permitted vertical deformations of the stabilizer bar on both sides are 61.2 millimetres [4,7].

When simulating a dry road surface without vertical unevennesses is considered.

For the simulation of the test drives with the trolleybus multibody models the driving approach using a so called “mean wheel” (according to the Ackermann principle – e.g. [9]) was applied. The trajectories of a motion of the “mean wheel”, i.e. of the fictitious wheel with the centre of the wheel trace in projection of the centre of the steering front axle to the road, were the tracks trajectories of the real bus. The “mean wheel” steering angle is determined on the basis of the tangent slope to the trajectory of the “mean wheel” motion in the given time and on the basis of the deviation of the “mean wheel” position from the trajectory in the given time. The weight of the influence of the deviation of the “mean wheel” position from the trajectory of motion in the given time is optional and thus the driver reaction time can be set. In dependence on the “mean wheel” steering angle the instantaneous steering angles of the wheels of the steered front axle (or its knuckle pins) are determined in the trolleybus multibody models (e.g. [4,10,11]).

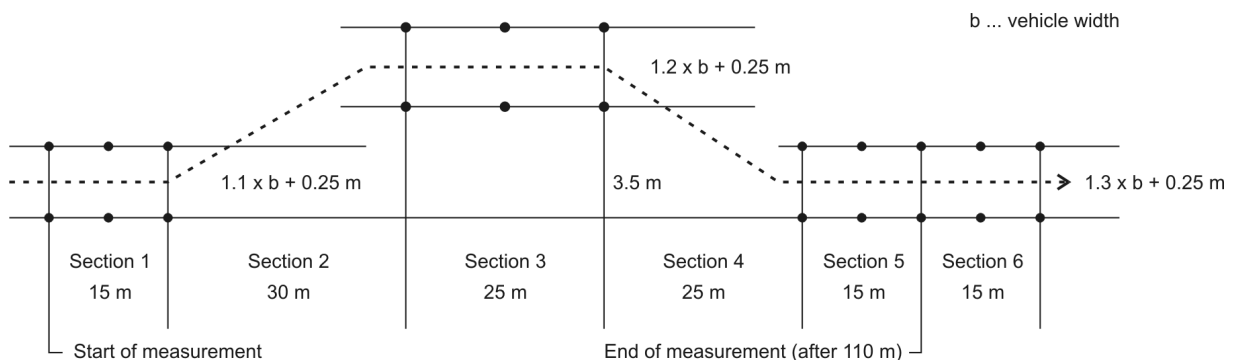


Fig. 3 Scheme of the test track for the severe double lane-change manoeuvre according to ISO 3888-1 [12]

The simulations were performed with the multibody models of the trolleybus both with the empty and the fully loaded vehicle and both with and without the rear section stabilizer bar. The monitored quantities were the same as at development of the stabilizer bar of the ŠKODA 22 Tr articulated trolleybus (e.g. [10,13]): the time histories and the extreme values of the angle of mutual

position of the trolleybus front and rear sections, the rear section roll angle, the lateral acceleration of the rear section above the rear axle, the relative deflections of the rear axle suspension and of the torsional deformation of the articulated joint. Further during the simulations with the trolleybus multibody models with the rear section stabilizer the extreme values of the time histories of the stabilizer bar vertical deformation were monitored.

The time histories of the rear section roll angle and torsional angle of the articulation at the simulations of the severe double lane-change manoeuvre according to ISO 3888-1 are given in Fig. 4 and Fig. 5. The values of the angles in all the graphs are given in degrees.

The time histories of the monitored quantities are of the positive values in accordance with the orientation of the axes of the right hand Cartesian system of coordinates "123" from Fig. 2.

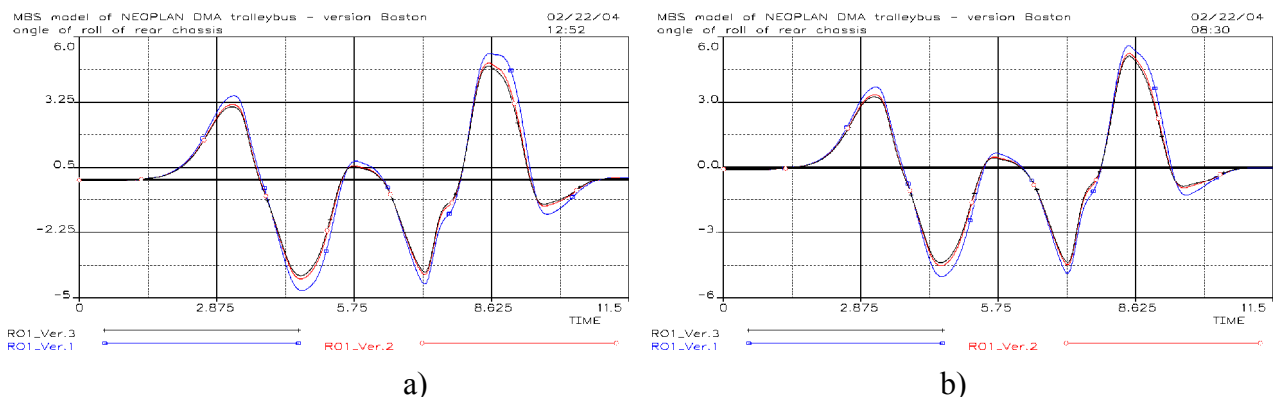


Fig. 4 Time histories of the rear section roll angle during the simulations of the severe double lane-change manoeuvre according to ISO 3888-1 at speed 50 km/h (RO1_ver.1 – without a stabilizer bar, RO1_ver.2 – with a stabilizer bar of diameter 42 mm, RO1_ver.3 – with a stabilizer bar of diameter 45 mm): a) empty trolleybus; b) fully loaded trolleybus

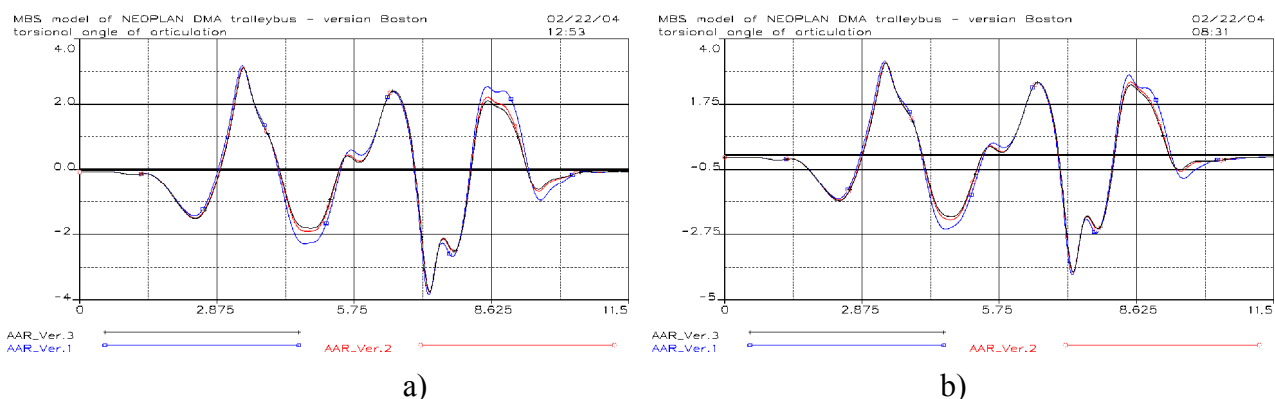


Fig. 5 Time histories of the torsional angle of the articulation during the simulations of the severe double lane-change manoeuvre according to ISO 3888-1 at speed 50 km/h (AAR_ver.1 – without a stabilizer bar, AAR_ver.2 – with a stabilizer bar of diameter 42 mm, AAR_ver.3 – with a stabilizer bar of diameter 45 mm): a) empty trolleybus; b) fully loaded trolleybus

Conclusions

Severe double lane-change manoeuvres (according to ISO 3888-1) and selected (more demanding) documented test drives with the ŠKODA 22 Tr low-floor articulated trolleybus focused on the driving stability evaluation were simulated with the multibody models of both the empty and the fully loaded NEOPLAN DMA trolleybus. Simulations were performed with the multibody models without the stabilizer bar and with two considered variants of the construction design of the rear section stabilizer bar. Results of simulations were used for the evaluation of the stabilizer bar construction design effect on the improvements in the driving stability of the trolleybus [4].

The following pieces of knowledge can be derived from the results of the severe double lane-change manoeuvres according to ISO 3888-1 and from the selected test drives with the ŠKODA 22 trolleybus:

1. The NEOPLAN DMA trolleybus has, on the basis of loading characteristics of the air springs, relatively rigid axles suspension, the consequence of which are small relative deflections in the course of air springs compression. When simulating any driving manoeuvre no relative deflections of the rear air springs, which would cause the contact of the rear section chassis and the air spring bump stops, were recorded (i.e. relative deflections smaller than -0.071 m [7]). No state, in which the rear shock absorbers could be damaged (i.e. relative deflections of the rear air springs greater than 0.103 m [7]), was identified in a rebound stage. Thus because of the possible "bump" of the rear section chassis to the air springs bump stops or the rear shock absorbers damage the stabilizer bar using would not be necessary. When simulating the severe double lane-change manoeuvre according to ISO 3888-1 (altogether 10 test drives [4]) and the stabilizer bar made of the steel rod of the circular section of diameter 42 mm is used the absolute maximum relative deflections of the rear air springs are decreased by 14.1 % on the average. When the stabilizer bar of diameter 45 mm is used the absolute maximum relative deflections are decreased by 17.6 % on the average. When simulating the selected test drives (altogether 5 tested situations [4]) and the stabilizer bar of diameter 42 mm is used the absolute maximum relative deflections of the rear air springs are decreased by 15.3 % on the average, when the stabilizer bar of diameter 45 mm is used the absolute maximum relative deflections are decreased by 19.1 %.
2. Nor rear section roll angle decreasing would be the reason for using the stabilizer bar in construction of the NEOPLAN DMA trolleybus. When simulating the severe double lane-change manoeuvre according to ISO 3888-1 and the stabilizer bar of diameter 42 mm is used the absolute maximum rear section roll angle is decreased by 8.5 % on the average, when the stabilizer bar of diameter 45 mm is used the absolute maximum rear section roll angle is decreased by 11 % on the average. When simulating the selected test drives and the stabilizer bar of diameter 42 mm is used the absolute maximum rear section roll angle is decreased by 11.1 % on the average, when the stabilizer bar of diameter 45 mm is used the absolute maximum rear section roll angle is decreased by 14 % on the average.
3. The maximal torsional deformation of the articulation recommended by its producer (the HÜBNER GmbH) is 3° [7]. When simulating the severe double lane-change manoeuvre according to ISO 3888-1 and the stabilizer bar of diameter 42 mm is used the absolute maximum torsional deformation of articulated joint is decreased by 2.1 % on the average, when the stabilizer bar of diameter 45 mm is used the absolute maximum torsional deformation of articulated joint is decreased by 2.8 % on the average. When simulating the selected test drives and the stabilizer bar of diameter 42 mm is used the absolute maximum torsional deformation of articulated joint is decreased by 4.7 % on the average, when the stabilizer bar of diameter 45 mm is used the absolute maximum torsional deformation is decreased by 6.1 % on the average.
4. When simulating driving manoeuvres with the multibody models of the NEOPLAN DMA trolleybus with the designed rear section stabilizer (disregarding the variant) time histories and extreme values of the angle of mutual position of the front and rear sections and of the lateral acceleration of the rear section above the rear axle almost do not differ from time histories and extreme values found during the simulations with multibody models of the trolleybus without the stabilizer bar.
5. When simulating driving manoeuvres with the multibody models of the NEOPLAN DMA trolleybus with the designed rear section stabilizer bar the variant with the stabilizer bar of diameter 45 mm does not influence substantially the change in time histories and magnitude of extreme values of the monitored quantities comparing the variant of the stabilizer bar of diameter 42 mm.
6. When simulating all the mentioned driving manoeuvres with the multibody models of the NEOPLAN DMA trolleybus with the designed rear section stabilizer the maximum permitted deformation of the stabilizer bar was not exceeded.

On the basis of pieces of knowledge from simulating the mentioned driving manoeuvres, despite not a fully sufficient effect completing the construction of the NEOPLAN DMA low-floor articulated trolleybus by the stabilizer bar of the rear section made of a steel rod of the circular cross-section of diameter 42 mm has been recommended. The aim of the stabilizer bar mounting is especially decrease in the torsional deformations and thus also in stress of the articulated joint.

Acknowledgement

The paper has originated in the framework of institutional support for the long-time conception development of the research institution provided by Ministry of Industry and Trade of the Czech Republic.

References

- [1] G. Genta, L. Morello, The Automotive Chassis, Volume 2: System Design, Springer Science+Business Media B.V., 2009.
- [2] K. Popp, W. Scheihen, Ground Vehicle Dynamics, Springer-Verlag, Berlin Heidelberg, 2010.
- [3] P. Maißer, C.-D. Wolf, A. Keil, K. Hendel, U. Jungnickel, H. Hermsdorf, P. A. Tuan, G. Kielau, O. Enge, U. Parsche, T. Härtel, H. Freudenberg, *alaska*, User Manual, Version 2.3, Institute of Mechatronics, Chemnitz, 1998.
- [4] P. Polach, Verification of the Influence of the Rear Carriage Sway Bar on the Drive Properties of the NEOPLAN DMA Low-floor Articulated Trolleybus Using Multibody Simulations, Research Report, ŠKODA VÝZKUM s.r.o., VYZ 0691/2004, Plzeň, 2004.
- [5] M. Blundell, D. Harty, The Multibody Systems Approach to Vehicle Dynamics, Elsevier Butterworth-Heinemann, Oxford, 2004.
- [6] S. Hegazy, H. Rahnejat, K. Hussain, Multi-Body Dynamics in Full-Vehicle Handling Analysis under Transient Manoeuvre, Vehicle System Dynamics. 34 (2000) 1-24.
- [7] P. Polach, Multibody Models of the NEOPLAN DMA Low-floor Articulated Trolleybus and Simulations of Selected Operational Situations for FEM Calculations, Research Report, ŠKODA VÝZKUM s.r.o., VYZ 0689/2004, Plzeň, 2004.
- [8] P. Polach, Utilization of Multibody Simulations at the Trolleybus Development, Manufacturing Technology, 13 (2013) 515-520.
- [9] O. Noréus, Modelling of Six-Wheeled Electric Transmission Terrain Vehicle, Licentiate Thesis, Royal Institute of Technology, Stockholm, 2007.
- [10] P. Polach, Verification of the Stabilizer Bar of an Articulated Trolleybus at the Severe Lane-Change Manoeuvre Simulation, in: J. Melcer (Ed.), Proceedings of the 4th International Conference on Dynamics of Civil Engineering and Transport Structures and Wind Engineering DYN-WIND'2008, University of Žilina, Papradno – Podjavorovník, 2008, pp. 137-142.
- [11] P. Polach, J. Václavík, Investigation of Lateral Dynamics of Triple Hybrid Hydrogen Bus, in: Z. Dimitrovová, J. R. de Almeida, R. Gonçalves (Eds.), Proceedings of the 11th International Conference on Vibration Problems, Associação Portuguesa de Mecânica Teórica, Aplicada e Computacional, Lisbon, USB flash drive, 2013.
- [12] Information on http://www.handling.cz/stranky/isotest_en.htm
- [13] P. Polach, Verification of the Stabilizer Bar of an Articulated Trolleybus, Engineering Mechanics. 15 (2008) 19-32.

Dynamic Time-History Response of Cylindrical Tank Considering Fluid - Structure Interaction Due to Earthquake

KOTRASOVÁ Kamila^{1,a*}, GRAJCIAR Ivan^{2,b} and KORMANÍKOVÁ Eva^{1,c}

¹Faculty of Civil Engineering TU, Vysokoškolská 4, 040 01 Košice, Slovak Republic

²Ricardo Prague, s.r.o., Czech Republic

^akamila.kotrasova@tuke.sk, ^bivan.grajciar@ricardo.com, email, ^ceva.kormanikova@tuke.sk

Keywords: cylindrical tank, earthquake, FEM, fluid – structure interaction

Abstract. Ground-supported cylindrical tanks are used to store a variety of liquids. The fluid develops a hydrodynamic pressures on walls and bottom of the tank during earthquake. This paper provides dynamic time-history response of concrete open top cylindrical liquid storage tank considering fluid-structure interaction due to earthquake. Numerical model of cylindrical tank was performed by application of the Finite Element Method (FEM) utilizing software ADINA. Arbitrary-Lagrangian-Eulerian (ALE) formulation was used for the problem analysis. Two way Fluid-Structure Interaction (FSI) techniques were used for the simulation of the interaction between the structure and the fluid at the common boundary.

Introduction

Large-capacity ground-supported cylindrical tanks are used to store a variety of liquids, e.g. water for drinking and fire fighting, petroleum, chemicals, and liquefied natural gas. Satisfactory performance of tanks during strong ground shaking is crucial for modern facilities. Tanks that were inadequately designed or detailed have suffered extensive damage during past earthquakes [2,4,6,7, 12].

The seismic analysis and design of liquid storage tanks is, due to the high complexity of the problem, in fact, really complicated task. Number of particular problems should be taken into account, for example: dynamic interaction between contained fluid and tank, sloshing motion of the contained fluid; and dynamic interaction between tank and sub-soil. Those belong to wide range of so called fluid structure interactions (FSI). The knowledge of pressures acting onto walls and the bottom of containers, pressures in solid of tanks, liquid surface sloshing process and maximal height of liquid's wave during an earthquake plays essential role in reliable and durable design of earthquake resistance structure/facility - tanks.

FEM - Fluid Structure Interaction of Liquid Filled Tanks

Seismic design of cylindrical liquid storage tanks has been adopted in [4,5,12]. The problem of fluid-structure interaction is very important in case of high tanks. The motion of fluid in the tank is possible to define using the simple quasistatic model, in which the inertial forces are defined by hydrostatic and hydrodynamic pressure on the tank wall.

Variety methods of discretization of the physical domain invented in the past gives the possibility to build more precise model. Finite element method (FEM) seems to be the most appropriate approach for such an investigation.

For the fluid-structure interaction analysis three different finite element approaches to represent the fluid motion are possible, Eulerian, Lagrangian and mixed methods. In the Eulerian approach, the velocity potential (or pressure) is used to describe the behaviour of the fluid, whereas the displacement field is used in the Lagrangian approach. In the mixed approaches, both the pressure and displacement fields are included in the element formulation.

In fluid-structure interaction analyses, fluid forces are applied into the solid and the solid deformation changes the fluid domain. For most interaction problems, the computational domain is divided into the fluid domain and solid domain, where a fluid model and a solid model are defined respectively, through their material data, boundary conditions, etc. The interaction occurs along the interface of the two domains. Having the two models coupled, we can perform simulations and predictions of many physical phenomena.

In many fluid flow calculations, the computational domain remains unchanged in time. Such problems involve rigid boundaries and are suitably handled in the Eulerian formulation of equilibrium equations [1, 3, 5, 8-12]. In the case where the shape of the fluid domain is expected to change significantly, modified formulation called Arbitrary Lagrangian-Eulerian (ALE) formulation was adopted to simulate the physical behaviour of the domain of interest properly. The ALE description is designed to follow the boundary motions rather than the fluid particles. Thus, the fluid particles flow through a moving FE-mesh. Basically, there are two different algorithms available for the generation of possibly moving mesh:

1. Remeshing of fluid domain, which is computationally expensive procedure.
2. Rezoning of FE-mesh of fluid domain. This procedure is quite fast while precise enough if no dramatic, changes of fluid domain is expected.

Governing Equations. Dynamic equilibrium of fluid domain involving effect of moving mesh is described by the modified Navier-Stokes equations. Let us assume temperature independent problem. Then the balance of momentum by ALE formulation is

$$\rho \left[\frac{\partial \mathbf{v}}{\partial t} + (\mathbf{v} - \mathbf{v}_b) \cdot \nabla \mathbf{v} \right] = \nabla(-p \mathbf{I} + \boldsymbol{\tau}) + \rho \mathbf{g}, \quad (1)$$

where ρ is the density of fluid, \mathbf{v} is the velocity of fluid, \mathbf{v}_b is the velocity of moving FE-mesh, p is the fluid pressure, \mathbf{I} is the identity matrix, $\boldsymbol{\tau}$ is the stress tensor and \mathbf{g} is the gravity acceleration. Dynamic equilibrium of the solid domain governs balance of momentum, e.g. in Cauchy form it is $\operatorname{div} \boldsymbol{\tau} + \rho_0(\mathbf{b} - \ddot{\mathbf{u}}) = 0$, where ρ_0 is the density of solid in an initial configuration, \mathbf{u} is the displacement, \mathbf{b} is the body load, $\boldsymbol{\tau}$ is the stress tensor. Together with traditional boundary conditions defined for the fluid domain (pressure and velocity), additional special conditions are considered: free surface, the interface between the fluid and gas and FSI boundary, common boundary between the solid and fluid.

Fluid Domain, Free Surface, Boundary conditions. Dynamic boundary condition for free surface express balance of forces between interactive forces of liquid and gas are $\mathbf{f}_l \cdot \mathbf{n} + \sigma K = -\mathbf{f}_g \cdot \mathbf{n}$, $\mathbf{f}_l \cdot \mathbf{t} + \sigma K = -\mathbf{f}_g \cdot \mathbf{t}$ and $\mathbf{f}_l \cdot \mathbf{s} + \sigma K = -\mathbf{f}_g \cdot \mathbf{s}$, where \mathbf{f}_l resp. \mathbf{f}_g are forces exerted by liquid, resp. gas, \mathbf{t} and \mathbf{n} are the tangent and normal to FSI surface and \mathbf{s} is the surface tension (if present). Kinematic boundary condition state that the velocity at a point of free surface moves together with point of FE-mesh. Thus $(\mathbf{v} - \mathbf{v}_b) \cdot \mathbf{n} = 0$.

FSI Boundary, conditions. The Dynamic boundary condition defines stresses at the common FSI boundary which are opposite and equal $\sigma_f = \sigma_s$. The kinematic boundary condition assumes velocities and displacements of the FSI boundary to be the same, i.e. $\mathbf{v}_f = \mathbf{v}_s$ and $\mathbf{u}_f = \mathbf{u}_s$, where indexes f, s stand for fluid and solid, respectively.

Discretization by Finite Elements. Any of unknown physical variables in the Finite element method is expressed in terms of nodal values instead of field value. That causes local discontinuity of the problem, but globally, with regards to the whole FE model all governing equations are satisfied.

Unknown variables (displacement, velocity and pressure) are approximated using so called shape functions \mathbf{N} . $\hat{\mathbf{u}} = \mathbf{N} \mathbf{U}$, $\hat{\mathbf{v}} = \mathbf{N} \mathbf{V}$, $\hat{\mathbf{p}} = \mathbf{N} \mathbf{P}$, where \mathbf{U}, \mathbf{V} , resp. \mathbf{P} are nodal values of initially unknown fields, \mathbf{N} are shape functions.

Applying one of the appropriate variation principles, governing equations are transformed into integral form, in which interpolations are easily incorporated and in numerical calculation. As the governing equations are basically nonlinear and time dependent, an appropriate linearization should be used together with a discretization in time domain. Plenty of methods by linearization and time discretization were published in the past. ADINA has implemented some of the most popular once [5,12].

Numerical Experiment and Conclusion

Let us have a ground supported circular tank with the following dimensions: mean radius $R = 7.0$ m and the height of walls $H_w = 7.5$ m. Tank's surrounding walls have the uniform thickness of 0.25 m. The base slab of the channel is $h = 0.4$ m thick. Circular tank is filled with water up to the height of 7.0 m. The water filled tank is grounded on a hard soil. The following material characteristics of tank are: Young's modulus $E = 35$ GPa, Poisson ratio $\nu = 0.20$, density $\rho = 2550$ kg/m³. Seismic excitation acts along the y -direction. As the excitation input we consider a horizontal earthquake load given by the accelerogram (Fig. 4) of the earthquake in Loma Prieta, California (18.10.1989).

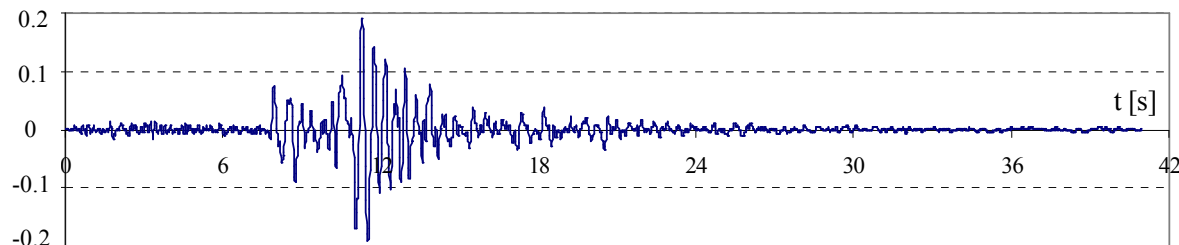


Fig. 4 Accelerogram Loma Prieta, California

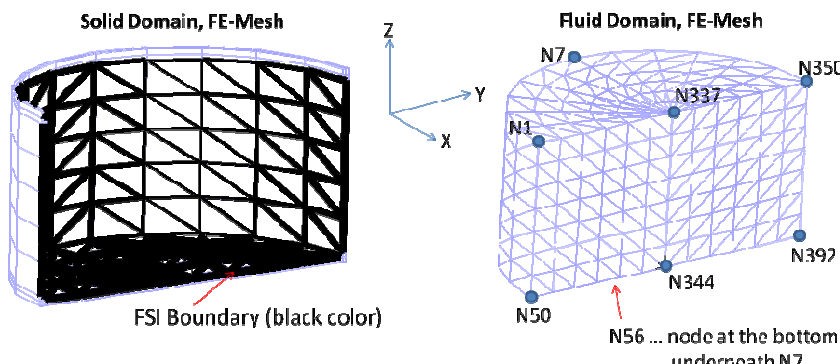


Fig. 5 FE-Model for 3D FSI analysis. FSI boundary on the solid domain at the left side, and fluid domain including nodes of interest (N350, N392, ...etc.) on the right side.

Dynamic time-history response of concrete open top cylindrical liquid storage tank was performed by application of the Finite Element Method (FEM) utilizing software ADINA. Arbitrary-Lagrangian-Eulerian (ALE) formulation was used for the problems. Due to the symmetry of the applied load and geometry of the tank, just half of the domain of interest was analyzed (Fig. 5). Two way Fluid-Structure Interaction (FSI) techniques were used for the simulation of the interaction between the structure and the fluid at the common boundary. The solid walls and base of the tank were modeled using 3D SOLID finite elements. The fluid inside the tank was modeled using 3D FLUID finite elements.

The resulting time dependent vertical displacements of fluid in node N350 of free surface is in Fig. 6. The maximum movement of the free surface of the fluid measured at node 350 is $u_{\max} = 25.94$ mm. The maximum value $p_{\max} = 80353$ Pa measured at node 392 and in time 21.36 s is seen from the response of the pressure over the fluid domain in dependency of time measured at the bottom, Fig. 7. Corresponding stress distributions is plotted in Fig. 8. Time variation of the Von

Misses stress at area of concern (plane of symmetry) is shown in Fig. 8. From there, we can see, that the maximum value of stress with regards to time is 1.99 MPa measured at time 21.2 s (Fig. 8).

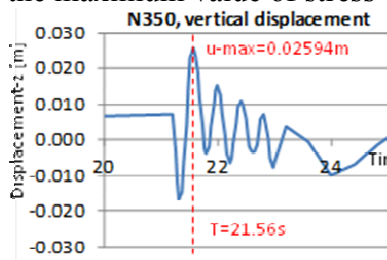


Fig. 6 Time dependent response of the vertical movement of the free surface in node 350

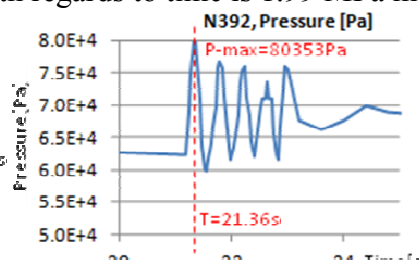


Fig. 7 Time dependent response of the pressure at the bottom in node 392

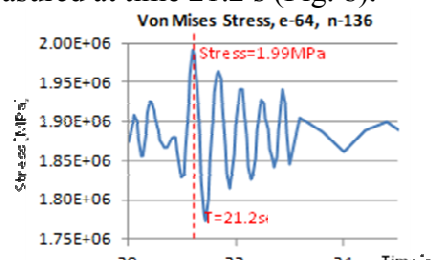


Fig. 8 Time dependent response of the Von Mises Stress in node 136

Acknowledgements

Preparation of the paper was supported by the Scientific Grant Agency of the Ministry of Education of Slovak Republic and the Slovak Academy of Sciences under Project 1/0201/11.

References

- [1] G. K. Batchelor, An introduction to fluid dynamics. Cambridge University Press; 1967.
- [2] J. Benčat, D., Papán, Buildings Structure Response Due to Rail-Way Traffic Prediction Model In: ICSV18, 18th International Congres on Sound Vibration, 10 - 14 July 2011, Rio de Janeiro, Brazil, p. 1-8.
- [3] J. Habenberger, J. Schwarz, Damping effects of the fluid in cylindrical liquid storage tanks. Earthquake Engineering and Structural Dynamics, 2005.
- [4] N. Jendželovský, J. Sumec, Stress-strain fields of the reinforced water tower under seismic loads. In: 9th international scientific conference VSU' 2009, 4 - 5 June, 2009, Sofia, Bulgaria, Vol. 1. Sofia. L. Karavelov civil engineering higher school, 2009. p. I76-I-80.
- [5] E. Kock, L. Olson, Fluid-structure interaction analysis by the finite element method-a variational approach. International Journal for Numerical Methods in Engineering, Vol. 31, Issue 3, p. 463-491, March 1991, John Wiley & Sons, Ltd.
- [6] J. Králik, Dynamic analysis of soil-fluid-tank interaction due to earthquake even. In: Dynamika tuhých a deformovatelných těles 2012, sborník přednášek z 10. mezinárodní conference, 10. - 12. října 2012, Ústí n. Labem, Česká republika.
- [7] J. Melcer, Experimental testing of a bridge. Applied Mechanics and Materials, Volume 486, 2014, Pages 333-340.
- [8] H. Lamb, Hydrodynamics. 6th ed New York, Dover Publications; 1945.
- [9] V. Michalcová, S. Kuznětsov, S. Pospíšil, Models of load on buildings from the effects of the flow field, Transactions of the VŠB – Technical University of Ostrava, Civil Engineering Series. Vol. 13, Issue 2, pp. 91–97, ISSN 1804-4824, DOI: 10.2478/tvbsb-2013-0014.
- [10] C. Nitikitpaiboon, K. J. Bathe, An arbitrary Lagrangian-Eulerian velocity potential formulation for fluid-structure interaction. Computers & Structures, 1993. Vol. 47, No. 4/5, p. 871–891, Great Britain.
- [11] L. G. Olson, K. J. Bathe, Analysis of fluid-structure interactions. A direct symmetric coupled formulation based on the fluid velocity potential. Computers & Structures, 1985, Vol. 21, No. 1/2, p. 21–32. U.S.A.
- [12] EN 1998-4: 2006 Eurocode 8. Design of structures for earthquake resistance. Part 4: Silos, tanks and pipelines, CEN, Brussels, 2006.
- [13] Theory and Modeling Guide, Volume I: ADINA, December, 2012.

Engineering Approach of Seismic Analysis of Piling Quay Walls Subject to Redistribution of Lateral Earth Pressure

ZHDAMIROV Vladimir^{1,a} and KOROVKIN Vladimir^{1,b*}

¹Department of Water-managements and water works, St. Petersburg Polytechnic University,
Polytechnique 29, 195251 St. Petersburg, Russia

^ajesus1teeth@gmail.com, ^bkorovkin40@yandex.ru

Keywords: soil mechanics, lateral earth pressure, seismic lateral earth pressure, generalized dynamic factor, factor of seismicity, anchored sheet pile wall

Abstract. Proposed an engineering method for calculating the fine quay walls of the seismic action. At the initial stage is the stress-strain state of the walls of the static load taking into account the redistribution of lateral earth pressure. In the presence of an earthquake is determined by seismic lateral earth pressure on the wall from the effects of inertia forces, added mass of water pressure and dynamic load from various forms of oscillations of the wall. Seismic load fluctuations wall defined by dynamic spectral method as a result of decomposition of seismic vibrations in a series of major modes of vibration. The results of the proposed calculation realized in the program «SCAD», and have been compared with «Plaxis - 2D» results.

Introduction

Issue of seismic stability of retaining structures studied by Russian scientists: Ivanov P.L. [1]. Kulmach P.P. [2] EA Ascension [3] Yakovlev [4] etc. and foreign: Ishihara K. [5] Papadrakakis M. etc. [6], Paz R. [7], Garevski M. [8], Wai-Fah Chen [9] etc.

In Russia, the principles of calculation of the seismic action on structures are a basis for regulatory documents [10,11] and various directories. The focus of the research of seismic stability of retaining walls was paid to the lateral earth pressure, which determines the operation of such facilities.

Basically theoretical and experimental works on this problem are limited to consideration of rigid or flexible retaining walls without excluding redistribution of soil pressure adjustment. This is due to the fact that the accepted theory of earth pressure on retaining wall sliding soil prism is adopted as a rigid body [2]. However, as experience shows, it is not true.

As used in the regulations values resulting seismic pressure adduced for active and passive earth pressure structures [10,11]. In fact, the lateral earth pressure depends on the magnitude and direction of movement of the wall [12]. It differs from the limit, presenting a mixed problem with the prelimit and limit area, that available for numerical methods. However, numerical methods based on continuum model do not correctly describe the earth pressure on retaining wall [13]. Redistribution of lateral pressure on the height of the wall is more consistent with a model of a granular medium [14].

Seismic Earth Pressure on Retaining Wall Considering Movement

Account in determining the movement of soil seismic lateral pressure is used to determine the bearing capacity of the reserve structure. For example, if the ground pressure of the jet at the immersed portion of the base wall is less than the limit, then the structures have a certain reserve carrying capacity. Seismic earth pressure on retaining at most unfavorable horizontal force of inertia power engineering using kinematic theory ground contact pressure is equal to [15]:

$$\sigma_{c,x,y} = K_{o,d} \sigma_{x,y}, \quad (1)$$

where $\sigma_{c,x,y}$ – the intensity of seismic horizontal pressure at a depth y ; $K_{o,d} = (1 \pm 2K_c(L)(1 \pm \operatorname{tg}\varphi(\delta)))$ – generalized dynamic factor, containing $K_c(L)$ – seismicity coefficient taking into account the distance of the object to hearth of earthquake [15], $\varphi(\delta)$ – function of the angle of internal friction, taking into account the soil conditions of the displacement (from the initial to the limit), $0 \leq \varphi(\delta) \leq \varphi$. The sign «+» refers to a shift in the wall from the ground, and the sign “-” respectively - on the ground.

For example. The displacement of the wall backfill implementing active pressure at value $\varphi = 30^\circ$, $\operatorname{tg}\varphi(\delta) = \operatorname{tg}\varphi$, for seismic coefficient values $K_c = 0.0 \div 0.4$ we will have $K_{o,d} = 1.0 \div 2.3$. By moving wall on a charge that implements passive to the above conditions, we have $K_{o,d} = (1.0 \div 0.66)$.

The obtained values of $K_{o,d}$ for two limiting cases of displacement wall at $\varphi = 30^\circ$ close to the values of seismic pressure given in the work [11]. $K_{o,d}$ value for the cases of exact work [11] does not consider.

Complex Method of Calculating the Sheet Pile Wall at Earthquake

The initial data is taken diagram lateral pressure static calculation fine quay wall built by mirroring [12]. This method allows you to get redistributed epure lateral earth pressure on the deformed wall (Fig. 1a). In the first stage of a dynamic calculation is performed by a conventional static analysis program SCAD at high lateral loads [16]. In relation to the calculated beam is taken from the top of the pillar to the anchor node, respectively, and at the bottom - at the subgrade. The beam is exposed to seismic soil pressure (1) and the hydrodynamic pressure of the added mass of water on the wall [17]. To take into account the compliance of the anchor node used wall portion with a conditional factor of subgrade resistance $K_{p,ank}$. Efforts in the wall of the first stage of the calculation are shown in Fig. 1b, c. The second stage of the calculation of the oscillations of the wall during an earthquake is related to the definition of the parameters of vibrations of the beam [18]. To account for fluctuations in the beam will apply mass at nodes of the beam, dividing it lengthwise into 10-12 portions. Options of 3 ownership oscillations (Fig. 1f): periods, frequency eigenvalues are determined by the program SCAD [16].

Design bending moment in the sheet pile wall M_d represents the sum of moments of the residual M_{ost} (from the dynamic effects of the added mass of soil and water , Fig. 1b, c) and fluctuation M_f (oscillation of the wall, Fig. 1g, h), and the anchor force R_{ad} represents the sum of forces from the above values[19]

$$M_d = M_{ost} + M_f, \quad (2)$$

$$R_{ad} = R_{a,ost} + R_{a,f}. \quad (3)$$

Illustration of calculation wall earthquake is shown in Fig. 1.

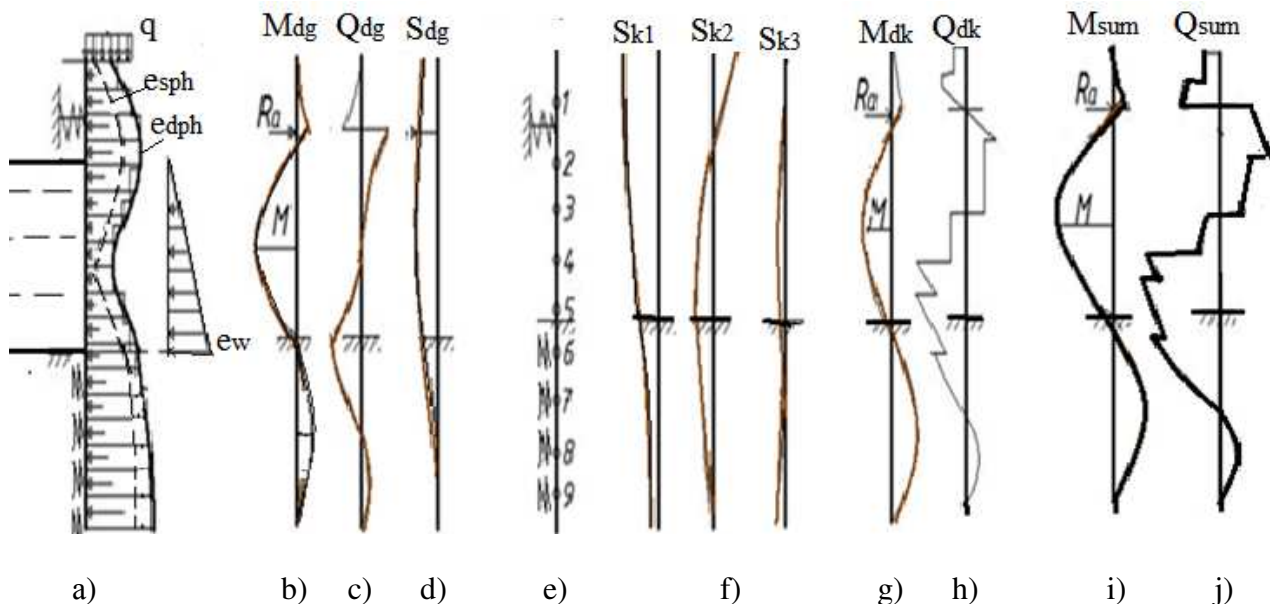


Fig.1. Scheme of the dynamic calculation sheet pile wall. a) Redistributed diagrams of lateral earth pressure: static e_{sph} (dotted line) and dynamic, e_{dph} (solid line), the pressure of the added mass of water e_w (triangular - naked manual ultrasonic inspection); b), c), d) Bending moment M_{dg} , shear forces Q_{dg} and elastic line the walls dynamic effects of soil S_{dg} ; e) Wall design scheme for dynamic analysis of the system with n degrees of freedom; f) The eigenmodes of the system S_{k1}, S_{k2}, S_{k3} ; g) and h) Bending moment from fluctuations M_{dk} and shear forces from fluctuations Q_{dk} ; i) and j) The total bending moment M_{sum} , shear forces Q_{sum} in the wall of the sheet by the earthquake.

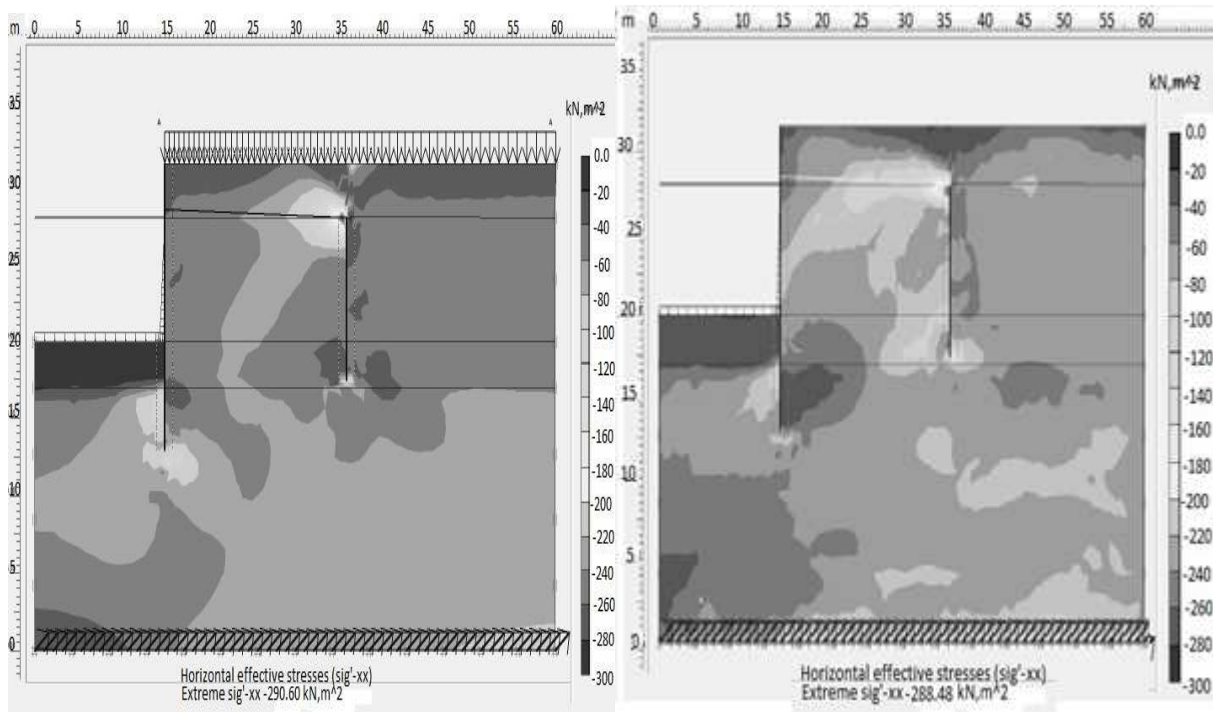
Implementation of the Proposed Complex Method of Calculating Seismic Impact on the Wall

Example. Define static and dynamic forces in anchor revetment of the tongue Larsen VII type, a free height of 12 m, immersed in a two-layer foundation soil of sand $\varphi = 32^\circ$, $\gamma = 18.8 \text{ kN/m}^3$, $E = 28 \text{ MPa}$ with depth of 3 m and clay $\varphi = 12^\circ$ and $c = 20 \text{ kPa}$, $E = 20 \text{ MPa}$. During the operating the wall subjected to earthquake intensity 9 points.

Static calculation. Results source static analysis using the Kulon diagrams of lateral pressure (no pressure redistribution) were bending moment in the wall equal to $M = 700.39 \text{ kNm}$. The results of the static analysis, taking into account the redistribution of revetment pressure were bending moment in the wall equal to $M = 523.6 \text{ kNm}$ (Table 1) [12].

Dynamic calculation. To calculate the dynamic effects in the SCAD program used previously established design model sheet pile wall with static analysis: knots, rods, sections geometric characteristics, the characteristics of elastic foundation [17]. Create a new dynamic impact of seismic load, taking into account (1) for the transformed diagrams of lateral earth pressure. For this we should to select the kind of exposure - "seismic" at tab of program SCAD «Seismic impact of» selected number accounted forms of natural vibrations, orientation schemes and loads coefficients for soil, seismic category, rate of structures. In the selected type of loading effects are created like a inertial properties of nodes. The values of the masses m_i in each of the nodes are taken from the mass matrix with a positive sign. Calculation results of dynamic loads on the walls were bending moment equal to $M = 943.8 \text{ kNm}$ (Table 1).

For comparison, we calculated the program «Plaxis» and «Plaxis - 2D» [20]. Below are stress contours on the wall of the static and dynamic effects.



a) Contours of the horizontal stresses
in static exposure

b) Contours of horizontal stresses
in the dynamic action

Fig. 2 Stresses in the ground mass if berthing facilities

Calculation results are shown in Table1.

Table 1 Efforts in the wall using different solutions

Proposed methods for calculating	Proposed settlement	Manual... [11]	«Plaxis»	«Plaxis 2D»
Sheet pile wall -Sections				
Static bending moment , [kNm]	523.6	544.2	549.49 _K	-
Static reaction in the anchor on 1RM, [kN]	285.2	215.2	305. 22	-
Dynamic bending moment	943.9	1017.6	-	864.1
Dynamic response in the anchor	370.2	445.5	-	360.1 _K
Sheet pile wall of truboshpunta				
Static bending moment , [kNm]	738.7	653.3	657.4	-
Static reaction in the anchor on 1RM,[kN]	345.5	209.8	348.2	-
Dynamic bending moment	1331.6	1221.7	-	1033.7
Dynamic response in the anchor	448.5	434.3	-	417.8

Note: efforts to anchor the proposed method and Manual... [11] are given without irregularity coefficient tension rods.

Analysis of the Results of the Calculation

Number of Table 1 shows that the values of the dynamic forces in the wall, resulting in a foreign program «Plaxis 2D» somewhat smaller than the Russian calculations.

The results of calculation show that the proposed method of calculating the fine quay walls more strongly reacts to changes in the stiffness of the facial element. In the proposed method at the time of replacement of the static calculation of the tongue on the 912 mm diameter truboshpunkt leads to a change in the form of diagrams to a parabolic saddle. This increases the time span and the value of the anchor reaction compared with the Coulomb Diagrams.

Conclusion

1. Have shown the practical formula for determination seismic lateral earth pressure on retaining wall on the basis of the kinematic theory of engineering ground contact pressure.
 2. Proposed an engineering method for calculating the fine quay walls of the seismic action, taking into account depending on the lateral pressure on the deformation of the wall.
 3. Calculation results show that Russian standards of calculating berthing facilities for seismic loads [11] have a certain margin of safety in the computation effort (20%) compared with the overseas program «Plaxis 2D».
 4. Comparison of the calculation results of the proposed method with the program «Plaxis 2D» yet - shows them more or less similar for their flexible sheet pile wall and the difference in the efforts (to 30%) in the direction of increasing the proposed method for the rigid wall. This is due to the fact that the program «Plaxis 2D», using a continuum model takes into account the impact of flexibility wall interface by a factor that takes into account the influence of the friction forces on the ground wall. However, in the case of a rigid wall, a working scheme free support coefficient interface unable to accommodate the redistribution of soil pressure on the height of the wall caused by the displacement of its bottom base of soil compacting. Taking account of this phenomenon, the discrete media inherent in the proposed method of calculation leads to an increase in pressure in the upper side wall portion, compared with a Coulomb while decreasing it in the lower part. This trend persists in static and dynamic effects on the fence.
 5. Evidently, that in seismic regions in the construction of berthing facilities, using flexible sheet piling is more justified than the increased stiffness. In this case, the action of seismic load deflection of the wall plays the role of an additional damper. Moreover, the additional lateral redistribution wall pressure therein reduces effort compared with Kulon linear pressure.
- In connection with the above when calculating the fine harbor wall stiffness increased seismic impact on the program «Plaxis 2D» recommended calculated efforts to introduce a correction factor of the order of $K = 1.1-1.3$.

References

- [1] P.L. Ivanov, Primers and base waterworks, Graduate School, Moscow, 1985, pp. 352.
- [2] P.P. Kulmach, V.Z. Filippennok, N.G. Zaritovskiy, Marine waterworks. Part II, Berthing, Offshore structures and bank protection, LVVISU, St. Petersburg, 1991, pp. 391.
- [3] E.A. Ascension, Dynamic instability of soils. Moscow, Editorial URSS, 1999, pp. 263.
- [4] P.I. Yakovlev, Application of the theory of limit states of stress and determination of the coefficient of lateral pressure for flat walls under seismic conditions, in the book: Foundations, published, submitted to journal of Budevilnik, 9, Kiev, 1976, pp. 93-98.
- [5] K. Ishihara, Soil behavior during earthquakes. Translated from English, ed. Fadaeva AB, MB Lisyuk, St. Petersburg. NGO Georeconstruction–Fundamentproject, 2006, pp. 384.
- [6] M. Papadrakakis, M. Fragiadakis, N. Lagaros (Ed.), Engineering seismology, geotechnical and structural earthquake, 2011, pp. 585.

-
- [7] R. Paz, International handbook of earthquake and engineering seismology. International handbook of earthquake engineering: codes, programs, and examples. New York, 1994.
 - [8] M. Garevski, Earthquake engineering in Europe. Atilla Ansal, 2010.
 - [9] Wai-Fah Chen, Chen, Chen, Handbook earthquake engineering, CRC Press, 2002.
 - [10] Construction in seismic regions. SP 14.13330.2011. Updated edition SNIP II- 7-81, National Standard, Moscow, 2011.
 - [11] Manual accounting seismic effects in the design of marine hydraulic structures such as revetment. RD 31.3.06-2000, MTRF, Moscow, 2001.
 - [12] V.S. Korovkin, Engineering kinematic theory of the contact pressure of the soil and its application to the static calculation of thin quay walls: submitted to journal of Engineering and Construction Journal, 6 (2013) 39-49.
 - [13] Plaxis B.V. P.O., Box 572, 2600 A N Delft, Netherland, 2002.
 - [14] A.N. Badanin, A.K. Bougrov, A.V. Krotov, Justification of the first critical load grainy medium sandy base: submitted to Journal of Engineering Construction magazine, 9 (2012).
 - [15] V.Y. Gusch, V.S. Korovkin, Using engineering theory ground contact pressure applied to seismic lateral pressure. Proceedings of the scientific - practical conference with international participation ICF. Part 1. Published of Polytechnic University, St. Petersburg, 2012, pp. 44-46.
 - [16] M.V. Kolomine, V.S. Korovkin, A practical way to determine the lateral pressure from the earthquake epicenter, depending on. Proceedings of the conference ICF, Part 1, Polytechnic University, St. Petersburg, 2012, pp. 55-56.
 - [17] V.S. Karpilovsky, etc., Computer complex SCAD. Publishing House of the DIA, Moscow, 2004, pp. 592.
 - [18] N.S. Tovstukha, V.S. Korovkin, Dynamic calculation of the sheet pile wall on program SCAD, Proceedings of the conference ICF, Part 1, Polytechnic University, St. Petersburg, 2012, pp. 68-69.
 - [19] M.P. Fedorov, etc., Information and computer technology in construction, Application SCAD program for solving dynamics, Polytechnic University, St. Petersburg 2009, pp. 230.
 - [20] B.V. Plaxis, Plaxis 2D Dynamic. P.O. Box 572, 2600 AN Delft, Netherlands, 2012.

Safety of Nuclear Power Plants against the Aircraft Attack

KRÁLIK Juraj^{1,a*}

¹Faculty of Civil Engineering, Slovak University of Technology in Bratislava

Radlinského 11, 813 68 Bratislava, Slovak Republic

^ajuraj.kralik@stuba.sk

Keywords: safety, aircraft, nonlinear analysis, reinforced concrete, impact, nuclear power plant

Abstract. This paper presents the nonlinear dynamic analysis of the reinforced concrete building of nuclear power plant to the aircraft impact. The dynamic load is defined in time on the base of the simulation of the airplane impact considering real stiffness, masses, direction and velocity of the flight. The dynamic response is calculated in the system ANSYS using the transient nonlinear analysis solution method. The damage of the concrete wall is evaluated in accordance of the standard NDRC considering the spalling, scabbing and perforation effects. The simple and detailed calculation of the wall damage is compared.

Introduction

The last accidents of the NPP in Chernobyl and Fukushima give us the new inspiration to verify the safety level of the NPP structures. The International Atomic Energy Agency set up a program [7,8] to give guidance to its member states on the many aspects of the safety of nuclear power reactors. One from the safety risk of NPP structures is the possibility of the aircraft attack to the NPP structures [6,12,14,16]. In the case of the possibility of the aircraft impact we must consider the probability of the aircraft attack [5,13], the definition of the impact load in dependency of the plane type [1,2,7,12,14], the behavior of the reinforced concrete structures under the high strain speed [2,3,6,9,10,14,16,17] and the effective methods to solve of the probability of failure [4,9,10,15].

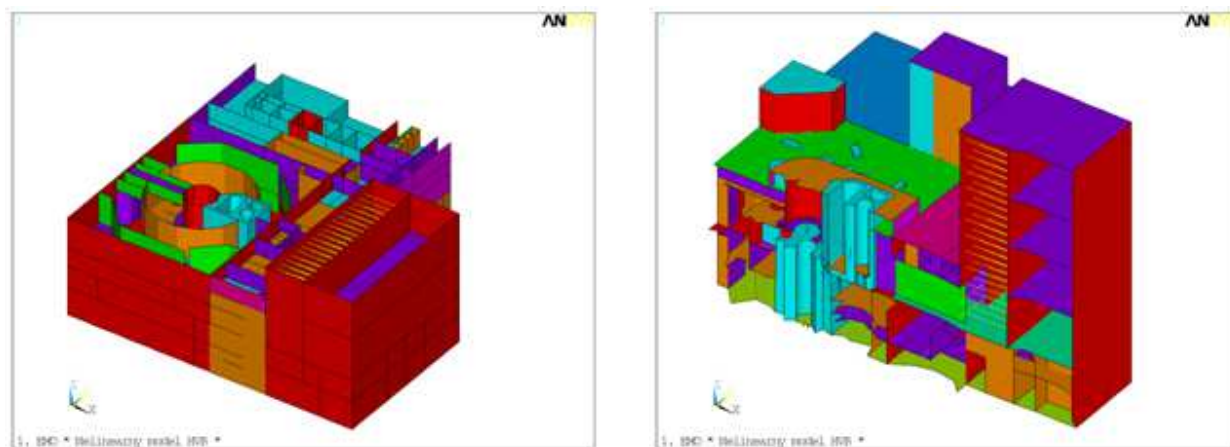


Fig. 1 Calculation model of NPP building

Calculation model of NPP building The NPP WWER 440 building consists of six objects (Fig.1) - reactor building, bubbler tower, air-conditioning centre, turbine building, and lengthwise side electrical building and cross side electrical building [9]. The calculation model of the NPP building [9] consists of the beam, shell and solid elements. The FEM model consists of 20 681 elements with 91 890 degrees of freedom [9].

Model of Aircraft Impact

There is assumed with the aircraft impact of the lightweight jet business fighter LEARJET 25. The plane LEARJET 25 is the metallic biplane with the tail in the form T (Fig. 2). The total length of plane is 13.192 m, the height of fuselage is 2.53 m and in the tail 4.62 m. There is proposed the masses of the full plane with the passenger equal to 6.27 ton, the plane speed 155 m/s and the manipulation in the interval $0^\circ - 50^\circ$. The breaking off the wings and the loss of the fuel is proposed in the case of the flight through the steel structures of the reactor hall.

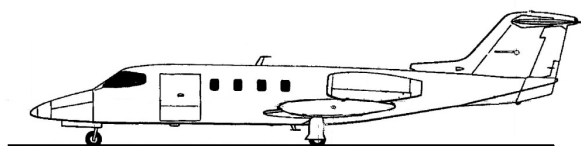


Fig. 2 Airplane LEAR JET 25

The critical section of the NPP structures were estimated on the base of the previous static analysis and the orientation of flay was defined come out from the technical information of the manufacturer. The three critical places were defined: LC1 - the plane attack to the wall of the bubble tower, LC2 - the plane attack to the roof of the bubble tower, LC3 - the plane attack to the plate of the box of the steam generator. All accident are proposed for the flay direction of 50° (Fig. 3).

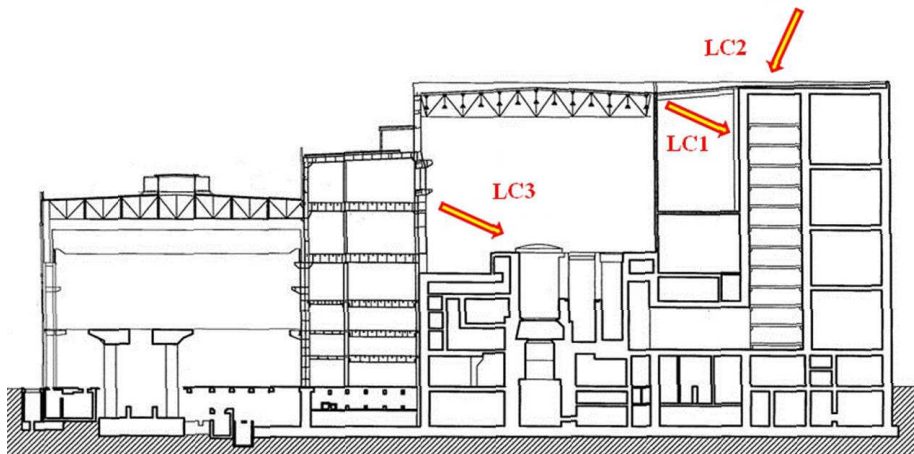


Fig. 3 Scheme of the aircraft attack to the NPP steam generator and the bubble tower

The load functions in the time were determined in agreement with the standard DOE [3] in the calculation program Riera_Code [1] based on the technical parameters of the plane Lear Jet (geometry, stiffness, fuselage masses, flay velocity in the moment of impact, operate possibilities and others).

Table 1 Load function for aircraft of Learjet 25

Airplane Learjet 25 for impact velocity 155 ms^{-1}							
Time [ms]	0.0	24.0	32.5	48.0	50.5	56.0	90.0
Force [MN]	0.0	11.0	11.0	30.0	30.0	15.0	0.0

Penetration of the RC Wall

For assessment of the reinforced walls or plates resistance, some simplified relations for the calculation of missile penetration or perforation of the wall according to [6] can be used based on the results of experimental tests.

The penetration depth (x_c) of the crushed mass of the engine casing is given by the modified NDRC equation for the diameter missiles

$$x_c = \alpha_c \sqrt{4KWN D \left(V / (1000D) \right)^{1.8}}, \quad \text{for } x_c / (\alpha_c D) < 2, \quad (1)$$

where x_c is the crushed casing penetration depth in inches, V is the engine velocity in ft/sec, D is the average outer diameter of the engine casing in inches, W is the total engine weight (in lbs), $K = 180/(f_c')^{1/2}$, $N = 0.72$ (flat-nose missile), f_c' is the concrete strength in psi, and $\alpha_c = 0.5$ is the penetration reduction factor to account for missile deformability as suggested in [6].

The wall thickness required to prevent scabbing (t_s) can be computed using the reduced Chang formula

$$t_s = \alpha_s 1.84 (200/V)^{0.13} (MV^2)^{0.4} \left(1/(D/12)^{0.2} \right) \left(1/(144f_{cd})^{0.4} \right), \quad (2)$$

where $M = W/g$ and $g = 32.2$ ft/sec². The factors of 12 and 144 used in equation (2) are used to convert the units of casing diameter (inches) and concrete compressive strength (psi) to the units (ft, psf) used in the empirical Chang formula. The recommended value for α_s is 0.55.

The reduced Degen formula [6] is used to calculate wall thickness to prevent perforation (t_p)

$$t_p = \alpha_p D \left(2.2(x_c/\alpha_c D) - 0.3(x_c/\alpha_c D)^2 \right), \quad \text{for } x_c / (\alpha_c D) \leq 1.52. \quad (3)$$

The recommended value for α_p is 0.6. The exit velocity of the engine may be estimate using the relationship cited by Kar [6] and attributed to CEA-EDF :

$$v_R^2 = (v_{in}^2 - v_p^2) / \left(1 + (W_{cp}/W) \right), \quad \text{for } v_{in} > v_p, \quad (4)$$

where v_R is the residual velocity of the missile after wall perforation, v_{in} is the initial impact velocity of the missile prior to wall impact, and v_p is the missile velocity that just initiates perforation, W_{cp} represents the weight of the concrete plug ejected by the perforating missile with weight, W .

The target wall thickness for the missile attack to the reinforced concrete structures is determined in the Table 2 on the base of the standard requirements [6].

Tab. 2 Target wall thickness for the missile penetration

Lear Jet 25	Target Missile Penetration ($V_R = 0,0$)		
	Spalling - x_s [m]	Scabbing - t_s [m]	Perforation - t_p [m]
Wall thickness [m]	0.1984	0.2314	0.576

The previous analysis shows us that the safety depth of the reinforced concrete wall or plate in the case of the aircraft of the plane Learjet 25 is equal 0.576 m.

Nonlinear Dynamic Analysis of the Reinforced Concrete Structure

FEM model consists the layered shell elements SOLID181 with the concrete and steel layers. The material model takes into account the orientation of the cracks and the reinforcements in the NPP plates and walls.

The non-linear dynamic equilibrium equations in semi-discrete form is given by

$$\mathbf{M}\ddot{\mathbf{r}}_n + \mathbf{C}\dot{\mathbf{r}}_n + \mathbf{p}(\mathbf{r}_n, \dot{\mathbf{r}}_n) = \mathbf{f}_n, \quad (5)$$

where \mathbf{M} and \mathbf{C} are matrices of mass and damping, $\mathbf{p}(\mathbf{r}_n, \dot{\mathbf{r}}_n)$ is vector of internal resisting forces, $\ddot{\mathbf{r}}_n$, $\dot{\mathbf{r}}_n$, \mathbf{r}_n are the vectors of acceleration, velocity and displacement and \mathbf{f}_n is the vector of external forces in the time t_n . The internal resisting forces $\mathbf{p}(\mathbf{r}_n, \dot{\mathbf{r}}_n)$ are evaluated as

$$\mathbf{p}_n = \int_{\Omega} \mathbf{B}_n^T \boldsymbol{\sigma}_n d\Omega \quad \text{and} \quad \boldsymbol{\sigma}_n = \mathbf{D}_{ep} \mathbf{B}_n \mathbf{r}_n, \quad (6)$$

where the elastic-plastic matrix \mathbf{D}_{ep} is based on the Hill anisotropy theory and the bilinear kinetic hardening material model and the strain-displacement matrix \mathbf{B}_n is defined for the theory of the large rotations.

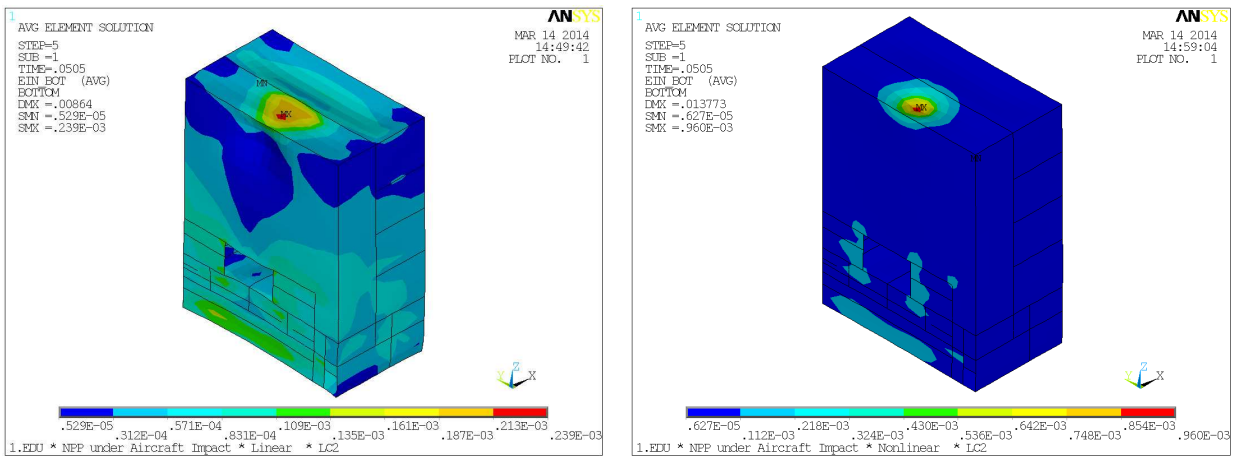


Fig. 4 The behavior of the strain intensity for the load case LC2 - linear and nonlinear solution

Table 3 The strain intensity in the RC structure under aircraft in FEM model

Structural segment	Elastic strain of shell element [%]			Elastic-plastic strain of shell element [%]		
	Bottom	Middle	Top	Bottom	Middle	Top
Wall BT	0.016638	0.0035238	0.011024	0.027842	0.0075763	0.015421
Plate BT	0.025027	0.0062563	0.034068	0.122060	0.0103870	0.103590
Plate BSG	0.026995	0.0049293	0.019217	0.045238	0.0049309	0.035405

Note - BT - Bubbler Tower, BPG - Box of Steam generator

Summary

This paper presented the results from the linear and nonlinear dynamic analysis of the reinforced concrete building of nuclear power plant under the aircraft impact. The accident scenario assumes the aircraft impact in three critical points (wall BT, plate BT and plate BSG). The load function was determined in the program Riera_Code on the base of the comparison study with the reference aircraft. The dynamic response was calculated in the system ANSYS using the transient nonlinear method. The strain intensity in the critical places increases from 1.4 to 4.9 times in the nonlinear analysis in comparison with the linear solution. The wall or plate of the NPP reinforced concrete structure may be locally cracked after the aircraft impact, but the integrity of the containment structure will be safe and reliable. The reinforced concrete wall or plate with the higher thickness as 60 cm is resistant to the aircraft of the plane Learjet 25 in accordance of the standard [6]. The criteria of the damage of the concrete wall in the standard NDRC are more conservative than the results from the nonlinear analysis of the aircraft impact. The nonlinear detailed analysis gives us the more accurate results.

Acknowledgements

This article was created with the support of the Ministry of Education, Science, Research and Sport of the Slovak Republic within the Research and Development Operational Programme for the project "University Science Park of STU Bratislava", ITMS 26240220084, co-funded by the European Regional Development Fund and with support of Grant Agency of the Slovak Republic (VEGA) (grant No. VEGA No. 1/1039/12).

References

- [1] V. Adamík, Aircraft load function from the impact of JAS 39 GRIPEN, LEAR JET 25 and AIRBUS A 320, Research report No. 5090, Pardubice – April, 2013.
- [2] M.Y.H. Bangash, T. Bangash, Explosion-Resistant Buildings. Design, Analysis, and Case Studies. Springer Berlin Heidelberg New York, 2006.
- [3] Z. Čada, P. Hradil, V. Kanický, V. Salajka, Seismic Analysis of a Building Structure Considering Uncertainties of its Dynamic Properties. ANSYS Conference and 29. CADFEM Users meeting 2011. Stuttgart, 2011, pp. 1-5.
- [4] R. Čajka, M. Krejsa, Measured Data Processing in Civil Structure Using the DOPROC, Method, Advanced Materials Research. 859 (2013) 114-121.
- [5] DOE STANDARD, Accident Analysis for Aircraft Crash into Hazardous Facilities, Appendix C, DOE – STD3014 – 2006, October 1996, Riaffirmation May, 2006, USA Department of Energy, Washington, DC 20585, 2006.
- [6] ERIN, Resistance of Nuclear Power Plant Structures Housing Nuclear Fuel to Aircraft Crash Impact, (Safeguards Material), Final Report by ABS Consulting, Anatech, and ERIN Engineering, Electric Power Research Institute, Paolo Alto, CA, February, 2003.
- [7] IAEA Safety Standards, Advanced Nuclear Plant Design Options to Scope with External Events, IAEA-TECDOC-1487, Vienna, February, 2006.
- [8] J. Králik, Comparison of Probabilistic and Deterministic Assessments for Evaluation of Seismic Safety of Nuclear Power Plants in Slovakia. First European Conference on Earthquake Engineering and Seismology, 3-8 September, Geneva, Switzerland, pp 422, 2006.
- [9] J. Králik, Safety and Reliability of Nuclear Power Buildings in Slovakia. Earthquake-Impact-Explosion. Published by STU Bratislava, 2009, 307p.
- [10] J. Králik, Probabilistic Safety Analysis of the Nuclear Power Plants in Slovakia. Journal of KONBiN, Safety and Reliability Systems, Ed. VERSITA Central European Science Publishers, Warszawa. 14-15 2-3 (2010) 35-48.
- [11] M. N. Monotti, Reinforced Concrete Slabs - Compatibility Limit Design, Dissertation work, Swiss Federal Institute of Technology Zurich, 2004.
- [12] NEI 07-13, Revision 8P, Methodology for Performing Aircraft Impact Assessments for New Plant Designs, ERIN , Palo Alto, CA, April, 2011.
- [13] NEA/CNRA/R(2011)12, Proceedings of the Forum on the Fukushima Accident: Insights and Approaches, JT03312480, Nov. 2011, OECD.
- [14] I. Němec, Š. Sychrová, I. Ševčík, J. Kabeláč, Study of a Nuclear Power Plant Containment Damage Caused by Impact of a Plane, International Refereed Journal of Engineering and Science (IRJES). 1 4 (2012) 48-53.
- [15] D. Novák, M. Vořechovský, R. Rusina, Small-sample Probabilistic Assessment - Software FReET, ICASP 9, 9th International Conference on Applications of Statistics and Probability in Civil Engineering, San Francisco, USA, July 6-9, 2003, pp. 91-96.
- [16] T. Sugano, Local Damage to Reinforced Concrete Structures Caused by Aircraft Engine Missiles: Part 2, Evaluation of Test Results, Nuclear Engineering and Design, Vol. 140, 1993, pp. 407-423.
- [17] O. Sucharda, J. Brožovský, Verified Non-linear Model for Reinforced Concrete Beams. Advances in Remote Sensing, Finite Differences and Information Security, Proceedings of the 5th WSEAS International Conference on Finite Differences - Finite Elements - Finite Volumes - Boundary Elements, Praha, WSEAS Press, 2012, pp. 27-32.

Failure Probability of NPP Communication Bridge under the Extreme Loads

Juraj Králik^{1,a*} and Juraj Králik, jr.^{2,b}

¹Faculty of Civil Engineering, Slovak University of Technology in Bratislava
Radlinského 11, 813 68 Bratislava, Slovak Republic

²Faculty of Architecture, Slovak University of Technology in Bratislava
Námestie slobody 19, 812 45 Bratislava, Slovak Republic

^ajuraj.kralik@stuba.sk, ^bkralik@fa.stuba.sk

Keywords: safety, reliability, probability, failure, extreme loads, bridge, nuclear power plants

Abstract. The safety and reliability of the communication steel bridge of the nuclear power plant under extreme loads is considered in this paper. The extreme load from the wind and the earthquake is defined for the probability of exceedance 10^{-4} by year on the base of the last results from the investigation in the Slovakia. The deterministic and the probabilistic assessment to verify of the safety and reliability of the structure are presented. The uncertainties of the input data and the calibration of the load factors are discussed. The advantages and disadvantages of probabilistic analysis are discussed. The advantages of the utilization the LHS method to analyze the safety and reliability of the structures are presented.

Introduction

This paper deals with the resistance of the steel bracing systems of the bridge between two buildings in the nuclear power plants (NPP) [7]. The international organization IAEA in Vienna [2,3] set up the design requirements for the safety and reliability of the NPP structures. The methodology of the seismic analysis of the structure behavior and the design of the structure under extreme loads are the object of the various authors [6,7,8,9,10,11,14,15,16,17,19]. In the case of NPP structures the characteristic values of the seismic loads are determined on the base of the IAEA requirements [2] by mean return period of the extreme loads which is equal to one per 10^4 years [11]. The methodology of the probabilistic analysis of the structure reliability is described in various papers and practical applications [5,8,11,12,13,15,16]. The reliability analysis is based on the partial factor methods in accordance of the Eurocode 1990 [2]. In the present the method of the partial factor is favorable in the practice. The Eurocode 1990 [1] and JCSS [4] recommends the use of three levels of the reliability analysis. Level III methods are seldom used in the calibration of design codes because of the frequent lack of statistical data. The measure of reliability in Eurocode 1990 [1] is defined by the reliability index β . The reliability index depends on the criterion of the limited state. The standard JCSS [4] required the measure of reliability in dependency on the safety level. The probability of the failure P_f can be determined using simulation method on the base of MONTE CARLO, LHS and others.

Load and Load Combination

The load combination of the **deterministic calculation** is considered according to ENV 1990 [1] and IAEA [4] for the ultimate limit state of the structure as follows:

Deterministic method – extreme design situation

$$E_d = G_k + Q_k + A_{Ed}, \quad (1)$$

where G_k is the characteristic value of the permanent dead loads, Q_k - the characteristic value of the permanent live loads, A_{Ed} - the design value of the extreme loads, $A_{Ed,k}$ - the characteristic design value of the extreme loads.

In the case of **probabilistic calculation** and the ultimate limit state of the structure the load combination [1] we take following:

Probabilistic method – extreme design situation

$$E = G + Q + A_E = g_{\text{var}} G_k + q_{\text{var}} Q_k + a_{\text{var}} A_{E,k}, \quad (2)$$

where g_{var} , q_{var} , a_{var} are the variable parameters defined in the form of the histogram calibrated to the load combination in compliance with Eurocode and JCSS requirements.

The extreme wind as well the seismic load was considered for the same return period 10^4 years [2]. The peak ground acceleration was set up as 0.15 g for the horizontal direction [11]. The spectrum acceleration response was calculated for the locality Mochovce in the three characteristic frequency values. The seismic response was solved by linear response spectrum method. The spectral analysis results from linear behavior of structures and the appropriate damping due to structure plasticity is considered by proportional damping for the whole structure or separately by materials.

Uncertainties of Input Data

The uncertainties of the input data – action effect and resistance are for the case of the probabilistic calculation of the structure reliability defined in JCSS and Eurocode 1990.

Table 1 Probabilistic model of input parameters

Name	Quantity	Charact. value	Variable paramet.	Histogram	Mean	Stand. deviation	Min. value	Max. value
Material	Young's modulus	E_k	e_{var}	Normal	1	0.120	0.645	1.293
Load	Dead	G_k	g_{var}	Normal	1	0.010	0.921	1.079
	Live	Q_k	q_{var}	Gumbel	0.60	0.200	0	1
	Earthquake	$A_{E,k}$	a_{var}	Gama(T.II)	0.67	0.142	0.419	1.032
	Wind extrem	$A_{W,k}$	w_{var}	Gumbel	0.30	0.150	0.500	1.032
Resistance	Steel strength f_{sk}	F_k	f_{var}	Lognormal	1	0.100	0.726	1.325
Model	Action uncertaint	θ_E	$T\theta_{\text{var}}$	Normal	1	0.100	0.875	1.135
	Resistance uncert.	θ_R	$T\theta_{\text{var}}$	Normal	1	0.100	0.875	1.135

The stiffness of the structure is determined with the characteristic value of Young's modulus E_k and variable factor e_{var} (Table 1). A load is taken with characteristic values G_k , Q_k , $A_{E,k}$, $A_{W,k}$ and variable factors g_{var} , q_{var} , a_{var} and w_{var} (Table 1). The uncertainties of the calculation model are considered by variable model factor θ_R and variable load factor θ_E for Gauss's normal distribution.

Extreme Wind Load

The wind load was determined from the meteorology research work in the locality Mochovce [18]. The design wind load is determined for the probability of the exceedance 10^{-2} per year and the extreme wind load for the probability 10^{-4} per year. The mean wind velocity for probability 10^{-2} per year (or 10^{-4} per year) of the is equal to 27.2 m/s (or 38.7 m/s) and the maximum peak to 40.0 m/s (or 53.9 m/s). In the case of the extreme wind the value of the extreme basic wind pressure is defined in the Eurocode as the 2.0 times higher as the design basic value.

Seismic Analysis of the NPP Structures

On the base of the experience from the reevaluation programs in the membership countries IAEA in Vienna the seismic safety standard No. 28 was established at 2003 [2]. The seismic load for the

Mochovce site was defined by peak ground acceleration (PGA) and local seismic spectrum in dependence on magnitude and distance from source zone of earthquake. Firstly the value of PGA was defined at 1994 ($PGA_{RLE} = 0.1$ g) follow in accordance of the results of seismological monitoring this locality at 2003 ($PGA_{UHS} = 0.142$ g and $PGA_{HS} = 0.143$ g).

Computational Model of the Bridge Structure

The steel bridge connects the auxiliary building, reactor building and ventilating chimney of the JEMO NPP [7]. The length of bridge structures is equal 20.3 and 23 m. The bottom level of the bridge is at +6.0 m and the top level at +10 m.

The total width of bridge is 5 672 mm and the height is 7 260 mm. The principal longitudinal beams are made from the steel profile I and 2U. The transversal beams are from the I profiles. The bridge is supported by columns from I profiles at modulus 4.7 m. The horizontal bracing system is made from 2L profiles at bottom and top level of bridge. The support structures of the technology pipes is from the 2T profiles. The roof panel of BDP are putting on steel profile panels type VSZ. The FEM model was set up by link, beam and shell elements in program ANSYS [7]. This model has 5 858 elements and 4 876 nodes.

The comparisons of the modal characteristics are presented in the Table 2.

Table 2 Modal characteristics of the bridge

Model	Mode X		Mode Y		Mode Z	
	Frequency [Hz]	Mass fract. [%]	Frequency [Hz]	Mass fract. [%]	Frequency [Hz]	Mass fract. [%]
Original	3.89	54.10	1.81	39.69	7.37	6.71

Recapitulation of the Numerical Analysis

The elements of the bridge steel structure were designed in accordance of the Eurocode requirements described below. The results from the design check of the deterministic analysis are shown in Table 3. There are described the safety level of the critical elements of the bridge structures with the support in accordance of the Eurocode [1].

Table 3 Comparison of the design check of the original and upgraded bridge

Load case	Capacity ratio of Bridge Elements [%]			
	Column	Longitud. Beam	Cross Beam	Bracing
Extreme wind	65.0	49.1	54.8	68.9
Earthquake	51.7	90.3	97.7	63.8

The probabilistic analysis was realized using 1000 LHS simulations in program FReET [15]. The uncertainties of the input data was considered in the form of the histograms (see Table 1). The density of the probability of the failure (Fig. 2) presents the reliability function for the case of the combination of the action of the normal forces and bending moments [11].

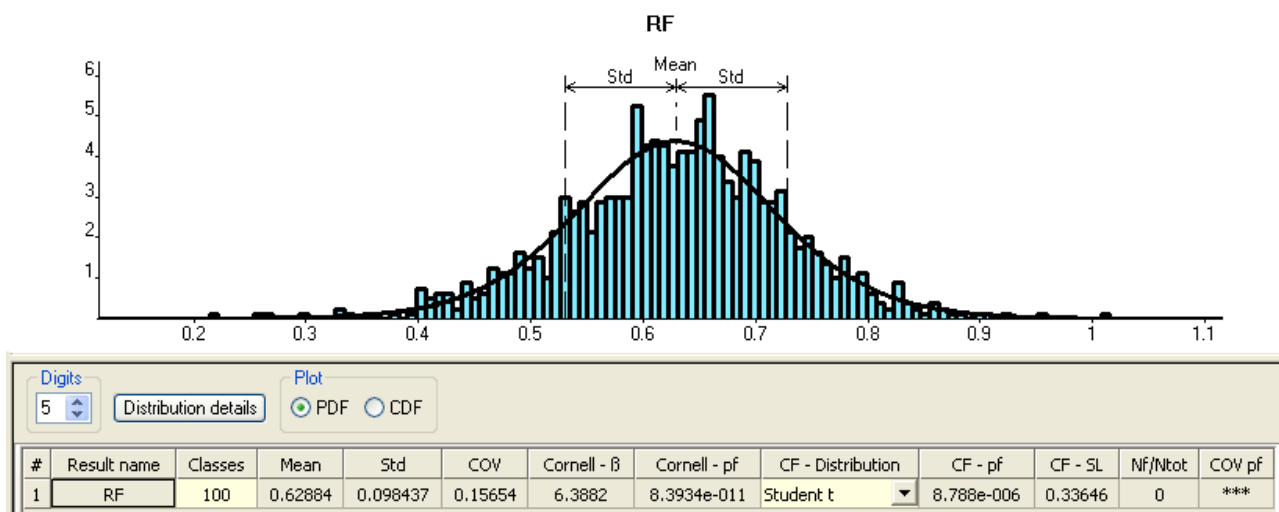


Fig. 2 The density of the reliability function RF – bracing system

Conclusion

This paper presents the reliability analysis of the steel bridge support resistance due to extreme loads – wind and earthquake. The extreme loads were defined for mean return period equal to one per 10^4 years in accordance of the IAEA requirements for NPP structures. The reliability of the bridge was calculated using the deterministic and probabilistic analysis. The uncertainties of the input data – action effect and resistance were considered by the partial factors in the case of deterministic analysis and in the form of the histograms on the base of the Eurocode and JCSS. The critical elements of the structure were identified on the base of the deterministic analysis. The effect of the extreme wind was worse than earthquake SL-2 with $PGA = 0.15$ g. The probability of the bridge bracing failure was equal to $P_f < 10^{-6}$ on the base of the LHS simulation.

Acknowledgement

This article was created with the support of the Ministry of Education, Science, Research and Sport of the Slovak Republic within the Research and Development Operational Programme for the project "University Science Park of STU Bratislava", ITMS 26240220084, co-funded by the European Regional Development Fund and with support of Grant Agency of the Slovak Republic (VEGA) (grant No. VEGA No. 1/1039/12).

References

- [1] EN 1990 (2002), Eurocode – Basis of structural design, CEN Bruxelles.
- [2] IAEA, Safety Report Series No. 28, Seismic Evaluation of Existing Nuclear Power Plants, IAEA, Vienna, 2003.
- [3] IAEA Safety Standards, Extreme external events in the design and assessment of nuclear power plants, No. IAEA-TECDOC-1341, Vienna, March, 2003.
- [4] JCSS-OSTL/DIA/VROU-10-11-2000, Probabilistic Model Code, Part 1 Basis of Design, Working material, <http://www.jcss.ethz.ch/>, 2001.
- [5] P. Konečný, J. Brožovský and V. Křivý, Simulation Based Reliability Assessment Method using Parallel Computing. Proceedings of 1st International Conference on Parallel, Distributed and Grid Computing for Engineering, Civil Comp Proceedings, 90 (2009), pp. 542–549.

- [6] K. Kotrasová, I. S. Leoveanu and E. Kormaníková, A Comparative Study of the Seismic Analysis of Rectangular Tanks According To EC8 and IS 1893, In Buletinul AGIR, No. 3/2013, Julie-Septembrie, pp. 120-125.
- [7] J. Králik, V. Salajka and Z. Čada, SO 802/1-03. Communication Bridge between NPP and SO 801/1-02, Static and dynamic calculation of structures, UJV Rez, Energoprojekt Praha, 2008.
- [8] J. Králik, J. Králik, jr. Deterministic and Probabilistic Analysis of the Steel Bridge Support Resistance due to Extreme Loads, 10th International Scientific Conference VSU 2010. Vol. 1, Proceedings. Sofia, Bulgaria, 3.-4.6.2010, Sofia: L.Karavelov Civil Engineering Higher School Sofia, 2010, pp. 104-109.
- [9] J. Králik, Deterministic and Probabilistic Analysis of Steel Frame Bracing System Efficiency, Trans Tech Publications, Switzerland, Applied Mechanics and Materials. 390 (2013) 172-177.
- [10] J. Králik, J. Králik, jr. Deterministic and Probabilistic Analysis of Non-symmetrical Wind Effects to Symmetrical High Rise Buildings. Proc. ESREL, Reliability, Risk and Safety, Theory and Applications, CRC Press/A.Balkema Book, Taylor&Francis Group, Prague, Czech Republic, 7-10 September, 2009, Vol. 2, pp. 1393-1396.
- [11] J. Králik, Safety and Reliability of Nuclear Power Buildings in Slovakia. Earthquake – Impact - Explosion. Ed. STU Bratislava, 2009, 295p.
- [12] M. Krejsa, P. Janas and R. Čajka, Using DOProC Method in Structural Reliability Assessment., Online available since 2013/Feb/13 at www.scientific.net, Trans Tech Publications, Switzerland, Applied Mechanics and Materials. 300-301 (2013) 860-86.
- [13] M. Krejsa, Probabilistic Failure Analysis of Steel Structures Exposed to Fatigue. Key Engineering Materials, Advances in Fracture and Damage Mechanics XII. Editors, A. Milazzo and M.H. Aliabadi. Zurich, Switzerland, Trans Tech Publications. 577-578 (2013) 101-104.
- [14] J. Melcer, Experimental testing of a bridge, Trans tech Publications, Switzerland, 2014, Applied Mechanics and Materials, 486 (2014) 333-340.
- [15] J. Melcher, Z. Kala, J., Kala, The Analytical and Statistical Approaches to Lateral Beam Buckling, In proc. Structural Stability Research Council, University of Florida, University of Florida, 2000.
- [16] D. Novák, K. Bergmeister, R. Pukl and V. Červenka, Structural assessment and reliability analysis for existing engineering structures, theoretical background. Structure and infrastructure engineering. 9 2 (2009) 267-275.
- [17] V. Salajka, P. Hradil and J. Kala, Assess of the Nuclear Power Plant Structures Residual Life and Earthquake Resistance, Trans Tech Publications, Switzerland, Applied Mechanics and Materials. 284 – 287 (2013) 1247-1250.
- [18] SHMU, Climatic and Hydrologic Conditions and the Radioactivity Background of the Locality Mochovce, Rep. 7-200-2011, SHMU, Bratislava, 2011.
- [19] A. Tesár, J. Melcer, Structural monitoring in advanced bridge engineering. John Willey & Sons, Ltd.2008. International Journal for Numerical Methods in Engineering. 74 (2008) 1670–1678.

Structure Analysis Loaded by Interior Blast Effect

MAKOVIČKA Daniel^{1, a*} and MAKOVICKA Daniel, Jr.^{2, b}

¹CTU in Prague, Klokner Institute, CZ-166 08 Praha 6, Šolínova 7, Czech Republic

²Static and Dynamic Consulting, CZ-284 01 Kutná Hora, Šultysova 170/8, Czech Republic

^adaniel.makovicka@klok.cvut.cz, ^bd.makovicka@makovicka.cz

Keywords: masonry, dynamic analysis, blast effect, response, assumption, angle of failure

Abstract. The paper determines the parameters of the explosion wave excited by a terrorist charge and assumption of the building structure of a railway station based on dynamic analysis. Certain simplified methods according to various publications, according to our own experimental results and according to 3D computations based on detailed calculation modelling of the interior of the room are compared to determine the explosive effects. Equivalent static analysis was applied to the dynamic response of the structural elements of the selected room. The damage caused to these structural elements is weighted on the basis of the angle of failure of the central axis / surface, and on the basis of the limit stress state of these structures.

Introduction

When a small charge explodes in the internal space of a building, a pressure wave is formed by the explosion that applies a load on the surrounding internal elements of the structure (Fig. 1). The pressure effects of even a small charge are usually high, and the primary consequence is that a window or a door structure may be broken and the pressure is released into the surrounding areas. Although the exhaust vents open, the load transmitted to the surrounding walls of the room, and to the ceiling and floors, is quite high, and the corresponding magnitude must first be estimated. This magnitude depends on numerous parameters that have an impact on the load level, and therefore it is appropriate to adopt simplifying assumptions. The load of the surrounding structure of the room can be determined either by means of relatively accurate calculations which take into account the internal space of the room, the composition of the explosive, and which deal with the interaction of the internal environment (air and combustion product mixture) with the structure of the room itself. Alternatively, simpler approximate procedures can be applied; these procedures are based on determining the parameters of the explosion load in a free space and then approximating them to the load in a semi-enclosed space (after the exhaust vents have opened).

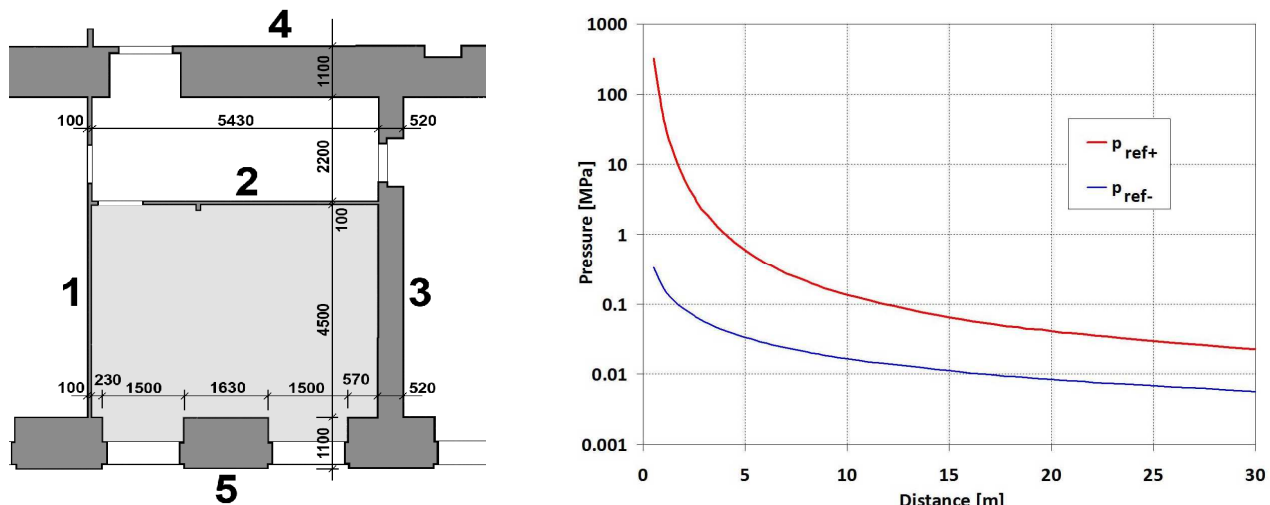


Fig. 1 Ground plan of a room and pressures p_{ref+} and p_{ref-} in dependence on distance R of the charge from the walls

Dynamic Load

After an explosion in the enclosed space of rooms in a building structure, with closed relieving vents, the load is increased by approximately 50% due to reflection from the surface of the walls, the ceiling and the floor of the room; the duration of the overpressure is thus roughly double.

After a normal (perpendicular) impact of the explosion wave on a solid obstacle in the open air conditions, a reflected wave is formed with the reflection overpressure p_{ref} that loads the building structure from the outside. The overpressure value in the reflected wave corresponds to approximately twice the value of the overpressure for low overpressure values p_+ of approximately up to 5 MPa (up to eight times the value for high overpressures of the order of several MPa) in the incident wave [1,2,3].

$$p_{load+} \approx 2 p_{ref+} \quad p_{load-} \approx 2 p_{ref-} \quad (1)$$

For bounded space the resulting load of the surrounding structures and its duration can be expressed approximately as follows:

$$p_{load+} \approx 1.5 p_{ref+} \quad t_{load+} \approx 2 \tau_+ \quad (2)$$

Formulas similar to those for the overpressure phase of the load also apply approximately to the underpressure phase.

The reflective overpressure $p_{ref} = p_{ref}^f = p_{ref+}$ in the rooms can also be calculated directly according to a method described in [3,4]. To determine the reflective overpressures and impulses, their values in the band $\bar{R} < 2 \text{ m/kg}^{1/3}$ must either be read from the published curves [4], or their approximate values must be determined using the derived exponential relationships:

a) Reflective overpressure:

$$p_{ref}^f = 14.554 \times \bar{R}^{-1.4587} \quad [\text{MPa}] \quad \text{for } 0.05 < \bar{R} \leq 0.5 \text{ m/kg}^{1/3}, \quad (4)$$

$$p_{ref}^f = 5.76 \times \bar{R}^{-2.762} \quad [\text{MPa}] \quad \text{for } 0.5 < \bar{R} \leq 5 \text{ m/kg}^{1/3}, \quad (5)$$

b) Reflective impulse:

$$I_{ref}^f = 0.345 \times \sqrt[3]{C_w} \times \bar{R}^{-1.857} \quad [\text{kPa.s}] \quad \text{for } 0.05 < \bar{R} \leq 0.5 \text{ m/kg}^{1/3}, \quad (6)$$

$$I_{ref}^f = 0.5823 \times \sqrt[3]{C_w} \times \bar{R}^{-1.0976} \quad [\text{kPa.s}] \quad \text{for } 0.5 < \bar{R} \leq 5 \text{ m/kg}^{1/3}, \quad (7)$$

where $\bar{R} = \frac{R}{\sqrt[3]{C_w}}$ is the reduced distance from the epicentre of the explosion, R is the distance [m],

and C_w is the equivalent mass of the charge [kg TNT].

When substituting input values C_w into the relationships above, two differences from the calculations of the reflective overpressure and the reflective impulse in the open space outside the building must be taken into account:

a) Here, the indices f denotes the detonation conditions in the free air space in the room, and the following is substituted for the charge size C_w :

$$\text{b) } C_w = C_N k_{TNT-p} k_E \quad k_G = C_N k_{TNT-p} k_E \quad (8)$$

where C_N is the mass of the used charge of the (actual) explosive [kg], k_{TNT-p} is the pressure tritol equivalent, k_E is the charge seal coefficient, $k_G = 1$ is the geometry coefficient of the impact wave spreading in the free air space and k_B is the cover mass [kg] divided by the explosive mass. The seal coefficient can be determined using the relationship

$$k_E = 0.2 + 0.8 / (1 + k_B). \quad (9)$$

Mechanical Characteristics of Structure Loaded by an Explosion

When dynamically loaded by an explosion, masonry structure displays almost linear elasticity up to the point of failure [5]. The structure should be analysed using the following load combinations [3,6] applied to the whole structure together with an instantaneous loss of primary vertical support:

a) static analysis: $\delta (1.2D + 0.25L), \quad (10)$

b) dynamic analysis: $D + (0.25 \text{ or } 0.50)L, \quad (11)$

or for alternate load path method (checking if residual load-carrying capacity upon notional removal of a selected load-bearing element [2,6,7])

$$(0.9 \text{ or } 1.2)D + (0.5L \text{ or } 0.2S) + 0.2W_n, \quad (12)$$

where: D is dead load ($1.2D$ or $1.0D$ is usually recommended), L is live load, S is snow load for roof and W_n is wind load for periphery structure elements (walls columns window, door, etc.) and δ is dynamic load factor.

For frame structures a column removal should be analysed for one floor above ground. The exterior locations of columns to be removed include the middle of the short side and long side and the corner of the building.

The real elastic modulus E is an important material quantity for calculating the response of masonry to the load due to an explosion. It can be estimated according to the deformability modulus E_{def} stated in the design standards, based on the experimentally verified experience [5] of the authors of this paper:

- a) For the response of an undamaged structure near the failure limit $E \approx 0.5E_{def}$,
- b) For a structure already damaged by visible cracks: $E \approx 0.1E_{def}$.

The loading capacity of the brick masonry is decided in accordance with the standards used to design the bending compression / tensile strength of the masonry, with a certain margin of safety, given by the coefficients of the load, combination, etc.

If the loading capacity R_{tf} is exceeded, a crack appears in the structure of the material. Thus the most unfavourable condition must apply to a safe structure, based on comparing the stress state or the deformation magnitude. The following relationship applies to the stress combination:

$$\min (\sigma_g \pm \sigma_{expl}) \geq -R_{tf} \text{ or upon adjustment } \sigma_{expl} - \sigma_g \leq R_{tf}, \quad (13)$$

where σ_{expl} is stress caused by the effects of the pressure wave when there is an explosion, σ_g is the normal stress at a given place (a joint) caused by the overburden weight itself.

In structural design based on limit state theory, it is usually more suitable to consider the carrying capacity strength moment, possibly in combination with the normal force, rather than the carrying capacity limit R_{tf} . This stress criterion must be supplemented by an evaluation of the deformation of the structure.

Satisfying acceptance criteria for linear and nonlinear static analysis consist in obtaining the actual internal forces caused by load combinations and compare them with member capacities. An indicator DCR (Demand-Capacity Ratio [6]) is defined by

$$\text{DCR} = Q_{UD} / Q_{CE}, \quad (14)$$

where Q_{CE} is expected ultimate, unfactored capacity and Q_{UD} is actual force (demand) in structural member or joint (bending moment, shear or axial force).

For reinforced concrete structures allowable DCR = 2.0 for typical structural configurations and DCR = 1.5 for atypical structural configurations. For steel structures allowable DCR values depend on section compactness, and are in the range (1.0 – 3.0) for typical structural configurations. The criteria for atypical structural configurations are multiplied by 0.75, but not less than 1.0. For the dynamic analysis the acceptance criteria may differ from the static ones. Moreover, the analytical results of the linear static approach are not compatible with the results from the nonlinear static and nonlinear dynamic approaches.

As a rule, the limit deformation value (shift or angular displacement) determines the actual destruction of the wall; the limit deformation value corresponds to the critical angle of the partial turning of the central line of the structure due to its bending. The limit angular displacement ψ at the failure limit is:

$$\psi = \arctg (x_m / (0.5 h_{span})), \quad (15)$$

where x_m is the maximum achieved dynamic displacement caused by the explosion load and h_{span} is the span of the plate ceiling structure or the height of the wall structure within one storey, or the span of any beam, the height of a column, etc.

Evaluations of structures loaded by an explosion based on dynamic displacement and rotation round the central line of plate, wall or beam systems during the action of a dynamic load of this type have been of very topical interest in recent times, as regards the process of evaluating the effects of an explosion on a structure. In earlier publications [2,3,5,8], the authors applied this procedure to various types of materials and structure systems, and on the basis of an experimental comparison they determined the failure angle ψ_{\max} , i.e. the angle where damage is caused to the structure by breaking (Table 1). The stability of the structure with the cracks should be assessed in order to prevent any collapse of the structure due to the formation of plastic joints and cracks.

Table 1 Limit failure angle ψ_{\max} [°] upon breaking of the material [2]

Type	Structure material	ψ_{\max} [°]
1	Concrete C16/20 to C40/50	6.5
2	Masonry, full bricks 10, mortar 4 or mortar 10	5.0
3	Masonry, cement bricks, mortar 4	4.5
4	Masonry, cellular concrete or perforated precise blocks, mortar 4	4.0
5	Steel S235	10.5
6	Wood, hard and soft	12
7	Window glass, thickness 3 mm	6

As for impact phenomena (very rapid) during bending stress of the structure, the ductility coefficient k_m can usually be considered to be equal to 3 to 5 for masonry, and from 5 to 10 for reinforced concrete, steel and wood. As for the load due to the impact wave, the dynamic load factor including consideration of the ductile behaviour of the structure is found to be in the range $\delta = 1 \sim 2$ (DoD UFC Guidelines [6] recommends 2.0 and other works conclude that the use of a fixed dynamic load factor of 2.0 is highly conservative).

Evaluating the Failure Probability for a Specific Room

The equivalent static calculation of the wall uniformly and continuously loaded by load p_{load+} with duration of its effect t_{load+} was used to determine the failure hazard. In this procedure, the nature of the boundary conditions (support of the wall board) is chosen. As concerns the partition walls of a specific building, the individual wall board elements were considered to be independent, for the sake of simplification, hinge-mounted along their entire circumference. From the viewpoint of uncertainty in the simplified effect of the pressure wave from the explosion, even such a simplification is acceptable and justified for an engineering estimate of the explosion effects.

When calculating the load level p_{load+} , the load is found to be in the range of units of MPa or hundreds of kPa inside a room (Fig. 1), based on the position of the charge inside the room. When comparing such high loads with the carrying capacity of the windows and doors, it reaches several units of kPa. It is apparent that such window and door openings will be smashed (destroyed) and will enable the pressure to be released into the surrounding (external or internal) areas.

Table 2 shows the calculated bending moments in the middle part of the wall board in vertical and horizontal directions, maximum deflection y at the centre of the wall board and the angle ψ of angular displacement of the centre line of the wall board. The angle of 5° was chosen as the limit angle ψ at which the wall board masonry breakdown occurs (fracture, sweeping out of brick fragments, etc.) For the sake of transparency, the individual walls of the room are numbered and these numbers are shown in the ground plan of the room in Fig. 1.

It follows clearly from Table 2 that thin partition walls up to 150 mm in thickness will be destroyed by the explosion. As the explosion pressures markedly exceed the carrying capacity of such thin partition walls, the ruins of the partition walls will be swept into the surrounding areas. Thick bricked walls and interwindow pillars 900 mm and more in thickness will be destroyed only if the charge is placed in their vicinity, at a distance of about 1 m. For distances of the charge of more than 2 m, such a massive structure will transfer the explosion pressures without collapsing and without any other serious defects. Of course, the plaster will be damaged, cracks will appear in the walls, brick fragments may fall out, etc., but the structure will not collapse. If a massive carrying wall or pillar (more than 900 mm in thickness) collapses under this ceiling, it is likely that the ceiling structure will fall through and damage will also occur to higher floors.

Table 2 Failure risk estimation of structural parts (Fig. 1)

Structural element		Distance of charge	Explosion load	Load duration	Vertical moment	Horizontal moment	Displacement	Rotation	Failure estimation
		R [m]	p_{load+} [MPa]	t_{load+} [s]	M_{ver} [kNm]	M_{hor} [kNm]	y [mm]		
1	Wall 6700×2800×100	2.5	5.09	0.008	116	45	2282	117.0	Expected
2	Wall 5430×2800×100	5	0.89	0.011	28	11	557	43.4	Expected
3	Wall 6700×2800×520	3	3.15	0.009	409	160	57	4.7	Partial failure
4	Wall 5430×2800×1100 mm	1	64.74	0.005	10202	4122	151	12.3	Probable
		2	9.27	0.007	2 030	820	30	2.5	Improbable
5	Pillar 1630×2800×1100 mm	1	64.74	0.005	9227	4050	44	6.3	Partial failure
		4	1.52	0.010	369	162	2	0.3	Improbable

Conclusion

An example of a railway station room was used to discuss the explosion and the building safety hazard when a terrorist charge is brought into the building in a suitcase and is equipped with a system for initiating the charge after it has been placed in the building and the terrorist has left. Due to uncertainties in all parameters of the explosion load, a simplified methodology has been presented here derived by the authors for small charges [2,3,9].

The response of the structure is evaluated on the basis of the results of the equivalent static calculation for the elastic-plastic system. The explosion hazard of the structure is evaluated on the basis of internal forces and deflections of the structure. The structure response was assessed based on the results of a 3D dynamic computation according to the magnitude of internal forces and displacements, and partial rotation of the central line of beam or slab cross-sections of the structure. Currently, structure assessment methodology based on partial rotation of the cross-sections has been in the process of development [9]; it corresponds to the most recent research trends. The authors used limit values determined experimentally upon explosion load of brick-layered, reinforced concrete and window glass boards based on comparing their own [2,3,8,9] and other published results [6].

The example of a specific room is used to analyze its exposure and also the hazard to the entire building based on various possible distances of the charge from the carrying building structure.

Acknowledgement

The study is based on outcomes of the research project VG20122015089 supported by the Ministry of the Interior of the Czech Republic.

References

- [1] J. Henrych, The dynamics of explosion and its use, Academia, Prague, 1979.
- [2] D. Makovička, Explosion hazard to buildings and design load parameters, in: N. Jones, C.A. Brebbia (Eds), Structures Under Shock and Impact VI, WIT Press, Southampton, 2000, pp. 373-382.
- [3] D. Makovička, B. Janovský, Handbook of explosion protection for buildings (in Czech), CTU Publishing House in Prague, 2008.
- [4] W.E. Baker, W.E., P.S. Westine, P.A. Cox, et al., Explosion hazards and evaluation, Elsevier, Amsterdam 1983.
- [5] D. Makovička, Failure of masonry under impact load generated by an explosion, Acta Polytechnica. 39 1 (1999) 63-91.
- [6] DoD UFC Guidelines, Design of buildings to resist progressive collapse, Unified Facilities Criteria (UFC) 4-023-03, Department of Defence (DoD), 2005 (with updates from 2009 and 2010).
- [7] ASCE 7, Minimum design loads for buildings and other structures, American Society of Civil Engineers, 2005.
- [8] D. Makovička, D. Makovička, Simplified evaluation of a building impacted by a terrorist explosion, in: N. Jones, C.A. Brebbia (Eds), Structures Under Shock and Impact XI, WIT Press, Southampton, 2010, pp. 93-104.
- [9] D. Makovička, D. Makovička, Blast resistant design and limits of the response of a structure to an external explosion, in: G. Schleyer, C.A. Brebbia, (Eds), Structures Under Shock and Impact XII, WIT Press, Southampton, 2012, pp. 229-239.

Single Degree of Freedom Analysis of Steel Beams under Blast Loading

FIGULI Lucia^{1,a*} and PAPAN Daniel^{2,b}

¹ Department of Technical Sciences and informatics, Faculty of Special Engineering, University of Žilina, Ul. 1. Mája 32, 010 26 Žilina, Slovak Republic,

² Department of Structural Mechanics, Faculty of Civil Engineering, University of Zilina,
Univerzitná 8215/1, 010 26 Žilina, Slovak Republic

^alucia.figuli@fsi.uniza.sk, ^bdaniel.papan@fstav.uniza.sk,

Keywords: SDOF model, blast loading, blast wave dynamic analysis

Abstract. The paper deals with the analysis of steel beams subjected to blast load approximated as a one degree system of freedom (SDOF). It requires knowing the parameters of blast pressure wave, its effect on structure and the tools for the solution of dynamic analysis. The blast wave is estimated with linear decay and exponential decay using positive and negative phase. The results of SDOF model are compared with the corresponding experimental accelerations and strain time-histories. There is a described dynamic analysis for such structure.

Introduction

The elements from the sectors of the critical infrastructure are objects, which can cause extensive damage not only in terms of protection of human life and health, but also to the economy and to performance of the state functions; are [6]. The elements of the critical infrastructure are the second most important target, right after the human targets. Resistance of the security tools used for protection of an object as well as resistance of the building particles of an object both play a significant role in protection of the critical infrastructure. If it is inadequate, the probability of a successful security breach is higher and so is the probability of the actual attack on this object [7]. The possibility of a terrorist attack stems from the instability and unpredictability of developments in the security field in the world. Bombing tactics can be applied on all elements of the critical infrastructure sectors or on personal targets [8]. This article presents the results of scientific research at the Faculty of Special Engineering, University of Zilina.

Experimental Tests

We did field tests using ANFO explosives on 21st January 2014. The field tests took place at Military Technical and Testing Institute Zahorie. The field tests were focusing on the measurement of overpressure and its influence on steel beams. POLONIT was used as the explosive. The weight of charges were selected: 2.3 kg (pipe bomb), 4.5 kg (bomb belt) and 9 kg (bomb vest – it was not detonated because of a high overpressure of 4.5 kg explosive which caused a damage of construction with steel beams). The explosives were used together with 25 g of ignition explosive PLNp10. The sensors were placed in the height of 1.6 m in the angle of 45° from the normal line in the distances 2 m, 5 m and 10 m from the source of the explosion. One of the sensors was orientated in parallel with steel beams in the distance of 5.5 m opposite of gabion wall and in the distance of 3 m from the source of explosion (we wanted to record the reflected blast wave). The explosive charges were placed at a wooden base in the height of 10 m. The structure consists of steel frame and four wide flange steel beams HEB 100 and 12 steel beams IPE 120 with span length of 1770 mm. For convenience the beams were tested in the vertical positions and simply supported. They were loaded mainly to bending caused by the blast pressure as the axial stress due to self-weight was practically negligible. All the beams were pinned at the top and roller supported at the bottom (see Fig. 1). The mechanical characteristic, the nominal static yield and ultimate strength of the HEB 100

section were 313 and 441 MPa. The nominal static yield and ultimate strength of the IPE 120 section were 330 and 452 MPa.

During the blast test pressure, strain and acceleration were measured. Maximum overpressure was measured using blast pressure sensors type 137A23 and 137A24 PCB Piezotronics. The sensors were placed in the height of 1.6 m in the angle of 45° from the normal line in the distances 2 m, 5 m and 10 m from the source of the explosion. One of the sensors was orientated in parallel with steel beams in the distance of 5.5 m opposite of gabion wall and in the distance of 3 m from the source of explosion (we wanted to record the reflected blast wave). The strain time histories were measured at the middle of beams number 2, 5, 12, 15 by surface strain sensors and accelerations by the accelerometers.



Fig. 1 Field tests: a) blast pressure sensors

b) steel beams

Blast Loading

Steel beams are loaded by blast wave. The source for the blast load is a detonation of the explosive. For any explosion, the charge weight and the standoff distance are used to determine the shock wave loaded at given point. The real detonation of spherical charge runs in such way that the detonation wave extends from the centre of the charge in all directions. Its front strikes against the surrounding environment at the charge brim. From this point the blast wave extends and after the gas explosions the reflected one is distributed. The blast wave profile has two phases – positive and negative one. Its real form is approximated with the regular shape with one peak and then it drops below the ambient pressure (Fig. 2).

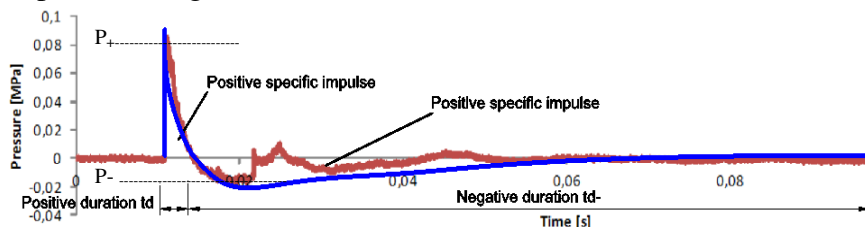


Fig. 2 Real and approximated blast wave time history, P_0 - ambient pressure, P_+ - peak value of overpressure, P_- - under pressure, t_A - arrival time of blast wave, t_d - duration time of blast wave

A pressure time history of blast wave is idealized as a triangular pulse having a peak force P_+ and positive duration t_d . The simplest form assumes a linear decay

$$P(t) = P_+ \left(1 - \frac{t}{t_d}\right). \quad (1)$$

The most realistic idealised pressure time history of blast wave can be described with mathematical function (Eq. 2), where b is a shape parameter important for the shape of negative phase. Our research concludes that the shape parameter $b = 1.1$ describes the pressure time history the most satisfactory way

$$P(t) = P_+ \left(1 - \frac{t}{t_d}\right) e^{-bt/t_d} . \quad (2)$$

Equivalent SDOF System

The analysis of dynamic response of blast-loaded structures is very complex. To simplify the analysis, the structure is idealized as a single degree of freedom (SDOF) system. Therefore, so called single degree of freedom system is a springmass-damper system where the mass is allowed to move in only one direction. For structures under the impulsive loads (blast loads) damping has much less importance because the maximum response will be reached in a very short time, before the damping forces can absorb much energy from the structure. The effects of damping are hardly ever considered in blast design because of the following reasons:

- (1) Damping has very little effect on the first peak of response which is usually the only cycle of response that is of interest.
- (2) The energy dissipated through plastic deformation is much greater than that dissipated by normal structural damping.
- (3) Ignoring damping is a conservative approach [1].

To make the SDOF system response equivalent to that of the real system, equivalent SDOF factors are used to obtain the effective mass, force, and resistance terms [3]. Equivalent SDOF factors for simply supported beams are in Table 1.

Table 1 Equivalent SDOF factors for simply supported beam

Loading diagram	Strain range	Load factor K_L	Mass factor K_M	Spring constant
uniform	elastic	$K_L = \int_0^L \frac{p(x)\phi^2(x)dx}{pL} = 0.64$	$K_M = \int_0^L \frac{m(x)\phi^2(x)dx}{mL} = 0.50$	$\frac{384EI}{5L^3}$

We have to transform the real mass of the beam to equivalent mass using load factor (Table 1) where ϕ is the shape function. In the next step it is necessary to determine equivalent force-total load applied on the structural element is multiplied to obtain the equivalent concentrated load for the equivalent SDOF system using load factor K_L .

Mechanical properties are very important in determining the resistance of a structure subjected to blast loads. The mechanical properties, especially yield stress, of steel under dynamic loading condition are quite different from that under static loading. The stresses that are sustained under dynamic conditions gain values that are remarkably higher than the static compressive strength. This enhancement is described in terms of the dynamic increase factor (DIF), which can be evaluated for different steel grades. Details of dynamic increase factor c are written in [1]. For our beams $c = 1.29$ and $a = 1.1$.

In our field test we have managed measured only two explosions. In explosion n. 1 (1 kg) and No. 2 (2.3 kg), the maximum pressure have been not recorded. In explosion No. 5 strains and accelerations have been not recorded. Therefore we can compare only two set of results.

Table 2 Strain and acceleration of test beams and SDOF system

Test No.	Charge	Test P+ [kPa]	Positive impulse $\tau+$ [s]	Beam	Strains [$\mu\epsilon$]			Accelerations [m/s^2]				
					Test min	Test max	SDOF linear decay	SDOF exponential decay	Test min	Test max	SDOF linear decay	SDOF exponential decay
3	Polonit - 2.3 kg + 25 g PLNp10	122.8	0.00423	T1 HEB 100	-98.28	96.81	165.03	143.64	-1005.20	1044.63	435.57	391.14
				T2 IPE 120	-162.74	154.71	195.00	162.45	-1039.11	712.27	546.81	503.52
				T3 IPE 120	-153.66	186.73	195.00	162.45	-781.55	1013.61	546.81	503.52
				T4 HEB 100	-70.46	95.33	165.03	143.64	-205.07	352.33	435.57	391.14
4	Polonit - 4.5 kg + 25 g PLNp10	153.4	0.00367	T1 HEB 100	-215.05	250.97	189.78	172.67	-875.62	1044.63	544.11	476.25
				T2 IPE 120	-282.07	154.00	226.97	197.54	-756.96	1032.90	683.07	615.57
				T3 IPE 120	-279.97	322.79	226.97	197.54	-1034.82	1043.45	683.07	615.57
				T4 HEB 100	-205.85	160.98	189.78	172.67	-232.10	432.39	544.11	476.25

Summary

The results of SDOF model (loading function with linear and exponential decay) were compared with the corresponding experimental accelerations and strain time-histories. SDOF model with the exponential decay could predict reasonably well the strain obtained from the experimental measurements. The acceleration results are different from experimental ones. It can be caused by badly prepared steel frame, where the beams were pinned. After the explosion No. 4 the steel frame showed no stiffness. We would like to continue with these tests after the deficiencies and focus on model based on finite elements methods too.

Acknowledgements

This contribution is the result of the research supported by project APVV 0471-10 Critical Infrastructure Protection in Sector Transportation

References

- [1] UFC 3-340-02 Structures to Resist the Effects of Accidental Explosions.
- [2] J.M. Biggs, Introduction to Structural Dynamics, 1964 ISBN 07-005255-7.
- [3] H.A. Buchkoldt, Structural dynamics for Engineers.
- [4] A.A. Nassr, A.G. Razaqpur, M.J. Tait, M. Campidelli, S. Foo, Single and multi degree of freedom analysis of steel beams under blast loading, Nuclear Engineering and Design 242, 2012.
- [5] R.W. Clough, J. Penzien, Dynamics of Structures, Berkley USA, 1995.
- [6] Z. Dvořák, E. Sventeková, Evaluation of the resistance critical infrastructure in Slovak Republic. Novi sad : s.n., 2012.
- [7] D. Vidriková, Z. Dvořák, V. Kaplan, The current state of protection of critical infrastructure elements of road transport in the condition of the Slovak Republic, Transport means 2011, 2011.
- [8] Š. Jangl, V. Kavický, Detection explosives, ammunition and improvised explosive device, EOD future in the light of NATO EOD Demonstrations and Trials 2012, a book of papers, Trenčín, NATO EOD Centre of Excellence, 2012, p. 43-53.

Impact Resistance of Thin-Walled Shell Structures

REHACEK Stanislav^{1,a*}, HUNKA Petr^{1,b}, CITEK David^{1,c}, KOLISKO Jiri^{1,d}
and SIMUNEK Ivo^{1,e}

¹Klokner Institute, CTU in Prague, Solinova 7, 166 08 Prague, Czech Republic

^astanislav.rehacek@klok.cvut.cz, ^bpetr.hunka@klok.cvut.cz, ^cdavid.citek@klok.cvut.cz,
^djiri.kolisko@klok.cvut.cz, ^eivo.simunek@klok.cvut.cz

Keywords: impact load test, concrete, drop-weight test, steel fibers, specimen

Abstract. Fibre-reinforced composite materials are becoming important in many areas of technological application. In addition to the static load, such structures may be stressed with short-term dynamic loads or even dynamic impact loads during their lifespan. Dynamic effects can be significant especially for thin-walled shell structures and barrier constructions. Impact loading of construction components produces a complex process, where both the characteristics of the design itself and the material parameters influence the resultant behavior. It is clear that reinforced concrete with fibers has a positive impact on increasing the resistance to impact loads. Results of impact load tests carried out on drop-weight test machine are presented in this paper. The results are supplemented by compression strength test.

Introduction

The goal of the project is to establish new procedures for evaluating the impact resistance of cementitious composites. An appropriate shape of test specimens, ways to support the test specimens and the method of measurement were chosen on the basis of experiments [1,3,4,6]. The load tests of specimens reinforced with different fibre content of reinforcement were made afterwards. The rectangle specimens 700×300, of thickness 50 mm were selected for drop-weight test. The load tests of specimens reinforced with different type of fibre reinforcement were made afterwards. The drop-weight tests were supplemented by mechanical tests, compressive strength.

Mix Design

Each mix design, with different type of reinforcement is given in Table 1.

- Unreinforced concrete – Mix design A.
- The polypropylenes Fibers FORTA FERRO TM 54 were used in Mix design B.
- The synthetic Fibers CHRYSO FIBRE S50 were used in Mix design C.
- The synthetic Fibers CHRYSO FIBRE S-CRETE 500 were used in Mix design D.

Table 1 Mix design A to D

MIXTURE	A	B	C	D
Concrete component	[kg/m ³]	[kg/m ³]	[kg/m ³]	[kg/m ³]
CEM I 42.5 R	380	380	380	380
Microfume	15	15.3	15.5	15.5
Fine 0 - 4mm	886	894	886	897
Aggregate:	Coarse 4 - 8mm	282	275	272
	Coarse 8 - 16mm	555	551	557
Superplasticizer, Chysos	3.69	3.69	3.69	3.54
Air Entrainers, Chysos	0.69	0.77	0.69	0.69
Polypropylene Fibers Forta Ferro TM 54	-	2	-	-
Synthetic Fibers Chryso Fibre S50	-	-	2	-
Synthetic Fibers Chryso Fibre S-CRETE 500	-	-	-	2
Water	165	157	157	157

Test Specimens

All test specimens were made into wood moulds, compacted on vibratory table. Specimens were demoulded after 24 hours and then stored in water according to EN 12390-2 [5] for 28 days. The test specimens were stored in dry place up to the test. Before testing, the specimen were measured and weighed.

Drop-Weight Test

The Drop-Weight test was carried out in Drop-Weight test machine. The rectangle specimens (700×300×50 mm) were supported along the shorter sides. The blows were introduced through a 9.5 kg hammer, falling continually from 10 cm height. The hammer head with these parameters was used - diameter 35 mm, rounding end (diameter 120 mm). The number of blows to the first visible crack (First-crack strength) and the number of blows to the failure (Failure strength) were monitored. For the mix design A (unreinforced concrete), the first-crack strength = failure strength. The test results are shown in Table 2 and Fig. 2. Experimental setup is visible in Fig. 1.



Fig. 1 Experimental setup – Drop-Weight test

Table 2 Test results - Drop-Weight test

Mix design/specimen number	Drop-weight test results	
	Fall from 10 cm	
	First-crack strength (blows)	Failure strength (blows)
A/1	2	2
A/2	3	3
A/2	2	2
B/1	2	4
B/2	2	4
B/3	3	5
C/1	2	6
C/2	2	11
C/3	2	9
D/1	4	7
D/2	4	6
D/3	2	4

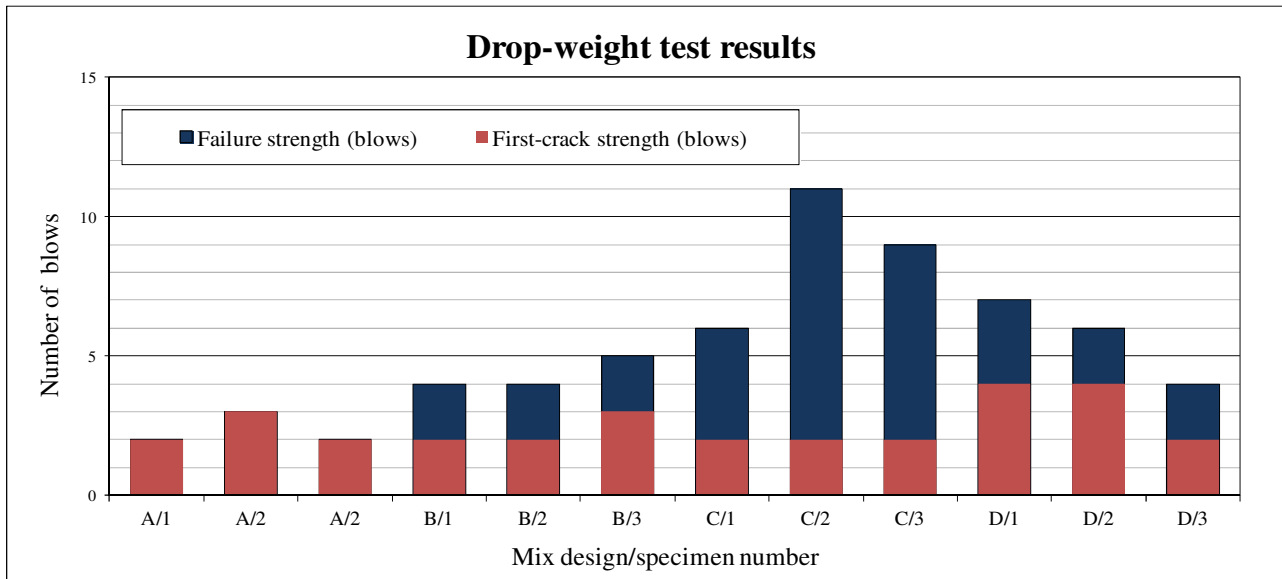


Fig. 2 Test results - Drop-Weight test

Mechanical Tests

The drop-weight tests were supplemented by mechanical tests - compressive strength. Not recorded significant influence of the addition of a specific type of fibers on the mechanical properties was found. Any proposed formulation meets the requirements set out in the proposal. The test results are shown in Table 3.

Table 3 Test results - mechanical test

Mix design		A		B		C		D	
Specimen-test	age of test [days]	com. strength [MPa]	density [kg.m ⁻³]	com. strength [MPa]	density [kg.m ⁻³]	com. strength [MPa]	density [kg.m ⁻³]	com. strength [MPa]	density [kg.m ⁻³]
Cylinder - com. strength	28	61.8	2300	56.7	2260	56.1	2280	54.4	2280
Prism - com. strength	28	56.5	2260	53.4	2250	58.0	2260	55.3	2260

Summary

The percentage increases of the different mixtures are shown in Table 4. As a basis for comparison, mix design A (unreinforced concrete) is chosen.

Table 4 Test results

Shape of the specimen	Type of test	Parametr	Mixture			
			A	B	C	D
Rectangle specimens	Dynamic load test, drop-weight test	Failure strength (blows)	2.3	4.3	8.7	5.7
		Increase [%]	-	87	278	-12
Cylinder	Compressive strength	Compressive strength [Mpa]	61.8	56.7	56.1	54.4
		Increase [%]	-	-8	-9	-12
Prism	Compressive strength	Compressive strength [Mpa]	56.5	53.4	58	55.3
		Increase [%]	-	-5	3	-2

The results obtained so far can be summarized as follows:

- Rectangle specimens 700×300 and 50 mm thickness were selected as the optimum form the test.
- The amount of 2 kg/m³ fibers reinforcement was chosen for the test.
- In mix design C and D synthetic Fibers were used (CHRYSO FIBRE S50 and CHRYSO FIBRE S-CRETE 500).
- In mix design B polypropylenes Fibers were used (FORTA FERRO TM 54).
- The Drop-weight test shows the overall increase of failure strength between the mix designs.
- The increase in failure strength between unreinforced concrete (mix design A) compare to mix design C and D (synthetic Fibers) is significantly bigger than the increase between unreinforced concrete (mix design A) compare to mix design B (polypropylenes Fibers).
- For the mix design A (unreinforced concrete), the first-crack strength = failure strength.
- The drop-weight tests were supplemented by mechanical tests - compressive strength. Not significant influence of the addition of a specific type of fibers on the mechanical properties was found.

Acknowledgements

This contribution is the result of the research supported by the grant projects 14-19561S.

References

- [1] A. Bentur, S. Mindess, N. Banthia, The behaviour of concrete under impact loading, Experimental procedures and method of analysis, Matériaux et Constructions, 19 (113) 371-378.
- [2] J. Kolisko, M. Dudikova, T. Klecka, Bending test fiber reinforced concrete with polypropylene fibers. Effect of the shape of the test beam, 6 Conference Special Concrete, Sekurkon Prague, Beroun, 2009, pp. 186-193.
- [3] A. Bentur, A. Mufti, N. Banthia, Fibre reinforced concrete, Present and future, Canadian Society for Civil Engineering, October, 1998.
- [4] N. Banthia, S. Mindess, A. Bentur, M. Pigeon, Impact testing of concrete using a drop weight impact machine, Experimental Mechanics, 29 1 (1989) 63–69.
- [5] EN 12390-2, Hardened Concrete - Part 2: Making and curing specimens for strength tests, German version.
- [6] S. Rehacek, P. Hunka, J. Kolisko, L. Kratochvile, Two type of impact load tests, tested on fibre reinforced concrete specimens, Concrete and Concrete Structures, 2013, Zilina, University of Zilina, 2013, pp. 278-283.

Impact Loading of Concrete Slabs

JENDŽELOVSKÝ Norbert^{1,a} and VRÁBLOVÁ Kristína^{1,b*}

¹Slovak University of Technology, Faculty of Civil Engineering, Radlinského 11, 813 68 Bratislava,
Slovak Republic

^anorbert.jendzelovsky@stuba.sk, ^bkristina.vrablova@stuba.sk

Keywords: impact loading, concrete slabs, impact force, FEM-model

Abstract. In this article the impact loading of concrete slabs has been presented. Different methods for calculation of impact forces have been considered. Numerical models of two slabs with different boundary conditions have been analyzed using the Finite Element Method in ANSYS software. In the final part of the paper, z -direction displacements and bending moments of models have been compared.

Introduction

The main motivation why to investigate and calculate the effects of impact load upon structures is that it can induce internal forces which might result in failure of structure. The accidental actions are mentioned in Eurocodes, specifically in EN 1991-1-7 and EN 1991-1-6. Dynamic impact is described in detail in EN 1991-1-7 while EN 1991-1-6 mentions accidental action as impact from construction vehicles, cranes, building equipment or materials in transit, which match our design situation closer, but it does not provide any formulas or standard values for structural design. [4]

Impact in Eurocode EN 1991-1-7

Impact is an interaction between a structure and a moving object. During the impact, the kinetic energy of the moving object is transferred to deformation of a structure. In design, equivalent static force for expression of the dynamic interaction force is commonly used. In fact, Eurocode mentions following fields of the impact application:

- impact from road vehicles,
- impact from forklift trucks,
- impact from trains,
- impact from ships,
- the hard impact of helicopters on roofs.

Eurocode distinguishes between two kinds of impacts: the hard impact (where the energy is mainly dissipated by the impacting object) and the soft impact (where the energy is absorbed by structure) [3].

By the Comité Euro-International du Béton [5] beam can be idealized as a single degree of freedom system. This document also categorizes the impacts into soft and hard ones.

Here, a single spring-mass system is proposed for modeling of soft impact while a two spring-mass model is used for hard impact (Fig. 1).

To improve and speed up the performance in civil engineering practice, the designers have to use simplified methods given in Eurocodes. In this article the authors focus on numerical methods for calculation of the effects of impact force on concrete slabs.

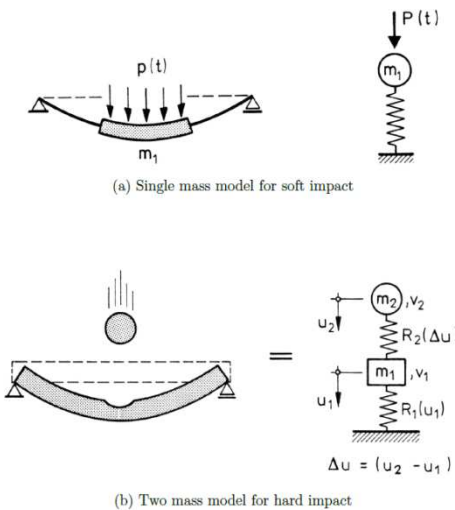


Fig. 1 Mass-spring model for impact [5]

Calculation of Impact Force

It is not easy to find a value of the impact force. The value of impact force can be calculated from the formula of momentum:

$$\vec{F} = \frac{\Delta \vec{p}}{\Delta t} = \frac{m \Delta v}{\Delta t}, \quad (1)$$

where Δv stands for impact velocity, m is a mass of falling object and Δt is time of impact. The problem is to find the value of impact time. Different sources present different methods of calculation [1,2]. The most suitable way how to obtain the value of Δt is an experiment. The impact time depends on natural angular frequency of structure:

$$\omega = \sqrt{\frac{k}{m}}, \quad (2)$$

where k is the stiffness of construction and m is construction mass [1,2].

Numerical Example

Two 2D models of concrete slabs in ANSYS were created, which differed in boundary conditions. The first model (Model A) (Fig. 2a) was supported in corners and the second model (Model B) (Fig. 2b) was supported on four edges by fixing of z -direction displacements. The geometry of both models was identical: span 7×7 m and thickness 180 mm. Models were made from 2D elements SHELL43 with material properties of concrete, i.e. Young's modulus 30 GPa, Poisson's ratio 0.15 and density 2500 kg/m³.



Fig. 2a Model of a slab supported in corners



Fig. 2b Model of a slab supported on four edges

As a first step, the impact force of falling object had to be calculated. The object with the mass $m = 50$ kg, which was falling from the height $h = 10$ m, was considered. The courses of the impact forces on Model A and Model B are in the Fig. 3.

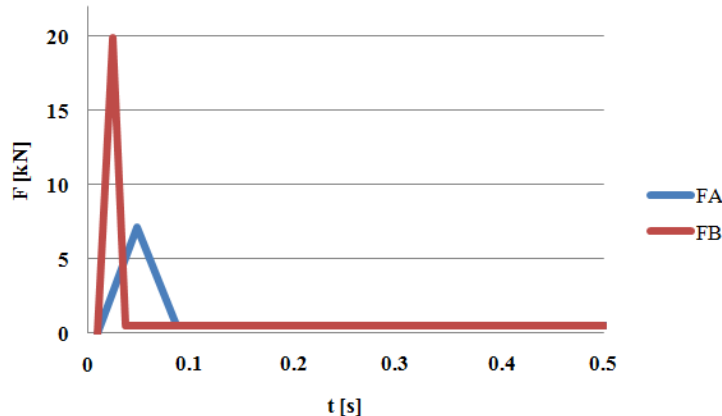


Fig. 3 The course of impact force on structure

From the Fig. 3 it is clear, that impact time of force considered in Model B is smaller than impact time of force considered in Model A. The values of impact forces are also different and depend on length of impact time. These facts yield from the formula of momentum while differences between models yield from different stiffness of slabs.

Conclusion

The z -direction displacements were monitored in 4 points. The location of points is presented in Fig. 4. The damping constants were chosen 5 % for both models.

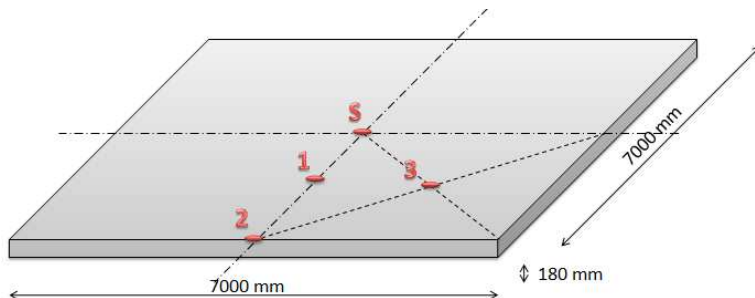


Fig. 4 Location of monitored points

Negative values of displacements represent displacements below the level of slab and positive values represent displacements above the level of slab. Model A becomes stable in 4 seconds after the action of impact force. The course of the displacements (in points described in Fig. 4), as well as the deformed shape of slab in time of maximum z -direction displacements are presented in Fig. 5. Model A reached also positive values of z -direction displacements nevertheless the impact force was smaller than in Model B. It is because of smaller rigidity of the slab in Model A.

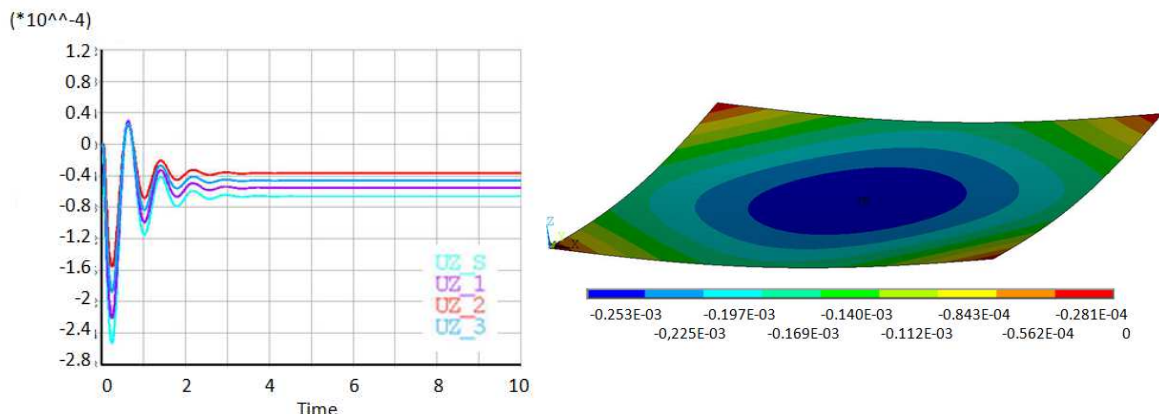


Fig. 5 Course of z -direction displacements and deformed shape of Model A

Model B became stable in 0.6 seconds. Its displacement did not reach positive values. The course of displacements in points “1”, “2”, “3” and “S” can be observed in Fig. 6, where one can also see the deformed shape in time of maximum z-direction displacements.

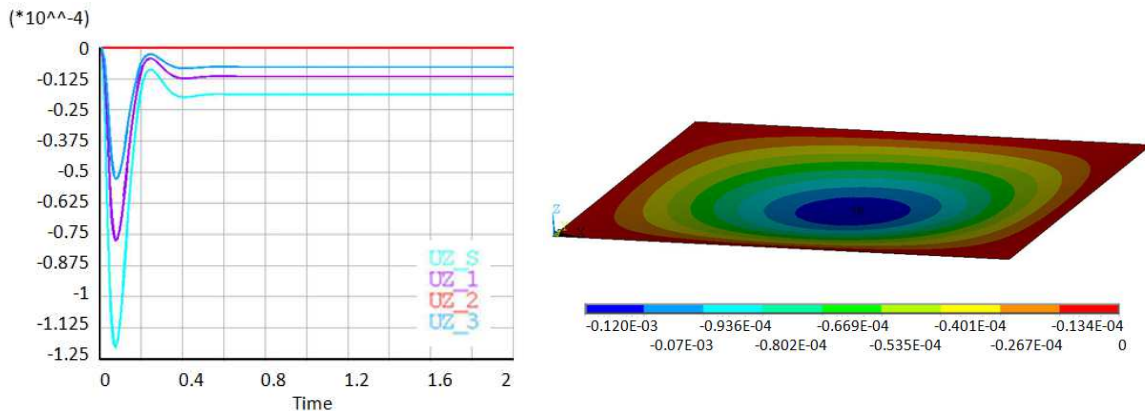


Fig. 6 Course of z -direction displacements and deformed shape of Model B

Summary

The comparison of models A and B is in Table 1. The maximum values in point “S”, the time when they were reached and respective maximum bending moments on slabs are presented here. Bending moments in x - and y -directions are identical because the slabs are symmetric. The maximum value of z -direction displacement is in Model A, because it has a smaller rigidity. One can also observe the same behaviour in bending moments. The stiffness of the models also affected the time needed for stabilizing and course of displacements as seen in the Figs. 5 and 6. Stiffer Model B needed only 0.6 seconds for stabilizing compared with 4 seconds of the Model A.

Table 1 The values of displacement and bending moments in x - and y -directions for S node

		Model A	Model B
w	[m]	-2.53×10^{-4}	-1.20×10^{-4}
t	[s]	0.24613	0.077061
m_x	[kNm/m]	0.44096	0.137085
m_y	[kNm/m]	0.44096	0.137085

Acknowledgements

This paper was written with the support of Slovak Grant Agency VEGA. Registration number is 01/0629/12.

References

- [1] S.P. Timoshenko, Vibration in engineering, (In Russian), Fizmatgiz, 1959.
- [2] D. Kuchárová, J. Melcer, Dynamics of building structures, (In Slovak), EDIS publishers’ ŽU, Žilina, 2000.
- [3] EN 1991-1-7 Actions on structures- General actions- Accidental actions.
- [4] EN 1991-1-6 Actions on structures- General actions- Actions during execution.
- [5] CEB, Concrete structures under impact and impulsive loading, Synthesis report, Comité Euro-International Du Beton, Bulletin D’Information, No.187, 1988.

Analysis of High Velocity Impact on Composite Structures

ŽMINDÁK Milan^{1,a*}, PELAGIĆ Zoran^{1,b} and BVOČ Maroš^{1,c}

¹University of Zilina, Faculty of Mechanical Engineering, Department of Applied Mechanics,
Univerzitná 8215/1, 010 26 Zilina, Slovak Republic

^amilan.zmindak@fstroj.uniza.sk, ^bzoran.pelagic@fstroj.uniza.sk, ^cmaros.bvoc@gmail.com

Keywords: impact mechanics, finite element method, wave propagation, composite materials

Abstract. In the recent years a big focus is subjected to the response of structures subjected to out-of-plane loading such as blasts, impact, etc. not only to homogenous materials, but also to heterogeneous materials, such as composites. Such form of loading can cause considerable damage to the structure. In the case of layered composite materials the damage can have several forms, starting from damage in layers up to delamination and full damage of the construction. This paper describes the investigation of shockwave propagation in composite structures caused by impact loading. The composite consists of carbon fibers in a polymer matrix, in which the fibers are much stiffer than the matrix. Finite element simulations were carried out for a “bird” strike impact on a composite wing leading edge. Results show a good impact resistance and good damping abilities of shockwaves.

Introduction

Fiber reinforced polymers (FRP) are most commonly used materials in various fields of industry. In the recent years quickly developing industries such as aerospace, ship and car industry almost completely rely on composite materials, especially on layered polymers reinforced with glass, aramid or carbon fibers and sandwich constructions consisting of FRP coatings with a foam core. Such constructions offer high strength at low weight, which considerably improve their performance (higher loading capacity, lower fuel consumption, etc.) especially in ship and aerospace industry [1]. These materials also have good antiballistic properties, for example modern bulletproof vests are made from aramid fibers.

The development and investigation of dynamic properties of such materials is time consuming, cause of the high amount of experiments needed. A good alternative is the usage of numerical simulations which gained a large popularity in the field of investigation of static and dynamic behavior of constructions, especially the finite element method (FEM). The simulations carried out in this paper were performed in the commercial FE software LS-DYNA. It is supposed that readers are familiar with the basics of continuum mechanics and basic simulation methods of classical problems in statics and dynamics using (FEM).

Mechanics of Impact Phenomena

Subjecting a structure to impact loading (impulse-type forcing) leads to the propagation of waves in the structure as an effect of forces associated with volume deformation. The main wave forms in solids are [2]:

- Longitudinal waves (Fig.1a): the characteristic particle motion is of compressional or stretching character. The wave propagation direction is parallel to the particle motion.
- Shear waves (Fig.1b): are characterized by transverse particle movements to the propagating wave direction. After longitudinal waves, they are the second fastest waves propagating in a structure. Alternative forms of shear waves are *bending waves*, which occur in structures of finite bending stiffness.

- Rayleigh waves (Fig.1c) are waves have a characteristic elliptic movement of particles, the propagation direction is parallel to the particle motion. They propagate along surfaces which thickness exceeds many times the wave height.

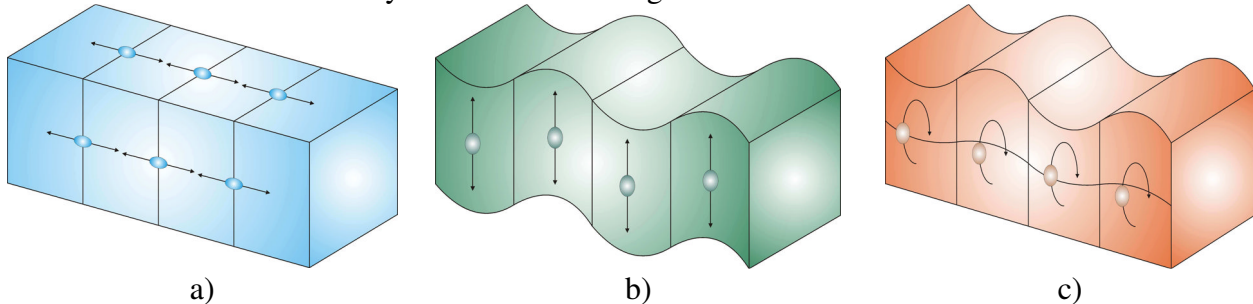


Fig. 1 Different wave types a) Longitudinal waves, b) Shear waves, c) Rayleigh waves

Recently the most successful method for modeling the dynamic response of a structure is FEM [3]. The solution in the form of time integration can be, depending on the problem, accomplished via implicit or explicit methods. Although implicit methods are unconditionally stable (they are not dependent on the time step size), for wave propagation problems explicit methods have shown more suitable, because they do not require stiffness, mass and damping matrix decomposition. The system of equations has the form

$$\mathbf{M}\ddot{\mathbf{u}}_{(t)} + \mathbf{C}\dot{\mathbf{u}}_{(t)} + \mathbf{K}\mathbf{u}_{(t)} = \mathbf{F}_{(t)}^{\text{ext}}. \quad (1)$$

The solution of this system is carried out for each time step via the explicit central difference method. Here, the acceleration in time t has the form

$$\ddot{\mathbf{u}}_{(t)} = \mathbf{M}^{-1}[\mathbf{F}_{(t)}^{\text{ext}} - (\mathbf{C}\dot{\mathbf{u}}_{(t)} + \mathbf{K}\mathbf{u}_{(t)})] = \mathbf{M}^{-1}[\mathbf{F}_{(t)}^{\text{ext}} - \mathbf{F}_{(t)}^{\text{int}}], \quad (2)$$

where $\mathbf{F}_t^{\text{ext}}$ is the vector of external forces and $\mathbf{F}_t^{\text{int}}$ is the vector of internal forces given as

$$\mathbf{F}_t^{\text{int}} = \sum \left(\int_{\Omega} (\mathbf{B}^T \boldsymbol{\sigma}_n d\Omega + F^{hg}) \right) + F^{\text{cont}}. \quad (3)$$

Velocities and accelerations have the form

$$2\Delta t \dot{\mathbf{u}}_{(t)} = \mathbf{u}_{(t+\Delta t)} - \mathbf{u}_{(t-\Delta t)}, \quad (4)$$

$$\Delta t^2 \ddot{\mathbf{u}}_{(t)} = \mathbf{u}_{(t-\Delta t)} - 2\mathbf{u}_{(t)} + \mathbf{u}_{(t+\Delta t)}. \quad (5)$$

The starting procedure has the form

$$\mathbf{u}_{(t-\Delta t)} = \mathbf{u}_{(0)} - \Delta t \dot{\mathbf{u}}_{(0)} + \frac{\Delta t^2}{2} \ddot{\mathbf{u}}_{(0)}. \quad (6)$$

By applying zero initial conditions to the displacements and velocities, the starting procedure has the form

$$\ddot{\mathbf{u}}_{(t-\Delta t)} = \mathbf{M}^{-1} \mathbf{F}_{(0)}^{\text{ext}}. \quad (7)$$

The stability of the central difference method depends on the length of the time step, which has to be divided into the shortest natural domains in the finite element mesh. The critical time step is computed by following relation

$$\Delta t^{crit} = \frac{2}{\omega_{\max}}, \quad (8)$$

where ω_{max} is the maximum natural circular frequency. The calculation is based on Courant-Friedrichs - Lewy condition (CFL condition) for solving partial differential equations numerically by the method of finite differences

$$\omega_{max} = 2 \frac{c}{l}, \quad (9)$$

where c is the wave speed in the material and l is the characteristic length. By substitution (Eq. 8) into (Eq. 7) we obtain relation for critical time step

$$\Delta t = \frac{l}{c}, \quad (10)$$

where Δt is time required for wave propagation in rod with length l . During time step calculation, ANSYS LS-DYNA program check size of all finite elements. For the numerical stability of calculation was used coefficient 0.9 for time step reduction

$$\Delta t = 0.9 \frac{l}{c}. \quad (11)$$

Characteristic length of a shell element is given as

$$l = \frac{A}{\max(l_1, l_2, l_3, l_4)} \quad (12)$$

where A is the element area, l_i are lengths sides of the (Fig. 2). For triangular shell element the relation has the form

$$l = \frac{2A}{\max(l_1, l_2, l_3)}. \quad (13)$$

Wave propagation velocity in a shell element is given by relation

$$c = \sqrt{\frac{E}{\rho(1-\mu^2)}} \quad (14)$$

where E is the Young modulus, ρ is mass density and μ is the Poisson number.

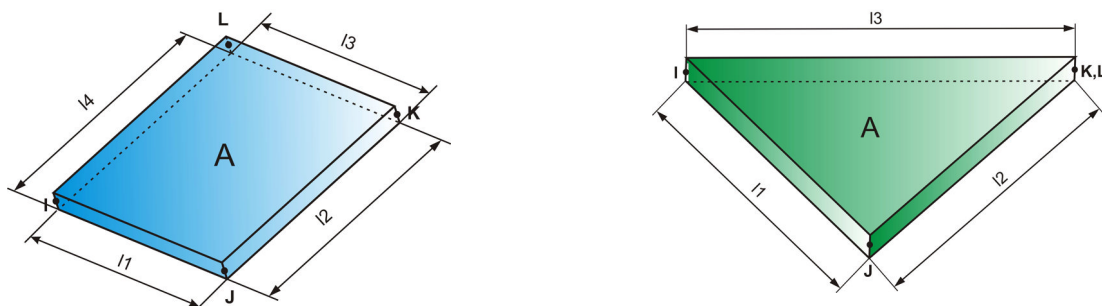


Fig. 2 Quadrilateral and triangular shell element

Homogenization

There are several homogenization methods already developed and described in literature [4]. A possible approach is the phenomenological approach, in which the constitutive performance of the different materials is characterized by a constitutive law and the composite response is obtained with a combination of these different laws. This procedure, although limits the complexity that can have the composites microstructure. This has been successfully applied to the simulation of carbon nanotube reinforcements.

The other possible approach corresponds to a full homogenization, where the performance of the material is obtained from a FE simulation of a Representative Volume Element (RVE). Generally, a RVE is used to describe a 2D or 3D periodic microstructure [4]. The homogenization scheme is shown in Fig. 3.

In this work the homogenization was made on the microstructural level for which the computer program VAMUCH (Variational Asymptotic Method for Unit Cell Homogenization) was used [5]. We note that this software can be used to homogenize arbitrary heterogeneous materials with arbitrary microstructure by providing a unit cell of the structure.

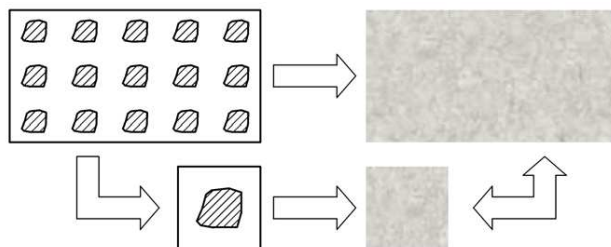


Fig. 3 Homogenization process

Woven carbon fabric composite was used (Fig. 4) as material for the wings leading edge. It consists from two or more warp fibers alternatively interfaced with two or more welt fibers. It is known that this weave type has good mechanical properties and that it is stronger than plain weave, but it is less stable. Heavy weight fabrics made from thick (high tex) fibers have to be used to avoid excessive crimping.

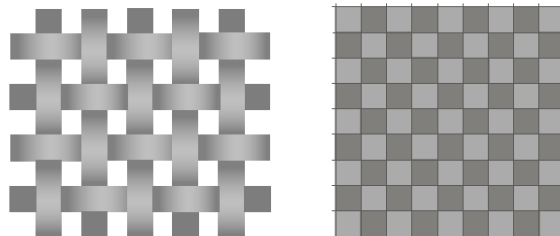


Fig. 4 Woven fabric composite

The material model input data of the homogenized unit cell had orthotropic properties. The studied structure consisted of regular quadrilateral elements. After this it was necessary to assign correct material orientation to each element, which responds to the fiber orientation of the fabric. For this purpose the ANSYS Parametric Design Language (APDL) was used to generate the checkerboard pattern.

Simulation of Shockwave Propagation on a Wing Leading Edge

The FE model of the wings leading edge was modelled in the commercial software LS-DYNA. The airfoil type NACA 65(2) - 415 $a = 0.5$ (Fig. 5a) was used on the wing segment.

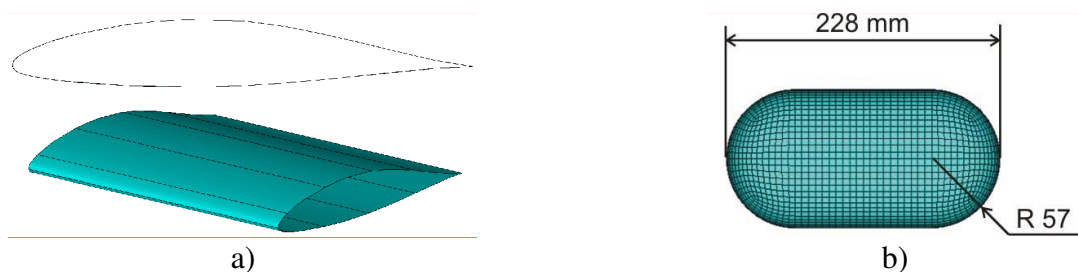


Fig. 5 a) Wing airfoil and investigated wing segment b) "bird" impactor geometry

The FE model consists of the bird impactor model (Fig. 5b) and the wings leading edge. For the leading edge, the highest cord thickness of the airfoil was chosen (Fig. 6a). On this edge the boundary conditions were applied (the whole edge was clamped). As stated in the upper chapter, the wing segment was meshed using a developed algorithm in the APDL environment. The total

thickness of the composite leading edge is 2 mm. The wing ribs, used as wing reinforcement on the edges are made from 3mm aluminum. The bird model was modelled as a hydrodynamic viscous liquid with a total mass of 1.8 kg. The bird's initial velocity was 60 m.s^{-1} .

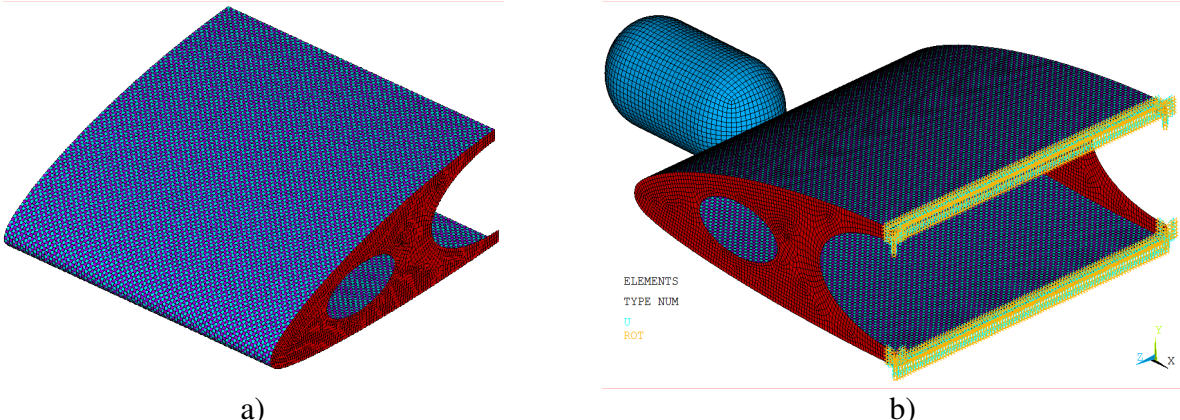


Fig. 6 a) FE mesh of segment wing b) Applied boundary conditions

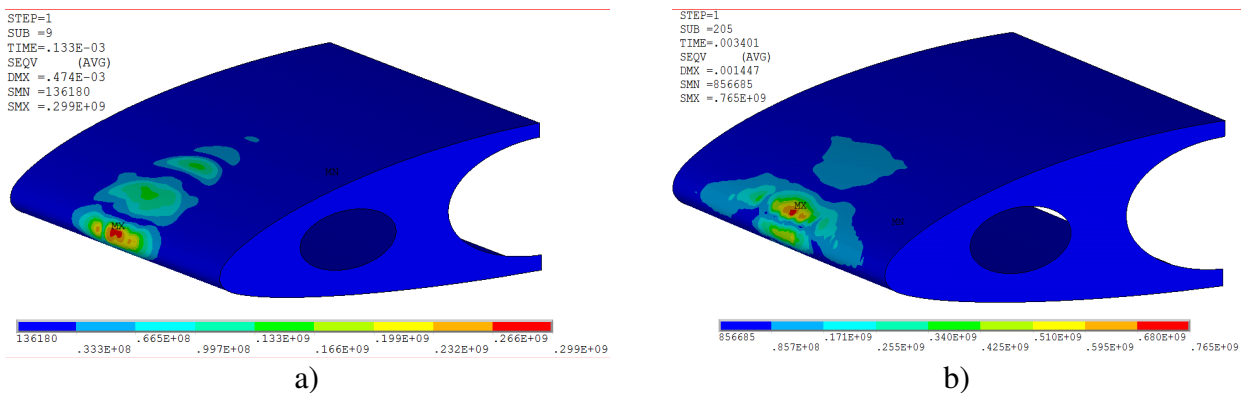


Fig. 7 a) von Misses stress course at time $1.33 \times 10^{-4} \text{ s}$
b) von Misses stress Course at time $3.4 \times 10^{-3} \text{ s}$

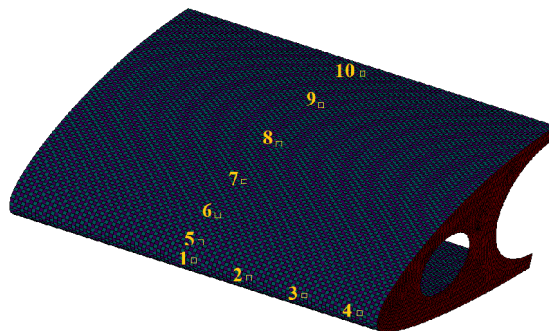


Fig. 8 Investigated nodes in the structure

The total simulation time of the impact was $5 \times 10^{-3} \text{ s}$. The von Misses stress criterion was used to evaluate the shockwave propagation through time. The course of the shockwave at the beginning of the impact is shown in Fig. 6b. Fig. 7a shows the von Misses course at the final time step. Table 1 summarizes maximal von Misses stresses in all investigated nodes (Fig. 8). Nodes 12 to 13 are on the other side of the wing profile. The maximum stress value is 765 MPa in the contact location between the bird and the wing leading edge at time $t = 3.4 \times 10^{-3}$ (Fig. 7b). The time course history is shown in Fig. 9.

Table 1 Von Misses stress in investigated nodes

N	Stress [MPa]	N	Stress [MPa]	N	Stress [MPa]	N	Stress [MPa]
1	594.82	5	680.32	9	98.71	13	162.27
2	360.01	6	163.57	10	80.99	14	114.41
3	183.26	7	199.40	11	264.31	15	137.81
4	91.53	8	118.25	12	176.34	16	145.02

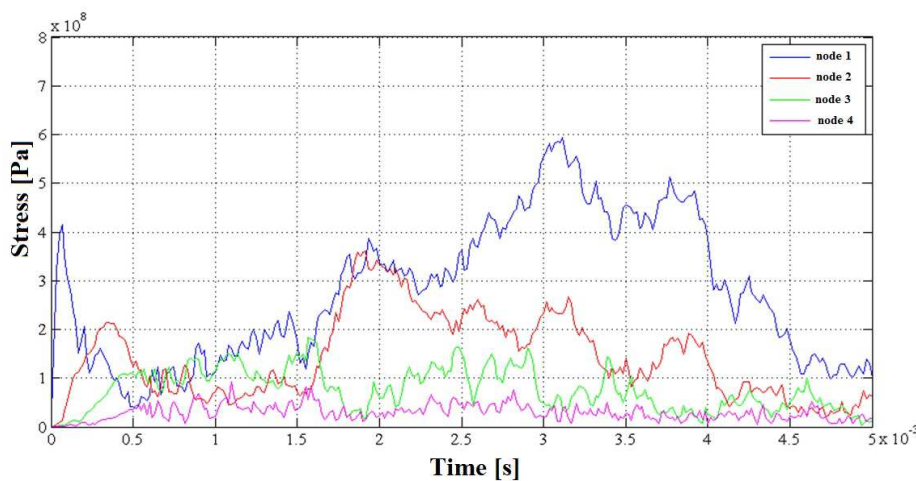


Fig. 9 Time history course of von Misses stress in different points

Summary

A series of finite element simulations of low velocity impact on wing leading edge is presented by using LS-DYNA software.

The maximum von Misses stress and their time-courses in different points of the structure were evaluated. As the shock waves are discontinuities in mechanical fields and they propagate with a large speed, numerical models are both computer time and memory consuming and so they require very effective computational technique to be solved correctly.

Acknowledgements

The authors gratefully acknowledge the support by the Slovak Grant Agency VEGA 1/1226/12

References

- [1] T. Sakakibara, et. al., Simulation of ball impact on composite plate with PP30% LGF. 12th International LS-DYNA Users Conference, 2012.
- [2] V. Kompiš, M. Vančo, V. Ferencey, Shock waves propagation in composite materials. Mechanical Engineering, 61 2 (2010).
- [3] S. Abate, Impact Engineering of Composite Structures. Udine, Springer, 2011, pp.180-186.
- [4] Q.H. Quin, Q.S. Yang, Macro-Micro Theory on Multifield Coupling Behavior of Heterogenous Materials, Springer, 2008.
- [5] W. Yu, T. Tang, Variational asymptotic method for unit cell homogenization of periodically heterogeneous materials. Int. J. of Solid and Structures. 44 11-12 (2007) 3738-3755.

Environmental Noise and Annoyance in the Urban Area at Different Time Intervals

ARGALÁŠOVÁ L'ubica^{1,a,*}, JURKOVIČOVÁ Jana^{1,b}, ŠEVČÍKOVÁ Ľudmila^{1,c},
ŠTEFÁNIKOVÁ Zuzana^{1,d}, HIROŠOVÁ Katarína^{1,e}, BABJAKOVÁ Jana^{1,f},
KÁNOVICSOVÁ Andrea^{1,g} and FILOVÁ Alexandra^{1,h}

¹ Institute of Hygiene, Faculty of Medicine, Comenius University, Špitálska 24, 813 72 Bratislava,
Slovak Republic

^alubica.argalasova@fmed.uniba.sk, ^bjana.jurkovicova@fmed.uniba.sk,

^cludmila.sevcikova@fmed.uniba.sk, ^dzuzana.stefanikova@fmed.uniba.sk,

^ekatarina.hirosova@fmed.uniba.sk, ^fjana.babjaková@fmed.uniba.sk,

^gandrea.kanovicsova@fmed.uniba.sk, ^halexandra.filova@fmed.uniba.sk,

Keywords: environmental noise, urban area, young healthy individuals, annoyance, health risk assessment

Abstract. Environmental (community) noise, particularly road traffic noise, has attracted widespread attention in recent decades as a major environmental health concern. The aim of the study was to determine the impact of environmental noise on psychosocial well-being of young healthy individuals and to follow the time trends of exposure in the period of 10, 15, 20, 25 years. The validated methodology was used to assess noise annoyance, interference with activities and sleep disturbance; the objectification of noise levels was done by direct measurement using sound level analyzer with a module for frequency analysis. The results revealed the sharp increase during the years 1989 and 1999 (the period of political and socio-economic transformation and the changes in traffic management) and the decrease in the year 2013. The findings of our study indicate the need for preventive measures to reduce environmental noise exposure in residential areas and to emphasize the importance of the elaboration of methods for environmental noise exposure risk assessment.

Introduction

Environmental (community) noise, particularly road traffic noise, has attracted widespread attention in recent decades as a major environmental health concern [1,2]. In Slovakia, the rapid development in traffic density connected with the economic transformation since 1990 has brought new problems in relation to environmental noise, particularly road traffic noise [3]. Road traffic noise represents a frequent, unavoidable and continuously increasing environmental factor in big cities throughout the world [4].

In the European Union, about 56 million people (54%) living in areas with more than 250 000 inhabitants are exposed to road traffic noise of more than average L_{DEN} (day-evening-night) 55 dB per year, which is thought to be risky to health [5]. WHO estimated that in high-income western European countries (population about 340 million people), at least 1 million healthy life years (disability-adjusted life-years) are lost every year because of environmental noise [4].

Annoyance is the most prevalent community response in a population exposed to environmental noise. The other most investigated non-auditory health endpoints for noise exposure are perceived disturbance and annoyance, cognitive impairment (mainly in children), sleep disturbance, and cardiovascular health impairment [5,6]. It can result from noise interfering with daily activities, feelings, thoughts, sleep, or rest, and might be accompanied by negative responses, such as anger, displeasure, exhaustion, and by stress-related symptoms [7].

Aim of the Study

The aim of the study was to determine the impact of environmental noise on psychosocial well-being of young healthy individuals, to assess noise annoyance as the most prevalent community response and to follow the time trends of exposure in the period of 10, 15, 20, 25 years.

Methods

The validated methodology according to the recommendations of experts from ICBEN was used to assess noise annoyance, interference with activities and sleep disturbance; the objectification of noise levels was done by direct measurement method using sound level analyzer with a module for frequency analysis [8].

Exposure Assessment. Equivalent (L_{Aeq}) noise levels were assessed for both the control and exposed groups living in the Slovakian capital Bratislava (about half a million inhabitants) by a Brüel-Kjaer measuring technique - calibrated integrating sound level meter type 2230 in the years 1989, 1999, 2004 and sound level analyzer with a module for frequency analysis type 2250 in the years 2009 and 2013.

The exposed group was made of students living in noisy area (the dormitory at Comenius University), whereas the control group was made up of students living in quiet areas of other dormitories and residential areas surrounding Bratislava proper. For the exposed and the control group, A-weighted outdoor equivalent noise levels were measured manually during a 24 hour period; there were 20 measuring stations assessed and the arithmetic averages were calculated.

Two separate measurements were done at both the exposed and control areas during the regular work week in both the spring and autumn. All measurements were recorded according to the standard STN ISO 1996-1,2 method during the day (6.00–12.00), afternoon (12.00–18.00), evening (18.00–22.00) and night (22.00–6.00). The time interval of each measurement was 15 min. Measuring stations were situated 2 m from the building facades. The average equivalent noise levels ($L_{Aeq,24h}$) were calculated and compared for exposed and control areas.

Subjective Response, Psychosocial Well-Being and Annoyance. Subjective response was assessed by a validated noise annoyance questionnaire administered in person, modified in the course of 10, 15, 20 and 25 years [9,10,11,12]. Besides questions on personal (age and gender), behavioral (smoking, coffee and alcohol consumption) and home characteristics (building construction and type of residence), it also included questions on possible non-auditory health effects (noise annoyance from different sources, interference with various activities and sleep disturbance). Window orientation to quiet or noisy streets, flat location, and length of stay in a flat were included into the questionnaire as well.

We used a three graded scale (Not at all annoys; Moderately annoys; Annoys) in the period between 1989 – 1999 and a five-graded verbal scale (Not at all annoys; Slightly; Moderately; Very; Extremely) during the years 2000–2013, that was developed and recommended by experts from the ICBEN (The International Commission on the Biological Effects of Noise) [8].

For statistical purposes, however, it was necessary to dichotomize (Not at all + Slightly; Moderately + Very + Extremely) or trichotomize (Not at all + Slightly; Moderately, Very + Extremely) the answers.

Study Samples. The source population was composed of medical students enrolled at Comenius University. The respondents represented a homogenous sample of young healthy individuals of comparable age, education and lifestyle. The response rate was 90%. Only those students living in the Bratislava agglomeration were eligible to participate in the study.

There were 511 university students (166 in the exposed and 374 in the control group) in the sample from 1989. In the group from 1999 there were 857 probands (374 in the exposed area and 483 in the control area). In the sample from 2004 there were 808 students (305 in the exposed area and 503 in the control area). In the sample from 2009 there were 659 probands (280 in the exposed area, 379 in the control area). In the sample from 2013 there were 932 students (340 in the exposed area, 557 in the control area) [9,10,11,12].

Students significantly differed by the flat location in relation to noise exposure, length of stay in the given area, position of a flat in the floor height, windows orientation, satisfaction with flat surrounding and spirits intake (higher spirits intake in the exposed group). They significantly did not differ by age, gender and the other behavioral and life style characteristics.

Statistical Analysis. Bivariate and stratified analyses (presented as crude odds ratio, Mantel-Haenszel weighted odds ratios) were used to calculate community noise annoyance risks and the risks of interference with various activities.

Multiple logistic regression was carried out to adjust for different covariates (e.g. gender, age, windows orientation, length of stay in a residence, smoking, spirits intake, etc.). Covariates in the logistic regression analysis were considered as categorical data.

The risks were followed in the time intervals of 10, 15, 20, 25 years and the time trends were assessed.

The major tools in our statistical analysis were Epi Info™, Version 7.1.1.1, 2013 and S-Plus 6.0.

Results and Discussion

Based on the results of measurements of noise exposure in the exposed and control site, we found a continuous increase in traffic noise burden in the exposed area at intervals of 10, 15, 20 and 25 years beyond the health risk zone and the European and Slovak limit values [1,2,13] (Fig. 1).

The monitoring of sound levels in the exposed area, with particular reference to the evening time bands in the year 2013 showed an increase especially in this time interval when the noise is acting particularly troublesome for students (Table 1).

In the composition of the traffic flow the number of passenger cars was predominant, there were also trucks, buses and trams, which are particularly noisy [18].

The traffic flow composition in the evening was similar in terms of number of passenger cars and trams to traffic flow during the day, which demonstrates its continuity on the busy roads in Bratislava.

Table 1 Time dynamics of noise levels in the exposed housing facility (student dormitory Družba, Botanická 25, Bratislava), April 2013

Time intervals	Sound level L _{Amin} (dB)	Sound level L _{Amax} (dB)	Sound level L _{Aeq} (dB)	Road traffic flow composition
17.00-18.00	58.6	75.5	67.5	A 5460, B 36, L 60, T 72
20.00-21.00	52.1	81.3	66.9	A 4644, B 12, L 12, T 60

Legend: A - automobile, B - bus, L - lorry, T - tram

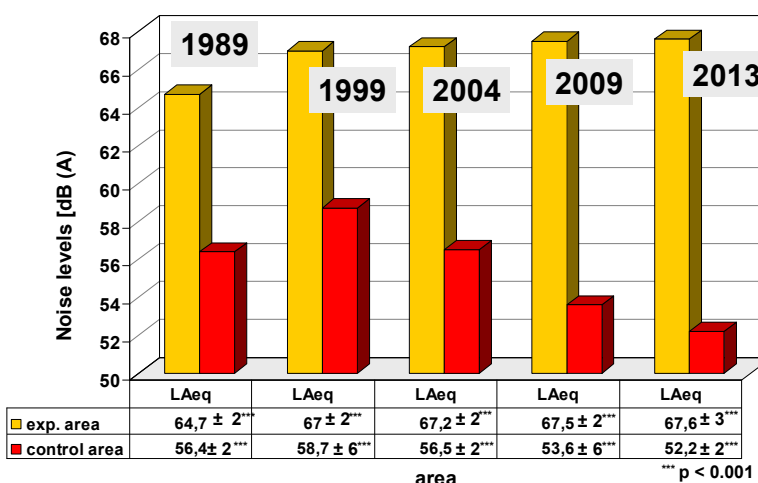


Fig. 1 Noise levels in the observed areas

Table 2 Risks from community noise annoyance (years 1989, 1999, 2004, 2009, 2013)

Noise annoyance (type of noise)	Risks in 1989	Risks in 1999	Risks in 2004	Risks in 2009	Risks in 2013
	OR (95 % CI)				
Industry	+ 1.62 (1.14-2.35)**	+ 3.49 (2.48-4.21)**	+ 1.90 (1.51-2.42)***	+ 2.27 (1.76-2.98)***	+ 1.63 (1.28-2.09)***
Aircraft	+ 0.46 (0.22-0.92)*	+ 0.87 (0.62-1.22)	+ 1.01 (0.74-1.36)	+ 0.64 (0.44-0.91)*	+ 0.91 (0.62-1.34)
Road traffic	+ 2.56 (1.93-3.42)***	+ 6.01 (4.97-7.95)***	+ 4.97 (4.34-6.43)***	+ 5.41 (4.28-7.25)***	+ 3.31 (2.68-4.08)***
Neighborhood	+ 1.71 (1.29-2.27)***	+ 2.43 (1.99-3.03)***	+ 2.15 (1.73-2.78)***	+ 2.48 (1.99-3.19)***	+ 1.70 (1.39-2.08)***
Entertainment facilities	+ 1.51 (0.90-2.52)	+ 3.90 (3.19-5.46)***	+ 3.65 (3.20-5.12)***	+ 3.60 (2.85-4.90)***	+ 2.43 (1.96-3.01)***
Railways	0.56 (0.31-0.98)*	2.06 (1.58-2.71)**	+ 2.28 (1.73-3.01)***	+ 1.41 (1.04-1.92)*	+ 2.08 (1.53-2.82)***
House equipment	+ 0.57 (0.40-0.80)*	+ 1.25 (0.98-1.58)	+ 1.08 (0.83-1.41)	+ 1.22 (0.94-1.58)	+ 0.97 (0.70-1.35)

Legend:

*** p < 0.001

** p < 0.01

* p < 0.05

+ Mantel-Haenszel odds ratio

CI = confidence interval; OR = odds ratio

We observed a sharp increase of value risks causing road traffic noise annoyance and interference with various activities over 10 years ($OR_{MH} = 2.56$ (95% CI = 1.93–3.42) in 1989 and 6.01 (95% CI = 4.97–7.95) in 1999) with slightly decreasing trend at the interval of 25 years ($OR_{MH} = 3.31$ (95 % CI = 2.68–4.08 in 2013)). However, the logarithmic trend is increasing (Fig. 2). Interference with sleep and rest disturbance by road traffic noise has been currently the most important issue ($OR_{MH} = 3.07$ (95 % CI = 2.43–3.89)).

In addition to road traffic noise we observed an increase in noise annoyance from railways – trams ($OR_{MH} = 2.08$ (95% CI = 1.53–2.82 in 2013)). The important issue remains still the noise annoyance from the entertainment facilities ($OR_{MH} = 2.43$ (95% CI = 1.96–3.01 in 2013)), and from the neighbourhood (OR_{MH} = 2.08 (95% CI = 1.53–2.82 in 2013)) (Table 2, Fig. 2).

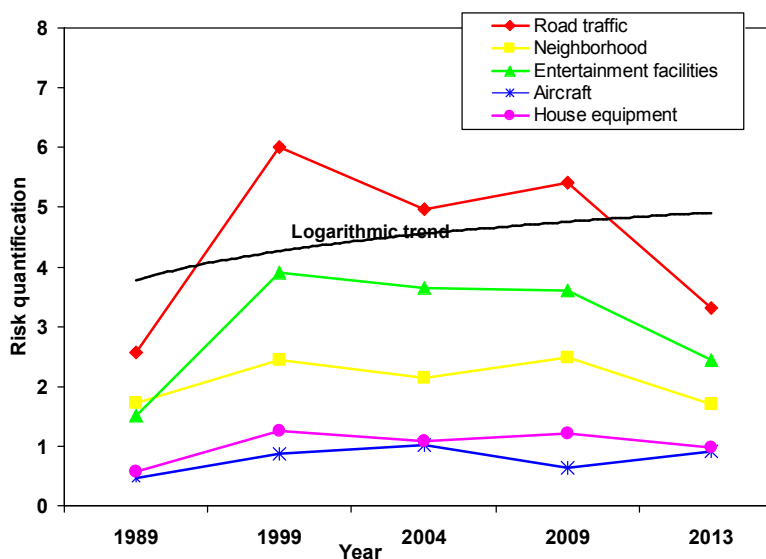


Fig. 2 Risks from community noise annoyance

The sharp increase of road traffic noise annoyance ($OR_{MH} = 2.56$ (95 % CI = 1.93–3.42) in 1989 and 6.01 (95 % CI = 4.97–7.95) in 1999) could be attributed to the period of political and socio-economic transformation and the changes in traffic management in our country.

The decreasing trend of road traffic noise annoyance in 2013 could be explained by adjustment and the change in subjective perception to road traffic noise, the other noise sources (entertainment facilities, neighbourhood), or by the other confounding factors (dwelling sound insulation).

Our results are comparable with the other studies comparing "annoyance", distortion of psycho-social-well-being and sleep disturbances in the exposed (noisy) and control areas [14,15,16,17]. Noise annoyance showed strong correlation with noise levels, personal characteristics and housing conditions according to authors in Belgrade, Serbia [14,15]. The most annoying noise sources were construction, road traffic and leisure/entertainment activities in Skopje, Macedonia [17]. The contribution and strength of our study is in the time trend analysis in 10, 15, 20 and 25 year interval.

Summary

Our study identified the association between environmental noise and noise annoyance in the course of 25 years. Road traffic noise annoyance is still an important issue. The sharp increase during the years 1989 and 1999 could be attributed to the political and socio-economic transformation and the changes in traffic management in our country. The decrease in the year 2013 could be explained by adjustment and the change in subjective perception to road traffic noise, the other noise sources (entertainment facilities, neighbourhood), or by the other confounding factors (dwelling sound insulation). The contribution and strength of our study is in the analysis of noise burden population trends and the elaboration of methods for environmental noise exposure risk assessment. The findings of our study indicate the need for preventive measures to reduce environmental noise exposure in residential areas and for future research in this field.

Acknowledgements

This contribution is the result of the research supported by the ESF-OPV project „MPH study programme development at Comenius University in Bratislava in English language (Master of Public Health).“ ITMS code of the project: 261402300093.

References

- [1] B. Berglund, T. Lindvall, D.H. Schwela (Eds), Guidelines for Community Noise, WHO, Geneva, 2000.
- [2] Ch. Hurtley (Ed.), Night noise guidelines for Europe. WHO, Geneva, 2009.
- [3] L. Argalášová-Sobotová, L. Mihalčík, M. Jajcay, J. Jurkovičová, L. Ševčíková, Noise as a public health problem in Slovakia, in: G. Belojević et al. (Eds.) Needs assessment of capacity building on health risk assessment of environmental noise: Case studies. WHO, Copenhagen, 2012, pp. 17-26.
- [4] L. Fritschi, L.A. Brown, R. Kim, D. Schwela, S. Kephalopoulos, Burden of disease from environmental noise. Quantification of healthy life years lost in Europe. WHO, Geneva, 2011. Information on http://www.who.int/quantifying_ehimpacts/publications/e94888.pdf.
- [5] M. Basner, W. Babisch, A. Davis, M. Brink, Ch. Clark, S. Janssen, S. Stansfeld, Auditory and non-auditory effects of noise on health. *The Lancet*. Published online October 30, 2013 [http://dx.doi.org/10.1016/S0140-6736\(13\)61613-X](http://dx.doi.org/10.1016/S0140-6736(13)61613-X).
- [6] D. Ouis, Annoyance from road traffic noise: a review. *J. Environ. Psychol.* 21 (2001) 101-120.
- [7] L. Sobotová, J. Jurkovičová, J. Voleková, L. Ághová, Community noise annoyance risk in two surveys. *IJOMH* 14 (2001) 197-200.
- [8] J.M. Fields, R.G. de Jong, T. Gjestland et al., Standardized general-purpose noise reaction questions for community noise surveys: Research and recommendation. *J. Sound. Vib.* 242 (2001) 641–679.
- [9] L. Ághová, J. Voleková, J. Jurkovičová, J. Šitár, Psychohygienic aspects of noise load in the urban environment, in: Psychology in ecological problems solving. Institute of experimental psychology SAS, Bratislava, 1992, pp. 63-66.

-
- [10] J. Jurkovičová, L. Sobotová, L. Ághová, J. Voleková, Noise exposure risks in two noise annoyance surveys after ten years, in: Proceedings inter.noise, 29th International Congress on Noise Control Engineering, Nice, France 2000, 27.-30. august, Imprimé par Jouve, Paris 2000, pp. 2852-2855.
 - [11] L. Sobotová, J. Jurkovičová, Z. Štefániková, L. Ševčíková, L. Ághová, Community noise annoyance assessment in an urban agglomeration. Bratisl. Lek. Listy, 107 (2006) 214-216.
 - [12] L. Sobotová, J. Jurkovičová, Z. Štefániková, L. Ševčíková, L. Ághová, Community response to environmental noise and the impact on cardiovascular risk score. Sci. Total Environ., 408 (2010) 1264-1270.
 - [13] The Ministry of Health Decree Nr. 549/2007 laying down details on the permissible values of noise, infrasound and vibration requirements and the objectification of noise, infrasound and vibration in the environment (in Slovak).
 - [14] B. Jakovlevič, K. Paunović, G. Belojević, Road-traffic noise and factors influencing noise annoyance in an urban population. Environ. Int., 35 (2009) 552-556.
 - [15] K. Paunović, B. Jakovljević, G. Belojević, Predictors of noise annoyance in noisy and quiet urban streets. Sci. Total Environ., 12 (2009) 3707-3711.
 - [16] J. Björk, J. Ardö, E. Stroh, H. Lökvist, P.O. Östergren, M. Albin, Road traffic noise in southern Sweden and its relation to annoyance, disturbance of daily activities and health. Scan. J. Work. Environ. Health, 32 (2006) 392-401.
 - [17] G. Ristovska, D. Gjorgjev, A. Polozhani, M. Kocubovski, V. Kendrovska, Environmental noise and annoyance in adult population of Skopje: a cross-sectional study. Arh. Hig. Rada Toksikol, 60 (2009) 349-355.
 - [18] E. Panulinová, S. Harabinová, The noise pollution problem in the tram route, in: Proceeding of SGEM, 13th International Multidisciplinary Scientific Geoconference: Ecology, Economics, Education and Legislation, Albena, Bulgaria 2013, 16-22 June, STEF92 Technology Ltd, Albena 2013, Vol. 1, pp. 1059-1064.

3D Traffic Noise Simulation

MELOVA Tatiana^{1,a*}, KOLOUSEK Martin^{2,b} and PRISCAK Tomas^{1,c}

¹Valbek, s.r.o., Kutuzovova 11, 831 03 Bratislava, Slovak Republic

²Valbek, s.r.o., Vanurova 505/17, 460 01 Liberec, Czech Republic

^amelova@valbek.sk, ^bmartin.kolousek@valbek.cz, ^cpriscak@valbek.sk

Keywords: simulation, noise pollution, noise cloud, vegetation growth

Abstract. The main task of this contribution was to explain the ways of the spread of noise pollution from the traffic. Descriptive simulation explains justification of each road construction by a simple way. It is confirmed that the projects which had contained a noise study simulation were easier to enforce for public than those without it. Also vegetation growth simulation in different time horizons is already slowly becoming an important part of the urban transport projects, due to the increasing of environmental pressure. Practice shows that the design value of these simulations is increasing because of the rising of the global traffic load.

Introduction

More and more the large-scale projects have been faced with reactions from the public on the negative effects that the project will bring to the everyday life of people in the affected area. In order to refute these concerns, it is important illustratively and simply shows the real impact of the construction on the affected territory. This can be achieved by the most modern computational methods, for instance by graphical traffic noise simulation.

The effort of these simulations is to offer quality projects with the greatest added value. This value means the use of modern sophisticated computational tools and inputs in the project preparation. They must be designed in view of the high efficiency in regard to the available resources.

Understanding of the project is even more important if the project is being presented to the public. Because of the public is not familiar with design practices and procedures. In these cases is the real space for deploying of complex visualizations. This way of the communication with the public is crucial. The practice shows that not always a quality project is accepted by the public. That all is caused just because of the poor illustrative presentation. Moreover, these simulations have presented complex projects by easily understandable form to the public. This way of presentation gives to investor's hands really powerful tool for promoting of their project.

Technology of Noise Visualization "Acoustic Cloud"

Other analytical methods are acoustic studies. Noise as one of the public health risks has been considered in the design of transportation projects even more often. It is shown that taking into account the results of the noise study in the initial phase of the project has a positive effect on the last stages of project documentation. It seems to be particularly advantageous to use of 3D models of noise pollution within the visualization of these structures, instead of traditional noise maps. The main advantage of this view comparison to the conventional 2D noise presentation is the complete clarity and transparency for the public. As a basis for making the noise pollution visualization are being used data from the program Cadna A (Fig. 1) [1].

It is one of the most widely used computer programs for the prediction and assessment of environmental noise impact to the environment.

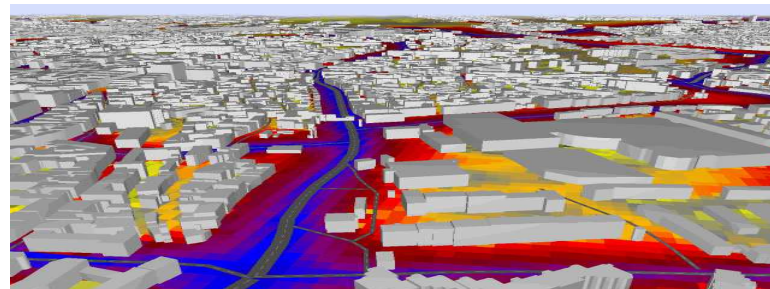


Fig. 1 View of the noise spreading in the program Cadna A

Current development is focused mainly on the so-called acoustic 3D visualization. The acoustic cloud can be displayed on request of the investor in the 3D model. There is possible to create any view from any angle in a wide range of details. Autodesk 3D Studio Max is used for visual processing (Fig. 2) [2]. As the input data format is DXF output from the program Cadna A [1]. The imported data are further processed by using a script invented by us, which greatly speed up following work with data. The animation can be created either on the 3D model of the country, or the whole scene can be incorporated into a real video. On request of the designer or contractor it is possible to simulate different conditions for the calculation and view. For transportation structures we can compare different versions of the project at various times and their impact on the environment. It is also possible to consider many types of noise barriers such as walls or new objects and their influence on noise transmission (Fig. 4).

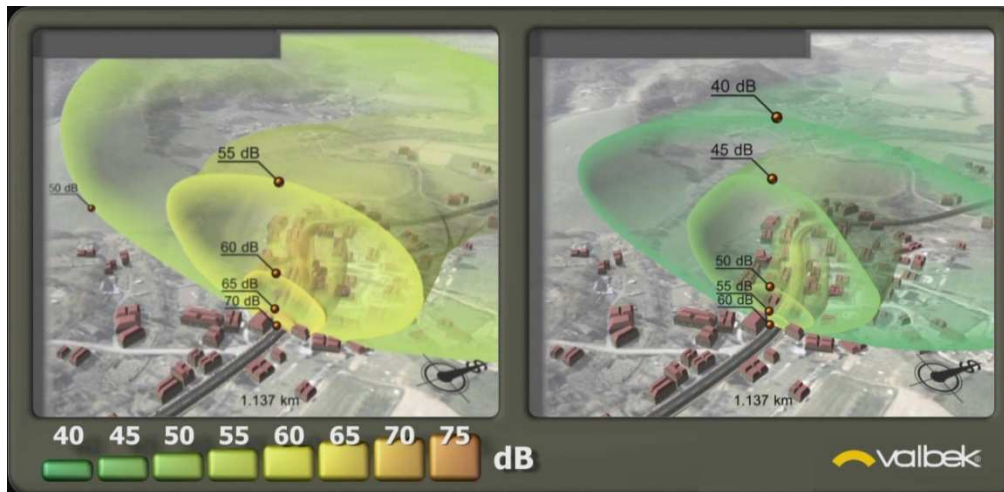


Fig. 2 Acoustic cloud displayed in program Autodesk 3D Studio Max

Probably the most telling presentation of noise pollution is an acoustic cloud animation directly in real video (Fig. 3). Making such a simulation is time-consuming and technically demanding, but at the same time due to its realism, the most representative. At the beginning is the providing of the video footage of interest area by using a small pilotless aircraft. After that, it is necessary to select images that best match to the requirements of the investor. Then we have calculated the trajectory of the camera in 3D space by using a technique called "match moving". The interest area model, 3D models and acoustic cloud seen in the background have been created by the program 3D Studio Max [2]. The last phase is the final rendering by using software V – ray [3]. The colour corrections are realized in the program named Fusion. The result is a highly realistic video. The main advantage is the clarity and clearness, because things are easier to understand for people if they are presented visually. Designers and investors get into their hands a powerful tool for negotiating with the authorities and public. So if the worries about over noise pollution have already been rejected in the beginning, there is not usually a problem to enforce such a construction.

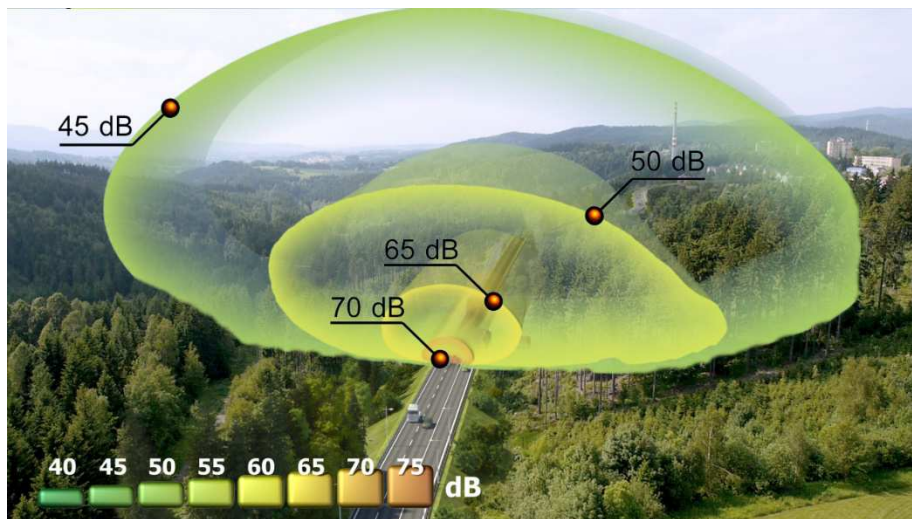


Fig. 3 Acoustic cloud displayed in real video

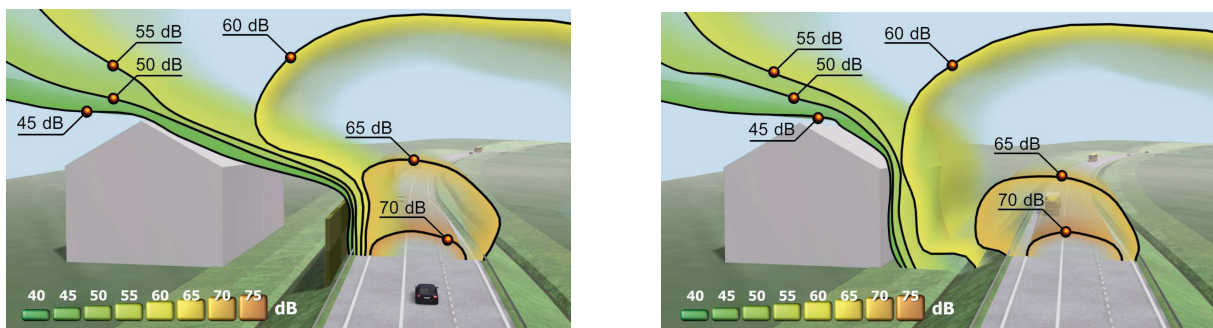


Fig. 4 Demonstration of noise behaviour with and without noise barrier

Vegetation Growth Simulation

It is worth noting further use of another visualisation technology, and it is a simulation of the growth of vegetation. The technology enables 3D modelling of all types of vegetation. It has simulated according to their growth patterns based on statistical analysis of the morphological development of any plant. With this technology, it is possible to model and visualize 3D ecosystems and show their evolution in the range of years with extreme realism (Fig. 5).

This simulation is based on the research project AMAP. CIRAD - French research centre, which is one the most advanced international agronomic research centre [4]. It has devoted to the vegetation research simulation more than 30 years. Currently there is a database with more than 4.000 species of plants. The technology developed in this project allows the creation of 3D models of all types of vegetation. Just generated models of vegetation growth it can be easily fitted into a model for future road construction. It is easy to imagine the extent of vegetation at different times and seasons. The database of available plants for our climate zone covers the most common vegetation species. Of course, this method does not remain just a static animation. Among other things, this technology offers the possibility to upload these data directly to the internet. It can be linked for example with the option of entering GPS coordinates. A website visitor could easily enter the coordinates of his house or apartment and thus determine the development and influence of various traffic factors in his surrounding area.

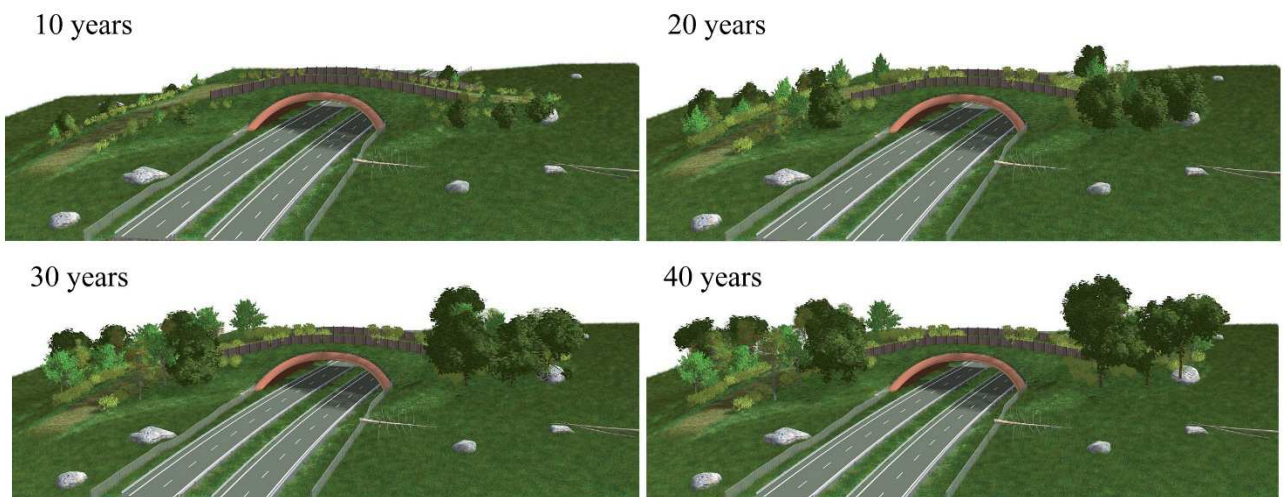


Fig. 5 Vegetation growth simulation at different ages

Summary

Visual presentation of the information is the simplest and most representative way to promote any good design. The main advantage is that even a common man can judge the necessity of sometimes very extensive structure. This is the key point to the success of every investor. Our goal is continuous improvement of these new technologies for the presentation of acoustic and vegetation studies. Making the outputs of complex computer programs easier understandable to a wider public.

References

- [1] Cadna A, Reference manual, Release 3.8, (2008).
- [2] Autodesk 3D Studio Max, Online manual.
- [3] V-ray, Online manual on http://www.vray.com/vray_for_3ds_max/manual/
- [4] Information on <http://amap.cirad.fr/fr/index.php>

Monitoring of Tram Traffic Noise in the Small Curve Radius

Eva Panulinová^{1a*} and Slávka Harabinová^{1b}

¹Institute of Structural Engineering, Faculty of Civil Engineering,
Technical University of Košice, Vysokoškolská 4, SK-040 02 Košice, Slovak Republic

^aeva.panulinova@tuke.sk, ^bslavka.harabinova@tuke.sk

Keywords: tram traffic noise, roadway diameter, calculation of noise levels, wheel squeal noise

Abstract. An excessive noise exposure not only decreases work quality and productivity, it also negatively affects human health. The most accurate data on noise levels can be obtained by measurements; however this approach is really time-consuming and its application is sometimes rather complicated. More frequently, calculation methods are used. The design methodology suggested by Liberko has been used for the calculations in Slovakia since 1991 [1]. As has been proved by experience, there is a need to re-evaluate some parts of the Slovak calculation methods and extend the number of initial parameters, so that much higher accuracy could be achieved. To meet the paper objectives, the comparative measurements were carried out at the selected points in Košice. The results obtained underwent spectral and statistic analysis. The performed measurements and analyses were focused on the evaluation of influence of small curve radius on tram traffic noise.

Introduction

The layout/location of the railway line is one of the parameters that at all events influence the level of noise caused by tramway transport. Providing that the ride of the tramway car is ideally straight in line, the forces that develop in a curve influence the acoustic situation in the vicinity of a moving tramway car. This parameter has not yet been taken into account in calculations. The paper presented analysis of tram traffic noise, particularly influence of a track curve radius on noise emission.

Defining the Problem

The quick movement of a tramway car that leads to a twitch, especially on the inner rail of the railway line, is one of the reasons for higher noise emission in curves in comparison with the straight line. A short-term noise of excessive acuteness that occurs during this movement results from impulse sliding - a wheel slide during its ride in track curves with small radii.

Wheel-to-rail friction occurs in such rotational motion, while the wheel moving on the outer side of the curve is forced to transverse motion by the moving wheel flange. Such forced wheel guidance does not arise in the wheel moving on the inner side of the curve (Fig. 1).

When the stress in the wheel exceeds a certain specified magnitude, a sudden recoil movement and subsequent release occurs. This happens periodically and leads to the oscillation of wheels. Depending on the existing frequency, the sound that is thus emitted into the environment is perceived as a short-term noise manifested by unpleasant creaking and wailing. This noise is marked in the paper as a wheel squeal noise.

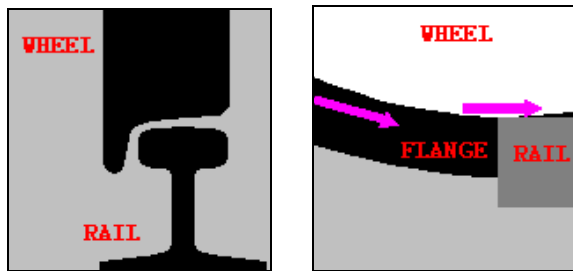


Fig. 1 Schematic of wheel/rail interface [3]

According to Möhler [4], the basic criterion for the characterization of a wheel squeal noise is the difference ΔL between the maximum ($L_{A\max}$) and equivalent noise level (L_{Aeq}) at a reference measurement point (the measurement point situated at a distance of 7.5 m from the railway line axis in the height of 1.2 m above the top of the rail head).

In $\Delta L = L_{A\max} - L_{Aeq}$ (dB) :

- $\Delta L > 8 \text{ dB}$ - a wheel squeal noise occurs,
- $\Delta L = 5 \text{ to } 8 \text{ dB}$ - a soft wheel squeal noise occurs,
- $\Delta L < 5 \text{ dB}$ - a wheel squeal noise does not occur.

Experimental Measurements

The knowledge acquired from foreign literature determined the selection of the limitary magnitude of the track curve radius. As Möhler has it [4], the presence of a distinct short-term noise is best recognized during the ride of a car in the curves of the radii below 50 m.

Therefore, the measurement points were classified in three groups:

- track curve sections with the radius lower than 50 m,
- track curve sections with the radius greater than 50 m, and
- those in the straight line.

The selection specified above allowed for a comparison of single measurement points in various situations.

All measurements were carried out in approximately equal meteorological conditions by means of which the influence of unfavourable weather conditions was avoided. The location of the "before" reference acoustic measurements campaign and a typical noise time history are presented in Fig. 2 hereafter:

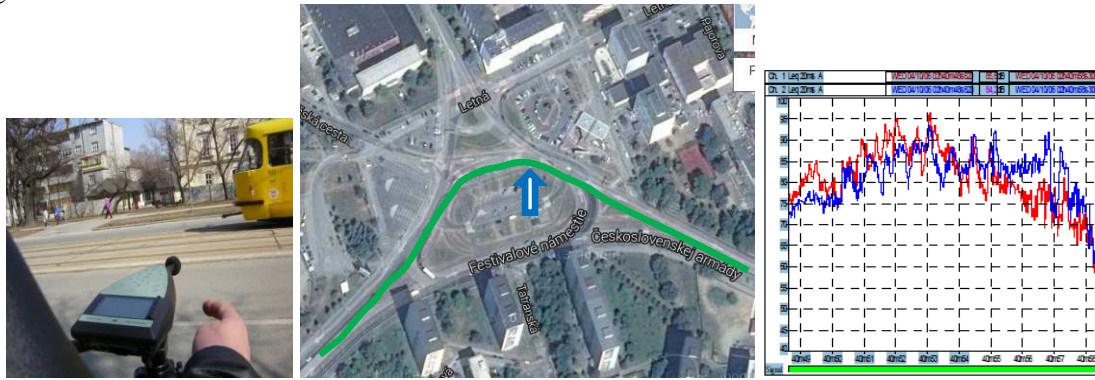


Fig. 2 Location of a typical acoustic measurement in a small curve

It directly recorded equivalent, maximum, minimum, and other complementary noise levels in the external environment, were measured with the characteristic F and weight filter A. At least 25 measurements were conducted and the data recorded in each out of 10 selected measurement points.

Results of Experimental Measurements

The results were evaluated and submitted to spectrum and statistic analyses. As far as statistics methods are concerned, descriptive statistics, correlation and regression analyses, as well as the χ^2 test of good conformity were used.

After a detailed analysis it can be stated that:

- In all measurement points in the track curve sections with the radii r not greater than 70 m, the occurrence of a louder noise was identified, specified in a tone variety spectrum as a disturbing noise, marked in the paper as a wheel squeal noise (Q-sound).
- In the measurement points in the track curve sections with r below 50 m, the occurrence of wheel squeal noise was recorded in 80 % of all measurements, whereas in the points with r lower than 70 m a wheel squeal noise occurred in 51 % of measurements and in straight line sections it occurred only as an exception - 5 % (Fig. 3).

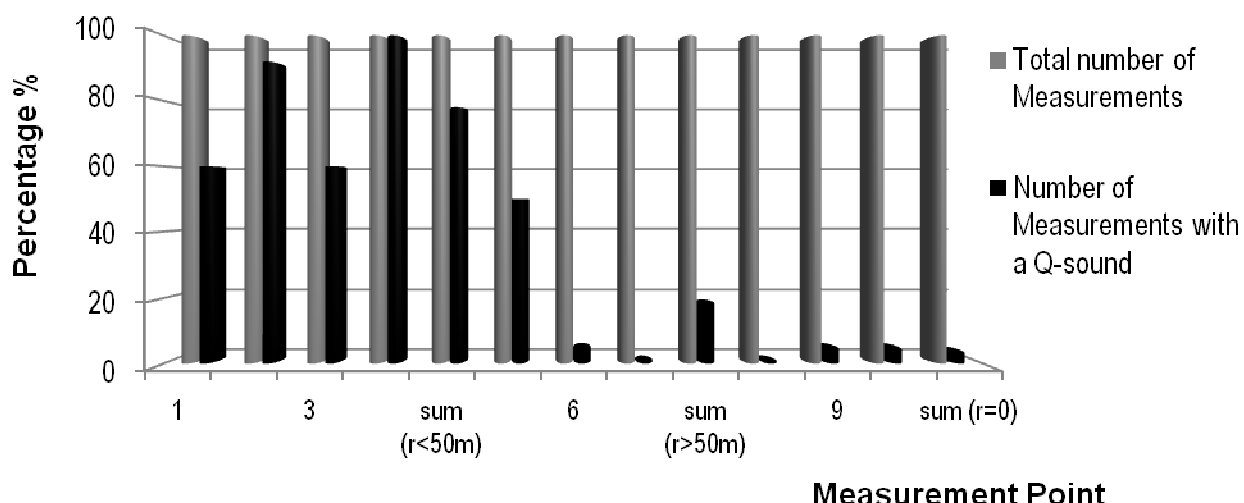


Fig. 3 The percentage of wheel squeal noise (Q-sound) occurrences in the measurement points of a track curve

- The wheel squeal noise occurred in 60 % of measurements in one straight line section with the very bad technical condition of the permanent way (which was detected by a visual inspection).
- In the spectrum distribution of measurements with a wheel squeal noise, noise levels of medium frequency (315 to 1600 Hz) dominated and the characteristic peak of a spectrogram occurred in the majority of cases around the frequency of 500 Hz (Fig. 4).

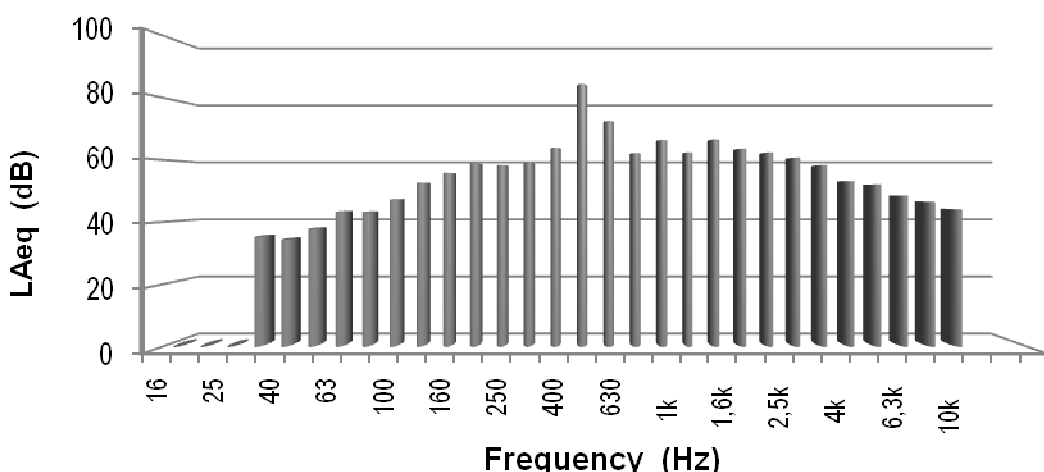


Fig. 4 The third-octave spectrum of equivalent noise level with the identified wheel squeal noise

- It has been proved by means of regression and correlation analyses that the radii r over 70 m have a lower degree of dependence, which means they influence the resulting noise level less than those up to 70 m.
- The difference between the measurements in the sections with the radii below 50 m and those in the straight line is 3.7 dB(A), and between the measurements in the sections with the radii over 50 m and those in the straight line 1.1 dB(A).
- The resulting noise level in the sections with the radii up to 50 m is greatly affected by the presence of a wheel squeal noise, while the resulting noise level in the sections with the radii over 50 m depends on their radii. The resulting noise level in the straight line sections is influenced by the car velocity and the technical shape of the permanent way.

Conclusions

In conclusion, it can be said that the experimental measurements proved the occurrence of a louder noise, specified on in a tone variety spectrum as a disturbing noise, marked in the paper as a wheel squeal noise. As this is the component of noise emission that causes the most unpleasant feelings, it should not be neglected in the prognoses of noise cause by tramway transport, particularly not in the routes with curves of small radii.

Wheel-squeal on other tram operating systems may also be related to maintenance issues. Identification of specific high-noise emitting tram cars through such technology as the noise camera will provide an opportunity to identify the major mechanisms for wheel squeal noise from maintenance or engineering problems.

Acknowledgements

This contribution is the result of the research supported by the Scientific Grant Agency of the Ministry of Education of the Slovak Republic and the Slovak Academy of Sciences under Project 1/0201/11.

References

- [1] M. Liberko, Guidelines for calculation of traffic noise levels, VÚVA Brno, 1991.
- [2] STN ISO 3095 (28 1304) - Acoustic - Measurement of noise emitted by rail vehicle.
- [3] Ch. Coleman, Railroad Wheel FA from http://www.spikesys.com/Trains/whel_faq.html, 23 February 2014.
- [4] U. Möhler, Schallemissionen von Schienennahverkehrsbahnen, Zeitschrift für Lärmekämpfung, 6/1998.
- [5] Odegaard & Danneskiold-Samsøe : A Study o European Priorities and Strategies for Railway Noise Abatement – Final Report, Report 01.980, prepared for the EU Commission, Directorate General for Energy and Transport, February 2002, from <http://www.eurailnoise.dk/desktopdefault.aspx?panel>, 2 February 2014.
- [6] J. van den Brink, Curve Squeal, CM 2000, 2000.
- [7] Ruiten van C J M, Mechanism of Squeal Noise Generated by Trams, Journal of Sound and Vibration. 120 2 (1988) 245-253.
- [8] L. Argalášová, J. Jurkovičová, A. Filová, J. Babjaková, A. Kánovcová, L. Sevčíková, The analysis of risks and the health consequences of environmental noise exposure in the urban agglomeration (in Slovak), FFP. 2 (2013) 5-7.

The Efficiency of Dynamic Relaxation Methods in Static Analysis of Cable-Membrane Structures

HÜTTNER Miloš^{1,a}, MÁCA Jiří^{1,b} and FAJMAN Petr^{1,c}

¹Department of Mechanics, Czech Technical University in Prague - Faculty of Civil Engineering,
Thákurova 7; 166 29, Prague 6, Czech Republic

^amilos.huttner@fsv.cvut.cz, ^bmaca@fsv.cvut.cz, ^cfajman@fsv.cvut.cz

Keywords: dynamic relaxation, cable-membrane, kinetic damping, viscous damping, iteration

Abstract. This paper is focused on the static analysis of cable-membrane structures using the dynamic relaxation method. Several different processes of dynamic relaxation method are compared in this paper. The techniques with viscous damping and the techniques with kinetic damping are used. The efficiency and stability of each process are compared to selected 3D examples of cable-membrane structures. The effect of mass distribution along the structure is also of interest and it is studied in the paper.

Introduction

The cable-membrane structure is idealized into a system of nodes and lines in the case of numerical analysis. The line consists of either a cable element or an edge of the membrane element. The equilibrium position of unsupported nodes is searched during static analysis. It is considered a large displacement of the nodes and small deformation of elements.

The most common numerical methods for the solution of geometrically non-linear response of structure are the force density method and the dynamic relaxation method (DRM). Unlike the force density method, the DRM does not require matrix manipulations for the solution of the system of non-linear equilibrium equations [1]. The efficiency and applicability of some dynamic relaxation techniques in the analysis of cable-membrane structures are examined in this paper.

Used Elements

Cable Element. The bar carries only axial force and it connects the endpoints i and j . Homogeneous material with a constant cross-section throughout its length is assumed. The internal force T_k in one cable element k can be calculated according to the known Eq. 1.

$$T_k = \frac{E_k A_k}{r_k} (r_k - s_{0,k}), \quad (1)$$

where E_k is the elastic modulus, A_k is cross sectional area, r_k is current length of line k and $s_{0,k}$ is initial length of line k . The elastic stiffness $S_{k,cable}^E$ for the cable element can be calculated as:

$$S_{k,cable}^E = \frac{E_k A_k}{s_{0,k}}. \quad (2)$$

Membrane Element. For membrane structures the natural strain triangular element can be used for calculation of internal forces. This element has only in-plane stiffness so the element formulation is with respect to displacements in the local coordinate directions. Isoparametric behavior of the element is considered. Using equations of equilibrium, it is possible to convert the

surface stress within the element into forces along the sides of the triangle. General application of this element is described in [2].

The elastic stiffness $S_{k,\text{edge}}^E$ for the edge k of the membrane element j can be calculated as:

$$S_{k,\text{edg}}^E = \frac{3}{2} \cdot \frac{E_j d_j A_j}{(s_{0,k})^2}. \quad (3)$$

where E_j is the elastic modulus of membrane, d_j is the thickness of the membrane, A_j is the area of the membrane element and $s_{0,k}$ is initial length of the edge k .

Dynamic Relaxation Method

DRM is an explicit iterative technique which converts a static system to an artificially dynamic one by adding fictitious inertia and damping forces. When the artificial dynamic system returns to its static state, a solution to the original static problem is obtained [3].

The first mention of the method are in [4,5]. This theory was further developed and its detailed overview can be found in Barnes [6], Topping [2] or Lewis [1]. The kinetic damping theory was proposed by Cundall [7]. Practical examples of the application can be seen in [1,2,3]. The analysis of cable structures using the DRM is to see in [8, 9].

Principle. The basic unknowns form nodal velocities, which are calculated from nodal displacements. The discretization from timeline with time step Δt will be performed. During the step Δt a linear change of velocity is assumed. Acceleration during the step Δt is thus considered to be constant. By substituting the above assumptions the velocity for joint i in direction m (x , y and z) can be expressed in a new time point $t + \Delta t / 2$ thus:

$$v_{im}^{(t+\Delta t/2)} = v_{im}^{(t-\Delta t/2)} \frac{M_{im} / \Delta t - C_{im} / 2}{M_{im} / \Delta t + C_{im} / 2} + \frac{R_{im}^t}{M_{im} / \Delta t + C_{im} / 2}, \quad (4)$$

where R_{im}^t is residual force (i.e. out of balance) at joint i in the direction m and at time t ,
 M_{im} is the fictitious mass at joint i in the direction m ,
 C_{im} is the viscous damping factor for joint i in the direction m ,
 $v_{im}^{(t+\Delta t/2)}$ is velocity at joint i in the direction m and at time $t + \Delta t / 2$.

Current coordinate x (and similarly for y and z) of the joint i at the time point $t + \Delta t$ can be expressed as follows:

$$x_i^{(t+\Delta t)} = \Delta t \cdot v_{ix}^{(t+\Delta t/2)}. \quad (5)$$

From the imbalance (between external and internal forces) in node i one can calculate the residual force for the corresponding node in time t

$$R_{im}^t = P_{im} - \sum_k T_{km}^t - \sum_k T_{0,km}, \quad (6)$$

where P_{im} is the external load at joint i in the direction m .
 T_{km}^t is the tension force in the direction m of the line k entering into joint i at time t .
 $T_{0,km}$ is the initial prestress in the direction m of the line k entering into joint i .

The initial force T_k in line k is calculated as the sum of $T_{k,cable}$ of the cable element and $T_{k,edge}$ of the edge of the membrane element. If the sum of the link force $T'_k < 0$ the force is compressive so T'_k must be set equal to zero.

Algorithm. The acceptable error of residual forces R_{lim} must be defined before starting the calculation. The iteration process can be outlined as below:

Preprocessing:

- Set initial conditions.
- Set fictitious masses, the fictitious damping factor and the size of a time step. Usually $\Delta t = 1\text{s}$.
- Determine the initial residual forces for the each degree of freedom from Eq. 6.

The general iterative steps:

- Determine velocities for the each degree of freedom from Eq. 4.
- Update the coordinates from Eq. 5.
- Determine the current residual forces for the each degree of freedom from Eq. 6.

If $\max|R_{im}| < R_{lim}$ then stop the algorithm. Otherwise continue the DRM iteration from step d).

Factors of Calculation

The stability and the speed of calculation depend on the appropriate choice of the fictitious parameters. This paper focuses on the effect of the damping, the line stiffness and the distribution of the mass.

Damping Factors. The damping factor that causes the structure to approach the static position most rapidly should be used for the analysis. This factor is called the critical damping factor. The critical damping factor may be estimated by undertaking an undamped mode [2].

The requirement for a two-stage solution procedure involving the determination of the viscous damping coefficient is rather inconvenient. For this reason the method has been superseded by the dynamic relaxation technique with kinetic damping [7]. When the technique of kinetic damping is employed, the viscous damping coefficient is taken as zero. At a kinetic energy peak, velocities are set to zero and the whole system is restarted from the current configuration [1].

It can be deduced that the kinetic energy peak has occurred when the current value of the kinetic energy is smaller than that in a previous iteration. The peak of the kinetic energy can be approximation with a quadratic curve [1] or with a line [2].

Stiffness Factors. The stiffness of the line connection determines the value of the fictitious mass. To ensure the stability of the calculation, it is appropriate to apply the following relationship

$$M_{im} = M_i = \frac{\Delta t}{2} S_i, \quad (7)$$

where S_i is lumped stiffness at the node i and it can be calculated as

$$S_i = \sum_k S_k, \quad (8)$$

where S_k is the stiffness of line k entering into joint i . The stiffness is given as a sum of two components – namely, the geometric stiffness $S_k^G = T_k / r_k$, and the elastic stiffness S_k^E that is for cable element calculated from Eq. 2 and for edge of the membrane element from Eq. 3. T_k is tension force in line k and r_k is current length of line k .

Used Processes

Twelve dynamic relaxation processes is examined in this paper. Table 1 gives an overview of selected attributes for individual processes, where “C” indicates the calculation with critical damping factor, “KQ” indicates the calculation with kinetic damping with a quadratic curve approximation of the peak [1] and “KL” indicates the calculation with kinetic damping with a linear approximation of the peak [2]. The symbol “S” denotes the calculation of the stiffness using Eq. 8, “S/2” denotes that the stiffness is divided 2 (by [1]). The symbol “Mi” denotes the calculation of the mass using Eq. 7, “M” denotes that the mass is the same for all nodes and it is calculated as $M = \max(M_i)$.

Table 1 Outline of the processes

process	1	2	3	4	5	6	7	8	9	10	11	12
damping	C	C	C	C	KQ	KQ	KQ	KQ	KL	KL	KL	KL
stiffness	S	S	S/2	S/2	S	S	S/2	S/2	S	S	S/2	S/2
mass	Mi	M	Mi	M	Mi	M	Mi	M	Mi	M	Mi	M

Examples

The efficiency of the processes was studied on one cable structure (verification of methods) and two cable-membrane structures. In all cases, computations were stopped when the vector of residual forces was reduced to 0.1% of its original value.

Cable Spatial Net. The cable structure is taken from Lewis [1] and it was used in [9]. The structure has 45 degrees of freedom. Its initial geometry is generated using a pre-tension force of 90 kN in the x direction, (except for the central cable where it is 120 kN) and 30 kN in the y direction, plus a point load $P_{iz} = 4.8$ kN at all free nodes. Under these initial load conditions, the plan dimensions of the structure are as shown in Fig. 1, with the values of z coordinates, in meters, in Table 2. The symmetry of the initial configuration about the x and y central axes is maintained. The structure is subjected to a further increase in load by $P_{iz} = 2.0$ kN at all free nodes. The cross-sectional area of the cables is assumed to be 350 mm^2 in the x direction and 120 mm^2 in the y direction. The elastic modulus is 160 kN/mm^2 [1].

All results of converging methods correspond to the results shown in [1]. The accuracy of the coordinates is ± 0.01 mm and the accuracy of the cable forces is ± 0.02 kN.

Table 2 z -coordination of the cable spatial net

node	1	2	3	6	7	8	9	13	14	15	16
$z - \text{coor.}$	1.0	2.0	3.0	0.0	0.8195	1.4096	1.6769	0.0	0.6870	1.1478	1.3176

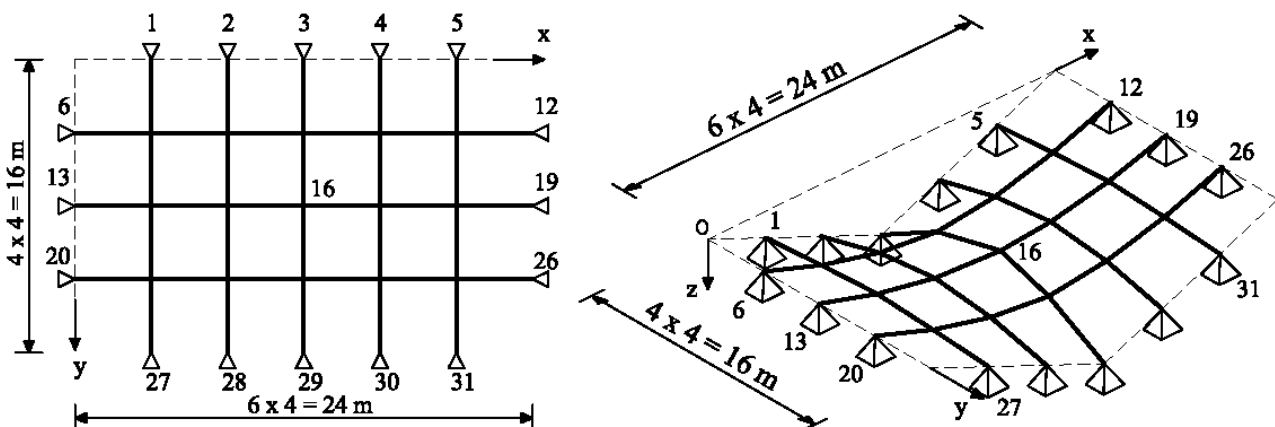


Fig. 1 a) Plan view of cable spatial net b) Perspective view

Simple Cable-Membrane Roof. It is a fictitious cable-membrane structure with 27 degrees of freedom. The initial setting of construction is shown in Fig. 2. The joints 6-10, 11-15, 16-20, 2-22, 3-23 and 4-24 are connected with the cable elements. The load $P_z = 6.0 \text{ kN}$ acts at all free nodes. All cables have parameters: $E = 160 \text{ kN/mm}^2$, $A = 62.5 \text{ mm}^2$. All membranes have parameters: $E = 500 \text{ N/mm}^2$, thickness $d = 1 \text{ mm}$ and Poisson's ratio 0.2.

The accuracy of calculation for all the processes was: $\pm 0.1 \text{ mm}$ for the unknown coordinates and $\pm 0.02 \text{ kN}$ for the forces in the cable elements.

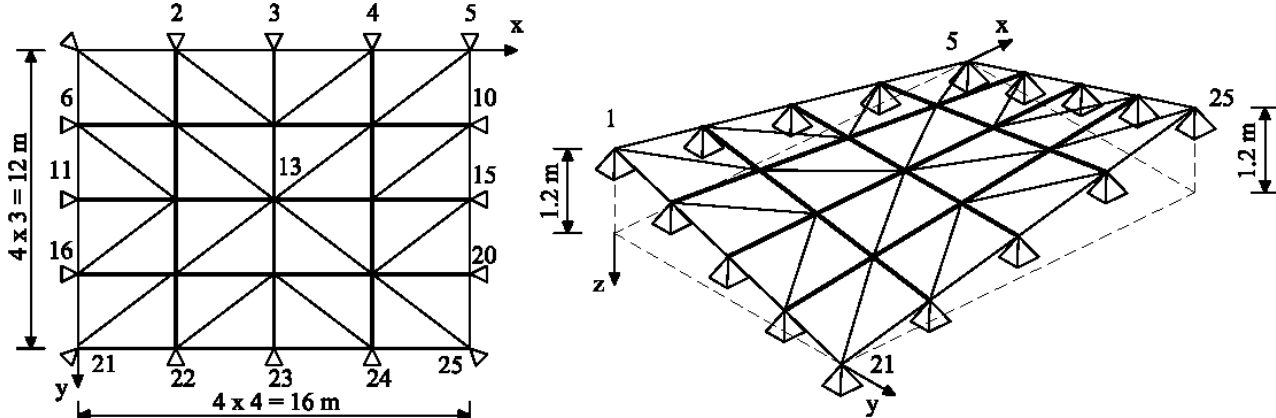


Fig. 2 a) Plan view of simple cable-membrane roof. b) Perspective view

Advanced Cable-Membrane Roof. It is a fictitious cable-membrane structure with 387 degrees of freedom. The initial setting of construction is shown in Fig. 3. All coordinates are equal to zero. The joints 1-19, 19-133, 133-115 and 115-1 are connected with the cable elements. The structure is loaded with a uniform vertical load $q_z = 2 \text{ kN/m}^2$. The structure is, in the direction x and in the direction y , prestressed with the force 1 kN.

All cables have parameters: $E = 150 \text{ kN/mm}^2$, $A = 40 \text{ mm}^2$. All membranes have parameters: $E = 700 \text{ N/mm}^2$, thickness $d = 1 \text{ mm}$ and Poisson's ratio 0.2. The structure was also numerically analyzed in the commercial software Easy. Stat from Technet GmbH. The used processes exhibit a deviation 5% in the determination of the unknown coordinates and 15% in the determination of the cable forces. The deviation is probably due to the different approximations of membranes.

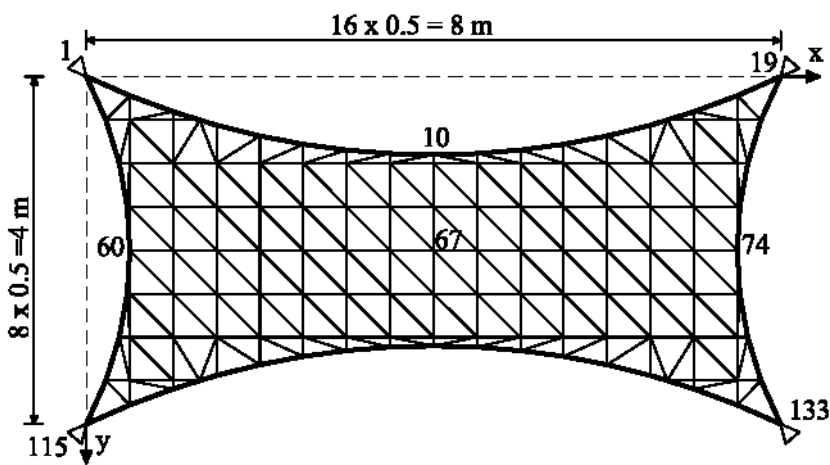


Fig. 3 Plan view of the advanced cable-membrane roof

Results. The overall ranking of methods sorted by the number of errors (sum of all examples), and the total number of iterations are shown in Table 3. It is evident that use the sum of elastic and geometric stiffness divided by 2 is unstable (processes 3, 4, 7, 8, 11 and 12). Furthermore, it appears that the processes that use the same mass for the whole structure (odd processes) are faster than methods that use different masses for each joint (even processes). It is advisable to use techniques with kinetic damping. The difference of approximation of the peak kinetic energy is negligible.

Table 3 The outline of number of iterations

process	5	9	6	10	1	2	8	11	7	12	4	3
example 1	127	132	136	137	138	138	-	-	-	-	-	-
example 2	172	179	183	182	232	230	123	127	127	129	157	159
example 3	696	710	1484	1632	1633	2096	-	-	-	-	-	-
total no. of iterations	995	1021	1803	1951	2003	2464	123	127	127	129	157	159
errors	0	0	0	0	0	0	2	2	2	2	2	2

Conclusions

It was shown that the dynamic relaxation is suitable for static analysis of cable-membrane structures. It was found that use the sum of elastic and geometric stiffness divided by 2 is unstable. It is advisable to use techniques with kinetic damping. Furthermore, it appears that the processes that use the same mass for the whole structure are faster than methods that use different masses for each joint. The difference in approximation of the peak kinetic energy is negligible.

Acknowledgements

The results presented in this paper are outputs of the research project “P105/11/1529 - Cable - membrane structures analyses” supported by Czech Science Foundation and project “SGS14/029/OHK1/1T/11- Advanced algorithms for numerical modeling in mechanics of structures and materials” supported by the Czech Technical University in Prague.

References

- [1] W.J. Lewis, Tension Structures: Form and Behaviour, Thomas Telford, London, 2003.
- [2] B.H.V. Topping, P. Iványi, Computer Aided Design of Cable Membrane Structures, Saxe-Coburg Publications, Kippen, Stirlingshire, Scotland, 2007.
- [3] M. Rezaiee-Pajand, S.R. Sarafrazi, H. Rezaiee, Efficiency of Dynamic Relaxation Methods in Nonlinear Analysis of Truss and Frame Structures, Computers and Structures 112-113 (2012) 295-310.
- [4] A.S. Day, An Introduction to Dynamic Relaxation, The engineer (1965) 218-221.
- [5] J.H.R. Otter, Computations for Prestressed Concrete Reactor Pressure Vessels Using Dynamic Relaxation, Nuclear Structural Engineering 1 (1964) 61-75.
- [6] M.R. Barnes, Form and Stress Engineering of Tension Structures, Structural Engineering Review 6 (1994) 175-202.
- [7] P.A. Cundall, Explicit Finite-difference Methods in Geomechanics, Proceedings E.F. conf. numerical methods in geomechanics. Blacksburg, 1976, 132-150.
- [8] S. Kmet, M. Mojdis, Teoretical and Experimental Analysis of Cable Domes, in 14 Conference on Civil Structural and Environmental Engineering Computing, 2013 Cagliari, editor B.H.V. Topping, paper 146.
- [9] M. Hüttner, J. Máca, P. Fajman, Analysis of Cable Structures using the Dynamic Relaxation Method, in 14 Conference on Civil Structural and Environmental Engineering Computing, 2013 Cagliari, editor B.H.V. Topping, paper 145.

Form-Finding of Membrane Structures and Necessary Stabilization of this Process

LANG Rostislav^{1,a*}, NĚMEC Ivan^{2,b} and ŠEVČÍK Ivan^{3,c}

¹Institute of Structural Mechanics, Faculty of Civil Engineering, Brno University of Technology,
Veveří 331/95, CZ-602 00 Brno, Czech Republic

²Institute of Structural Mechanics, Faculty of Civil Engineering, Brno University of Technology,
Veveří 331/95, CZ-602 00 Brno, Czech Republic

³FEM consulting, s.r.o., Veveří 331/95, CZ-602 00 Brno, Czech Republic

^alang.r@fce.vutbr.cz, ^bnemec.i@fce.vutbr.cz, ^csevcik@fem.cz

Keywords: membrane structure, form-finding, optimization process, stabilization, isotropic prestress, anisotropic prestress, Cauchy stress tensor, second Piola – Kirchhoff stress tensor, Euler – Almansi strain tensor, Green – Lagrange strain tensor

Abstract. The aim of this contribution is a form-finding process. It is the problem of initial pre-stressed shape generation of membrane constructions. The contribution deals with specific aspects of this process and the necessity of introducing stabilization with regard to its practical application. Individual examples will show the results of methods described in this paper.

Introduction

In recent decades we may witness a new trend in civil engineering. This new trend is remarkable in favouring textile application in architecture. Modern membrane constructions weigh very little, have attractive shapes and an ability to bridge large spans. Their rigidity and bearing capacity are derived merely from the membrane state of tension. This aspect requires the application of sufficient pre-stressing insuring the existence of mere tension forces during the whole durability of the membrane construction [1,2,3].

As the result of negligible bending rigidity of those constructions the shape and tension cannot be separated. Therefore solving membrane constructions leads to geometrically nonlinear calculations. Even the membrane construction design itself, i.e. its shape and pre-stressed design, is geometrically nonlinear process known as form-finding [4].

Form-Finding

Form-finding is a special branch of general structural optimization. The form-finding process is on the border of structural mechanics and art. Its task is to find a neat shape defined by the stress distribution, influencing this membrane and insuring sufficient geometric rigidity.

As stated by Kai-Uwe Bletzinger [4], in comparison with usual concept of structural mechanics, the inverse problem is solved by the form-finding process. This process is defined by prescribing the stress distribution, which becomes a control parameter in the process of generating the shape. In this regard, it is an inversion of the usual tasks of structural mechanics, where tensions are reaction of the material to deform the structure. The changes of tension in the form-finding process are not derived from structural deformation, however, the deformations are the result of prescribing the tension.

Determining the Shape Through Prescribing the Tension

As presented below, each spatial equilibrium system of forces acting on the membrane defines clear shape. By the repeated application of pre-stressing, the membrane structure converges to the shape

that is defined by this pre-stressing. Later it will be shown that it does not matter if the initial positions are different.

On the infinitesimally small surface of membrane the initial and final configuration can be described, i.e. its position in the material and spatial coordinates (Fig. 1).

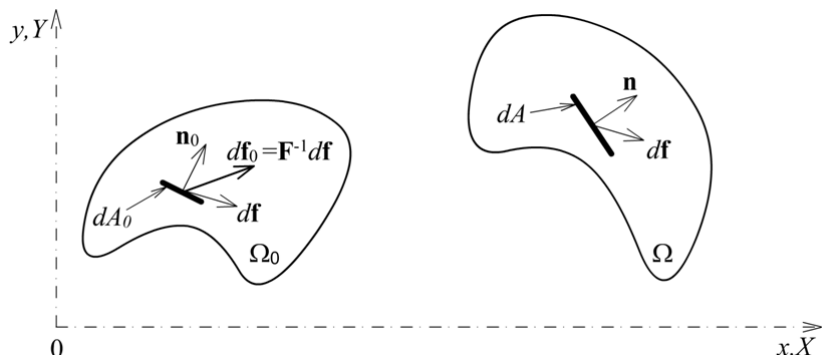


Fig. 1 Initial and final configuration [5]

- dA_0 infinitesimal small area of the membrane in the original configuration,
- dA infinitesimal small area in the resulting configuration corresponding to the small area dA_0 ,
- df_0 force acting on the non-deformed small area dA_0 , transformed into the material coordinates,
- df force acting on the small area dA in the spatial coordinates,
- n_0 unit normal to the small area dA_0 in the material coordinates,
- n unit normal to the small area dA in the spatial coordinates,
- F deformation gradient.

On this infinitesimally small surface can be defined the strain and stress tensors:

- σ Cauchy stress tensor defined in spatial coordinates,
- \hat{e} Euler – Almansi strain tensor defined in spatial coordinates,
- S Second Piola – Kirchhoff stress tensor defined in material coordinates,
- E Green – Lagrange strain tensor defined in material coordinates.

Next the principle of virtual work will be applied. It shows that energy and work are independent of the coordinate system, nevertheless it has to be ensured that a corresponding and energetically conjugate stress is assigned to the appropriate degree of deformation [5].

$$\delta W = \delta W^{\text{int}} + \delta W^{\text{ext}} = 0. \quad (1)$$

As mentioned above, the equilibrium force system defines unique shape of the membrane. Pre-stressed membrane in the equilibrium position without external loads is defined by the Eq. 2

$$\delta W = \delta W^{\text{int}} = 0. \quad (2)$$

and consequently it can be written,

$$\delta W = t \cdot \int_{\Omega_0} S : \delta E d\Omega_0 = t \cdot \int_{\Omega} \sigma : \delta \hat{e} d\Omega. \quad (3)$$

where t is thickness of the membrane.

As the resulting shape of the membrane structure is not known, it has to be found. Prescribed pre-stressing is applied to the original shape of the membrane and this actually represents the second

Piola – Kirchhoff stress \mathbf{S} . The resulting configuration from the first iteration is considered as the initial configuration for the next iteration. If the pre-stressing is applied to the membrane repeatedly, membrane stabilizes at the equilibrium position and deformation tensors $\hat{\mathbf{e}} = \mathbf{E} = 0$. Now, Eq. 3 is fulfilled and the initial configuration is equated with the resulting configuration, i.e. with the Cauchy stress $\boldsymbol{\sigma}$ identifying themselves with the second Piola - Kirchhoff stress \mathbf{S} . This way the shape of the membrane for prescribed pre-stressing has been found. Form-finding leads to the solution of the iterative process. This process is indicated as the updated reference strategy URS by the authors Bletzinger and Ramm [4].

An analogous proof can be performed in the situation of pressurized membranes where material is subjected to both pre-stressing and pressure on the inner surface of the membrane.

$$\delta W = \delta W^{\text{int}} + \delta W^{\text{ext}} = t \cdot \int_{\Omega_0} (\mathbf{S} : \delta \mathbf{E} - \vec{p} \cdot \delta \mathbf{u}) d\Omega_0 = t \cdot \int_{\Omega} (\boldsymbol{\sigma} : \delta \hat{\mathbf{e}} - \vec{p} \cdot \delta \mathbf{u}) d\Omega = 0 \quad (4)$$

The Required Pre-Stressing is Specified as the Controlling Parameter in the Process of Form-Finding

The main problem of the form-finding process, however, is the determination of the spatial system of forces in equilibrium, which usually can not be defined in advance. The exception is the isotropic stress field, which can be physically simulated using the soap film analogy. From the mathematical point of view this is a special case because the shape obtained when applying isotropic pre-stressing, is the shape with minimum area in closed borders [6,7]. The soap film analogy was used in life-work of German architect and engineer Frei Otto.

Isotropic pre-stressing mostly leads to a good geometrical rigidity and in the case of an isotropic material also to its uniform utilization. Based on the soap film analogy there were created many programs that enable generating the shapes of minimum areas.

There are many cases, however, where it is necessary to pre-stress membrane anisotropically. This requirement may be caused by a variety of reasons, including the use of orthotropic material (orthotropy in the warp and weft), request for another form or other inclinations, or the fact that in the given boundary conditions, the existence of a shape with isotropic pre-stressing is physically impossible.

In this case it is necessary, through the process of form-finding, to generate anisotropically pre-stressed membrane. As mentioned above, each spatial force system in equilibrium specifically defines the resulting shape, but as mentioned later, such an equilibrium system of forces is usually not possible to be determined in advance. The reason is that in the anisotropic system of forces in equilibrium, the measure of the anisotropy in each point is generally different. This fact has resulted in many stabilization processes, which lead not only to finding the final shape, but also to finding the equilibrium of anisotropic pre-stressing itself.

The Stabilization of Form-Finding Process Leads to the Finding of the Equilibrium of Anisotropic Pre-Stressing

Repeated application of constant orthotropic pre-stressing all over the membrane leads to singular resulting shape, resulting in uncontrolled deformation and this shape becomes unusable (Fig. 2). This is a consequence of repeated prescription of physical nonequilibrium system of forces.

To prevent this uncontrolled deformation, various stabilizations have been proposed. In the paper [4] as a possible stabilization method named Element size control, preventing stretching of finite elements greater than the user specified, is used. In the paper [4] examples based on this method are presented too.

During the work of the author team a stabilization method, based on the influencing of originally specified orthotropic pre-stressing in each iteration by the coefficient dependent on the total

elongation, without, however, the maximum elongation definition. Further stabilization method was tested using the coefficient depending merely on the previous iteration.

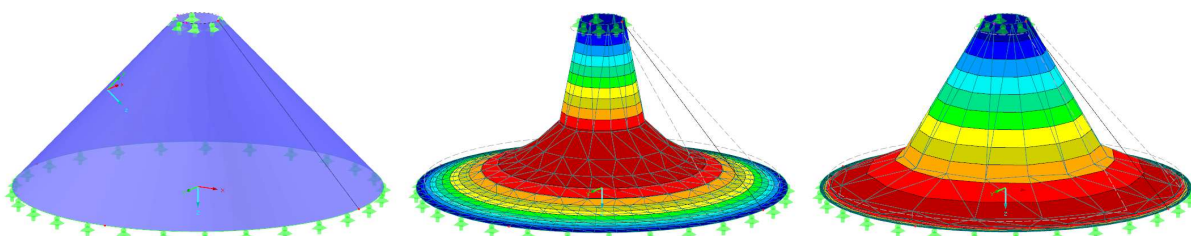


Fig 2. Constant orthotropic prestress all over the membrane. From left: initial shape, the shape after 10 iteration, the shape of the 50th iteration and uncontrolled finite element deformation

The above-mentioned methods are possible stabilizations, however, it is necessary to be aware that there may experience the following effects. Element size control method and a method using a coefficient depend on the overall deformation are dependent on initial approximation of the shape of the membrane. Method that uses a coefficient depending only on the previous iteration reduces the effect of the initial membrane approximation, does not, however, guarantee such a good calculation stability.

Designing the stabilization

The aim of this paper is to suggest stabilization, leading to the generation of appropriately pre-stressed shape of membrane structures.

The designed stabilization is based on defining the pre-stressing in one direction of orthotropy and defining the average value of pre-stressing in the second direction of orthotropy. In the first iteration, there will be applied nonequilibrium system of forces with specified values of tension in warp and weft. In following iterations, there will be applied value of tension in one of directions again (specified by users) and as a result of nonequilibrium of specified force system, the values in the second direction will be modified. However, the modified prestress in the second direction will have the same mean value as mean value of prescribed prestress.

This method was programmed and consequently tested. The designed stabilization has good numerical stability.

Examples of generated pre-stressed shapes

a) Membranes with isotropic pre-stressing

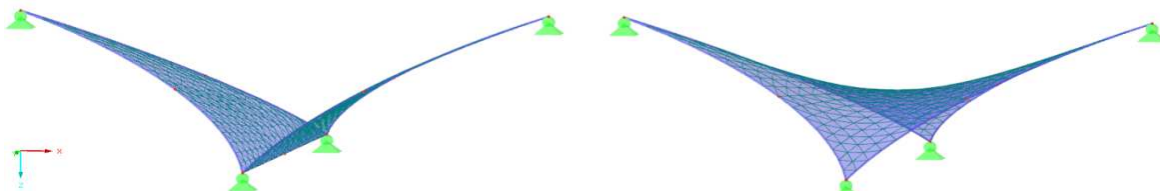


Fig. 3 Different starting shapes of membrane structures with identical boundary conditions

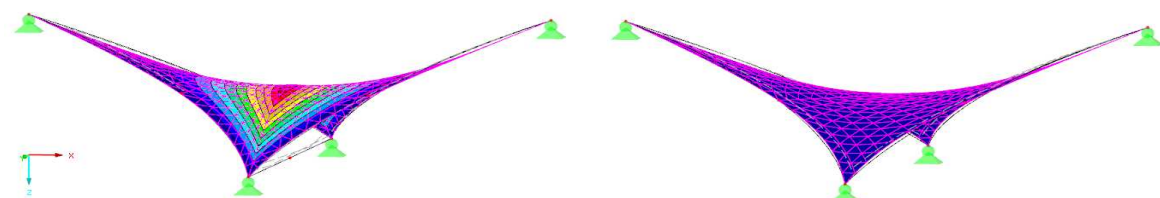


Fig. 4 Resulting shapes of isotropically pre-stressed membranes

The text above stated that the unique shape was defined by the requirement for the equilibrium of pre-stressing. This assertion is proved by the isotropically pre-stressed membrane whose shape is generated from different initial geometries. Through definition of the same pre-stressing the resulting shape is the same. This fact can be seen in the Fig. 4. Isolines in Fig. 4, 6 and 7 represent the necessary deformation to generate resulting equilibrium shape for given prestress.

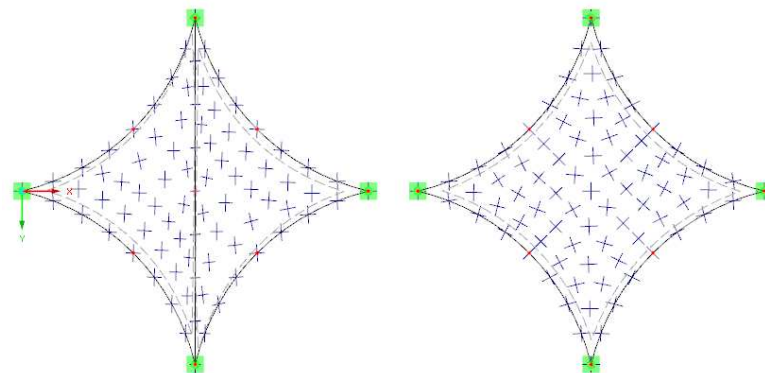


Fig. 5 Isotropic pre-stressing

In Fig. 6, we can see the result of the requirement of the isotropic pre-stressing in the cone membrane. It is obvious that it is a physically unrealistic requirement, which proves strangling during the calculation of the shape. If we simulate the task through the soap film analogy experiment, in the given boundary conditions the bubble would be pinched and broken as simulated in Fig. 6.

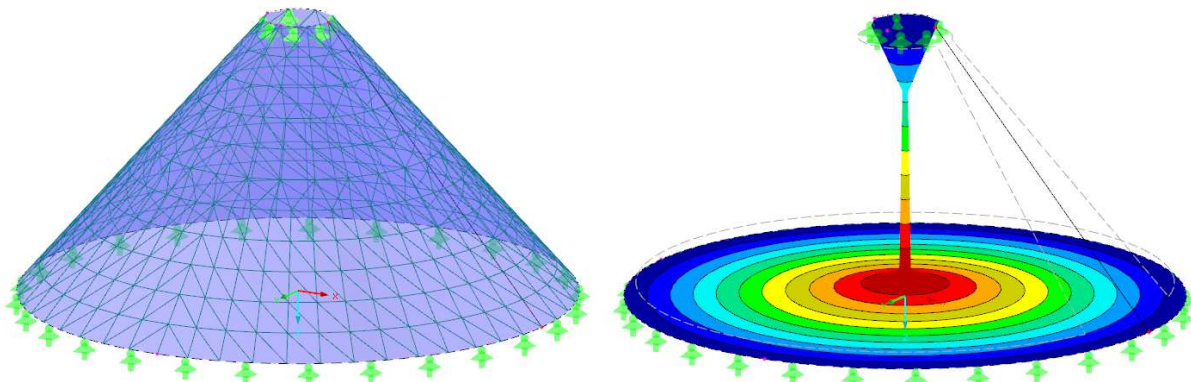


Fig. 6 Infeasible requirement of isotropic pre-stressing

b) Anisotropic pre-stressed membrane through a proposed stabilization

Through the proposed stabilization the shapes of cone membranes shown in Fig. 8 were generated. The resulting shapes are again independent of the initial geometry.

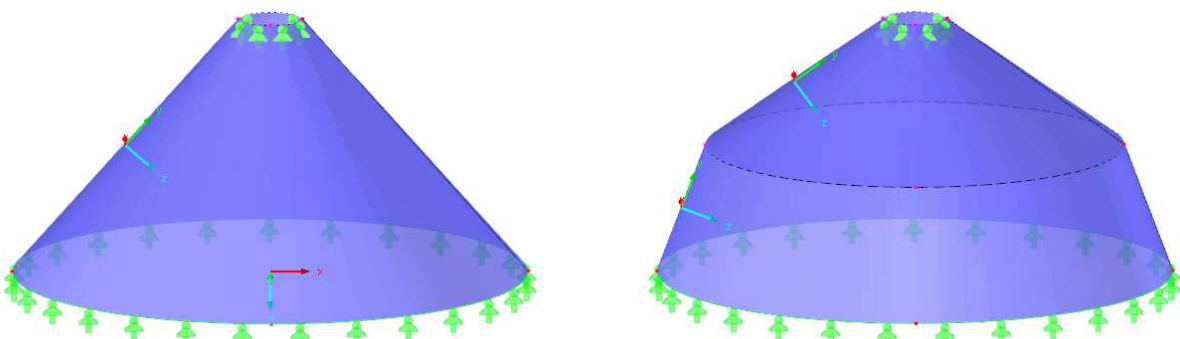


Fig. 7 Different starting shapes of membrane structures with identical boundary conditions

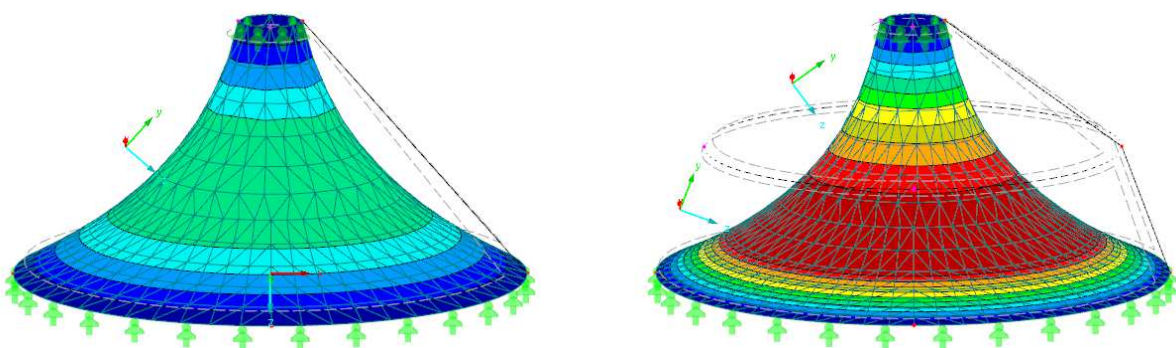


Fig. 8 The same resulting conical shapes of anisotropically prestressed membranes

Conclusions

Membrane structures are stable and reliable, provided that merely tensile stress affects them throughout their existence. This ensures sufficient pre-stressing, which is tied with the shape of these structures. The project office needs such a tool, which allows generating pre-stressed membrane shapes. The size and orientation of pre-stressing depend on the specific requirements of the designer and boundary conditions. This is in direct dependence on the required geometric rigidity and the direction of the applied load, therefore these parameters of the pre-stressed size and orientation are the responsibility of structural engineers.

The aim of the described methods of generating the initial pre-stressed shapes, however, is the possibility of creating these shapes. Without the use of form-finding, the shapes can not be generated.

All the examples given in the article were computed in the RFEM program developed by Ing. Dr. habil. K. Dlubal, s.r.o., in cooperation with the FEM Consulting s.r.o. In this program the functionality of the form-finding, at present containing two different stabilization methods for generating the initial shapes of membrane structures, is currently being prepared.

References

- [1] K.-U. Bletzinger, E. Ramm, Structural optimization and form finding of light weight structures, Comput. Struct. 79 (2001) 2053–2062.
- [2] E. Oñate, B. Kröplin, Textile Composites and Inflatable Structures, first ed., Springer, Dordrecht, 2005.
- [3] P. Wriggers, P. de Mattos Pimenta, New Trends in Thin Structures: Formulation, Optimization and Coupled Problems, Springer Verlag, Vienna, 2010.
- [4] K.-U. Bletzinger, E. Ramm, A general finite element approach to the form finding of tensile structures by the updated reference strategy, Int. J. Space Struct. 14 (1999) 131–146.
- [5] I. Němec, et al., Finite Element Analysis of Structures: Principles and Praxis, first ed., Shaker Verlag, Aachen, 2010.
- [6] F. Otto, B. Rasch, Finding Form: Towards an Architecture of the Minimal, first ed., Axel Menges, Exeter, 1996.
- [7] I. Němec, R. Lang, Design and Analysis of the Membrane Structure, Transactions of the VŠB - Technical University of Ostrava, Mechanical Series 1/2013 (2013) 51-54.

Vibrations in the Assessment of Construction State

ZOLTOWSKI Bogdan^{1,a*} and ZOLTOWSKI Mariusz^{1,b}

¹University of Technology and Life Sciences, Bydgoszcz, Poland

^abogzol@utp.edu.pl, ^bmazolto@utp.edu.pl

Keywords: technical diagnostics, identification, modeling, modal analysis

Abstract. The knowledge of the dynamic state and structure of the system allows describe its behavior, and allows creating prognosis models of the system behavior in the function of dynamic evolution time, based on the model of the technical state symptoms growth. Most often, however, there are no known equations describing behaviors of the system in the function of dynamic evolution time, which accounts for the need to apply new tools to examine the dynamic state. There is, therefore, the requirement to experimentally verify analytical technical models as the proper one is a model which is verified in practice. An experiment is, therefore, often only an inspiration for further researches leading to the optimization of the construction.

In this work presented are chosen problems of machines' technical state diagnosis with the use of identification and technical diagnostics methods. Relations between methods of dynamic state evaluation and methods of technical state evaluation were indicated. Example modal analysis results illustrate the complexity of projecting dynamic state researches into diagnostic researches of machine state evaluation.

Introduction

Destruction processes of technical systems force the need to supervise changes of their technical state. It is possible with the use of technical diagnostics methods. Methods and means of modern technical diagnostics are a tool of machine state diagnosis, which is the basis of decisions made at each stage of their existence.

Many previous works of the author [1,2,3,4,5] clearly indicate connections between machine dynamics and technical diagnostics, especially vibration diagnostics. The bases of identification, modeling and concluding fully convince towards the dominating role of vibrations in machine state identification [6,7,8,9]. Properly planned and realized experiment is the base to obtain diagnostically sensitive signals which processed will determine state diagnosis procedures. The processing includes: creation of numerous signal measures in time domain, frequencies and amplitudes, selection and reduction of the number of signal measures, creation and analysis of effectiveness of cause-and-effect models, as well as evaluation of the righteousness of made diagnostic decisions.

The realization of these tasks is possible only through broad support from information technology, which in this work is presented in the form of SIBI programs. Practical applications of the presented ideas have been verified in researches on complex objects exploited in difficult climate conditions.

Dynamics and Diagnostics

Into quality measures of machine's technical state, i.e. its dynamics, included is the level of vibration amplitudes, as well of the machines as the lot, and also of relative vibrations of separate elements and parts. Overall vibrations of the machine can be perceived as an external symptom while they are responsible for the level of interferences emitted into the environment. Relative vibrations of separate elements, however, influence mainly the state of internal forces in the machine, i.e. at its level of dynamic stress amplitudes.

Identification can concern both the construction of models and the reconstruction of the examined model state, which leads straight to the problem of technical diagnostics. The process of diagnostic identification includes: modeling (symptom or structural), identification experiment (simulation and/or real), estimation of diagnostic parameters (state features or symptoms), diagnostic concluding.

The specificity of diagnostic identification tasks is different from general identification in the way that it includes a number of additional elements enhancing this process. They are:

- constructing models of diagnostic signals generation,
- choosing features of object structure state and diagnostic symptoms,
- modeling cause-and-effect relations,
- evaluating the accuracy of choosing variables for the model,
- determining boundary values of the symptoms,
- states classifying and determining of periodicity a diagnosis.

Methods of identification can be divided concerning: the kind of identified model, the kind of experiment, identification criterion applied, as well as estimation procedure applied. In general these are: methods of analysis, time, frequency, correlation, regression, factor analysis, as well as iteration methods described in works of many authors [2,4,6,5,8].

For simple objects a good tool to evaluate their changeable dynamic state are methods of simple identification, which use amplitude - frequency spectrum. Searching resonance frequency and amplitude value in this frequency with the use of tests (impulse, harmonic and random) are relatively well mastered in research techniques of our enterprises [2,5].

Another way of describing and analyzing the dynamic state of machines is a modal analysis used as a theoretical, experimental and exploitation method. It uses frequencies of own vibrations, values of suppression and forms of vibrations to describe the changing machine state, and it is used to improve the finished elements method. The presented procedures are based on the knowledge of the system model, and the conclusions drawn from the actions on the models depend on their quality. Depending on the aim of the performed dynamic analysis of the object, different requirements are set for the constructed models, and their evaluation is conducted with different experimental methods.

Description of Object State Changes

The dynamic state of the object can be, in the easiest case, described with a model of 1 degree of freedom – Fig. 1. A conventional description of this model is known relations (Eq. 1-4) indicating that vibrations well reflect the state of the machine. A description of this model can be achieved within m, k, c categories, or through a, v, x researches.

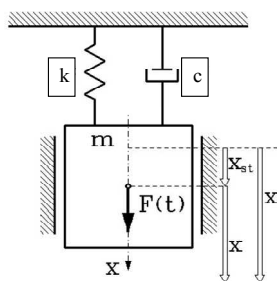


Fig.1 System model of 1 degree of freedom

$m, k, c =$ vibration process (a, v, x)

$$m\ddot{x} + c\dot{x} + kx = F(t), \quad (1)$$

$$x = A \sin(\bar{\omega}t + \varphi), \quad (2)$$

$$v = \frac{dx}{dt} = A\bar{\omega} \cos(\bar{\omega}t + \varphi), \quad (3)$$

$$a = \frac{d^2x}{dt^2} = \frac{dv}{dt} = -A\bar{\omega}^2 \sin(\bar{\omega}t + \varphi). \quad (4)$$

Identification of his model (Eq. 1) from the experimental side is the a , v , x measurements for different time moments, which reflects the changes of the object state and is widely applied in vibration diagnostics. The solution of the task in the m , k , c , categories, however, requires a number of solution conversion of the equation (Eq. 1) for determining

$$c_{kr} = 2m\bar{\omega}, \quad c_{kr} = 4\pi mf, \quad k = m \cdot \bar{\omega}^2, \quad k = 4\pi^2 mf^2. \quad (5)$$

Determining the value (5) requires realizing identification experiment from which the frequency f or frequency ω can be determined. Here is useful the simple identification or modal analysis directly giving the values of own frequencies ω from the stabilization diagram – Fig. 2.

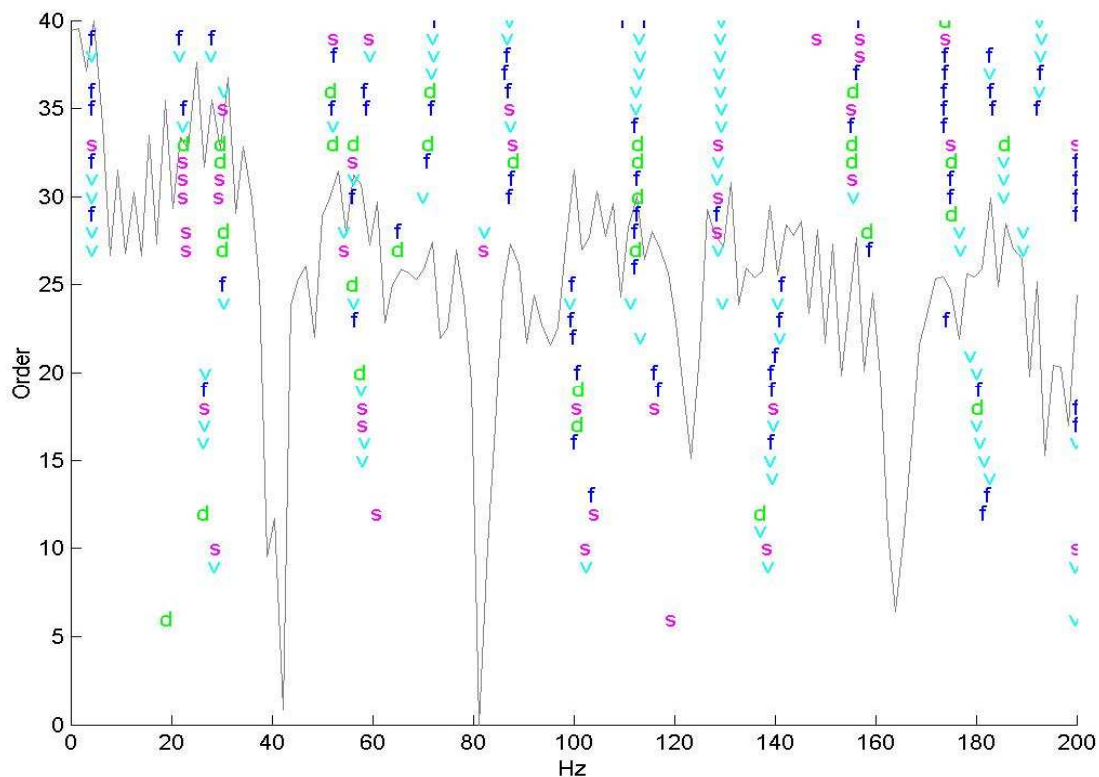


Fig. 2 Stabilization diagram for ω determination

The problem becomes more complicated for models of many degrees of freedom (more than 3). Here also the problem of object state identification can be solved from the measurement side (a , v , x), while from the side of determining m , k , c own problem needs to be solved.

$$(K - \omega^2 M) q_0 = 0. \quad (6)$$

Equation (Eq. 6) presents a linear system of homogeneous algebraic equations

$$\begin{aligned} (k_{11} - \omega^2 m_{11}) q_1 + (k_{12} - \omega^2 m_{12}) q_2 + \cdots + (k_{1n} - \omega^2 m_{1n}) q_n &= 0, \\ (k_{21} - \omega^2 m_{21}) q_1 + (k_{22} - \omega^2 m_{22}) q_2 + \cdots + (k_{2n} - \omega^2 m_{2n}) q_n &= 0, \\ \dots &\dots \\ (k_{41} - \omega^2 m_{41}) q_1 + (k_{42} - \omega^2 m_{42}) q_2 + \cdots + (k_{4n} - \omega^2 m_{4n}) q_n &= 0. \end{aligned} \quad (7)$$

A solution for $q \neq 0$ exists when the main matrix determinant $(K - \omega^2 M) = 0$, i.e. $\det(K - \omega^2 M) = 0$. Solving the system of Eq. 7 own values can be determined, and from them the frequencies of own vibrations, indispensable for the object identification $\left(\lambda = \omega^2 = \frac{k}{m} \right)$.

Identification Researches Software (SIBI)

More and more frequently conducted identification researches of machine dynamic state, used for the evaluation of the state changes, fault development and location of the occurred state causes, were the basis for creating a specialized software system. It allows acquiring and processing measurement data, creating many measures of diagnostic signals, examining their diagnostic sensitivity, statistic processing and diagnostic concluding. The program was named Information System of Identification Researches (System Informatyczny Badań Identyfikacyjnych – SIBI). The structure of the program is a module construction which includes the following modules (Fig. 3).

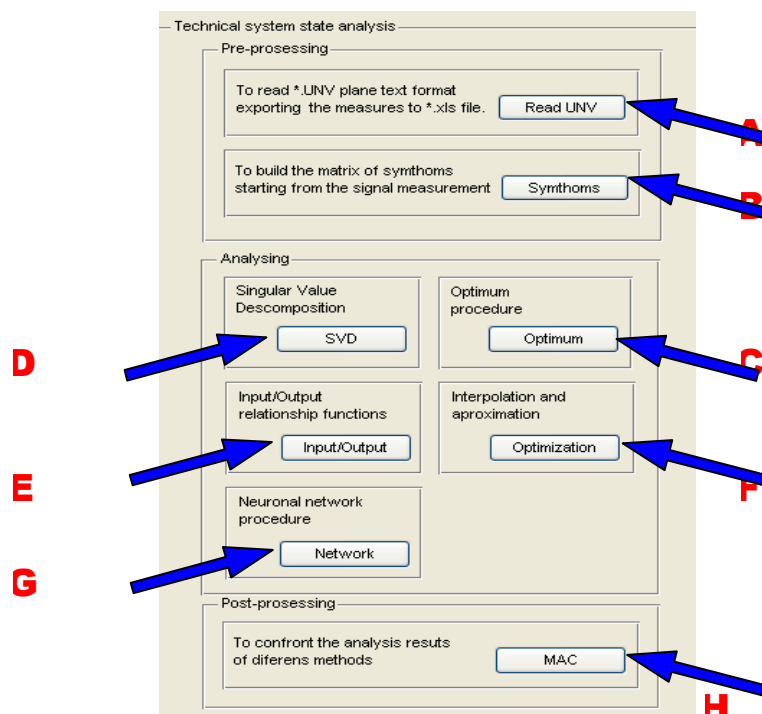


Fig.3 Main dialog box of SIBI program

- Read unv module which allows processing data from UNV format into XLS format.
- Symptoms module which allows defining, determining and creating matrix of many measures of vibration processes. Modules A and B are part of software responsible for acquiring and processing vibration processes in order to acquire observation matrix of vibration estimators.
- Optimum module uses the method of ideal point for individual evaluation of the sensitivity of measured symptoms of vibration processes.
- SVD module used for determining generalized damage measures, and for the evaluation of damage development. Using the SVD method allows a multidimensional description of the state of the examined object.
- Input/Output module used for the analysis of similarities between vibration processes, and for determining different exploitation measures of the examined object.
- Optimization module used for creating models and data in genesis (with approximation and interpolation methods), diagnosis and prognosis of object states.
- Network module using neuron nets for state classification on the basis of obtained results in the form of time rows.

H. MAC module is a procedure that allows the comparison of different vectors understood as a measure of the input and output of the system. C, D, E, F, G modules are elements of 2 parts of the software allowing the performance of statistic concluding and cause-and-effect relations, as well as visualization of the obtained results.

Cause-and-Effect Modeling

Many state measures acquired in experiments requires the reduction of over measurement, which is possible with the use of OPTIMUM procedure (statistic evaluation of separate measures) or SVD (for the multidimensional approach). Optimized set of symptoms is the basis of constructing cause-and-effect, most often regressive, multidimensional models (Fig.4).

$$y = -2.68w_1 - 0.54\text{row}_1 - 0.49x_1 + 2.01w_2 + 0.35\text{row}_2 + 2.26x_2 - 0.27H(f) + 0.06H(f)L + +0.02g_2x_1 - 92.3\text{ARMS}(t) + 12.99\text{bkurt} + 239.69\text{Cs} - 200.58I - 44.37$$

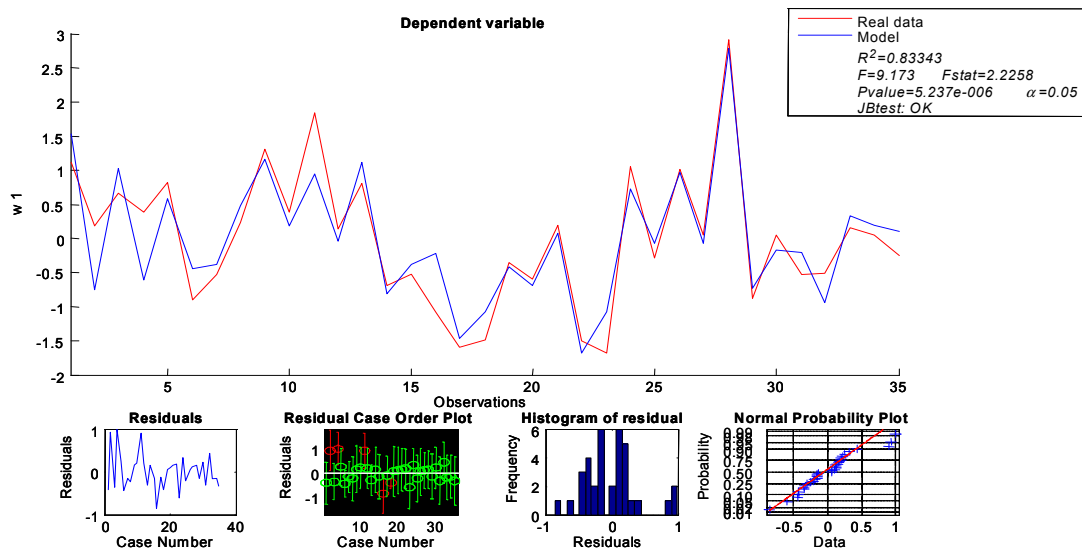


Fig. 4 Regressive model determination

The wellness of the model is evaluated with the help of the determination coefficient R^2 , and the number of component symptoms determines its accuracy – Fig. 5.

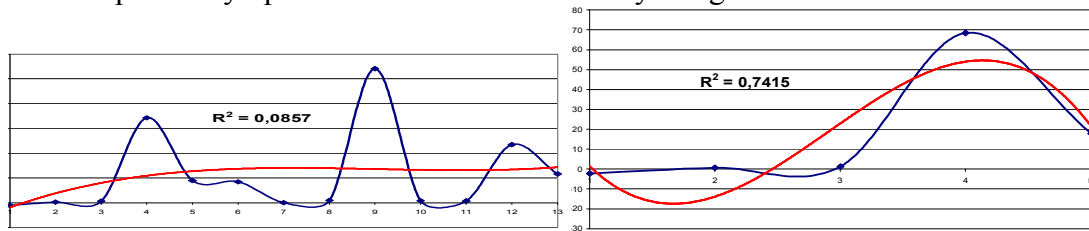


Fig. 5 The influence of the number of symptoms measured on the accuracy of the model

Conclusions

Presented in this work considerations, concern the modeling of object dynamic state with the use of description and researches within the range of identification, distinguishing modal analysis and ideas directly supporting different methods of forming machine dynamics.

The knowledge of the dynamic state and structure of the system allows of describe its behavior, and allows creating prognosis models of the system behavior in the function of dynamic evolution time, based on the model of the technical state symptoms growth. Most often, however, there are no known equations describing behaviors of the system in the function of dynamic evolution time, which accounts for the need to apply new tools to examine the dynamic state.

There is, therefore, the requirement to experimentally verify analytical technical models as the proper one is a model, which is verified in practice. An experiment is, therefore, often only an inspiration for further researches leading to the optimization of the construction.

References

- [1] J.S. Bendat, A.G. Piersol, Methods of analysis and measurement of random signals, [in Polish] PWN, Warszawa, 1996.
- [2] C. Cempel, Vibroacoustical Condition Monitoring, Ellis Hor. Ltd., Chichester, New York, 1991.
- [3] W. Cholewa, J. Kiciński, Technical diagnostics. Reversediagnosticmodels. [in Polish] Wydawnictwo Politechniki Śląskiej, Gliwice, 1997.
- [4] J. Giergel, T. Uhl, Identification of mechanicalsystems, [in Polish] PWN, Warszawa, 1990.
- [5] H. Kaźmierczak, J. Kromulski, Methods of parametric identification in application into construction diagnostics, Exploitation problems, [in Polish], 6/93, MCNEMT, Radom, 1993.
- [6] H. Tylicki, Optimization of the process of vehicle mechanical state prognosis, [in Polish] Rehabilitation thesis, No 86, ATR Bydgoszcz, 1999.
- [7] T. Uhl, Computer-enhanced identification of mechanical construction models, [in Polish] WNT, Warszawa, 1997.
- [8] B. Żółtowski, Diagnostic identification of technical objects, Problems of machines exploitation, [in Polish] Z.1 (105), PAN, 1996.
- [9] B. Żółtowski, Machine diagnostics basic, [in Polish] Wyd. ATR, Bydgoszcz, 1996.
- [10] B. Żółtowski, Multidimensional monitoring of the track-vehicle interface of a railway system, Besanson, 2007.
- [11] B. Zoltowski, L. Castañeda, Monitoreo Multidimensional de la Interfase Vía-Vehículo de un Sistema Ferroviario, Congreso Internacional de Mantenimiento – ACIEM – Marzo 2007, Bogotá, Colombia.

Assessment State of Masonry Components Degradation

ZOLTOWSKI Mariusz^{1a*}

¹University of Technology and Life Sciences, Bydgoszcz, Poland

^amazolto@utp.edu.pl

Keywords: degradation, optimization, destruction of material, modeling, modal analysis

Abstract. The chosen problems of identification of the destruction state of wall elements in this work were introduced. It was showed a possible relationship between methods of opinion of dynamic state and methods of destruction opinion of the wall elements. Near they utilizations experimental modal analysis illustrate the complexity problems and need of optimization of number component measuring the examples - results of investigations.

Introduction

If the problem of logging was observed the growth of interest in universally and the modern information processing with investigations for needs of construction, production and exploitation of building constructions. The growth of requirements, along with caused with use of many modern technologies, the development of computer diagnostic devices, the enabling the detection and location developing damages.

The test of dynamic opinion in state of walls elements in this work was undertaken with the help of tremblings, using hereinto function FRF appointive in experimental modal analysis [14]. The processing was subjected was the gain over in investigations of walls vibrations elements information more far, and particularly the optimization under in relation to usefulness of appointed measures to differentiation of destruction state of wall element. It the utilization the method of OPTIMUM as well as method SVD was proposed [1,5,12,14,16,17].

Identification of Dynamic State

The technical reality then the result of analysis models which describe her less or more correctly. The identification can concern both the building of models of object how and the reproduction of state of studied object, which leads to problems of diagnostics directly. The process of diagnostic identification hugs [1,6,7,8,15,17]:

- * modeling
- * identification experiment (simulating and / or real),
- * the estimation of diagnostic parameters (the features of state or symptoms),
- * diagnostic inference.

It is possible that the existing methods of identification can divide on method of identification of static properties and dynamic. The methods of identification were it been possible to divide with regard on: the kind of identified model, kind of experiment the, applied criterion of identification, or else the applied procedure of estimation [1,2,6,7,15].

The methods of identification of straight line are a good tool of opinion for changes their dynamic state, using phantom frequency. Search in this frequency the resonance frequency and value of amplitude with the help of the tests: impulse, harmonic and accidental they are composed in investigative technicians our enterprises comparatively well.

Modal analysis is different way of description and analysis the dynamic state, practical as theoretical, experimental and exploational modal analysis. She uses the frequency the natural oscillation and figures of tremblings of to description of changes state of machines as well as it serves to improvement of method of elements complete.

Identification Straight Line and Folded

The change of state (the destruction of walls elements) described with signal can be reflected in variables values of level (the parameters), tremblings or in change the transmittion from point of damage to the point the receipt.

Identification Straight Line. It is in majority of uses with identification of straight line it where the changes of value of mass were marked was - the m , stiffness - the k , suppression - the c , or the change of parameters of profiles frequency (the phantom). It tasks about identification of straight line which should:

- mark the structure of model, that is the value and mutual connections between mass elements (the m), springy (the k) and the dumping (the c);
- mark the profiles frequency arrangements or only sure gathering of their parameters.

The investigations of changes transmittion reflecting the dynamic properties of object it was it been possible was to conduct three methods [5]:

- with the help of impulse test (knock hammer);
- with the help of harmonic test (signal from generator);
- with the help of accidental test (stimulation many resonances simultaneously).

Experimental Modal Analysis. Experimental modal analysis is the technique of investigation of property dynamic objects, both on stage construction and in exploitation. The identification experiment in experimental modal analysis depends on extortion the tremblings near simultaneous measurement of strength the object extortionary and the answer of arrangement, the most often in figure of phantom, or the accelerations of tremblings.

The relation of strength extortionary, the movement on entry of arrangement to value the acceleration of tremblings on exit with arrangement (Fig.1) is the function FRF.

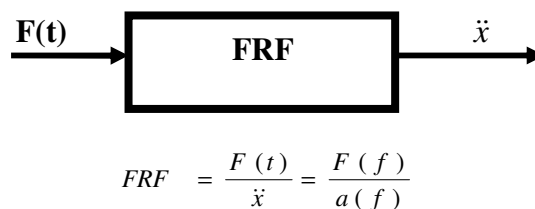


Fig. 1 Function FRF

More far processing the signal of extortion and answer in field of time it was transformed to ghostly field and marks for studied states of destruction the FRF.

It having registered the vibration signal for needs marking FRF, it has been possible without larger difficulties to mark in field of time many different measures of vibration process, frequency and amplitudes. It lets then the chance of searching of description of destruction of walls elements, and for the best vibrations measures. This requires however the selection of information by optimization, that is the search in sense the best measures of enlightening the size of destruction, what was introduced further in method of OPTIMUM.

OPTIMUM Method

Measured vibration signals in different prepare they imitate the development of destruction of walls elements [11]. Using with techniques to self - characterize in support mighty optimizations about measurements of distance from ideal point sensibility the measured measures of vibration process in relays the state of walls elements [1,7,9,12].

The results of measurements of vibration process for different states of destruction (introduced in Table 1) they are subject to the walls elements the statistical opinion with the help of the different criterions.

Table 1 Measures of vibration process for different states of destruction of walls elements

State	Parameter 1	Parameter 2	Parameter 3	Parameter 4	Parameter 5	Parameter 6	Parameter 7	Parameter 8
1	0.00	0.99	0.03	0.01	0.85	0.28	0.96	0.73
2	0.03	0.98	0.04	0.10	0.76	0.47	0.95	0.67
3	0.14	0.94	0.08	0.10	0.39	0.59	0.94	0.06
4	0.16	0.94	0.12	0.11	0.12	0.02	0.94	0.28
5	0.21	0.90	0.14	0.13	0.92	0.46	0.91	0.29
6	0.25	0.90	0.20	0.14	0.14	0.64	0.87	0.34
7	0.25	0.84	0.22	0.15	0.82	0.29	0.80	0.26
8	0.26	0.83	0.23	0.20	0.40	0.12	0.79	0.59
9	0.27	0.81	0.23	0.21	0.40	0.67	0.73	0.62
10	0.30	0.64	0.29	0.25	0.11	0.32	0.65	0.28
11	0.30	0.62	0.31	0.27	0.90	0.24	0.61	0.61
12	0.33	0.62	0.42	0.29	0.17	0.76	0.59	0.68
13	0.37	0.52	0.53	0.34	0.78	0.42	0.59	0.26
14	0.37	0.50	0.55	0.34	0.93	0.01	0.56	0.19
15	0.39	0.48	0.61	0.39	0.35	0.45	0.53	0.44
16	0.40	0.47	0.62	0.43	0.63	0.37	0.48	0.24
17	0.40	0.41	0.67	0.49	0.80	0.96	0.46	0.02
18	0.42	0.34	0.68	0.49	0.34	0.29	0.43	0.84

the changeability of symptoms

$$f_1 = \frac{s_j}{\bar{y}} \quad (1)$$

s_j - standard deviation, \bar{y} - value average. The correlating with state of destruction, sometimes the exploitation of object

$$f_2 = r(y, w). \quad (2)$$

It marking in turn of value the averages and standard deviation of measured symptoms (Table 1) was marked by received criterion f_1 . Delimitation among state and every of measures the coefficient of correlation qualified as a second criterion f_2 .

Making further the maximization of received criterions and standardization to maximum value (Table 2) it receives oneself statistical profiles of their sensibility, which further permits to mark the co-ordinates of ideal point.

Table 2 Criterion of optimization of measured parameters

	Parameter 1	Parameter 2	Parameter 3	Parameter 4	Parameter 5	Parameter 6	Parameter 7	Parameter 8	Parameter 9	Parameter 10
f1	0.54	0.63	0.58	0.65	0.53	0.62	0.51	0.56	0.47	0.73
max(f1)	0.73									
f1*	0.74	0.85	0.79	0.89	0.72	0.85	0.70	0.77	0.64	1
f1**	1									
f2	0.95	0.99	0.99	0.98	0.00	0.16	0.99	0.05	0.15	0.98
max(f2)	0.99									
f2*	0.96	1	0.99	0.99	0.00	0.16	0.99	0.05	0.15	0.98
f2**	1									
Li	0.25	0.14	0.20	0.10	1.03	0.84	0.29	0.97	0.91	0.01
1/Li	3.91	7.10	4.98	9.41	0.96	1.18	3.41	1.02	1.09	94.83
wi	0.03	0.05	0.03	0.07	0.00	0.01	0.02	0.00	0.00	0.74

This makes possible the marking from ideal point distance of individual measures with dependence [12]

$$L = \sqrt{(1-f_1^*)^2 + (1-f_2^*)^2} \quad (3)$$

as well as the marking the coefficients of sensibility (the weight) the individual measures

$$w_i = \frac{1}{L_i \cdot \sum_{i=1}^n L_i}, \quad \text{where: } \sum w_i = 1. \quad (4)$$

The introduced algorithm was possible easily to realize in programme Excel, getting qualitative in a row of measured symptoms. Final result of such conduct of for the example - 10 measures was showed on Fig. 2.

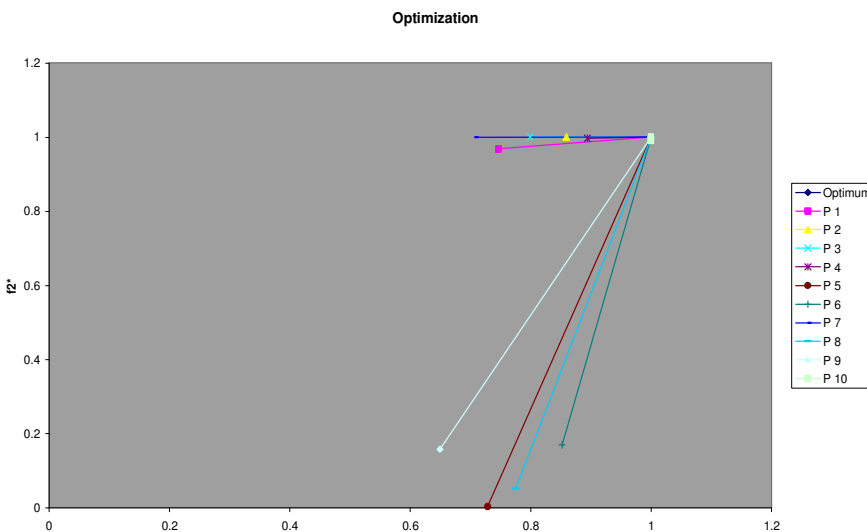


Fig. 2 Result of working of method of OPTIMUM

The registered temporary vibration signal process transferred to sheet Excel is the basis for more processing in field of time, frequency and amplitudes, giving many measures enabling the decomposition of output signal on signals individual evolve one self the damages of elements. Gaining over many partial measures is possible near utilization programme: SYMPTOMS PROGRAMME, in which it was possible to mark 38 measurements defined for opinion of destruction state. Supervising the destruction of wall state was led by utilization programme called OPTIMUM of usefulness of these measures (the choice of informative measures) as well as the SVD (part of symptoms in supervising the development of damage).

The example - results of investigation of sensibility on Fig.3 were showed valid of many vibrations measures of the chosen wall element.

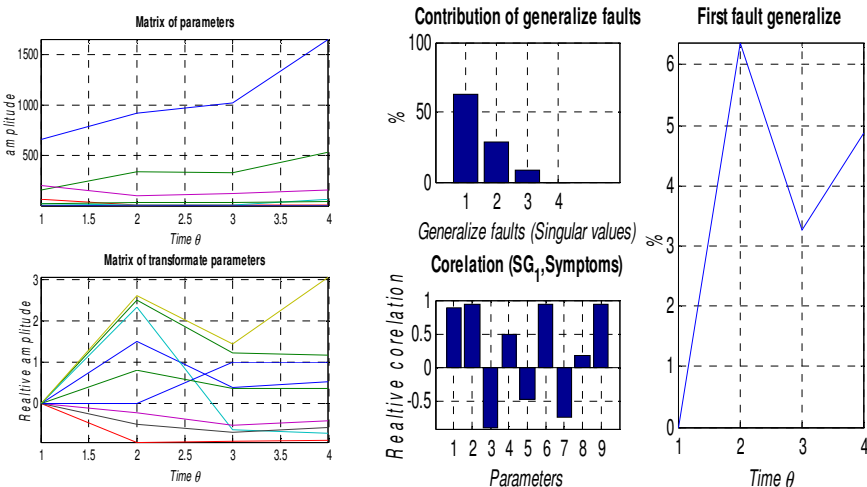


Fig. 3 Results of investigations the method the SVD

The draught of operation on decision process consists since moment of conquests the state information of machine, by her accumulation and the processing, until moment of choice and the delivery of settled decision to realization.

Summary

Introduced in this study the consideration of modern approach to modeling of dynamic state of building constructions, near utilization with range of identification, with distinction of modal analysis and questions the description and investigations supporting the directly different ways of formation of dynamics of construction. Nascent in this way evolutionary dynamic models guilty to perfect the methodology and the inference in opinion of dynamic state, more and more often used to optimization of construction as well as helping the exploational decisions.

The problems of optimization are important question of this area of investigations, in this the reduction of quantity of information and search the best symptoms of state of destruction material of construction. The proposed method of OPTIMUM permits on choice of the best measures by defined the criterions of quality usefully.

The modeling the changes of dynamic state and supply of objects, from regard the changing burden as well as the individual approach to changes of state every element this really the beginning in range of utilization of evolutionary models.

References

- [1] A. Ameljańczyk, Optimization in problems steering and management. Ossolineum, Wrocław, 1984.
- [2] J.S. Bendat, A.G. Piersol, Method of analysis and measurement of random signals. PWN, Warszawa, 1996.
- [3] R.D. Bishop, G.M. Gladwell, S. Michaelson, Matric analysis of tremblings. PWN, Warszawa, 1972.
- [4] J.T. Broch, Mechanical Vibration and Shock Measurements. Brüel & Kjaer, 1980.
- [5] C. Cempel, Practical Wibroakustyka. Warszawa, PWN, 1989.
- [6] P. Eykhoff, Identification in dynamic arrangements, BNI, Warsaw, 1980.
- [7] J. Giergiel, T. Uhl, Identification of mechanical arrangements. PWN, Warszawa, 1990.
- [8] J. Giergiel, Mechanical trembling. AGH, Kraków, 2000.

- [9] J. Kaczmarek, Basis of theory of trembling and dynamics of machines. Szczecin, 1993.
- [10] F. Morrison, Art of modelling of dynamic arrangements. WNT, Warszawa, 1996.
- [11] W.M. Paczkowski, Chosen problems of discrete evolutionary optimization. Papers of PS, No. 554, Szczecin, 1999.
- [12] H. Tylicki, Optimization of process of forecasting of technical state of motor vehicles. Qualifies for professorship trial No. 86, ATR Bydgoszcz, 1999.
- [13] T. Uhl, W. Lisowski, Practical problems of analysis of modal construction. CCATIE, Kraków, 1996.
- [14] T. Uhl, By computer helped identification of models constructions. WNT, Warszawa, 1997.
- [15] M. Żółtowski, R. Orłowicz, Chosen questions of acoustic isolation of wood ceilings. ZN ATR, Bydgoszcz 2005.
- [16] M. Żółtowski, Identification of the vibration threats of building objects, ZN ATR, Bydgoszcz 2005.
- [17] M. Żółtowski, Measurements of property of acoustic materials. DIAGNOSTICS, PTDT, PAN, Vol.33, 2005.

Numerical Modeling of Cylindrical Tank and Compare with Experiment

JENDŽELOVSKÝ Norbert^{1,a} and BALÁŽ Lubomír^{1,b*}

¹Slovak University of Technology, Faculty of Civil Engineering, Radlinského 11, 813 68 Bratislava,
Slovak Republic

^anorbert.jendzelovsky@stuba.sk, ^blubomir.balaz@stuba.sk

Keywords: modeling, finite element method, experiment, eigenfrequencies, cylindrical tank

Abstract. This paper deals with a problem of eigenfrequencies of cylindrical tank (steel water tank). For an ANSYS analysis of eigenfrequencies some numerical models of cylindrical tank are used and finally results got by these models are compared with experimental results in laboratory. In final part of the paper some crucial results are presented both in a graphical and numerical way.

Introduction

The dynamic task differs from the static one in two important aspects. The dynamic problem doesn't have a single solution, like the static problem. The solution must be defined at all time points, meaning that the dynamic task changes by one dimension - time, compared to the static one. In the fact, the second and more essential difference for the case of the static problem is that the internal forces of tension and deformation depend exclusively on the external load and can be determined through the procedure based on a balance of forces. However, if the load changes in time, the resulting deformations, internal forces, and tensions depend not only on this load, but also the fictitious forces acting against the acceleration and producing time-varying deformations [1].

In this paper we focus on comparison of the computational model of a steel cylindrical tank created through the finite element method (FEM), as well as the results of experimental research we carried out at our workplace. In both parts of the research we tried to find the vibration shapes and frequencies of the cylindrical tank, represented by the available model.

The cylindrical shell (steel water tank) was modelled using the ANSYS computer program. Given the experimental sample, a model ignoring the overpressures on the cylinder's surface was created. The filling was modelled using two types of elements designed to model fluids, being FLUID30 and FLUID80 [2,6]. Several calculation procedures applicable for the specific design situations are recommended.

Model and experimental sample (steel tank) parameters:

Height: 0.87 m

Diameter: 0.56 m

Wall and bottom thickness: 1.1 mm

Material: steel ($E = 210 \text{ GPa}$)

Load: water ($\gamma = 10 \text{ kN/m}^3$)

The issue of solving the cylinder tank's interaction with the fluid has a great justification in mechanics, because the liquid's weight significantly affects the tank's response, similarly to [7]. The movement of the liquid filling in a solid cylinder can be expressed as the sum of two separated contributions – “solid impulse” and “convection.” The solid impulse component exactly meets the borderline conditions on the walls and the bottom of the tank, but causes (incorrectly in regard to the wave action in dynamic response) zero pressure on the level of the free liquid surface in a static situation. The convective component doesn't change the borderline conditions and ensures compliance with the correct balance condition on a free surface [3,5].

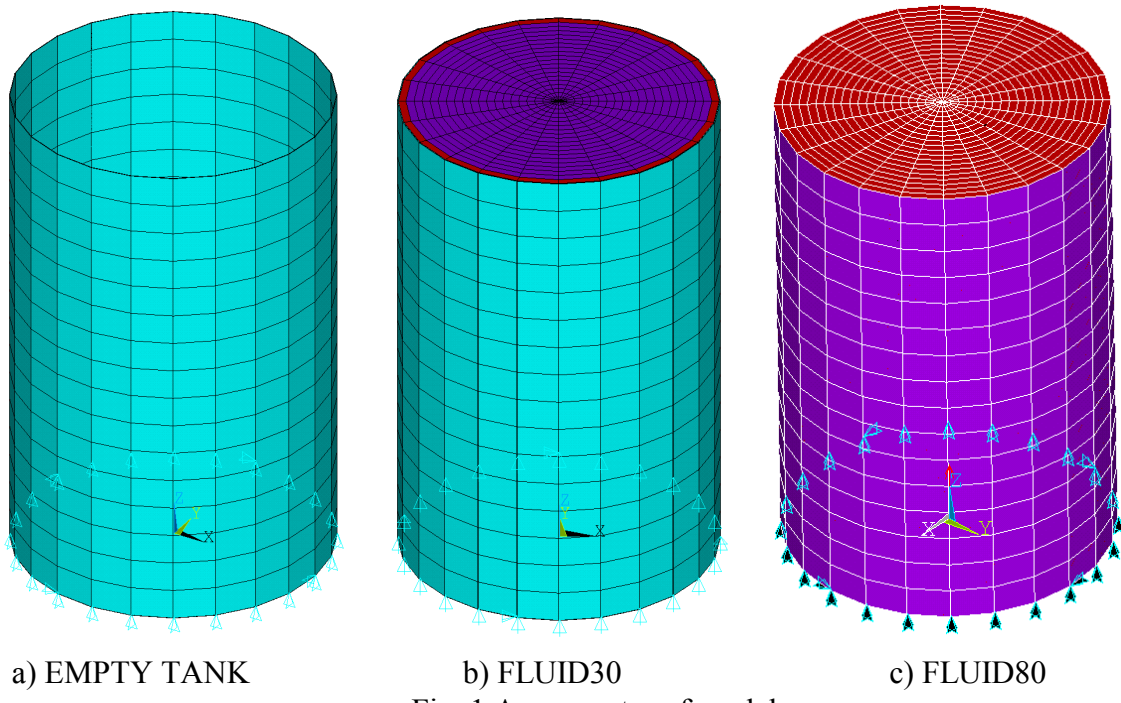


Fig. 1 Axonometry of models

Experimental Measurements of the Tank's Frequencies

We used a portable measuring apparatus for the measurement (Fig. 5). This apparatus consists of hardware and software evaluation device. To measure changes in acceleration utilizing the structure's fictitious characteristics, we used five piezoelectric accelerometers by Brüel & Kjaer. For measurements we used a 16-channel A/D converter. All accelerometers were set to the same sampling frequency – 10 000 samples per second, while the length of the measured time record was 5 seconds. To evaluate the results, we used the licensed LabVIEW program.



Fig. 2 Experimental Sample

Fig. 3 Prepared Model



Fig. 4 Detail of the Accelerometer



Fig. 5 Amplifier

Accelerometer Records

In the following graphs we present the records of the cylinder tank construction's acceleration. According to Fig. 3 we placed the sensors, the accelerometers, on the outside of the tank. Fig. 6 and 7 show the acceleration graphs for an individual accelerometer with a strong highlight of the horizontal stroke in the experimental model.

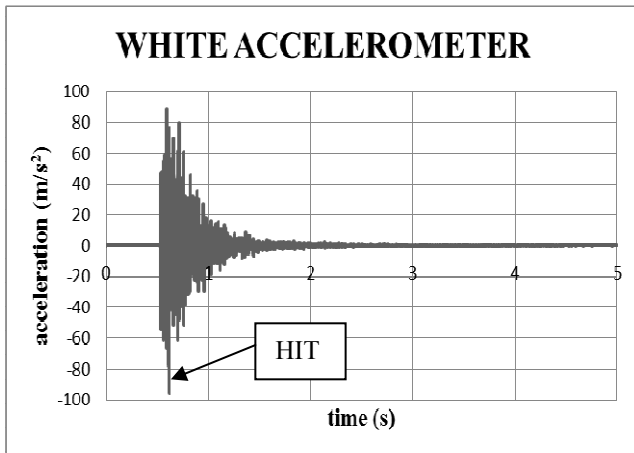


Fig. 6 White Accelerometer

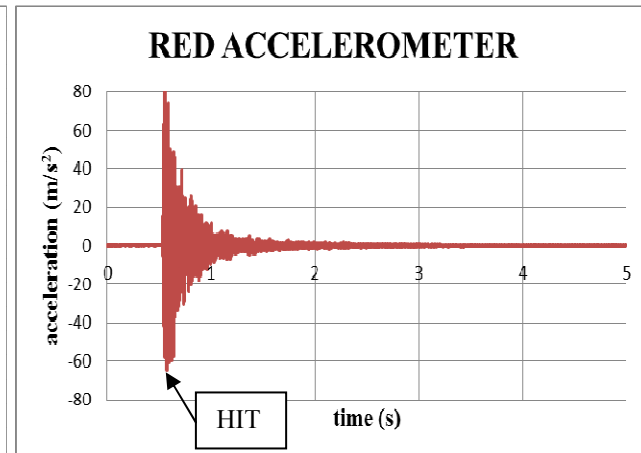


Fig. 7 Red Accelerometer

From the presented acceleration results in time we determined the period of oscillation $T(s)$, and then calculated the first frequency according to the relationship (Eq. 1). More detailed information can be found in [1,4,8].

$$T = 0.0232 \text{ s}, f_e = \frac{1}{T} = \frac{1}{0.0232} = 43.103 \text{ Hz} \quad (1)$$

Summary

This initial analysis provides a picture of the importance of proper finite element selection for fluid modeling. In any case, it's important to put the analysis results through experimental measurements that will prove or disprove the adequacy of the used elements for the given issue type. Our findings

show that for the static analysis, we can use any FLUID30 or FLUID80 element, but for the dynamic analysis the FLUID80 finite element is more suited.

Element FLUID30 represents Euler's approach and element FLUID80 represents Lagrange's approach. The type of elements are detail describe in [2,6,8]. When you use FLUID30 will be created unsymmetric system of equations. The find eigenfrequencies and custom shape in this calculation is very difficult. For small constructions is this problem a little. When we have a large and real construction is this problem very difficult and the results are almost always wrong.

Table 1 First eigenfreqncies of cylindrical tank

FIRST EIGENFREQUENCIES		
“FLUID30”	“FLUID80”	“EXPERIMENT”
40.48 Hz	45.64 Hz	43.103 Hz

Acknowledgements

This paper was written with the support of Slovak Grant Agency VEGA. Registration number is 01/0629/12.

Knowledge transfer between scientific research and engineering practice enabled by company Biogas Budča Ltd. Elektrárenská 1 Bratislava 831 04.

Responsible representative: Ing. Viliam Bendel, Šípová 3/A , Bratislava, phone +421 903900654, e-mail: bendel@europea.sk

References

- [1] M. Sokol, K. Tvrdá, Dynamics of building structures, Bratislava 2011, STU Publishing, 212 p. (in Slovak).
- [2] Z. Mistriková, N. Jendželovský, Static Analysis of the Cylindrical Tank Resting on Various Types of Subsoil, Journal of Civil Engineering and Management. 18 5 (2012) 744-751.
- [3] K. Kotrasová, E. Kormaníková, Frequency analysis of the base plate on Winkler model subsoil model, Pozemné komunikácie a dráhy, Vol. 6, 1-2/2010, (in Slovak).
- [4] K. Kotrasová, E. Kormaníková, Frequency analysis of fluid in rectangular ground- supported tank, 12th International Multidisciplinary Scientific GeoConference and EXPO, SGEM 2012, Varna, Bulgaria, Vol. 3, June 2012, pp. 693-69817.
- [5] E. Juhásová, J. Benčat, V. Krištofovič, Š. Kolcún, Expected seismic response of steel water tank, 12th European Conference on Earthquake Engineering, London, 2002.
- [6] J. Sumec, N. Jendželovský, Seismic analysis of reinforced concrete water tank, Proceedings of the 4th International Conference on Dynamics of Civil Engineering and Transport structures and Wind Engineering, DIN-WIND 2008.
- [7] M. Mrózek, A. Nevařil, Z. Čada, M. Braťka, Contemporary approaches to seismic analysis of tank with fluid, Engineering mechanics 2009, National conference with international participation, Svatka, CR, 11.-14.5.2009, pp. 186-187, Praha, Czech Republic, 2009.
- [8] V. Salajka, Odezva nádrží s kapalinou na seismické buzení, Technické listy, 2007, 1, Brno, Czech Republic, 2007, p. 1-2, (in Czech).

Non-Destructive Tracking of Structural Changes of Concrete Mixtures During Thermal Stress

KUSÁK Ivo^{1,a*}, LUŇÁK Miroslav^{1,b} and CHOBOLA Zdeněk^{1,c}

¹Department of Physics, Faculty of Civil Engineering, Brno University of Technology,
Veveří 95, 602 00 Brno, Czech Republic

^akusak.i@fce.vutbr.cz, ^blunak.m@fce.vutbr.cz, ^cchobola.z@fce.vutbr.cz

Keywords: impedance spectroscopy, dielectric losses, loss factor, conductivity losses, polarization losses, concrete structure, thermal stress

Abstract. This paper deals with the application of the method of impedance spectroscopy to testing of cement-based composites prepared from a mix of cement mortar and quartz sand, which were intentionally degraded by high-temperature treatment (in the temperatures range from 25 °C to 400 °C). The monitoring of structural changes in the thermal stress is very important, for example for determining the reliability of the whole structure. Based on the Debye theory of dielectric the models were created, their applications and received parameters measured dielectric material is characterized and discussed the uniqueness of determining the values of model parameters. Development of electrical parameters and permittivity at each temperature areas reliably show these structural changes and thus the structural reliability.

Introduction

The concrete is for its high ability to resist the action of compressive force and for its durability widely used as the main structural material in modern construction. Concrete, however, has some shortcomings. One of them is limited toughness, or brittleness, due that the concrete structure can collapse suddenly or even explosively. This problem increases with the size and strength of concrete structures. If is the breaking limit locally exceeded, can result in disaster, without prior warning, ie without plastic deformation prior to collapse. Effects of hight temperatures amplifies this problem.

There are a number of large concrete structures such as television towers, dams, bridges, protective covers nuclear power plants that are at risk of exposure to high temperatures, whether as a result of fire, nuclear accident or terrorist attack. Exposure to high temperatures can be a shock (rapid heating or rapid cooling) or long term. If the concrete is exposed to high temperatures, changing its mechanical and chemical behavior, especially allowable stress and compressive strength, elastic modulus and Poisson's ratio, and more. These changes depend on the rate of change of temperature, extremes of temperature, duration of the fire and the type of concrete.

The monitoring of structural changes in the thermal stress is very important, for example for determining the reliability of the whole structure. The method that was used for this monitoring is called impedance spectroscopy.

Analysis of impedance spectra [1,2] variances in the $\tan \delta(f)$ and $\text{Im } Z(f)$ or $\text{Re } Z(f)$ of the of inhomogeneous materials is a part of the impedance spectroscopy which is still waiting for its development. At present, one is not able to determine unambiguously the individual material component contributions to the total electric conductivity and polarization at various frequencies of the exciting field. Materials having higher electric resistance values (over 500 kΩ) can be regarded – under certain simplifying assumptions – as dielectrics. A theory of dielectric polarization was formulated by Debye for homogeneous materials. However, experiments carried out on real materials and the respective conclusions did not show to be in agreement with the fundamentals theories. Therefore it seems most appropriate description using the model "Havriliak-Negami" [7], which describes the behavior of the material comprehensively. With these models we are able to

determine for example, the relaxation time τ , or complex values of permittivity ε^* (including their components).

The relaxation polarization [4,5] is a phenomenon which is characterized by slow response, by contrast to the elastic polarization, in which the recovery is almost instantaneous. Let polar particles of different kind exist in a dielectric being only loosely bound to their neighbours. These particles will simultaneously perform oscillations and chaotic displacements with respect to their environment. If an external electric field is applied, these thermal movements will be gradually aligned with the direction of this electric field. In this way, there arises a non-symmetric distribution of electric charges, thus giving rise to a dipole moment. Both the polarization growth and decrease (after the external electric field is switched off) are proceeding slowly. The relaxation polarization is temperature dependent, being always accompanied by dielectric losses and dielectric heating.

Experimental

Mortars were produced using a CEM I Portland cement (Českomoravský Cement - Heidelberg Cement Group); aggregates to cement ratio of 2 and water to cement ratio (W/C) of 0.55. Siliceous sand (maximum size of 2 mm) and shredded automobile tires (size in the range of 1-2 mm) were used as aggregates. Each mortar composition and its plasticity are presented in Table 1.

Mortar specimens (prisms: 40 mm×40 mm×160 mm) were prepared. The specimens were left in the moulds for 24 hours, then cured in water for 27 days and finally air-cured for 32 days at laboratory temperature (25 ± 2 °C).

After initial curing, the specimens were dried at a temperature of 60 °C for two days. Subsequently, the specimens under investigation were heated in a furnace at the temperatures of 200 °C, 300 °C and 400 °C with a temperature increase rate of 5 °C/min. A dwell of 60 minutes at the maximum temperature was provided, in order to find out the effect of high temperature on them. After heat treatment, the specimens were left to cool down spontaneously at laboratory.

Table 1 Mortar composition and relevant plasticity

Code	Cement [g]	Sand [g]	Rubber aggregates [g]	Water [g]	Total water [g]	W/C	Plasticity [cm]
H1	500	1000	-	275	275	0.55	15.5
H2	500	750	250	275	275	0.55	13.0

Results and Discussion

For a mixture H1 were at loss factor depending identified four curves (Fig. 1). The curve for the reference sample (without annealing) is located between the values of $\tan \delta$ 0.4 - 0.7, and contains next two maxima and two local minima. Maximum occurs at a frequency of 1 kHz. The shape of the curve indicates the next two maxima: one in the low frequency and the other in f bigger than 1 MHz. From these peaks, we assume a higher representation of polarization losses compared to conduction losses. The second curve - for the sample annealed lower temperature (200 °C) is close by the values and by the shape to the curve of the dissipation factor of the reference sample, but there are noticeable decreases of values for the area of dominance of polarization losses at low frequencies and the presence of local maxima around the frequency value about 105 Hz. But notice a slight increase in values in the range of 100 Hz to 1 kHz. Sample H1 annealed by temperature of 300 °C as well as H1 annealed 400 °C resulted mutually almost identical curves of loss factor , the curves are significantly different from the previous two dependencies. For frequencies up to 1 kHz are values of $\tan \delta$ about 0.6 then dependence is decreasing. In the frequency range from 1 kHz to 1 MHz symptoms disappeared polarization losses, the shape of the curve corresponds to the

conduction losses. Sluggish values of loss factor for the frequency of excitation electromagnetic field up to 1 kHz are unusual and suggest a superposition of several narrower curves of polarization losses. A mixture of H2 (Fig. 2), containing 25% less sand where the missing quantity is replaced by crushed rubber, shows differences in the spectrum of the dissipation factor as compared with a mixture of H1. For no-annealed sample (H2) reaches $\tan \delta$ values of 0.3 to 0.6, which is less than H1. H2 annealing by temperature 200 °C was spectrum of $\tan \delta$ large increasing in values up to 1.0 between the frequencies of 40 Hz to 1 kHz. The tail of the curve from 1 kHz to 1 MHz is decreasing (decrease of polarization losses up to 0.1), only the effect of conductivity losses is visible. The present of rubber created by the heat stress better connections with components of concrete and filled the open pores at the sample.

A further annealing at high temperatures of 300 °C and 400 °C it came to degradation of the rubber and its connection with the particles of concrete and is likely to leak part of the rubber out of the sample. The sample became more porous, carbon of rubber component adhered on the surface of sample and the surface became more conductive. Curves of loss factor for the samples after annealing of 300 °C and 400 °C, extremely decreased to the values 0 to 0.2, with a slight visibility of polarization losses in the region of 40 Hz to 1 kHz. For higher frequencies the values of $\tan \delta$ are low at the limit of measurability.

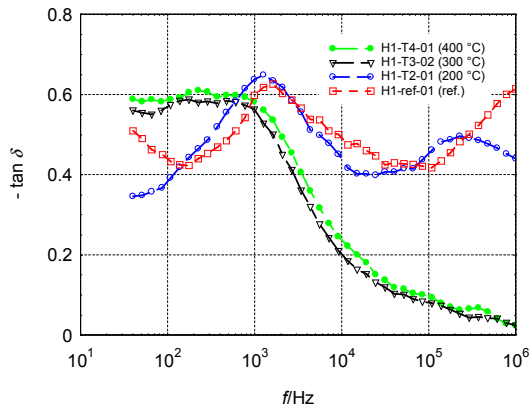


Fig. 1 Loss factor versus frequency diagram
(H1-reference sample without rubber
aggregates)

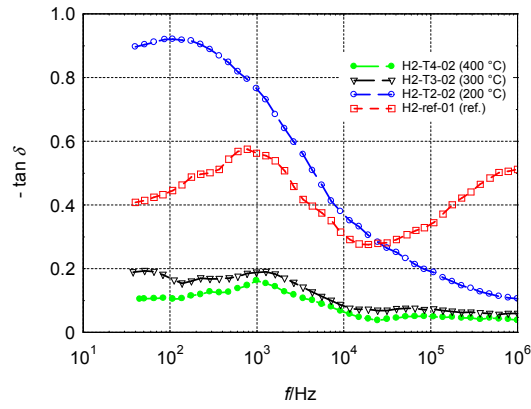


Fig. 2 Loss factor versus frequency diagram
(H2-sample with the addition of rubber
aggregates)

In the graphs Fig. 3 and Fig. 4 are marked discrete values of relative permittivity and impedance components for a frequency 1 kHz of excitation electric field for the various phases of the thermal stress of the reference sample and the sample H1 and H2 blended with rubber. The relative permittivity of the sample before annealing H1 starts at 350, sample H2 at the 200. Thermal stressing the permittivity falls and together values are leveling after annealing 300 °C around value of 30.

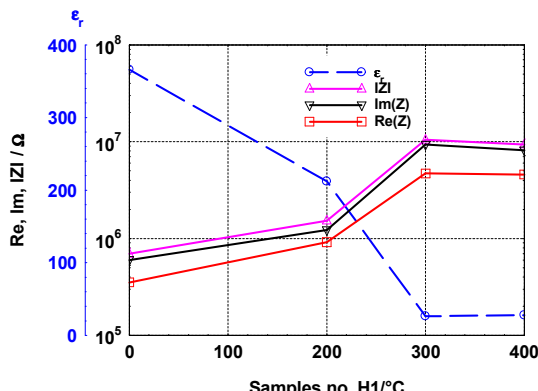


Fig. 3 Permittivity values and impedance parts
for a mixture of H1 (for 1 kHz)

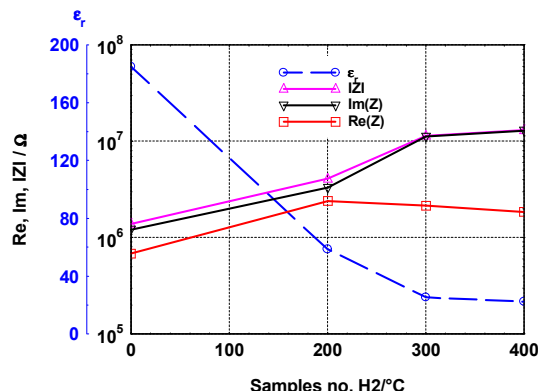


Fig. 4 Permittivity values and impedance parts
for a mixture of H2 (for 1 kHz)

Size of electric impedance and its components has the opposite trend. Before annealing reach values between 3×10^5 to 2×10^6 Ω. Annealing 200 °C values increased almost of magnitude. A further annealing at 300 °C values increased higher rate than in the previous step. Stabilization there was in this case it is close to 10^7 Ω. In all cases the impedance values and imaginary components of the sample with rubber is higher than the reference sample. The real component of the impedance in the sample with a rubber (H2) at the annealing temperature to 200 °C is higher than H1, after annealing of 300 °C and 400 °C, the value of Re (Z) and H2 decreased slightly, while H1 has increased considerably. It is obvious to assume that after annealing of 300 °C and more, there was a carbonization of sample components which contribute to the conductivity of the material.

Summary

The paper described the change of the electrical parameters of cement samples with and without admixture of rubber granules. The samples were thermally loaded and put them in the context of changes in the structure of samples with relative permittivity, loss factor and impedance components. The relative permittivity of samples by using rubber granulate as an additive achieves lower levels in a wide range of temperatures (for reference value of frequency 1 kHz).

Acknowledgements

This paper was elaborated with the financial support of the European Union's "Operational Programme Research and Development for Innovations", No. CZ.1.05/2.1.00/03.0097, as an activity of the regional Centre AdMaS "Advanced Materials, Structures and Technologies".

This paper has been prepared with the financial support of the project „SUPMAT – Promotion of further education of research workers from advanced building material centre“. Registration number CZ.1.07/2.3.00/20.0111. The project is cofunded by European Social Fund and the state budget of the Czech Republic.

References

- [1] I. Kusák, M. Luňák, Comparison of Impedance Spectra of Concrete Recorded with Utilizing Carbon Transition Paste, Advanced Materials Research, Trans Tech Publication, Switzerland, 2014.
- [2] M. Luňák, I. Kusák, Z. Chobola, Dielectric Properties of Concrete Specimens after Heat Stress, Applied Mechanics and Materials, Trans Tech Publications, Switzerland, 2014.
- [3] T. Ficker, L. Topolář, I. Kusák, Is componential strength analysis of concrete possible?, Magazine of Concrete Research, England, 2013.
- [4] I. Kusák, M. Luňák, P. Schauer, Tracing of Concrete Hydration by Means of Impedance Spectroscopy (New Tool for Building Elements Testing), Applied Mechanics and Materials, Trans Tech Publications, Switzerland, 2013.
- [5] L. Pazdera, L. Topolář, V. Bílek, J. Smutný, I. Kusák, M. Luňák, Measuring of Concrete Properties during Hardening, In ESA 2010. 1. CZ, Palacky University, 2010, pp. 311-318.
- [6] M. Luňák, I. Kusák, L. Pazdera, L. Topolář, V. Bílek, Monitoring of cement-based material solidification, focusing on electrical properties, ESA 2010. 1. CZ, Palacky University, 2010, pp. 233-240.
- [7] M. Cabeza, P. Merino, A. Miranda, X.R. Novoa and I. Sanchez, Impedance spectroscopy study of hardened Portland cement paste, Cement and Concrete Research, 2002, pp. 881-891.

Fatigue of Steel Specimens at Low Temperatures

TESAR Alexander^{1, a*} and SEDLAR Marek^{1,b}

¹Institute of Construction and Architecture, Slovak Academy of Sciences,

Dubravská cesta 9, 845 03 Bratislava 45, Slovak Republic

^aalexander.tesar@savba.sk, ^bmarek.sedlar@savba.sk

Keywords: fatigue, steel specimens, low temperature, FETM-technique, micro-mechanical modelling, steel specimen, ultimate behaviour

Abstract. Fatigue of steel specimens at low temperatures is treated in present paper. Micro-mechanical modeling is used for numerical analysis of the problem. The numerical treatment of non-linear problems appearing is made by updated Lagrange formulation of motion. Each step of iteration approaches the solution of the linear problem. Numerical and experimental assessment is submitted in order to demonstrate the efficiency of the approach suggested.

Introduction

The fatigue at low temperatures is the focus of intense research because of fatigue disaster prevention of steel specimens adopted in slender structures, such as space and offshore facilities, guyed masts, cable roofs, long-span bridges, lines of high voltage air conductors, etc. Required is sophisticated analysis order to answer the questions associated with fatigue reliability of such structures. For the fatigue assessment the model is suggested adopting the analysis on the micro-mechanical level and considering the ultimate behaviour of micro-mechanical string elements configurated in 3-D space mesh. In this paper is presented:

1. mathematical formulation of the problem,
2. description of the ultimate fatigue at low temperatures adopting the micro-mechanical string modeling,
3. analysis and experimental assessment of the problem.

Behaviour at Low Temperatures

When a steel specimen consists of densely packed inclusions, their interaction effects may play a dominant role in the fatigue of the resulting continuum at low temperatures. The concept of transformation strain is to be used when elastic medium contains periodically distributed inclusions or micro-mechanical voids in the material. Because of the periodicity, the transformation strains are regular functions of space, time and temperature. The periodicity is exploited in an effort to obtain estimate for transformation strains used to approximate mechanical properties of steel specimens at low temperatures.

The Washizu's variation principle is adopted below in order to include initial stress and strain components due to isothermal deformation in time. The stress in the micro-element in the 3-D mesh at the beginning of time increment studied is considered as initial stress with thermal strain increment. The variation principle adopted is then written in terms of time rate quantities given by

$$I = \left\{ \int_V [S_{ij} \varepsilon_{ij} + 0.5 W_{ij} u_{ki} u_{kj} - (\dot{\varepsilon}_{ij}^0 + 0.5 \dot{\varepsilon}_{ij}) S_{ij}] dV - \int_{A1} r_i^{(1)} u_i dA1 - \right. \\ \left. - \int_{A2} s_i (u_i - w_i) dA2 \right\} (dt)^2 + \left\{ \int_V W_{ij} \varepsilon_{ij} dV - \int_{A1} r_i u_i dA1 - \int_{A2} p_i (u_i - w_i) dA2 \right\} dt , \quad (1)$$

where W_{ij} and S_{ij} are the Piola-Kirchhoff stress tensors for initial stress and strain rate, respectively, p_i and s_i are the Lagrange surface traction and its time rate quantity, respectively, r_i and $r_i^{(1)}$ are prescribed on the surface area $A1$ and w_i on the area $A2$. The volume V is bounded by surface area $A = A1 + A2$. The total strain rate ε_{ij} is composed of the initial strain rates ε^0_{ij} and ε'_{ij} , corresponding to instantaneous stress rate S_{ij} . To evaluate the strain rate, thermal expansion coefficient at temperature T is $\alpha(T)$ and at temperature $T + dT$ is $\alpha(T + dT)$. By expanding $\alpha(T + dT)$ into Taylor series, the average thermal strain rate is obtained.

Fatigue Analysis

It is in the nature of things that fatigue cracks are initiated as a result of cumulative ultimate damage process in the specimen. As with any other ultimate state, the assessment of fatigue consists in demonstrating that the strength is higher compared with relevant ultimate fatigue strength resistance of the steel specimen at low temperatures.

Adopting the above approach, the run of the ultimate fatigue analysis is given by:

1. Micro-mechanical modeling of specimen configuration in space, time and temperature.
2. Updated calculation of stress and strain in space, time and temperature as well as of cyclic structural response in each step of forcing being stated in all micro-elements of the 3-D model adopted.
3. Automatic comparison with ultimate fatigue strength specified in the Wöhler curve of the steel specimen studied.
4. Initiation of cracks in micro-mechanical elements trespassing the ultimate fatigue strength.
5. Updated calculation of the propagation of cracks in space, time and temperature.

The regime of crack initiation and propagation is rather complex. One or several cracks develop and propagate slowly along the critical regions of the specimen studied. For shear forcing the cracks turn inside of the body in a direction that is quasi-perpendicular to the tension. The fatigue cracks appear and propagate there consequently until total collapse of the specimen studied.

Application

Above approach was adopted for numerical and experimental research of the fatigue behaviour of steel specimens used as standard structural components in the high voltage air conductors (Fig. 1). Such specimens are subjected to heavy static and dynamic loads at low temperatures. The model used in numerical analysis of the problem is submitted in Fig. 2.

In numerical and experimental assessment the tests of static and dynamic behaviour as well as of the fatigue of above steel specimens studied at low temperatures were made. The standard stress-strain curve of typical specimen is plotted in Fig. 3. For numerical solution the above approach was adopted.

For experimental research the pulsator with loading capacity of 6000 kN, available at the Institute of Construction and Architecture of Slovak Academy of Sciences in Bratislava, Slovak Republic, was used (Fig. 4). For low temperatures was developed special insulated tube device, filled with dry ice, where the specimens were located during experimental research (Fig. 5). The model used is in Fig. 6.



Fig. 1 Steel specimen studied

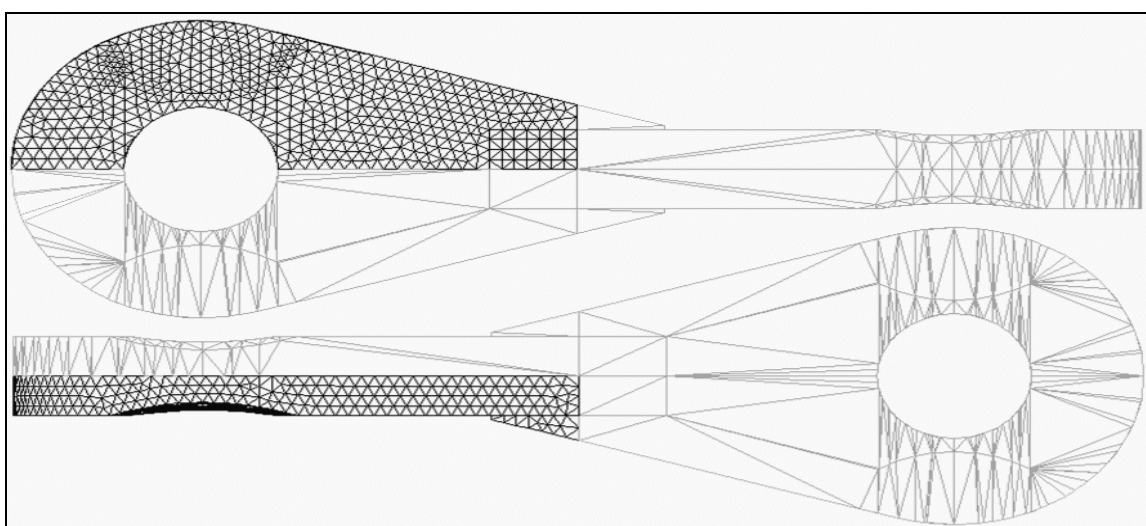


Fig. 2 Calculation mesh adopted

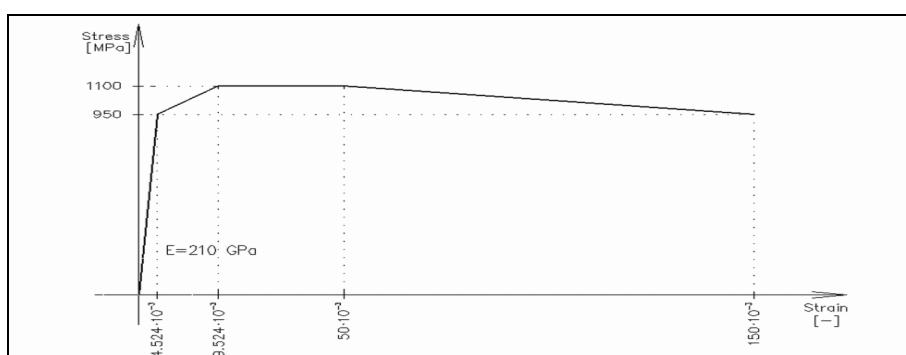


Fig. 3 Stress-strain curve of the standard specimen studied



Fig. 4 Pulsator with loading capacity of 6000 kN



Fig. 5 Insulated tube filled with dry ice

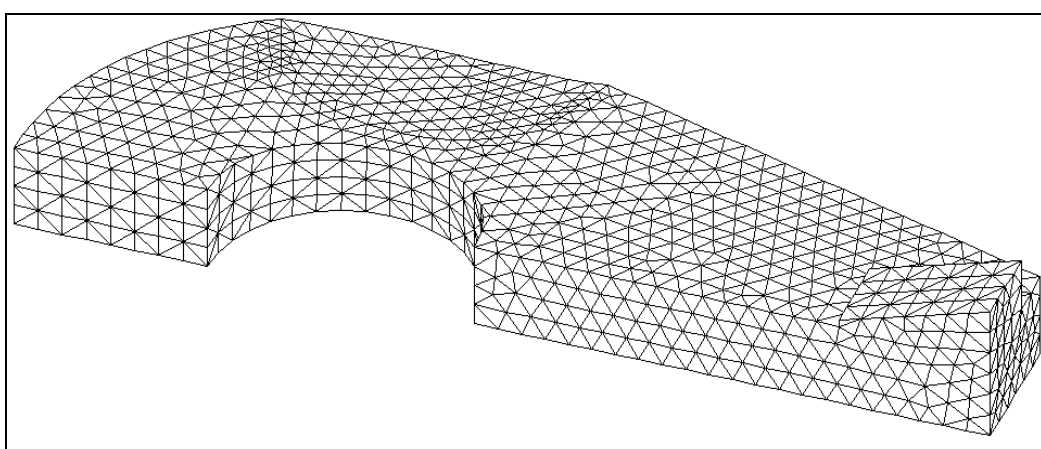


Fig. 6 3D-model used for calculation (4944 solid elements, 1889 nodes)

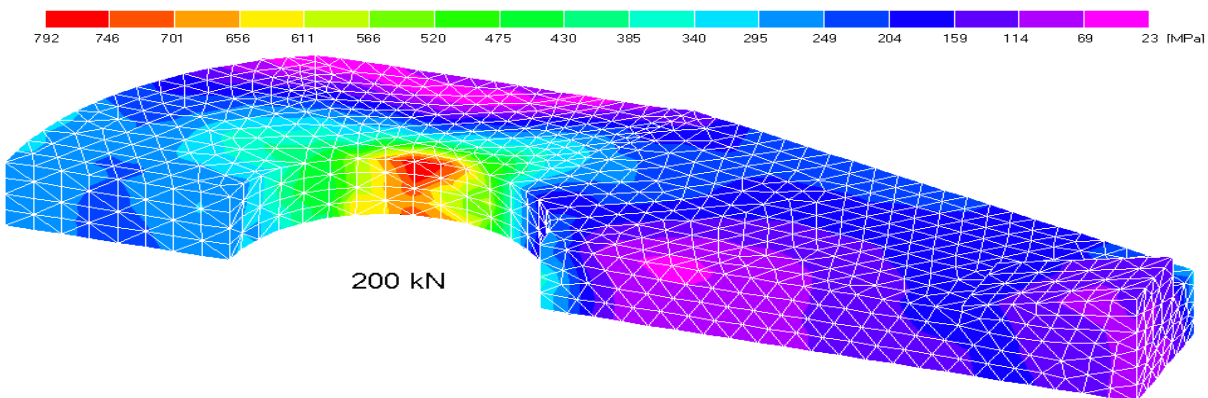


Fig. 7 Stress configuration at axial load level 200 kN

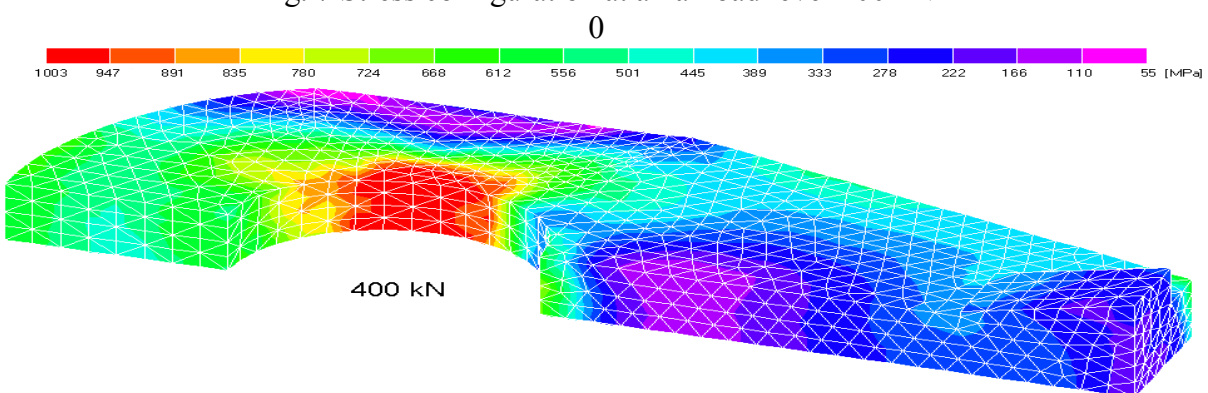


Fig. 8 Stress configuration at axial load level 400 kN

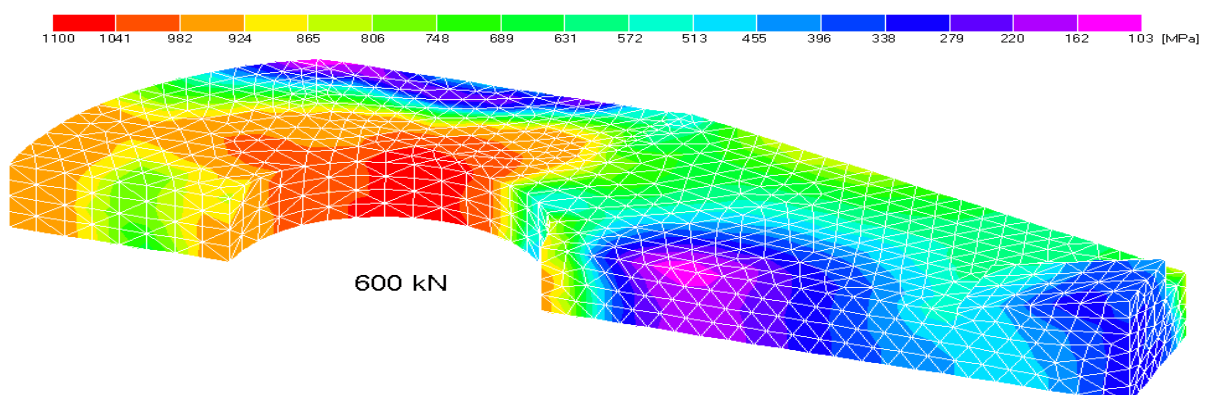


Fig. 9 Stress configuration at axial load level 600 kN

Table 1 Some results of static testing

Specimen Nr.	Temperature [°C]	Ultimate axial force in [kN]	
		calculated	tested
4	- 60	642	640
5	- 60	628	625
8	- 30	614	610
9	- 30	639	635

Table 2 Some results of fatigue testing

Specimen Nr.	Temperature [°C]	Upper & lower load amplitudes [kN]		Upper & lower force amplitudes [kN]		Frequency [Hz]	Number of cycles	
		calculated	tested	-	-		-	-
3	25	450	100	400	200	3.7	5276	5300
6	- 60	400	200	-	-	2.8	4157	4180
7	- 30	400	200	-	-	2.8	2364	2400

Seven specimens were tested at temperatures from -60°C until +25°C. Simultaneously they were subjected to axial forcing updated until collapse of the specimen.

Static testing:

1. Updated increase of the axial static load until the level 450 kN, with following decrease on the level 79 kN (the laboratory weight of the testing platform).
2. Updated increase of the axial static load until collapse of the specimen studied.

Fatigue testing:

1. The updated increase of the static load until the level of 400 kN with following decrease on the level 100 kN.
2. Repeated increase of the static load on the level 400 kN.
3. The dynamic part of testing with specification of the frequency as well as of low and upper amplitude levels of vibrating axial forces and with start of the fatigue testing.
4. After obtaining the amplitude level required, the numbering of cycles continued until the fatigue collapse of the specimen.

The comparisons and evaluations of the results are in Figs. 7 - 9 and in Tables 1, 2.

Conclusions

Theoretical, numerical and experimental results presented in this paper provide some image concerning the ultimate fatigue behavior of 3-D steel specimens at low temperatures as well as on the efficiency of the micro-mechanical approach suggested.

Acknowledgements

Authors are indebted to the Grant Agencies VEGA and APVV, Slovak Republic, for supporting the research presented.

References

- [1] A. Tesar, Transfer Matrix Method, KLUWER Academic Publishers, Dordrecht/Boston/ London, 1988.
- [2] A. Tesar, J. Svolik, Wave distribution in fibre members subjected to kinematic forcing. Int. Journal for Communication in Numerical Mechanics, 9, 1993.

Dynamic Heat Transfer through the External Wall of a Timber Structure

SKOTNICOVÁ Iveta^{1,a}, LAUSOVÁ Lenka^{2,b*} and BROŽOVSKÝ Jiří^{3,c}

^{1, 2, 3} Faculty of Civil Engineering, VŠB-Technical University of Ostrava,
Ludvíka Poděště 1875/17, 708 33 Ostrava-Poruba, Czech Republic

^aiveta.skotnicova@vsb.cz, ^blenka.lausova@vsb.cz, ^cjiri.brozovsky@vsb.cz

Keywords: numerical simulation, heat field, heat flux, experimental measurements, temperature response, light weight building structure

Abstract. The article compares results of temperature and heat flux measurements in the external wall of the real timber structure with the results obtained by numerical modeling using the finite element method in the ANSYS software. The measured temperature values are compared with the results obtained from numerical simulation of the dynamic heat transport using non-stationary boundary conditions. In the article there is evaluated a suitability of theoretical numerical calculations for a thermal field and heat flux prediction in a building structure.

Introduction

The main aim of this paper is a comparison of experimental measurement results and numerical analysis of a temperature development and a heat flux value in the external structure [1, 2] of the real timber structure in winter period. Experimental measurements of the temperature response were made in the real timber building of the passive standard placed at the site of the Faculty of Civil Engineering at the Technical University of Ostrava. Material based on a timber has got the main influence on the thermal comfort of the inside setting [3]. Comparison of temperature and heat flux distribution in the structure was processed for the selected two days in winter. The target of this analysis is a verification of a suitability of numerical simulation methods application for a thermal field and thermal flux prediction in the light timber building structure.

For a theoretical analysis of thermal behavior there was chosen a numerical implicit method – the finite element method in the ANSYS software. This method is suitable for a solution of non-stationary multidimensional thermal tasks and enables to get solution of thermal problem in the finite number of discrete places (nodes) of the generated mesh in the whole area or just in the part of it.

Comparison of the experiment results and thermal behavior numerical simulation of the external wall of the timber structure was assessed for the chosen detail (see Fig. 1). Theoretical analysis of detail was carried out for the real boundary conditions for a winter period obtained by experimental measurements.

Experimental Measurements

External structures of the assessed timber passive house are solved as diffusion open structures with wood fibre thermal insulation. Table 1 shows the composition of the assessed detail of the external wall and basic thermal technical properties of used building materials.

There are placed sensors (1-5 – see Fig. 1) in the external walls for a long-term temperature monitoring (and also humidity) in the cross structure profile. There was also the ambient temperature measured by shielded temperature sensor as well as the interior air temperature.

The local heat flux by the peripheral wall was measured in two places simultaneously with the temperature measurement in the structure by heat flux sensors (see Fig. 1).

Fig. 2 and Fig. 3 demonstrate time dependent temperature of the external wall in winter time for two chosen days in January (26.1. - 27.1. 2013), when the external air temperature reached low

values close to standard values [4, 5]. Measured temperatures show how the structure due to its thermal insulated properties deals with the winter low temperature on the external surface. Whereas external surface of the structure was loaded by the difference of surface temperatures during the day which fluctuated between -13.9 °C and -3.1 °C, inside of the structure including internal surface show very little differences in temperatures (between 17.8 °C and 18.8 °C – see Table 2 - time dependent temperature of the inside surface was influenced with the internal temperature and operation mode of heating).

The average value of heat flux in the measuring point was derived from the measured values of heat flux which was $q = 1.8 \text{ W/m}^2$.

Table 1 Composition of the external wall of the timber passive house in solved detail

External wall	Layer thickness	Density	Thermal conductivity coefficient	Specific heat capacity	Thermal diffusivity
	$d [\text{m}]$	$\rho [\text{kg/m}^3]$	$\lambda [\text{W/(m.K)}]$	$c [\text{J/(kg.K)}]$	$a [\text{m}^2/\text{s}]$
Fermacell board	0.015	1250	0.320	1000	2.56×10^{-7}
Wood fibre thermal insulation	0.060	50	0.039	2100	3.7×10^{-7}
Fermacel Vapor board	0.015	1250	0.320	1000	2.56×10^{-7}
Wood fibre thermal insulation/ Wall SW90 beam	0.300	50	0.039	2100	3.7×10^{-7}
Fermacell board	0.015	1250	0.320	1000	2.56×10^{-7}
Wood fibre thermal insulation	0.080	0.053	2100	1.00×10^{-7}	0.053
Wood fibre thermal insulation	0.060	0.047	2100	0.93×10^{-7}	0.047
Baumit plaster	0.007	0.800	850	5.23×10^{-7}	0.800

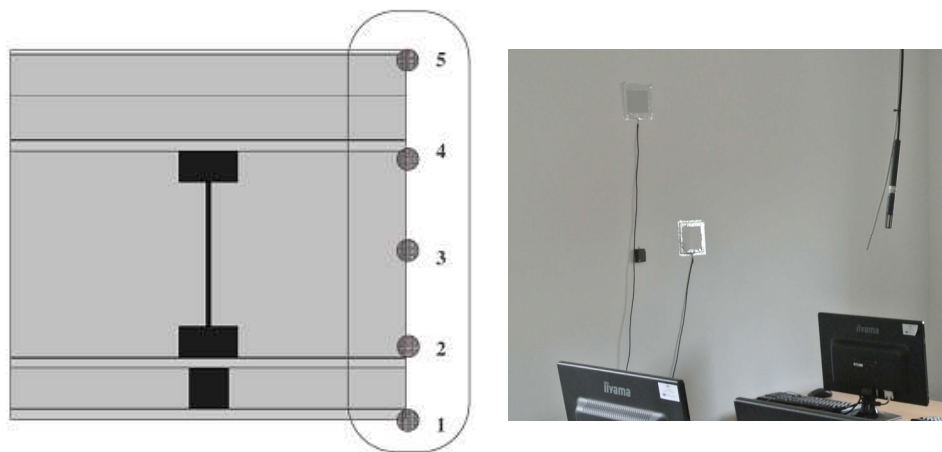


Fig. 1 Placing temperature sensors (1-5) and a heat flux sensor to the structure

Numerical Simulation Calculation

Numerical calculation by the finite element method in the ANSYS software has been used for numerical modeling of a thermal performance and a heat flux value.

The solved model of the peripheral structure has been created by applying the finite elements of PLANE55 type (Fig. 4). Width of the model corresponds to the axial distance between the timber

pillars of the peripheral wall (0.6 m). Each material has been defined by thermal and technical features: density, specific heat capacity, thermal conductivity coefficient.

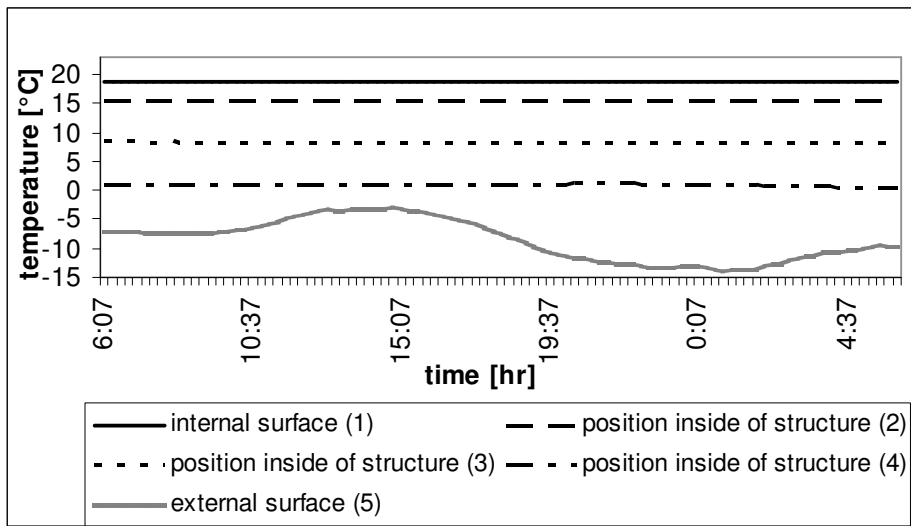


Fig. 2 Time course of temperature in sensors of the external wall

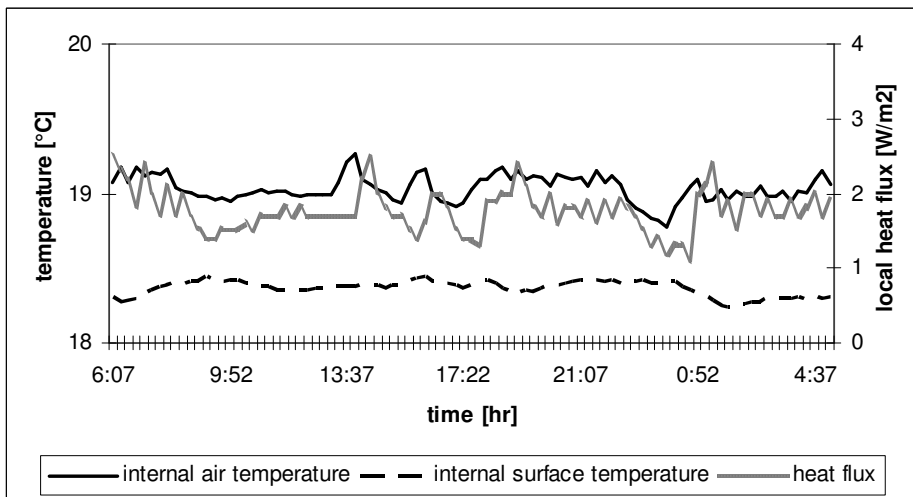


Fig. 3 Time course of heat flux in the external wall

Thermal analysis has been solved as a two-dimensional non-stationary task. The non-stationary task requests loading of time and time step. The time step equal to the time step of measurements (3600 sec.) has been applied for calculations. The total duration of the assessed time interval has been chosen as 24 hours.

The initial condition of calculation describes temperature distribution in the body at the beginning of the phenomenon in time t_0 and it has been applied by simulation calculation of a heat field for stationary conditions ($\theta_{se} = -6.5^\circ\text{C}$, $\theta_{si} = 18.8^\circ\text{C}$) and this state was further used as an initial condition for non-stationary calculations. The initial condition of a heat field distribution was verified by simulation calculations, so that the initial thermal state of the structure corresponded to the real measured temperatures.

All boundary conditions of calculations have been defined as the Dirichlet boundary conditions. External surface temperatures of the structure have been substituted from the real measured values. For the internal structure side the boundary conditions have been considered constant during the whole time interval 24 hours. The boundary conditions for the calculation of heat flux in the structures have been set up for stationary boundary conditions - external and internal surface

temperature of the structure was achieved for the average real measured values ($\theta_{se} = -8.6 \text{ }^{\circ}\text{C}$, $\theta_{si} = 18.8 \text{ }^{\circ}\text{C}$) see Fig. 4.

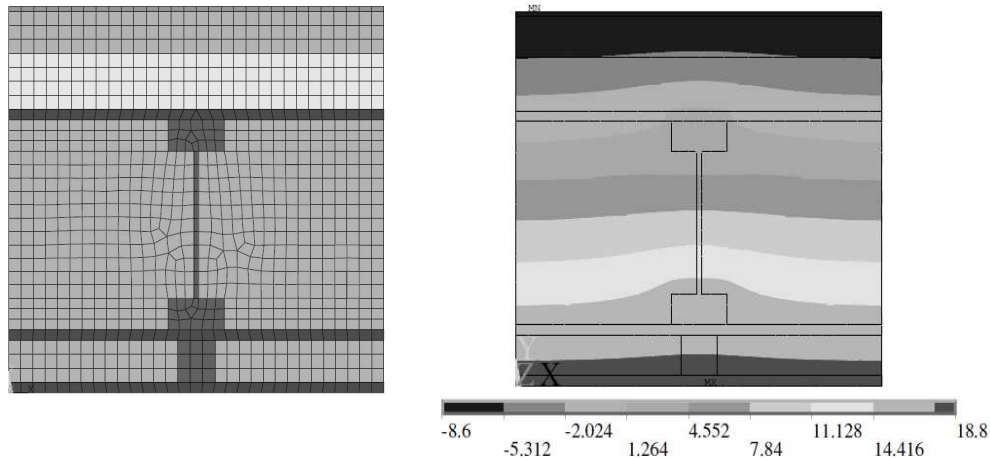


Fig. 4 Numerical model PLANE55 and thermal field for stationary boundary conditions

Table 2 shows the calculated and measured temperatures in individual positions of the temperature sensors for solved external wall detail in the selected hours from the both representative days in winter period.

Table 2 Experimental temperatures and numerical calculation during the selected day in January

	time [hour]	temperature [°C]					time [hour]	Sensor					
		sensor						1	2	3	4	5	
		1	2	3	4	5		1	2	3	4	5	
Experim.	6:00	18.7	15.6	8.4	1.2	-7.3	22:00	18.8	15.6	8.4	1.2	-12.9	
Ansys		18.8	15.5	8.3	1.1	-7.3		18.8	15.5	8.3	1.1	-12.9	
Experim.	10:00	18.8	15.8	8.4	1.1	-7	2:00	18.7	15.6	8.4	0.9	-13	
Ansys		18.8	15.7	8.8	1.0	-7		18.8	15.5	8.3	1.0	-13	
Experim.	14:00	18.8	15.6	8.4	1.0	-3.2	5:00	18.7	15.6	8.2	0.4	-10.1	
Ansys		18.8	15.5	8.5	0.9	-3.2		18.8	15.7	8.5	0.2	-10.1	
Experim.	18:00	18.8	15.6	8.3	1.1	-7.6							
Ansys		18.8	15.5	8.4	1.0	-7.6							

Fig. 4 shows the temperature field in the selected detail of the wall with timber column which causes thermal bridge. This temperature distribution was determined for stationary boundary conditions for which heat flux was calculated.

Fig. 5 shows a result of theoretical calculation of heat flux on that inner surface of the structure. The graph shows a significant increase of the flux at the place of a thermal bridge. The calculated value of the local heat flux $q = 1.8 \text{ W/m}^2$ is obtained at the center between the columns. The value of heat flux determined by numerical simulation at the point between the columns is the same as the measured mean value of the local heat flux. A value of heat flux for inhomogeneous surface structures obtained by analytical calculation would be affected by the temperature field deformations due to the thermal bridge. Therefore, numerical calculation is more accurate method for determining the heat flux in the structure.

The value of heat flux is important for deriving of the heat transfer coefficient (thermal transmittance) U -value of a structure. To determine this value, however, there is needed to evaluate the average value of heat flux across the whole characteristic detail, which will be the subject of further analysis [6].

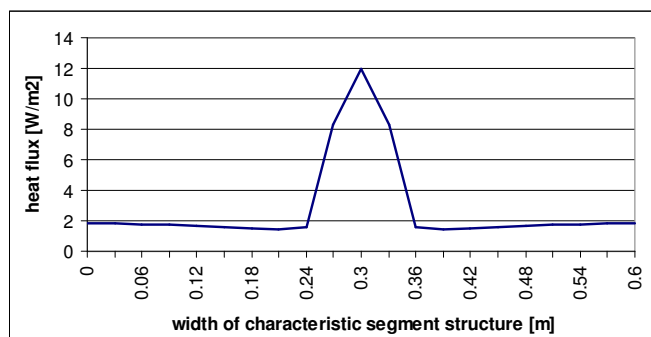


Fig. 5 Heat flux on the inner surface of the structure

Conclusion

The aim of the article is a comparison of the experimental measurement results and numerical simulation of a heat field and a heat flux in the external wall structure of the real timber building in winter and also verifying of suitability for using numerical method based on dynamic simulation of heat transfer for the prediction temperature distribution inside of the light building structure. The assessment of the obtained results can be summarized in the following points:

- Simulation calculations of heat transfer with the non-stationary boundary condition very well correspond with the measured values in each thermal sensor position. The obtained temperature distribution in dependence on time much better describes the real conditions than stationary solution.
- Calculated heat flux corresponds to the average value of measured heat flux in the assessed place, by numerical simulation there is determined the influence of the thermal bridge in the structure. All results of simulation calculations have got sufficient accuracy.

Acknowledgement

The work is supported from funds of the Conceptual development of science, research and innovation for 2014 allocated to the VŠB-Technical University of Ostrava by the Ministry of Education, Youth and Sports of the Czech Republic.

References

- [1] Barrios, Guillermo et al. Envelope wall/roof thermal performance parameters for non air-conditioned buildings Energy and Buildings. DOI: <http://dx.doi.org/10.1016/j.enbuild.2012.03.030>, 50 (2012), pp. 120–127.
- [2] I. Skotnicova, Z. Galda, P. Tymova, L. Lausova, Experimental Measurement and Numerical Simulation of Dynamic Thermal Performance of External Timber Frame Wall. Advanced Materials Research, Vol. 899 (2014), pp. 126-130, DOI:10.4028/www.scientific.net/AMR.899.126.
- [3] M. Kalousek, D. Beckovsky. Thermal comfort of lightweight building in summer time. Healthy buildings 2006, Lisbon, TU Lisbon, pp. 64–67.
- [4] ČSN 73 0540 Thermal protection of buildings. Prague, Czech Office for Standards, Metrology and Testing, 2011, 356 p.
- [5] ČSN 73 0548 Calculation of thermal load of air-conditioned spaces. Prague, Czech Office for Standards, Metrology and Testing, 1986, 30 p.
- [6] B. Taraba, Z Michalec, V. Michalcova, T. Blejchar, M Bojko, M Kozubkova, CFD simulations of the effect of wind on the spontaneous heating of coal stockpiles, Fuel. 2014, vol. 118, pp. 107-112, ISSN 0016-2361, DOI: 10.1016/j.fuel.2012.10.064.

Carrying Capacity Definition of Steel-Concrete Beams with External Reinforcement under the Fire Impact

VATULIA Glib^{1,a*}, OREL Yevhen^{1,b} and KOVALOV Maksym^{1,c}

¹Ukrainian State Academy of Railway Transport, Feuerbach square, 7, 61050 Kharkiv, Ukraine

^avatulya@kart.edu.ua, ^borel@kart.edu.ua, ^cbmgs@kart.edu.ua

Keywords: steel-concrete beam, structure fire resistance, fire-resistance rating, fire standard temperature conditions, limiting state, mathematical model, finite-element method

Abstract. The authors proposed the results of fire resistance evaluation of steel-concrete beams with external sheet reinforcement at standard temperature range of fire in the room and justified specifications for flame-retardant coat due to design standards. In order to analyze fire resistance the three-dimensional computer models have been developed taking into account basic conditions of beams loading and bearing as well as non-linear "stress-strain" dependencies of concrete and external reinforcement.

Introduction

Application of calculation method of fire resistance analysis and assessment of beams with external steel sheet reinforcement helps evaluate fire-resistance rating of the structures due to the impact of possible fire from the sides and bottom of the beam (three-sided heating). Calculations have been performed with the subsequent analysis of beams limit states according to the selected criteria of fire-resistance rating.

ANSYS software package used during the investigations gives the possibility to calculate the heat transfer, describe the stress-strain state of the structures in various sections and provides joint solution of these problems.

The calculation methodology was elaborated according to the existing technical approaches and design standards for fire-resistance rating definition of reinforced concrete and steel-concrete structures [1,2].

The authors considered concrete beams with external steel sheet reinforcement with the thickness values varying from 2 to 4 mm (Fig. 1) as object of research.

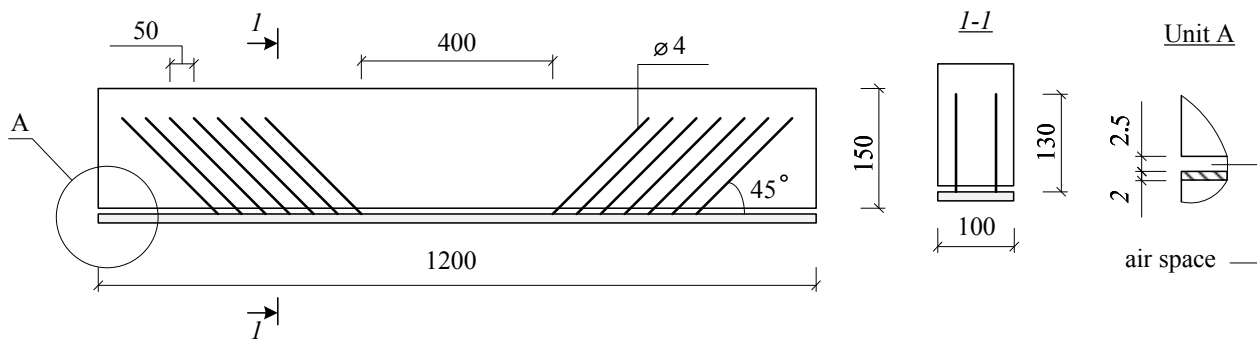


Fig. 1 Design model of steel-concrete beam

Beams were made from C20/25 concrete, with density value of 2300 kg/m³ and normal humidity of 3%, corresponding to the conditions of concrete hardening during 28 days. Bearing steel sheet was made from St.3 structural steel; fixing anchors were made of A240 reinforcement steel with the diameter of 4 mm.

It's assumed that minimal fire resistance rating for proposed steel-concrete beams will be chosen among several values R15, R30, R45 and R60. Cause and fire scenario are not considered [2-4].

The authors used finite-element method as the resolving equations of stress-strain state definition of steel-concrete beams [5]. Determination of fire resistance was done on the basis of computer simulations using mathematical models of crack formation according to the working strength theory, models of plastic deformation and plastic strain hardening of concrete compression area and steel elements tension, size and location of the finite elements and boundary conditions taking into account the structure symmetry.

The verification of proposed finite element models and calculation has been performed by comparing the obtained results with experimental data of steel-concrete beams destruction under the mechanical load [6]. Convection and radiation boundary conditions have been imposed to created finite element models. Radiation boundary conditions have been laid on the formed finite-element mesh with the surface effect of radiative heat transfer.

Thermal and physical characteristics of the materials used in calculations have been taken according to [1]. The coefficient of heat conductivity was described by the power polynomial, and the specific heat was described by piecewise linear function.

Boundary conditions on heated and unheated side correspond to the boundary conditions of III type and take into account the convective and radiative heat transfer. Only radiative heat transfer occurs in the air space. Heat transfer parameters have been taken in accordance with [7].

As a result of calculation the temperature-time relationship curves were plotted in different points of the cross-section under standard fire impact (Fig. 2). Analyzing them it's possible to make a preliminary determination of the occurrence of fire resistance rating using conditional criterion of "critical temperature". It is assumed that when the steel temperature reaches 500°C stress values in external sheet reinforcement reach the yield point and lose its ability to resist the power loads. On the basis of this hypothesis, we can conclude that the fire resistance rating of proposed beams occurs on the 400th second (7th minute) of standard fire impact.

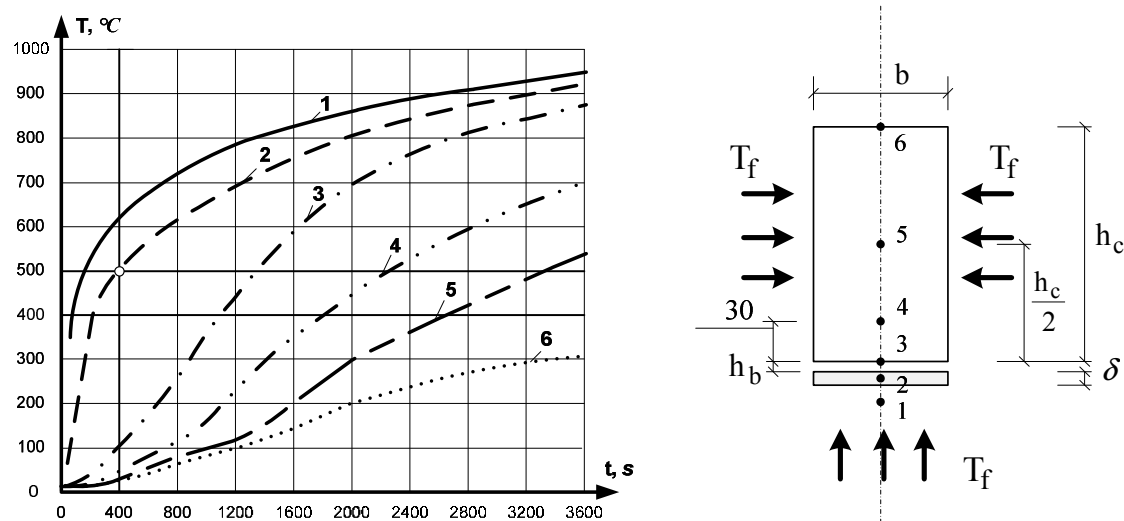


Fig. 2 Temperature-time relationship curves in different points of beam cross-section under standard fire impact: 1 – standard temperature range of fire; 2 – temperature in steel sheet; 3 – temperature in bottom concrete layer; 4 – temperature in concrete layer, located on 30 mm from bottom; 5 – temperature in middle concrete layer; 6 – temperature in upper (unheated) concrete layer

Loss of system invariability occurs on the 20th minute. Let us plot the chart of maximum flexure from standard fire impact due to more accurate determination of limiting state occurrence (Fig. 3).

The obtained chart of flexure has atypical behavior for regular reinforced concrete beams, because of the flexure excursion from the 2nd till the 5th minute of the fire impact. It happens due to rapid heating of external steel sheet reinforcement up to the temperature of 400°C and after that the character of temperature excursion slows down. At this time the sheet reinforcement sharply

expands, which results in the flexure increase and extensive crack formation of the concrete. Using the known procedure of fire resistance rating determination, described in [2], we have drawn tangent to the chart plots before and after inflection of the curve. The point of intersection characterises the fire resistance rating of investigated beams, which is equal to 18 minutes.

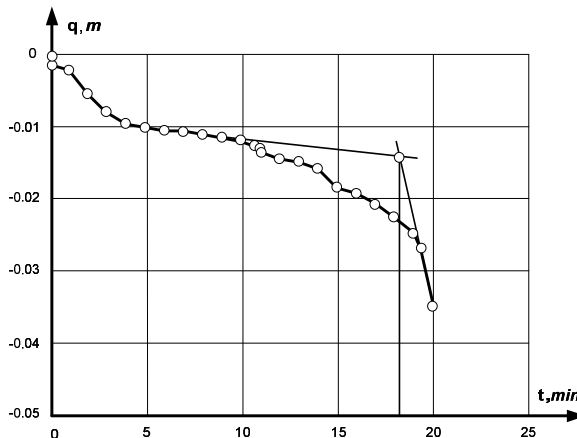


Fig. 3 Chart of maximum flexure from standard fire impact

As a result it is possible to ensure the R15 fire resistance rating, which is equal to fire resistance degree of IVa and IIIa type according to [8].

In order to provide the required fire resistance rating of steel-concrete beams several types of fire protection has been examined: Conlit SL150 Rockwool mineral wool coat, Piro-Safe FlamoPlast SP-A2 fire retardant intumescence coating and Natresk fire-retardant coating. The adhesion and cohesive properties of Natresk gypsum based fire retardant coating remain invariable during the temperature interval of standard fire. Piro-Safe FlamoPlast SP-A2 intumescence coating is sprayed only on external steel sheet reinforcement.

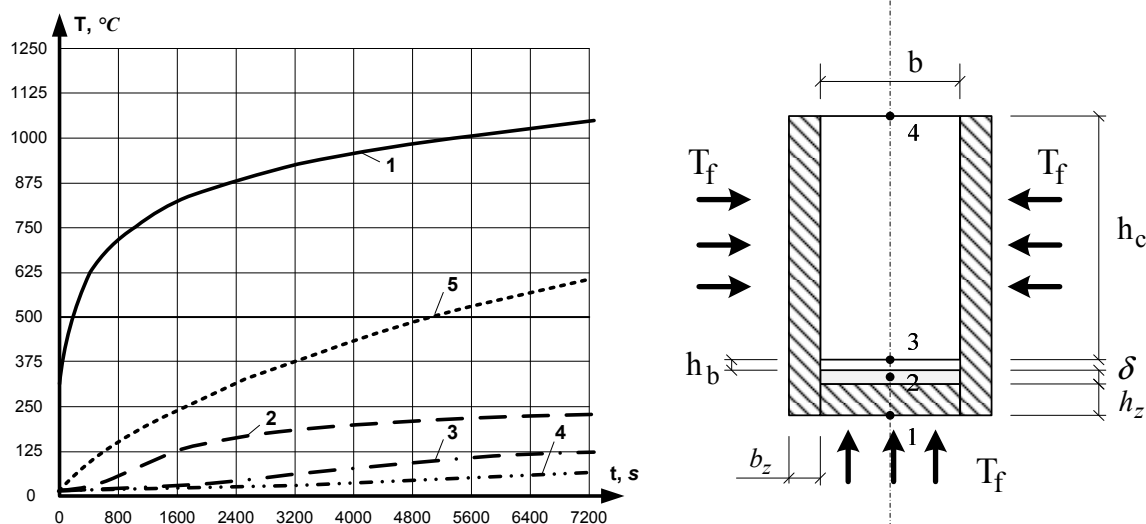


Fig. 4 Temperature-time relationship curves in different points of beam cross-section with Conlit SL150 flame-retardant coat from mineral wool board (thickness 25 mm) under standard fire impact:
 1 – temperature in flame-retardant coat; 2 – temperature in steel sheet; 3 – temperature in bottom concrete layer; 4 – temperature in upper (unheated) concrete layer; 5 – maximum temperature in concrete with Natresk fire-retardant coating

The temperature-time relationship curves in different points of beam cross-section with Conlit SL150 flame-retardant board and Natresk gypsum based coating (Fig. 4), Piro-Safe FlamoPlast SP-A2 intumescence coating (Fig. 5), and charts of maximum flexure (Fig. 6) have been built under the standard fire impact on the basis of the obtained results.

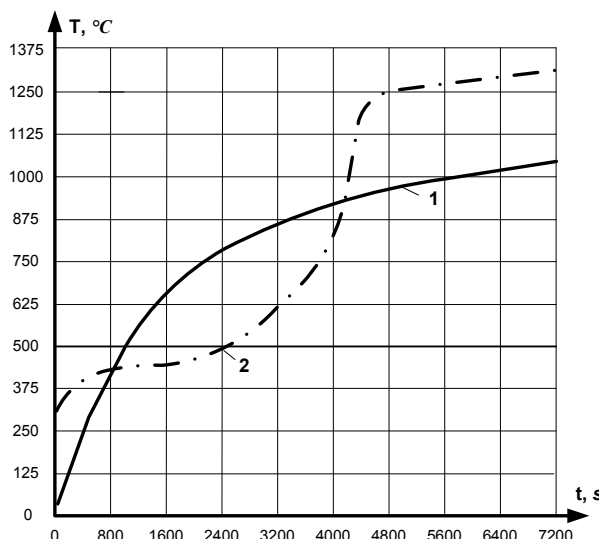


Fig. 5 Temperature-time relationship curves in beam with Piro-Safe FlamoPlast SP-A2 intumescent coating (thickness 1.1 mm) under standard fire impact: 1 – temperature in concrete; 2 – temperature in steel sheet

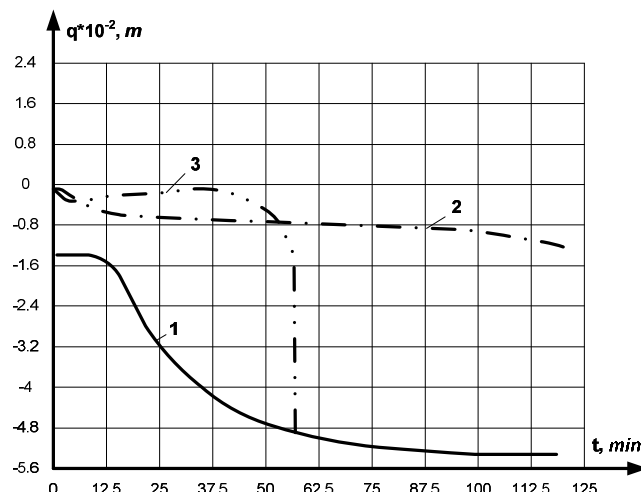


Fig. 6 Charts of maximum flexure of beam with flame-retardant coat under standard fire impact: 1 – Conlit SL150 mineral wool board; 2 – Natresk coating; 3 – Piro-Safe FlamoPlast SP-A2 coating

Summary

As a result of the investigation we proved that examined flame-retardant coatings help to ensure demanding rate of fire resistance of concrete beams with external steel sheet reinforcement under standard fire impact. It's enough to use plates with a minimum thickness of 25 mm and Conlit Glue, to provide fire resistance of proposed beams over 120 min for Conlit SL150 Rockwool fire-retardant mineral wool coat. The utilization of Natresk fire-retardant coating, with minimum 10 mm thickness helps to provide fire resistance rating for more than 100 min. The Piro-Safe FlamoPlast SP-A2 fire retardant intumescent coating with thickness range from 1 to 1.5 mm provides fire resistance within the period of time from 47 to 69 min. Thus, it is necessary to use 1 mm coating to ensure R15, R30, R45 fire resistance ratings. The coating of not less than 1.3 mm should be used to provide R60 rating.

References

- [1] EN 1992-1-2:2004 Eurocode 2: Design of Concrete Structures, Part 1-2: General rules - Structural Fire Design, Brussels, 2004.
- [2] A.F. Milovanov, Fire Resistance of Reinforced Concrete Structures, Strojizdat, Moscow, 1986.
- [3] B. Barthelemy, G. Cruppa, Fire Resistance of Building Structures, Strojizdat, Moscow, 1985.
- [4] Z. Huang, I.W. Burgess, R.J. Plank. Behavior of reinforced concrete structures in fire, Proc. Int. Workshop Struct. in Fire. 2006.
- [5] R.B. Caldas, R.H. Fakury, João Batista M Sousa JR. Finite element implementation for the analysis of 3D steel and composite frames subjected to fire. Lat. Am. j. solids struct. [online]. 2014.
- [6] M.A. Kovalov, Stress-Strained and Limit State of Steel-Concrete Beams under the Short-Term Static Loading. PhD Manuscript, Kharkiv, 2008.
- [7] DBN V.1.2-7-2008 Main Requirements for Structures and Buildings. Fire Safety, Ukrarhbudinform, Kiev, 2008.
- [8] DBN V.1.1-7-2002 Fire Resistance. Fire Safety of Structures and Buildings, Libra, Kiev. 2003

Mathematical Modelling of Thin-Walled Cold-Rolled Cross-Section

FLODR Jakub^{1,a}, KREJSA Martin^{1,b*}, MIKOLASEK David^{1,c},
SUCHARDA Oldrich^{1,d} and ZIDEK Libor^{2,e}

¹VSB - Technical University Ostrava, Faculty of Civil Engineering, Department of Structural Mechanics, Ludvika Podeste 1875/17, 708 33 Ostrava - Poruba, Czech Republic

²VSB - Technical University Ostrava, Faculty of Civil Engineering, Laboratory of Building Materials, Ludvika Podeste 1875/17, 708 33 Ostrava - Poruba, Czech Republic

^ajakub.flodr@gmail.com, ^bmartin.krejsa@vsb.cz, ^cdavid.mikolasek@vsb.cz,
^doldrich.sucharda@vsb.cz, ^elibor.zidek@vsb.cz

Keywords: numerical modelling, wind engineering, thin-walled cold-rolled cross-section, steel structure, trapezoidal sheet, finite element method, FEM, ANSYS

Abstract. The purpose of the paper is to perform a static analysis of a thin-wall cold-rolled steel cross-section of a trapezoidal sheet by means of a mathematical model developed in ANSYS, commercially available software applications. The trapezoidal sheets are used typically as an external cladding which covers the structures of steel halls. Investigating into behaviour of the trapezoidal sheets subjected to extreme loads represents an urgent issue in wind engineering. A physical tension test has been performed in order to verify and confirm the mathematical model. Experiments have been performed to prove results of the static analysis into the behaviour of a load-carrying structure formed by a thin-wall cross-section.

Introduction

In past years the thin-wall cold-rolled cross-sections have become a preferred solution for external cladding of the buildings. The main advantages include a low weight, speed of production/assembly and low price. A disadvantage is that the static/dynamic/stability behaviour of the thin-wall structure is rather complicated [2,11], the reason being that the structures are rather lean and the shape of load-carrying element sis rather complex. This means that the design calculation and reliability assessment of that structure or load-carrying element are rather demanding. A detailed investigation into influence and conditions which may occur in relation as well as some experiments (such as [1,6,10,13]) would be really needed so that the thin-wall load-carrying elements could be used more frequently. This paper focuses on creation of a numerical model which would correspond as much as possible to the real behaviour of a thin-wall cross-section. The verified numerical model (such as [4]) can be used then for further verification of reliability [9] of thin-wall cross-sections.

Creation of a Mathematical Computational Model

The creation of a mathematical computation model of a thin-wall cold-rolled steel cross-section of a trapezoidal sheet was divided into two parts. First, a physical tension experiment was performed in a thin-wall steel cross-section in order to obtain real material characteristics of the steel cross-sections which are needed for definition of a correct numerical model. Then, the results of the tension test were applied using a complex numerical model which was created so that model and the physical experiment could be verified. The computational numerical models were developed using Finite Element software - ANSYS 12 (as in [8,12]). Three computational models with different finite elements were created for the numerical model. Four-node shell elements - SHELL 181, eight-node volume elements - SOLID 185 and twenty-node elements - SOLID 186 were used for that purpose. When developing a numerical model, attention was paid to definition of suitable boundary conditions.

A deformation load was introduced into the model. In order to make the attachment in the tearing equipment ideal, the finite elements with CP function were used which made it possible to use an even dislocation for some finite elements. Then, a complete numerical model was created – it was in line with the physical experiment. A trapezoidal cross-section including two swinging supports and one fixed support as well as a load grate with all components was modelled. The model used a combination of shell elements - SHELL 181 and rod elements - BEAM 188. The numerical model used deformation loads in the upper part of the load press where the press was in a contact with the loading equipment. The numerical model was developed step by step and included influence of non-linear behaviour (as in [3,7]). Complex models are non-linear in terms of geometry, structure and physics. For solving then, a Newton-Raphson method was used. For more detailed description of a gradual development of computational models and non-linearity included see Table1.

Table 1 Numerical calculation, overview of solution alternatives

<i>Alt.</i>	<i>Type of task</i>	<i>Solving method</i>	<i>Type of nonlinearities</i>
A	without imperfections	nonlinear	constant
B	without imperfections	2 nd order theory	constant
C	stability, imperfections	2 nd order theory, Eugen Buckling Analysis	constant, geometric (loaded)
D	geometric nonlinearity, imperfections	2 nd order theory	constant, geometric (loaded)
E	alt. D, multi linear working diagram	2 nd order theory	constant, geometric, physical
F	alt. C, multi linear working diagram	2 nd order theory	constant, geometric, physical
G	alt. A, multi linear working diagram	2 nd order theory	constant, physical

Much attention was paid during the development of a numerical model to the creation of the computational grid. The final mathematical model was created by 100 000 finite elements. Considering the physical non-linearity, the computation took much time.

Analysing the Calculation Results by Means of the Verified Computational Model

The final computational model of the tension test was created by gradual modification/replacement of the finite elements and boundary conditions. The numerical model output can be described as a multi-linear isotropous material model with hardening. It followed from the creation of the mathematical model that the shell elements were not suitable for that solution as they were not able to take into account changes in the cross-section thickness. This is the reason why the volume finite elements were used – they were able to take this fact properly into account. During the experiment, attention was paid to the relation between the loading force and the final displacement. This relation was also monitored in the numerical model. The numerical model was modified so that it could correspond at best to the results of the tension test.

The second numerical model with several variants was used in order to investigate into the influence of different types of non-linearity. The outcome of the numerical model was the dependence of the force on the displacement in the press head. These values were monitored in both the numerical model and physical experiment. The force/displacement chart proves that the rigidity is different in each numerical model. A rather interesting finding is that the imperfections obtained from the stability calculation and those from the initial deformation caused by the loading grate did not have much influence on the final results which was proved by the multi-linear working diagram. The required displacement in a press head (20 mm) was not reached for each variant of the solution. Some computational models were not able to transfer that deformation and the calculation failed before reaching the value, the reason being intensive collapse of elements in the numerical model.

Analysing the Calculation Results and Comparing them with the Experiment

When developing the numerical model, the main objective was to create a model which should be as close as possible to the proposed physical experiment. When preparing the experiment, it was necessary to keep in mind limitations of the building material laboratory – the main limitation was a limited space in the room where the test press is installed. Several untypical specimen of a thin-wall cross-section were produced. Joint supports were prepared for rotating the trapezoid cross-section in the supporting points. The testing equipment was represented by a continuous beam with two spans. The trapezoidal sheet cross-section was 60 mm high and 700 mm wide. The loading grate can be regarded as an arm of balance where the elements are linked with each other by means of joints and can deform in different ways. The loading grate was attempting to create in test specimen internal forces caused by the continuous load.

Five tests of the trapezoidal cross-sections (SATJAM T60/235, 1 mm thick) were performed. The press loaded the structure by deformations and the loading process was divided into two stages. First, the structure was loaded up to 20 kN so that all parts could sufficiently settle. Then, the load was removed. Afterwards, a new additional load was introduced and both the loading force and final displacement in the press head were measured (can be used as [5]).

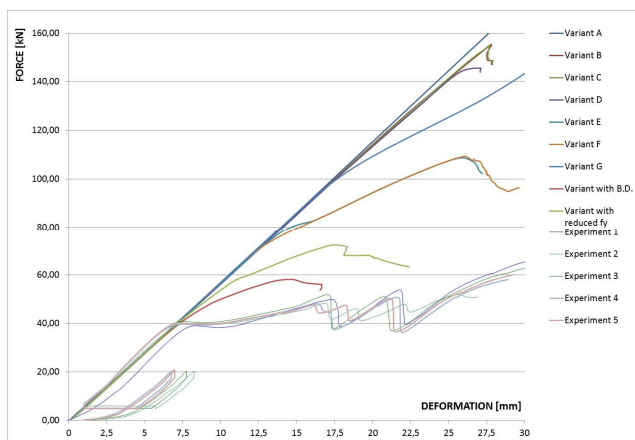


Fig. 1 Comparison of the results:
the force-displacement diagram

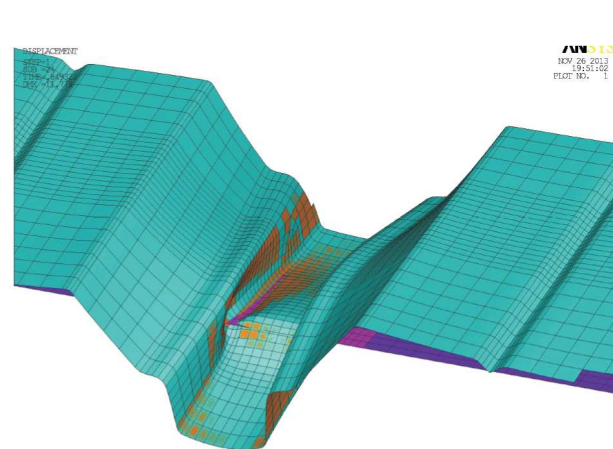


Fig. 2 Deformation of a numerical model
in the point of support

The numerical models are able to transfer considerably higher forces than those obtained by the physical experiment (Fig. 1). The multi-linear working diagram was modified and the tension in the yield point was reduced, while the slope between the points in the working diagram was maintained. The behaviour of the trapezoidal sheets was linear up to ca. 40 kN. Then, local swelling started appearing in the sheets and parts of the test specimen started collapsing – in particular, in the points of support. In the same time, similar deformation appeared in supporting points. The flange sheets started swelling too – this appeared in both the numerical model (see Fig. 2) and the experiment.

Summary

This paper dealt with creation of a mathematical model which would describe in a sufficient detail the behaviour of a thin-wall cross-section in bend. First, a numerical model of a tension test was created – it was in line with the physical experiment and failures in the model were similar to those in the physical experiment. Then, a multi-linear isotropic material model was derived. The model included reinforcement and was used as a rather complex numerical model of a loading grate and trapezoidal sheet system. This numerical model was created on the basis of the physical experiment. If it is assumed that the material behaves in an elastic way, the mathematical model can be regarded, after comparing it with the results of the experiment, as sufficiently accurate. The model can be used then for primary verification of reliability of the thin-wall cold-rolled steel cross-sections.

Acknowledgements

This paper was drafted thanks to the financial support aimed at conceptual development of research, science and innovations granted for the year 2014 to the VSB-TU by the Czech Republic's Ministry of Education and Sport.

References

- [1] P. Agel, A. Lokaj and M. Rosmanit, Load bearing capacity tests of mechanical joining on timber-concrete beam, Procedia Engineering. 65 2013 434-439.
- [2] M.C.M. Bakker, M. Rosmanit and H. Hofmeyer, Elastic post-buckling analysis of compressed plates using a two-strip model, Thin-Walled Structures. 45 5 (2007) 502-516.
- [3] I. Balazs, J. Melcher, Geometrically nonlinear numerical analysis of beams of mono symmetric thin-walled cross-sections loaded perpendicularly to the plane of symmetry. Transactions of the VSB – Technical University of Ostrava, Civil Engineering Series. Vol. XIII, Issue 2 (2013), pp. 1–12.
- [4] R. Cajka, M. Krejsa, Validating a computational model of a roof light steel structure by means of a load test, Applied Mechanics and Materials. 501-504 (2014) 592-598.
- [5] R. Cajka, M. Krejsa, Measured data processing in civil structure using the DOPROC method, Advanced Materials Research. 859 (2014) 114-121.
- [6] M. Karmazinova, Lateral flexural-torsion buckling of thin-walled cold-formed steel beams with holes-design resistance evaluation based on test results, Applied Mechanics and Materials. 368-370 (2013) 1683-1687.
- [7] Z. Kala, J. Kala, Sensitivity analysis of stability problems of steel structures using shell finite elements and nonlinear computation methods. AIP Conference Proceedings. Vol. 1389 (2011), pp. 1865-1868.
- [8] J. Kralik, M. Baran, Numerical analysis of the exterior explosion effects on the buildings with barriers, Applied Mechanics and Materials. 390 (2013) 230-234.
- [9] M. Krejsa, P. Janas and R. Cajka, Using DOPROC method in structural reliability assessment, Applied Mechanics and Materials. 300-301 (2013) 860-869.
- [10] J. Melcer, Experimental testing of a bridge, Applied Mechanics and Materials. 486 (2014) 333-340.
- [11] M. Nagyova, M. Psotny and J. Ravinger, Stability and friction, Pollack Periodica. 5 3 (2010) 63-70.
- [12] O. Sucharda, J. Brozovsky and D. Mikolasek, Numerical modelling and bearing capacity of reinforced concrete beams, Key Engineering Materials. 577-578 (2014) 281-284.
- [13] V. Urban, V. Krivy and L. Fabian, Experimental testing of the weathering steel road bridge in Ostrava, Advanced Materials Research. 849 (2014) 228-233.

Experimental Study of Torsion of Guyed Mast Shaft

URUSHADZE Shota^{1,a*}, PIRNER Miroš^{1,b} and FISCHER Ondřej^{1,c}

¹Institute of Theoretical and Applied Mechanics, AS CR, v.v.i., Prosecká 76, 190 00 Prague,
Czech Republic

^aurushadze@itam.cas.cz, ^bpirner@itam.cas.cz, ^cfischero@itam.cas.cz

Keywords: dynamics of guyed masts, dynamic response, swivelling of the shaft, wind tunnel, aerodynamic model

Abstract. The torsion of the mast shaft has been monitored on several masts in the Institute of Theoretical and Applied Mechanics (ITAM) since 2005. The occurrence of this phenomenon is conditioned by the fact that the guy ropes are attached out of the axis of the mast shaft. An experimental mast-shaft model of 15 m height guyed in 3 directions was used for the more detailed study of its rotational motion. The excitation was realized by transversal auxiliary rope drawn by harmonic human force in resonance. The displacement of the shaft top results in translation caused by the guy force and the rotation, caused by the eccentricities of the guy-ropes, attached out of the shaft axis. The resulting movement of the shaft support is an elliptical orbit. The shaft of our experimental mast was equipped in two levels with accelerometers for registration of horizontal x , y motions. The two x , y signals in two levels were monitored and analysed.

Introduction

The problem of rotational movement (torsion) of guyed masts during wind-excited vibration has become important in previous Czechoslovakia after the collapse of the mast of the TV transmitter Bohemia-West, Krašov on the January 1st, 1979. It was a triangular lattice tubular mast of the height 312 m, fixed at the base in both, bending and torsion, anchored in 4 levels into 3 directions. The highest anchorage was at the height 285 m, its guy was cca 330 m long, inclined cca 60°. On that critical day, in moderate wind, some of the longest guys started to sway with the planes of their sags, synchronizing step by step their rhythm with the torsional vibration of the whole shaft, and this stationary movement lasted for several hours. The transversal amplitudes of the long guys, as well as the transversal forces in the suspension points, were considerable, exciting the shaft torsion in their upper hangers and heavy transversal loading on the lower ones. These were realized as a well designed flat steel tie, but even those, after many times repeated bending perpendicular to its plane and probably over the yield point, could not resist. The tie loosed, the anchorage plucked off, the highest span with the cantilever (101 m) fell down, fortunately without other damages. The rest of the mast had to be, of course, demolished. Anchoring of two guy-levels in one block. The lower one remained undamaged, while the flat – steel tie, connecting the rectification element of the upper guy with the block, broke due its repeated transversal bending induced by torsion vibration of the shaft, combined with synchronized wobbling of the guys. The mast of course, collapsed (see Fig. 1).

The described collapse has revealed that such a classical structure like the mast had not been fixed perfectly in space - one of its degrees of freedom, namely the rotation about the vertical axis (the axis of the shaft) remains unbound. The shaft was usually supported on a hinge and the guys were arranged so that they intersect the shaft axis and are not able to resist to moments (eccentric loadings) in horizontal plane. But such loadings usually do not occur on masts, thus it was not necessary to compensate this degree of freedom and small (infinitesimal) shaft rotations were tolerated. If nevertheless a special mast should resist to eccentric loads (e.g. wind loads on antennae or pick-up elements on long cantilevers outside the shaft).

The statics of guyed masts was sufficiently elaborated as early as the first half of the 20th century, also with respect to the nonlinearity of the effect of ropes [1].

The basis for the dynamics of guyed masts was published by Koloušek [5], with the use of his deformation method. Since then the field of dynamics of guyed masts has extended by the knowledge of the effects of nonlinear phenomena, parametric resonance and self-excitation. Out of these, let us state at least [6,7].

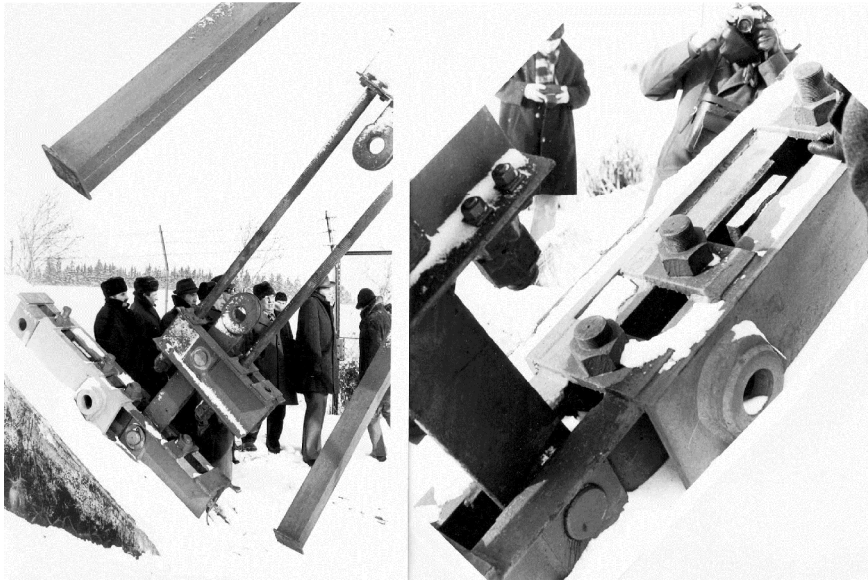


Fig. 1 The rest of the flat steel tie of the anchorage of the longest guy. The undamaged anchorage of the shorter (last-but-one) guy is on the same block, ahead

The theoretical analysis of the mast should always be corrected on the basis of monitoring of the real structure.

From the measuring of the dynamic response of masts or of their models it was known that the resulting movement of the shaft in ground plan appears as an ellipse, whose major semi-axis forms an angle less than 90° with the direction of the wind. Usually low intensity of turbulence and smooth surface of the shaft are conditions for the regularity and intensity of the vortex shedding. High intensity of turbulence disturbs the regularity of the shedding and thus also the cross-wind direction excitation and then the ellipse becomes more a circle [2,4].

Torsion or Swivelling of the Mast Shaft

The shifting from zero position will result in changes of the forces in the ropes and moments in the points of connection to the shaft, which are out of the axis of the shaft. If the shaft is guyed by three ropes, there are 6 points on the elliptical track, in which the sum of the moments from the eccentric connection of the ropes is zero, and thus also the swivelling is zero (see Fig. 2). These points delimit the domains with positive or negative rotation of the shaft. The zero points may lie close to each other; in such case the domains prevail with their size at the apexes of the ellipse. If the ellipse degenerates into a line, there are two domains of rotation which differ in the plus/minus sign.

The frequency of torsion f_{tor} or swivelling of the shaft depends on the position of the zero points on the ellipse (see Fig. 2): if the zero points are far enough from each other, the torsion of the shaft is governed by the 6 domains of moments and the frequency of swivelling f_{tor}

$$f_{tor} = 3 f_b, \text{ where } f_b \text{ is the frequency of bending.} \quad (1)$$

If points 2 and 3 merge into one, and so do points 5 and 6, then:

$$f_{tor} = f_b. \quad (2)$$

Under certain conditions¹ there also appear other ratios of f_{tor} and f_b .

¹ These conditions include the fact that the point of intersection of guy ropes; forces may lie "behind" the centre of gravity of the shaft cross section; "behind" means out of the orbit.

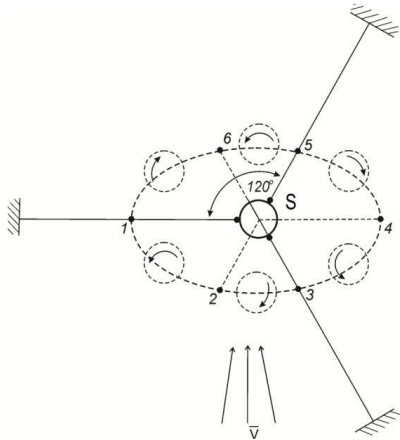


Fig. 2 Rotation of the shaft owing to the eccentricity of the ropes

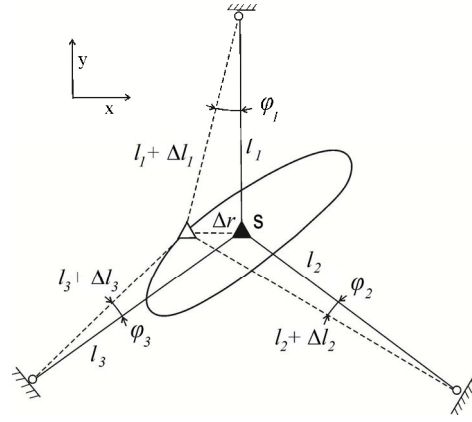


Fig. 3 Deriving the length strain of the ropes

The proof of the occurrence of moments which swivel (torsion) the shaft will be made using a simple calculation model, in which we take into account only static effects. The ropes are in a horizontal plane, without sag. Fig. 3 shows the ground plan of a shaft of triangular cross section, guyed in one level by three ropes (1., 2. and 3.).

When moving the shaft by Δr in the direction of X-axis, the ropes 1. and 2. of a length of l_1 and l_2 will lengthen by

$$\left. \begin{aligned} \Delta l_1 &= \sqrt{l_1^2 + \Delta r^2} - l_1 \\ \Delta l_2 &= l_2 (\cos \varphi_2 - 1) + \Delta r \cdot \cos(30^\circ - \varphi_2) \\ \text{and the 3rd rope will shorten by} \\ \Delta l_3 &= \frac{l_3 - \Delta r \cdot \cos 30^\circ}{\cos \varphi_3} - l_3 \end{aligned} \right\} \quad (3)$$

where l_i are the lengths of rope.

When Δr is \parallel the axis X then $\Delta y = 0$, $\Delta x = \Delta r$,

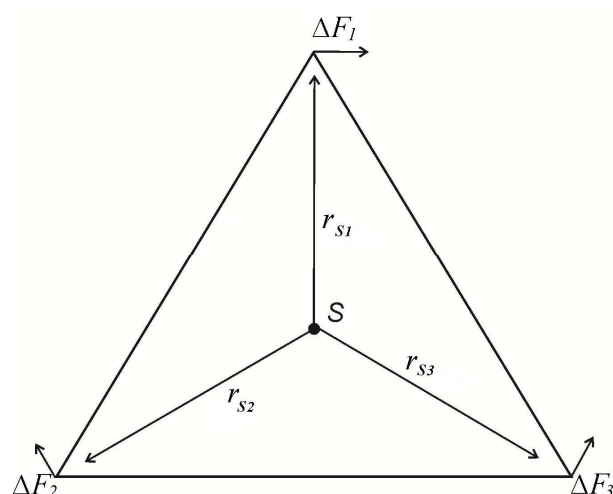


Fig. 4 Components of forces and their moment arms to the rotation axis

$$\cos \varphi_i = \frac{l_i}{l_i + \Delta l_i}, \quad (4)$$

$$k_i = \frac{A \cdot E}{l_i}, \quad (5)$$

$$\Delta F_i = k_i \cdot \Delta l_i. \quad (6)$$

Using the length transformations of the ropes Δl_i and the chosen spring constant k_i of the rope we will determine the increments of forces in the ropes ΔF_i , whose components on the arms r_{si} create the resulting moment (see Figure 4)

$$M = \sum_1^3 \Delta F_i \cdot r_{si}. \quad (7)$$

Monitoring of Torsion (Swivelling) on a Mast-Shaft Model

The torsion of the mast shaft was monitored on experimental mast-shaft model of 15 m height guyed in 3 directions (see Fig. 5).

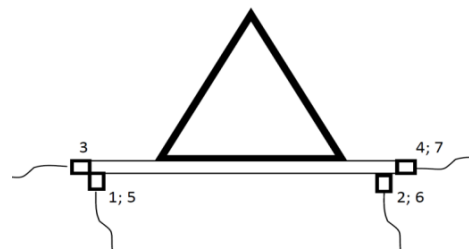


Fig. 5 View of the mast and position of the sensors

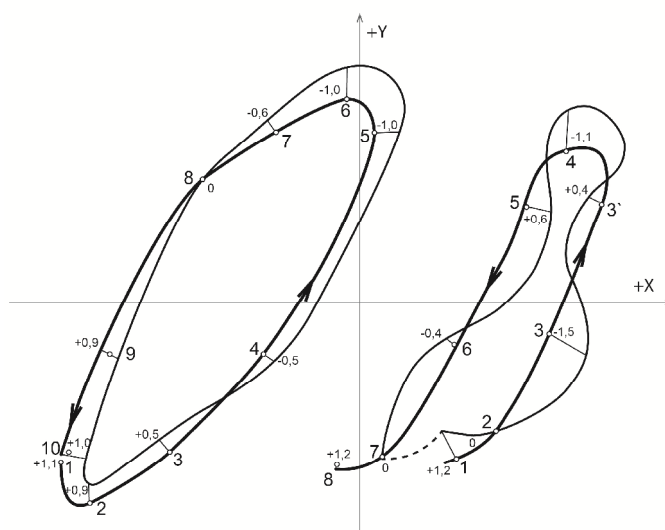


Fig. 6 Two examples of mast-top trajectories with different rocking – torsion ratios. The thick line – orbit, the distance between thick and thin line - value of the torsion

Fig. 6 shows the records of the plotter of the orbit and the course of swivelling of the shaft relative to it.²

² The deviations from ideal elliptical orbits and the courses of swivelling are caused, for example by imperfect smoothness of the air flow.

The movements of the shaft were monitored at a height of 6.7 m and 13 m by means of two accelerometers Endevco, type 86, the signals of which could have been mutually added or subtracted. The distance of the parallel axes from the accelerometers was 525 mm. An example of analysis is in Fig. 7. The agreement of the frequency of flexural vibration with the frequency of torsional vibration is obvious; other ratios of frequencies did not occur.

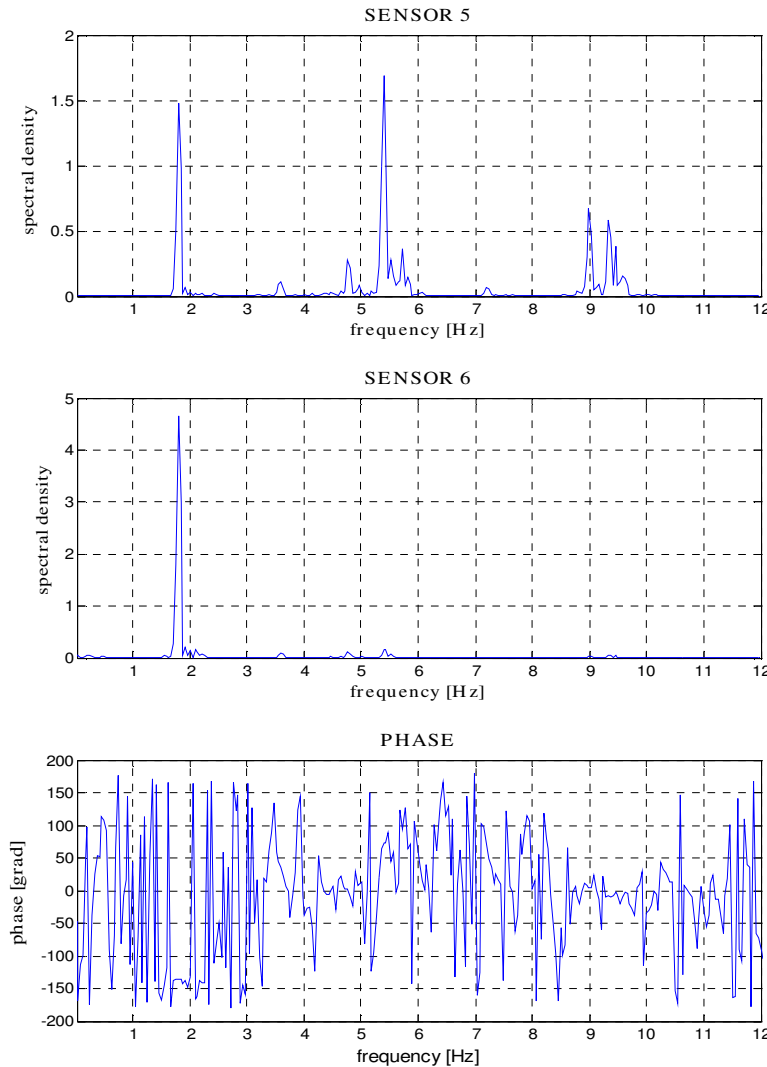


Fig. 7 Power spectral densities and the phase shift

Monitoring of Swivelling on a Small Model

In more detail and more stable aerodynamic conditions was the phenomenon of swivelling of the mast shaft examined on a simple model. The shaft is a tube of hardened PVC, of an outer diameter of 75 mm, supported by a point at the bottom. It is guyed by three cables. The mass ratio of tube mass to the cables mass is 12.

The flexural rigidity of the shaft is not modelled; the bending is substituted by the tilting. That is why there are no higher shapes of tilting and the orbit is always close to ellipse.

The top end of the shaft is outside the tunnel, therefore it was equipped with a horizontal arm with two accelerometers attached on its ends; the distance between the accelerometers is 566 mm, alternatively 165 mm - see Fig. 8. Accelerometers 1 and 2 sense the motion in the direction perpendicular to the horizontal arm. Besides the two accelerometers on the horizontal arm there is also the third accelerometer at the upper end of the shaft, which senses the motions perpendicular to the direction of the above pair of accelerometers.

The mast model was adjusted within the admissible limits by means of stressing of the wires and increasing of the mass concentrated on the top of the shaft. The values of the mass and guy force were changed. The air flow velocity was $\bar{V} = 10 \div 50$ m/s. The flow was not modified by the turbulence generator.

As stated above, the ratio of flexural to torsional frequency can be either 1:3 (the orbit is an ellipse or a circle) or 1:1 (the orbit is a line). The analysis of the model's response showed that there may be also other ratios of frequencies.

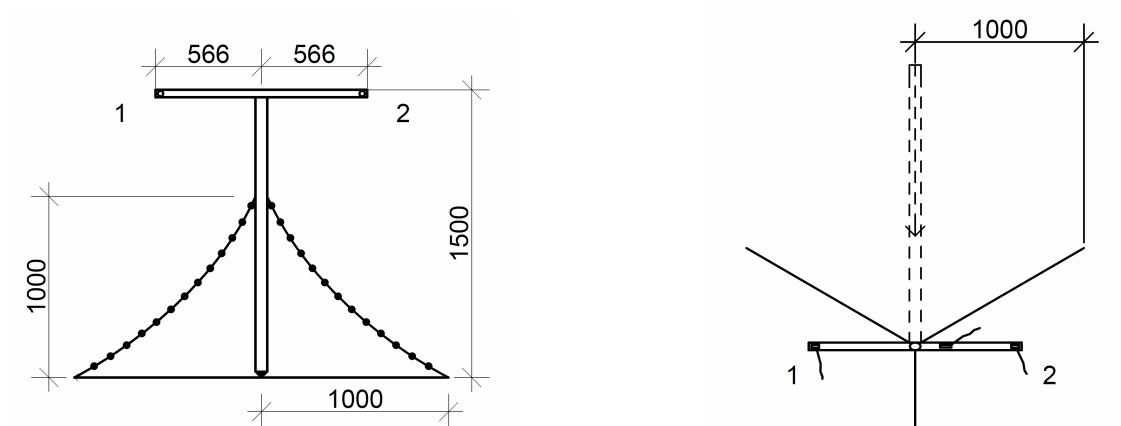


Fig. 8 Diagram of the model of guyed mast (side view and ground plane)

Conclusions

Systematic monitoring of torsion (swivelling) of guyed mast shafts has been performed in ITAM since 2005. The presented example of experimental verification describes the analysis of dynamic response of the shaft.

The simple static calculation model serves for making the proof of the occurrence of the moment, affecting the shaft, which is guyed by three ropes. The exact theoretical solution of the real phenomenon assumes the introduction of dynamics of guy ropes, which vibrate in 3D shapes during the shaft's movement along the orbit and it's torsion (swivelling), as well as a detailed determination of the aerodynamic characteristic of the shaft cross-section with respect to the conditions of aerodynamic instability [3].

Acknowledgements

The support of the grant MPO TIP FR-TI3/654 is gratefully acknowledged. Identification code of research project of the ITAM AS CR v.v.i. RVO: 68378297.

References

- [1] F. Bleich, 1933, Stahlhochbauten, Berlin.
- [2] O. Fischer, M. Pirner, 1987, Dynamics of guyed masts, Study 2/87, Academia, Prague, (In Czech).
- [3] O. Fischer, J. Náprstek, M. Pirner, Dynamic response of guyed masts to wind action. Proceedings Congress IASS, Madrid, 1979.
- [4] V. Koloušek, et all., Wind effects on civil engineering structures, Academia-Elsevier, Prague, 1983.
- [5] V. Koloušek, Solution statique et dynamique de pylones d'antenne harbenes, Mem. De IAIPCV, VII, Zürich, 1947.
- [6] U. Peil, Collapse behaviour of guyed masts under gales and guy-rupture, Proceedings 2nd EECWE, Prague, 1998.
- [7] B.F. Sparling, Comparison of frequency and time domain analyses for guyed masts in turbulent winds, IASS, Group 4 on Masts and Towers, Oslo, Norway, 2001.

New Results in Dynamics Stability Problems of Elastic Rods

LALIN Vladimir Vladimirovich^{1,a} and KUSHOVA Daria Aleksandrovna^{2,b*}

^{1,2}Saint-Petersburg State Polytechnical University, Institute of Civil Engineering, Department of structural mechanics and building structures, Saint-Petersburg, Polytechnicheskaya st., 29, Russian

^alalin@cef.spbstu.ru, ^bdasha_kushova@mail.ru

Keywords: large displacements and rotations, conjugate pairs of strain and stress vectors, the functional of variational formulation, the stability equations, dynamic stability, dynamic approach to study the stability problem, dynamic stability criterion

Abstract. This article is about the nonlinear dynamic stability problems of the exact (Cosserat) theory of elastic rods. There is examined the general geometrically nonlinear theory with no restrictions on displacements and rotations being imposed.

In this article, it is shown that the variational problem can be defined as the search for the stationary point of the Hamilton's functional.

The new exact solutions of the stability problems for different types of the end fixities of the rod were obtained taking into account bending, shear and longitudinal stiffness.

Introduction

Traditional approach of variational formulation of the nonlinear rod deformation problems is to use the variational equation in the form of principle of virtual displacements [1-18]. In this work, considering the case of plane problem, it is shown that using of the conjugate pairs of strain and stress vectors [19], the variational problem can be defined as a problem of search for the stationary point of the Hamilton's functional. The static equations for plane and spatial problems are derived from Lagrange functional in our paper [20]. In this paper, we obtain the dynamic equations derived from the Hamilton's functional.

Problem Formulation

In this paper, the general geometrically nonlinear theory of elastic rods is examined, with bending, shear and tension-compression stiffness being taken into account and no restrictions imposed on displacements and rotations. In the plane problem every point of this rod has three degrees of freedom: two translational degrees and one rotational degree.

We take the disposition of originally rectilinear rod along X - axis of the right Cartesian coordinate system of X, Y, Z (see Fig. 1a) with unit vectors {i}, {j}, {k} respectively as the reference unstressed configuration (RC). In RC every point of the rod can be identified by the x_0 coordinate, where $0 \leq x_0 \leq L$, L is length of the unstrained rod.

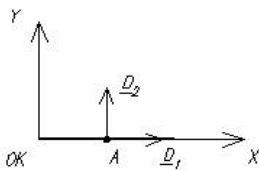


Fig. 1a Reference configuration (RC) of the rod

In the exact theory of elastic rods every point of the rod is connected with three basis vectors of unit length (directors), we denote its vectors as $\{D_i\}$ in the RC. For the originally rectilinear rod without any natural twisting we can assume that $\{D_1\}$ vector is in the direction of the rod axis, $\{D_2\}$ and $\{D_3\}$ vectors are in the directions of the principal central axes of cross section (Fig. 1a), where $\{D_i\} = \text{const } (x_0, t)$, $\{D_1\} = \{i\}$, $\{D_2\} = \{j\}$.

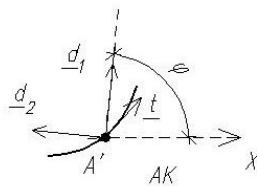


Fig. 1b Actual (deformed) configuration (AC) of the rod

Figure 1b shows the actual (deformed) configuration of the rod (AC). Position of every point of the rod in the AC can be defined by the vector $\{r\}(x_0) = x(x_0)\{i\} + y(x_0)\{j\}$. The directors in the rotated position are denoted as $\{d_i\} = \{d_i\}(x_0, t)$, where $\{d_1\}$ vector is not necessarily coincides with $\{t\}$ - unit vector, tangent to the rod axis in the AC. In the plane problem the rotation of the directors is given by vector $\{\Phi\}(x_0, t) = \varphi(x_0, t)\{k\}$. Functions $x(x_0, t)$, $y(x_0, t)$, and $\varphi(x_0, t)$ are three degrees of freedom in the plane problems of the geometrically nonlinear deformation of the rod.

Formulation of the geometrically nonlinear problem for the physically linear rod consists of three sets of Eq. 1–3 [20, 22].

Equations of motion

$$\begin{cases} \rho \ddot{x} - (N \cos \varphi - Q \sin \varphi)' - q_x = 0 \\ \rho \ddot{y} - (N \sin \varphi + Q \cos \varphi)' - q_y = 0 \\ \frac{\rho}{A} J_z \ddot{\varphi} - M' - x'(N \sin \varphi + Q \cos \varphi) - y'(Q \sin \varphi - N \cos \varphi) - m = 0, \end{cases} \quad (1)$$

where q_x , q_y , and m – distributed power and moment loads respectively, ρ - linear density, J_z – moment of inertia, A - cross-section area. Dotted values indicate the time derivative, $\ddot{x} = d^2 x / dt^2$ and $(\dots)'$ will denote derivative with respect to x_0 .

The components of deformations ε , Γ , ψ are defined through the functions $x(x_0, t)$, $y(x_0, t)$, and $\varphi(x_0, t)$ by geometrical Eq. 2

$$\begin{cases} \varepsilon = x' \cos \varphi + y' \sin \varphi - 1 \\ \Gamma = -x' \sin \varphi + y' \cos \varphi \\ \psi = \varphi' \end{cases} \quad (2)$$

Hooke's law for the physically linear material:

$$N = k_1 \varepsilon, \quad Q = k_2 \Gamma, \quad M = k_3 \psi \quad (3)$$

where k_1 , k_2 , and k_3 – longitudinal, shear, and bending stiffness of the rod, respectively.

Let us take the classical Euler problem (hinged rod shown in Figure 2) as an example. The equilibrium configuration is rectilinear, with only T-compression force acting.

Boundary values are

$$x_0 = 0: x = 0, y = 0, M = 0 \quad (4)$$

$$x_0 = L: y = 0, M = 0, N = -T. \quad (5)$$

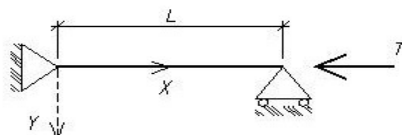


Fig. 2 Design model of the rod

The Hamilton's functional can be written in the following way

$$H(x, y, \varphi) = \int_{t_1}^{t_2} \int_0^L \left[\frac{1}{2} \left(\rho \dot{x}^2 + \rho \dot{y}^2 + J_z \left(\frac{d\varphi}{dt} \right)^2 \right) - \left(\frac{1}{2} (k_1 \varepsilon^2 + k_2 \Gamma^2 + k_3 \psi^2) \right) \right] dx_0 dt - T(x(L) - L) \quad (6)$$

The first variation of the Hamilton's functional

$$\delta H(x, y, \varphi, \delta x, \delta y, \delta \varphi) = - \int_{t_1}^{t_2} \int_0^L \left[\rho \dot{x} \delta \dot{x} + \rho \dot{y} \delta \dot{y} + \frac{\rho}{A} J_z \delta \varphi \dot{\varphi} - k_1 \varepsilon \delta \varepsilon - k_2 \Gamma \delta \Gamma - k_3 \psi \delta \psi \right] dx_0 dt - T(x(L) - L) \quad (7)$$

Integrating Eq. 7 by parts and using the conditions $\delta x(0, t) = 0$, $\delta y(0, t) = \delta y(L, t) = 0$, it is easy to show that the condition $\delta H = 0$ result in the equations of motion (1) and natural boundary values $M(0, t) = M(L, t) = 0$, $N(L, t) = -T$.

The stability equations as a local linearization of motion equations are

$$\begin{cases} -(N \cos \varphi_0 - Q \sin \varphi_0)' + \theta'(N_0 \sin \varphi_0 + Q_0 \cos \varphi_0) + \\ + \theta(N_0 \sin \varphi_0 + Q_0 \cos \varphi_0)' + \rho \ddot{u} = 0 \\ -(N \sin \varphi_0 + Q \cos \varphi_0)' - f'(N_0 \cos \varphi_0 - Q_0 \sin \varphi_0) - \\ - f(N_0 \cos \varphi_0 - Q_0 \sin \varphi_0)' + \rho \ddot{v} = 0 \\ -M' - u'(N_0 \cos \varphi_0 + Q_0 \sin \varphi_0) - \\ - x_0'(N \sin \varphi_0 + Q \cos \varphi_0 + N_0 \theta \cos \varphi_0 - Q_0 \theta \sin \varphi_0) - \\ - v'(Q_0 \sin \varphi_0 - N_0 \cos \varphi_0) + y_0'(N_0 \theta \sin \varphi_0 - N \cos \varphi_0 + \\ + Q \sin \varphi_0 + Q_0 \theta \cos \varphi_0) + \frac{\rho}{A} J_z \theta = 0, \end{cases} \quad (8)$$

where $u(x, t)$, $v(x, t)$, and $\theta(x, t)$ – variations of functions x_0 , y_0 , and φ_0 , respectively; N , Q , M , ε , Γ , ψ – variations of the internal forces and strains correspond to u , v , and θ . Functions u , v , and θ satisfy the principal boundary values of the original meet Eq. 1–5.

In Eq. 8 the quantities with the inferior index 0 denote the equilibrium state characteristics, satisfying the system of Eq. 1–5.

The exact solution of the nonlinear system Eq. 1–5 is

$$M_0 = 0, \quad Q_0 = 0, \quad \varphi_0 = 0, \quad \Gamma_0 = 0, \quad q_y = 0, \quad y_0 = 0, \quad q_x = 0.$$

$$N_0 = -T, \quad \varepsilon_0 = x_0' - 1 = \frac{N_0}{k_1}, \quad \cos \varphi_0 = 1, \quad \sin \varphi_0 = 0.$$

Thus, the stability equations can be written in the following way

$$\begin{cases} -N' + \rho \ddot{u} = 0 \\ T\theta' - Q' + \rho \ddot{v} = 0 \\ -M' - Q(1 - \frac{T}{k_1}) - T(-x_0' \theta + v') + \frac{\rho}{A} \theta J_z = 0 \\ \begin{cases} N = k_1 u' \\ Q = k_2 (-x_0' \theta + v') \\ M = k_3 \theta' \end{cases} \end{cases} \quad (9)$$

Then, for the homogeneous rod, whose stiffness does not depend on x , we obtain the following system, replacing the N , Q , M by expression them through the components of deformations:

$$\begin{cases} \rho \ddot{u} - k_1 u'' = 0 \\ \rho \ddot{v} + T \dot{\theta} - k_2 \left[v' - \left(1 - \frac{T}{k_1} \right) \theta \right] = 0 \\ \frac{\rho}{A} \ddot{\theta} J_z - k_3 \theta'' - k_2 \left[v' - \left(1 - \frac{T}{k_1} \right) \theta \right] \left[1 - \frac{T}{k_1} + \frac{T}{k_2} \right] = 0 \end{cases} \quad (10)$$

In the derived system Eq. 10 the first equation describes the longitudinal deformations and does not depend on the second and third equations. Consequently, the stability is verified only by the second and third equations.

The general solution of the second and third equations of system Eq. 10 satisfies the boundary values, can be written in the following way:

$$\begin{aligned} v &= \sum_{n=1}^{\infty} v_n \sin \frac{n\pi x}{L} \cos \omega t \\ \theta &= \sum_{n=1}^{\infty} \theta_n \cos \frac{n\pi x}{L} \cos \omega t \end{aligned} \quad (11)$$

We obtain a system of homogeneous algebraic equations for the amplitudes v_n , θ_n for each number «n». From the condition that the determinant of this system equal zero, we obtain an equation for determining the frequency ω . Buckling condition $\omega = 0$ gives the equation for determining the critical force Eq. 12.

The quadratic equation

$$T^2 \left(\frac{1}{k_2} - \frac{1}{k_1} \right) + T - \frac{k_3 n^2 \pi^2}{L^2} = 0. \quad (12)$$

Examining the solution of the equation where $n = 1, 2, 3, \dots$, one can find that the critical (minimal) force value is obtained at $n = 1$ and is calculated from the quadratic equation [22]

$$T^2 \left(\frac{1}{k_2} - \frac{1}{k_1} \right) + T - T_E = 0, \quad (13)$$

where $T_E = \pi^2 k_3 / L^2$ – Euler's force [23].

Hence, we obtain a unique positive value T

$$T = \frac{\sqrt{1 + 4T_E \left(\frac{1}{k_2} - \frac{1}{k_1} \right)} - 1}{2 \left(\frac{1}{k_2} - \frac{1}{k_1} \right)}. \quad (14)$$

Solution (13) is the exact solution of the stability problem of the rod when longitudinal, shear and bending stiffness are taken into account.

In the same way we have obtained the exact solutions of the stability problems for different types of end fixity of the rod. It appears that for all boundary values, equation (13) and the solution (14) retain their form, differing only by the value of the Euler force T_E .

Summary

1. The formulation of the dynamic problems of the geometrically nonlinear deformation of the elastic beam was obtained as a system of the differential equations.
2. The Hamilton's functional for the variational formulation of the dynamic problems of the geometrically nonlinear rods was proposed.
3. The equations of the plane problems of the dynamic stability as a local linearization of the equations of motion were obtained.
4. The exact solutions of the equilibrium stability problems for different types of end fixity of the rod were obtained taking into account bending, shear and tension stiffness.

References

- [1] D.P. Goloskokov, P.A. Zhilin, Obshaja nelinejnaja teoriya uprugih sterzhnej s prilozheniem k opisaniju jeffekta Pojntinga, Deposited VINITI No. 1912-V87, Dep., 20 p. (Russian)
- [2] V.V. Eliseev, Mehanika uprugih sterzhnej, Saint-Petersburg, SPbSPU, 1994, 88 p. (Russian)
- [3] P.A. Zhilin, A.D. Sergeev, Ravnovesie i ustojchivost' tonkogo sterzhnja, nagruzhennogo konservativnym momentum. Mehanika i processy upravlenija, Trudy SPbSPU, 1994, No. 448, pp. 47-56. (Russian)
- [4] P.A. Zhilin, A.D. Sergeev, T.P. Tovstik, Nelinejnaja teoriya sterzhnej i ee prilozhenija, Trudy XXIV letnej shkoly: Analiz i sintez nelinejnyh mehanicheskikh kolebatel'nyh sistem, Sankt-Peterburg, 1997, pp. 313 – 337 (Russian).
- [5] P.A. Zhilin, Prikladnaja mehanika, Teoriya tonkih uprugih sterzhnej, SPb, Izd-vo SPbSPU, 2007, 102 p. (Russian).
- [6] V.V. Eliseev, T.V. Zinoveva, Mehanika tonkostennyh konstrukcij, Teoriya sterzhnej, SPb, Izd-vo SPbSPU, 2008, 96 p. (Russian).
- [7] G. Jelenic, M.A. Crisfield, Geometrically exact 3D beam theory: implementation of a strain-invariant finite element for static and dynamics. Comp. Meths. Appl. Mech. Engng, 1999, No. 171, pp. 141-171.
- [8] A. A. Shabana and R.Y. Yakoub, Three dimensional absolute nodal coordinate formulation for beam elements theory. ASME Journal of Mechanical Design, 123 4 (2001) 606–613.
- [9] J. N. Reddy, An Introduction to Nonlinear Finite Element Analysis. Oxford University Press, 2004, 482 p.
- [10] S.S. Antman, Nonlinear problems of elasticity, Springer, Berlin Heidelberg New York, 2005, 835 p.
- [11] J. Gerstmayr, A.A. Shabana, Analysis of thin beams and cables using the absolute nodal coordinate formulation. Nonlinear Dyn. 45 1-2 (2006) 109-130.
- [12] A.A. Shabana, Computational continuum mechanics. Cambridge University Press, 2008, 349 p.
- [13] P. Wriggers, Nonlinear finite element methods. Springer-Verlag Berlin Heidelberg, 2008, 566 p.

- [14] S. Krenk, Non-linear modelling and analysis of solids and structures. Cambridge University Press, 2009, 361 p.
- [15] A. Ibrahimovic, Nonlinear Solid Mechanics. Springer Science+Business Media B.V. 2009, 585 p.
- [16] D. Bigoni, Nonlinear solid mechanics: bifurcation theory and material instability. Cambridge University Press, 2012, 550p.
- [17] S. Coskun, B. Öztürk, Elastic Stability Analysis of Euler Columns Using Analytical Approximate Techniques, Advances in Computational Stability Analysis, Dr. Safa Bozkurt Coskun (Ed.), 2012, DOI 10.5772/45940.
- [18] V.P. Bagmutov, A.A. Belov, A.S. Stoljarchuk, Jelementy raschetov na ustojchivost'. Ucheb. Posobie. V. P. Bagmutov, A. A. Belov, A. S. Stoljarchuk. – Volgograd: IUNL VolgGTU, 2010, 56 p. (Russian).
- [19] V.V. Lalin, Razlichnye formy uravnenij nelinejnoj dinamiki uprugih sterzhnej. Trudy SPbGTU, 2004, No. 489, pp. 121-128, (Russian).
- [20] V.V. Lalin, D.A. Kushova, Geometricheski nelinejnoe deformirovanie i ustojchivost' ploskikh uprugih sterzhnej s uchetom zhestkostej na rastjazhenie-szhatie, sdvig i izgib. International Journal for Computational Civil and Structural Engineering, 9 4 (2013) 178-185, (Russian).
- [21] I.M. Gelfand, S.V. Fomin, Variacionnoe ischislenie. M.: GIFML, 1961, 228 p. (Russian).
- [22] V.V. Lalin, L.A. Rozin, D.A. Kushova, Variacionnaja postanovka ploskoj zadachi geometricheski nelinejnogo deformirovaniya i ustojchivosti uprugih sterzhnej. Inzhenerno – stroitelnyj zhurnal, 36 1 (2013) 87-96, (Russian).
- [23] A.V. Perelmuter, V.I. Slivker, Ustojchivost' ravnovesija i rodstvennye problem. Vol. 1, Moscow, SKAD SOFT, 2010, 647 p. (Russian).

Fatigue Damage Accumulation under the Complex Varying Loading

MELNIKOV Boris^{1, a*} and SEMENOV Artem^{1, b}

¹Saint-Petersburg State Polytechnical University, Russia

^amelnikovboris@mail.ru, ^bsemenov.artem@googlemail.com

Keywords: low-cycle fatigue, plasticity, damage, complex loading, identification

Abstract. Fatigue analysis of steel parts of structures, which are subjected to complex irregular loading programs caused by wind, thermal, wave loads, earthquakes and combined imposed actions, requires in some cases using special methods of stress-strain evaluation. The model of the low cycle fatigue nonlinear damage accumulation is developed with taking into account the history of the deformation process. The damage is defined on the base of considering the quasi-static accumulation of maximal strain (stress) and hysteresis loops. The identification of material constants of the model is discussed. Application of the damage model for fatigue analysis of the antennas, pipelines, basements and fasteners units is considered and a comparison with experiments is given.

Introduction

During variable macroscopically elastic deformation of structures the local plasticity may occur in the stresses concentration zones and can result in low- or high-cycle fatigue failure. In this regard, the question arises, what the mechanism of fatigue failure (low- or high-cycle) is realized. The criterion of failure mechanism estimation is a fact of presence or absence of mechanical adaptation of material to considered loading regime, which can be determined numerically, particularly with help of the multimodel method of plasticity analysis [1,2].

In the case of mechanical adaptation the micro-plasticity hysteresis is only observed and for fatigue resistance estimation the models of high-cycle fatigue are applicable. Usually the high-cycle fatigue is associated with a large service life. If there is no mechanical adaptation under cyclic mechanical loading then the macro-plastic hysteresis is observed, resulting in low-cycle fatigue failure with a short service life.

There is a wide range of fatigue-life prediction models proposed in literature (see review in [3-6]) including approaches based on stress-life, strain-life and inelastic energy models. The model proposed in the below represents mixed strain/energy class of models, addressed to the low-cycle fatigue and transition from low-to-high cycle fatigue and it is applicable for multi-axial complex non-proportional loading cases.

Model for the Low-Cycle Fatigue Damage Accumulation

For the evaluation of fatigue resistance there is important to take into account the quasi-static accumulated maximal strain or stress in the stress concentration zone and also the influence of induced anisotropy of material. Moreover, it is necessary to take into account the cyclic and instant strain contributions of damage. Respectively, the damage can be estimated by the following equation:

$$D = F\left(\frac{\varepsilon_{\max}}{\varepsilon_p}\right) + \sum_{k=1}^N f\left(\frac{\Omega_k}{\omega_p}\right) + \sum_{k=1}^N \varphi\left(\frac{\omega_k}{\omega_p}\right), \quad (1)$$

where D is the damage, ε_{\max} is the maximal eigenvalue of strain tensor for history of loading, Ω_k is the irreversible work of quasi-static plastic deformation in k^{th} cycle; ω_k is the irreversible work of cyclic plastic deformation in k^{th} cycle; ε_p , ω_p are material constants, namely, the limit plastic strain and work for quasi-static strain in the experiments (Fig. 1).

The scheme of evaluation of D , mentioned above, is close to given in [3]. Since $F\left(\frac{\varepsilon_{\max}}{\varepsilon_p}\right)$,

corresponding to the part of D caused by uni-axial loading, is equal zero if the load ratio is $R = -1$, then failure in this case may be regarded as the effect of nonreversible cyclic deformation work. Hence, for one cycle:

$$\varphi\left(\frac{\omega_k}{\omega_p}\right) = \left(1 - \frac{\varepsilon_{\max}}{\varepsilon_p}\right) \frac{1}{N_p}, \quad (2)$$

where N_p is a number of cycles before failure at $R = -1$.

The first term in (1) forms the instant-plastic strain accumulation; for metals it can be specified simply as $F\left(\frac{\varepsilon_{\max}}{\varepsilon_p}\right) = \frac{\varepsilon_{\max}}{\varepsilon_p}$. Further, assuming independency of $\varphi\left(\frac{\omega_{mid}}{\omega_p}\right)$ and R , based on experimental results with $R \neq -1$, we obtain:

$$f\left(\frac{\Omega}{\omega_p}\right) = \left(1 - \frac{\varepsilon_{\max}}{\varepsilon_p}\right) \frac{1}{N_p} - \varphi\left(\frac{\omega_{mid}}{\omega_p}\right), \quad (3)$$

where N_p is a number of cycles before failure at $R \neq -1$, ω_{mid} – average loop area for N_p cycles, $\omega + \Omega = \oint \sigma_{ij} d\varepsilon_{ji}^p$.

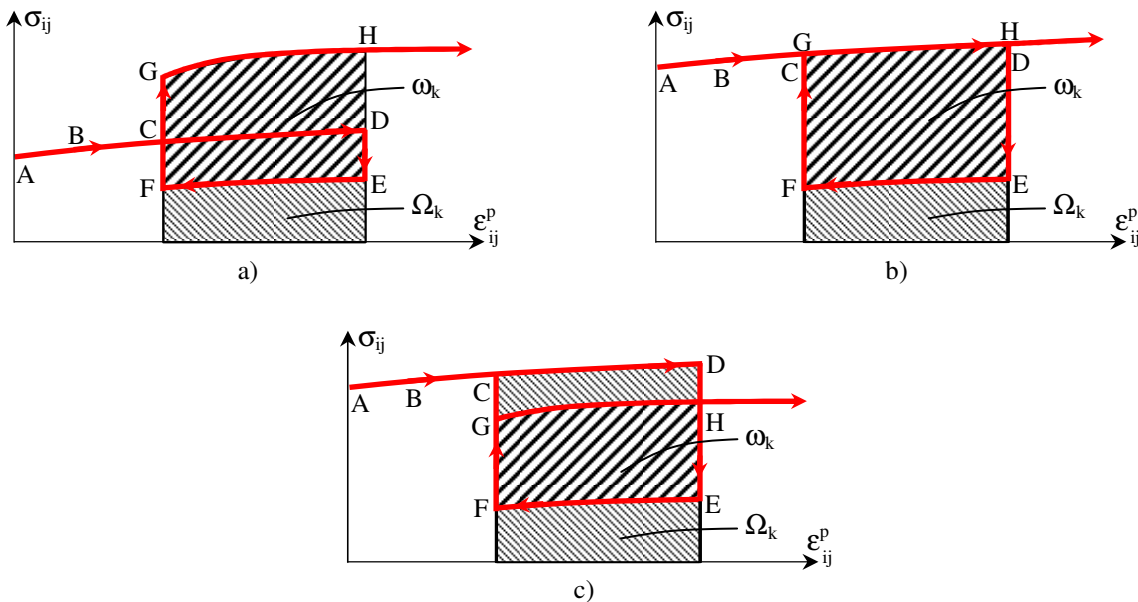


Fig. 1 Typical cases of cyclic deformation and corresponding decompositions of plastic work

Verification of the Damage Criterion on Tubular Specimens under Complex Cyclic Loading

The predictive capability of the damage accumulation model (1) was investigated by testing tubular specimens made of X18H10T steel under complex cyclic loading with partial and full unloading. Specific work of plastic deformation before failure calculated using structural model of plasticity [1,2,7,8] and multi-surface theory of plasticity with one active surface [1,2,8] was defined as 343 MPa and 467 MPa. Experimental value under axial tension is 436 MPa. The Odquist parameter is equal 0.466, 0.560 and 0.555, respectively.

Verification of the Damage Criterion on Box-Shaped Beams under Cyclic Three Point Bending

Experiments were carried out on box-shaped beams under cyclic three point bending scheme. The plate thickness, from which beams were prepared, was 4 mm, the width was 6 and 3 cm. Material characteristics: yield stress $\sigma_Y = 300$ MPa, ultimate stress $\sigma_U = 450$ MPa, true tensile resistance $\sigma_S = 800$ MPa, area under «true» stress-strain curve $\omega_p = 420$ MPa. Comparison of the computed results and experimental data is given in the Table 1. It was assumed that the crack initiation (failure) takes place if the crack length is about 0.1 mm.

Table 1 Comparison of model (1) predictions with experimental data

Exp. №	Beam length, m	Section height, mm	Maximal tension	$\varphi\left(\frac{\omega}{\omega_p}\right)$	Number cycles before failure	
					Prediction by Eq. 1	Experimental data
1	0.58	68	42	0.0028	100	237
2	0.58	68	50	0.0143	30	24
3	0.27	38	25	0.0184	70	64
4	0.27	38	30	0.0453	32	16
5	0.27	38	30	0.0468	49	16

Influence of Stress Gradient at the Stress Concentration

The quality of the surface (roughness, scratches, sharp transitions, edges) essentially affects the behavior fatigue of structures (according [9] data at the depth 0.125-0.22 mm) and attenuates the strength properties. The yield stress decreases to 40% from integral value [9].

In the stress concentration zones the stress gradient may be large enough. The maximum tension estimated in the concentration zone results in lower durability value, comparing to the experiments. The possible explanation is following: using this approach the estimated value reflects formation of microcracks in the maximal concentration point and does not take into account the number of plastic reversals necessary for its diffusion.

Peterson [10] supposed to determine fatigue life by the moment when microcrack would develop at some distance δ from the notch root. Firstly this approach was used for determining the notch factor in the case of static failure. Further investigations [11,12] were addressed to the high- and low-cycle fatigue. But this approach does not consider plastic deformation in the concentration zone. The size δ in the [11,12] is considered as material characteristic, without dependence on the notch size and cyclic loading level. Also, the scheme does not take into account the stress state inhomogeneity influence on the fatigue failure.

The proposed method for analytical-experimental evaluation of the fatigue resistance of structural elements consists of two steps. The first step represents experimental determination of δ

characteristics and the second step encompasses computing of the number of cycles prior failure of element of structure.

At the first step the experimental evaluation of fatigue curves for the both, smooth standard specimens, and notched specimens at different R-values (load ratio) is carried out. Then the cyclic stress-strain state at the stress concentration zone for the notched specimens is analyzed by the finite-element method. Based on results of numerical analysis, experiments using the fatigue model the value of durability δ is determined. The investigations had shown that the durability prediction can be improved by using instead δ the $\bar{\delta} = \delta\bar{G}$ where gradient of maximum principle stress is defined by

$$\bar{G} = \frac{1}{\sigma_1} \left. \frac{\partial \sigma_1}{\partial x} \right|_{x=0}. \quad (4)$$

Examples of Durability Analysis for Various Elements of Structures

The damage model (1) was applied to predict the durability of elements of pipelines designed for the severe climate environments; the results were compared to the experimental investigations data.

The proposed approach results were confirmed by the results of the measurement of acoustic emission and radio-acoustic emission for the fixing cylindrical elements of aerials. In analysis, the three possible directions of hypothetical cracks (parallel to cylinder axis, normal to it, and slanted, at 45° angle) were investigated. Numerical analysis was planned so that the significant plastic deformation occurs under the maximum possible loading by the moment when the crack grows up 0.02 m. At the first loading cycle in the most stressed point the plastic deformation appears, but in the following cycles no plastic strain develops. The stabilization and adaptation of the hysteresis loop is observed (Fig. 2). Material conforms to the cyclic zero-to-tension loading and low-cyclic fatigue would not take place. The acoustic emission data confirmed this conclusion. The difference between experimental and calculated durability indices was less than 15%.

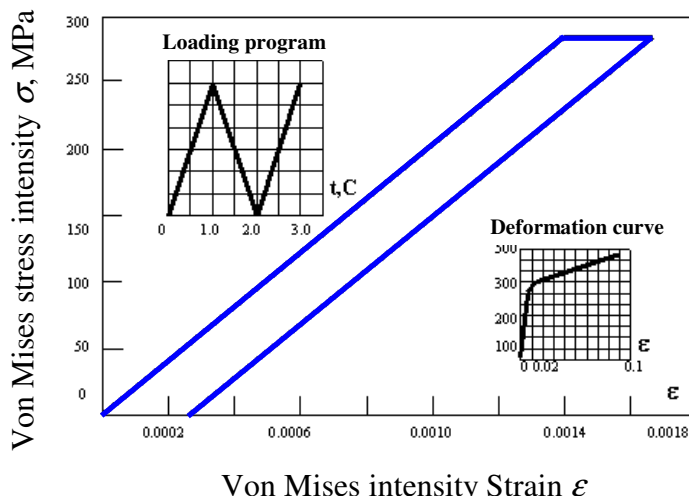


Fig. 2 Adaptation of the hysteresis, observed in fixing element of aerials

The experimental investigations of damage were carried out and the results were compared with predicted by the damage model (1) for the most stressed and most responsible elements of pipeline system (Fig. 3).

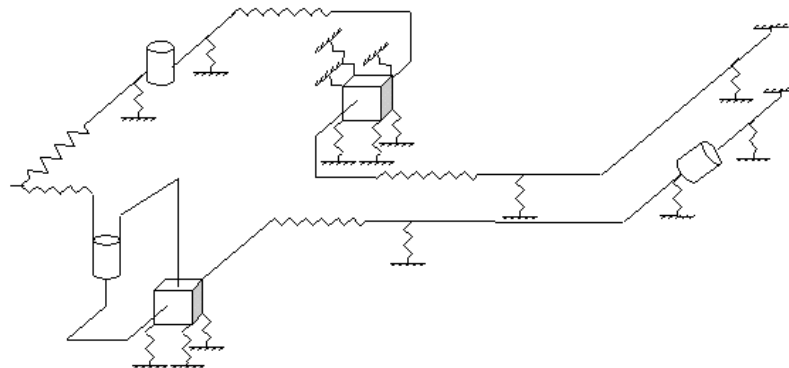


Fig. 3 Schematic presentation of system of pipelines

Durability analysis was performed for the input pipeline flange connection subjected to axial force with the low cyclic component. The material is steel 45. The considerable stress concentration was observed in the zone of abrupt diameter change. Secondary plastic deformation did not rise in the hole. The high-cycle fatigue model was used for the durability evaluation. Fig. 4 shows computed (1) and experimental (2) curves.

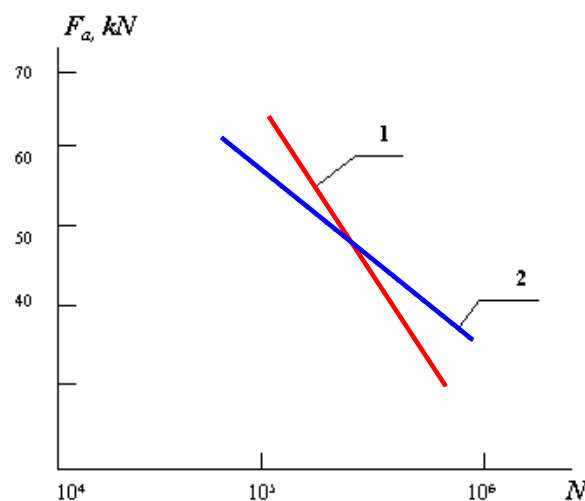


Fig. 4 Experimental and calculated durability curves for the pipeline element

The proposed damage model (1) is addressed for the durability prediction in the macroscopic crack initiation stage. In all considered examples the number of cycles for the crack initiation dominates over the number of cycles for the crack propagation. In practice there are also inverse situations, too. In this case the direct methods of fatigue crack propagation should be used based on the Paris law and its generalization [3-6, 13] or methods based on the continuum damage mechanics [14,15].

In accordance with [16-18] the developed method can be extended to the concrete objects as well.

Summary

Application of the proposed model of nonlinear fatigue damage accumulation with taking into account the history of deformation process and loading multiaxiality demonstrates satisfactory accuracy in comparison with the experimental data for the tubular specimens, box-shaped beams, elements of aerials and pipelines.

Acknowledgements

This work was supported by the Russian Fund for Fundamental Research, project 12-08-00-943a.

References

- [1] B.E. Melnikov, A.S. Semenov, Strategy of multimodel analysis of elastic-plastic stress-strain state, Berlin Proc. of 6 th Int. Conf. on Comp. Civil and Build. Eng.-Berlin. (1995) 1073-1079.
- [2] B.E. Melnikov, A.S. Semenov, Creation and application of hierarchical sequence of material models for numerical analysis of elasto-plastic structures, ZAMM Zeitschrift fur Angewandte Mathematik und Mechanik. 76 (1996) 615-616.
- [3] S. Suresh, Fatigue of Materials, Second Edition, Cambridge University Press, 1998.
- [4] J. Schijve, Fatigue of Structures and Materials, 2nd Edition, Springer, 2009.
- [5] S.S. Manson, G.R. Halford, Fatigue and durability of structural materials, ASM Int., 2006.
- [6] P.A. Pavlov, Foundations of engineering computation the mechanisms parts on fatigue longevity strength, Mashinostroenie, 1988 (in Russian).
- [7] A.S. Semenov, B.E. Melnikov, M.Yu. Gorokhov, V. Ulbricht, Prevention of cyclic instability at the modeling of elasto-plastic deformation at large strains under proportional and non-proportional loading, Proc. of SPIE, 6597 (2007) 659-710.
- [8] I.N. Izotov, N.P. Kuznetsov, B.E. Melnikov, A.G. Mityukov, A.Y.Musienko, A.S. Semenov, Modification of the multisurface theory of plasticity with one surface. Comparison with experimental data, Proc. of SPIE, 4348 (2001) 390-397.
- [9] V.T. Troschenko, V.V. Pokrovsky, A.V. Prokopenko, Metal slopes under cyclic loading, Kiev: Nauk. dumka, 1987 (in Russian).
- [10] R.E. Peterson, Application of stress concentration factors in design, Proc. Society Expirim, Stress Analysis. 1 (1943) 120-129.
- [11] O'Donnell, Pordy. Fatigue strength of units with cracks, 2 (1964) 147-159.
- [12] P.A. Fomichev, J. Polak, Method of calculating the endurance of specimens with a stress raiser. Strength of Materials, 9 (1989) 100-103.
- [13] A. Semenov, S. Semenov, A. Nazarenko, L. Getsov, Computer simulation of fatigue, creep and thermal-fatigue cracks propagation in gas-turbine blades, Materiali in Tehnologije, 46 (2012) 197-203.
- [14] J. Lemaitre, R. Desmorat, Engineering damage mechanics: ductile, creep, fatigue and brittle failures, 2005.
- [15] A.S. Semenov, S. Saehn, B.E. Melnikov, Computer simulation of kinked fatigue crack propagation at sharp notches, Proc. of SPIE, 3687 (1999) 427-436.
- [16] A. Sprince, G. Fischer, L. Pakrastish, A. Korjakin, Crack propagation in concrete with silica particles. Advanced Materials Research, 842 (2014) 470-476.
- [17] A. Sprince, A. Korjakin, L. Pakrastish, Time-dependent behavior of high performance fiber-reinforced concrete. Advanced Materials Research, 705 (2013) 75-80.
- [18] O.N. Popova, T.L. Simankina, The service life estimation method for the structural elements of residential buildings, Magazine of Civil Engineering, 7 (2013) 40-42.

Probability and Sensitivity Analysis of Plate

TVRDÁ Katarína^{1a*}

¹Slovak University of Technology in Bratislava, Department of Structural Mechanics,
Radlinského 11, 813 68 Bratislava, Slovak Republic

^akatarina.tvrda@stuba.sk

Keywords: probability, sensitivity, plate, Monte-Carlo method, statics analysis, Gauss distribution, triangular distribution, finite element method

Abstract. This paper deals with some problems of the ceiling plate, made of the Cobiax-system. Cobiax provides a system to produce voided, biaxial, flat plate slabs as a high-quality concrete solution for large spans and slim slabs. Plastic voids in the shape of spheres or flattened spheres are contained in steel cages and put into concrete structures to create longer spans and reduce vertical loads. The presented plate is made of cobiax balls with a diameter of 27 cm located outside the area of columns. Probability analysis of Monte-Carlo method in software Ansys is presented. Input parameters are changing according to Gauss or triangular distribution.

Introduction

One of the possible solutions of static analysis and expertise is also an assessment of the reliability of structures. ANSYS software allows assess the structure on safety or a failure based on probability analysis using Monte Carlo methods. A number of papers dealing with probability analysis may be found in works of authors [1,2,3,4]. Such calculations can contribute to the safety of the structures.

Static analysis

We will deal with the static analysis of the ceiling plate loaded by uniformly distributed load $q = 6.5 \text{ kN/m}^2$ (Fig.1). The plate is made of concrete B30/37 class with a modulus of elasticity $E = 33 \text{ GPa}$ and the thickness of plate is $h = 0.4 \text{ m}$.

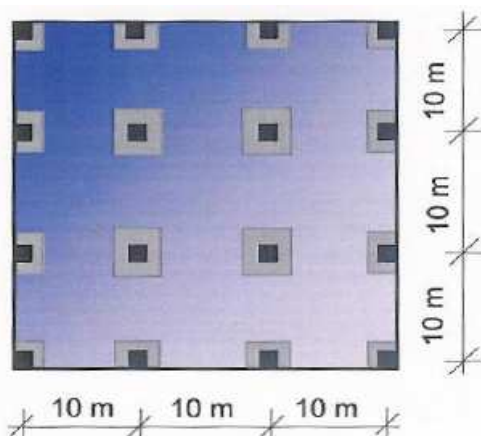


Fig. 1 Ceiling plate

Dead load of $0.4 \times 25 \text{ kN/m}^3 = 10 \text{ kN/m}^2$ was in columns location compared with dead load $0.4 \times 25 \text{ kN/m}^3 - 2.86 = 7.14 \text{ kN/m}^2$ at location of balls with a diameter of 27 cm. Manufacturer of the Cobiax prescribed in this case to reduce the flexibility of the modulus on $E_b = 0.92 \times 33 \text{ GPa} = 30.366 \text{ GPa}$ and recommended a maximum load reduction of 2.86 kN/m^2 . The static scheme is in Fig 2.

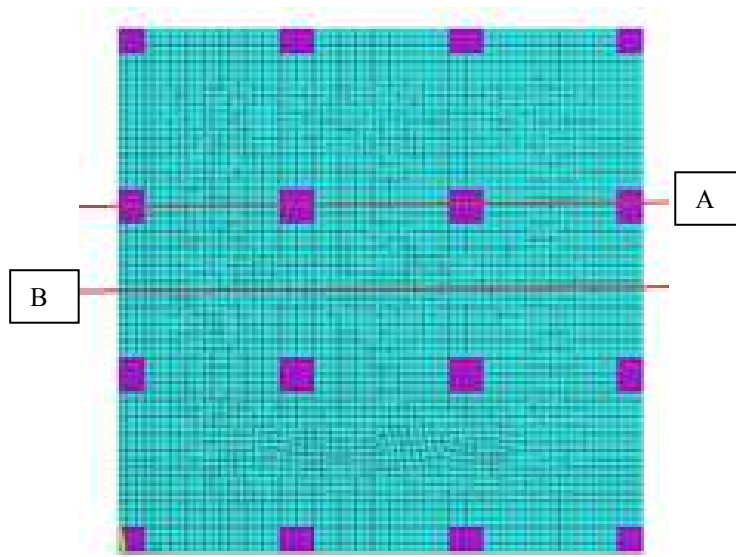
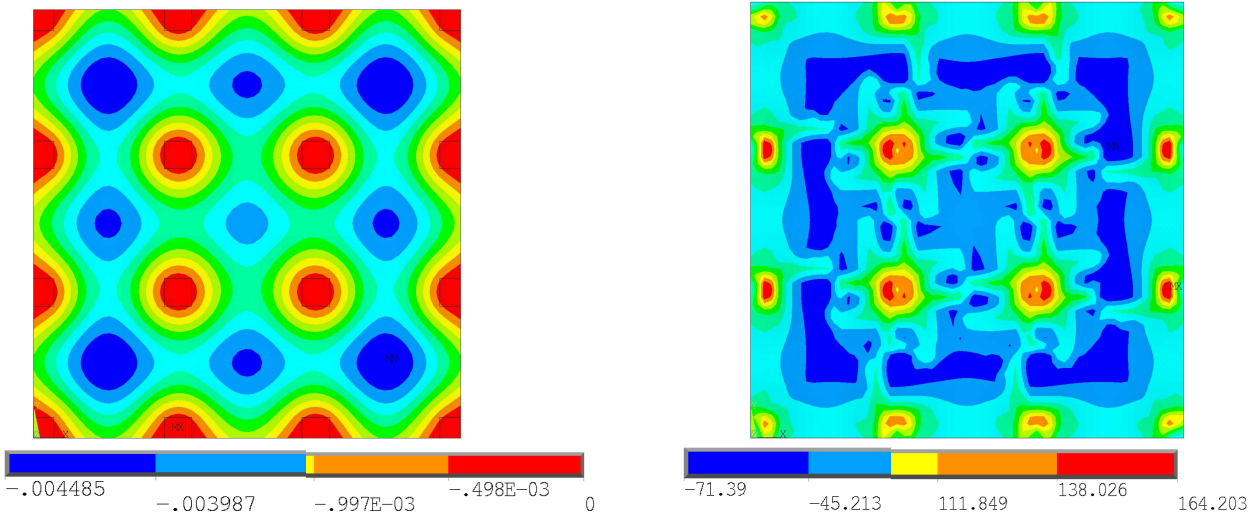
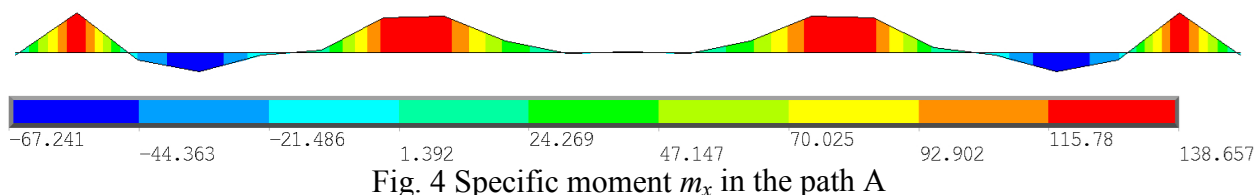
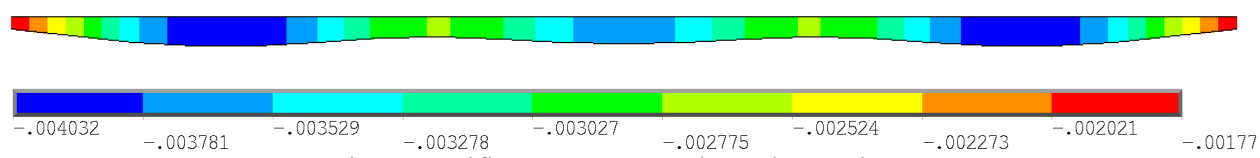


Fig. 2 Static scheme

The resulting stress, strain and internal forces of the ceiling plate are presented in the following figures.

Fig. 3 Deflection w and specific moment m_x Fig. 4 Specific moment m_x in the path AFig. 5 Specific moments m_x along the section B

Probability analysis

As we know, any building structure is subjected to certain specified tolerances in the manufacture of the construction of dimension proportions. We can also specify the load, modulus, which may be randomly changed. This analysis, which deals with all these uncertainties and the variation, is called

the probability analysis. The method used for this purpose was the Monte Carlo method with a direct sampling and number of cycles was set to 120500. In this case it was set 5-output parameters as the maximum deflection (PRIEH), maximum specific moment mx (MAX_MX), maximum specific force (MAX_Vxz), Misses stress (NAP), reliability (CO), which varied depending on the four input parameter. The input parameters were: modulus of elasticity for the Cobiax plate (E_{kob}), for full plate ($E_{_}$), uniformly distributed load ($q_{_}$), and the thickness of the plate ($h_{_}$).

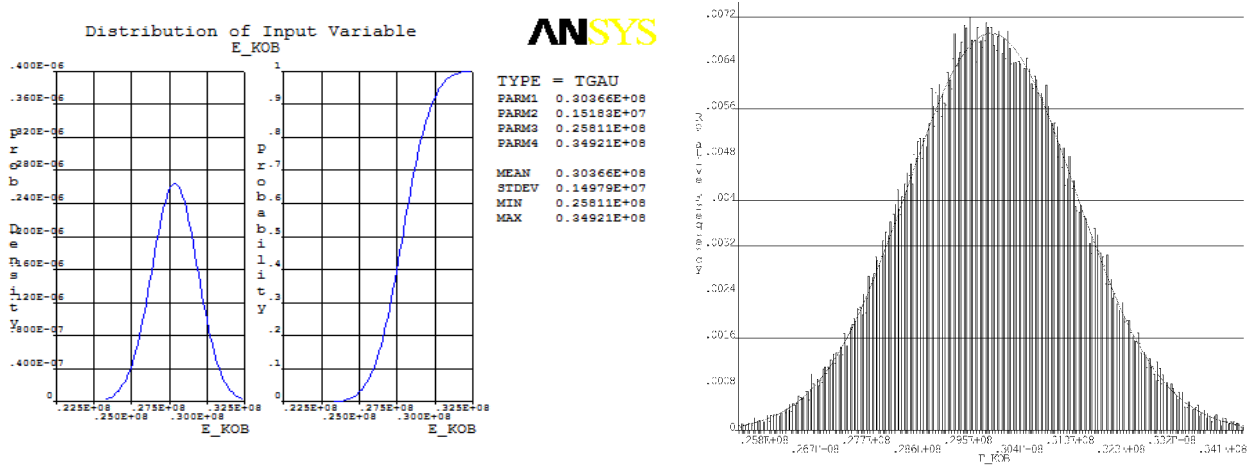


Fig. 6 Distribution and histogram of input variable E_{kob}

Type and distribution of some inputs are given in the following Table 1 and Fig. 6. From Fig. 6 it is clear, that input variable E_{kob} has a Gauss distribution.

Table 1 Input Variable

Variable	Distribution	Min	Max
E_{kob}	TGAU	0.05 x 30366e3	0.85 x 30366e3
$E_{_}$	TGAU	0.05 x 33e6	0.85 x 33e6
$q_{_}$	TGAU	0.05 x 13.64	0.85 x 13.64
$h_{_}$	TRIA	0.35	0.45

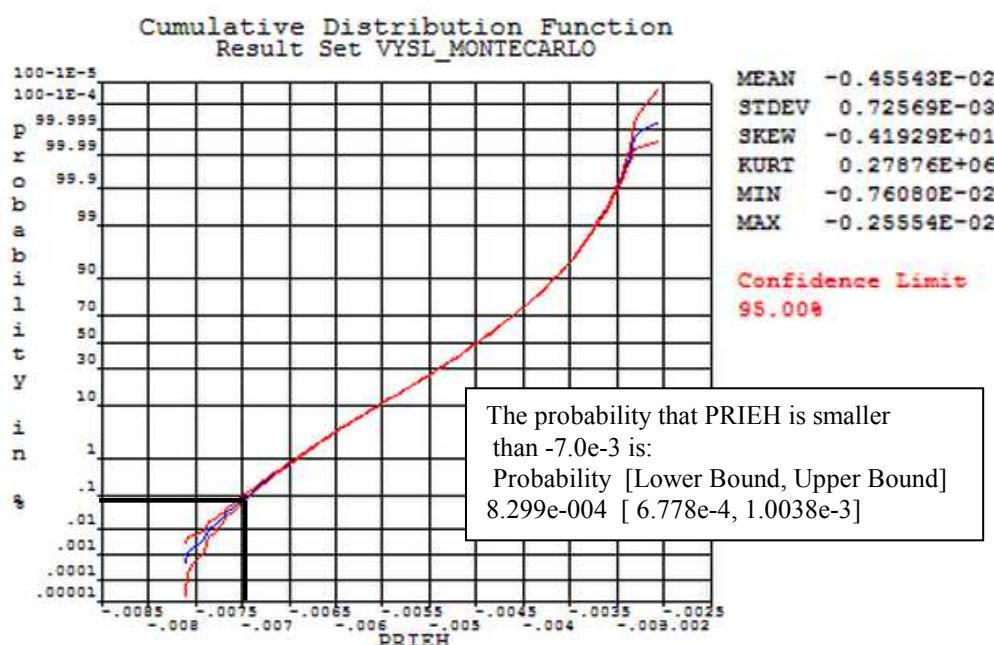


Fig.7 Cumulative distribution function of max. deflection PRIEH

According to the CDF - Cumulative Distribution Function (Fig. 7) we can determine probability of the corresponding parameter PRIEH (the maximum value of deflection). The output shows the probability (Fig. 7) that max deflection is less than -0.007 m, representing that the design is at 8.3e-2 (0.083 %) unreliable.

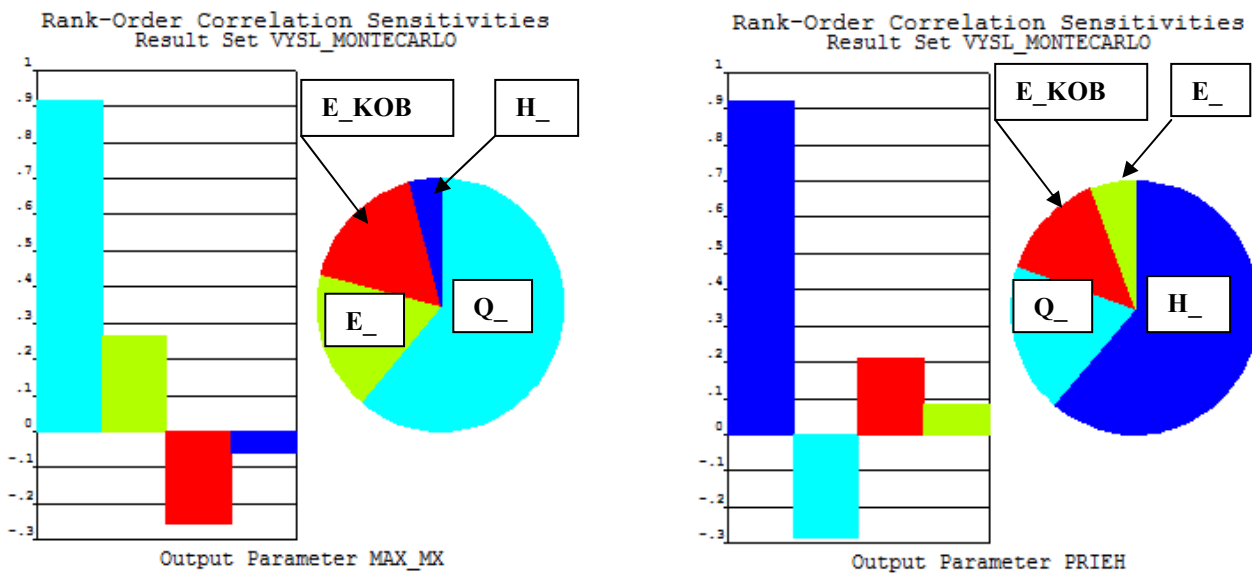


Fig. 8 Rank-order correlation sensitivities of output variable MaX_MX and PRIEH

Sensitivity analysis (Fig. 8) showed that the input parameter E_{-} (module of elasticity) most affected on the output PRIEH-deflection of the plates and parameter Q_{-} (uniformly distributed load) on the output parameter Max_Mx (specific bending moment).

Summary

The aim of this analysis was to determine the probability of failure of structures, and then to determine its reliability depending on the input parameters. In our case, there has been a failure 0.0366 (see Fig.7), when exceeding the limit deflection -0.007 m. The simulation method Monte Carlo was used in program ANSYS. The 120500 simulations were calculated in the time 432000 sec. The probabilistic analysis gives us more complex information than the deterministic analysis.

Acknowledgements

This contribution is the result of the research supported by the grant from Grant Agency of VEGA in Slovak republic No. 1/0480/13, No. 1/1186/12.

References

- [1] P. Marek, J. Brozzetti, M. Gustar, Probabilistic Assessment of Structures Using Monte Carlo Simulation Background, Exercises and Software, ITAM CAS, Prague, Czech Republic, 2003.
- [2] J. Kralik, Reliability analysis of structures using stochastic finite element method. Edition of scientific papers, Vol. 77, STU Bratislava, 2009.
- [3] S. Kmet, M. Tomko, J. Brda, Time-dependent analysis of cable trusses Part II. Simulation-based reliability assessment. Structural Engineering and Mechanics. 38 (2011) 171-193.
- [4] A. Haldar, S. Mahadevan, Probability, reliability and Statistical Methods in Engineering Design. John Wiley&Sons. New York, 2000.

Strain-Life Approach: Application for Fatigue Design of Ship Superstructure Critical Detail

PETINOV Sergei^{1,a*}

¹St.Petersburg Polytechnic University, 29 Polytechnicheskaya Str., 195251 St.Petersburg, Russia

^asergei.petinov@gmail.com

Keywords: strain-life format of fatigue, fatigue damage accumulation, FEA modeling of structures, fatigue of ship structures, expansion joints in superstructures

Abstract. Strain-Life approach to fatigue analysis of structures being developed since early 1960s recently was considered applicable in Civil Engineering, in particular, for fatigue evaluation of bridge structure with integrated abutments.

To exemplify the approach and display the problems of its implementation in fatigue design, in-service reliability of structures, an example of fatigue design of a ship superstructure critical detail is presented. The detail is located at expansion joint ending in the superstructure which is frequently applied in ship design aimed at reducing stresses in a long superstructure caused by the general bending deformation of ship hull. Specific of the detail is the high local stress concentration which may result in fatigue damage menacing integrity of the ship hull.

In the example of fatigue design of the expansion joint the modified «Strain-Life» criterion for fatigue of material is applied along with empirical relationship providing evaluation of the local strain. This version of the approach allows assessment of fatigue properties of the detail without utilizing Neuber's formula and presenting the loading history in the block-type format. The results of analysis allowed selection of the expansion joint detail of the superstructure geometry and construction procedure at a shipyard providing necessary reliability.

Introduction

The current S-N (Stress-Life) approaches to fatigue analysis and design of structures are based on assumption that material of structure deforms elastically in service loading conditions. Respectively, the design S-N curves are limited from the left side by the number of cycles prior to failure equal to $N = 10^4$, which approximately corresponds to the stress amplitude (nominal!) equal to the yield stress. The mechanics of fatigue damage of a welded joint material is implied (not definitely specified) as built into the design S-N curves based on analysis of results of fatigue testing of the typified welded joints.

Considering effects of stress concentration in critical locations of structure within the Hot-spot stress approach or the Notch-stress approach [1,2] by multiplying the nominal stress range by the respective stress concentration factors or calculation the respective stress, again, follows the presumable linear elastic material behavior in critical locations. Referring the characteristic stress to the classed S-N curve makes rather an illusion of proper assessment of damage; in fact, it means evaluation of the damage with uncertainty, somewhat on the conservative side.

In the high-stress range of the service loading the input of this over-estimation of fatigue damage in the total sum typically is insignificant due to stochastic properties of excitation. At the moderate service loading, in the high-cycle regime, which provides the predominant damage, the above approaches neglecting the effects of material microplasticity at critical locations, again, over-estimate the damage.

What is important, fatigue tests of typified welded joins are being carried up at cyclic loading with positive load ratio (ratio of the minimum to the maximum load in the cycle) to avoid buckling in the compressive part of the load cycle. This means the design S-N curves are related to the mentioned type of loading. Specific of the procedure is the termination of test when initiated and grow-

ing fatigue crack notably affects the specimen compliance preceding complete fracture. Respectively, when applied to assessment of fatigue resistance of a structural detail, the state of damage, corresponding crack size occurs uncertain.

The Strain-Life approach considered in the present rules as optional may be regarded a more accurate technique for fatigue analysis and design of structures by the mentioned reasons. The approach includes an appropriate Strain-Life criterion for fatigue failure of material and it needs in evaluation of the local (elastic-plastic) strain at a notch under applied nominal stress to enter the criterion. The local strain can be obtained by using the elastic-plastic cyclic finite-element software; however, even with the present facilities it appears a laborious and timely procedure when a service range of nominal stress should be accounted.

Strain-Life Approach

The procedure application for the purposes of fatigue design is illustrated in the below in case of a ship superstructure critical detail. The approach is based on application of a Strain-Life relationship for fatigue failure material criterion. As appropriate for the present analysis, the Coffin-Tavernelli's version [3] of the criterion is selected:

$$\Delta\varepsilon = \Delta\varepsilon_p + \Delta\varepsilon_e = CN^{-\alpha} + 2\sigma_f/E \quad (1)$$

where $\Delta\varepsilon_p$ is the plastic strain range, C and α are the empirical parameters, material constants, $\Delta\varepsilon_e$ is the elastic strain component, approximately defined in Eq. 1 by σ_f , conventional fatigue limit stress at fully reversed loading; E is the modulus of elasticity.

Criterion (Eq. 1) should be corrected, namely, its «elastic» component, to consider effects of stress concentration and of service loading irregularity. Effect of stress concentration can be reflected by introducing multiplier K_t/K_f , where K_t is the theoretical stress concentration factor, K_f is the fatigue notch factor. The latter may be estimated by using Peterson's formula [4]: $K_f = 1 + (K_t - 1)/(1 + g/r)$, in which r is the notch root radius, g is the «structural parameter», around the size (depth) of the initial crack. For the hull steels this parameter may be approximated by $g = 0.38(350/\sigma_u)^{1.16}$, where σ_u is the tensile strength of steel. The service loading irregularity effect, decrease of fatigue limit stress, might be taken into account as recommended in [5] according which the «cut-off» fatigue limit stress, minimum damaging stress, drops down; correction factor is $\omega=0.55$. Consequently, (1) is rewritten as:

$$N(\Delta\varepsilon) = (CE/\sigma_f)^{1/\alpha} (E\Delta\varepsilon/\sigma_f - 2\omega K_t/K_f)^{-1/\alpha}. \quad (2)$$

Criterion (Eq. 2), as well as (Eq. 1), provides conservative evaluation of fatigue properties of a structure, since it underestimates the fatigue lives approximately, in the range of $10^4 < N < 10^6$ cycles, as indicated Manson in discussion of [3].

The following step in the procedure is the evaluation of the elastic-plastic cyclic strain, $\Delta\varepsilon$, at a critical location. Neither the inelastic finite-element analysis facilities nor the Neuber's heuristic formula-based approach [6] are used here. Instead, **conditional** generalized cyclic diagram of steel under the scope is applied. Such diagrams for hull steels were derived based on the parametric experimental studies of local strain evolution at varied stress concentration, nominal stress amplitude and mean stress [6]. Analysis of test results revealed similitude of material cyclic behavior which allowed deriving the cyclic diagrams, strain range at the notch root related to nominal stress range in a structural component:

$$\Delta\varepsilon = (K_t S_n / E) \left(1 + M_s(r, t) F(\sigma_m) (AK_t S_n / S_c - 1)^\beta \right) \quad (3)$$

where S_n is the nominal stress range, S_c is the cyclic proportionality stress range, A and β are empirical parameters, $M_s(r,t)$ is the correction for effects of the notch size, the stress state at the notch root, $M_s(r,t) = M_0 / \left(1 + (a/t)^s (r/t)^q\right)$; here t is the thickness of the notched component, r is the notch root radius, M_0 , a , s and q are empirical parameters; $F(\sigma_m)$ is the correction for the influence of mean stress on the plastic strain range, $F(\sigma_m) \approx 1 + B\sigma_m / (K_t S_n)$, where σ_m is the nominal mean stress, B it an empirical parameter.

Eq. 3 provides evaluation of the local strain at a notch root in a structural detail; the limiting condition is $r/t \geq 1.0$, required in analysis of structural details with holes and openings. Application of Eq. 3, as seen, needs only in the elastic stress analysis (FEA) to obtain the stress concentration factor («theoretical»). Further, fatigue damage under random loading histories based on the linear damage summation is found as [6]:

$$D = N_s (\sigma_f / CE)^{1/\alpha} \int p(S_n) (E \Delta \epsilon(S_n) / \sigma_f - 2\omega K_t / K_f)^{1/\alpha} dS_n \quad (4)$$

where $p(S_n)$ is the probability density of the long-term (representative of the life-long service) nominal stress distribution, N_s is the service number of load cycles required by appropriate rules for design.

It should be noted that the criterion (Eq. 1) may be replaced in Eq. 4 e.g., by the Manson's criterion, if appropriate [10].

Application of the Approach

The above approach application is illustrated in example of fatigue design of a fast ship superstructure detail. The detail is the superstructure side at the expansion joint cut, close to the main deck, Fig. 1. The long superstructures are frequently subdivided into several parts to reduce the stress caused by the hull bending at seaway in superstructure and, respectively, save its weight.

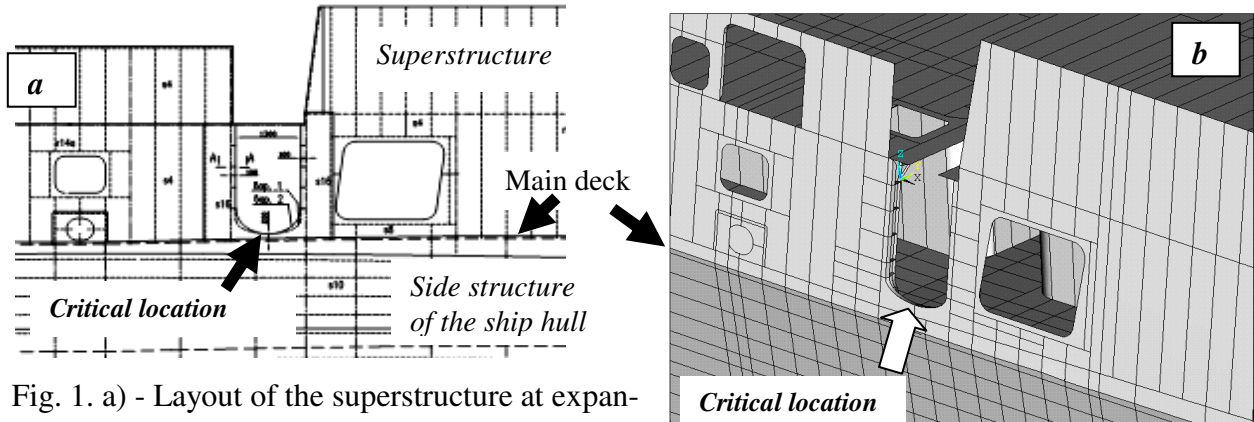


Fig. 1. a) - Layout of the superstructure at expansion joint cut; b) - geometrical model of the critical area

In design procedures of ship and marine structures the loading history is presented by the continuous long-term probability distribution function of wave loading through the service life [8], [9]. In the design stage the loading history may be estimated using a simplified approach: via calculation of ship hull (girder) bending moments (in vertical and horizontal planes) in seaway given in the rules and characterized by the recommended probability to exceed. The stress at the critical location shown in Fig. 1 is caused by the hull bending in vertical plane and hull bending in horizontal plane due to three-dimensional shape of the wave systems in seaway.

The stress in the flange at the cut ending is magnified by the cut shape; respective stress concentration factors must be calculated by the finite-element method. The local FE model was designed as a fragment of representative block which included part of the ship hull and superstructure extended from the considered location to the fore and aft parts where another cuts in the superstructure are located. The latter is shown in Fig. 2. Apart from that, the FE mesh was completed with rod elements at the flange corner so that the stress normal to the cut profile would be obtained.

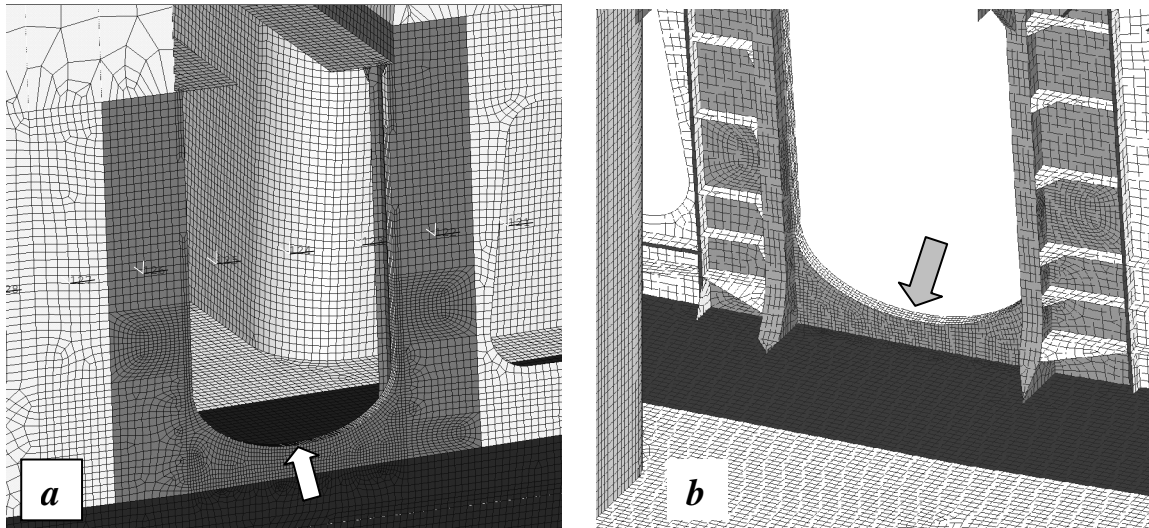


Fig. 2 FE model of the superstructure side: a) – view from outside; b) – as seen from inside the superstructure. Arrow shows the critical location

Girder bending moments in vertical and horizontal planes were applied to the global model of the representative block to model behavior of the superstructure blocks, their «opposite bending» induced by the hull bending in vertical plane.

In general, participation of the hull shear deformation in local normal stress concentration must be considered. However, in the case of semi-circular or semi-elliptical shape of the cut lower part profile the maximum stresses due to bending and shear are not superimposed [4,6]. This allowed considering the bending modes only in fatigue assessment of the detail.

The bending moments were used as defined in the rules [7]. Bending moment range in the vertical plane, for the mid-part of the hull:

$$\Delta M_v = 0.30 k_v B L^2 C_w (C_b + 0.257) \quad \text{kNm}, \quad (5)$$

where k_v is the moment distribution factor depending on the ship's speed; in this analysis $k_v = 1$ for the central part of the hull and moderate speed, L, B are ship length and breadth, respectively, $C_w = 10.75 - (3 - 0.01L)^{1.5}$ is the «effective» wave height defined by the bending moment at exceedance $Q = 10^{-8}$, C_b is the block coefficient.

The bending moment range in horizontal plane, for the mid-part of the hull:

$$\Delta M_h = 0.44 L^{2.25} (d + 0.30B) C_b (1 - \cos(2\pi x/L)) \quad \text{kNm}, \quad (6)$$

where d is the draught in considered load condition.

The respective nominal stress ranges are: due to bending in vertical plane - $S_v = \Delta M_v / W_{min}$, where W_{min} is the section modulus of the hull upper deck, and due to bending in horizontal plane: $S_h = \Delta M_h / W_h$; W_h is the section modulus of the ship side structure. Since these modes of bending

at any time moment differ by a random phase angle, the total combined nominal stress at the detail location is obtained as the sum of random correlated variables [8]:

$$S_{com} = S_v (1 + (S_h / S_v)^2 + 2 \cdot \rho_{vh} (S_h / S_v))^{1/2} \quad (7)$$

where $\rho_{vh} = 0.1$ is the average correlation factor of vertical and horizontal bending moments [8].

The long-term probability distributions of bending moments and related stresses are approximated by the two-parameter Weibull formula [7,8]:

$$Q(S > S_1) = \exp(-(S_1 / a_s)^k) \quad (8)$$

which is read as the probability to exceed a stress range S_1 ; a_s, k are the scale and shape parameters of the distribution, respectively.

Scale and shape parameters of the Weibull nominal stress distributions (Eq. 8) for the ship under the scope: $a_s = S_{max} / (\ln N_s)^{1/k}$, $N_s = \eta \cdot 10^8 = 0.47 \cdot 10^8$, is the intended service life load cycles, where $\eta = 0.47$ is the «usage» factor, the fraction of service life spent on a seaway. The shape parameter, according [7], is $k = 2.21 - 0.54 \lg L = 1.081$, L is the ship length. The wave-induced bending moments and nominal stress characteristics at the detail location are given in Table 1 (probability of exceedance is $Q = 1/N_s = 2.1 \cdot 10^{-8}$).

Table 1 Bending moments and nominal stress characteristics at the critical location

Plane of bending	Bending moment range, kNm	W_{min}, W_h, m^3	Nominal stress range, MPa	Scale parameter, a_s , MPa
Vertical	$4.719 \cdot 10^5$	1.9961	236.4	16.594
Horizontal	$2.098 \cdot 10^5$	2.8750	73.0	5.124
Combined stress, Eq. 7	-	-	254.6	17.872

It was assumed in the analysis that material of the welded joint of the superstructure side plating and the flange was uniform, on condition the due mechanical finishing of the weld material were provided (the shipyard followed the recommendation). Material, higher strength steel of the 390 Grade ($\sigma_y = 390$ MPa); the fatigue resistance is characterized by the fatigue limit stress $\sigma_f = 112$ MPa (amplitude), fully reversed axial cyclic loading. The parameters of the criterion (Eq. 2) are: $C = 0.400$, $\alpha = 0.653$. The Eq. 3 parameters, for the steel under the scope: $A = 1.25$ and $\beta = 1.20$; $M_0 = 0.107$, $a = 0.203$, $s = 0.25$ and $q = 1.20$; mean stress was not considered in analysis since for the ship considered it is typically insignificant; consequently, $F(\sigma_m) = 1$.

The results of analysis for the versions of the detail geometry are summarized in Table 2.

Table 2 Results of fatigue analysis of the expansion joint detail

Shape version	2	3	4	5	6
L^* , width, mm	1300	1300	1400	1300	1400
H, minor semi-axis	550	425	425	425	425
Flange, mm	80x18	80x18	80x18	80x30	80x30
$K_t^{(com)}$	2.28	2.11	1.85	2.00	1.82
D, damage index	1.128	0.798	0.300	0.530	0.288

As may be seen, the versions of geometry 4 and 6, specific by elongated semi-elliptic shape, provide favorable safety margin for the structure. Respectively, the analysis allowed the shipyard choosing the necessary geometry of the detail and the proper finishing of the welded joint of the side shell and flange.

Conclusion

The Strain-life criterion-based procedure of fatigue design provides considering elastic-plastic behavior of material at a critical location in structure and effects of stress concentration in the whole range of service stress. Also, exhaustion of fatigue resistance according the procedure means fatigue crack initiation within the local stress evaluation area. Although this is not precise definition of the crack size, the damage assessment in the sufficiently fine FE model of a critical location may provide the necessary clarification [10].

Acknowledgement

Mr. A. Ridiger's assistance in design of the FE models is acknowledged.

References

- [1] A. Hobbacher, Recommendations for Fatigue Design of Welded Joints and Components, IIW Doc. XIII-2151r1-07 / XV-1254r1-07 (2007).
- [2] W. Fricke, Guideline for the Fatigue Assessment by Notch Stress Analysis for Welded Structures, IIW-Doc. XIII-2240r1-08/XV-1289r1-08 (2008).
- [3] L.F. Coffin, J.F. Tavernelli, Experimental Support for Generalized Equation Predicting Low-Cycle Fatigue. Trans. ASME, Ser. D. 4 (1962) p.533.
- [4] R.E. Peterson, Stress Concentration Factors, A Handbook, J.Wiley & Sons, Hoboken, NJ, USA (1989).
- [5] EUROCODE 3: Design of steel structures – Part 1-9: Fatigue (EN 1993-1-9-2005) BSI, June (2006).
- [6] S.V. Petinov, Fatigue Analysis of Ship Structures. Backbone Publishing Co., Fair Lawn, NJ, USA (2003).
- [7] Det Norske Veritas: Fatigue Assessment of Ship Structures. Classification Notes № 30.7. Hovik, Norway (2010).
- [8] E.H. Cramer, et al. Fatigue Design of Ship Structures, Proceedings, PRADS-95. Seoul, Korea, pp. 2.898-2.909 (1995).
- [9] S. S. Manson, U. Muralidharan, A Modified Universal Slopes Equation for Estimation of Fatigue Characteristics of Metals. Journal of Eng. Math. and Tech. ASME, 110 (1988).
- [10] S.V. Petinov, R.V. Guchinsky, Fatigue of a Fillet-welded Joint Assessment by the FEA Simulation of Damage Accumulation. Magazine of Civil Engineering. 22 (2011) 5-9.

Simulating Couette Flow Using the Meshless Local Petrov-Galerkin Method

MUŽÍK Juraj^{1,a*}

¹University of Zilina, Univerzitna 8215/1, 010 26 Zilina, Slovak Republic

^ajuraj.muzik@fstav.uniza.sk

Keywords: meshless analysis, meshless Petrov-Galerkin method, Navier-Stokes equation

Abstract. The paper deals with use of the meshless method for incompressible fluid flow analysis. There are many formulations of the meshless methods. The article presents the Meshless Local Petrov-Galerkin method (MLPG) – local weak formulation of the Navier-Stokes equations. The shape function construction is the crucial part of the meshless numerical analysis in the construction of shape functions. The article presents the radial point interpolation method (RPIM) for the shape functions construction.

Introduction

Incompressible Navier-Stokes flow in two dimensions is one of the several major problems in fluid mechanics that have been extensively studied both theoretically and numerically. In general, the formulation of incompressible Navier-Stokes equations using primitive variables is often used, but it has limitation in approximating the velocity and pressure. The meshless Local Petrov-Galerkin method (MLPG) is truly meshless method which requires no elements or global background mesh, for either interpolation or integration purposes. The first article applying MLPG method to compute convection-diffusion and incompressible flow was by Lin and Atluri [1]. In their work, two kinds of upwind schemes were constructed to overcome oscillations produced by convection term. They applied the upwind schemes to solve incompressible flow problem based on primitive variables formulation and added the perturbation term to the continuity equation to satisfy Babuška-Brezzi condition. But there still persists the problem of perturbation parameter determination for high Reynolds number problems. The present paper focuses on the MLPG primitive variable method using fractional step method to achieve velocity-pressure decoupling to solve incompressible viscous flow [2].

Meshless Shape Function Formulation - Radial Point Interpolation

Using radial basis functions (RBF) is one of the best solutions to construct the meshless shape function. Multi-quadratic RBF function is one of the most popular radial function [3] and is defined as

$$R_i(\mathbf{X}) = (r_i^2 + \varepsilon^2)^q \quad (1)$$

where r_i is the distance between the desired point (\mathbf{X}) and the field node i (\mathbf{X}_i) defined simply as 2D euclidean distance. Constants ε and q in the Eq. 1 are constants that depend on the type of problem. The RPIM interpolation augmented with polynomials can be written as

$$u(\mathbf{X}) = \sum_{i=1}^n R_i(\mathbf{X})a_i + \sum_{j=1}^m p_j(\mathbf{X})b_j = \mathbf{R}^T(\mathbf{X})\mathbf{a} + \mathbf{p}^T(\mathbf{X})\mathbf{b} \quad (2)$$

where $R_i(\mathbf{X})$ is the radial basis function (RBF), n is the number of RBFs, $p_j(\mathbf{X})$ is polynomial basis function, m is number of polynomial basis function, a_i and b_j are interpolation coefficients. In order

to determine a_i and b_j a support domain is formed for the point of interest at \mathbf{X} , and n field nodes are included in the support domain. Interpolation coefficients can be determined by enforcing the Eq. 2 to be satisfied at these n nodes surrounding the point of interest \mathbf{X} . This leads to n linear equations, one for each node. The equation system in matrix form can be expressed as

$$\mathbf{U}_s = \mathbf{R}\mathbf{a} + \mathbf{P}_m\mathbf{b} \quad (3)$$

where \mathbf{U}_s is the vector of displacement function values, the RBF moment matrix is and the \mathbf{P}_m is polynomial moment matrix. Eq. 3 can be subsequently rewritten as

$$u(\mathbf{X}) = \mathbf{R}^T(\mathbf{X})\mathbf{a} + \mathbf{p}^T(\mathbf{X})\mathbf{b} = [\mathbf{R}^T(\mathbf{X}) \quad \mathbf{p}^T(\mathbf{X})] \begin{bmatrix} \mathbf{a} \\ \mathbf{b} \end{bmatrix} \quad (4)$$

and following set of equations is used to obtain unknown vectors of parameters a, b

$$\tilde{\mathbf{U}}_s = \begin{bmatrix} \mathbf{U}_s \\ \mathbf{0} \end{bmatrix} = \begin{bmatrix} \mathbf{R} & \mathbf{P}_m \\ \mathbf{P}_m^T & \mathbf{0} \end{bmatrix} \begin{bmatrix} \mathbf{a} \\ \mathbf{b} \end{bmatrix} = \mathbf{G} \begin{bmatrix} \mathbf{a} \\ \mathbf{b} \end{bmatrix}. \quad (5)$$

Using Eq. 5 we can obtain

$$u(\mathbf{X}) = [\mathbf{R}^T(\mathbf{X}) \quad \mathbf{p}^T(\mathbf{X})] \mathbf{G}^{-1} \tilde{\mathbf{U}}_s = \tilde{\Phi}^T(\mathbf{X}) \tilde{\mathbf{U}}_s \quad (6)$$

and finally the RPIM shape functions corresponding to the nodal velocity vector $\Phi(\mathbf{X})$ are obtained as

$$\Phi^T(\mathbf{X}) = [\phi_1(\mathbf{X}) \quad \phi_2(\mathbf{X}) \quad \dots \quad \phi_n(\mathbf{X})]. \quad (7)$$

Then the velocity field approximation can be written using the RPIM shape functions and nodal displacements

$$u(\mathbf{X}) = \Phi^T(\mathbf{X}) \mathbf{U}_s = \sum_{i=1}^n \phi_i u_i \quad (8)$$

and the I -th derivatives of velocity field $u(\mathbf{X})$ are easily obtained as

$$\Phi^{(I)}(\mathbf{X}) = \left[\frac{\partial^I \mathbf{R}^T(\mathbf{X})}{\partial \mathbf{X}^I} \quad \frac{\partial^I \mathbf{p}^T(\mathbf{X})}{\partial \mathbf{X}^I} \right] \mathbf{G}^{-1}. \quad (9)$$

Note that \mathbf{G}^{-1} usually exists for arbitrarily scattered nodes. Therefore, there is no singularity problem in the RPIM as a small number of nodes are used in the local support domain [4].

Governing Equations and Fractional-Step Algorithm

The governing equations for unsteady incompressible viscous fluid flow are Navier-Stokes equations with the continuity equation in the convection term [2,5]. This equation can be written as

$$\frac{\partial u}{\partial t} = \frac{1}{Re} \left(\frac{\partial^2 u}{\partial x^2} + \frac{\partial^2 u}{\partial y^2} \right) - u \frac{\partial u}{\partial x} - v \frac{\partial u}{\partial y} - \frac{\partial p}{\partial x} + f_x \quad (10)$$

$$\frac{\partial v}{\partial t} = \frac{1}{Re} \left(\frac{\partial^2 v}{\partial x^2} + \frac{\partial^2 v}{\partial y^2} \right) - u \frac{\partial v}{\partial x} - v \frac{\partial v}{\partial y} - \frac{\partial p}{\partial y} + f_y \quad (11)$$

$$\frac{\partial u}{\partial x} + \frac{\partial v}{\partial y} = 0 \quad (12)$$

where u and v are the velocities in x and y direction respectively, p is the pressure, f_x and f_y are the body forces, Re is Reynolds number. Eq. 10 and Eq. 11 are the momentum equations and Eq. 12 is the continuity equation. A fractional-step algorithm is used to solve this problem (see [2,3]). The time derivative of the velocity vector in a momentum Eq. 10 and Eq. 11 can be replaced with a difference approximation and following relation is obtained

$$\frac{u^{n+1} - u^n}{\Delta t} = \frac{1}{Re} \left(\frac{\partial^2 u^n}{\partial x^2} + \frac{\partial^2 u^n}{\partial y^2} \right) - u^n \frac{\partial u^n}{\partial x} - v^n \frac{\partial u^n}{\partial y} - \frac{\partial p^n}{\partial x} + f_x^n \quad (13)$$

$$u^{n+1} = u^n + \Delta t \left[\frac{1}{Re} \left(\frac{\partial^2 u^n}{\partial x^2} + \frac{\partial^2 u^n}{\partial y^2} \right) - u^n \frac{\partial u^n}{\partial x} - v^n \frac{\partial u^n}{\partial y} + f_x^n \right] - \Delta t \frac{\partial p^n}{\partial x} \quad (14)$$

and

$$\frac{v^{n+1} - v^n}{\Delta t} = \frac{1}{Re} \left(\frac{\partial^2 v^n}{\partial x^2} + \frac{\partial^2 v^n}{\partial y^2} \right) - u^n \frac{\partial v^n}{\partial x} - v^n \frac{\partial v^n}{\partial y} - \frac{\partial p^n}{\partial y} + f_y^n \quad (15)$$

$$v^{n+1} = v^n + \Delta t \left[\frac{1}{Re} \left(\frac{\partial^2 v^n}{\partial x^2} + \frac{\partial^2 v^n}{\partial y^2} \right) - u^n \frac{\partial v^n}{\partial x} - v^n \frac{\partial v^n}{\partial y} + f_y^n \right] - \Delta t \frac{\partial p^n}{\partial y} \quad (16)$$

where upper indexes n and $n+1$ indicate the time step. Eq. 14 and Eq. 16 are explicit formula for convection and viscous terms and the implicit one for a pressure term. To simplify Eq. 14 and Eq. 16 we used the fractional step approximation (see e.g. [2]). According this approximation the intermediate velocities \tilde{u}^n and \tilde{v} are computed using simplified momentum equation

$$\tilde{u}^n = u^n + \Delta t \left[\frac{1}{Re} \left(\frac{\partial^2 u^n}{\partial x^2} + \frac{\partial^2 u^n}{\partial y^2} \right) - u^n \frac{\partial u^n}{\partial x} - v^n \frac{\partial u^n}{\partial y} + f_x^n \right] \quad (17)$$

$$\tilde{v}^n = v^n + \Delta t \left[\frac{1}{Re} \left(\frac{\partial^2 v^n}{\partial x^2} + \frac{\partial^2 v^n}{\partial y^2} \right) - u^n \frac{\partial v^n}{\partial x} - v^n \frac{\partial v^n}{\partial y} + f_y^n \right]. \quad (18)$$

When we compare Eq. 14, 16 and Eq. 17, 18 we get

$$u^{n+1} = \tilde{u}^n - \Delta t \frac{\partial p^n}{\partial x} \quad (19)$$

$$v^{n+1} = \tilde{v}^n - \Delta t \frac{\partial p^n}{\partial y}. \quad (20)$$

The intermediate velocities \tilde{u}^n and \tilde{v}^n does not satisfy the continuity Eq. 12. The velocities u^{n+1} and v^{n+1} must satisfy the continuity equation which implies

$$\frac{\partial^2 p^n}{\partial x^2} + \frac{\partial^2 p^n}{\partial y^2} = \frac{1}{\Delta t} \left(\frac{\partial \tilde{u}^n}{\partial x} + \frac{\partial \tilde{v}^n}{\partial y} \right) \quad (21)$$

Eq. 21 is the Poisson's equation with non-zero source term [2]. The Eq. 19 and Eq. 20 are solved explicitly by updating nodal values for velocities. The pressure Eq. 21 is solved using MLPG over problem domain with boundary conditions $p^n|_{\Gamma_u} = p^{-n}$ and $\partial p^n/\partial n = q^{-n}$.

The MLPG Method and the Local Weak Formulation

The meshless Local Petrov-Galerkin method (MLPG) is truly meshless method which requires no elements or global background mesh, for either interpolation or integration purposes. In MLPG the problem domain is represented by a set of arbitrarily distributed nodes. The weighted residual method is used to create the discrete system equation by integrating the governing equation over local quadrature domains. The quadrature domain can be arbitrary in theory, but very simple regularly shaped domain, such as rectangles for 2D problems are often used for ease of implementation [6]. A generalized local weak form of the pressure Poisson Eq. 21 defined over local sub-domain Ω_s can be written as

$$\int_{\Omega_s} \left[\left(\frac{\partial^2 p^n}{\partial x^2} + \frac{\partial^2 p^n}{\partial y^2} \right) - \frac{1}{\Delta t} \left(\frac{\partial \tilde{u}^n}{\partial x} + \frac{\partial \tilde{v}^n}{\partial y} \right) \right] w d\Omega = 0 \quad (22)$$

where p is the trial function, w is the test function defined as

$$w(r_i) = \begin{cases} 1 - 6r_i^2 + 8r_i^3 - 3r_i^4 & r_i \leq 1 \\ 0 & r_i > 1 \end{cases}; \quad r_i = \frac{\|x - x_i\|}{d_s} \quad (23)$$

where d_s is the size of the local quadrature domain, so it is evident that weighting function value is zero on its boundary. Using the divergence theorem the Eq. 22 has changed to

$$\int_{\Omega_s} \left(\frac{\partial p^n}{\partial x} \frac{\partial w}{\partial x} + \frac{\partial p^n}{\partial y} \frac{\partial w}{\partial y} \right) d\Omega - \int_{\Gamma_{su}} \frac{\partial p^n}{\partial n} w d\Gamma = \int_{\Gamma_{sq}} \bar{q} w d\Gamma - \frac{1}{\Delta t} \int_{\partial\Omega_s} (\tilde{u}^n n_1 w + \tilde{v}^n n_2 w) d\Gamma + \frac{1}{\Delta t} \int_{\Omega_s} \left(\tilde{u}^n \frac{\partial w}{\partial x} + \tilde{v}^n \frac{\partial w}{\partial y} \right) d\Omega \quad (24)$$

Because unknown nodal values of the pressure \mathbf{p} , are constants which can be moved out of the integral the equation, Eq. 24 can be changed to discrete system of linear equations, where global "stiffness" matrix is defined as

$$K_{ij} = \int_{\Omega_s^i} \left(\frac{\partial \varphi_j}{\partial x} \frac{\partial w_i}{\partial x} + \frac{\partial \varphi_j}{\partial y} \frac{\partial w_i}{\partial y} \right) d\Omega - \int_{\Gamma_{su}^i} \frac{\partial \varphi_j}{\partial n} w_i d\Gamma \quad (25)$$

and the right-hand side "load" vector is

$$f_i = \int_{\Gamma_{sq}} \bar{q} w d\Gamma - \frac{1}{\Delta t} \int_{\Gamma_{su}^i} (\tilde{u}^n n_1 w_i + \tilde{v}^n n_2 w_i) d\Gamma - \frac{1}{\Delta t} \int_{\Gamma_{sq}^i} (\tilde{u}^n n_1 w_i + \tilde{v}^n n_2 w_i) d\Gamma + \frac{1}{\Delta t} \int_{\Omega_s^i} \left(\tilde{u}^n \frac{\partial w_i}{\partial x} + \tilde{v}^n \frac{\partial w_i}{\partial y} \right) d\Omega \quad (26)$$

Numerical Example

In this section the MLPG solution of Navier-Stokes equations developed in the previous sections is validated by solving the Couette flow example as a benchmark problem of fluid flow simulation [7]. The problem domain (see Fig.1) is formed by regular nodal model with 41x81 nodes and nodal spacing of $n_s = 0.025$.

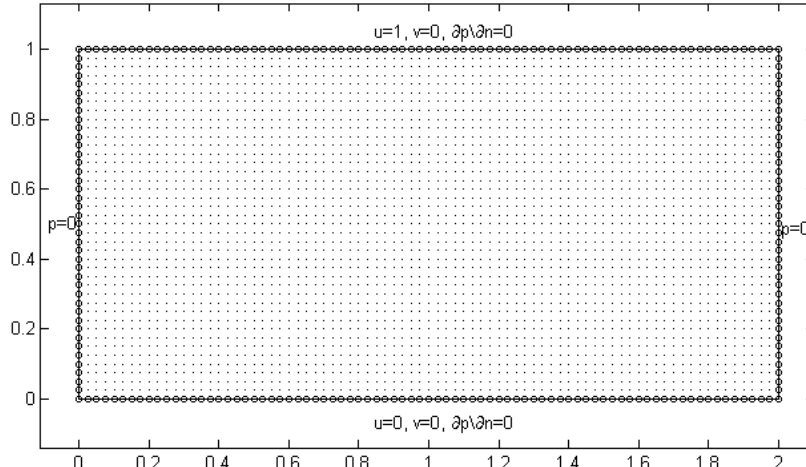


Fig. 1 Network and boundary conditions for Couette flow

The plain Couette flow is defined as viscous flow between two parallel plates with zero external pressure gradient. The bottom plate is stationary and the upper plate is moving with constant velocity and the distance between plates $h = 1$ (see Fig.1). The exact solution of the unsteady Couette flow is often reported as

$$u(y, t) = y + \frac{2}{\pi} \sum_{k=1}^{\infty} \frac{(-1)^k}{k} \sin(k\pi y) e^{-k^2\pi^2 t\nu} \quad (27)$$

where ν is the kinematic viscosity of fluid [8]. Rectangular computational domain (see Fig. 1) has been used to solve Couette flow. Because the laminar Couette flow is valid only for very low Reynolds' number, our computations have been carried out with $Re = 1$. The time step has been constant $\Delta t = 0.0001$ [3].

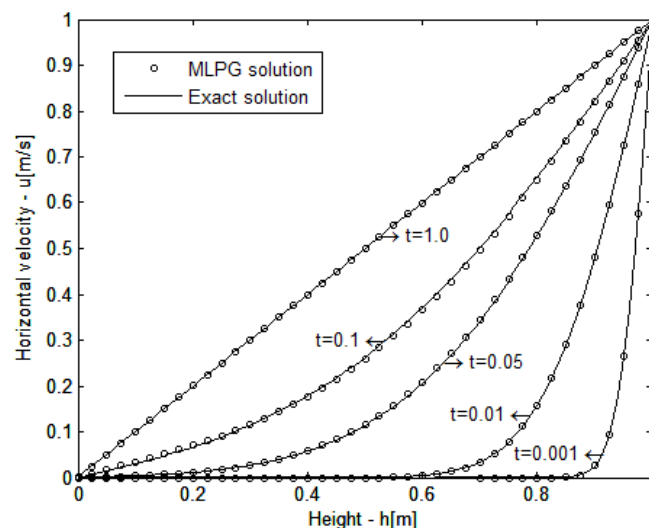


Fig. 2 Comparison of results for Couette flow

Horizontal velocity distribution at various time intervals has been compared with the corresponding exact solution according Eq. 27 and presented in Fig. 2.

Conclusions

In this article, a numerical algorithm using the Meshless Local Petrov-Galerkin (MLPG) method for the incompressible Navier-Stokes equations is demonstrated. To deal with convection term, the fractional step method was adopted and the set of recurrent equations was derived for time stepping procedure. The ability of the MLPG code to solve fluid dynamics problems was presented by solving Couette flow problem with reasonable accuracy when compared to exact solution.

Acknowledgement

This contribution is the result of the project supported by Scientific Grant Agency of Slovak Republic (VEGA) No. 1-0789-12.

References

- [1] H. Lin, S.N. Atluri, The Meshless Local Petrov-Galerkin (MLPG) Method for Solving Incompressible Navier-Stokes Equations, Computer Modeling in Engineering & Sciences 2 (2001) 117–142.
- [2] C. Sataprahma, A. Luadsonga, The Meshless Local Petrov-Galerkin method for simulating unsteady incompressible fluid flow. Journal of the Egyptian Mathematical Society, Available online 5 December 2013.
- [3] K. Kovarik, J. Muzik, M.S. Mahmood, A meshless solution of two-dimensional unsteady flow. In: Engineering Analysis with Boundary Elements. 36, **5** (2012), 738-743.
- [4] K. Kovarik, A meshless solution of two dimensional density-driven groundwater flow. Boundary elements and other mesh reduction methods XXXIII. – Southampton, pp. 253-264, WIT Press, 2011.
- [5] F. Schlosser, J. Sramek, Deformation parameters of the asphalt mixtures. In: Materials, methods & technologies : journal of international scientific publications, 7, **1** (2013), 215-224.
- [6] J. Izvoltova, A. Villim, Identification of observations errors by Gauss-Jacobi algorithm [Aplikacia Gauss-Jacobiho algoritmu pri identifikacii chyb merania]. In: Civil and environmental engineering scientific technical journal, 8, **1**, (2012), 13-17.
- [7] K. Kovarik, D. Sitanyiova, S. Masarovicova, Water-engineering construction [Vodohospodarske stavby]. University of Zilina, 2008, 217 p.
- [8] J. Gergisak, J. Sramek, A. Urdova, Dependence of retroreflection of microprismatic sheeting on their cleanliness. Theoretical foundation of civil engineering, XXII Slovak - Polish - Russian Seminar, Žilina, Slovak Republic, Moskva, Izdatel'stvo ASV, 2013, pp. 687-692.

A 2-D Meshless Model for Soil Subsurface Settlement

MUŽÍK Juraj^{1,a*}

¹University of Zilina, Univerzitná 8215/1, 010 26 Zilina, Slovak Republic

^ajuraj.muzik@fstav.uniza.sk

Keywords: meshless methods, numerical methods, meshless local Petrov-Galerkin method, moving least squares, Heaviside step function

Abstract. The paper deals with use of the meshless method for soil subsurface settlement analysis. There are many formulations of the meshless methods. The article presents the Meshless Local Petrov-Galerkin method (MLPG) – local weak formulation of the equilibrium equations. The main difference between meshless methods and the conventional finite element method (FEM) is that meshless shape functions are constructed using randomly scattered set of points without any relation between points. The Heaviside step function is test function used in the meshless implementation presented in the article. Heaviside test function makes weak formulation integral very simple, because only body integral in governing equation is due a body force.

Introduction

In the Local Petrov-Galerkin method, the problem domain is represented by a set of arbitrarily distributed nodes. The weighted residual method is used to create the discrete system equation. The weighted residual method is, of course, in integral form, and a background mesh of cells is still required for the integration. The major idea in MLPG is, however, that the implementation of the integral form of the weighted residual method is confined to a very small local subdomain of a node. This means that the weak form is satisfied at each node in the problem domain in a local integral sense. Therefore, the weak form is integrated over a "local quadrature domain" that is independent of other domains of other nodes. This is made possible by use of the Petrov-Galerkin formulation, in which one has the freedom to choose the weight and trial functions independently.

Shape Functions in Meshless Sense – Moving Least Squares Method (MLS)

The creation of the shape or trial functions is the crucial part of meshless numerical analysis. The moving least squares method (MLS) is used to construct the shape function based on set of scattered nodes. There is no predefined relationship between nodes such as element in finite element analysis.

Consider the task of finding an approximate solution $u^h(x)$, while knowing the true solution, u_a at selected points x_a . Then in a least squares sense minimization of the expression $[u^h(x_a) - u_a]^2$ for each a is the objective. Suppose a polynomial approximation is chosen so that

$$u^h(x) = g_1 + g_2 x + g_3 x^2 + \dots + g_{m+1} x^m. \quad (1)$$

The approximation is then written in matrix form

$$u^h(x) = \mathbf{p}^T(x)\mathbf{g}. \quad (2)$$

Using the above the least squares functional is written with the approximation substituted in for $u^h(x)$

$$J = \frac{1}{2} \sum_{a=1}^n \{u^h(x_a) - u_a\}^2 = \frac{1}{2} \sum_{a=1}^n \{\mathbf{p}^T(x_a)\mathbf{g} - u_a\}^2. \quad (3)$$

Now recall that compact support for each node a is intended. Therefore, the local solution is influenced by the local nodes. Whereas nodes far away have no influence. Hence, each summation term, indexed by a , in the least squares functional is weighted by a weight function w_a , which limits the term's influence to point a and usually several surrounding nodes. Based on this intuition the functional J is modified and becomes a weighted least square functional as follows:

$$J = \frac{1}{2} \sum_{a=1}^n w_a \left\{ \mathbf{P}^T(x_a) \mathbf{g} - u_a \right\}^2. \quad (4)$$

Next, it is necessary to minimize J with respect to each g_i . However, before this operation, it is helpful to first write the functional in matrix form. To this end, the functional J is written as follows:

$$J = \frac{1}{2} (\mathbf{Pg} - \mathbf{u})^T \mathbf{W} (\mathbf{Pg} - \mathbf{u}) \quad (5)$$

where the terms \mathbf{W} are defined as 4th order quartic spline function values with $q = |x-x_a|/\rho_a$

$$w(q) = \begin{cases} 1 - 6q^2 + 8q^3 - 3q^4 & q \leq 1 \\ 0 & q > 1 \end{cases}. \quad (6)$$

The \mathbf{g} vector is k by 1 and the \mathbf{u} vector is n by 1. Now, set $\partial J / \partial g = 0$. This yields the following:

$$(\mathbf{Pg} - \mathbf{u})^T \mathbf{WP} = 0. \quad (7)$$

Transposing the whole equation yields

$$(\mathbf{WP})^T (\mathbf{Pg} - \mathbf{u}) = 0. \quad (8)$$

Multiplying through gives

$$\mathbf{P}^T \mathbf{WPg} - \mathbf{P}^T \mathbf{Wu} = 0 \quad (9)$$

and finally

$$\mathbf{P}^T \mathbf{WPg} = \mathbf{P}^T \mathbf{Wu}. \quad (10)$$

Now define the moment matrix $\mathbf{A} = \mathbf{P}^T \mathbf{WP}$ and $\mathbf{B} = \mathbf{P}^T \mathbf{W}$. Note that \mathbf{A} is k by k and \mathbf{B} is k by n . Using these definitions Eq. 10 becomes

$$\mathbf{Ag} = \mathbf{Bu}. \quad (11)$$

Solve now for the unknown coefficient \mathbf{g}

$$\mathbf{g} = \mathbf{A}^{-1} \mathbf{Bu}. \quad (12)$$

Substitute this into the first part of Eq. 2

$$u^h = \mathbf{P}^T(x) \mathbf{g} = \mathbf{P}^T(x) \mathbf{A}^{-1} \mathbf{Bu}. \quad (13)$$

The approximations u^h are usually written as

$$u^h = \boldsymbol{\phi}^T \mathbf{u} = \sum_{a=1}^n \phi_a u_a . \quad (14)$$

Comparison of Eq. 14 with Eq. 13 reveals that the vector of MLS shape functions is

$$\boldsymbol{\phi}^T = \mathbf{p}^T(x) \mathbf{A}^{-1} \mathbf{B} . \quad (15)$$

Notice that the \mathbf{A} and \mathbf{B} matrices depend on \mathbf{W} . The \mathbf{W} matrix in turn is a function of the x_a and the evaluation point x . Hence every time a new evaluation point x is chosen the matrices \mathbf{A}^{-1} and \mathbf{B} are recomputed to calculate the MLS shape functions based on the Eq. 15.

Weak Formulation of Equilibrium Equations

Consider a solid mechanics boundary problem defined over domain Ω . For a field node I , the governing equation is satisfied using a locally weighted residual method, leading to a weak form equation for this node. The local weighted residual form defined over a local quadrature domain Ω_q bounded by Γ_q is defined as

$$\int_{\Omega_q} W_I (\sigma_{ij,j} + b_i) d\Omega = 0 \quad (16)$$

where W_I is the test function usually centered at node I . Eq. 16 is applied to all the nodes in the domain Ω .

When the local weighted residual formulation rather than the global energy principle is used to create discretized equation system node by node, the compatibility of the shape functions in whole domain is not required. As long as the field approximation is continuous at any point in the local quadrature domain Ω_q , the shape function is differentiable and the resultant integrand is integrable, the solution will exist. So the local weak-form method only requires the local compatibility in the local quadrature domain Ω_q . The first term on the left hand side of the Eq. 16 can be integrated by parts

$$\int_{\Omega_q} W_I \sigma_{ij,j} d\Omega = \int_{\Gamma_q} W_I n_j \sigma_{ij} d\Gamma - \int_{\Omega_q} W_{I,j} \sigma_{ij} d\Omega \quad (17)$$

where n_j is the j^{th} component of the unit outward normal on the boundary. Substituting Eq. 17 back to the Eq. 16 the following form is obtained

$$\int_{\Gamma_q} W_I \sigma_{ij} n_j d\Gamma - \int_{\Omega_q} [W_{I,j} \sigma_{ij} - W_I b_i] d\Omega = 0 . \quad (18)$$

The boundary of the local quadrature domain is composed by three parts $\Gamma_q = \Gamma_{qi} \cup \Gamma_{qu} \cup \Gamma_{qt}$ (Fig. 1) where

- Γ_{qi} is the internal boundary of the quadrature domain, which does not intersect with global boundary Γ ;
- Γ_{qt} is the part of the natural boundary that intersects with the quadrature domain;
- Γ_{qu} is the part of the essential boundary that intersects with quadrature domain.

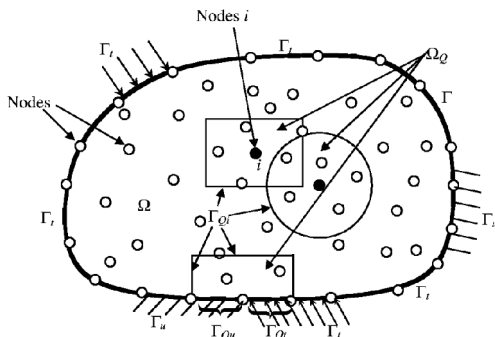


Fig. 1 Domains and their boundaries. Problem domain Γ boundary bounded by its boundaries including essential (displacement) boundary Γ_u , natural (force or free) boundary Γ_t ; quadrature domain of Ω_Q and its boundary including the interior boundary Γ_{Qi} that is located within the problem domain, the essential boundary Γ_{Qu} that intersects with Γ_u and natural boundary Γ_{Qt} that intersects with Γ_t .

Therefore, the Eq. 18 can be rewritten as

$$\int_{\Gamma_{qi}} W_I \sigma_{ij} n_j d\Gamma - \int_{\Gamma_{qu}} W_I \sigma_{ij} n_j d\Gamma - \int_{\Gamma_{qt}} W_I \sigma_{ij} n_j d\Gamma - \int_{\Omega_q} [W_{I,j} \sigma_{ij} - W_I b_i] d\Omega = 0 . \quad (19)$$

For the local quadrature domain located entirely within global domain, there is no intersection between Γ_q and the global boundary Γ . For such a case there is no integral over Γ_{qt} and Γ_{qu} and Eq. 19 is simplified to

$$\int_{\Gamma_{qi}} W_I \sigma_{ij} n_j d\Gamma - \int_{\Omega_q} [W_{I,j} \sigma_{ij} - W_I b_i] d\Omega = 0 . \quad (20)$$

In this local weak form, Eq. 19 and Eq. 20, the Petrov-Galerkin method can be used, in which the trial and test functions are selected from different function spaces. Because the resulting integrals are complicated there is need to simplify them by proper choice of the test function. The promising approach is to use the Heaviside step function as test function. The Heaviside function is defined as value of 1 over the quadrature domain and 0 outside

$$W_I = H_I[\mathbf{x}] = \begin{cases} 0 & \mathbf{x} \notin q \\ 1 & \mathbf{x} \in q \end{cases} . \quad (21)$$

Using the Heaviside step function as test function, the volume integrals in the Eq. 19 and Eq. 20 will vanish except for the body force term, resulting in following formulation

$$\int_{\Gamma_{qi}} \sigma_{ij} n_j d\Gamma - \int_{\Gamma_{qu}} \sigma_{ij} n_j d\Gamma = \int_{\Gamma_{qt}} \sigma_{ij} n_j d\Gamma - \int_{\Omega_q} b_i d\Omega \quad (22)$$

and for the quadrature domain completely within the global domain

$$\int_{\Gamma_{qi}} \sigma_{ij} n_j d\Gamma = - \int_{\Omega_q} b_i d\Omega . \quad (23)$$

Numerical Example of Soil Body Subjected to Strip Loading

The MPLG model has been verified with the computation of the soil foundation problem. Because there is no exact analytical solution of this kind of problem, the model of the embankment slope was calculated using conventional finite element code for geotechnical problems. The soil material was modeled using standard Mohr-Coulomb elasto-plastic model with parameters described in

Table 1. The loading strip is situated in the middle of the surface side with width of 6 [m] and intensity $q = 500$ [kPa]. All displacement boundaries are assumed to be fixed along the normal direction and free along the tangential direction. Regular nodal distribution is used in computation with nodal spacing $n_c = 0.9$ [m]. For displacement comparison the same model was calculated using FEM and the displacement at the depth of 6.5 [m] was compared with meshless solution.

Table 1 Soil parameters used in the numerical example [7]

Soil parameter	Value
γ – volumetric weight	18 [kNm ⁻³]
E – Young modulus	5000 [kPa]
v – Poisson ratio	0.3 [-]
φ – internal friction angle	23 [°]
c – cohesion	10 [kPa]
ψ – dilatation angle	0 [°]

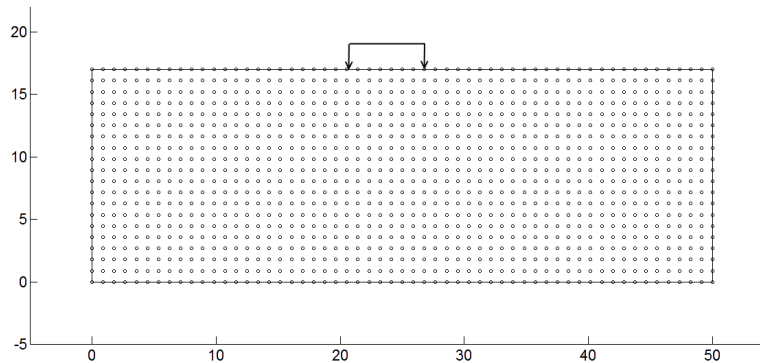


Fig. 2 Soil foundation geometry and dimensions (in meters) with strip load $q = 500$ [kPa]

The process of simulation is typical for any analysis of problems of material nonlinearity. We divide the process into two stages. At the first stage the, the foundation is loaded only by the gravity force of the soil mass. The simulation at this stage is based on linear elasticity with the K_0 procedure to obtain in situ stresses [7]. After in situ stress is obtained the analysis comes to second stage, and strip load is applied incrementally. This loading is divided into 25 loading steps. The main indicator of the MLPG accuracy in elasto-plastic type of analysis is the stress field over the problem domain. The stress field obtained using MLPG was compared with stress field from FEM analysis for same model [8].

The maximum vertical stress component σ_y variation difference over the model domain computed by MLPG and FEM (Plaxis) is 9.8 [%].

The comparison of the displacement results (MLPG vs FEM) which represents the settlement of soil body is plotted in the Fig. 3.

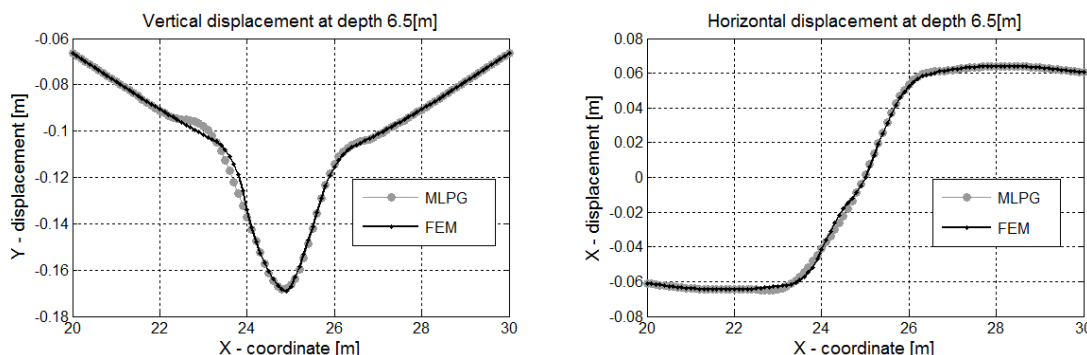


Fig. 3 Comparison of the horizontal and vertical displacements respectively at depth = 6.5 [m]

Conclusion

The described meshless numerical method MLPG represents alternative to the conventional numerical methods most usually used in geotechnical engineering, like FEM. The area of the meshless methods based on local weak form is still under development. The influence of the nodal meshless shape function types (RPIM, MLS), and shape function parameters should be also investigated with the corresponding types of engineering problems. The article also represents the ability of MLPG to solve the geotechnical tasks with accuracy comparable with FEM implementations.

Acknowledgement

This contribution is the result of the project supported by Scientific Grant Agency of Slovak Republic (VEGA) No. 1-0789-12.

References

- [1] K. Kovarik, A meshless solution of two dimensional density-driven groundwater flow. Boundary elements and other mesh reduction methods XXXIII. – Southampton, pp. 253-264, WIT Press, 2011.
- [2] Y.T. Gu, G.R. Liu, A meshless Local Petrov-Galerkin (MLPG) formulation for static and free vibration analyses of thin plates. Computer Modeling in Engineering & Sciences, pp. 463-476, 2001.
- [3] K. Kovarik, Numerical simulation of groundwater flow and pollution transport using the dual reciprocity and RBF method. Komunikacie – Communications, 12 3a (2010) 5-10.
- [4] K. Kovarik, D. Sitanyiova, S. Masarovicova, Water-engineering construction [Vodohospodarske stavby]. University of Zilina, 2008, 217 p.
- [5] J. Izvoltova, A.Villim, Identification of observations errors by Gauss-Jacobi algorithm [Aplikacia Gauss-Jacobiho algoritmu pri identifikacii chyb merania]. In: Civil and environmental engineering, 8 1 (2012) 13-17.
- [6] M. Drusa, D. Lamich, J. Vlcek, S. Heviankova, M. Kyncl, M. Marschalko, I. Yilmaz, T. Bouchal, M. Bendova, D. Kubecova, D. Krcmar, M. Bednarik, Verification of the results of the geotechnical monitoring using finite element method. SGEM 2013, GeoConference on science and technologies in geology, exploration and mining, 13th international multidisciplinary scientific geoconference, 2013, pp. 533-540.
- [7] G. Nguyen, An influence of different values of soils shear strength parameters on the size of spread foundation with an inclined eccentric load. Theoretical foundation of civil engineering, XXI Russian-Slovak-Polish 2012, Warszawa, Politechnika Warszawska, 2012, pp. 451-456.
- [8] M. Drusa, D. Lamich, J. Vlcek, S. Heviankova, M. Kyncl, L. Kais, M. Marschalko, I. Yilmaz, T. Bouchal, M. Bendova, D. Kubecova, D. Krcmar, M. Bednarik: Design limits of reinforced soil structures in difficult geological conditions. SGEM 2013, GeoConference on science and technologies in geology, exploration and mining, 13th international multidisciplinary scientific geoconference, 2013, pp. 71-78.

Experimental Study and Mathematical Modeling of Bond of Different Types Winding Glass-Plastic Reinforcement with Concrete

BENIN Andrey^{1,a*}, BOGDANOVA Galina^{1,b} and SEMENOV Sergey^{2,c}

¹Petersburg State Transport University, Moskovsky pr., 9, Saint-Petersburg, Russia

²Saint-Petersburg State Polytechnical University, Politehnicheskaya 29, Saint-Petersburg, Russia

^abenin.andrey@mail.ru, ^bnich@pgups.edu, ^csemenov.serg@ksm.spbstu.ru

Keywords: pullout test, GFRP, bond, nonlinear concrete models, flat winding

Abstract. The experimental studies of flat and relief glass-plastic reinforcement bond with concrete were conducted. The comparative analysis of obtained experimental data with results of other researchers in field of reinforcement and concrete bond was made. It was identified that composite reinforcement with flat winding has better bond characteristics in comparison with steel reinforcement and other winding types of composite reinforcement. The analytical dependencies, allowing simulation the process of fiber-plastic reinforcement bond with concrete, were obtained. The finite element modeling of deformation process of concrete foundation of transport constructions with fiber-plastic reinforcement was made.

Introduction

The glass fiber reinforcement plastic (GFRP) bars are widely used in structural engineering as reinforcement of concrete structures. First structure with GFRP reinforcement was built in Germany in 1986 [1]. Wide using of GFRP bars related to a unique combination of high strength, corrosion resistance and low cost. Application of GFRP bars for reinforcement of corrodible structures (such as buildings of chemical plants, supporting structures bridges etc.) and structures liable to electrochemical processes (such as track facilities liable to roaming current, electrolysis bath etc.) is most rational for life provision.

However GFRP bars have weaknesses, one of main is low operational temperature (up to 150°C). This limitation is due to polymer matrix properties. This boundary can be extended up to 300°C with loosing carrying capacity up to 15% [1] by using special polymers [2] (phenolformaldehyde resin and resin based on cycloaliphatic compounds). The second problem is anisotropy of GFRP which causes changing of the bond-slip behavior between GFRP bar and concrete.

There are a numerous reviews [3,4] devoted to bond-slip behavior of GFRP bars and paper analysis of influence on bond-slip diagram of: GFRP surface (type and disposition of the ribs) [5], freeze – thaw cycles [6,7], temperature [8,9], hydrostatic pressure [10], cyclic loadings [11-13] and complex loading program [14].

The first objective in this paper is to compare experimental results of bond-slip behavior of GFRP bars with flat winding and concrete with of GFRP bars with ordinary windings and steel bars. The second is to demonstrate possibility of using GFRP bars with flat winding as reinforcement in the tram track deck.

Mechanical Properties of GFRP Bars

In this research GFRP bars with modified flat winding made by LLC “Plast-Composite” [16] was used. The main mechanical properties are shown in Table 1. One of the difficulty of these experiments was to fix GFRP bars into the grips. It was crushed during fixture procedure in standard grips due to low transverse strength of the GFRP. There are two methods to solve this problem: using special anchors (see Fig. 3, pos. 3) glued onto the end of GFRP bar [18], using special grips with controlled fixture force and special jaws with friction providing shells. The

second method was realized by Zwick Roell Group. These grips allow to fixing and carrying out the tests of the GFRP bar up to 10 mm diameter.

Table 1 Mechanical properties of the GFRP bars with modified flat winding

Profile number	Tensile strength [MPa]		Rupture strain [%]		Tension elastic modulus [GPa]	
	Tech. spec. [16]	Measured value	Tech. spec. [16]	Measured value	Tech. spec. [16]	Measured value
6	no less than	1200	up to	2,3	no less than 50	55.8
8	1000	1160	5.6	2,5		54.6
10		1130		2,6		54.5
12		1125		2,9		54.2

Bond-Slip Behavior of GFRP Bars in Concrete

The main difference from the steel rebar bond-slip behavior is the weak adhesion GFRP and concrete. This is the reason of importance of the ribs construction and disposition. There are two main approaches to the increasing bond strength: creation of the ribs and covering surface GFRP bar of the sand (Fig. 1).

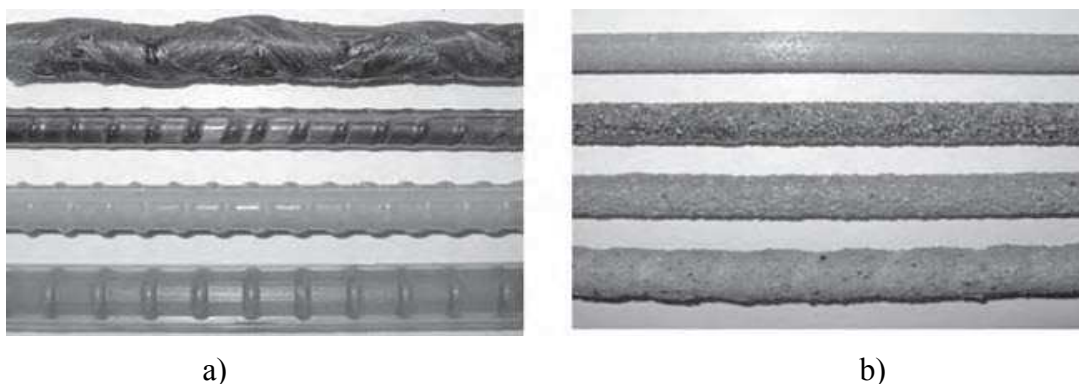


Fig. 1 The main type of the GFRP bar surface: a) ribbed, b) sand coated [15]

There are two standard methods of bond diagram obtaining: pull-out test [17,18] and four point bending test [17,19].

Some authors noted that first method gives overestimated force value due to hydrostatical component of stress tensor caused by supporting plate and the second method gives more realistic results for bending structures. However standard [18] recommends using pull-out test, moreover a lot of researchers already used it their work. In this work pull-out test was used also (Fig. 2).

The results of pull-out test of GFRP bars with flat winding and comparison with GFRP bars with another type of winding [5] and steel rebar are shown in Fig. 3.



Fig. 2 GFRP bar pull-out test: a) test equipment and specimen; b) LVDT sensor for GFRP bar slip measurement

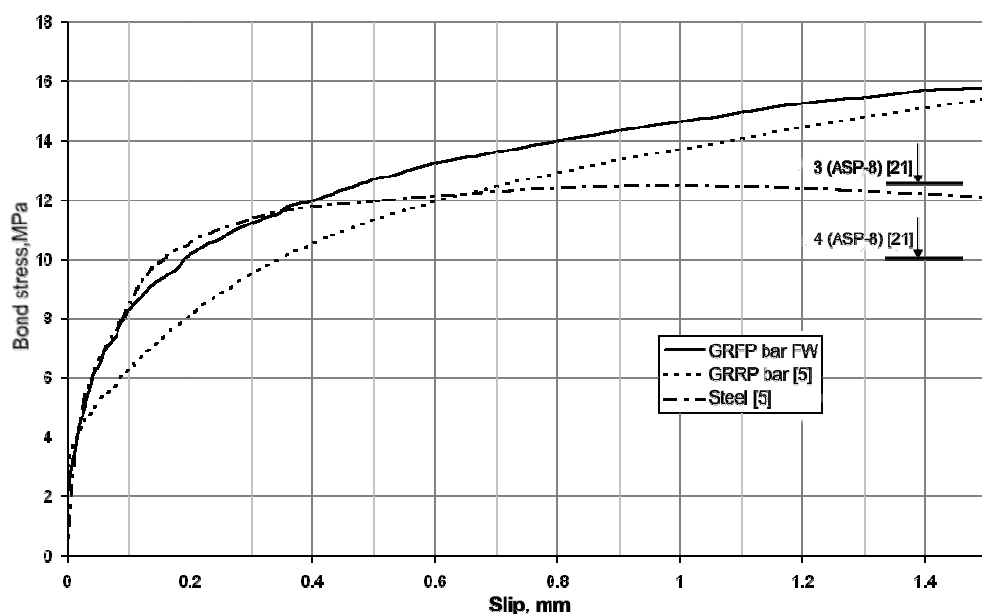


Fig. 3 Bond-slip diagram for GFRP bar with flat winding Ø12 (solid line), GFRP with ribs [5,21] (dashed line and maximal levels of the bond stress) and steel rebar [5] (dot-dash line) and concrete B35

GFRP bars (present research and [5]) demonstrate better bond properties than steel rebar. GFRP bar with flat winding has same initial section of the diagram as steel rebar.

The Tram Track Deck With GFRP and Steel Fiber Reinforcement

Preliminary finite-element calculation of the concrete deck under loading from tram and automobile was carried out. Input data for calculation was geometry of concrete plate 12 m length and 6.6 m width. Plate lay on compacted sand and gravel foundation, concrete ballasting was carried out.

There is asphalt concrete cover on the plate. Load on the plate pass through the Ri 60 rail. Load by the tram axis is 85 kN. There is a four axis in the tram, track width is 1524 mm, base is 7500 mm, distance between pair wheels is 1940 mm. Action from automobile transport is possible instead tram load. According to the Russian rules loan on the axis was 11.5 kN. Track width is 1900 mm, another parameters was get arbitrarily (worst case): base is 2500 mm, approach of neighbour automobile is 2500 mm.

Express finite element (FE) modeling using elastic models of concrete was carried out (Fig. 4).

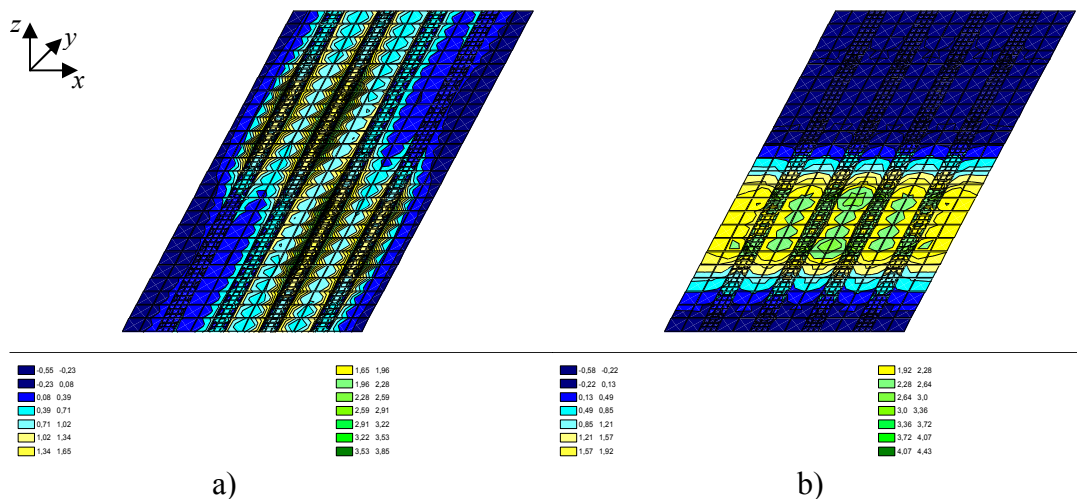


Fig. 4 Bending moments for worst case loading: a) transversal (M_y), b) longitudinal (M_x)

More detailed analysis of deformation process using nonlinear concrete models [22-23] and anisotropic material for the discrete disposed [24] GFRP bars is required.

Obtained results allowed to set concrete design class to B35 and necessary reinforcement of concrete foundation by GFRP bars with diameter 12 mm.

There are two full scale models of concrete tram deck made from concrete with fibers and concrete reinforced by GFRP bars were prepared.

Cyclic loading tests of two full scale models of tram track deck with glass fiber and GFRP bars reinforcement was carried out. The concrete block (deck) covered by asphaltic concrete with tram rail Ri60 and damping system (Fig. 5) was loaded by cyclic load $F_{\min}=5$ kN, $F_{\max}=42.5$ kN.

There are no sufficient displacements (max 1.6 mm) and stresses (max 0.6 MPa) were observed during loading process (12 million cycles). Thereby both types of foundation (made from concrete with fibers and concrete reinforced by GFRP bars) was passed the test under required by rules number of cycles, corresponding to 25 years of operating, without any damage.

Summary

GFRP with flat winding demonstrate good tensile properties with better bond properties than steel rebars. It can be recommended as replacement of steel rebars in reinforced concrete structures especially liable to aggressive environment. Detailed analysis of bond-slip interaction GFRP and concrete using nonlinear models is required.



Fig. 5 Full scale model of tram track deck

The experimental results demonstrated that the track construction complies with cyclic loads requirements after 25 years operational period and is applicable for use under tram track construction in Saint-Petersburg on both fibrous concrete and glass-plastic reinforcement foundations. Meanwhile, the first type of formation was less labor-intensive, the second type was more economical.

Acknowledgements

This contribution is the result of the research supported by the Russian Fundamental Research Program, Project 12-08-00943.

References

- [1] L. Franke, Behavior and Design of High-Quality Glass-Fiber Composite Rods as Reinforcement for Prestressed Concrete Members, Report, International Symposium CP/Ricem/i Bk, Prague, pp. 171-174.
- [2] ACI Committee 440, State-of-the-Art Report on Fiber Reinforced Plastic (FRP) Reinforcement for Concrete Structures, American Concrete Institute, Detroit, Michigan, 1996, 68 p.
- [3] E. Cosenza, G. Manfredi, R. Realfonzo, Behaviour and modeling of bond of FRP rebars to concrete, Journal of Composites for Construction. 1 2 (1997) 40-51.
- [4] Z. Achillides, K. Pilakoutas, Bond Behavior of Fiber Reinforced Polymer Bars under Direct Pullout Conditions, Journal of Composites for Construction. 8 2 (2004) 173–181.
- [5] M. Baena, L. Torres, A. Turon, C. Barris, Experimental study of bond behaviour between concrete and FRP bars using a pull-out test, Composites: Part B. 40, 2009, pp. 784–797.
- [6] J.F. Davalos, Y. Chen, I. Ray, Effect of FRP bar degradation on interface bond with high strength concrete, Cement & Concrete Composites, 30, 2008, pp. 722–730.
- [7] J. Alves, A. El-Ragaby, E. El-Salakawy, Bond Strength of Glass FRP Bars in Concrete Subjected to Freeze-Thaw Cycles and Sustained Loads, Proc. of CICE 2010 - The 5th International Conference on FRP Composites in Civil Engineering, September 27-29, 2010 Beijing, China.

- [8] A. Katz, N. Berman, L.C. Bank, Effect of high temperature on bond strength of FRP rebars, Journal of Composites for Construction. 3 2 (1999) 73-81.
- [9] A. Katz, N. Berman, Modeling the effect of high temperature on the bond of FRP, Cement & Concrete Composites, 22, 2000, pp. 433-443.
- [10] L.J. Malvar, Bond stress-slip characteristics of FRP rebars, Technical report TR-2013-SHR, 1994.
- [11] C.E. Bakis, S.U. Al-Dulaijan, A. Nanni, T.E. Boothby, M.M. Al Zahrani, Effect of cyclic loading in bond behavior of GFRP rods embedded in concrete beams, J. Composite Tech. Res., 20 1 (1998) 29–37.
- [12] J. Alves,A. El-Ragaby, E. El-Salakawy, Effect of fatigue loads on the bond strength of glass FRP bars to concrete Proc. of Annual Conference - Canadian Society for Civil Engineering 2, 2010, pp. 1018-1027.
- [13] J.Y. Lee, C.K. Yi, B. Kim, Y.G. Cheong, Bond degradation of glass fibre reinforced plastic bars in concrete subjected to tensile cyclic loads, Journal of Reinforced Plastics and Composites. 32 7 (2013) 463–475.
- [14] J. Alves, A. El-Ragaby, E. El-Salakawy, Durability of GFRP Bars, Bond to Concrete under Different Loading and Environmental Conditions., J. Compos. Constr. 15 3 (2011) 249–262.
- [15] V.S. Hota, Ganga Rao, Narendra Taly, P.V. Vijay, Reinforced concrete design with FRP composites, Taylor & Francis Group, 2006, 400 p.
- [16] TU 2296-001-30604955-2012. Armatura kompozinaya polimernaya (rus).
- [17] RILEM Recommendations for the Testing and Use of Construction Materials 1994 618 p.
- [18] ISO 10406-1 Fibre-reinforced polymer (FRP) reinforcement of concrete — Test methods Part 1: FRP bars and grids, 2008.
- [19] ISO 10080 Steel for the reinforcement of concrete - Weldable reinforcing steel - General, 2005.
- [20] EN 1992-1-1:2004: Eurocode 2: Design of concrete structures General rules for building.
- [21] V.G. Hozin, A.A. Piskunov, A.R. Gizdatullin, A.N. Kuklin, Sceplenie polimerkompozitnoi armature s cementnim betonom, Proceedings of KGASU. 23, 1, 2013, pp. 214-220.
- [22] A.V. Benin, A.S. Semenov, S.G. Semenov, Fracture simulation of reinforced concrete structures with account of bond degradation and concrete cracking under steel corrosion. Advances in Civil Engineering and Building Materials. 2nd Int. Conf. CEBM. Hong-Kong. Chang, Al Bahar & Zhao (Eds), 2012 Taylor & Francis Group, London, pp. 233-237.
- [23] A.V. Benin, A.S. Semenov, S.G. Semenov, Fracture analysis of reinforced concrete bridge structures with account of concrete cracking under steel corrosion, Advanced Materials Research. 831 (2014) 364-369.
- [24] A.V. Benin, S.V. Elizarov, Account of discrete arrangement of reinforcement in calculation of reinforced concrete elements, Application of codes, design and regulations, Proceedings of the International Conference held at the University of Dundee, Scotland, UK on 5-7 July 2005, London, Tomas Telford Publishing, 2005, pp. 491-498.

Fatigue Assessment of Concrete Members Strengthened by FRP Materials

ČAVOJCOVÁ Alena^{1,a*} and MORAVČÍK Martin^{1,b}

¹ University of Žilina, Faculty of Civil Engineering, Department of Structures and Bridges,
010 26 Žilina, Slovak Republic

^aalena.cavojcova@fstav.uniza.sk, ^bmartin.moravcik@fstav.uniza.sk

Keywords: fatigue, concrete, FRP, cyclic loading

Abstract. Fatigue and fatigue damage leads to a change in material properties that can lead to the element failures. Generally, it is necessary to verify the influence of the fatigue effects on the concrete members according to European standard EC2, [1]. FRP materials have been possibly used for the fatigue damage structure rehabilitation. There we can apply the condition of the limit boundaries stress on concrete and limit force in FRP material theoretical approach. Fatigue assessment will be analyzed for T-beam cross section with reinforcement and strengthened FPR material in this paper.

Introduction

Fatigue as a negative effect induces changes in the properties concrete members. Increase damage is growing with increasing cyclic loading. In exceeding limits occurs to irretrievable damage – collapse of element.

EC2 recommended to verification of fatigue by limit stress in the concrete and in the reinforcement of concrete structures. Verification is performed separately, independently for both carrier materials. Dependence number of cycles and amplitude of stress decide for verification reinforcement. The values are subtracted from appropriate S-N curve. In concrete is verified boundary values amplitude of stress. Analysis of sensitivity was also performed given to greater sensitivity of reinforcement on fatigue loading. Analysis of sensitivity was performed in our research in our concrete beam. We used different reinforcement ratio.

Fatigue damage members needs reconstruct - the additional reinforced or else externally strengthened. Application FRP materials are very effective to increase to resistance of fatigue loading. Strengthened members must verify on fatigue. Assessment not find in simultaneously valid EC2.

In article, we are focused on verification of fatigue on non-strengthened members and strengthened member with using Germany regulations DAfStb Guideline [3]. Guideline is new materials for make new EC 2, which will be published in 2020.

Verification of Fatigue with Applicable EC 2

Fatigue resistance is recommended verified by simplified method of equivalent stress amplitude. It used boundary value stress $\sigma_{c,max}$ and $\sigma_{c,min}$ and fatigue resistance of concrete $f_{cd,fat}$ according to (Eq. 1) in concrete. Reinforcement it controlled limits of standards according (Eq. 2).

$$\frac{\sigma_{c,max}}{f_{cd,fat}} \leq 0.5 + 0.45 \frac{\sigma_{c,min}}{f_{cd,fat}} \leq 0.9, \quad (1)$$

$$\gamma_{F,fat} \Delta \sigma_{S,eq} (N^*) \leq \frac{\Delta \sigma_{R,sk} (N^*)}{\gamma_{S,fat}}. \quad (2)$$

Our monitoring beam satisfied the condition (Eq. 1) from terms verifications of concrete. Reinforcement must unsatisfied (Eq. 2), (Fig. 1). Reinforcement we must resist control limit 10^6 cycles. The graph (Fig. 1) shows fatigue resistance $\Delta\sigma_{R,sk}$ and number of cycles for design loading in beam $\Delta\sigma_{S,eq}$.

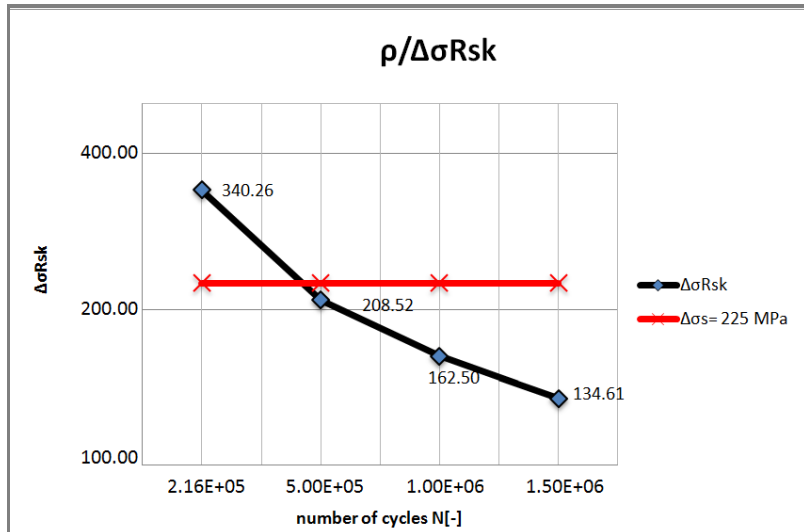


Fig. 1 Dependence of number of cycles and fatigue resistance for design loading

Fatigue resistance is directly dependent on the reinforcement elements. Analysis shows that elements with a small reinforcement ratios are prone to failure for N^* cycles in graph (Fig. 2). Resistance of these members must be solved additionally. Members with a higher reinforcement ratio are resistant to fatigue loading.

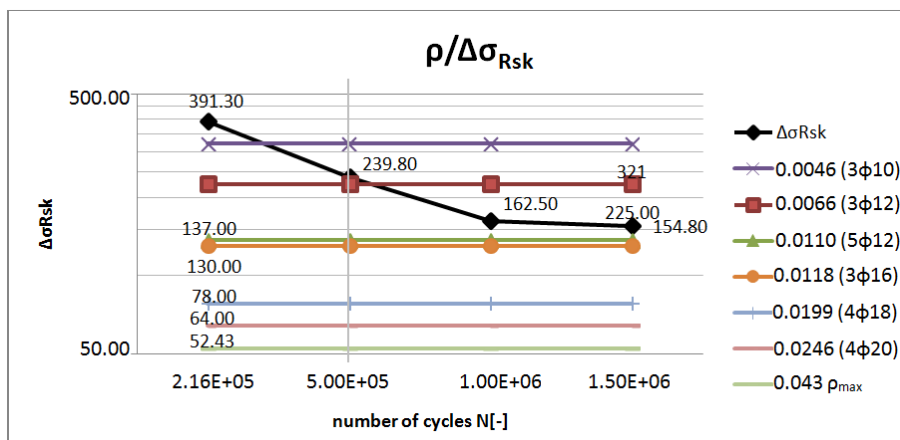


Fig. 2 Fatigue resistance of beams with different ratio reinforcement

Application Strengthened with FPR Materials

One possibility of modern strengthened reinforced members is application of FRP materials. Fatigue assessment must satisfy limit boundary stress in structure and force in FRP material. In the world exists more ways strengthened. [4-6].

On beam (Fig. 3) is designed system of strengthened NSM (Near surface mounted). Application is in to the tension zone T-cross section. Used is strip type MBRACE CFK 150/2000, cross-section 20/1.4 mm and following characteristics $F_{Luk} = 1850 \text{ N/mm}^2$, $E_L = 165\,000 \text{ N/mm}^2$, [5]. The graph (Fig. 4) is result of static loading in numerical models. There is dependence on deflection and force for non-strengthened beam and strengthened beam. The strength of concrete was design C35/45 and reinforcement B 500B. The second beam was strengthened system NSM into the groove.

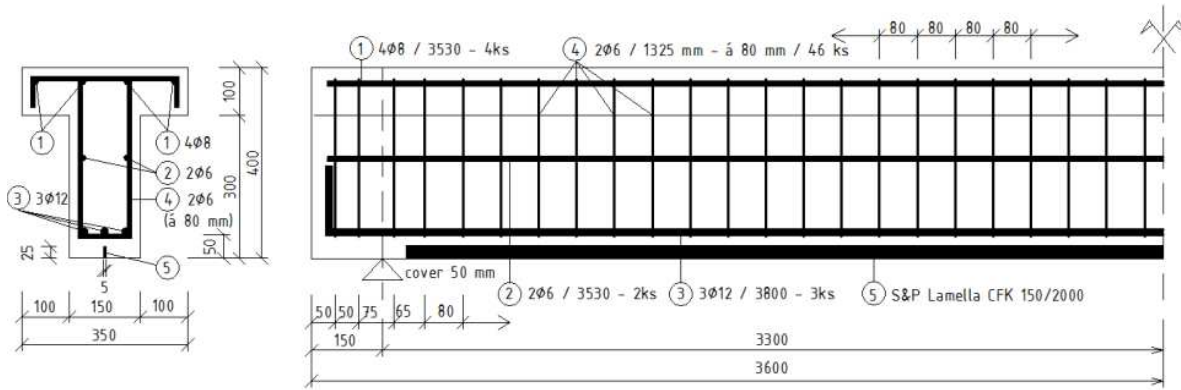


Fig. 3 Cross and longitudinal section with NSM

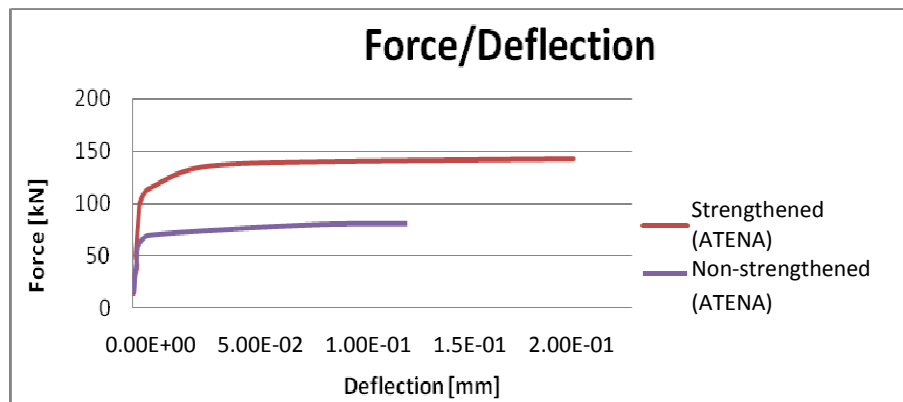


Fig. 4 Deflection in strengthened and normal beam

Application Strengthened according guideline

Germany guideline [2] recommended process for verification of strengthened structure application of FRP materials. The guideline defines calculation according different type's strengthened (external, internal – type NSM). Recalculation is based on calculation according to strains and forces result from concrete F_{cd} (Eq. 3), reinforcement F_{s1d} (Eq. 4) a strip FRP F_{Ld} (Eq. 5) according equations 3-5.

$$F_{cd} = b \left(\frac{-\varepsilon_c}{-\varepsilon_c + \varepsilon_{L,0} + \varepsilon_{LRd,max}} \right) d_L f_{cd} \left(1 + \frac{2}{3\varepsilon_c} \right), \quad (3)$$

$$F_{Ld} = a_L E_L \varepsilon_L, \quad (4)$$

$$F_{s1d} = a_{s1} f_{yd}. \quad (5)$$

Design resistance (Eq. 6) is calculated under in effect one strip in the groove.

$$m_{Rd} = F_{s1d} (d - k_a x) + F_{Ld} (d_L - k_a x). \quad (6)$$

According [2] NSM system has sufficient fatigue resistance, if it satisfies the conditions:

$$F_{Ld} \leq 0.6 F_{bL,Rd} = 0.6 \left(b_L \tau_{bLd} \sqrt[4]{a_r} \left(26.2 + 0.065 \tanh \left(\frac{a_r}{70} \right) (l_{bL} - 115) \right) 0.95 \right). \quad (7)$$

Where: F_{bLRd} is design bond resistance that depends on the bond length and maximum bond stress of adhesive.

$$\Delta\sigma_L \leq \frac{500}{t_L}. \quad (8)$$

Where: $\Delta\sigma_L$ is stress in strip and t_L is strip thickness. In Table 1, we can see calculation our beam according [2].

Table 1 Results

DAfStb Guideline	$m_{Rd} > m_{Ed}$	$60.25 > 31.40 \text{ kNm/m}$
Resistance	$m_{Rd} > m_{RdI}$	$60.25 > 46.81 \text{ kNm/m}$
	$F_{Ld} < 0.6 F_{bLRd}$	$9.9 < 10.7 \text{ kN}$
Fatigue	$\sigma_L < 500/t_L$	$354.8 < 357 \text{ N/mm}^2$

Conclusion

Performed sensitivity analysis showed that elements designed with higher reinforcement ratio satisfied condition of fatigue resistance. But such members are often over dimensioned almost two times from the global structural resistance point of view. Possibility to increase structural resistance and do not to apply so much reinforcement is used elements based on FRP materials. One FRP strip applied in the tensioned zone of the beam can satisfy the fatigue resistance as can be seen at our example.

Acknowledgements

This contribution is the result of the research supported by VEGA 1/0517/12, APVV-0736-12 and The research is supported by European regional development fund and Slovak state budget by the project Research centre of University of Žilina, ITMS 26220220183.

References

- [1] EN 1992-1-1 Eurocode 2: Design of concrete structure, Part 1-1: General rules and rules of buildings.
- [2] Deutscher Ausschuss fur Stahlbeton, German committee for Structural Concrete, Commentary on the DAfStb Guideline "Strengthening of Concrete Members with Adhesively Bonded Reinforcement" with Examples.
- [3] Technical specification BASF MBRACE CFK 150/2000.
- [4] P. Koteš, P. Kotula, F. Bahleda, M. Brodňan, Experimental investigation and numerical modelling of concrete structures with GFRP members. 6th CCC Congress Mariánske Lazne 2010 „Concrete Structures for Challenging, Mariánske Lázně, ČR, 2010, pp.149-154.
- [5] K.Gajdošová, Stress and Crack Width Control According to EN 1992. In: Design of concrete structures using eurocodes: International workshop: Proceedings, konferencia. Vienna, Austria, 2012. Technische Universität Wien, 2012, pp.199–202.
- [6] J. Halvoník, V. Borzovič and J. Dolnák, Experience with design of prestressed concrete bridges according to Eurocode. : Design of concrete structures using EN 1992-1-1: First International Workshop. Prague, CR, 201, pp. 61-71.

Investigation of the Bond Behavior of UHPC

ČÍTEK David^{1,a*}, HUŇKA Petr^{2,b}, ŘEHÁČEK Stanislav^{3,c} and KOLÍSKO Jiří^{4,d}

^{1,2,3,4}Klokner Institute, CTU in Prague, Solinova 7, 166 08 Prague, Czech Republic

^adavid.citek@klok.cvut.cz, ^bpetr.hunka@klok.cvut.cz, ^cstanislav.rehacek@klok.cvut.cz,
^djiri.kolisko@klok.cvut.cz

Keywords: UHPC, bond of reinforcement, prestressed girders, pull out test

Abstract. Ultra High Performance Concrete - UHPC has become increasingly used. Its outstanding features are generally known. It is a fact that the bond of the reinforcement in UHPC is better than that in ordinary concrete, but this bond needs to be quantified. The aim of the experimental research was to determine the average bond stress between prestressing strands and different types of UHPC and to show very significant increase in the average shear stress in bond with UHPC compared to ordinary concrete. In order to determine the bond capacity, an experimental research was carried out. Experimental details of the models in real structures – parts of prestressed girders made from UHPC, were tested in the laboratory and the results were compared with specimens prepared according to standard. The influence of different material properties and different anchorage length of prestressing strands to bond behavior of UHPC was examined in pull out tests. Test results of bond test led to the conclusion that the application of UHPC can significantly reduce the anchorage length of reinforcement compared with the ordinary concrete.

Introduction

The bond of reinforcement and concrete is one of the fundamental parameters of reinforced concrete structures. It affects the anchorage length of reinforcement and along with it, the design of the construction. The tensile strength of the reinforcement is transferred by the uneven shear stress at the contact between the reinforcement and the concrete. Anchor length must be established so that this tensile force in the reinforcement is reliably transferred to the surrounding concrete.

Previous research [1] was aimed at determination of the bond behavior of UHPC and ordinary reinforcement. In the experiments it was verified by the fact that the excellent material properties of UHPC materials have a very significant impact on the bond behavior of the material. The following part of the experimental program is aimed at verification of the influence of material properties on the bond behavior of concrete and strands, which has the different shape and character from ordinary reinforcement.

Bond of Reinforcement and Test Methods

There are few methods how to measure average shear stress in the bond. ČSN 73 1333 – Testing of bond behavior of prestressing strands and concrete was used for the test. The test samples are prescribed by a cube 150×150×150 mm with prestressing strand. This reinforcement use a wooden wedge at the bottom of the mold centered and mounted in such a way that the resulting reinforcement anchorage length of strand is 140 mm (Fig. 1).

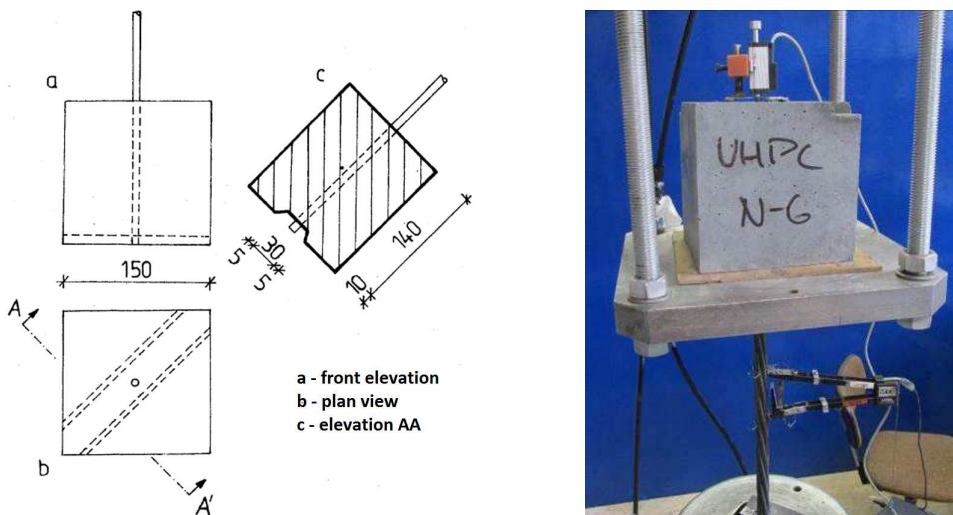


Fig. 1 Scheme of the test specimen and specimen prepared for pull out test

During the test, the test sample was inserted into the test device and the embedded reinforcement is pulled out. The tensile force in the reinforcement and slip of the unloaded upper end of the reinforcement are measured during the test. The measured force is translated to the average shear stress in bond for the entire length of the anchor length.

Bond of Prestressing Strands and UHPC – Standard Test Specimen

One part of the experiment was focused on determination of the bond of prestressing strands with two types of UHPC and comparison of the average shear bond stress of prestressing strands with the ordinary concrete C45/55. A pull out test was used. The steel strands with 15.7 mm in diameter embedded in concrete with anchorage length of 140 mm were pulled out of a cube 150×150×150 mm using the test equipment. In this case was used the method according to CSN 73 1333.

The results show very significant increase in the average shear stress in bond with UHPC compared to concrete C45/55 (Fig. 2). There is no sudden drop of stress for test samples with the strands, when the reinforcement is pulled out as samples with reinforcing bars. The graph (Fig. 2) shows the growth of the average shear stress after initial slip of the strand. This is due to twisting of the prestressing strand when it is pulled out from concrete. No rotation of specimen in loading device is possible. A similar pattern is also reflected in the ordinary concrete [2].

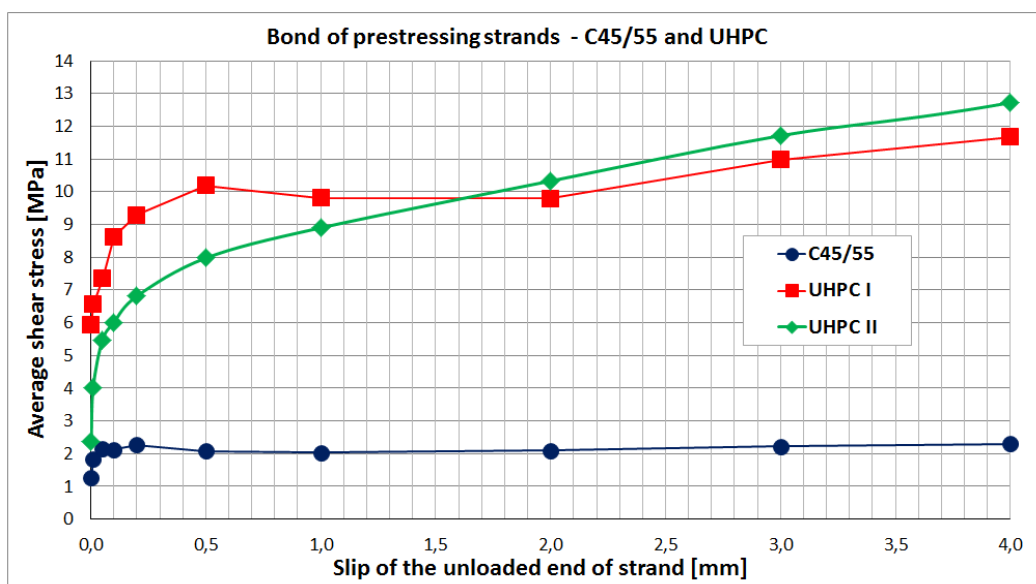


Fig. 2 Comparison of the bond behavior of strands embedded in UHPC and C45/55

Bond of Prestressing Strands and UHPC – Ends of Prestressed Girders

The second part of the experimental verification of bond of strands and UHPC was focused on determination of the average shear stress of prestressed girders made from UHPC (Fig. 3). The girders were cut after the bending test, and the ends of the prestressing strands adjusted by cutting so that the individual cables can be pulled out using the same procedure as in standardized elements - cubes. These tests were complementary to the amount of material tests and the informative aim was to determine the effect of the anchorage length of the strands on the average shear stress in bond. The undamaged ends of girders after the bending test were selected and suitable reinforcement for subsequent preparation to pull out test was selected too. The summary of results is shown in graph in Fig. 4.



Fig. 3 Prestressed girders made from UHPC – end with prestressing strands

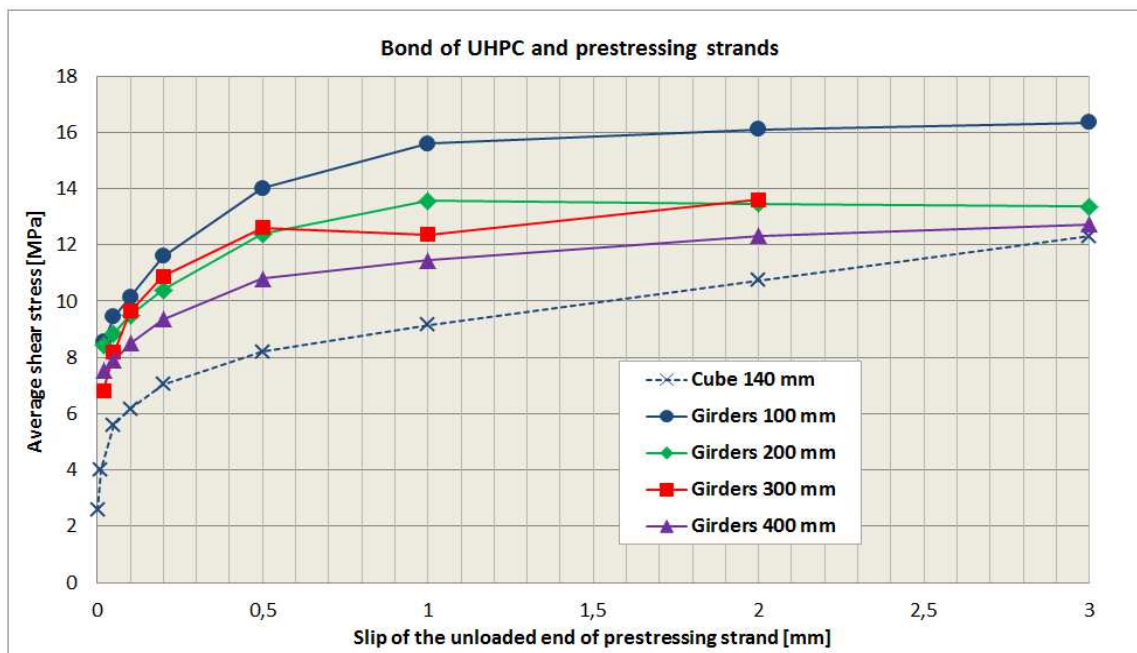


Fig. 4 Comparison of the bond of strands embedded in UHPC with different anchorage length

Summary

The aim of the experiment was to determine the average shear stress of bond between prestressing strands and two different types of UHPC and ordinary concrete and verification of different behaviors and demonstrate significantly better bond behavior than the ordinary concrete C45/55. Results indicated a significant difference between the two types of concrete. Test specimens made from UHPC (with compressive strength higher than 150 MPa) were compared with ordinary concrete and a significant increase in the bond of the strands with UHPC was found. Different behavior of the load - displacement diagrams can be explained by differences in the composition of each mixture UHPC resulting in different tensile and compressive strength and even technological influences in the actual preparation of test specimens.

In the second part of the experiment two types of production of the test specimens for bond examination were compared. First production samples according to one hand, the production of non-standard samples by cutting the ends of prestressed beams after mechanical testing. Non-standard method samples were also cut to different lengths of the anchorage (100, 200, 300, 400 mm), and the effect of these anchor lengths on the average shear stress in bond was examined.

The results of average values of bond presented in the graph in Figure 4 shows a significant difference between the two methods of production. The difference between the standard procedure and testing of samples by cutting the real structures shows that the standardized procedure requires the reinforcement in the form of non-preloaded beams and reinforcement is pre-tensioned and anchored. The considerably lower values of shear stress in the case of standard test specimens indicate a conservative standard procedure compared to samples from the girders.

Samples of prestressed beams were also compared from the aspect of the values of bond affected by different anchorage length. As was expected, the observed relatively obvious difference between samples with embedment length of 400 mm (minimum of the average values) and samples with an anchor length of 100 mm (maximum of the average values). Different results can be explained in addition to the size effect, especially inequality and disparity during stress along the bonded reinforcement and therefore different levels of averaging in calculating the voltage of individual anchorage lengths.

The obtained experimental data serve as a the basis for further systematic experimental verification and more accurate information about the bond significantly higher values of UHPC with the prestressing strands so as to enable efficient design of prestressed elements.

Acknowledgements

This contribution is the result of the research supported by the research project GAČR 13-15175S. The tests were carried out in laboratory of Klokner Institut, Czech Technical University in Prague.

References

- [1] D. Citek, J.L. Vitek, Soudržnost betonářské výztuže a UHPC, Proceedings of 11th Conference Technologie Betonu, Jihlava, Czech Republic, 2013, pp. 87-92.
- [2] D. Citek, J.L. Vitek, Bond of Reinforcement and UHPC, Proceedings of 20th Czech Concrete Day 2013, Hradec Králové, Czech Republic, 27-28.11.2013.

Damage Detection and Localization on Cement Specimens

PLACHÝ Tomáš^{1,a*}, OKÉNKA Jakub^{1,b}, TESÁREK Pavel^{1,c}
and POLÁK Michal^{1,d}

¹Department of Mechanics, Faculty of Civil Engineering, Czech Technical University in Prague,
Thákurova 7, 166 29 Praha 6, Czech Republic

^aplachy@fsv.cvut.cz, ^bokenkaj@gmail.com, ^ctesarek@fsv.cvut.cz, ^dpolak@fsv.cvut.cz

Keywords: damage detection, health monitoring, impact excitation method, natural frequency, mode shape, cement specimen

Abstract. This paper is focused on cement specimen testing by impact excitation non-destructive technique. The impulse excitation method was used for measuring of the natural frequencies and modes of longitudinal, transversal and torsional vibration of the specimens. The objective was to find dynamic properties of the specimens without a crack, with a crack and with a healed crack by cement paste and based on their comparison detect and localize the crack.

Introduction

The detection of cracks in cement specimens was only one part of the project mainly focused on the examination of the capability of bacteria to heal a crack in cement specimens – bioremediation of cement. In literature [1], it is estimated that structures made from autoremediation cement will have 30 % longer life than the others. So the motivation for this part of our work was to test the method for detection and localization of a crack in cement specimens and also detection and quantification of the remediation of a crack.

Description of the Tested Specimens

For the purpose of the tests the cement paste from the cement CEM I 42.5 R of the factory in Radotín was used. The dimensions of the tested specimens were $40 \times 40 \times 160$ mm as it is recommended in [2]. The water cement ratio was 0.4. The standardized damage (crack) was made by putting the cooper plate of the thickness 0.1 mm to the fresh specimen to the depth of 20 mm. The cracks were situated in the four distances – 30, 40, 60 and 80 mm. The total number of the specimens was 15. For each distance of the crack three specimens were made and three more reference specimens without any crack. The cooper plate was pulled out from the specimen after 24 hours after its unmolding.

The Impulse Excitation Method

The impulse excitation method, which we used in our previous research [3, 4], was chosen for detection and localization of a crack. Three types of vibration were used for measuring the fundamental natural frequencies and mode shapes of longitudinal, transversal and torsional vibration of the specimens. Brüel&Kjær equipment was used for testing. The impact hammer Brüel&Kjær 8206 (Fig. 1 – on the left) with force transducer inside was used for excitation and the acceleration transducer Brüel&Kjær Type 4519-003 (Fig. 1 and 2) was used for the response measurement. Both signals, the excitation force and the acceleration, were recorded and transformed using Fast Fourier Transform (FFT) to the frequency domain, and the Frequency Response Function (FRF) was evaluated from these signals using the vibration control station Brüel&Kjær Front-end 3560-B-120 and program PULSE 13.4. The test was repeated five times for each specimen and resultant readings were averaged. From an averaged FRF, the fundamental resonant frequency was

determined for each specimen. For measuring of longitudinal, transversal and torsional vibration, the specimen measurement was set as it is shown in Fig. 1 and Fig. 2.



Fig. 1 The test arrangement for longitudinal vibration



Fig. 2 The test arrangement for transversal (left) and torsional (right) vibration

Results

At first the measurements of resonant frequencies was carried out on the reference specimens (without the crack), on the specimens with the open crack in the distance 30 mm, on the specimens 30 min after healing of the crack and then after 4 days. In all 3 figures (Fig. 3), there is visible that the crack has an influence onto the 1st resonance frequencies for all 3 types of vibration. The resonance frequencies decreased significantly for all three basic modes of vibration. Also new resonance frequencies were found. Especially for the transversal vibration, new modes of vibration appeared. The ratio between the 1st and the 2nd resonance transversal frequencies of cracked specimen decreased in comparison with the reference specimen. The same phenomenon was observed for the longitudinal vibration. After healing there was observed, that the new frequencies were vanished, main resonant frequencies were shifted onto reference position and ratios of the 1st and the 2nd frequencies returned to referent values.

On the chosen specimens, the complete modal analysis was carried out in a number of points on their surfaces (Fig. 4). The first natural mode shapes of longitudinal, transversal and torsional vibration were evaluated for the specimens without any damage, with crack and after remediation. Modal characteristics of the specimens – without and with the crack - were mutually compared. For comparison of natural modes, changes of a mode surface curvature $CAMOSUC_{(j),x}$ were used

$$CAMOSUC_{(j),x} = \left| \frac{r_{(j)XX,x+1} - 2r_{(j)XX,x} + r_{(j)XX,x-1}}{h^2} - \frac{r_{(j)YY,x+1} - 2r_{(j)YY,x} + r_{(j)YY,x-1}}{h^2} \right|, \quad (1)$$

where $r_{(j)XX,x}$ is the value of the j^{th} natural mode shape in the x^{th} measured point in damage state XX of the specimen, $r_{(j)YY,x}$ is the value of the j^{th} natural mode shape in the x^{th} measured point in the virgin state YY of the slab and h is the dimension of the net of measured points.

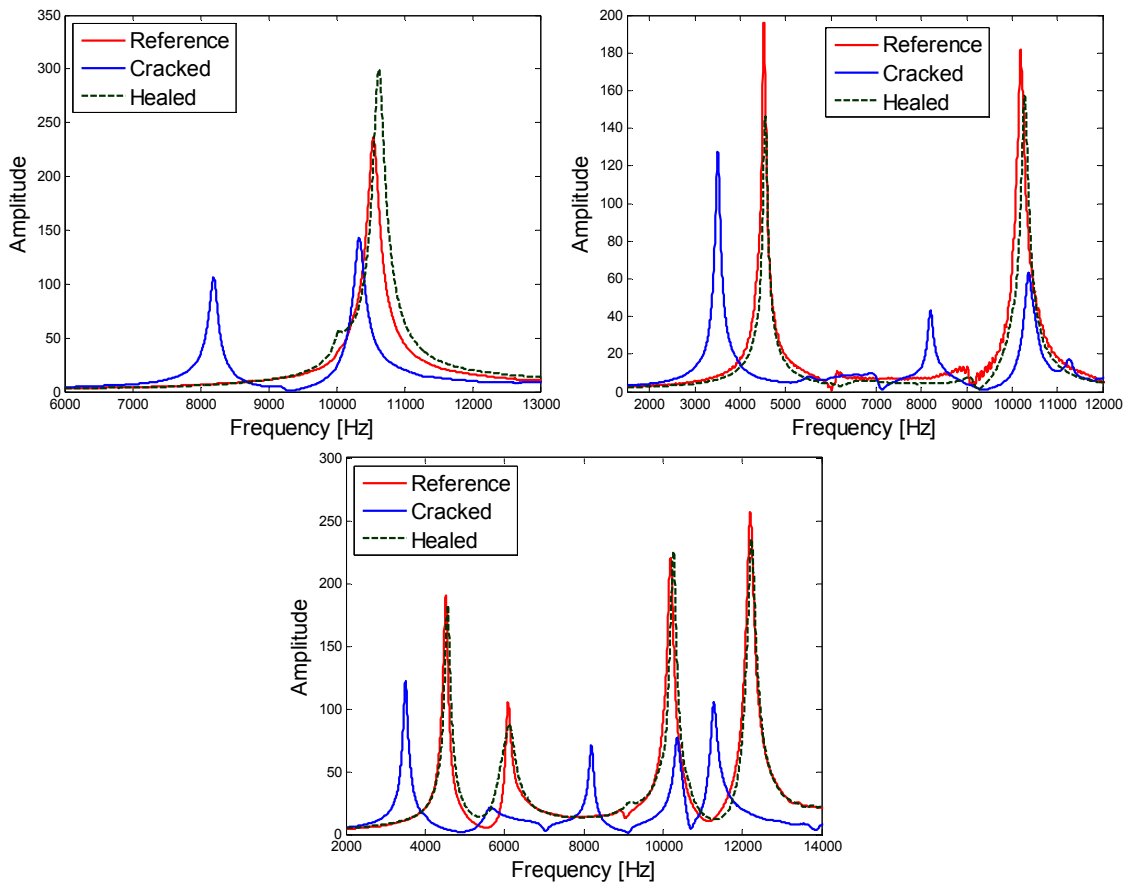


Fig. 3 The FRFs for longitudinal (upper left one), transversal (upper right one) and torsional (lower one) vibration

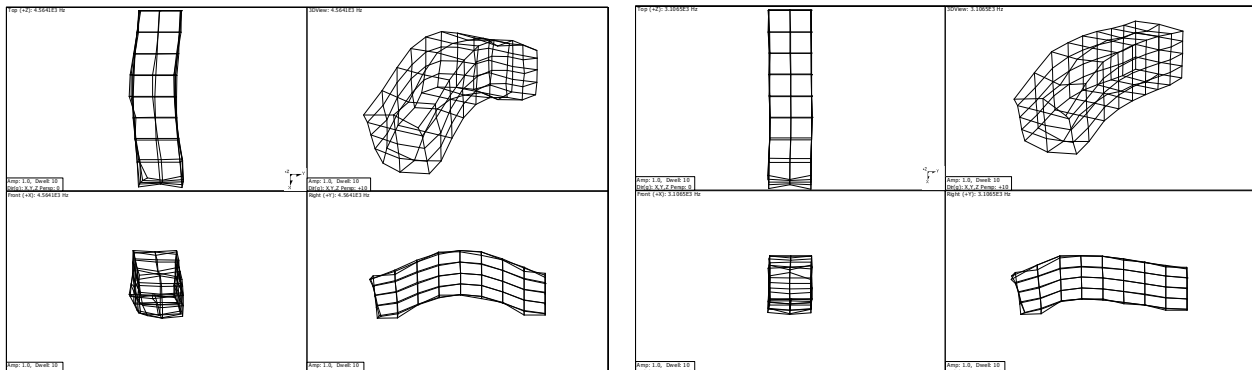


Fig. 4 The 1st natural mode shape of the transversal vibration – virgin state (left), crack in the distance 30 mm from the left end of the specimen (right)

Conclusion

The impulse excitation technique was used successfully for detection of a crack in cement specimens and for evaluation of the healing of a crack (Fig. 3). The detection of the crack based on the changes of the natural frequencies can be used successfully even for small cracks and also the degree of healing is very well visible from FRFs. This technique is very quick and nondestructive [5]. The localization of a crack using modal analysis gave us good results only for deep cracks (Fig. 5), approximately to the half of the cross-section. For shallow cracks, less than quarter of the cross-section, mode shape changes were very small.

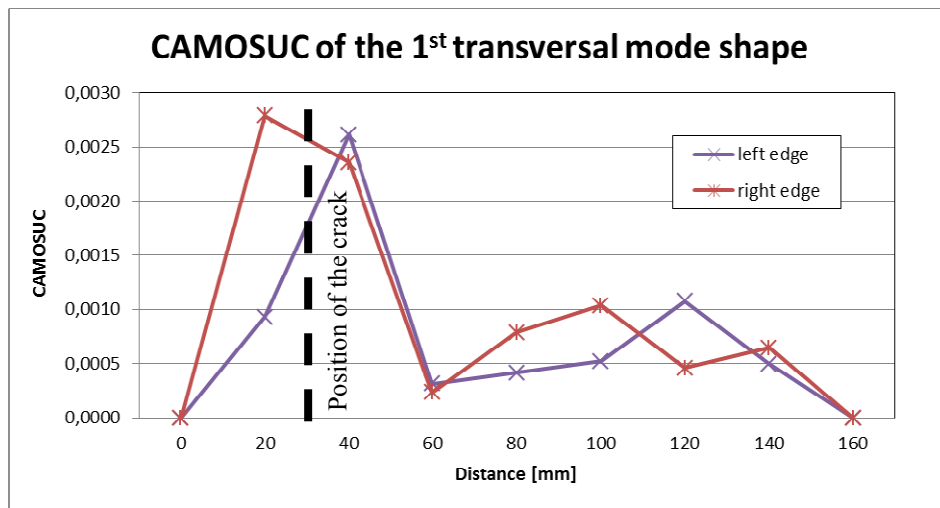


Fig. 5 The detection of a crack in the distance 30 mm using CAMOSUC of the 1st natural mode shapes (Fig. 4)

Acknowledgements

This contribution is the result of the research supported by the Technology Agency of the Czech Republic – Competence Centers under No. TE01020168 Centre for Effective and Sustainable Transport Infrastructure.

References

- [1] M. Wu, B. Johannesson, Mette Geiker, A review: Self-healing in cementitious materials and engineered cementitious composite as a self-healing material, *Construction and Building Materials*, 28.1 (2012) 571-583.
- [2] K. Van Tittelboom, N. De Belle, D. Van Loo, P. Jacobs, Self-healing efficiency of cementitious materials containing tubular capsules filled with healing agent, *Cement and Concrete Composites*, 33.4 (2011) 497-505.
- [3] T. Plachý, M. Polák, Damage detection and localisation on reinforced concrete slabs based on modal analysis, in: L. Collini (Ed.), 22nd Danubia-Adria Symposium on Experimental Methods in Solid Mechanics, DAS 2005, University of Parma / Ingegneria Industriale, Parma, 2005, pp. 247-248.
- [4] T. Plachý, P. Tesárek, A. Wilczynska, P. Padevět, Experiment in real conditions, Mechanical properties of gypsum block determined using non-destructive and destructive methods, in: International Conference on Engineering Mechanics, Structures, Engineering Geology, International Conference on Geography and Geology – Proceedings, 2010, pp. 418-423.
- [5] L. Melzerová, P. Kuklík, Non-destructive Tests of Modulus of Elasticity for the Glued Laminated Timber Beams, *Procedia Engineering*, 48 (2012) 409-412.
- [6] P. Padevět, O. Zobal, Changes of the Fracture Energy of Cement Paste with Addition of Fly Ash in Time, *Procedia Engineering*, 48 (2012) 513-519.

Two Examples of the Use of FRP Reinforcement to Strengthen Structures

PODOLKA Luboš^{1,a*}

¹Institute Department of Civil Engineering, University of Technology and Economics in Czech Budejovice, Street Circular No. 517/30, 370 01, Czech Budejovice, Czech Republic

^apodolka@mail.vstecb.cz

Keywords: composites, strengthening, anchorage, prestressed, FRP materials

Abstract. The paper describes experiments carried out in laboratories KU CVTU in Prague and subsequent demonstration of the application of their results in practice in two practical examples reinforcement structures, reinforced concrete frame and Reinforced Concrete Girder Bridge.

Introduction

The paper describes experiments carried out in laboratories KU CVTU in Prague and subsequent demonstration of the application of their results in practice in two practical examples reinforcement structures, reinforced concrete frame and Reinforced Concrete Girder Bridge.

The basis for the subsequent practical application of reinforced concrete circular columns multifunctional building in Olomouc, the experience gained during the experimental test consisting of a column of these dimensions 250×250×1500 mm of concrete C 12/15 with reinforcement 4 φ E12 and E10 φ stirrups of $a' = 200$ mm, which was amplified CFK fabric wrap SikaWrap Hex ® 230 C (305×1100 mm) at the top and bottom end. Over saturating the pad 50x250 mm thick 10 mm transverse tensile see photo.

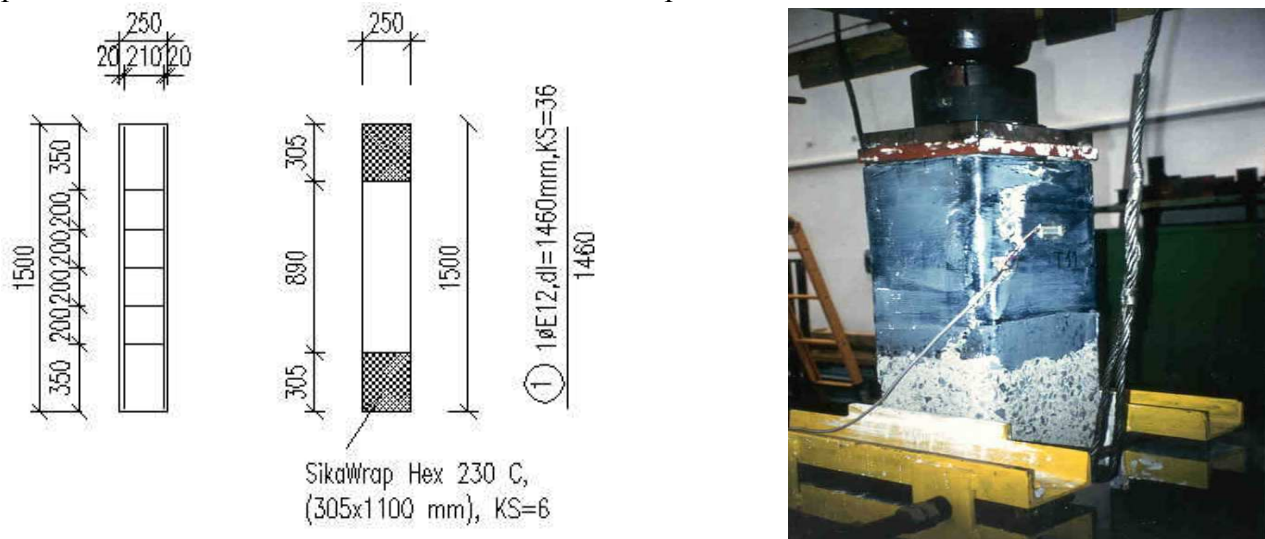


Fig. 1 View of the reinforcement scheme and designed the column FRP reinforcement wrap, respectively. View of a sample placed in the press.

Reinforced Columns Building City Center CPI Olomouc

The existing hotel has ten floors above ground and one underground floor. The other two dimensions are at about 17.0×37.0 m Next door is a three-storey outbuilding of about 16.0×35.0 m (two above ground and one underground floor. Existing hotel will be the reconstruction increased by one floor to the 11th overall Extension the hotel will be part of the plan also increased by one level height above terrain and the hotel will be about 36.0 m.

From a structural point of view, two floors and a basement designed as a reinforced concrete skeleton. The columns are circular 500 and 600 mm section. The ceilings are beamed reinforced concrete slabs with a thickness of 150mm. From the third floor support system is then designed as prefabricated reinforced concrete wall system with a transverse arrangement of load-bearing walls - of the panel system T 06 B. The thickness of the load-bearing walls is 150 mm. The thickness of ceiling panels is also 150 mm. Hotel is across the board based on the footings and passports in the level of viable layers of gravel. For existing hotel is contemplating an increase of one floor. The construction is tentatively proposed as a transverse wall system respecting supporting the construction of the lower floors. The walls are pre-designed masonry thickness 250 mm of brick blocks strength of 10 MPa and mortar strength of 5 MPa. The walls are imposed ceiling panels SPIROLL thickness 165 mm. Part of the ceiling structure at the point of installation of penetrations is designed as a steel-concrete ceiling with profiled steel sheet with a thickness of 50 mm above the concrete wave trapezoidal sheet of reinforced concrete C20/25-XC1 networks kari.

Draft Gain Column Structure

For the model was used documents available design documentation of the building in 1978. Material properties were considered by the project. The stiffness of the joints of panels was considered according to the available project documents regeneration of prefabricated houses from 2000 [1]. Technological procedure repair columns FRP wrap:

First the removal of the asbestos specialized company in compliance with all safety and health regulations. Second removal of asbestos and loose layers with a flat surface cross linking pole sander or water jet.

3rd repair and re-profiling the surface of composite columns repair mortars corresponding minimum concrete C20/25-XC1.

4th application of the primary layer of glue or paste (depending on the technology used for bonding fabrics).

5th Applying a layer of wrap roller.

6th applying a sealing layer of adhesive.

7th If we follow another layer of wrap will again be coated with a layer of glue or paste and Frequently Asked roller and wrap

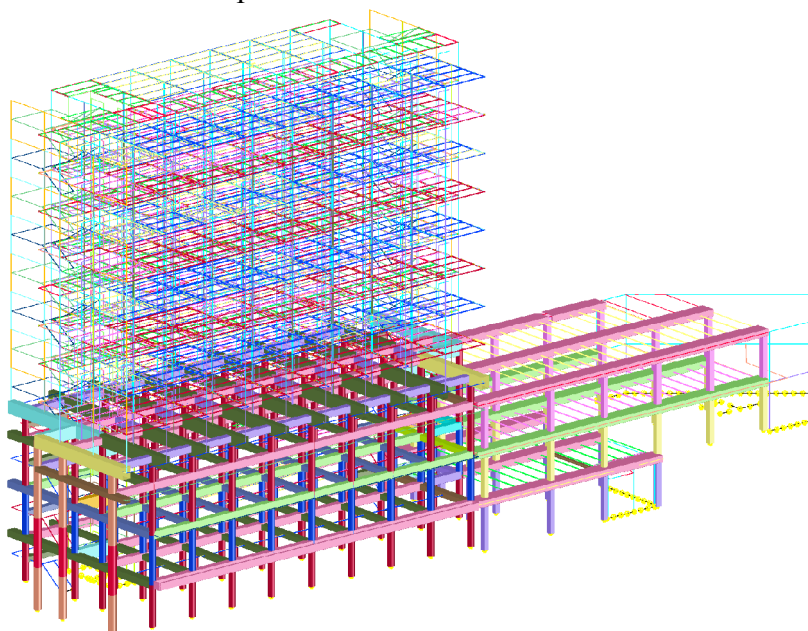


Fig. 2 3D model construction program created Recoc used to determine the internal forces in column [3]

Sample Calculation of Columns Gain FRP Wrap

Customer requirements was to increase the strength of columns using FRP wrap banding on the existing strength of C 12/15 on the strength of the C 16/20 and C 20/25 column at a diameter of 500 mm.

Table 1 Technical information used FRP wrap from the STADO CZ Ltd.

Technical information Stado Wrapping type G	
Properties belts	
Composition	Braided network little undulated, unidirectional fibers, polyester with a light attached to the carbon fibers.
Width	300 mm as standard sizes, the other can be delivered according to the order.
Color	black
Weight belt	300 g/m ²
Fiber content	100 %
The density of fibers	1.80 g/cm ³
Effective thickness of tissue	0.167 mm
Typical mechanical properties of the fibers	
Modulus of elasticity	240 GPa
Tensile	4300 MPa
Elongation at break	1.8 %

The requirement of min. wrapping reinforcement is to increase the strength of 6 MPa, ie $\sigma_x \geq 1.5$ MPa.

$$\gamma_f \sigma_x = \frac{f_{FRP} t_{FRP}}{r} \quad (1)$$

f_{FRP} tensile strength of the fabrics used (N/mm²)

t_{FRP} carbon fiber thickness (mm)

r the radius of the pole (mm)

the required level of security $\gamma_f = 1.75$.

$f_{FRP} = 4300$ N/mm²

$t_{FRP} = 0.167$ mm

$r = 500$ mm.

Determine the number of wraps column

$$t_{FRP} = \frac{\gamma_f \cdot \sigma_x \cdot r}{f_{FRP}} = \frac{1.75 \times 1.5 \times 500}{4300} = 0.305 \text{ mm} . \quad (2)$$

Column will be wrapped min. 2 layers of wraps.

The strength of the column after wrapping two layers of fabric Stado wrapping G

$$\sigma_x = \frac{f_{FRP} t_{FRP}}{r \gamma_f} = \frac{4300 \times 2 \times 0.167}{500 \times 1.75} = 1.64 \text{ MPa} . \quad (3)$$

Strength column after wrapping

$$f_{c,FRP} = f_c + 4\sigma_x = 15 + 4 \times 1.64 = 21.56 \text{ MPa} \geq R_{bg} = 20 \text{ MPa} \text{ min. control for concrete strength}$$

Classes C 16/20. Cylinder strength $f_{ck,FRP} = 21.56 / 1.25 = 17.25$ MPa.



Fig. 3, 4 View of non compact column or view of the depth removed the loose concrete in place of local failure.



Fig. 5, 6 A view of the gradual strengthening of the pillars supporting the structure when complete or view of the reinforced columns after removal of support.

The Second Experiment Prestressed Beam

The basis for reinforced bridge in Lounovicich the experience gained during the experiment on a beam dimensions $120 \times 180 \times 3000$ mm concrete C 25/30, slat sizes 50×1.2 mm, length 2800 mm. Structural strengthening using prestressed additional plates from the production of Precast Brno SpA, race composites, which is biased by means of a special device via a torque wrench. A strip is anchored by epoxy bonding adhesive from SKW-MBT S&P and pre-concreted anchors in concrete.

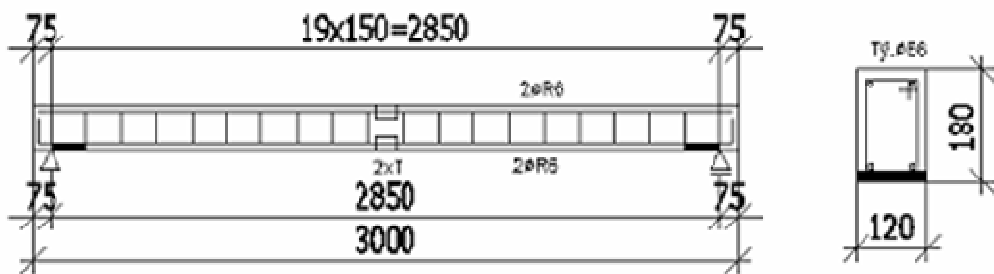


Fig. 7 View of the experimental sample reinforcement of reinforced prestressed FRP strips.

Strengthening of Reinforced Concrete Girder Bridge in Lounovice

The supporting structure consists of a continuous beam of two spans of the range 2×14.0 m. The beams are 0.3 m wide in the field is 0.95 m high longitudinal tapers are long 2.8 m from the intermediate supports. Height above the central support beam is 1.35 m. The beams have axis distance 1.6 m and the transverse direction are reinforced by cross bars to 3.5 m. Intermediate transoms are 0.2 meters wide and 0.85 m high, supporting crossbars are 0.3 meters wide and has a height equal to the beams. The main beams carry the concrete slab thickness 0.14 m, which is in connection with haunch beams 50/150 mm. The lower building forms one end abutments and intermediate supports. Saddles are made of limestone and granite blocks armored corners. Intermediate pillar is made entirely of granite blocks. Bridge are based on a flat concrete foundations rescued from undercutting sheet piling walls, the bottom surface is about 1.8 m below the bottom of the riverbed. Repair of the substructure will consist of re-profiling, cleansing and paired.



Fig. 8, 9 Looking at the bridge before rehabilitation.

Description of the Project Repair

Repair of the support structure includes both the expansion of the category of S7, 5 magnification unloading pavement consoles and clean, re-profiling and gain self supporting structure with prestressed and non-prestressed mechanically fastened carbon fibers and wrap.

For the design of the bridge amplification was performed in Scia calculate the beamed sloping grate modeling the geometry of the bridge, given critical load combination and the internal forces for individual beams forming a bridge structure.

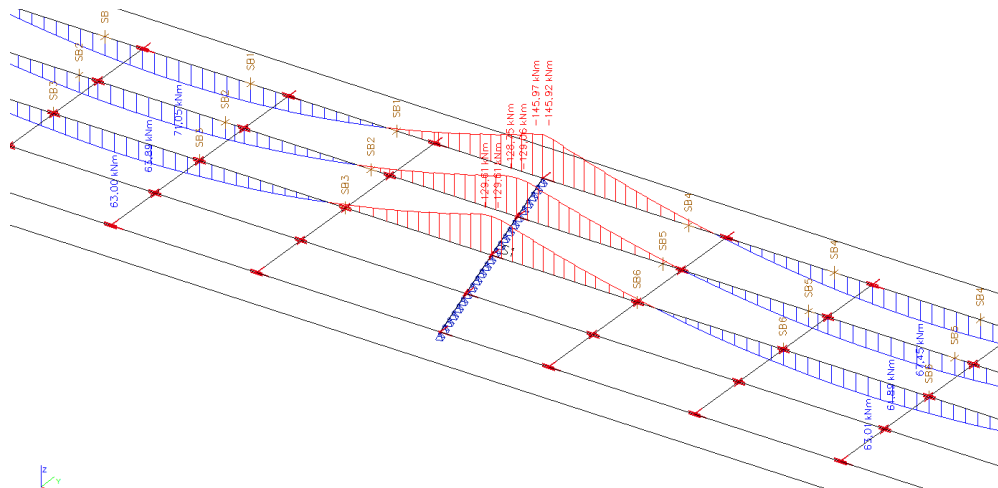


Fig. 10 View of the model created in the SCIA and determination of the bending moments you use to design a mechanically prestressed reinforcement anchored slats.

Experience of Implementing

As the largest problem in the application proved compliance with equality fins, as well as at the slightest cross prying there were split fins and it was necessary to replace a new one. Also expected stretch straps (verified by the certification of the plate with 50×1.4 mm to 0.07 % in laboratories KU Czech Technical University in Prague), i.e. the possibility of introducing forces into plates up to 70 kN, for a plate with 100×1.4 mm (140 kN) proved unrealistic and it was necessary to convert the structure into force achieved in the slats that moved using the plate with 100×1.4 mm at the level of 120 up to 125 kN and strips 50×1.4 mm at 65 up to 70 kN.



Fig. 11, 12 View of the mechanical anchorage of prestressed plates.



Fig. 13 View the final anchoring fins mechanically fastened using the front panels.

Acknowledgements

In conclusion, I would like to thank all participants of the construction for the opportunity to gain new experience in the remediation CPI Centrum in Olomouc PSJ SpA and bridge in Louňovice, i.e. the main contractor building Skanska CZ SpA, subcontractors STADO CZ Ltd., General designer METROPROJEKT PRAGUE SpA both in designing remediation and upon the realization that expired in 2013. Both buildings are already in operation.

References

- [1] Complete regeneration of the supporting structure prefab home building system T 06 B
- [2] CSN EN 1992-1-1 Eurocode 2: Design of concrete structures. Part 1-1: General rules and rules for buildings
- [3] RECO Program, a program for FEM structural analysis, web: www.recoc.cz
- [4] Data sheets for application of FRP fabrics, web: www.stado.cz
- [5] Externally bonded FRP reinforcement for RC structures Technical report on the "Design and use of externally bonded fiber reinforced polymer reinforcement (FRP EBR) for reinforced concrete structures" by 'EBR' working party of fib TG 9.3, July 2001, pp. 138.

Effect of Cement Dosage on Selected Mechanical Fracture Parameters of Concretes

ŠIMONOVÁ Hana^{1,a*}, HAVLÍKOVÁ Ivana^{1,b}, DANĚK Petr^{2,c},
LEHKÝ David^{1,d}, KUCHARCZYKOVÁ Barbara^{2,e} and KERŠNER Zbyněk^{1,f}

¹Brno University of Technology, Faculty of Civil Engineering, Institute of Structural Mechanics,
Veveří 331/95, 602 00 Brno, Czech Republic

²ditto, Institute of Building Testing

^asimonova.h@fce.vutbr.cz, ^bhavlikova.i@fce.vutbr.cz, ^cdaneck.p@fce.vutbr.cz,
^dlehky.d@fce.vutbr.cz, ^ekucharczykova.b@fce.vutbr.cz, ^fkersner.z@fce.vutbr.cz

Keywords: concrete, cement dosage, mechanical fracture parameters, three point bending fracture test, double-*K* fracture model, identification, artificial neural network, inverse analysis method

Abstract. Mechanical fracture parameters obtained from three-point bending tests on concrete specimens with a central edge notch are introduced in this paper. A total of four sets of specimens were tested. The concrete used in each set differed in cement dosage, which ranged from 250 to 405 kg per m³ of fresh concrete. Three specimens in each set were tested at the age of 28 days. Increasing the dosage of cement influences the mechanical fracture properties of concretes in both positive and negative ways.

Introduction

Project of the Grant Agency of the Czech Republic "Assessment and Prediction of the Concrete Cover Layers Durability" deals with the study of problems of concrete cover layers durability and contributes to development of the knowledge in the field of durability assessment and evaluation. Project is aimed especially at the determination of the transport characteristics of the concrete cover layers determined by the water and gas permeability methods. These so-called "durability parameters" are completed especially with the fracture parameters (e.g. fracture toughness and energy) and basic physical and mechanical properties of fresh and hardened concrete.

In this paper, authors are focused attention on mechanical fracture parameters of selected concrete determined via evaluation of records of experiments on specimens with stress concentrator. One of the fracture models applicable to concrete is the double-*K* model. This model combines the concept of cohesive forces acting on a fictitious (effective) crack increment with a criterion for crack propagation based on the stress intensity factor. Using double-*K* model is possible to determine the critical crack tip opening and fracture toughness of investigated concrete, respectively quantify – as indicated model name – two different levels of crack propagation: initiation, which corresponds to the beginning of the stable crack growth and the level of unstable crack propagation. Results obtained using double-*K* model are completed by selected parameters which were identified using artificial neural network based inverse analysis method [1].

Experimental Details

Materials. Tests were conducted on four sets of specimens differing in the material. Concrete of each set of specimens was different in dosage of Portland cement CEM I 42.5 R. Reference mixture (marked as REF) contains 250 kg/m³ of cement. The other mixtures, marked 0/1, 0/2 and 0/3, contain 305, 355 and 405 kg/m³ of cement, respectively. The consistency of fresh concrete was the same for all mixtures. Additional details regarding the concrete mixture compositions can be found in [2].

Specimens and Fracture Tests. Beam specimens (of nominal dimensions $100 \times 100 \times 400$ mm) with central edge notch were subjected to three-point bending (3PB) fracture tests. The notches were made with a diamond blade saw. The notches depths were approximately equal to 30 % of the depth of the specimen. The span length was equal to 300 mm. Three specimens from each set were tested at the age of 28 days. The fracture tests were carried out using a Heckert FPZ 100/1 testing machine with the load range of 0–10 kN.

Load versus displacement diagrams ($P-d$ diagrams) and load versus crack mouth opening diagrams ($P-CMOD$ diagrams) were recorded during the 3PB fracture experiments.

Application of the Double- K Fracture Model

The measured $P-CMOD$ diagrams are used to determine the fracture parameters of the double- K model. The unstable fracture toughness K_{Ic}^{un} is numerically determined first, followed by the cohesive fracture toughness K_{Ic}^c . When both of these values are known, the following formula can be used to calculate the initiation fracture toughness K_{Ic}^{ini} :

$$K_{Ic}^{ini} = K_{Ic}^{un} - K_{Ic}^c. \quad (1)$$

Details regarding the calculation of both unstable and cohesive fracture toughness can be found e.g. in [3,4].

Finally, according to Eq. 2 is determined the value of the load P_{ini} . This value can be defined as the load level at the beginning of stable crack propagation from an initial crack/notch and can be obtained using the expression:

$$P_{ini} = \frac{4 \cdot W \cdot K_{Ic}^{ini}}{S \cdot F_1(\alpha_0) \cdot \sqrt{a_0}}, \quad (2)$$

where $W = 1/6 BD^2$ is section modulus, B is specimen width, D is specimen depth, S is load span, a_0 is the initial notch length and $F_1(\alpha_0)$ is geometry function given by following equation:

$$F_1(\alpha_0) = \frac{1.99 - \alpha_0(1 - \alpha_0)(2.15 - 3.93\alpha_0 + 2.7\alpha_0^2)}{(1 + 2\alpha_0)(1 - \alpha_0)^{3/2}}, \quad (3)$$

where α_0 is ratio a_0/D .

Identification of Selected Parameters

Values of modulus of elasticity and parameters of the cohesive crack model (particularly the fracture energy and tensile strength) were identified from corrected $P-d$ diagrams [5] by inverse analysis using FraMePID-3PB software [1]. The cornerstone of the method is an artificial neural network which transfers the input data obtained from the fracture test to the desired material parameters.

The most important step in the whole procedure is the creation of the network and its training – the adjustment of its synaptic weights and biases. The training set is prepared numerically by the utilization of a finite element method (FEM) model which simulates a three-point bending test with random realizations of material parameters. The used FEM model was created in ATENA software; 3D Nonlinear Cementitious 2 material model was used to govern the gradual evolution of localized damage [6].

Measured and numerically derived $P-d$ diagrams with identified parameters are introduced in Fig. 1 for selected fracture test.

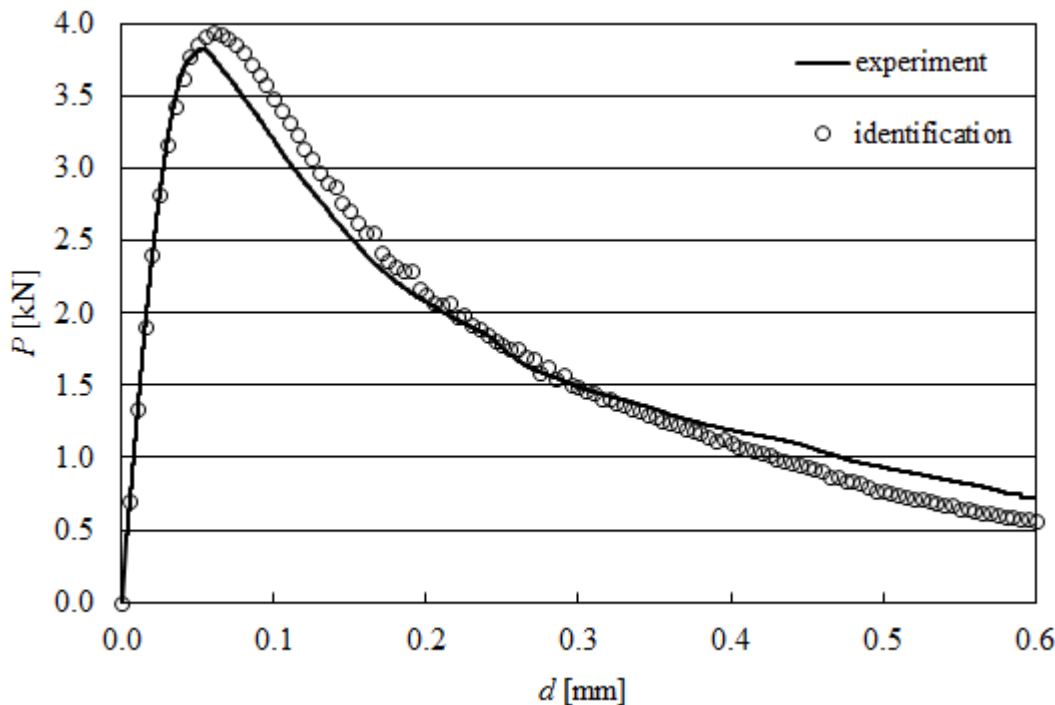


Fig. 1 P - d diagrams (specimen REF 2): measured and numerically derived with identified parameters

Results

The arithmetic mean and standard deviation values of the selected parameters are introduced in Table 1: elasticity modulus E , fracture energy G_F , tensile strength f_t , compressive strength f_c , unstable fracture toughness K_{lc}^{un} , the initiation level of stress intensity factor K_{lc}^{ini} , ratio K_{lc}^{ini}/K_{lc}^{un} , i.e. the ratio of initiation fracture toughness to unstable fracture toughness, and ratio P_{ini}/P_{max} , i.e. the ratio between the force at the beginning of stable crack propagation from an initial stress concentrator and the maximal force. The relative mean values of these properties are shown in Table 2 – the 100% value for each material parameter represents the values of those parameters for the reference concrete (REF).

Table 1 Mean values (standard deviations) of selected parameters of studied concretes

Parameter / Concrete	REF	0/1	0/2	0/3
E [GPa]	25.3 (2.4)	25.9 (1.8)	33.93 (–)	35.0 (4.0)
G_F [J/m ²]	155.1 (20.8)	174.2 (25.9)	153.7 (43.0)	133.9 (38.1)
f_t [MPa]	1.6 (0.1)	2.1 (0.1)	3.6 (0.3)	3.2 (0.3)
f_c [MPa]	21.4 (0.1)	33.3 (0.3)	44.9 (0.5)	55.6 (2.0)
K_{lc}^{un} [MPa·m ^{1/2}]	0.768 (0.064)	1.117 (0.248)	1.109 (0.109)	1.087 (0.258)
K_{lc}^{ini} [MPa·m ^{1/2}]	0.324 (0.084)	0.536 (0.213)	0.666 (0.025)	0.457 (0.131)
K_{lc}^{ini}/K_{lc}^{un} [–]	0.418 (0.075)	0.472 (0.095)	0.612 (0.102)	0.418 (0.021)
P_{ini}/P_{max} [–]	0.695 (0.134)	0.785 (0.164)	0.794 (0.009)	0.592 (0.107)

Table 2 Relative mean values of selected parameters of studied concretes in %

Parameter / Concrete	REF	0/1	0/2	0/3
E	100.0	102.4	134.0	138.3
G_F	100.0	112.3	99.1	86.3
f_t	100.0	131.3	225.0	200.0
f_c	100.0	155.6	209.8	259.8
K_{lc}^{un}	100.0	145.4	144.4	141.5
K_{lc}^{ini}	100.0	165.4	205.6	141.0
K_{lc}^{ini}/K_{lc}^{un}	100.0	112.9	146.4	100.0
P_{ini}/P_{max}	100.0	112.9	114.2	85.2

Conclusions

The authors focused their attention on mechanical fracture parameters of selected concretes determined via the evaluation of records of experiments performed on four sets of specimens with a stress concentrator. The concrete used in each set differed in cement dosage, which ranged from 250 to 405 kg per m³ of fresh concrete. Increasing the dosage of cement did not always cause an improvement in the mechanical fracture properties of the concrete. Increasing the dosage of cement generally had a positive effect on the following parameters of the tested concretes: elasticity modulus, tensile strength, compressive strength, unstable fracture toughness, and the initiation level of the stress intensity factor. Increasing the cement dosage had a negative effect on fracture energy in case of highest dosage.

Acknowledgements

This outcome has been achieved with the financial support of the Czech Science Foundation, project GA CR 13-18870S.

References

- [1] D. Lehký, Z. Keršner, D. Novák, FraMePID-3PB software for material parameter identification using fracture tests and inverse analysis, *Advances in Engineering Software*. 63 (2013) 1–8.
- [2] M. Matysík, L. Topolář, P. Daněk, T. Vymazal, I. Plšková, The effect of concrete quality on the acoustic emission parameters during three-point bending fracture test, *Advanced Materials Research*. 897 (2014) 149–152.
- [3] S. Xu, H.W. Reinhardt, Z. Wu, Y. Zhao, Comparison between the double-K fracture model and the two parameter fracture model, *Otto-Graf-Journal*. 14 (2003) 131–157.
- [4] X. Zhang, S. Xu, A comparative study on five approaches to evaluate double-K fracture toughness parameters of concrete and size effect analysis, *Engineering Fracture Mechanics*. 78 (2011) 2115–2138.
- [5] P. Frantík, J. Průša, Z. Keršner, J. Macur, About stability loss during displacement-controlled loading, in: Proceeding of International Conference on Fibre Concrete 2007, Prague, 2007.
- [6] V. Červenka, L. Jendele, J. Červenka, ATENA Program Documentation – Part 1: Theory, Červenka Consulting, Prague, Czech Republic, 2007.

The Effect of the Carbon Nanotubes on the Mechanical Fracture Properties of Alkali Activated Slag Mortars

TOPOLÁŘ Libor^{1,a*}, ŠIMONOVÁ Hana^{1,b}, ROVNANÍK Pavel^{1,c}
and SCHMID Pavel^{1,d}

¹Brno University of Technology, Faculty of Civil Engineering, Veveří 331/95, 602 00 Brno,
Czech Republic

^atopolar.l@fce.vutbr.cz, ^bsimonova.h@fce.vutbr.cz, ^crovnanik.p@fce.vutbr.cz,
^dschmid.p@fce.vutbr.cz

Keywords: alkali activation, slag, mechanical fracture properties, three-point bending test, acoustic emission

Abstract. New nanomaterials such as carbon nanotubes and nanofibres considerably improve performance of current building materials and they can contribute to new application facilities. Alkali activated slag is a material having a great potential to be used in practice. The main drawback of this material is a high level of autogenous and especially drying shrinkage, which causes a deterioration of the mechanical fracture properties. The aim of this paper is introduce the effect of carbon nanotubes admixture on the microstructure and mechanical performance of alkali activated slag mortars. The three-point bending tests of specimens with central edge notch were performed. Method of acoustic emission was used during this testing.

Introduction

Alkali activated aluminosilicate materials represent an alternative to ordinary Portland-cement based materials, reducing the environmental impact building industry and offering new superior properties. Alkali activated slag (AAS) is based on granulated blast furnace slag, which can be activated by alkali hydroxides, carbonates or the most preferably silicates [1]. Type and dosage of the activator as well as the way of curing have a significant effect on the hydration course and final mechanical properties [2].

The major disadvantage of AAS is an increased shrinkage during hardening period, caused by both autogeneous and drying shrinkage, which finally results in volume contraction, microcracking and deterioration of tensile and bending properties [3].

Acoustic emission method detects the stress waves generated from the place, where internal stress is distributed in the material. The causes of acoustic emission are structural changes, namely, micro-changes. Crack initiation and growth, crack opening and closure and dislocation movement, are possible acoustic emission sources at three-point bending tests. Acoustic emission method detects only the active changes in structure, which means that geometric discontinuities do not produce acoustic emission activity [4].

Our currently solved project is devoted to the investigation of effects of carbon nanotubes (CNTs) as nanosized reinforcement on the properties of alkali activated aluminosilicate materials and the main motivation is to reduce cracking tendency and improve tensile properties of these materials. This paper presents and discusses the comparison of selected mechanical fracture parameters of the material and parameters signals of acoustic emission for different quantity CNTs.

Experimental Part

Materials and Sample Preparation. Alkali activated slag mortars were composed of granulated blast furnace slag finely ground to a specific surface of $380 \text{ m}^2 \cdot \text{kg}^{-1}$ and sodium silicate solution with $\text{SiO}_2/\text{Na}_2\text{O} = 1.6$ and 43 % of dry mass. Quartz sand with a maximum grain size of 2.5 mm

was used as aggregate. Fresh mixture was prepared by mixing: 1000 g of slag, 400 g of silicate solution, 3000 g of sand and 211 g of water. First mixture marked as REF was reference without nanosized reinforcement. The other mixtures, marked CNT_0.5 and CNT_1.0, contain carbon nanotubes in amount 0.5 and 1.0 % of weight of slag, respectively.

AAS slurry was cast into prismatic moulds (40×40×160 mm) to set and after 20 h the samples were demoulded and immersed in water for another 27 days before testing. The three specimens were produced for all mixtures. Prior to testing of fracture properties the specimens were pull out from water immersion and stored in the air at laboratory conditions ($20 \pm 1^\circ\text{C}$, RH $45 \pm 5\%$).

Testing Methods. The three point bending (3PB) fracture tests were conducted on beam specimens with central edge notch. The initial notch was made before testing with a diamond blade saw. The depth of the notches was approximately 30 % of the depth of the specimen. The span length was equal to 120 mm. The fracture tests were carried out using a Heckert FPZ 10/1 testing machine in the range of 0–1000 N. The specimens were tested at the age of 28 days. Load versus displacement diagrams (F - d diagrams) were recorded (using HBM SPIDER 8) during the 3PB fracture experiments.

Values of elasticity modulus were determined from first (almost linear) part of F - d diagrams. Estimations of fracture energy values according to the RILEM method were calculated using work-of-fracture values [5]. The effective fracture toughness values were determined using the Effective Crack Model [6] which combines the linear elastic fracture mechanics and crack length approaches.

The values of bulk density and informative values of compressive strength (determined for fragments of the specimens, which were prepared from the broken specimens after the 3PB fracture tests) were also determined for all specimens.

The initiation of cracks during fracture tests was also monitored by method of acoustic emission (AE). AE is the term for the noise emitted by material and structures when they are subjected to stress. Types of stresses can be mechanical, thermal or chemical. This emission is caused by the rapid release of energy within a material due to events such as crack formation, and the subsequent extension occurring under an applied stress, generating transient elastic waves which can be detected by piezoelectric sensors. In this case method of AE detects and characterizes the development of process of the fracture crack and evaluates activity and evaluates the activity of the damage and only in his course of [7].

Results

The relative mean values of selected material properties obtained from recorded F - d diagrams [5, 6] using academic *StiCrack* software (modulus of elasticity, effective fracture toughness and specific fracture energy) are summarized in Table 1. This table also introduces informative values of compressive strength and values of bulk density. The 100% value for each material parameter represents the values of those parameters for the reference mixture (REF).

Table 1 Relative mean values [%] of determined parameters in relation to REF

Parameter	REF	CNT_0.5	CNT_1.0
Bulk density	100.0	100.1	95.0
Compressive strength	100.0	110.0	86.6
Modulus of elasticity	100.0	123.0	88.7
Fracture toughness	100.0	90.0	72.1
Fracture energy	100.0	65.6	64.4
Duration of AE signals	100.0	108.6	69.9

For illustration, Fig. 1 introduces values of modulus of elasticity (left) and values of fracture toughness (right) for examined materials. Values of fracture energy are introduced in Fig. 2 (left). The figures below show the mean values (obtained usually from 3 measurements) and standard deviation values of the selected parameters.

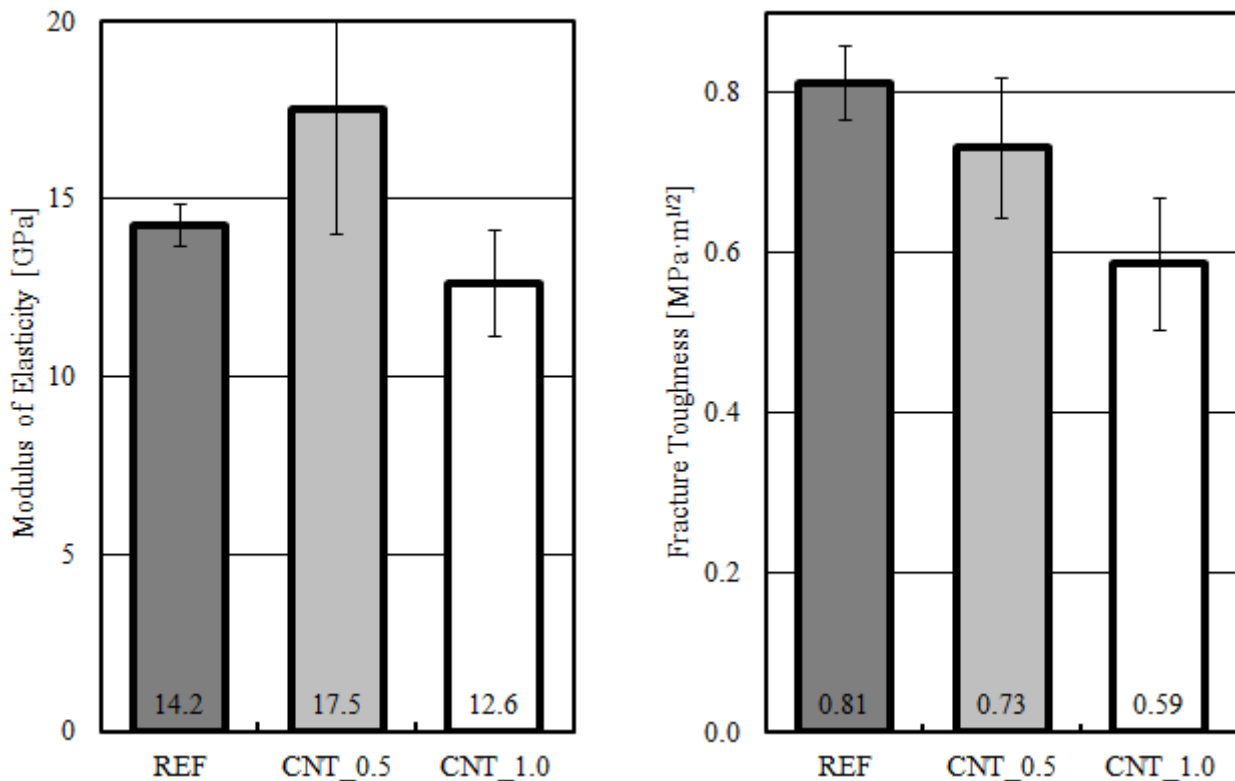


Fig. 1 Determined values (mean \pm standard deviation) for modulus of elasticity (left) and fracture toughness (right)

During tests an acoustic emission activity was recorded. The guard sensor eliminated mechanical and electrical noise. Acoustic emission system DAKEL with software XEDO has been applied for continuous monitoring of concrete structure loading. Four acoustic emission sensors were placed on specimen surface. To describe the origin of micro cracks during loading, we focused on the duration of acoustic emission signals. Duration is the time difference between the first and last threshold crossings. Results of signals duration AE in Fig. 2 (right) are given in the form of arithmetic mean (obtained from 3 independent measurements) and standard deviations as error bars.

Conclusions

The paper deals with the influence of quantities CNTs in alkali activated slag mortars on the selected mechanical fracture parameters determined from three-point bending of specimens with central edge notch. Informative compressive strength values were determined for fragments of the specimens, which were prepared from the broken specimens after the three-point bending tests.

Carbon nanotubes have no significant effect on values of bulk density. In case of compressive strength, elasticity modulus and duration of AE signals the addition of CNTs in amount 0.5 % of weight of slag leads to increase of these parameters values about 10, 23 and 9 %, respectively. Addition of CNTs in amount 1.0 % of weight of slag leads to decrease of these parameters values about 13, 21 and 30 %, respectively. Values of fracture toughness and fracture energy were decreased in both cases of addition of CNTs.

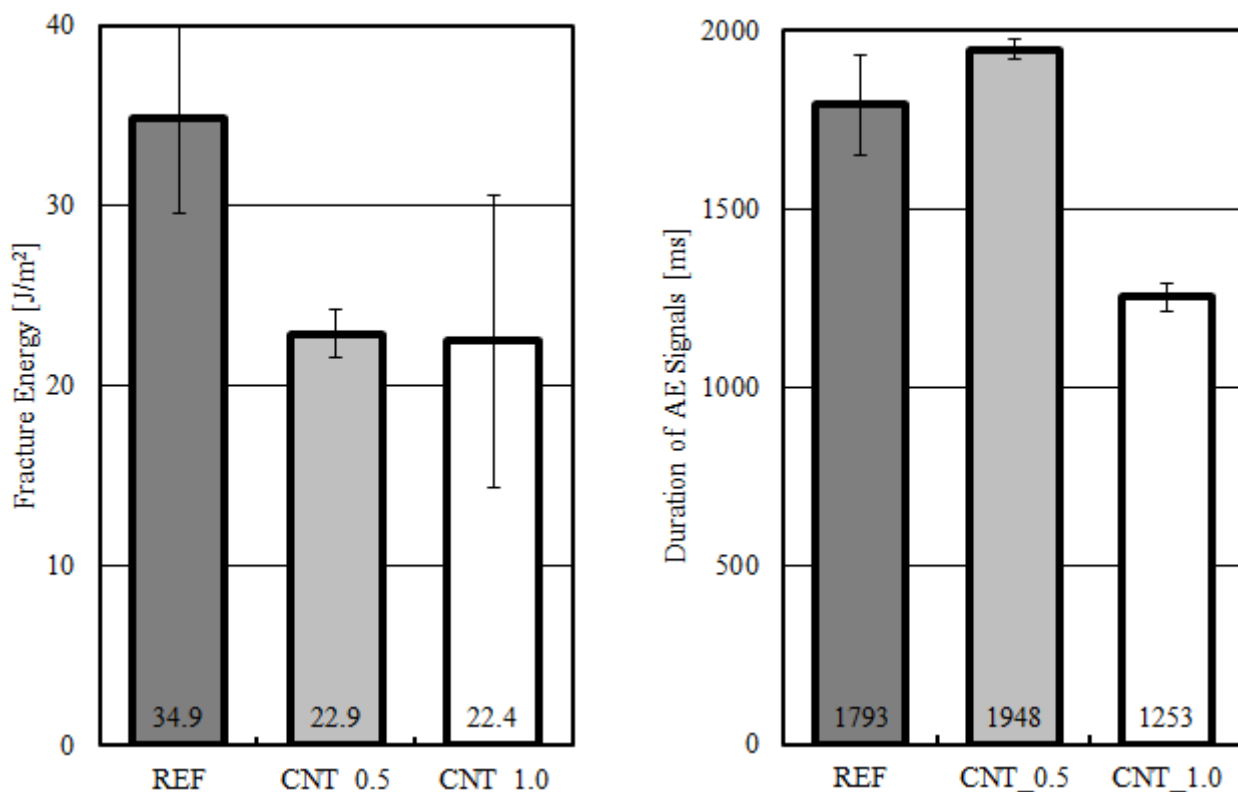


Fig. 2 Determined values (mean \pm standard deviation) for fracture energy (left) and duration of AE signals (right)

Acknowledgements

This research has been supported by the project of GACR No. 13-09518S. The authors greatly thank Dr. Miroslav Stibor for providing support for special calculations using *StiCrack* software.

References

- [1] C. Shi, P. V. Krivenko, D. Roy, Alkali-Activated Cements and Concretes, Taylor & Francis, Oxon, UK, 2006.
- [2] C. Shi, R. L. Day, Factors affecting early hydration characteristics of alkali-slag cements, *Cem. Concr. Res.* 26 (1996) 439–448.
- [3] M. A. Cincotto, A. A. Melo, W. L. Repette, Effect of different activators type and dosages and relation with autogenous shrinkage of activated blast furnace slag cement, in: G. Grieve, G. Owens (eds.), Proceedings of the 11th International Congress on the Chemistry of Cement, Durban, South Africa, 2003, 1878–1888.
- [4] M. Korenska, M. Manychova, L. Pazdera, L. Topolar, Monitoring of the damage in stone blocks by means of non-destructive methods, *Key Engineering Materials*. 592–593 (2014) 545–548.
- [5] RILEM Committee FMT 50, Determination of the fracture energy of mortar and concrete by means of three-point bend test on notched beams, *Material Structures*. 18 (1985) 285–290.
- [6] B. L. Karihaloo, Fracture mechanics of concrete. Longman Scientific & Technical, New York, 1995.
- [7] Ch. U. Grosse, M. Ohtsu, Acoustic Emission Testing. Springer-Verlag, Berlin, 2008.

Finite Element Analysis of Damage Modeling of Fiber Reinforced Laminate Plate

KORMANÍKOVÁ Eva^{1,a*} and KOTRASOVÁ Kamila^{1,b}

¹Technical University of Košice, Civil Engineering Faculty, Vysokoškolská 4, 04200 Košice, Slovak Republic

^aeva.kormanikova@tuke.sk, ^bkamila.kotrasova@tuke.sk

Keywords: damage mechanics, random-strength model, delamination, fiber reinforced layers, plate element, finite element analysis

Abstract. The paper deals with identifying the damage model for a bundle of T300 and AS4D fibers under tensile load. The damage model is implemented in ANSYS for a one-dimensional bar element to obtain the strain-stress response of a bundle of fibers. Delamination of a laminated plate, which consists of unidirectional fiber reinforced layers, is investigated. The methodology adopts the first-order shear laminated plate theory and fracture and contact mechanics. The latter technique allows for calculating individual components of the energy release rate along the lamination front. Numerical results are given for mixed mode delamination problems. Numerical example is performed by the commercial ANSYS code.

Introduction

Many modes of damage can be observed in composite materials, including matrix cracks, fiber breakage, fiber matrix de-bonding and more. The continuum damage mechanics represents all these damage modes by the effects they have on the meso-scale behavior of the material. One notable effect of damage is a reduction of stiffness, which can be used to define damage.

One of the most severe defects in composite laminate structures is delamination. Delamination originates from manufacturing imperfections, cracks produced by fatigue or low velocity impact, stress concentration near joints and free edges, or due to high interlaminar stresses. In the interface modeling technique, based on fracture mechanics, the critical energy release rate for particular delamination mode is used [1].

Random Strength Model

If a lamina is subject to tensile stress in the fiber direction, it is reasonable to assume that the matrix carries only a small portion of the applied load and no damage is expected in the matrix during loading. Then, the ultimate tensile strength of the composite lamina can be accurately predicted by computing the strength of fibers.

The Weibull expression is often used to describe the cumulative probability $F(\bar{\sigma})$ that a fiber of length δ will fail at or below an effective stress $\bar{\sigma}$ [2].

Then, the cumulative probability we can express

$$F(\bar{\sigma}) = 1 - \exp\left(-\frac{\delta}{L_0}\left(\frac{\bar{\sigma}}{\bar{\sigma}_0}\right)^m\right) \quad (1)$$

where the values of $\bar{\sigma}_0$ and m , which represent the characteristic strength of fiber, and the dispersion of fiber strength, respectively, can be determined from fiber strength experiments performed with a gauge length L_0 .

The maximum or critical bundle strength σ_{cr} is possible to obtain as

$$\sigma_{cr} = (\delta \alpha m)^{-1/m} \exp(-1/m) \quad (2)$$

The critical damage D_{cr} can be computed as the area fraction of broken fibers in the lamina prior to catastrophic failure, which turns out to be a function of Weibull shape modulus m only.

$$D_{cr} = 1 - \exp(-1/m) \quad (3)$$

Then, the product $\delta\alpha$ can be obtained as

$$\delta\alpha = \frac{(\sigma_{cr})^{-m}}{me} \quad (4)$$

where e is Euler's number.

Mixed-mode Analysis of Delamination

Fracture mechanics assumes that delamination propagation is controlled by the critical energy release rate (ERR). Delamination grows on the region of the delamination front where the following condition is satisfied

$$\left(\frac{G_I}{G_I^C}\right)^\alpha + \left(\frac{G_{II}}{G_{II}^C}\right)^\beta + \left(\frac{G_{III}}{G_{III}^C}\right)^\gamma \geq 1 \quad (5)$$

where α, β, γ are mixed mode fracture parameters determined by fitting to experimental test results.

$G_I^C, G_{II}^C, G_{III}^C$ are assumed to be material properties, independent of their location along the delamination front, and evaluated from experimental procedures. G_I, G_{II}, G_{III} are individual components of ERR. These components are of ERR are computed by using [2]

$$G_I(A) = \frac{1}{2} \frac{R_A^z \Delta w_{B-B'}}{\Delta_n \Delta_t} \quad G_{II}(A) = \frac{1}{2} \frac{R_A^n \Delta u_{nB-B'}}{\Delta_n \Delta_t} \quad G_{III}(A) = \frac{1}{2} \frac{R_A^t \Delta u_{tB-B'}}{\Delta_n \Delta_t} \quad (6)$$

where R_A^z, R_A^n, R_A^t are the reactions in the spring element connecting node A in the thickness z direction, normal n and tangential t directions to the delamination front,

$\Delta w_{B-B'}, \Delta u_{nB-B'}, \Delta u_{tB-B'}$ are the relative z, n, t displacements between the nodes B and B' located immediately ahead of the delamination front along its normal directions passing through A,

Δ_t and Δ_n are the characteristic mesh sizes in the normal and tangential directions of the delamination front (Fig. 1).

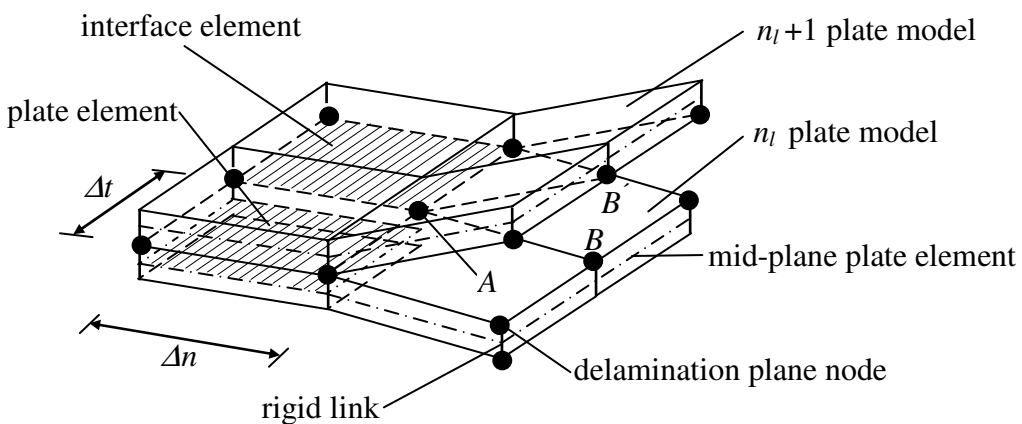


Fig. 1 Plate assembly in the neighborhood of the delamination front [2]

Example of Damage Modeling

The laminate plate consists of two sublaminates (1-1 model). The sublaminates consist of carbon epoxy UD composite [3]. Fiber volume fraction is 0.6.

The sublaminates are loaded by load mode I (opening load) $F = 1\text{N/mm}$. Diameters of the laminate plate are shown in Fig. 2.

The mechanical characteristics of the top layer (AS4D/9310) are: $E_x = 133.86\ 000$ GPa, $E_y = E_z = 7.706$ GPa, $G_{yz} = 2.76$ GPa, $G_{xy} = G_{xz} = 4.306$ GPa, $\nu_{xy} = \nu_{xz} = 0.301$, $\nu_{yz} = 0.396$, $F_{lt} = 1830$ MPa.

The mechanical characteristics of the bottom layer (T300/5208) are: $E_x = 136$ GPa, $E_y = E_z = 9.8$ GPa, $G_{yz} = 5.2$ GPa, $G_{xy} = G_{xz} = 4.7$ GPa, $\nu_{xy} = \nu_{xz} = 0.28$, $\nu_{yz} = 0.15$, $F_{lt} = 1550$ MPa.

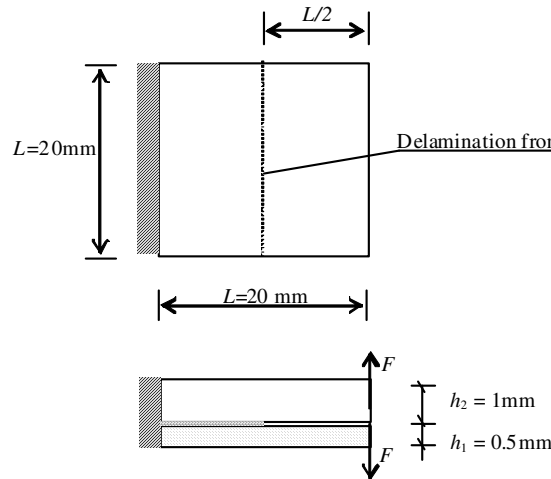


Fig. 2 Laminate geometry

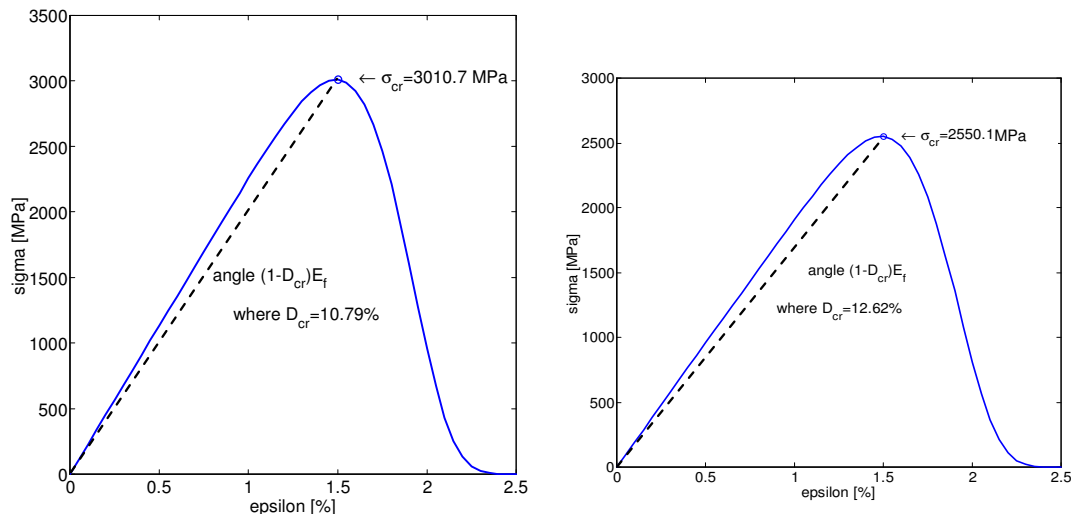


Fig. 3 Fiber tensile damage model for AS4D and T300 fibers, respectively

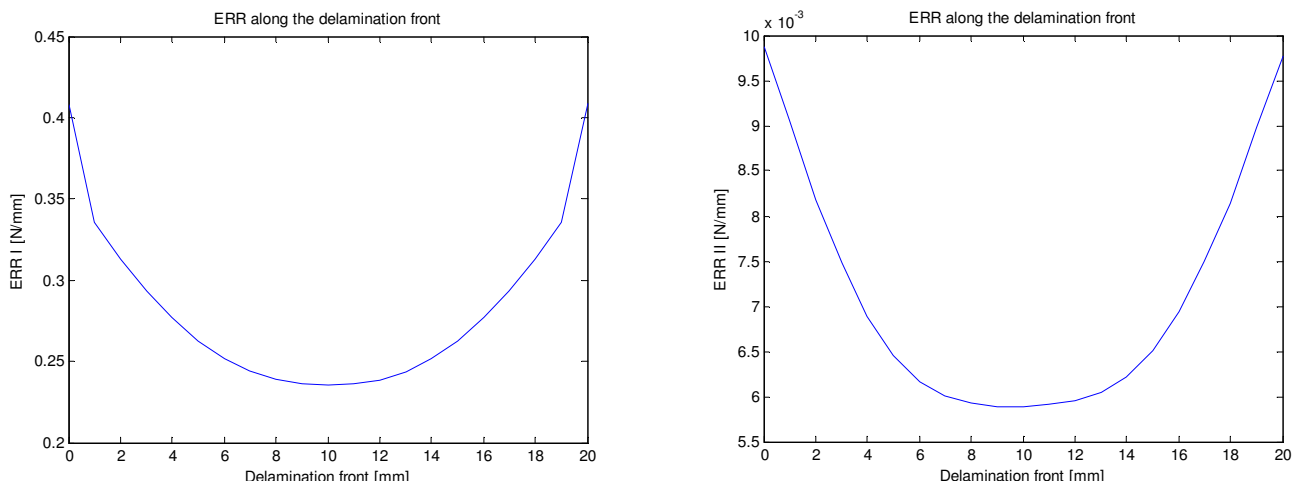


Fig. 4 ERR I and ERR II, respectively along the delamination front

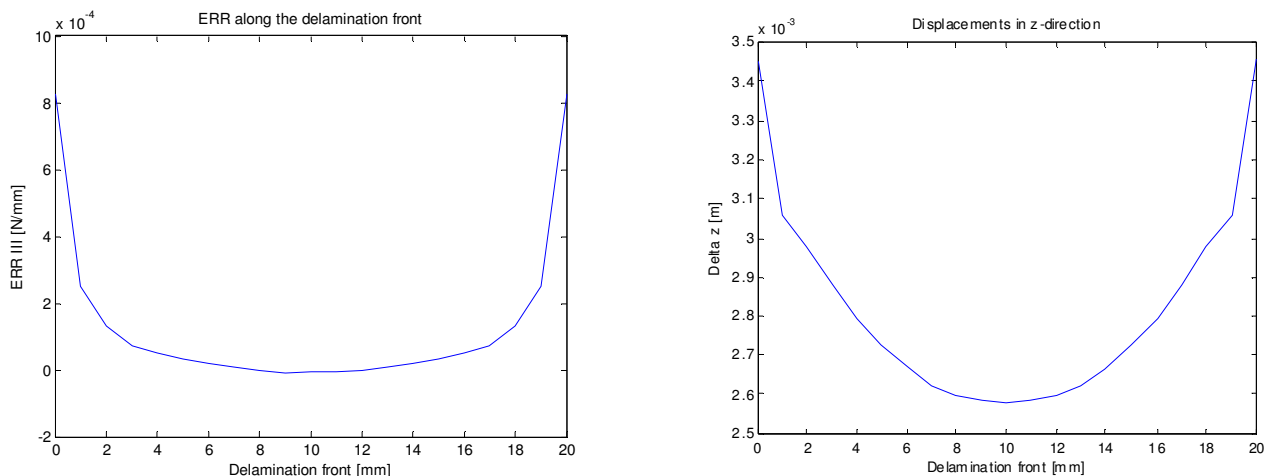


Fig. 5 ERR III and displacement in z -direction, respectively along the delamination front

Conclusion

The one-dimensional damage model [2] was implemented in program ANSYS. Then the strain-stress diagrams of carbon epoxy bundle of fibers were obtained (Fig. 3).

A two-layer laminate model which incorporates interface models based on the fracture and contact mechanics has been proposed. Delamination of the laminated plate was represented by two sublaminates. Sublaminates were modeled with the help of shear deformable elements SHELL181 in program ANSYS.

Individual components of ERR I, ERR II and ERR III along the delamination front in terms of interface variables were calculated (Figs. 4, 5a). One can see for load mode I that the largest values of ERR has the response mode ERR I. Other response modes ERR II and ERR III have minor influence on the whole ERR [4-6]. Fig. 5b shows relative displacements in the z -direction along the delamination front.

Unlike cracks in homogeneous media, which follow a path maintaining a pure mode I at their tip, delamination at the interface of the composite laminate plates involves coupled fracture modes.

Acknowledgement

This paper has been supported by the project VEGA 1/0201/11 Progressive methods for the solution of structural elements made of composite and other new-age materials.

References

- [1] I. Száva, M. Šejnoha, E. Kormaníková, et al., Selected Chapters of Mechanics of Composite Materials III. Derc Publishing House, 2013.
- [2] E. J. Barbero, Finite element analysis of composite materials, CRC Press, USA, 2008.
- [3] J. Vorel, M. Šejnoha, Documentation for HELP program, Theoretical manual and User guide, Czech Technical University in Prague, Faculty of Civil Engineering, 2008.
- [4] M. Žmindák, M. Dudinský, Finite Element Implementation of Failure and Damage Simulation in Composite Plates. In Eds, Ning HU: Composites and Their Properties. InTECh, 2012.
- [5] M. Mihaliková et al., Influence of strain rate on automotive steel sheet breaking. Chemické listy. Vol. 105, No. 17, 2011.
- [6] J. Králik, Probability Nonlinear Analysis of Reinforced Concrete Containment Damage due to High Internal Overpressure, In proc.: CCCT'04, August 14-17, 2004, Austin, Texas, USA, Editors Chu, HW, Savoie, M., Sanchez, B., Vol. 5, p. 65-68.

CHAPTER 2:

Wind Engineering

Analysis of Structures Having an Irregular Cross-Section Subjected to a Wind Load

JENDŽELOVSKÝ Norbert^{1,a*}

¹STU Bratislava, Faculty of Civil Engineering, Radlinského 11, 813 68 Bratislava, Slovak Republic

^anorbert.jendzelovsky@stuba.sk

Keywords: wind action, pressure coefficient, modeling, tall building

Abstract. The paper presents an analysis of wind effects acting upon the structures having an irregular shape. The calculation of pressure distribution around the perimeter of irregularly-shaped structure is presented. The example shows the analysis techniques employing both values from the valid standards and results of a numerical calculation of flux of an irregularly shaped structure.

Introduction

The principal idea of this article is to present methods of numerical analysis of structures loaded by wind. An irregular cross-section of the building is a matter of interest here. The standard Eurocode 1 [1] does not mention recommendations for calculation of wind pressure and wind forces coefficients for the cases of buildings having an irregular cross-section – irregular triangle with rounded corners. Only the solutions for buildings having rectangular and circular cross sections have been presented in the mentioned standard. This article presents the design calculations for a specific building.

Wind Effect

Overall wind forces acting upon the building structure are given by standard [1] according to the following relations:

The basic wind speed is defined as v_b (m/s). The mean wind speed varies with height according to the relation

$$v_m(z) = c_r(z)c_o(z)v_b, \quad (1)$$

where $c_o(z)$ is the orography factor = 1.0 (unless otherwise specified)

$c_r(z)$ is the roughness factor, which varies with height according to the equation

$$\begin{aligned} c_r(z) &= k_r \ln(z/z_0) && \text{for } z_{\min} < z < z_{\max}, \\ c_r(z) &= c_r(z_{\min}) && \text{for } z < z_{\min}, \end{aligned} \quad (2)$$

where z_0 is the roughness length and k_r is a terrain coefficient dependent on the roughness, determined from the relation:

$$k_r = 0.19 \left(\frac{z}{z_{0,H}} \right)^{0.07}. \quad (3)$$

Other values are taken from the table in standard [1], in which countries are classified with reference to their terrain roughness into Categories from 0 to IV.

Turbulence intensity $I_v(z)$ in a specific height is defined as the standard turbulence deviation σ_m divided by the mean wind speed v_m Eq. 1:

$$\sigma_v = k_r v_b k_i, \quad (4)$$

$$I_v(z) = \sigma_v / v_m(z). \quad (5)$$

Peak wind pressure q_p along the height z depends on the mean wind speed and the short-term fluctuations in wind speed

$$q_p(z) = (1 + 7I_v(z))1/2\rho v(z)_m^2. \quad (6)$$

Wind pressure w_e at the surface is defined:

$$w_e = q_p(z)c_{pe}, \quad (7)$$

where c_{pe} is pressure coefficient for exterior surfaces. The standard defines these coefficients for structures with rectangular cross-section as well as for those with circular cross - section, but here the value of the Reynolds number plays the crucial role:

$$\text{Re} = \frac{bv(z_e)}{v}, \quad (8)$$

where b is the diameter of the cylinder and v is the kinematic viscosity of air ($15 \times 10^{-6} \text{ m}^2/\text{s}$).

Numerical Example

Let us present an example of the analysis: a high-rise structure was considered (see Fig. 1) having a shape of an irregular triangle with rounded corners. The building's width is 40.08 m, the perpendicular dimension is 29.15 m. In the centre of building there is a reinforcing core containing elevator shafts and stairways. From the central core, walls diverge towards the building facade. Thickness of wall is from 200 to 300 mm, varying along the height of the building, ceilings are 200 mm thick. The building has 27 floors (25 above ground, 2 underground floors).

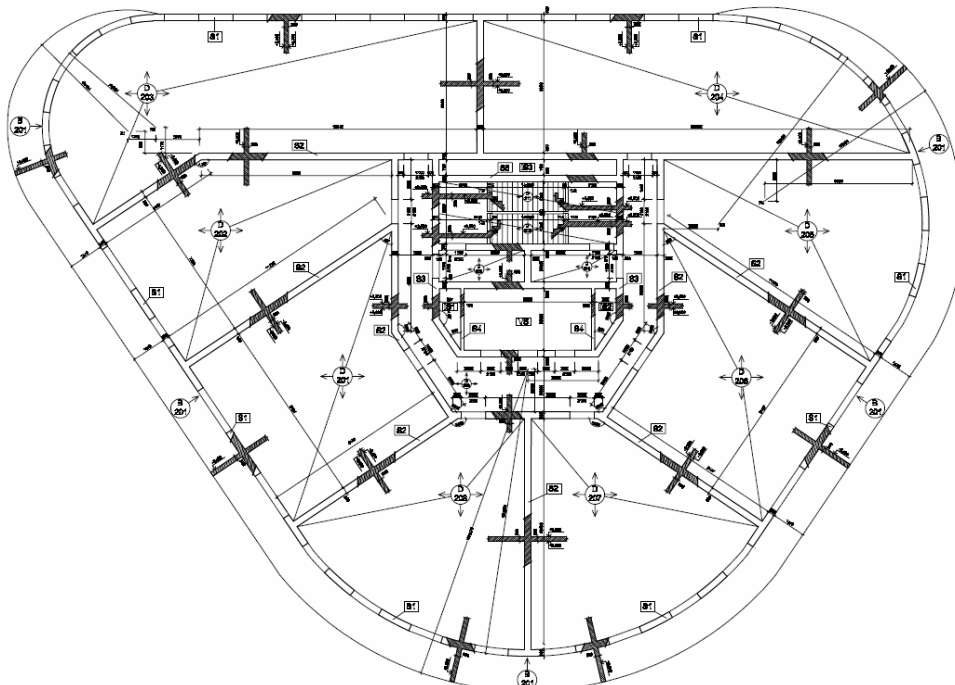


Fig. 1 Floor plan of building

There are several ways of calculating the external pressure coefficients. One way is to calculate a circular area with a cross-section identical with a ground plan of the building. Substitutive circle has a radius 17.00 m. For this circle the pressure coefficients were calculated (Fig. 2). Wind direction Y1 was considered. Load pressures in respective floors were calculated. Subsequently, the pressure load was converted to resultant forces in the directions x , y . The effects of acting of resultant forces upon the tall building core were investigated. In respective floors the values of resultant forces varied in relation to wind velocity along the height.

Another way is to calculate the pressure coefficients for the real shape of the structure presented in Fig. 3.

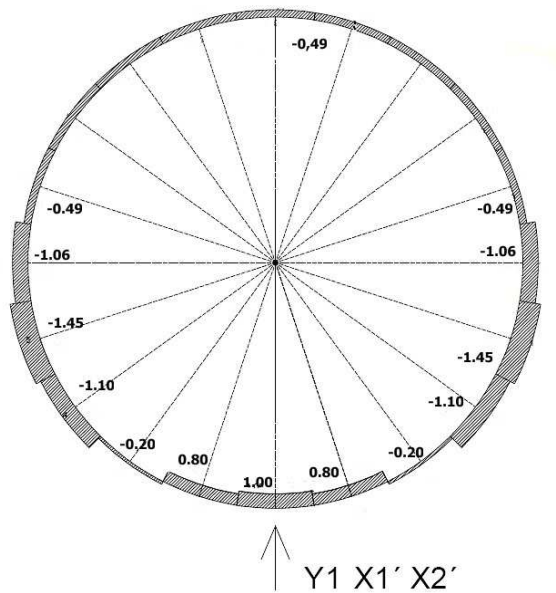


Fig. 2 Wind pressure on building with circular cross-section, pressure+, suction-

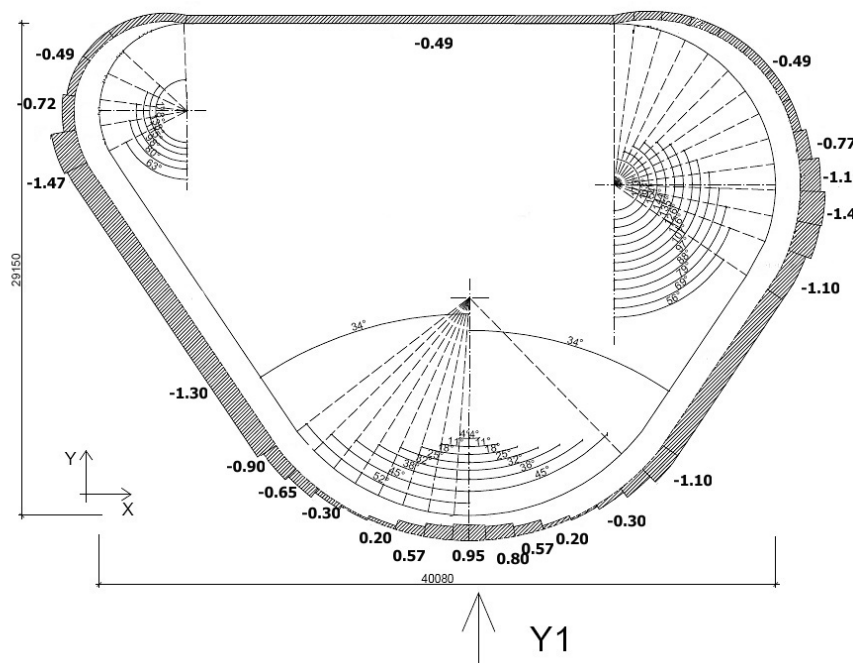


Fig. 3 Wind pressure on building with the real floor plan in the direction Y1

Coefficient of pressure in different parts of the contour was calculated as the wind load acting upon three circles. The radius of the bottom circle is $r = 13.0$ m, radius of the left circle is $r = 5.095$

m and radius of the right circle is $r = 9.50$ m. Equations for calculating the coefficient of pressure for the ring shape which are given in a standard regulation [1], were used. At direct walls, values of the coefficients at the end of one and the beginning of the second arch were averaged. Fig. 4 presents the wind acting in direction Y2. Here, the pressure coefficient was calculated firstly as for a vertical wall with a value of 0.95. Then, coefficients for three arches with different radii, considering the wind direction Y2 were calculated. On contact of the horizontal contour with right and left circles, the pressure coefficient was averaged. On two diagonals, coefficient was determined as the average value of the values at the ends of the arches.

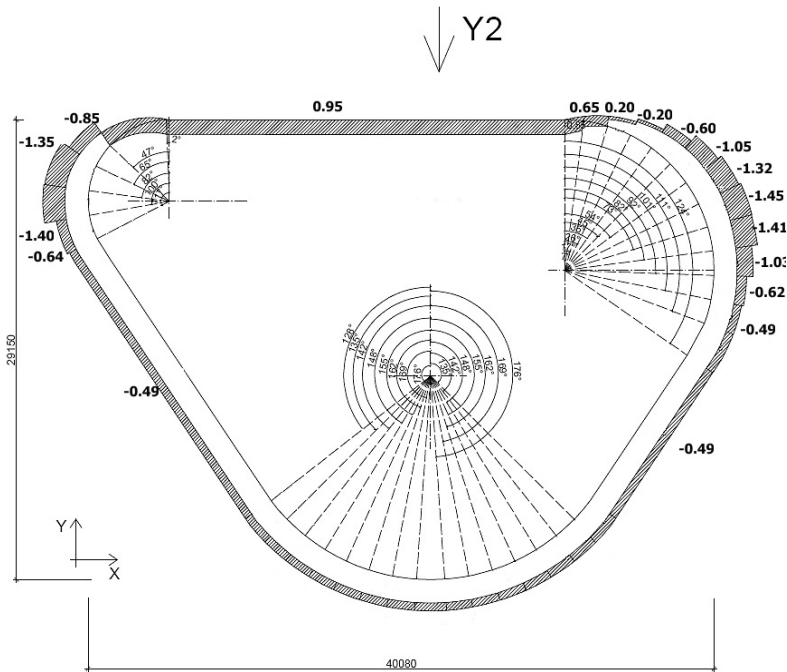


Fig. 4 Wind pressure on building with the real floor plan in the direction Y2

Conclusion

Values of the pressure coefficients on an irregular cross-section obtained by calculations presented above represent a starting point to further investigations of such cross-sections. Similar analyses have been presented in [2,3,4]. Next analyses of authors will focus on numerical modelling of pressure distribution using CFD based software. Another option is to use the wind tunnel STU Bratislava. On a scale model, the values of pressure along the contour can be experimentally measured there.

Acknowledgements

This contribution is the result of the research supported by Slovak Grant Agency VEGA, project No. 1/0629/12

References

- [1] Eurocode 1: Actions on structures. Part 1-4 General actions - Wind actions, 2007.
- [2] S. Huang, Q.S. Li, S. Xu, Numerical evaluation of wind effects on a tall steel building by CFD Journal of Constructional Steel Research, 63 5 (2007) 612-627.
- [3] J. Melcer, D. Kuchárová, Dynamics of Building Structures, EDIS, Žilina, 2000 (in Slovak).
- [4] O.C. Zienkiewicz, R.L Taylor, The Finite Element Method, Vol.3, Fluid Dynamics, Oxford, Butterworth Heinmann, 2000.

Influence of Walls and Ceiling on a Wind Flow in BLWT Tunnel

HUBOVÁ Ol'ga^{1, a}, KONEČNÁ Lenka^{2, b*} and LOBOTKA Peter^{3, c}

^{1,2,3} Slovak University of Technology in Bratislava, Faculty of Civil Engineering, Radlinského 11,
SK-813 68 Bratislava, Slovak Republic

^aolga.hubova@stuba.sk, ^blenka.konecna@stuba.sk, ^cpeter.lobotka@stuba.sk

Keywords: wind flow, BLWT tunnel, dynamic tests, calibration of measuring devices

Abstract. This paper deals with the determination of shadowing effects, caused by walls and a ceiling, in newly built Boundary Layer Wind Tunnel (BLWT). Short description of tunnel, measuring devices and the utilization of tunnel are mentioned. Fundamental measurements, necessary for basic analysis of simulated natural wind, are briefly described. Main part of this paper is devoted to additional measurements. These were done to detect the shadowing effects of walls and ceiling on the wind velocity in the cross-section of tunnel. Also the part of the cross-section of tunnel, where the calibration of Hot-wire anemometer is usually done, is analyzed in detail. The descriptions of additional measurements and analysis of obtained results are presented at the end of this paper.

Introduction

New universal BLWT tunnel (Fig. 1), launched by Slovak University of Technology in Bratislava at the end of 2012, contains two operating spaces – front space (FOS) and rear space (ROS). It is a vacuum tunnel with opened circuit of air flow. The air is induced in its front part. Then it comes into the FOS, where the uniform non-gradient wind flow with fluctuation less than 5 % is created. Here, due to the roughness of tunnel floor (length of roughness field is 14.4 m) the flow is modified. Finally, turbulent wind flow is created in ROS. The roughness of floor was created by a plastic film FASTRADE 20. The evaluation of vertical velocity profiles has proved, that this modification of tunnel floor matches the terrain categories III - IV (closely to IV), [1]. Total length of tunnel is 26.35 m. The cross-sections of both operating spaces are identical ($2.6 \text{ m} \times 1.6 \text{ m}$, $w \times h$). Due to its characteristics (two operating sectors with different kinds of wind flow, dimensions and technical parameters of tunnel), the tunnel can be used in various branches (civil and mechanical engineering, chemical industry, energetic industry, ecology).

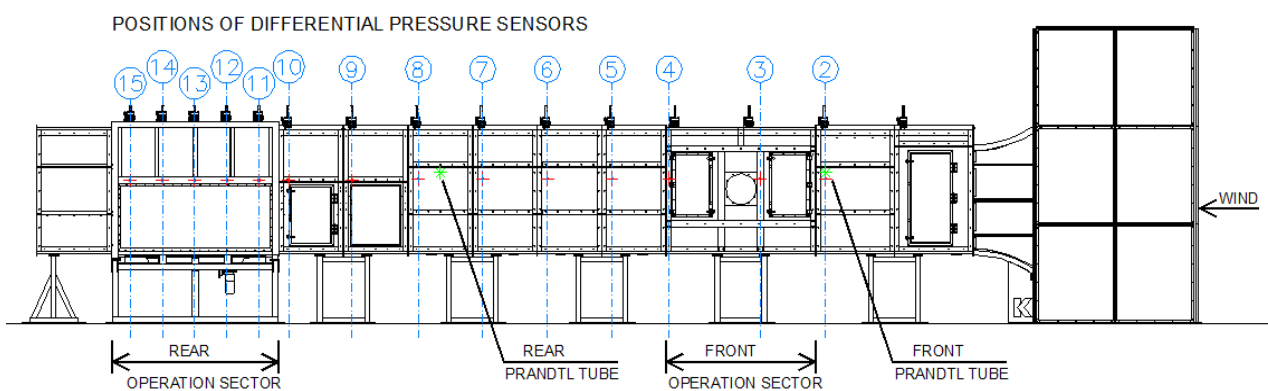


Fig. 1 Scheme of BLWT tunnel with positions of measuring devices

The FOS is suitable for the analysis of uniform non-gradient wind flow with the velocity up to 32 m/s, e.g. the determination of aerodynamic coefficients, wind response spectrum, resonance dynamic response, testing of section models. The ROS (the wind velocity from 0.3 to 20 m/s is

assumed during the tests) is suitable for the detection of effects caused by turbulent wind flow, e.g. the measurements of local pressure on the small-scale models, surface and overall wind load under various wind directions, wind effects upon the pedestrians, air purity (diffusion of emissions, trajectories of pollution), terrain and topographic studies. The development of turbulent layer has been monitored before. The change of wind velocity range was caused by roughness of length 14.4 m between both operating spaces.

Measuring Devices

15 *Differential Pressure Sensors* were placed at the cover along the tunnel, in height of 1 150 mm from tunnel floor (Fig. 1). They were used for permanent monitoring of pressures inside the tunnel. Each sensor had two measuring points, one on the left and the other on the right side. Resultant value of pressure was calculated as the average from both values. Maximum value of pressure inside the tunnel can be 1 000 Pa. If this value is exceeded, the tunnel could be damaged. However, for the maximum wind velocity these values were less than 700 Pa. These sensors played a very important role during the setting of ceiling, Fig. 2.

Two *Prandtl tubes* were placed in the tunnel (1st in FOS, 2nd in ROS). Both probes were fixed; only the movement in y-direction was allowed, i.e. probe could be pulled from the tunnel. It determined the value of wind velocity by method of difference between values of pressure in two places located on the cover of probe. An axis of total pressure p_c [Pa] was located on the front part of probe in the wind direction. Static pressure p [Pa] was measured in places, located in the cover of probe, with axes located perpendicularly to the wind direction:

$$p_c - p = \frac{1}{2} \rho U^2, \quad (1)$$

where ρ is air density [kg/m^3], U is mean value of wind velocity [m/s]. The values measured by Prandtl probes were used as reference values during the tests. During additional tests (mentioned below), only rear Prandtl probe was used. It had following coordinates: $y = 460$ mm (from wall), $z = 1 250$ mm (from tunnel floor), $x = 0$ (basic position).

Hot-wire Anemometer MiniCTA Type 54T42 (Dantec Dynamics) uses the method of constant temperature (CTA – Constant Temperature Anemometry) for the determination of wind velocity. It was used for the measurements of horizontal and vertical cross velocity profiles and turbulent intensity spectra. More information can be found in [2,3,4,5]. During additional tests, it was fixed on a cantilever beam of movable arm (Fig. 5d) and moving in 2D grid with distance step 50 mm (Fig. 4a,b). The calibration was required before each set of measurements. The wind velocity was continuously changing (because it depended on the air density, which is the function of temperature and barometric pressure). Thus, it was not possible to consider the same value of wind velocity for the same value of frequency of motor convertors. Therefore, it was necessary to make a new set of measurements (also the calibration) in regard to actual air conditions. Then, the set of current values of wind velocity was dedicated to the frequencies of motor convertors.

Almemo Type MA25902 with Thermo-Anemometer Probe Type FVA935TH5K2, [6], was used for the measurements of wind velocity. An advantage is its high accuracy in range from 0.2 to 20 m/s. It was fixed in the same way as it was in the case of Hot-wire anemometer (mentioned above, Fig. 5d). Almemo was used only for the control of measured values during the tests.

Measurements were fully automatized, i.e. the values of temperature, barometric pressure, wind pressures and wind velocity values were automatically recorded and analyzed in self-developed programs created in the software LabView (National Instruments).

Description of the Tests and Obtained Results

Basic measurements in both operating sectors contained horizontal cross velocity profiles in varied height levels, vertical velocity profiles and turbulent intensity spectra in ROS. The measurements were repeated for the heights of barrier: 150, 200 and 250 mm. The results gave the dimensions of simulated boundary layer ($2 \text{ m} \times (1.05 - 1.1 \text{ m})$, $w \times h$). These dimensions are affected by several factors, e.g. the roughness of tunnel floor, the setting of ceiling, and the walls. More information about basic measurements can be found in [3,4]. *Additional tests* were done to investigate the influences of shadowing effects of the walls and the ceiling.

Influence of ceiling. Adjustable ceiling of tunnel is created by 9 sandwich plates. By setting of ceiling (1st and 2nd modification, the panels of ceiling changed vertical position), uniform longitudinal pressure above the boundary layer was obtained. The example of longitudinal pressures for reference wind velocity $v_{ref} = 14.0 \text{ m/s}$ ($f = 26 \text{ Hz}$) is depicted in Fig. 2. In the place around 12th pressure sensor, small change in the trend of pressure ratio curve can be seen. Repeated tests confirmed that it was caused by position of movable arm located in this operating sector.

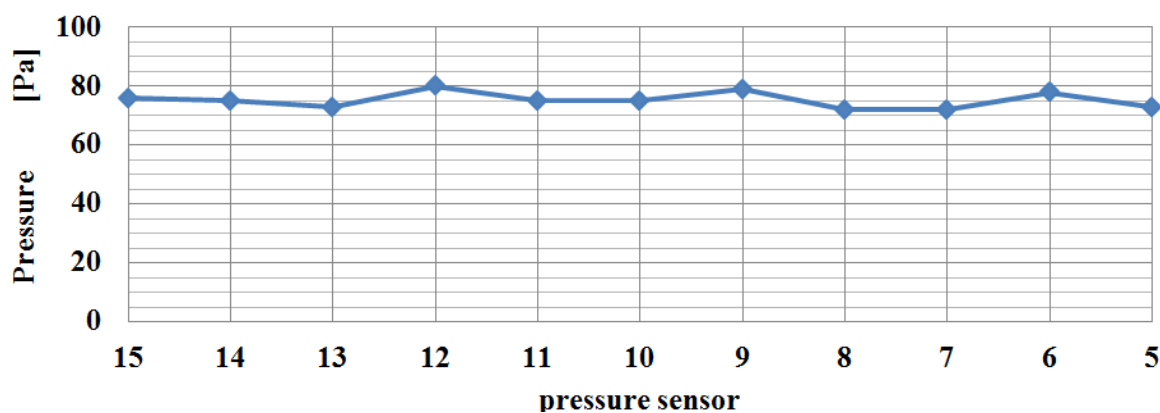


Fig. 2 Mean values of pressure distribution on the walls along the tunnel

Influence of walls. Almemo device was used for the measurements of horizontal cross velocity profiles at different heights (base height was $800 \text{ mm} \pm z$ above the tunnel floor) in FOS, Fig. 3 (U is mean wind velocity, U_r is reference wind velocity measured by Prandtl probe). Barometric pressure was 98 770 Pa, the temperature was $(18.3 - 18.6)^\circ\text{C}$, air density was $(1.1755 - 1.1742) \text{ kg/m}^3$ during the measurements. In horizontal cross velocity profiles the influence of walls up to 300 mm (from the walls) is evident, where the wind velocity significantly decreases.

Detailed test - influence of walls and ceiling. These tests were done in the area used for the calibration of Hot-wire anemometer. *First test was the measurement of mean values of wind velocity by Anemometer mini CTA.* The grid of measured points (Fig. 4a) was located 355 mm from reference (Prandtl) probe in the direction of wind flow (x -direction), Fig. 4b. This is the closest distance from reference probe allowed by given technical factors. Measured points were located every 50 mm in the direction of y -axis and z -axis (2D grid). This set of measurements was done for wind velocities 3.668; 9.33; 13.966 m/s (the frequencies of motor convertors f : 8; 18; 26 Hz). The analysis of obtained results proved that reference (Prandtl) probe creates a “shadow” (Fig. 5a, b and c), i.e. it affects the value of wind velocity in closed area significantly. The calibration of Hot-wire anemometer should rather be done next to the Prandtl tube, where the influence of Prandtl tube is not so significant – minimum distance is 510 mm from the wall.

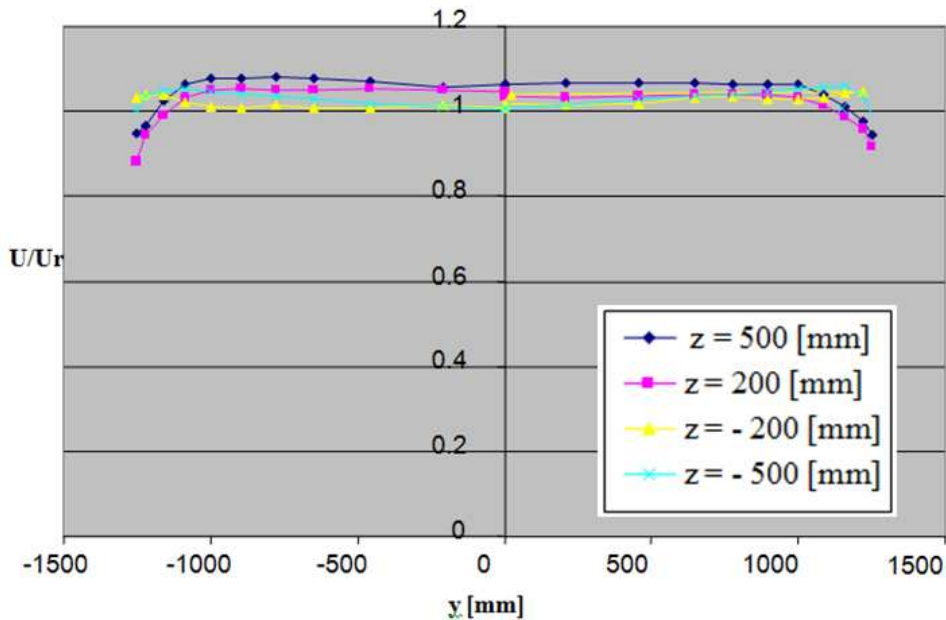


Fig. 3 Wind flow at different heights in FOS

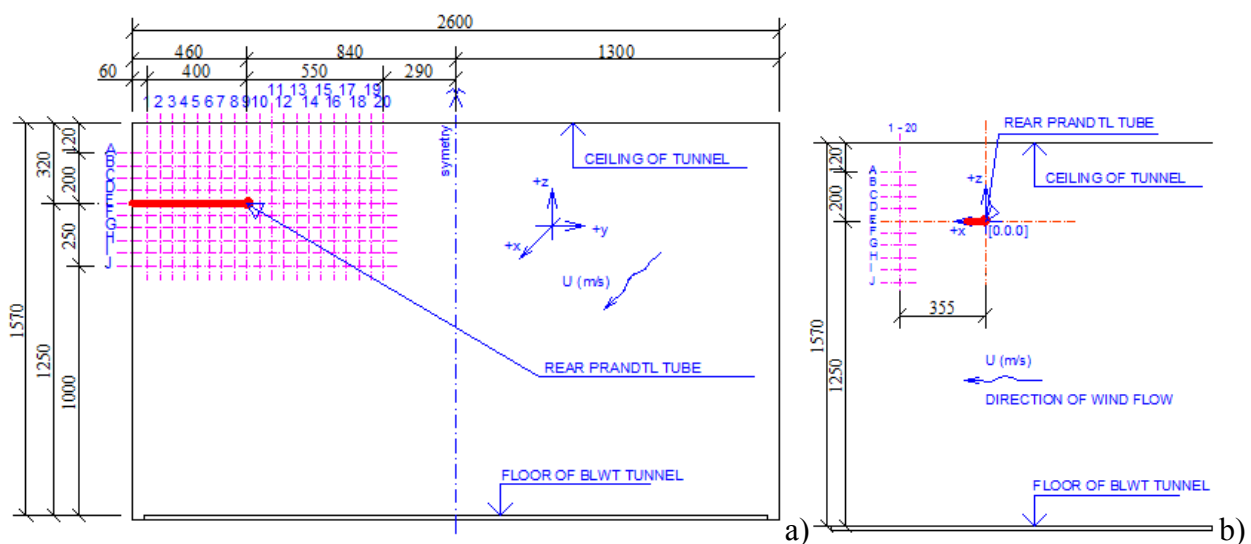


Fig. 4 2D grid of measured points - a) The cross-section of tunnel, b) The longitudinal section of tunnel

Second test was the measurement of horizontal cross velocity profiles by Almemo MA25902. This probe was fixed in the same way as it was during the first test, Fig. 5d. The profiles were measured in two axes in the direction of the cross-section of tunnel. First axis was located in a place of reference probe ($x = 0$ mm). Second axis was located in a place determined for the calibration ($x = 355$ mm from reference probe), Fig. 4 b. Both axes were placed in the same height from the tunnel floor, $z = 1250$ mm. The profiles were measured from 310 mm to 660 mm from the wall of tunnel (y -direction). This test was done for two cases. In first case, reference probe was fixed in its place (the measurements affected by reference probe). In second case, reference probe was removed (the measurements unaffected by reference probe). This set of measurements was repeated for two different wind velocities: 9.9 m/s ($f = 18$ Hz) and 14.7 m/s ($f = 26$ Hz).

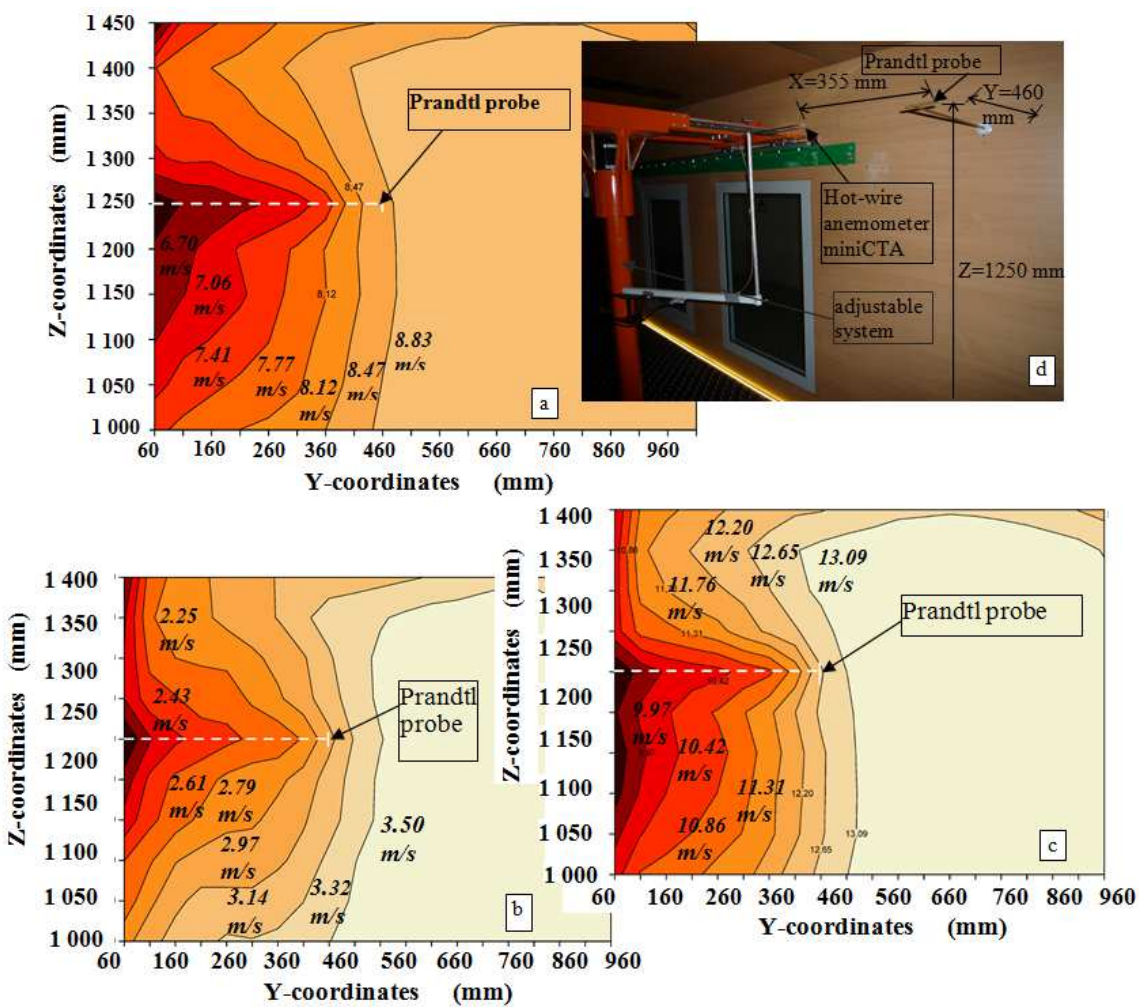


Fig. 5 Mean wind velocity distribution a) $v_{ref} = 3.668 \text{ m/s}$ ($f = 8 \text{ Hz}$); b) $v_{ref} = 9.33 \text{ m/s}$ ($f = 18 \text{ Hz}$); c) $v_{ref} = 13.966 \text{ m/s}$ ($f = 26 \text{ Hz}$), d) the photo from the test

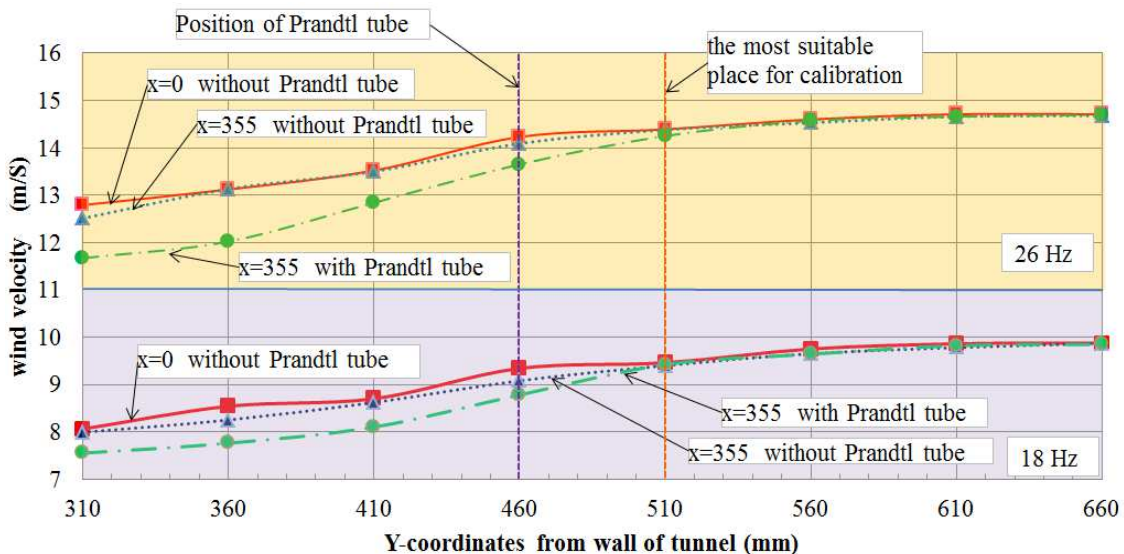


Fig. 6 Horizontal cross velocity profiles ($z = 1250 \text{ mm}$)

Prandtl tube has significant influence in the place considered for the calibration. The decrease of wind velocity was evident in horizontal cross velocity profiles up to 600 mm from the wall, Fig. 6. Prandtl tube was placed 460 mm from the wall, in area where the influence of wall arises. Therefore, this place is not suitable for the calibration. This problem can be solved in several ways,

e.g. using a longer Prandtl tube (longer than 600 mm). In spite of this influence of wall and with respect to the actual technical factors of this BLWT tunnel, the most suitable place for the calibration of Hot-wire Anemometer was determined in coordinates: $x = 355$ mm, $y = 510$ mm, $z = 1\,250$ mm.

Last test was the comparison of wind velocities measured by Almemo MA25902 and reference probe. Almemo was located in the most suitable place for the calibration of Hot-wire anemometer (the coordinates: $x = 355$ mm, $z = 1\,250$ mm, $y = 510$ mm). Reference probe was located in its position. This set of measurements was done in the same way as it is required in the case of calibration of Hot-wire anemometer, i.e. for 13 values of wind velocity (from 2.5 m/s to 16.4 m/s; the frequencies from 6 Hz to 30 Hz with step 2 Hz). For best results of statistical evaluation, this measurement was repeated 16-times.

The deviation of mean wind velocities measured by two different devices (Almemo MA25902 and Prandtl tube) in regard to the frequencies of motor convertors has a sinusoidal shape. Larger dispersion of measured values was more evident at low frequencies of motor convertors (up to 10 Hz). It might be caused by measurement principle of Prandtl tube (being not suitable for the measurement of velocity under 5 m/s). Polynomial function was determined from this sinusoidal shape.

$$y = 3 \times 10^{-7} x^5 - 3 \times 10^{-5} x^4 + 9 \times 10^{-4} x^3 - 0.0137 x^2 + 0.0887 x + 0.7875. \quad (2)$$

Where, y is the ratio $U_{Almemo}/U_{Prandtl}$ [-], x is the frequency of motor convertors [Hz]. After that, it was used for the determination of correction coefficients of calibration curve, used for the calibration of Hot-wire anemometer. It can be said that this device was calibrated with high accuracy with regard to reference (Prandtl) tube.

Conclusion

Additional tests helped to investigate the wind flow along the tunnel and shadowing effects of walls and ceiling on wind flow in detail.

Acknowledgements

This paper is supported by the grant no. VEGA 1/0480/13.

References

- [1] STN EN 1991-1-4 Eurocode 1, Actions on structures. Part 1-4: General actions, Wind actions, 2007, (In Slovak).
- [2] D. Zacho, O. Hubová, P. Lobotka, Simulating the natural wind in BLWT – wind tunnel in Laboratories of STU, In New Trends in Statics and Dynamics of Buildings, 11th International Conference, Bratislava, Slovak Republic, October 3-4, 2013, Bratislava, Slovak University of Technology, 2013, pp. 259-262.
- [3] O. Hubová, P. Lobotka: Natural wind simulation in the BLWT STU wind tunnel, In: ATF 2014, 3rd International Conference on Applied Technology, 6-7 May 2014, Vienna, Austria.
- [4] A. G. Davenport: Rationale for determining design wind velocities, J. Struct. Div., Proc. of the ASCE 86, 1960.
- [5] ASCE Manuals and Reports on Engineering Practice, no.67. Wind tunnel studies of buildings and structures. Aerospace Division of the American Society of Civil Engineers, ISBN 0-7844-0319-8, 1999, 145 p.
- [6] DIRECT INDUSTRY, [online],[cit. 2014-03-04]. Information on: <http://pdf.directindustry.com/pdf/ahlborn/thermo-anemometer-probe-type-fv-a935-th4-th5/17042-122516.html>

Response of Layered Plates to Effects of Wind

MARTON Pavol^{1,a*}

¹Department of Structural Mechanics, Faculty of Civil Engineering,
 STU Bratislava, Radlinského 11, SK-813 68 Bratislava, Slovak Republic

*pavol.marton@stuba.sk

Keywords: vibration, stress, stiffness, multilayer, plate, blast

Abstract. In the present article the response of layered plates to the effects of wind is analyzed. The computational model of layered plate meets the conditions of equilibrium shear stresses at the contact layers. The numerical experiment is applied to the layered glass plate with hinge supports at its edges. The dynamic effect of wind is analyzed in a dynamic calculation.

Introduction

In this paper the force variant is applied consisting in selection of tension function in the shape of the mixed third order polynomials. In the analysis the compliance of both the tension contact conditions and the kinematic contact is provided. The equivalent stiffness matrix of plate is defined. Wind loading is mediated by a wind speed record. Wind speed is simulated by discrete course with a time interval Δt .

Computational Model

The basic idea of the derivation of the stiffness matrix of layered rectangular element involves the application of girder stiffness relations for n-layered slab element in the definition of stiffness [3], [4]. A comparison of the relation of the beam bending stiffness and stiffness of homogeneous layered plates can be defined by formula

$$D = \frac{S}{12 S_1} \begin{bmatrix} 1 & v & 0 \\ v & 1 & 0 \\ 0 & 0 & 0.5(1-v) \end{bmatrix}, \quad (1)$$

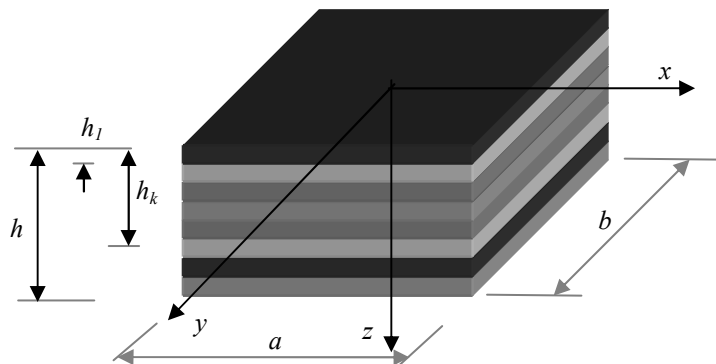


Fig. 1 Geometry of the layered plate element

where

$$S_1 = \sum_{k=1}^n (h_k - h_{k-1}) \frac{E^k}{1-v_k^2}, \quad S_2 = \sum_{k=1}^n (h_k^2 - h_{k-1}^2) \frac{E^k}{1-v_k^2},$$

$$S_3 = \sum_{k=1}^n (h_k^3 - h_{k-1}^3) \frac{E^k}{1 - \nu_k^2}, \quad S = 4 S_1 S_3 - 3 S_2^2. \quad (2)$$

Displacements are defined by relations

$$w(x, y) = a_1 + a_2 x + a_3 y + a_4 x^2 + a_5 x y + a_6 y^2 + a_7 x^3 + a_8 x^2 y + a_9 x^2 + a_{10} y^3 + a_{11} x^3 y + a_{12} x y^3 \quad (3)$$

The constants a_1, a_2, \dots, a_{12} are determined in a known manner by derivations w_x, w_y and by substituting the coordinates of the nodes. Introducing the relative coordinates $\xi = x/a, \eta = y/b$, the form function matrix is defined by the formula

$$N^t = [N_1^t \ N_2^t \ N_3^t \ N_4^t] \quad N_i = \frac{1}{8} \begin{bmatrix} (1 + \xi \xi_i)(1 + \eta \eta_i)(2 + \xi \xi_i + \eta \eta_i - \xi^2 - \eta^2) \\ a \xi_i (1 + \xi \xi_i)^2 (1 - \xi \xi_i)(1 + \eta \eta_i) \\ b \eta_i (1 + \eta \eta_i)^2 (1 - \eta \eta_i)(1 + \xi \xi_i) \end{bmatrix} \quad (i = 1 \dots 4). \quad (4)$$

The calculation of strain is defined by the equation

$$\varepsilon = B d, \quad (5)$$

where

$$B_i = \begin{bmatrix} \frac{\partial^2}{\partial x^2} N^t \\ \frac{\partial^2}{\partial y^2} N^t \\ 2 \frac{\partial^2}{\partial x \partial y} N^t \end{bmatrix}, \quad (6)$$

or

$$\underline{\underline{B}}_i = \frac{1}{8} \begin{bmatrix} B_{i11} & B_{i12} & B_{i13} \\ B_{i21} & B_{i22} & B_{i23} \\ B_{i31} & B_{i32} & B_{i33} \end{bmatrix}, \quad (7)$$

$$\begin{aligned} B_{i11} &= \frac{2}{a^2} (1 + \eta \eta_i) (1 - \xi_i^2 + 3 \xi \xi_i), \quad B_{i12} = \frac{2}{a} \xi_i^3 (1 + \eta \eta_i) (1 + 3 \xi \xi_i), \quad B_{i13} = 0, \\ B_{i21} &= \frac{2}{b^2} (1 + \xi \xi_i) (1 - \eta_i^2 + 3 \eta \eta_i), \quad B_{i22} = 0, \quad B_{i23} = \frac{2}{b} \eta_i^3 (1 + \xi \xi_i) (1 + 3 \eta \eta_i), \\ B_{i31} &= -\frac{2}{ab} [\xi_i (1 + \eta \eta_i) (\eta_i - 2\eta) + \eta_i (1 + \xi \xi_i) (\xi_i - 2\xi) + \xi_i \eta_i (2 + \xi \xi_i + \eta \eta_i - \xi^2 - \eta^2)], \\ B_{i32} &= \frac{2}{b} [\xi_i^2 \eta_i (1 + \xi \xi_i)^2 - 2 (1 + \xi \xi_i) (1 - \xi \xi_i)], \quad B_{i33} = -\frac{2}{b} [\xi_i \eta_i^2 (1 + \eta \eta_i)^2 - 2 (1 + \eta \eta_i) (1 - \eta \eta_i)]. \end{aligned} \quad (8)$$

Bending moments are defined by the relation of the nodes.

$$\begin{Bmatrix} M_x \\ M_y \\ M_{xy} \end{Bmatrix} = \frac{1}{8} D \left\{ S_{\underline{1}}, S_{\underline{2}}, S_{\underline{3}}, S_{\underline{4}} \right\} \begin{Bmatrix} \underline{d}_1 \\ \underline{d}_2 \\ \underline{d}_3 \\ \underline{d}_4 \end{Bmatrix}, \quad (9)$$

where

$$\begin{aligned} S_{i11} &= \frac{2}{a^2} (1 + \eta \eta_i) (1 - \xi_i^2 + 3\xi \xi_i) + \frac{2\nu}{b^2} (1 + \xi \xi_i) (1 - \eta_i^2 + 3\eta \eta_i), \\ S_{i12} &= \frac{2}{a} \xi_i^3 (1 + \eta \eta_i) (1 + 3\xi \xi_i), \quad S_{i13} = \frac{2\nu}{b} \eta_i^3 (1 + \xi \xi_i) (1 + 3\eta \eta_i), \\ S_{i21} &= \frac{2\nu}{a^2} (1 + \eta \eta_i) (1 - \xi_i^2 + 3\xi \xi_i) + \frac{2}{b^2} (1 + \xi \xi_i) (1 - \eta_i^2 + 3\eta \eta_i), \\ S_{i22} &= \frac{2\nu}{a} \xi_i^3 (1 + \eta \eta_i) (1 + 3\xi \xi_i), \quad S_{i23} = \frac{2}{b} \eta_i^3 (1 + \xi \xi_i) (1 + 3\eta \eta_i), \\ S_{i31} &= \frac{1-\nu}{ab} [\xi_i (1 + \eta \eta_i) (\eta_i - 2\eta) + \eta_i (1 + \xi \xi_i) (\xi_i - 2\xi) + \xi_i \eta_i (2 + \xi \xi_i + \eta \eta_i - \xi^2 - \eta^2)], \\ S_{i32} &= \frac{1-\nu}{b} [\xi_i^2 \eta_i (1 + \xi \xi_i)^2 - 2(1 + \xi \xi_i)(1 - \xi \xi_i)], \\ S_{i33} &= \frac{2}{b} [\xi_i \eta_i^2 (1 + \eta \eta_i)^2 - 2(1 + \eta \eta_i)(1 - \eta \eta_i)]. \end{aligned} \quad (10)$$

Stiffness matrix is defined by the equation

$$k_{ij} = B_{ij}^T D B_{ij} dA, \quad k = \begin{bmatrix} k_{11} & k_{12} & k_{13} & k_{14} \\ k_{21} & k_{22} & k_{23} & k_{24} \\ k_{31} & k_{32} & k_{33} & k_{34} \end{bmatrix}. \quad (11)$$

Calculation of Response of System without Damping

The response to the non-stationary load is determined by the kinetic equation [1], [2]

$$[M]\{\ddot{u}\} + [K]\{u\} = \{f(t)\}, \quad (12)$$

or after substitution

$$[D] = [M]^{-1} [K] \quad (13)$$

by the kinetic equations of the form

$$[E]\{\ddot{u}\} + [D]\{u\} = [M]^{-1} \{f(t)\}. \quad (14)$$

Free vibration equation solution

$$[E]\{\ddot{u}\} + [D]\{u\} = \{0\} \quad (15)$$

is

$$\{u\}_t = \cos \sqrt{D} t \{u\}_0 + \sqrt{D^{-1}} \sin \sqrt{D} t \{\dot{u}\}_0, \quad (16)$$

$$\{\dot{u}\}_t = \sqrt{D} \sin \sqrt{D} t \{u\}_0 + \cos \sqrt{D} t \{\ddot{u}\}_0. \quad (17)$$

From the Eq. 16 and 17 a solution is in the form

$$\{z(t)\} = \begin{bmatrix} U_{11} & U_{12} \\ U_{21} & U_{22} \end{bmatrix} \{z(0)\} = [U] \{z(0)\}, \quad (18)$$

$$[U_{11}] = [U_{22}] = \cos \sqrt{D} t = [E] - \frac{1}{2!} [D] t^2 + \frac{1}{4!} [D]^2 t^4 \dots ,$$

$$[U_{12}] = \sqrt{[D]^{-1}} \sin \sqrt{[D]} t = [E] t - \frac{1}{3!} [D] t^3 + \frac{1}{5!} [D]^2 t^5 \dots , \quad (19)$$

$$[U_{21}] = -\sqrt{[D]^{-1}} \sin \sqrt{[D]} t = -[D] \left([E] t - \frac{1}{3!} [D] t^3 + \frac{1}{5!} [D]^2 t^5 \right) .$$

The sectional integral of Eq. 12 for the case of immediately acting constant force is

$$\{u\}_2 = ([E] - [U_{11}]) [K]^{-1} \{f\} = ([E] - [U_{11}]) [D]^{-1} \{h\} = [W_{10}] \{h\}, \quad (20)$$

$$\{\dot{u}\}_2 = -[U_{21}] [K]^{-1} \{f\} = -[U_{21}] [D]^{-1} \{h\} = [W_{20}] \{h\}, \quad (21)$$

$$\{z_2(t)\} = [W_0] \{h\}. \quad (22)$$

In the numerical solution of the task formulated for the time step Δt , Fig. 2. The algorithm is given by

$$\{z\}_{i+1} = [U] \{z\}_i + [W_0] \{h\}_i. \quad (23)$$

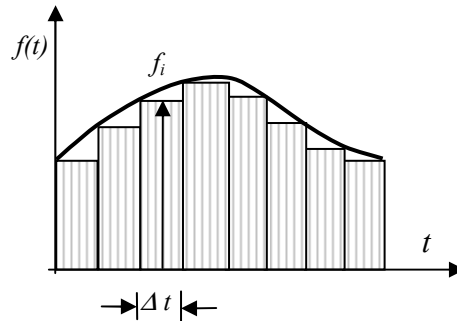


Fig. 2 Approximation of the load with a set of rectangular impulses

Model of the Blast Effects of Wind

Wind effect is modeled in the form of linearly increasing and linearly decreasing load for a period of 4 seconds. Model partly corresponds with the model by Sleigh [5].

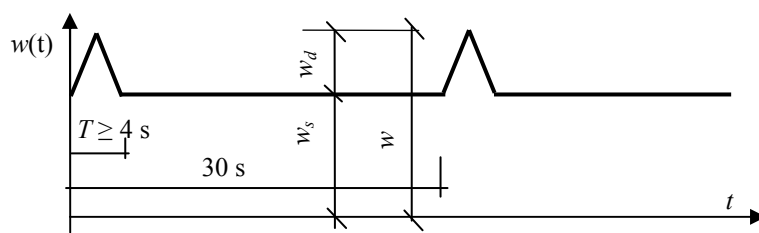


Fig. 3 Model of the blast effects of wind

Model of a Glass Panel

Panel is modeled as a layered glass plate reinforced by the steel grid in two layers, Fig. 4.

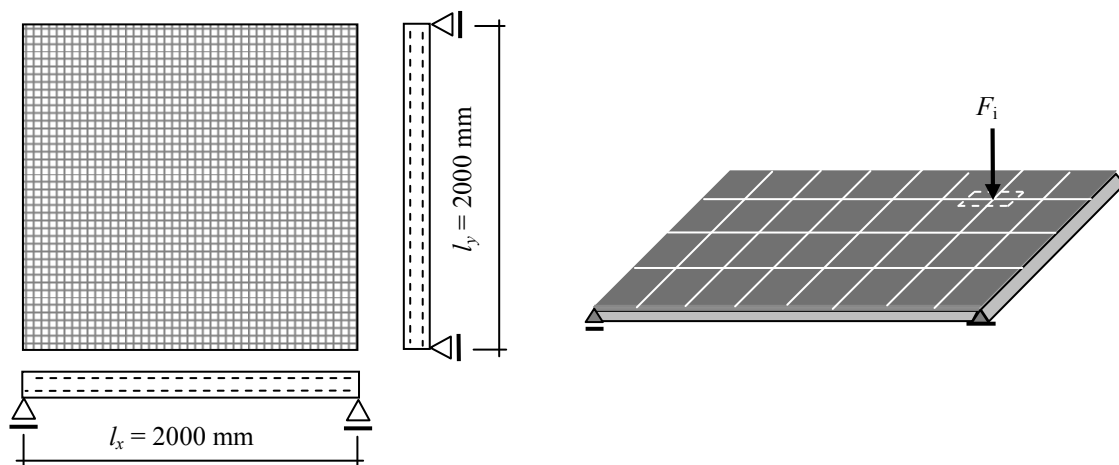


Fig. 4 Model of layered glass plate reinforced by steel grid, finite element and loading model

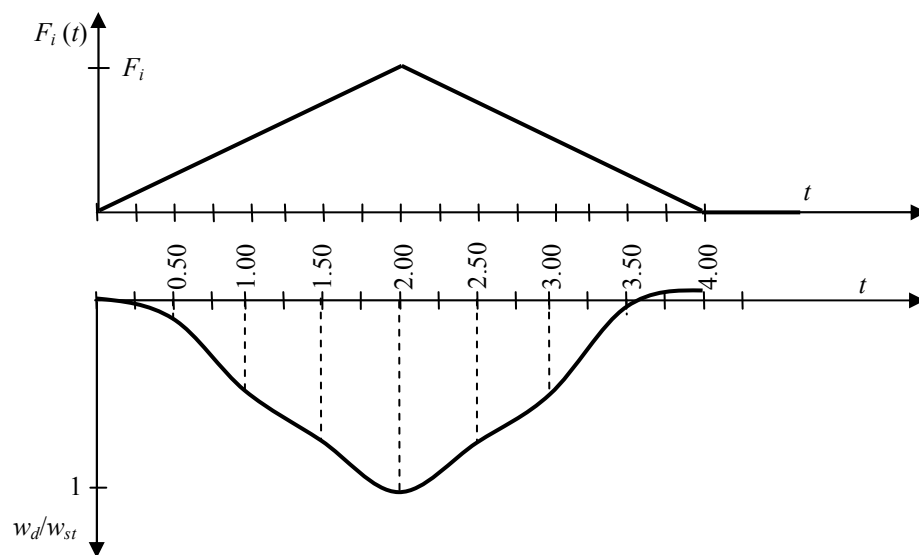


Fig. 5 Displacements due to the effect of the gust

Dynamic calculation was determined by dynamic factor w_d/w_{st} . The numerical values are shown in Table 1.

Table 1 Numerical values of dynamic factor

t (s)	w_d/w_{st}						
0.25	0.11	1.25	0.61	2.25	0.92	3.25	0.42
0.50	0.25	1.50	0.75	2.50	0.75	3.50	0.25
0.75	0.39	1.75	0.89	2.75	0.58	3.75	0.08
1.00	0.50	2.00	1.00	3.00	0.5	4.00	-0.01

Conclusion

This work has focused on derivation of the stiffness matrices, matrix of normal and shear stresses, fulfilling the equilibrium condition of shear stress on the contact layers. The presented methodology for the assessment of the response to the blast wind effects is universal and can be used also for solution of some related problems, e.g. calculation of the response of the structural systems to the technical seismicity effects due to explosion of the charge located either under or above the ground. The calculations proved that the dynamic effects of gusts are almost identical to static ones at high frequencies of plates.

References

- [1] P. Marton, Assesment of Response of the Layered Rectangular Plate to Loading by Sound Blast Waves. Proceedings of an International Conference Engineering Mechanics 2009, Svatka, Czech Republic, pp. 180-181.
- [2] P. Marton, Numerical Analysis of Multilayer Bar Systems by Nonstationary Process, Proceedings of Scientific Works, Charkov, 1989, pp. 69-72, (in Russian).
- [3] C.G. Lechnitzki, Anisotropic Plates, first ed., GITTL, Moscow, 1979, (in Russian).
- [4] K.W. Lorenz, W. Krings, Program with Sandwich Elements of Plates and Shells, Finite Elements in Static, Bochum, 1973, pp. 86-92, (in German).
- [5] Ch. Petersen, Progress Reports of the VDI Periodicals, No.11, VDI Verlag, Dusseldorf, 1971.

Response of Masts of Power Lines to the Blast Effects of Wind

MARTON Pavol^{1,a}

¹Department of Structural Mechanics, Faculty of Civil Engineering,
STU Bratislava, Radlinského 11, SK-813 68 Bratislava, Slovak Republic

^apavol.marton@stuba.sk

Keywords: speed record, power lines, insulator, conductor, mast

Abstract. This paper presents an analysis of the response of masts of power lines to wind gusts. The computational model of the masts is designed in two variants. The computational model of the first variant is the mast, in which the weight of insulators and conductors has been neglected. In the second variant, the effects of mass of insulators and conductors are modeled as a double pendulum. The values of wind pressure were obtained using a record of wind velocity.

Introduction

Power lines of very high voltage, Fig. 1, represent the system of masts, insulators, conductors and grounding cables. Masts can be categorized according to their function in transfer of the load into the supporting and reinforcing ones.

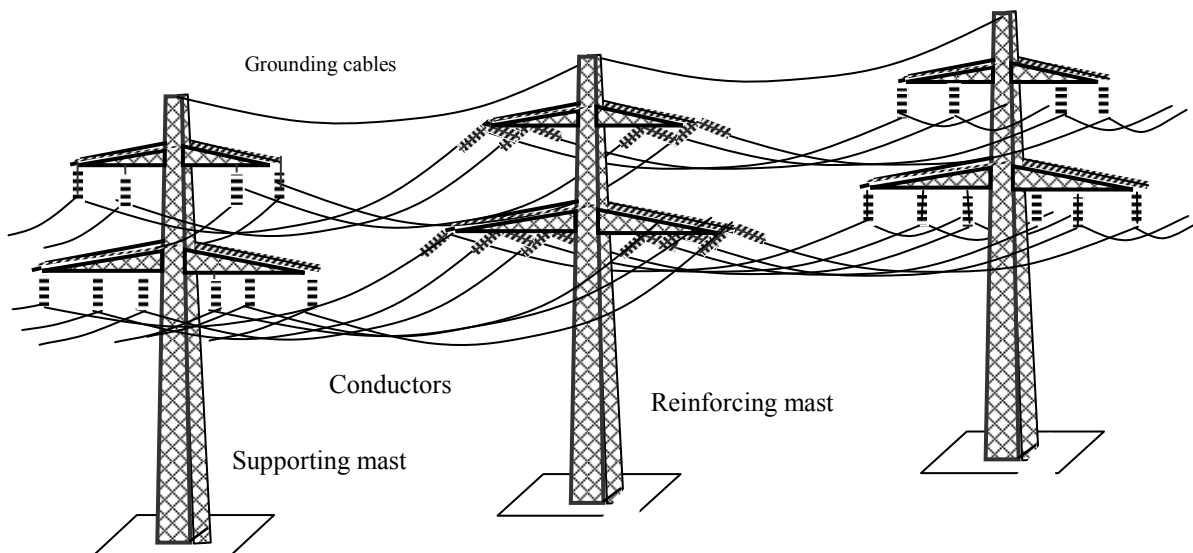


Fig. 1 Transmission masts

Function of reinforcing masts is the transmission of axial forces of the conductors, the horizontal load transfer due to the effects of wind and seismic effects, and transmission of vertical forces of self-weight of conductors and grounding cables (eventually ice coating) into the foundation of masts.

Supporting masts carry vertical loads from their self-weight, conductors, cables and grounding insulators and horizontal wind and seismic load.

In regard to the arrangement and different actions of individual components of the power line system, behaviour of masts is different. The load of power lines can act in the plane and in a plane perpendicular to the power line. The response of the system in different computational models was investigated.

Computational Model of Supporting Mast

Vibration in the plane perpendicular to the lines of supporting mast, Fig. 2a, is modeled as a set in sections with continuously distributed mass or mass concentrated in selected centers of weight of the mast, [1], [2].

Insulators, conductors and grounding cables are modeled as a physical pendulum Fig. 2b, or mathematical pendulum equivalent to physical pendulum, Fig. 2c. The simplest calculation model is shown in Fig. 2d.

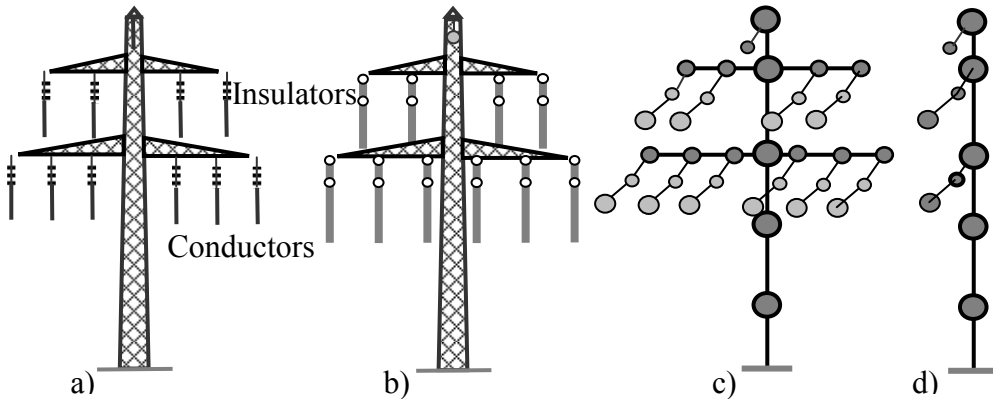


Fig. 2 Computational model of the supporting mast

Quasi-Static Calculation of the Response of the Mast to Wind Gust

Modeling the wind speed is simulated by course with discrete time interval Δt . Wind pressure $w(t)$ is depending on the wind speed stated by the generally valid relation for laminar flow, [3]

$$w(t) = c \cdot A \cdot q(t) = c \cdot A \frac{v^2(t)}{16} \quad (1)$$

Displacement due to the load impulse is given by

$$u(t) = w(\tau) W(t - \tau) d\tau, \quad (2)$$

where $W(t)$ is an influence function that is the response of systems with one degree of freedom to the unit impulse

$$W(t) = \frac{e^{-\delta \omega_0 t}}{m \sqrt{1 - \xi^2} \omega_0} \sin \sqrt{1 - \xi^2} \omega_0 t. \quad (3)$$

Displacement in time $\tau = k \Delta t$ and $t = j \Delta t$ is

$$u_j = \sum_{k=1}^{k=j-1} w_k W[(j-k) \Delta t]. \quad (4)$$

After the substitution, the elastic force in system with one degree of freedom after a single transformation is defined by the formula

$$F_j = 2 \pi \kappa \sum_{k=1}^{k=j-1} w_k e^{-\delta \kappa(j-k)} \sin 2\pi \kappa(j-k), \quad (5)$$

where δ is the logarithmic decrement.

Methodology of Wind Speed Record

- a) continuous chart recording wind speed is substituted by a discrete step system
- b) discrete values of wind speed shall be determined by discrete pressure values based on the unit area of wind $c.A = 1$
- c) the pressure values were averaged and represent the static value of wind pressure q_s
- d) the relation $w_d = w - w_s$ determines the maximum value of the dynamic component
- e) dynamic wind pressure will be standardized $q_d / q_{d,\max} \leq 1$
- f) the relative value of dynamic load is defined by the relation

$$\frac{F_j}{F_{jk,\max}} = 2 \pi \kappa \sum_{k=1}^{j-1} \frac{q_{dk}}{q_{d,\max k}} e^{\delta \kappa(j-k)} \sin 2\pi(j-k), \quad (6)$$

- g) the dynamic coefficient of increase in wind pressure (dynamic factor) is defined by the relation

$$\beta = \max \frac{F_j}{F_{j,\max}} - 1, \quad (7)$$

- h) impact factor is related to the maximum wind pressure resulting from the relation

$$\varphi = I + \beta \frac{q_{d,\max}}{q_{\max}}, \quad (8)$$

- i) for producing the sum of equations (6) it is appropriate to limit the correlation length of t_w [4]

$$t_w = t - \tau = (j - k)\Delta t = m \Delta t. \quad (9)$$

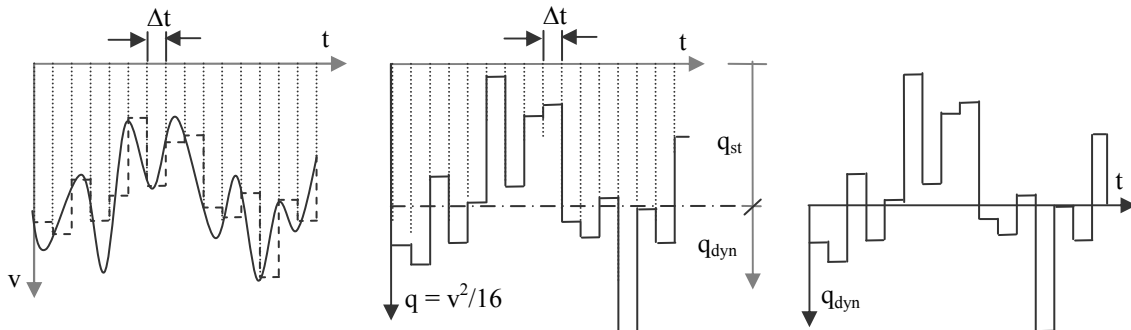


Fig. 4 Wind speed record

Table 1 Values of wind pressure

$q_s [\text{kNm}^{-2}]$	$q_{d,\max} [\text{kNm}^{-2}]$	$q_{\max} [\text{kNm}^{-2}]$	q_s / q_{\max}	$q_{d,\max} / q_{\max}$
0.588	0.458	1.046	0.56	0.44

- j) Determination of mean and maximum dynamic components of the wind pressure is in Table 2. It indicates maximum load ratio for different values of logarithmic decrement and vibration period of the non-damped natural vibration.

- k) Determination of the gust dynamic coefficient

From the values of Table 1 and Table 2 the calculation of the gust factor φ is given in Table 3.

Table 2 Determination of mean and maximum dynamic components of the wind pressure

δ	T_0 [s]				
	0.5	1.0	2.0	3.3	5.0
0.150	0.413	0.829	0.852	1.430	1.717
0.075	0.413	0.867	0.971	1.593	1.957
0.025	0.406	0.883	1.661	2.028	2.496

Table 3 Result of the calculation of the gust factor φ

φ	T_0 [s]				
	δ	0.5	1.0	2.0	3.3
0.150	0.742	0.925	0.935	1.189	1.315
0.100	0.738	0.927	0.952	1.242	1.353
0.075	0.742	0.941	0.987	1.261	1.421
0.050	0.743	0.938	1.010	1.328	1.524
0.025	0.739	0.959	1.291	1.452	1.658

Numerical Experiment

Within the numerical experiment the supporting mast response was analyzed, Fig. 4. Characteristics of the mast, insulators, conductors and grounding cables are shown in Table 4.

Table 4 Characteristics of the mast, insulators, conductors and grounding cables

No.	m	Sec.	l	EI	No.	m	Sec.	l	EI
-	kg		m	$\times 10^5$	-	kg		m	$\times 10^5$
1	462.4	0-1	4.0	12.34	7	163.8	6-7	3.0	1.234
2	436.1	1-2	4.0	9.939	8	134.3	5-9	1.6	
3	421.3	2-3	4.0	6.896	9	1932.0	8-9	7.1	
4	187.3	3-4	3.0	4.504	10	80.0	6-11	1.6	
5	245.7	4-5	2.0	3.030	11	966.0	10-11	7.1	
6	327.7	5-6	4.0	1.745	12	163.8	7-12	3.0	

Load characteristics are shown in Table 5. Gust factor is determined from Table 3 for $T_0 = 4.0$ s and the logarithmic decrement $\delta = 0.15$.

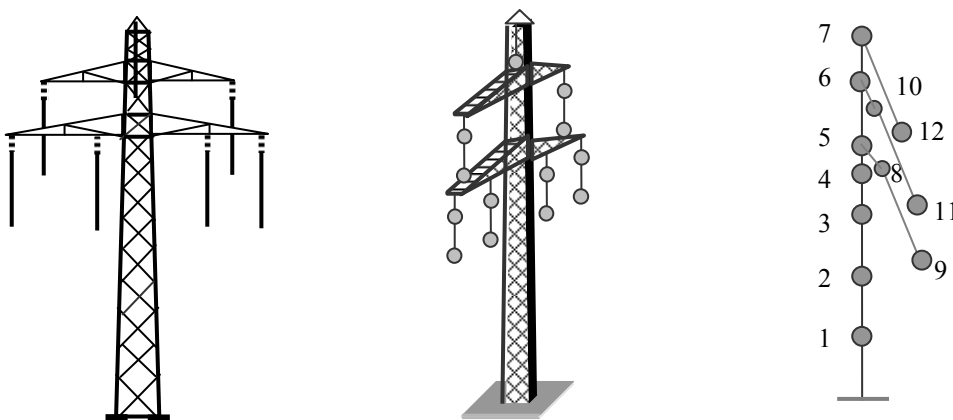


Fig. 5 Model of the mast with a load perpendicular to the power lines

Table 5 Load characteristics

Sect.	l	$c_{f,0}$	$q_p(z)$	c_f	A_{ref}	$w_p(z)$	i	F_i	φ	F_i	u_i	u_i^*
	m		Nm ⁻²		/ m'	Nm ⁻² /m		N	-	N	m	m
0-1	4.0	1.20	588	1.14	0.24	161	1	644	1.2	773	0.0008	0.0010
1-2	4.0	1.25	588	1.19	0.23	161	2	644	1.2	773	0.0034	0.0041
2-3	4.0	1.30	588	1.24	0.22	161	3	564	1.2	677	0.0077	0.0092
3-4	3.0	1.35	588	1.28	0.20	151	4	459	1.2	551	0.0120	0.0144
4-5	2.0	1.40	588	1.33	0.20	156	5	490	1.2	588	0.0160	0.0192
5-6	4.0	1.50	588	1.42	0.20	167	6	602	1.2	722	0.0260	0.0312
6-7	3.0	1.60	588	1.52	0.20	179	7	269	1.2	323	0.0350	0.0420
5-8	1.6	2.05	588	1.0	0.16	94	8	100	1.2	120	0.0170	0.0204
8-9	7.1	1.75	588	1.2	0.02	14	9	336	1.2	403	0.0180	0.0216
6-10	1.6	2.10	588	1.0	0.16	94	10	100	1.2	120	0.0260	0.0312
10-11	7.1	1.80	588	1.2	0.02	14	11	168	1.2	202	0.0260	0.0312
7-12	7.1	2.00	588	1.2	0.02	14	12	84	1.2	101	0.0350	0.0420

Calculated displacements both neglecting and considering the effects of wind on conductors and insulators are shown in Table 5, Fig. 5.

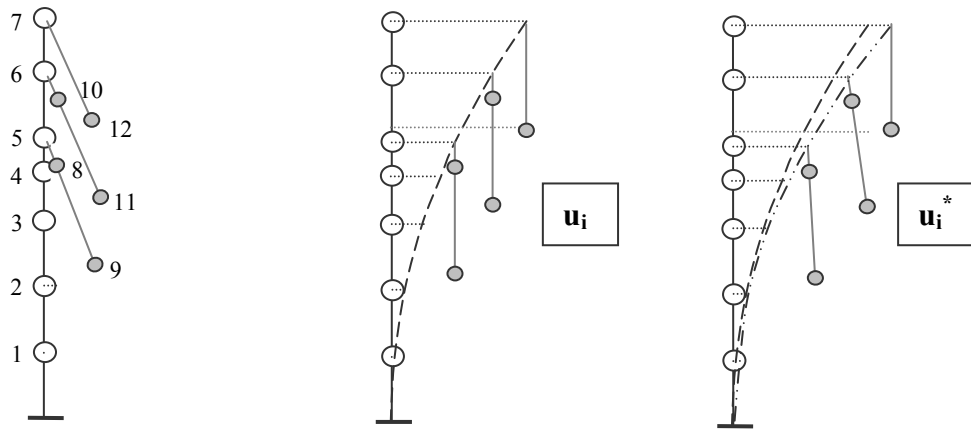


Fig. 5 The displacements in computational model of the mast in variants 1- u_i and 2- u_i^*

Conclusion

Numerical calculations of response of masts to the effects of wind confirmed the validity of the proposed calculation model, variant 2. Effect of self-weight of insulators and conductors, and grounding cables modeled as a pendulum resulted in a substantial reduction of the first two natural frequencies.

References

- [1] Ch. Petersen, Guyed Arrogated and Chimney Stones, first ed., Wilhelm Ernst und Sohn, Munchen, 1970.
- [2] P. Marton, Dynamic Investigation of Masts in the System of Power Lines, first ed., AS SVST, Bratislava, 1981.
- [3] Ch. Petersen, Progress Reports of the VDI Periodicals, No.11, VDI Verlag, Dusseldorf, 1971.
- [4] F. Steiger, Windmessungen an Antennenträgern, Stahlbau 34 (1965) 250-254.

Numerical and Experimental Investigations of Air Flow Turbulence Characteristics in the Wind Tunnel Contraction

MICHALCOVÁ Vladimíra^{1,a*}, KUZNĚTSOV Sergej^{2,b}, BROŽOVSKÝ Jiří^{1,c}
and POSPÍŠIL Stanislav^{2,d}

¹Faculty of Civil Engineering, VŠB-Technical University of Ostrava,
Ludvíka Poděště 1875/17, 708 33 Ostrava-Poruba, Czech Republic

²ÚTAM AV ČR, v.v.i., Centrum Excellence Telč, Batelovská 485, 58 856 Telč, Czech Republic

^avladimira.michalcova@vsb.cz, ^bkuznetsov@itam.cas.cz, ^cjiri.brozovsky@vsb.cz,
^dpospisil@itam.cas.cz,

Keywords: aerodynamics, wind tunnel contraction, CFD

Abstract. Characteristics of flow in contraction of rectangular cross-section are investigated numerically and experimentally so as to gain an additional insight into the contraction design. They observed velocity field and turbulent intensity in the area of contraction and downstream of it. Individual numerical models software Ansys Fluent are evaluated and compared with measurements in a wind tunnel.

Introduction

The crucial characteristics of a wind tunnel are the flow quality inside the test chamber and the overall performances. Three main criteria that are commonly used to define them are: a maximum achievable velocity, flow uniformity and the minimum turbulence level. Therefore, in general the aim of contraction design is to get a controlled flow in the test chamber, achieving the necessary flow performance and quality parameters [1,2,3,4].

The aim of the paper is to compare the results of physical and numerical modelling of the flow pattern in the course of flowing through the contraction with rectangular cross-section. The physical experiment took place in the climatic wind tunnel at the Institute of Theoretical and Applied Mechanics AS CR in Telč; numerical modelling was done at the Faculty of Civil Engineering of VŠB - TU using Ansys Fluent software. A smooth flow pattern with a constant vertical velocity profile of 10 m/s and with a turbulence intensity of approx. 1% was modelled before entry to the contraction in both approaches. The analysis is focused on evaluation of flow characteristics of the simulated process.

Physical Experiment

The testing section has a rectangular cross-section of 1.99 m (width) × 1.79 m (height). The total length of the incoming flow part of the aerodynamic section is 11.0 m, including the turbulent boundary layer development part with 9 m of length. This wind tunnel has been made for research and investigation of historical objects.

The main feature of the planned contraction of the Wind Tunnel CET will be a variable open-jet test section for full-scale and model small scale testing with a interior cross-sectional area according to Fig. 1 and Fig. 2. A variation in size is achieved by a rectangular contraction with two interchangeable outlet sections resulting in overall contraction ratios of 2.02 and test section speeds from 3 to 55 m/s. The main design criteria for the contraction shapes were avoidance of re-laminarization and boundary-layer separation as well as a velocity nonuniformity in the outlet cross-sectional area lower than 0.3 %. Additionally, it was desired that the interchangeable outlet sections should also be as short as possible in order to ease the handling of these components.

The air velocity field and the turbulence intensity are defined for the experiment. The results are evaluated at distances of 0.36 m after the contraction outlet. The distribution of velocity within the monitored cross-section is defined by a non-dimensional coefficient given by the ratio of actual velocity to its mean value in the given cross-section.

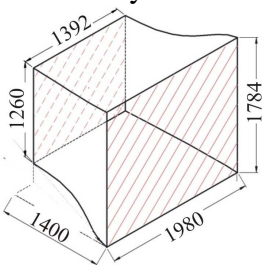


Fig. 1 Contraction diagram



Fig. 2 Contraction in tunnel: (a) downstream , (b) upstream view

Numerical Modelling

The following models were used: the RANS models, the Realizable k- ϵ and the SST k- ω , based on modelling of isotropic turbulence, the RSM model, resolving turbulences in an anisotropic way by direct computation of Reynolds stresses and the hybrid DES model with combination of the LES and the RANS methods. The DES models uses large vortexes in the centre of the flow pattern by direct simulation (LES method) and in the proximity of a wall, it uses the RANS method, in particular, it is SST k- ω here. In all models, the flow pattern was monitored by analysis of velocity and turbulence parameters. The results obtained from the above mentioned models were also compared with the experiment in collective cooperation [5]. Calculations can be also used for other tasks [6,7].

The computational area is 4.9 m long, whereas 0.5 m is made up of a rise; 1.4 m is the length of contraction, followed by a 3m long area after that according to Fig. 3. The computational grid uses 9×10^5 hex cells. In the transversal section in the contraction output in Fig. 4, there is a distinctive concentration in the surrounding of the connection of both areas for better data transmission at the boundary-line. The steady rise of cell sizes that are farther away from the boundary surfaces of the contraction for the purpose of correct computation at the wall is an important influence.

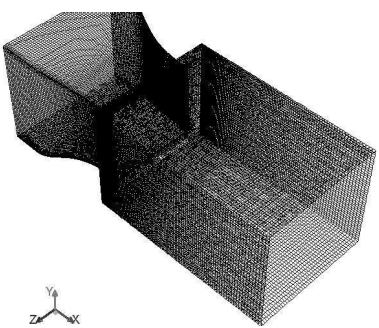


Fig. 3 Grid for numeric computation

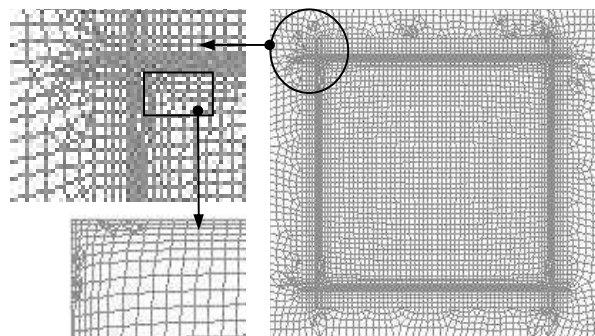


Fig. 4 Transversal section in the contraction output

Consistent types of marginal conditions were set up for all computations. At the inlet, it is the so-called velocity-inlet and at the outlet, it is the pressure-outlet condition. The marginal conditions on all the sides and lower and top areas of the computational area were defined by wall so that they correspond to the circumscribed space.

For the DES model, a time step of 5×10^{-4} second was selected; the computation simulated the flow for 4.3 seconds with the fact that averaging of quantities was set up after 1.6 seconds of the simulated process. Then it was possible to consider the flow pattern to be steady. The resulting time of the flow during temporal averaging of quantities represented approximately

a quadruple air exchange in the computational area. Some 8.6×10^4 iterations took place within one computation. The other models make it possible to resolve the task in a stationary way, but due to wrong convergence, the computations had to be done in a non-stationary way. For the RSM model, the time step was set to 1×10^{-3} seconds and 5.1×10^3 iterations were performed.

Results

The Fig. 5 shows distribution of velocity fields in the studied area which was obtained from the experiment. There is a result without the contraction on the left and the data obtained at a distance of 0.36 m after the contraction are show on the right. In Fig. 6 and Fig. 7, there are velocity coefficient isolines in transversal sections at a distance of 0.36 m after the contraction outlet defined from both the physical experiment and the numerical modelling. A minor increase in velocity near the walls round the perimeter of the contraction compared to the centre of the field. This is illustrated in Fig. 11 on the left (DES model).

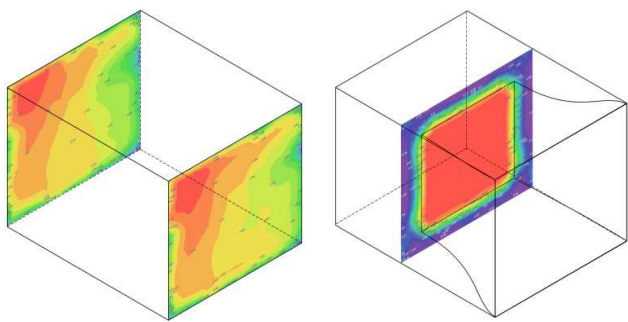


Fig. 5 Distribution of velocity fields (illustrative scheme, range of values without contraction 0.90-1.01)

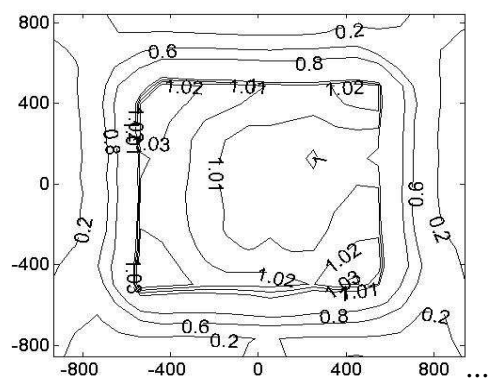
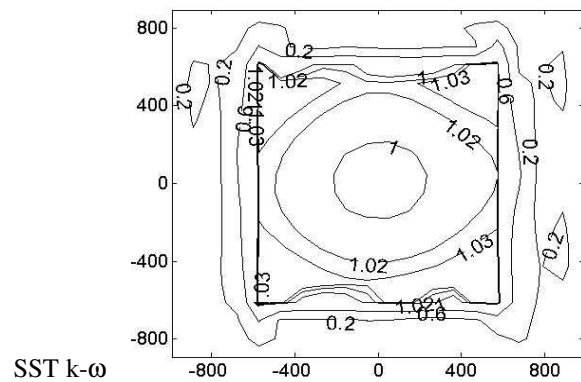
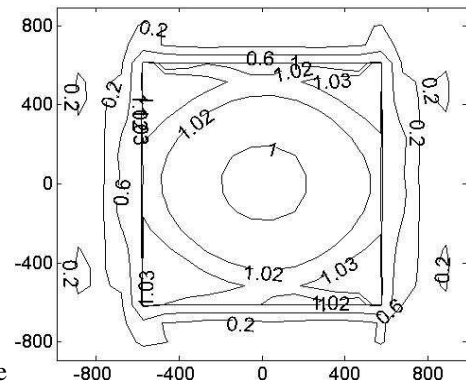


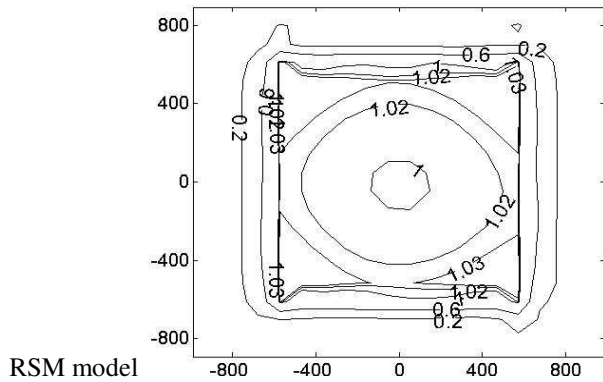
Fig. 6 Velocity coefficient isoline 0.36 m after contraction from experiment



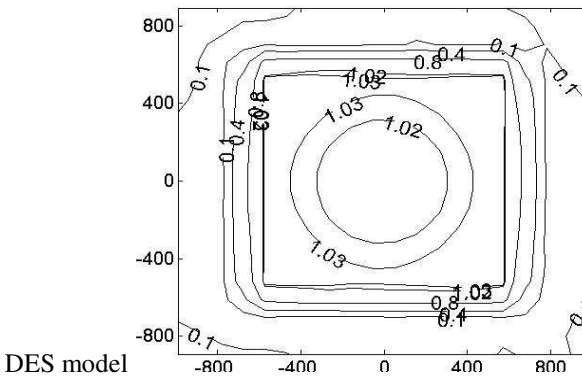
SST k- ω



Realizable



RSM model



DES model

Fig. 7 Velocity coefficient isoline 0.36 m after contraction from numeric modelling

There are turbulence intensity fields shown in Fig. 8. These data were obtained from the experiment. There is a result without the contraction on the left and the data obtained at a distance of 0.36 m after the contraction are show on the right. In Fig. 9 and Fig. 10 there are turbulence intensity isolines in transversal sections at a distance of 0.36 m after the output of the contraction defined both from the physical experiment and numeric modelling. The turbulence intensity was evaluated for the RSM and the RANS models. For the DES model, it is only possible to evaluate the intensity of large vortexes, therefore, the results differ slightly. Based on the isolines, the required decrease in intensity after flowing through the contraction is evident. This is illustrated in Fig. 11 on the right (SST k- ω model).

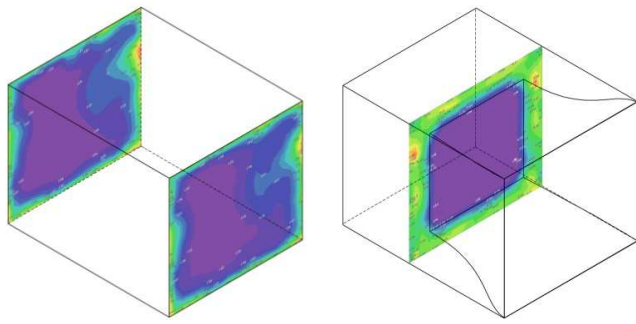


Fig. 8 Distribution of turbulence intensity fields
(illustrative scheme,)

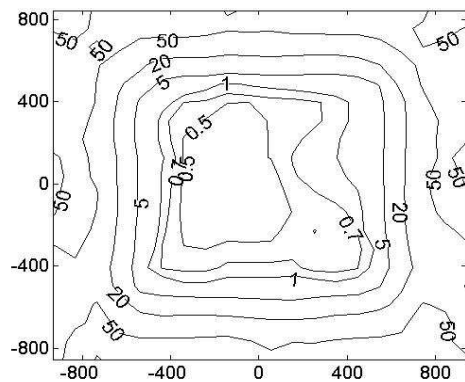
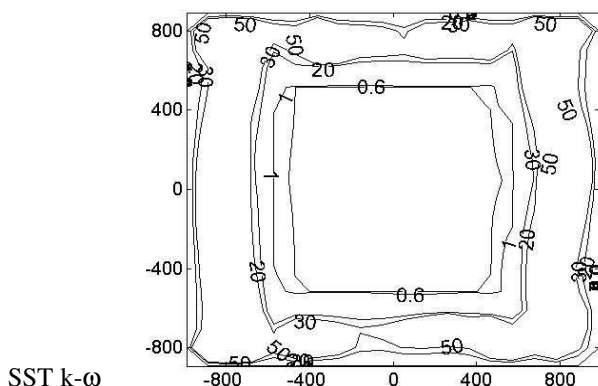
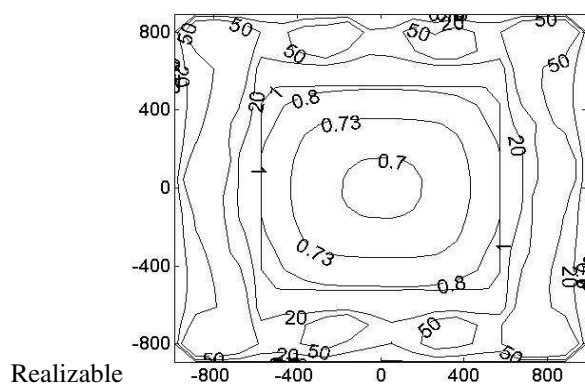


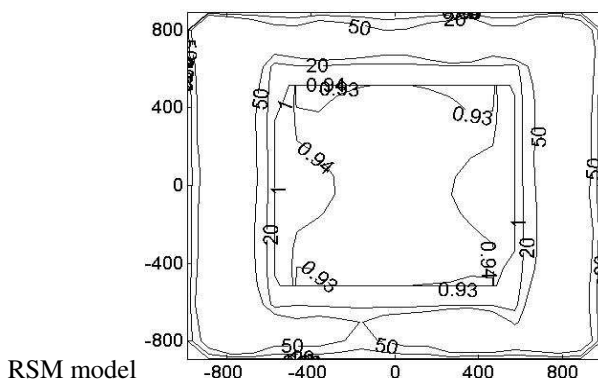
Fig. 9 Turbulence intensity 0.36 m [%]
after contraction from experiment



SST k- ω



Realizable



RSM model

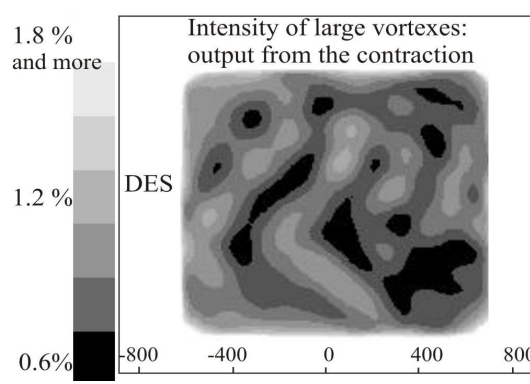


Fig. 10 Turbulence intensity isoline 0.36 m after contraction from numerical modelling



Fig. 11 Velocity field and turbulence intensity in contraction in vertical sections

Summary

Based on results from the experiment and from all computations, the required decrease in turbulence intensity by approx. was confirmed. The results also indicate a minor acceleration of velocity near the walls and around the perimeter of the contraction. Individual models show small differences in the description of velocity field values in the inner space.

The subject of the following investigation will be a measurement of velocity field inside the contraction. Based on this, it will be possible to determine the most suitable model which should serve for detailed description of the modelled process and for certificate of an optimum shape of the contraction for the most uniform velocity field possible and for the minimum possible turbulence at the outlet.

Acknowledgements

This contribution is the result of the research supported by the conceptual development of science, research and innovation for 2014 allocated to the VŠB-Technical University of Ostrava by the Ministry of Education, Youth and Sports of the Czech Republic.

This work was supported by the Grant Agency of the Academy of Sciences - project 14-12892S and by the institutional support RVO 68378297.

References

- [1] J.E. Sargison, G.J. Walker and R. Rosi, Design and calibration of a wind tunnel with a two dimensional contraction. In: Proceeding of the 15th Australian Fluid Mechanic Conference, Sydney, Australia, 2004.
- [2] F.M. Fang, J.C. Chen and Y.T. Hong, Experimental and analytical evaluation of flow in a square-to square wind tunnel contraction, Journal of Wind Engineering and Industrial Aerodynamics. 89 (2001) 247-262.
- [3] F.M. Fang, A design method for contractions with square end sections. Journal of Fluids Engineering. 119 (1997) 454-458.
- [4] T. Wolf, Design of a variable contraction for a full-scale automotive wind tunnel, Journal of Wind Engineering and Industrial Aerodynamics. 56 (1995) 1-21.
- [5] V. Michalcová, S. Kuznětsov, S. Pospíšil, Models of load on buildings from the effects of the flow field, Transactions of the VŠB – Technical University of Ostrava, Civil Engineering Series. 13, 2 (2013) 91–97.
- [6] I. Skotnicova, Z. Galda, P. Tymova, L. Lausova, Experimental Measurement and Numerical Simulation of Dynamic Thermal Performance of External Timber Frame Wall. AMR, Vol. 899, pp 126-130. DOI:10.4028/www.scientific.net/AMR.899.126.
- [7] E. Kormaniková, K. Kotrasová, Design of a variable Strength optimal design of the fiber reinforced composite on microscopic level, 12th International Multidisciplinary Scientific GeoConference and EXPO, SGEM 2012, Varna, Bulgaria, Code 101586, Vol. 3, pp. 499-506.

Wind Tunnel Study of Vortex Shedding behind Cooling Tower Models

MICHÁLEK Petr^{1,a*} and ZACHO David^{1,b}

¹Aerospace Research and Test Establishment (VZLU), Department of Aerodynamics,
Beranových 130, 199 05 Praha 9, Czech Republic

^amichalek@vzlu.cz, ^bzacho@vzlu.cz

Keywords: boundary layer wind tunnel, cooling towers, hot wire anemometry

Abstract. Wind tunnel measurements of vortex shedding behind cooling tower models were performed in VZLU. Two variants of cooling tower models were used, i.e. model with smooth wall outer surface and model with rough wall surface. Measurements were conducted using hot-wire anemometer. Time signal from the anemometer was transformed using Fast-Fourier routine into frequency spectrum. Measurements have shown significant differences between smooth and rough variant of model surface and dependency of vortex shedding frequency on Reynolds number.

Introduction

Cooling towers are used in order to dissipate unnecessary heat at power stations, industrial plants, etc. Cooling towers are in principle a large chimney with up to 100 m in diameter and 200 m in height. They are made mostly of reinforced concrete and have a rotational hyperboloid shape. They can be subjected to extreme loads, i.e. extreme wind speed, seismic activity, collision with airplanes. There is an effort to develop a composite reinforcement system, which would increase the stiffness of these cooling towers.

A possible dangerous phenomenon occurring in flows past a cylinder-like structure is vortex shedding. Vortex shedding behind some structures can drive them into violent oscillations that can damage or even destroy them. Frequency of vortex shedding is expressed by Strouhal number

$$St = f l / U. \quad (1)$$

where f is frequency of vortex shedding, l is characteristic dimension (e.g. diameter of the cylinder) and U is velocity of incoming flow. Strouhal number can also vary in dependence on Reynolds number.

Previous wind tunnel and field studies on cooling towers have studied wind pressures [1,2], gas dispersion from them [3] or interference effects between two towers [4], but vortex shedding was studied usually on circular cylinders and bluff bodies.

Wind tunnel and performance of the experiment

Wind tunnel measurement on cooling tower models is necessary to determine wind load on these structures and vortex shedding frequency. Wind load measured on scaled models in wind tunnel can be obtained in a more accurate way than by calculation according to Eurocode 1 [5]. Cooling tower model was manufactured using 3D printing. The cooling tower model was made in 1:400 scale, it is 330 mm high and 150 mm in diameter at the top. The model installed in the wind tunnel with hot-wire probes behind it is presented on Fig. 1.

There were two variants of the cooling tower outer surface, i.e. the smoothed original surface and roughened surface with glued abrasive material. These surface variations were made in order to study the effect on the tower surface roughness on the results. The reason for the roughness is that flow around round objects is more dependent on Reynolds number value than for rectangular objects. Round bodies with semi-aerodynamic shape possess higher critical values of Reynolds number, above them the flow patterns do not change, at least one magnitude higher than rectangular

bodies. Rough model surface has the same effect as increase of the Reynolds number, and thus decrease the difference between the model scale and real object in full scale. Increase of the Reynolds number by means of wind speed increase is not possible due to wind tunnel power limitation.



Fig. 1 Cooling tower model in the wind tunnel

Boundary layer wind tunnel (BLWT) is a special wind tunnel used for testing of civil engineering structures and gas dispersion experiments. BLWT in VZLU can simulate atmospheric boundary layer for agricultural, suburban or urban terrain according to Eurocode 1 [5]. The wind tunnel in VZLU is 15.6 m long, 1.8 m wide and 1.5 high with adjustable ceiling height and powered with 55 kW DC engine. For cooling tower model testing, suburban boundary layer – IIIrd category was used, because large areas around the power station are covered with woods. Properties of the boundary layer, such as vertical velocity profile U and turbulence intensity Iu , that were measured with hot-wire anemometer with single wire probe, are presented on Fig. 2, where R^2 is reliability coefficient of logarithmic fitting curve. Roughness length according to Fig. 2 was $z_0 = 0.83$ mm.

The modeled boundary layer has to correspond with the logarithmic law, which is defined for indifferent atmospheric layering as

$$U(z) = \frac{u^*}{k} \ln \left[\frac{z-d}{z_0} \right]. \quad (2)$$

Where u^* is frictional velocity (dynamic velocity) [m/s], $k = 0.4$ is von Karman's constant, z_0 is frictional height (aerodynamic roughness) [m], d is zero plane displacement [m], U is mean velocity [m/s] and z is vertical coordinate [m]. For more information about boundary layer adjustment in wind tunnels, please see the publications [6,7].

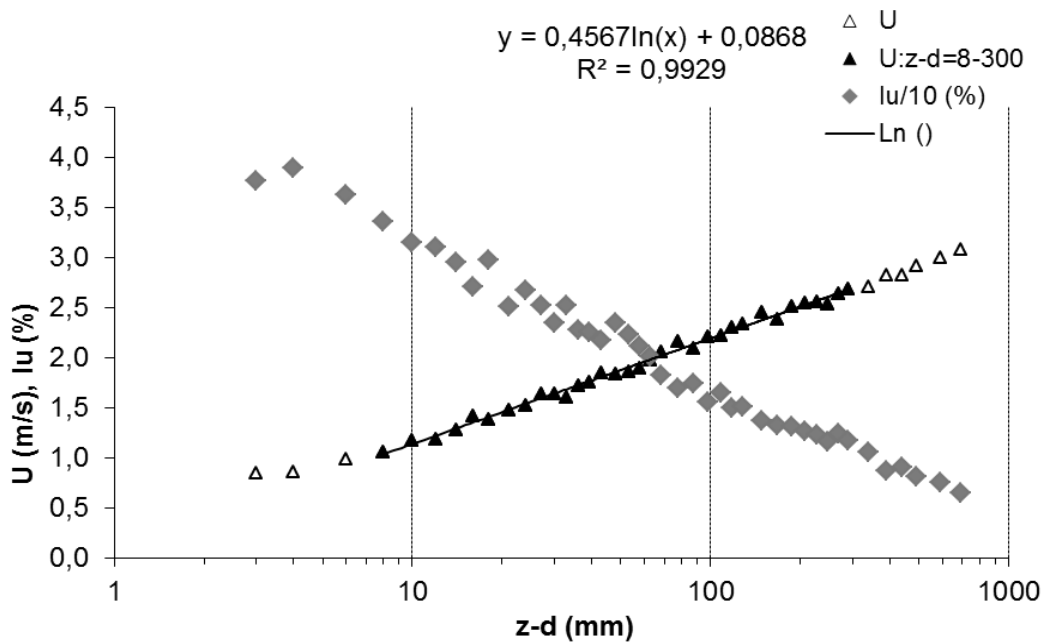


Fig. 2 Vertical velocity profile of the boundary layer

Cooling tower model was mounted in the wind tunnel and two hot-wire probes with one wire were mounted on a traversing device so that the probes could be moved in all three directions. Probe signal was processed using a constant temperature anemometer and then digitally sampled in a PC with LabView virtual instruments software. Two single-wire straight probes were connected to the constant temperature anemometer and the signals were sampled simultaneously and subtracted from each other. The LabView software then used Fast Fourier transform (FFT) to convert the resulting time signal into frequency spectrum, where peaks could be detected. Probes were moved in three directions x , y and z in order to find exact position behind the model where peaks were clearly visible on the online graph. Example of spectra with and without peak indicating presence of regular shedding of vortices behind rough tower is shown at Fig. 3. Presented spectra were calculated as an average of ca. 120 s sampling interval. Spectrum with peak was measured with probes located downwind of the cooling tower, i.e. “behind tower” and spectrum without peak was measured with probes located outside the area of tower wake, i.e. “outside tower”. Velocity above boundary layer in Fig. 3 was set to 15 m/s. As seen in Fig. 1, one probe was located behind the edge of the cooling tower in its narrowest diameter (at height 20 cm) and the second probe was located in ca. 15 cm horizontal distance, far enough beyond the wake of the model, where the peaks disappeared from the spectrum. In this configuration the peaks could be found for velocities above boundary layer 5 m/s and more. The remaining part of the spectrum represents a typical turbulent boundary layer spectrum with the part called “inertial subrange”, which corresponds with the $-5/3$ power slope curve. This inertial subrange is the range ca. 10 – 2000 Hz at Fig. 3. Higher frequencies were filtered out with the low pass filter, which was set to 3 kHz, sampling frequency was 9 kHz.

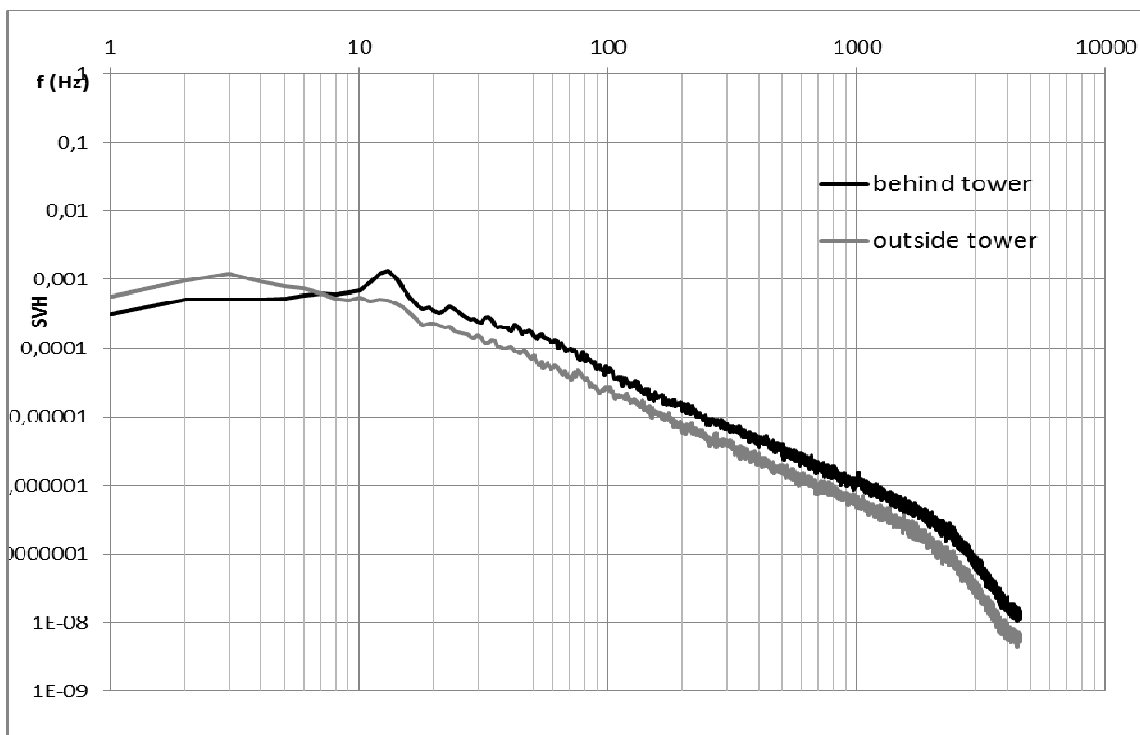


Fig. 3 Example of spectra with and without peaks

Measured and calculated peak frequencies for both model variants are presented at Table 1, where U is velocity at measured height (200 mm), Re is Reynolds number, f is detected frequency of peak and St is Strouhal number. Index 1 stands for model with smooth walls and index 2 for model with rough walls. Results indicate that rough variant of the model surface show lower peak frequencies and thus lower Strouhal numbers.

Table 1 Strouhal numbers for smooth (1) and rough (2) version

U (m/s)	$Re * 10^4$	f_1 (Hz)	St_1 (-)	f_2 (Hz)	St_2 (-)
2.6	2.3	3	0.153	-	-
4.3	3.81	5	0.153	5	0.153
6.0	5.31	6	0.131	6	0.131
8.5	7.53	10	0.153	8	0.122
11.1	9.83	13	0.153	10	0.118
12.8	11.3	15	0.153	13	0.133

Conclusion

Vortex shedding behind two variants of cooling tower models, either with smooth walls or with rough walls was measured in the boundary layer wind tunnel in VZLU. The measurements were made with two hot wire probes and the time signal was transformed into frequency spectrum using Fast-Fourier transform routine. Results showed that rough-wall variant of the model caused lower Strouhal numbers. These results will be used for comparison with CFD calculations of flow around cooling towers in full scale. Future work will also include measurements behind groups of cooling tower models, first of all determination of wind loads on cooling towers in groups, as they have been used in power plants.

Acknowledgement

Authors would like to thank the support granted by Technology agency of the Czech Republic under project TA02010382.

References

- [1] M. Pirner, Wind pressure fluctuations on a cooling tower, Journal of Wind Engineering and Industrial Aerodynamics. 10 (1982), 343-360.
- [2] M. Homola, Measurement of cooling tower group in aerodynamic tunnel 1.8 m, VZLU report Z 1541/67 Prague, 1967 (in Czech).
- [3] M. Schatzmann, A. Lohmeyer, G. Ortner, Flue gas discharge from cooling towers. Wind tunnel investigation of building downwash effects on ground-level concentrations, Atmospheric Environment. 21 (1987) 1713-1724.
- [4] M. Orlando, Wind-induced interference effects on two adjacent cooling towers, Engineering Structures. 23 (2001) 979-992.
- [5] ČSN EN 1991-1-4 Eurocode 1: Actions on structures – Part 1-4: General actions – Wind loads, Czech Institute for Normalization, Prague, 2007.
- [6] M. Jirsák, R. Ulman, Boundary layer simulation and its lower velocity limit. Proceedings of the 3rd ICWE, Eindhoven University of Technology, 2001, pp. 237-240.
- [7] Wind tunnel studies of buildings and structures, ASCE manuals and reports on engineering practice No.67, N. Isyumov (ed.), Virginia, 1999.

Analysis of Stochastic Resonance Phenomenon in Wind Induced Vibration of a Girder

POSPÍŠIL Stanislav^{1,a*} and NÁPRSTEK Jiří^{1,b}

Institute of Theoretical and Applied Mechanics ASCR, v.v.i., Prosecká 76, 19000, Prague 9, Czech Republic

^apospisil@itam.cas.cz, ^bnaprstek@itam.cas.cz

Keywords: nonlinear aero-elasticity, stochastic resonance, turbulence, aeroelastic divergence, wind induced vibration, wind tunnel experiments

Abstract. We study the response of a dynamic system to additive random noise and external deterministic periodic force to investigate vibration of a slender prismatic beam in a cross flow with a turbulence component. The aim of the study is to find such parameter combinations, which should be avoided in practice to eliminate response amplitude increase due to the effect of the stochastic resonance. We assume the non-linear oscillator (beam) with one generalized degree of freedom in the divergence-like regime. It is described by the version of the Duffing equation. We conduct the theoretical investigation with the use of relevant Fokker-Planck equation together with verification by numerical simulation of corresponding stochastic differential system. Real characteristics of a sectional model, fixed in the special stand allowing the snap-through effect, in the wind tunnel are employed.

Introduction

The response of various types of non-linear dynamic systems under random excitation has been studied during many years, as this mathematical model is inherent in a number of areas of physics including wind engineering and aero-elasticity, see e.g [1], [2]. Both latter branches deal very often with the vibration of slender structures under the excitation of deterministic (pseudo-steady wind) wind load with the combination of noisy (turbulence) additive force. It is still often assumed that contribution of the noise in the non-resonant part of the frequency spectra is decreasing the overall response of the structure, because it is acting in the disordering manner. The counter-intuitive property of the noise, its ability to induce ordering in non-linear non-equilibrium systems, has been demonstrated in the effect of the phenomenon called stochastic resonance (SR).

SR has been surmised in physical chemistry in early forties, see e.g. [3]. Many years later several branches in theoretical and experimental physics identified this phenomenon, see e.g. [4], or review paper [5]. Hundreds papers have been published until now, including also a couple of monographs, for instance [6]. Basically, SR occurs when the dynamical systems are perturbed by noise and in particular, when the system is subdued to an external periodic force applied together with some noise. The response of a bistable system heads towards the periodic switching between the semi-stable states. The dependence of the response on the additive noise intensity has a resonant form, hence an optimal (in the structural engineer's point of view - undesired) value of the noise intensity can be found. Moreover, in [7] it has been shown that a high-frequency periodic force can work as a noise and amplify the response to the low-frequency periodic signal in bistable systems.

In this paper, the response of a dynamic non-linear single degree of freedom (SDOF) system with cubic characteristic to a combination of additive random Gaussian white noise and external deterministic periodic force is studied. It is motivated by the most important and dangerous phenomenon of aero-elastic post-critical state - divergence - occurring at a prismatic slender beam in a cross-flow. This phenomenon manifests by stable periodic hopping between two nearly constant limits perturbed by random noises. The frequency of this hopping can be for certain combination of input parameters nearly constant and corresponding to external periodic force frequency. This state leads to high ratio of periodic component amplitude and intensity of the random component of the response process.

In such a case the system can be used as a harmonic selective resonator detecting the useful weak harmonic signal in the high noisy background. The aim of this paper is to investigate whether the undesired - harmful - SR can be achieved in the field of structures loaded by the turbulent wind. For this purpose we consider and model a beam vibration subjected to a weak periodic forcing with a double well potential and certain potential barrier and wind turbulence modeled as a white noise.

Mathematical Model and Basic Considerations

Let us assume the nonlinear mass-unity oscillator with one degree of freedom:

$$\begin{aligned}\dot{u} &= v; \\ \dot{v} &= -2\omega_b \cdot v - V'(u) + P(t) + \xi(t).\end{aligned}\quad (1)$$

The potential energy $V(u)$ being introduced in a form corresponding with the Duffing equation

$$V(u) = -\frac{\omega_0^2}{2}u^2 + \frac{\gamma^4}{4}u^4 \Rightarrow V'(u) = dV(u)/du = -\omega_0^2 \cdot u + \gamma^4 \cdot u^3 \quad (2)$$

and $\xi(t)$ is the Gaussian white noise of intensity $2\sigma^2$ respecting conditions:

$$\mathbf{E}\{\xi(t)\} = 0; \quad \mathbf{E}\{\xi(t)\xi(t')\} = 2\sigma^2 \cdot \delta(t - t'). \quad (3)$$

$P(t) = P_o \exp(i\Omega t)$ is external harmonic force with frequency Ω and amplitude P_o per unit mass. Symbols ω_0 and ω_b have a usual meaning of the circular eigen-frequency and circular damping frequency of the associated linear system. The linear part of the $V'(u)$ is negative making the system metastable in the origin, while the cubic part acts as stabilizing factor beyond a certain interval of displacement u .

If the intensity ξ is small enough, it will oscillate around either of the stable points with very small probability of switching to the other. If we increase the noise amplitude, then there is some higher probability that the response will jump from one basin to the other. If the noise level is just right, then the periodic forcing leads to oscillation between the wells with period Ω . In more general terms, there is stochastic resonance whenever adding noise to a system improves its performance or increases its signal-to-noise ratio. Note that the noise amplitude cannot be too large or the system can become completely random.

Fokker-Planck Equation - Starting Point

Taking into account that random noise in Eq. 1 has an additive character, the appropriate Fokker - Planck (FP), e.g. [8] equation with the diffusion and drift coefficient can be easily written out:

$$\kappa_u = v \quad \kappa_v = -2\omega_b \cdot v - V'(u) + P(t), \quad \kappa_{vv} = 2\sigma^2 \quad (4)$$

$$\frac{\partial p(u, v, t)}{\partial t} = -v \frac{\partial p(u, v, t)}{\partial u} + \frac{\partial}{\partial v}[2\omega_b \cdot v + V'(u) - P(t)]p(u, v, t), +\sigma^2 \frac{\partial^2 p(u, v, t)}{\partial v^2} \quad (5)$$

$$\text{together with boundary conditions: } \lim_{u, v \rightarrow \pm\infty} p(u, v, t) = 0; \quad p(u, v, 0) = \delta(u, v). \quad (6)$$

If the external excitation is only due to random component, Eq. 5 admits the closed form stationary solution of the Boltzmann type. For its various aspects and details, see e.g. [9], [10], [11] and other papers and monographs:

$$p_o(u, v) = K \cdot \exp\left(-\frac{2\omega_b}{\sigma^2} H(u, v)\right), \quad (7)$$

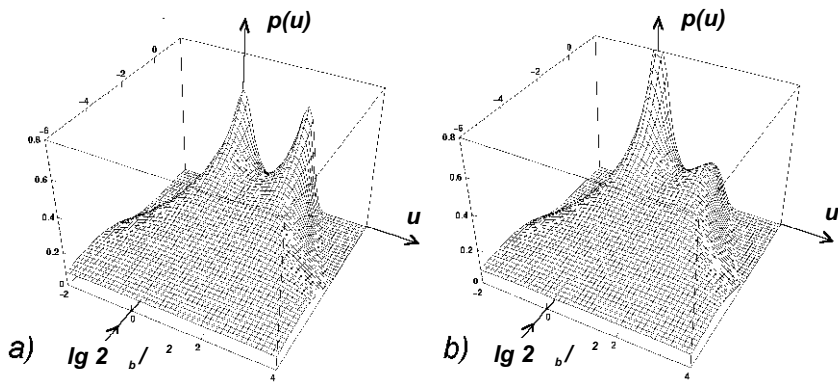


Fig. 1 Response PDF of the system excited by white noise only: (a) Symmetric potential; (b) Non-symmetric potential.

where K is the normalizing constant and $H(u, v)$ represents the Hamiltonian function of the basic system. In particular:

$$H(u, v) = \frac{1}{2}v^2 + V(u) = \frac{1}{2}v^2 - \frac{1}{2}\omega_0^2 u^2 + \frac{1}{4}\gamma^4 u^4. \quad (8)$$

It is evident that solution of Eq. 7 type can be provided for any arbitrary symmetric/non-symmetric potential including cases passing the system into monostable type. Probability density of the response has significantly non-Gaussian form, see Fig. 1.

When excitation force consists of both component, stationary solution of FPK Eq. 5 no more exists. In order to approximate its solution, the Eq. 7 can be used as a basic part, which should be multiplied by a space and time dependent series. The probability distribution function (PDF) can be expected periodic or cyclic-stationary in a certain meaning of the term in time coordinate for $t \rightarrow \infty$ and the Floquet theorem or the maximum entropy principle, e.g. [9] could also be alternatively used as a basic tool for the solution.

Example-Harmonically Excited Beam Under Influence of Turbulence Noise

The response of a beam, loaded by the wind with turbulent component, known as the aeroelastic divergence, initiated the idea to use the theory of stochastic resonance for the explanation of hopping of the beam in between two meta-stable positions, see [12]. This kind of response has been observed during the wind tunnel measurement focused on the self-induced vibration with the large amplitudes in the non-linear range using the special experimental stand. It represents the working mechanism sensitive to the excitation by the wind, see Fig. 2. The stand itself and the experiments focused on the bridge aeroelasticity are described more in detail in the papers [13] and [14] for the smooth flow. In order to arrange the clear modulation signal at the system, the excitation mechanism is attached which is able to excite harmonically the system with desired amplitude and the driving frequency. The SR mechanism works well with the almost over-damped system, however, low damping is not excluded from the analysis, because the SR mechanism is sensitive to any optimal combination of many parameters.

The system Eq. 1 for the unknown response $\varphi = u/r$ can be rewritten:

$$\begin{aligned} \dot{\varphi} &= \psi; \\ \dot{\psi} &= -\alpha \cdot \psi - \beta\varphi - \gamma\varphi^3 + A \sin(\Omega \cdot t) + \xi(t), \end{aligned} \quad (9)$$

with: $\alpha = 2\zeta\omega_0$, $\beta = \omega_0^2 - k_p d_0 / (mr) < 0$ and $\gamma = k_p r^2 / (2mL^2)$. The values of the parameters are the following: damping of the system $\zeta = 0.05$; system frequency $\omega_0 = 2.0$ [s^{-1}]; driving amplitude

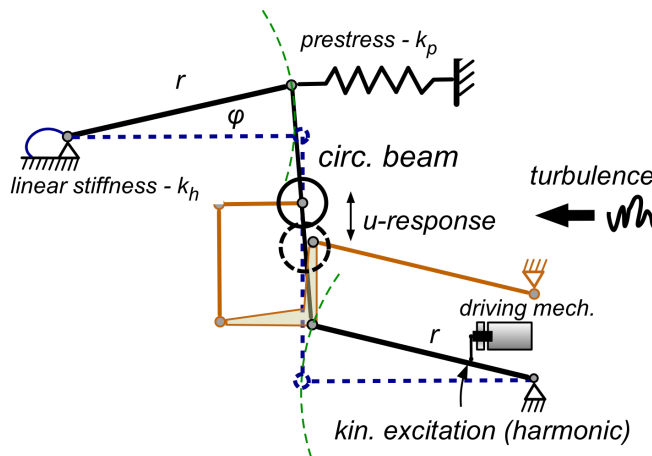


Fig. 2 The sketch of the experimental stand adjusted for the measurement of stochastic resonance phenomenon. The harmonic excitation is controlled by the electric engine. Turbulent wind is produced by the turbulence grids in front of the beam.

$A = 3^\circ$; mass $m = 5$ [kg]; pre-stressing stiffness $k_p = 820$ [N/m]; initial deformation $d_0 = 0.05$ [m] of the pre-stressing spring; lever length $r = 0.5$ [m]; length of the pre-stressing spring $L = 0.25$ [m]. The equation has been solved numerically for the time period 1000 [s] with the time step $\Delta t = 0.01$ [s].

The results of the stochastic resonance analysis are illustrated starting by Fig. 3, which presents the signal-to-noise ratio (SNR) as the function of the noise intensity expressed by σ^2 and the results (Fourier spectra) of the numerical simulations using the basic Eqs 9. In the individual spectral lines it can be seen the influence of rising white noise intensity σ^2 , which acts together with a harmonic force onto the system. For very low level of the noise the harmonic component is hardly able to overcome the inter-well barrier and therefore only seldom irregular jumps between stable points occur.

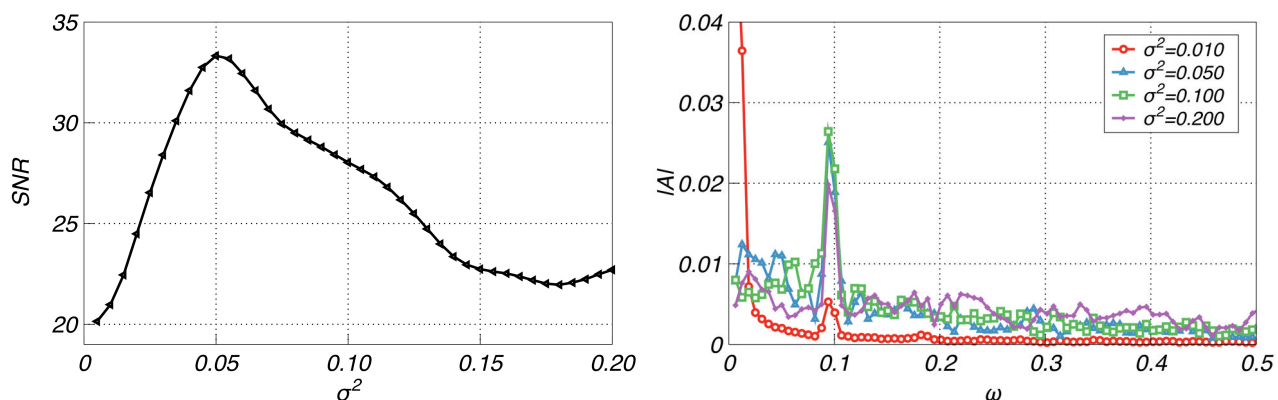


Fig. 3 Left - The spectral amplification of the system response due to stochastic resonance effect. The signal-to-noise ratio (SNR) as the function of various noise strengths (σ^2) due to stochastic resonance. Right - Fourier spectra of the response obtained by numerical solution of Eq. 9.

In local regimes the system response is relatively small and nearly linear. Optimal ratio of the noise intensity and the amplitude of the harmonic force results for its certain frequency in the system response containing a visible spectral peaks (amplification) corresponding with the frequency of the external harmonic modulation. The single peak (in the case of colored noise more peaks may appear) and thus the "optimal" noise strength can be identified.

Generally, the response is not harmonic and contains many higher harmonics. However its basic frequency is stable making possible to reconstruct the original harmonic component hidden in the

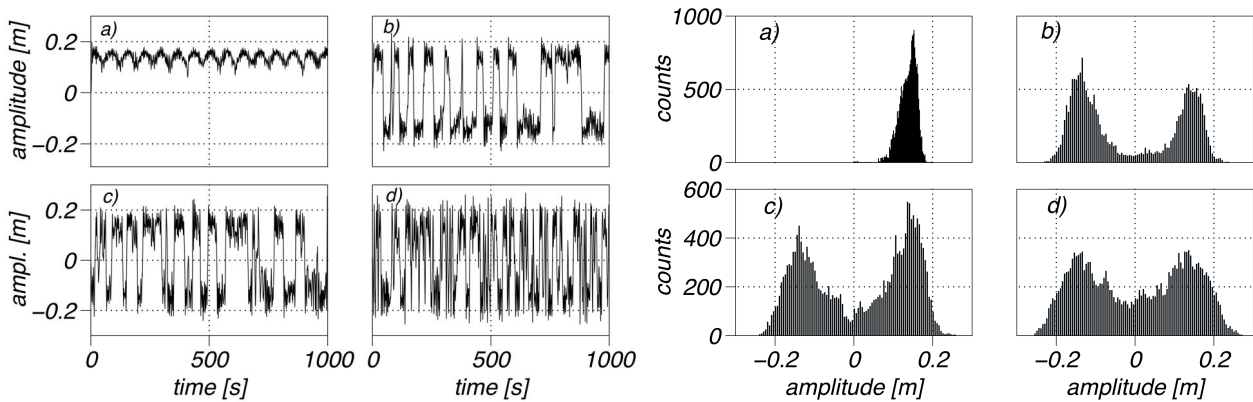


Fig. 4 Left - Response of the system with combined white noise and harmonic excitation with frequency $\Omega = 0.09$. Right - Probability density functions (histograms) of the response due to change of the noise intensity-turbulence. The curves (a), (b), (c) and (d) represent the noise intensity $\sigma^2 = 0.1, 0.5, 1.0$ and 2.0 respectively.

background. Fig. 4 demonstrates the state of large superiority of the noise. Increasing the noise level can counteract the aforementioned process and thereby the stochastic resonance effect can vanish. This figure shows also the sensitivity of the system. The curves (a), (b), (c) and (d) correspond to harmonic component frequency $\Omega = 0.09$ and noise intensity $\sigma^2 = 0.1, 0.5, 1.0$ and 2.0 respectively. Basically, certain frequency Ω leads to the stochastic resonance for certain noise intensity and damping level. To achieve this effect in practice, some sweeping of parameters or their optimization is necessary, because the dangerous effects of aeroelastic divergence should be avoided.

The influence of the noise is apparent in Fig. 4. When the noise strength is small, the mass remains in one well (say in the upper part of the response, or in the divergent position). Increasing the noise strength - case (b) and case (c) - the response is jumping from one well to another with clear periodic pattern. Further increase of the noise intensity - case (d) - leads to the more random jumping between the meta-stable positions of the mass.

Conclusions

The phenomenon of the stochastic resonance has been introduced as a theoretical tool of aeroelastic vibration analysis. This way reveals to be adequate observing carefully experimental results obtained by comprehensive measurements in a wind channel. With respect to those, the divergence manifests phenomenologically as a periodical hopping between two quasi-static positions with weak random perturbation. This effect can emerge under a relevant combination of periodic (nearly harmonic vortex shading) and random (white noise type) additive excitation as it has been observed experimentally.

Conditions of the theoretical stochastic resonance occurrence at the Duffing equation are qualitatively identical and therefore it has been adopted as an adequate theoretical model of the divergence phenomenon. The relevance of this model has been verified analytically by means of the Fokker-Planck equation as well as by numerical solution of corresponding Ito stochastic system.

The paper describes also the numerical simulation of the experimental stand used for the aeroelastic testing of profiles, before it has been tested in the turbulent flow. It shows, that under certain "optimal" value of the parameters, the signal-to- noise ratio of the response increases and the resonant-like peak occurs in the amplitude spectra.

This makes an optimistic perspective for the experimental analysis, which together with the analytical and numerical ones should continue to obtain better insight into the general tendencies when individual parameters of the system and the input signal are changed. Also other types of non-linearities in the system stiffness (especially non-symmetric) should carefully studied.

Acknowledgements

This work was supported by the Grant Agency of the Academy of Sciences - project 13-34405J and by the institutional support RVO 68378297.

References

- [1] G. V. Parkinson, J. D. Smith, The square prism as an aeroelastic nonlinear oscillator, Quart. J. Mech. Appl. Math. 17 (1964) 225-239.
- [2] M. Novák, A. G. Davenport, Aeroelastic instability of prisms in turbulent flow, Jour. Eng. Division, Proc. ASCE EM 96 (1970) 17-39.
- [3] H. A. Kramers, Brownian motion in a field of force and the diffusion model of chemical reactions. Physica, 4 (1940) 284-304.
- [4] M. E. Inchiosa, A. R. Bulsara, Signal detection statistics of stochastic resonators. Physical Review E, 53 (1996) 2021-2024.
- [5] L. Gammaiton, P. Hanggi, P. Jung and F. Marchesoni, Stochastic resonance. Reviews of Modern Physics, 70 (1998) 223-287.
- [6] M. D. McDonnell, N. G. Stock, C. E. M. Pearce and D. Abbott D. Stochastic Resonance, Cambridge University Press, 2008.
- [7] P. Landa, P. McClintock, Vibrational resonance. J. Phys. A, 33 (2000) L433.
- [8] V. S. Pugachev , I. N. Sinitsyn, Stochastic Differential Systems - Analysis and Filtering. J. Willey, Chichester, 1987.
- [9] J. Náprstek, Application of the maximum entropy principle to the analysis of non-stationary response of SDOF/MDOF systems. In: L. Püst and F. Peterka (Eds.), Proc. 2nd European Nonlinear Oscillations Conference - EUROMECH, Prague, 1996, pp. 305-308.
- [10] G. Q. Cai, Y. K. Lin, On exact stationary solutions of equivalent non-linear stochastic systems. Int. J. Non-Lin. Mech., 23 (1998) 315-325.
- [11] W. Q Zhu, G. Q. Cai and Y. K Lin, On exact stationary solutions of stochastically perturbed Hamiltonian systems. Prob. Eng. Mech., 5 (1990) 84-87.
- [12] J. Náprstek, S. Pospíšil, Response types and general stability conditions of linear aero-elastic system with two degrees-of-freedom. J. Wind Eng. Ind. Aerodyn. 111 (2012) 1–13.
- [13] R. Král, S. Pospíšil and J. Náprstek, Wind tunnel experiments on unstable self-excited vibration of sectional girders, J. Fluid Struct. 44 (2014) 235-250.
- [14] R. Král, S. Pospíšil and J. Náprstek, Experimental set-up for advanced aeroelastic tests on sectional models. Exp. Techniques, (2013) DOI: 10.1111/ext.12056

Numerical Estimation of Aerodynamic Characteristics of Footbridge Deck

ŠOLTÝS Róbert^{1,a*} and TOMKO Michal^{2,b}

^{1,2}Department of Structural Engineering, Technical University of Kosice, Vysokoskolska 4,
042 00 Kosice, Slovak Republic

^arobert.soltys@tuke.sk, ^bmichal.tomko@tuke.sk

Keywords: footbridge aerodynamics, computational fluid dynamics, vortex shedding

Abstract. For estimation of aerodynamic characteristics of cable-stayed footbridge deck a computational fluid dynamics (CFD) has been used. An incompressible fluid flow with Navier-Stokes equations has been applied. An adequate numerical model has been created to obtain accurate values of aerodynamic characteristics. Preliminary determination of simulation parameters have been estimated using laminar fluid flow model. Subsequently, Smagorinsky large-eddy simulation (LES) turbulent model has been applied with different simulation parameters to obtain converged values. The boundary layer separation regions and downwind vortex shedding have been observed.

Introduction

Cable-stayed and suspension bridges are sensitive to wind action. There are several well-known types of aerodynamic effects acting on bridge structures and their structural components. As the bridge span is increasing the aero elastic effects are more significant in their response. Such as vortex shedding induced vibrations, flutter and buffeting. Not long ago, bridge deck response has been predominantly estimated using wind tunnels but with increasing computer performance computational methods happens to be useful and power-full tools, supplementary to wind tunnel testing. For computation fluid flow past structures the most used method is computational fluid dynamics (CFD). Kuroda [1] investigated air flow past bridge deck of Great Belt East Bridge using laminar flow and aerodynamic results compared with wind tunnel results. For calculation aerodynamic characteristics and for investigation surrounding flow characteristics ADINA code [2] has been used with laminar and turbulent model.

Footbridge Deck Geometry Description

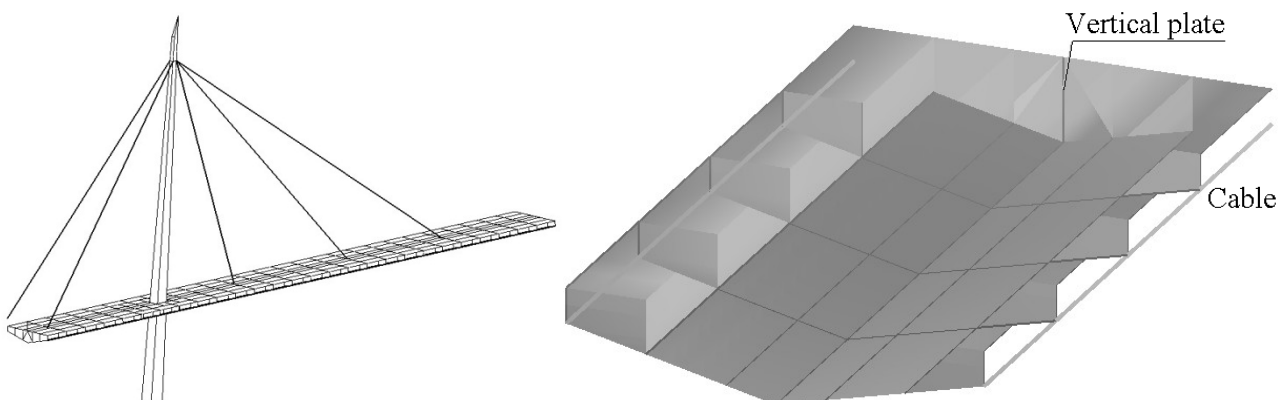


Fig. 1 View of footbridge (left), deck segments (right)

View of the investigated footbridge can be seen in Fig. 1-left. Footbridge deck (Fig. 1-right) material is intended to be steel plates with various thickness (8 to 20 mm). Footbridge deck with its dimensions, gravity center M_c and shear center S_c locations is shown in Fig. 2. Deck length is 67.7 m, width $B = 5.9$ m and height $H = 1.2$ m. Due to sharp edges in deck geometry, the cross-section is the bluff-body type. Therefore, boundary layer separation points can be easily predicted.

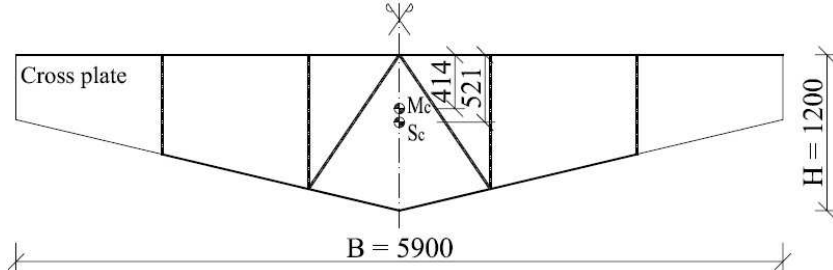


Fig. 2 Footbridge deck cross-section

Numerical Fluid Model - CFD

For computational representing surrounded air environment an incompressible fluid flow with Navier-Stokes equations (Eq. 1) have been applied

$$\frac{\partial v_i}{\partial t} + v_j \frac{\partial v_i}{\partial x_j} = \frac{1}{\rho} F_i - \frac{1}{\rho} \frac{\partial p}{\partial x_i} + \nu \Delta v_i, \quad \text{for } i = 1, 2, 3, \quad (1)$$

$$\text{where } \Delta v_i = \frac{\partial^2 v_i}{\partial x_j \partial x_j} = \frac{\partial^2 v_i}{\partial x_1^2} + \frac{\partial^2 v_i}{\partial x_2^2} + \frac{\partial^2 v_i}{\partial x_3^2},$$

ν , ρ , p are kinematic viscosity, fluid density and fluid pressure,

F_i is volumetric force intensity forcing unit fluid volume,

v_i is i -th velocity vector of i -th particle and

x is coordinate component.

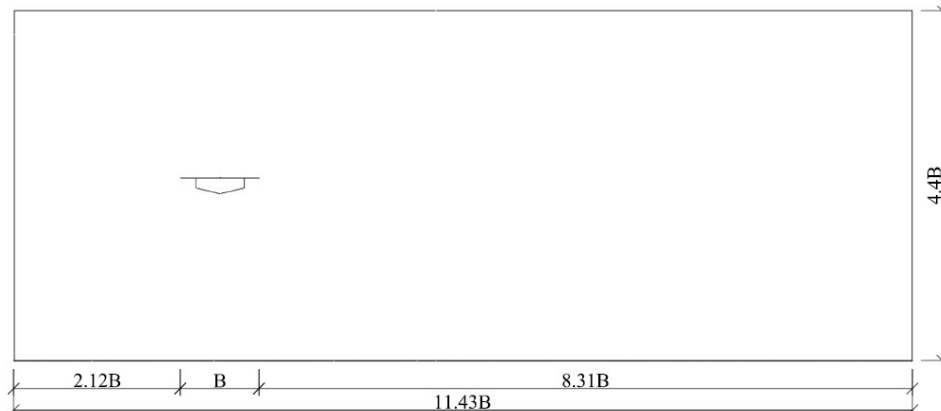


Fig. 3 Computational domain

Planar fluid model has been created representing air with temperature 20° and corresponding density $\rho = 1.205 \text{ kg/m}^3$ and dynamic viscosity $\mu = 18.205 \times 10^{-6} \text{ kg/ms}$. Inflow air velocity has been considered constant with $u = 20 \text{ m/s}$, which represents uniform flow. Computational domain has been meshed with quadrilateral finite volume elements using ruled-based algorithm. Two different meshes have been created, with coarse (19660 elements) and fine (36620 elements) density. Fluid-deck interface circumference has been divided into 340 elements in coarse and 480 elements in fine meshes. Computational domain dimensions and coarse mesh are shown in Fig. 3 and Fig. 4.

Symmetry boundary condition on top and bottom fluid computational domain outer edges has been considered. CFD model has been investigated using Laminar (for preliminary set-up computational parameters) and LES turbulent model with Smagorinsky constant $C_s = 0.1$.

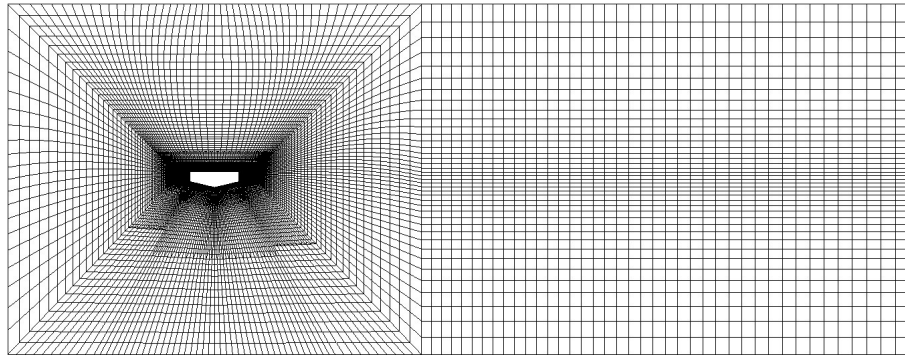


Fig. 4 Coarse mesh

Results

Before obtaining accurate results, estimation of appropriate CFD model input data has been necessary. Models with two different mesh densities have been solved with different time steps Δt , namely 0.005 s, 0.003 s, 0.002 s and 0.001 s. Acquired fluid-deck interface pressures have been integrated to compute drag force F_x in longitudinal x direction, lift force F_y in vertical y direction and pitch moment M to estimate drag c_d , lift c_l and pitch moment c_m coefficients according to

$$c_d = \frac{F_x}{\frac{1}{2} \rho A u^2}, \quad c_l = \frac{F_y}{\frac{1}{2} \rho A u^2}, \quad c_m = \frac{M}{\frac{1}{2} \rho A^2 u^2}, \quad (3a,b,c)$$

where A is windward area,

M is pitch moment around shear center S_c in deck cross-section plane.

Strouhal number has been calculated according to

$$S_t = \frac{f_{sh} H}{u}. \quad (4)$$

Vortex shedding frequency has been estimated from spectral density of drag coefficient time-course.

To choose proper model with proper set-up parameters, perfect would be realization of wind tunnel tests. Concerning the fact, no such tests have been realized, many numerical computational studies have been realized focusing on flow past circular cylinder [3,4] and fluid models adequacy has been compared to wind tunnel tests and numerical simulations performed by other authors [5], [6] and [7]. Computed aerodynamic characteristics for every time step and two mesh densities are shown in Table 1. Second column of Table 1 contains, besides Δt , the number of time steps per 1 simulated vortex shedding cycle (steps/cycle). As a proper fluid-flow model, turbulent LES model with fine mesh and $\Delta t=0.001$ s has been considered, regarding to converged drag c_d and pitch moment c_m coefficients. Obtained drag coefficient time courses are displayed on Fig. 5. Flow velocity distribution of LES model with $C_s = 0.1$, fine mesh and $\Delta t=0.001$ s can be seen in Fig. 6.

Table 1 Computed aerodynamic characteristics

Turbulent model, mesh density	Δt [s]; steps/cycle [-]	c_d [-]	c_l [-]	c_m [-]	S_t [-]	f_{sh} [Hz]
LAMINAR, coarse	0.005; (-)	$\doteq 0.63$	$\doteq 0.495$	$\doteq 0.158$	-	0
	0.001; (-)	$\doteq 0.612$	$\doteq 0.513$	$\doteq 0.156$	-	unsteady
LAMINAR, fine	0.005; (-)	-	-	-	-	unsteady
	0.003; (125)	0.613	0.418	0.160	0.159	2.65
	0.002; (185)	0.611	0.395	0.159	0.162	2.70
	0.001; (370)	0.604	0.391	0.160	0.162	2.70
	0.005; (-)	$\doteq 0.608$	$\doteq 0.5$	$\doteq 0.145$	-	0
TURBULENT, coarse	0.001; (-)	$\doteq 0.6$	$\doteq 0.5$	$\doteq 0.144$	-	unsteady
	0.005; (-)	0.541	0.796	0.134	-	0
TURBULENT, fine	0.003; (-)	0.541	0.773	0.137	-	0
	0.002; (180)	0.582	0.433	0.149	0.163	2.72
	0.001; (330)	0.597	0.310	0.148	0.181	3.02

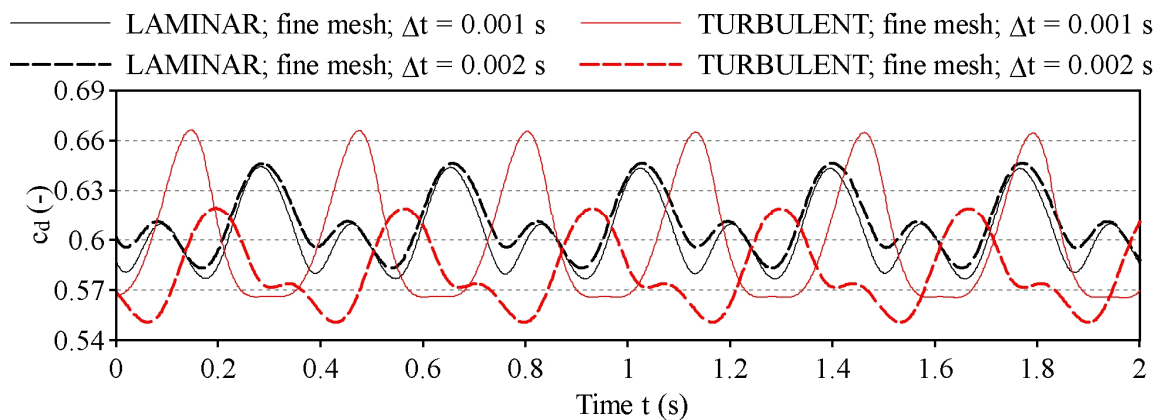
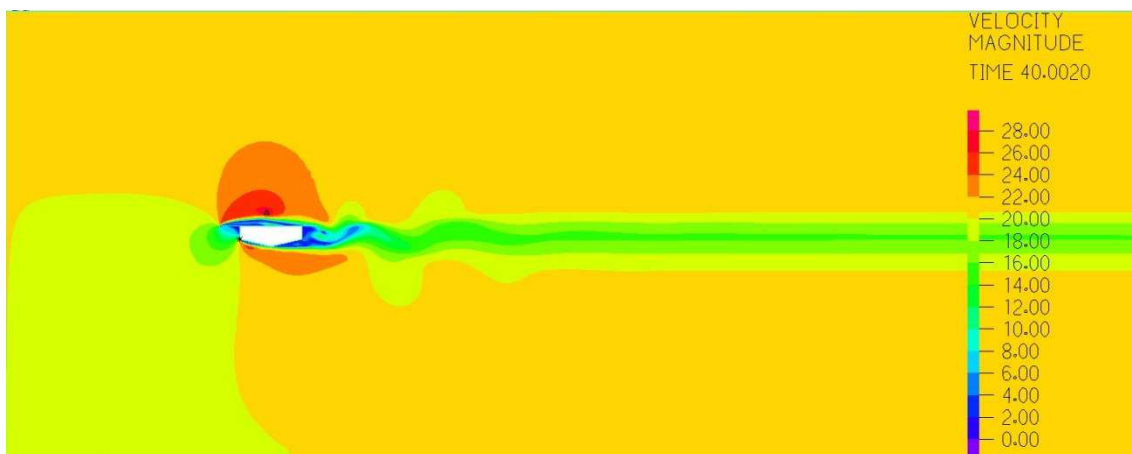


Fig. 5 Time-courses of drag coefficient

Fig. 6 Flow velocity distribution (model LES $C_s = 0.1$, fine mesh, $\Delta t = 0.001$ s)

Summary

The air flow past deck of cable-stayed footbridge using CFD numerical simulation method has been investigated with focus on aerodynamic characteristics and proper model set-up parameters. LES model is based on direct simulation of large eddies, which occur in space. Regarding to computational time requirements for solving 3D fluid flow model only planar LES turbulent with $C_s = 0.1$ model has been used, which represents a simplification. Concerning the bluff-body cross-section, boundary layer separation points on sharp edges have been observed as one could predict. Vortex shedding has occurred with frequency $f_{sh} = 3.02$ Hz and vortex path has been observed. Obtained aerodynamic characteristics will be used for examination of designed footbridge as well as the executed CFD model which will be extracted into 3D flow model for comparison with planar model.

Acknowledgements

The present work has been carried out within the project “Supporting of the Centre of excellent integrated research of advanced building structures, materials and technologies”, based on the Operational program Research and development, financed by the European Regional Development Fund of the European Union. The paper is carried out within the project No. 1/0321/12, partially funded by the Science Grant Agency of the Ministry of Education of Slovak Republic and the Slovak Academy of Sciences.

References

- [1] S. Kuroda, Numerical simulation of flow around a box girder of a long span suspension bridge, Journal of Wind Engineering and Industrial Aerodynamics 67&68 (1997) 239-252.
- [2] ADINA, Theory and modeling guide volume III: ADINA CFD & FSI, Version 8.7, ADINA R & D, Inc., Watertown, MA, USA (2010).
- [3] R. Soltys, M. Tomko, Numerical investigation of flow around cable with circular section, in: Young Scientist 2013, The 5th PhD. Student Conference of Civil Engineering and Architecture, Kosice (2013) 1-3.
- [4] R. Soltys, M. Tomko, S. Kmet, Wind spectral characteristics and aerodynamic characteristics of cables, in: Research activity of DSI, Kosice (2013) 129-132.
- [5] C. Wieselsberger, Neuere feststellungen über die gesetze des flüssigkeits und luftwiderstands. Phys. Z. (1921), (in German).
- [6] A. Roshko, Experiments on the flow past a circular cylinder at very high Reynolds number, Journal of Fluid Mechanics, 10 (1961).
- [7] M. Breuer, A challenging test case for large eddy simulation, high Reynolds number circular cylinder flow, International Journal of Heat and Fluid Flow, 21 (2000).

The Effect of the Crosswinds on the Stability of the Moving Vehicles

SKRÚCANÝ Tomáš^{1, a*} and GNAP Jozef^{1, b}

¹University of Zilina, Department of Road and Urban Transport, Univerzitná 1, 010 26 Žilina,
Slovak Republic

^atomas.skrucany@fpedas.uniza.sk, ^bjozef.gnap@fpedas.uniza.sk

Keywords: stability, crosswinds, heavy vehicles, tire cornering stiffness, rollover

Abstract. The article describes the effect of the crosswinds on the moving heavy road vehicles. It gives the mathematical descriptions of two extreme situations originated from the crosswinds – side deflection from the directness and the rollover of the vehicles. It also analyzes factors affecting the action of the wind on the vehicle, as a tire cornering stiffness, instantaneous vehicle weight, axle load, the position of the gravity center of the vehicle. Both situations present a greater risk for empty vehicles with tarpaulin superstructure, and therefore some types of them are addressed in the article.

Introduction

Crosswinds as the secondary effect of the move on the road in the open areas represent a significant risk for vehicles. The situation occurs when the impact of crosswinds cause that the vehicle deviates from a straight line or it rolls over. The risk is the greatest if the vehicle is light and large. Force exerted by the wind is directly proportional to the size of the area on which it acts. This area represents the side surface of the vehicle. Resistance to the action of the wind is a tire cornering stiffness, tire friction force and torque stability of the vehicle. The cornering stiffness and the friction are directly proportional to the instantaneous mass of the vehicle, the tire construction and ground surface. The position of the gravity center, the instantaneous mass and width axles affects the torque of stability.

Sideslip Angle and Tire Cornering Stiffness

The slip angle of a pneumatic tire is defined as "the angular displacement between the plane of rotation of the wheel (the direction in which the rim is pointing) and the path that the rolling tire will follow on the road surface." This path is made up of the successive footprints of the contact patch laid down as the tire rolls. In order for the vehicle to change direction, regardless of road speed or the radius of curvature, each of the vehicle's tires must assume some value of slip angle [1].

The sideslip angle occurs not only on the steering axle, but on the other axle action and it is influenced by factors such as centrifugal force on the vehicle when passing bend, crosswind, the sloping road, running around an obstacle such as a curb, and etc.

The difference between the values of the angle on the axles affects the dynamical behavior of the vehicle. If the sideslip angle on the front axle is greater than the rears, the vehicle behaves understeer. Otherwise, if the rear angle is greater than the front one, the vehicle behaves oversteer. This difference can be caused by the different axle load, different tire types between the axles. If we solve the effect of the crosswinds, the relative position of the wind force point and the vehicle gravity center is important for its behavior.

Cornering properties of the tire are particularly the effective inflation pressure, rotation speed, radial and lateral loads tire. The sideslip angle increases with the increasing radial and lateral load. Growth tire pressure results in an increase lateral stiffness and reduced the sideslip angle. In practice, the value of the sideslip angle ranges up to about 8° for radial tires.

Cornering stiffness of the tire is a tangent to the curve of the cornering characteristics of the lateral force at the sideslip angle of 0° (Fig. 2). The stiffness expresses the steepness of the increase

the lateral force in increasing the sideslip angle of the wheel in the linear range of cornering characteristics. It is approximately in the range of 0 - 3°. Directional stiffness is important in terms of vehicle handling [3].

For these small sideslip angles (Fig. 2, area I.), it is possible to use (Eq. 1) for the cornering stiffness.

$$C_\Omega = \frac{F_L}{\Omega}. \quad (1)$$

In this equation, the cornering stiffness means the C_Ω [N.deg^{-1}], F_L is the side force [N] and Ω the sideslip angle [deg].

To evaluate the effect of the normal load on the cornering ability of tires, a parameter called the cornering coefficient, which is defined as the cornering stiffness per unit normal load, is often used [4]

$$C_c = \frac{C_\Omega}{F_g}, \quad (2)$$

where the cornering coefficient is C_c [deg^{-1}]. This coefficient is similar to the coefficient of friction C_f . This replaces the C_c when the lateral force increases. Then, the tire lateral deformation is on the highest level and the tire is not able to resist the lateral force. The value of slipping is also increasing and then 100% slip comes.

The C_c is able to be equated to the C_f , so it is the quotient the lateral and radial forces.

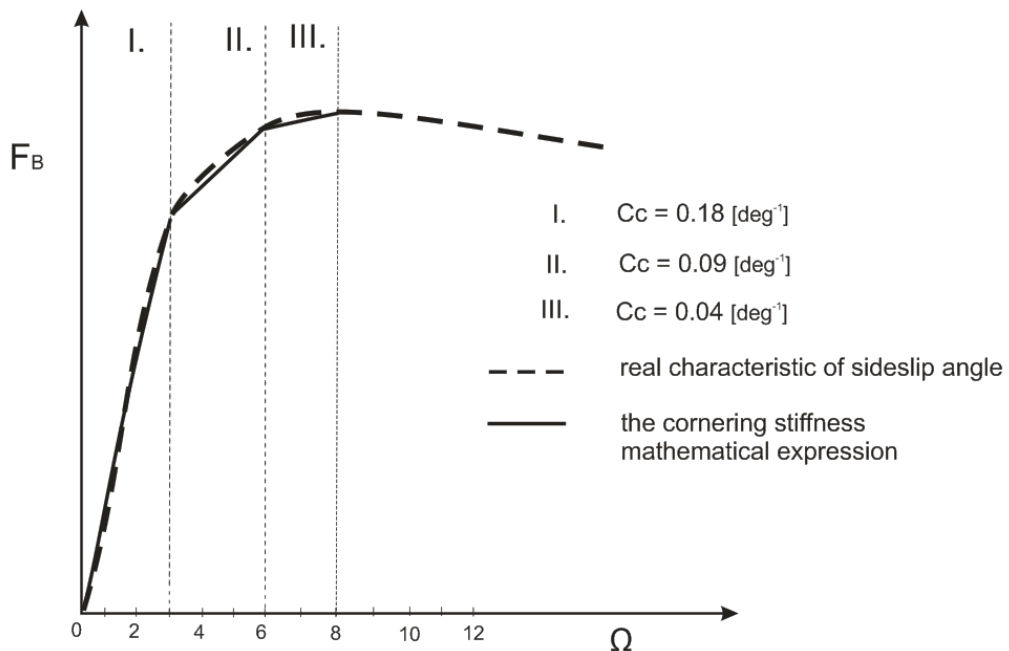


Fig. 2 Characteristic of the cornering stiffness

The basic value of C_c (I. area) was chosen according to the average values of C_c written in the Table 1. Only the values of the radial-ply tires are chosen because these types are the most often used. The average value C_c is cca 0.14 (by rated load, unless specified), but according to the characteristic of nominal load (Fig. 3), the value of 0.18 was chosen (Fig. 2). The empty vehicles are taken into account in calculations so it is not possible to consider the radial force on level of the maximum (100 %) but only 50% (empty vehicle / full loaded vehicle).

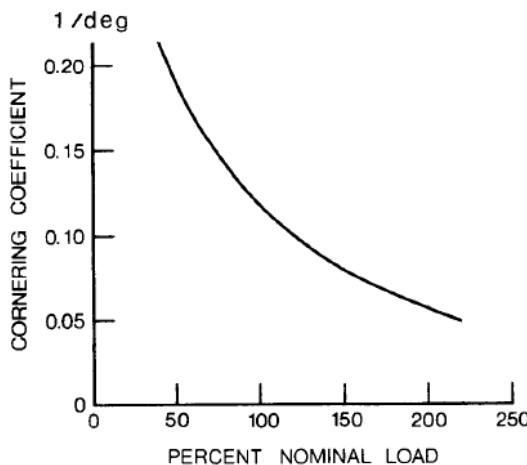


Fig. 3 Effect of normal load on the cornering coefficient [4]

Table 1 Cornering coefficients for truck tires [4]

Tire Type	Tire Construction	Cornering Coefficient (deg ⁻¹)
Michelin Radial XZA (1/3 Tread)	Radial-ply	0.1861
Michelin Radial XZA (1/2 Tread)	Radial-ply	0.1749
Michelin Pilote XZA	Radial-ply	0.1648
Michelin Radial XZA	Radial-ply	0.1472
Goodyear Unisteel G159, 11R22.5 LRF at 655 kPa (95 psi)	Radial-ply	0.1413
Michelin XZZ	Radial-ply	0.1370
Goodyear Unisteel 11, 10R22.5 LRF at 620 kPa (90 psi)	Radial-ply	0.1350
Goodyear Unisteel G159, 11R22.5 LRG at 792 kPa (115 psi)	Radial-ply	0.1348
Goodyear Unisteel 11, 10R22.5 LRF at 758 kPa (110 psi)	Radial-ply	0.1311
Firestone Transteel	Radial-ply	0.1171
Firestone Transteel Traction	Radial-ply	0.1159
Goodyear Unisteel R-1	Radial-ply	0.1159
Goodyear Unisteel L-1	Radial-ply	0.1121
Firestone Transport 1	Bias-ply	0.1039
General GTX	Bias-ply	0.1017
Goodyear Super Hi Miler	Bias-ply	0.0956
Goodyear Custom Cross Rib	Bias-ply	0.0912
Uniroyal Fleet Master Super Lub	Bias-ply	0.0886
Firestone Transport 200	Bias-ply	0.0789

For the next calculations in this article, the differences are considered zero. Thus, the vehicle is neither oversteering nor understeering. Its behavior is neutral. It is necessary to consider the weight distribution 50:50, the same tires on every axle and the action point of the crosswinds in the gravity center. In this case, we consider this difference zero, so the vehicle is cornering linearly.

The Crosswinds Impact

Airflow is a movement of the air mass. The airflow around the vehicle is manifested in the form of force effects on the bodywork. This effect is dependent on the specific weight of air ρ , coefficient of air resistance c_d , cross section area S and the squared speed of the airflow. The crosswinds impact F_w (*wind force*) is equated

$$F_w = \frac{1}{2} \rho_v c_d S v^2 . \quad (3)$$

This equation is used to express the air resistance while driving. When we consider the action of the wind on the side area of the vehicle (crosswind), values of some elements are different. The specific weight is the same value which represents the air density in the altitude 0 meters above sea level and the air temperature 15°C in $[\text{kg} \cdot \text{m}^{-3}]$. Squared speed is the speed of the crosswind regardless the vehicle speed $[\text{ms}^{-1}]$. Values $c_d [-]$ and $S [\text{m}^2]$ are different for different vehicles.

For the simplification, we consider the point of the crosswind action which is situated in the middle of the vehicle length and in the height H_o (Fig. 4). The gravity center is considered in the same position as the point O in the longitudinal direction (the same sideslip angles on all axles). The value of cross area S is the multiple of the vehicle length and height.

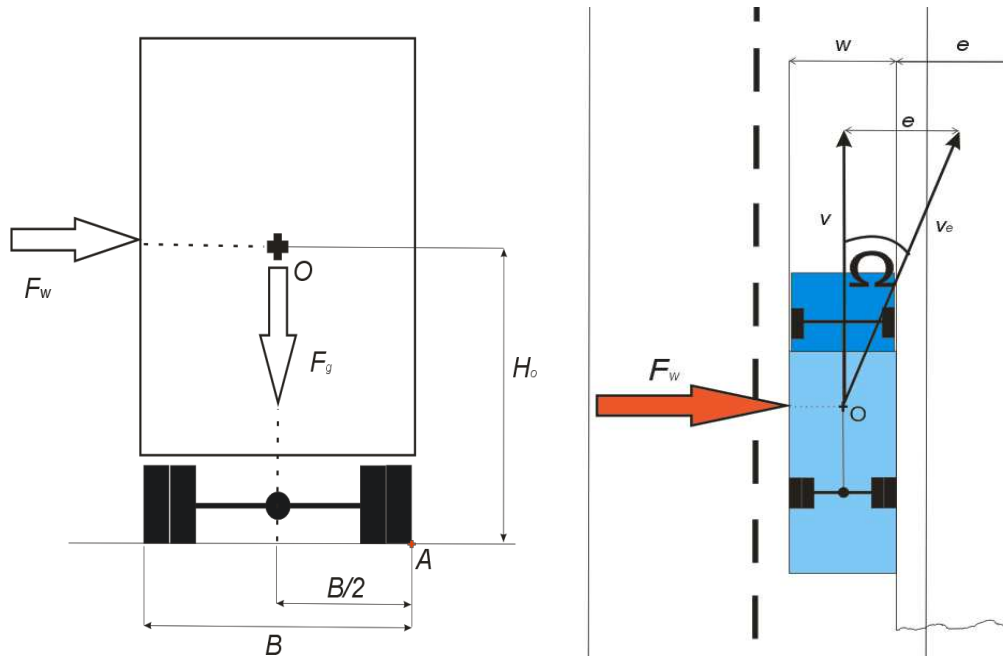


Fig. 4 Rolling torque and directional deviation of the vehicle

The directional deviation of the vehicle is dependent on the crosswind force and the cornering tire stiffness. These two factors influence the sideslip angle. It is possible to equate the deviation e related to the side slip angle. The angle is dependent on the vehicle speed and the driver's reaction time. This situation is drawn in the Fig. 5.

For quantification of the Ω value is used

$$\Omega = \frac{F_w}{F_g C_c}, \quad (4)$$

written in Table 2, where are written the deviations e equated by

$$e = \tan(\Omega v t_R) \quad (5)$$

according to the actual vehicle speed (90 kmh^{-1}). The reaction time is considered 1 s, which means a usual reaction time of healthy driver under normal conditions.

Other situation comes when the speed of crosswind is too high and the vehicle is empty. Then, the vehicle does not slip, but it rolls over. Resistance to the rollover depends on the height of the gravity center, its position in lateral direction, actual vehicle weight and the axle width. The height H_o amplifies the crosswind impact to roll over. With a higher value of the H_o , the rolling torque is increasing.

The torque sentences according to the Eq. 3 define the minimal crosswind speed needed to rollover (rolling speed) (Eq. 6). The torque is calculated to the border point A (Fig. 4). F_g represents the gravity force of the actual vehicle weight [N] and B is the axle width [m]

$$v_R = \sqrt{\frac{F_g \frac{B}{2}}{0.5 \rho c_d S H_O}} = \sqrt{\frac{mg \frac{B}{2}}{0.5 \rho c_d S H_O}} . \quad (6)$$

Table 2 Crosswind impact

DEVIATION			crosswind speed								
Gross weight [t]	Vehicle type	Empty weight [t]	Axle width [m]	Side area [sq.]	Rolling wind [km/h]	30	40	50	60	70	80
up to 7,5 (train 12)	truck	3.5	1.1	33	92	0.13	0.23	0.35	0.51	0.69	0.91
	trailer	1.5	1.1	20	82	0.18	0.32	0.50	0.72	0.98	1.28
up to 12	truck	6	1.1	44	104	0.10	0.18	0.27	0.40	0.54	0.70
up to 26 (train 40)	truck	11	1.2	38	158	0.05	0.08	0.13	0.19	0.25	0.33
	truck + trailer	4.5	1.2	30	114	0.09	0.16	0.25	0.36	0.49	0.64
up to 40	tractor + semitrail.	14	1.2	61	141	0.06	0.10	0.16	0.24	0.32	0.42
Gross weight [t]	Vehicle type	Empty weight [t]	Axle width [m]	Side area [sq.]	Rolling wind [km/h]	90	100	110	120	130	140
up to 7,5 (train 12)	truck	3.5	1.1	33	92	1.15	ROLLOVER				
	trailer	1.5	1.1	20	82	ROLLOVER					
up to 12	truck	6	1.1	44	104	0.89	1.10	ROLLOVER			
up to 26 (train 40)	truck	11	1.2	38	158	0.42	0.52	0.63	0.75	0.88	1.02
	truck + trailer	4.5	1.2	30	114	0.81	1.00	1.21	ROLLOVER		
up to 40	tractor + semitrail.	14	1.2	61	141	0.53	0.65	0.79	0.94	1.10	1.28

The Table 2 states the impact of the crosswind. On the left upper side (colorized gray), there is the head with all main descriptions. Table 2 is divided into in two parts, the upper part is the beginning and then the table continues downwards (according to the rising crosswind speed in the gray rows). The head of the continuing part is the second gray row. The numbers on the right are calculated values of the directional deviation e . If the deviation is higher than 1 m, the number is bold, bigger, underlined and red colorized. The first column of the right side (rolling speed) is the value of the airflow speed, whose action can cause the vehicle rollover.

Conclusions

The quantification and expression of the crosswind impact is written above (Table 2). From those numbers is clear, which types of freight vehicles are most vulnerable to the crosswind. The largest impact of crosswind is on the light trailers. These vehicles rollovers by the airflow speed 82 kmh^{-1} . It is necessary to stop the vehicle during strong windy weather and continue the carriage after the better weather conditions come. The best behavior have the heaviest vehicles – semitrailer sets and

heavy trucks. Thanks to their actual weight and axle width they reach higher directional stability and rolling torque.

References

- [1] C. Smith, Tune to win, Fallbrook: Aero Publishers, INC, 1978.
- [2] Š. Liščák, R. Matějka, V. Rievaj, M. Šulgán, Operational characteristics of vehicles, Žilina, EDIS publisher ŽU, 2004, (in Slovak).
- [3] J. Y. Wong, Theory of ground vehicles, 3rd ed., 2001 by John Wiley & Sons, Inc. Ottawa.
- [4] G. S. Vorotovic, B. B. Rakicevic, S. R. Mitic, D. G. Stamenkovic, Determination of Cornering Stiffness Through Integration of A Mathematical Model and Real Vehicle Exploitation Parameters, FME Transactions. 41 1 (2013).
- [5] G. Baffet, A. Charara, D. Lechner, Estimation of vehicle sideslip, tire force and wheel cornering stiffness, Control Engineering Practice. 17 11 (2009) 1255-1264.
- [6] T. Skrúcaný, Influence of tire pressure and deflector position on the fuel consumption of truck in conditions of chosen freight company, Diploma thesis, University of Žilina, 2013, Žilina.
- [7] L. Kruža, Construction of device for measuring tire cornering stiffness. Diploma thesis, Vysoké učení technické v Brně, 2011, Brno.
- [8] M. Sterling, A. D. Quinn, D. M. Hargreaves, F. Cheli, E. Sabbioni, G. Tomasini, D. Delaunay, C. J. Baker, H. Morvan, A comparison of different methods to evaluate the wind induced forces on a high sided lorry, Journal of Wind Engineering and Industrial Aerodynamics. 98 1 (2010).
- [9] M. Batista, M. Perković, A simple static analysis of moving road vehicle under crosswind, Journal of Wind Engineering and Industrial Aerodynamics. 128 5 (2014).

Estimation of Wind Energy Potential of the Territory

BADENKO Vladimir^{1,a*} and AREFIEV Nikolay^{1,b}

¹St.Petersburg, Polytechnicheskaya, 29, 195251, Russia

^avbadenko@gmail.com, ^barefiev@cef.spbstu.ru

Keywords: wind power, wind resources, wind energy projects, energy productions, geographic information systems (GIS), site selection

Abstract. Accurate information about the wind resource and the wind energy potential is required for federal and local authority policy initiatives that will expand the use of wind energy. This paper presents the experience of creating an information-analytical system (IAS), based on GIS technologies, for wind energy potential (theoretical and practically achievable) of Leningrad and Pskov regions, located in the North-West of Russia. IAS consists of GIS database coupled with models for support of decision making for regional planning. The paper presents the general methodological approaches and possible practical difficulties during the creation of such systems.

Introduction

An increase in public awareness regarding the negative impact of traditional power-generating methods on the environment has created a demand for developing environmentally friendly renewable energy [1]. Wind energy is a popular form of renewable energy and wind energy shows great potential in terms of power generation and economic viability [2].

The development of new wind energy projects requires a thorough analysis of land use issues and constraints [4]. In spite of the well-acknowledged environmental benefits of electricity generation from wind energy, there is increasing concern about impacts from wind turbines on local ecosystems [5]. Wind farm siting is an important first step in wind power development for governments and institutions. It is a formidable challenge to define the areas where it is technically and economically feasible to develop wind energy projects. Any site selection and assessment procedure must take into account the technical, economic, social (political) and environmental aspects of the future wind energy project [6]. In recent years geographical information systems (GIS) have become increasingly popular as a tool for the selection of optimal sites for different types of activities and installations, including siting of wind farm [1-7]. GIS was chosen as instrument because it provides a logical solution for analyzing a variety of spatially related data in a cost-effective way [7]. GIS allows carrying out an integrated assessment of technical and economic potential, for the determination of appropriate zones according to conflicting criteria [8]. A GIS-based approach had been developed for two case study regions in Germany to analyze the effect of different nature conservation criteria on the wind energy potential in quantitative terms [9]. In many researches had been pointed out that Multi-criteria Analysis coupled with GIS are the most convenient tools to facilitate decision making on site selection for considered problem [2,3,6,10].

In Russia under the current legal framework, the role of the regional authorities in creating the green energy policy and especially in wind park planning is rather passive. But according to current estimates, the technical resource of renewable energy sources, with great value of solar and wind energy, is about 4.5 billion tons of oil equivalent per year, which is more than four times as the total energy consumption in Russia now. For this reason some local authorities in Russia want to get information about green energy potential of territory in particular about wind energy potential. The objective of this study is to develop a GIS-based approach to support the decision making process connected with the site selection for wind energy projects for local authorities (Leningrad and Pskov regions) in Russia.

Materials and Methods

Leningrad and Pskov regions are located in the North-West part of Russia. Fig. 1 shows these regions with average annual wind distribution map of Russia [11,12] (on this small map regions under consideration are shown by black square). Also part of GIS database, which is used for considered regions, is presented in Fig.1. An information-analytical system (IAS) based on the GIS database for wind energy potential (theoretical and practically achievable) was created. IAS consists of GIS database coupled with models for support of decision making for regional planning concerning wind energy farm and adjoining problems. The GIS software used is MapInfo, but the developed framework can be operationalized using any GIS system with overlay and customizing capabilities. GIS data sets of land use, settlements, road network, electricity grid, wind potential, digital elevation models, spatial distribution of ecological factors, etc. were collected for Leningrad and Pskov regions from all type of sources including regional database and remote sensing data.

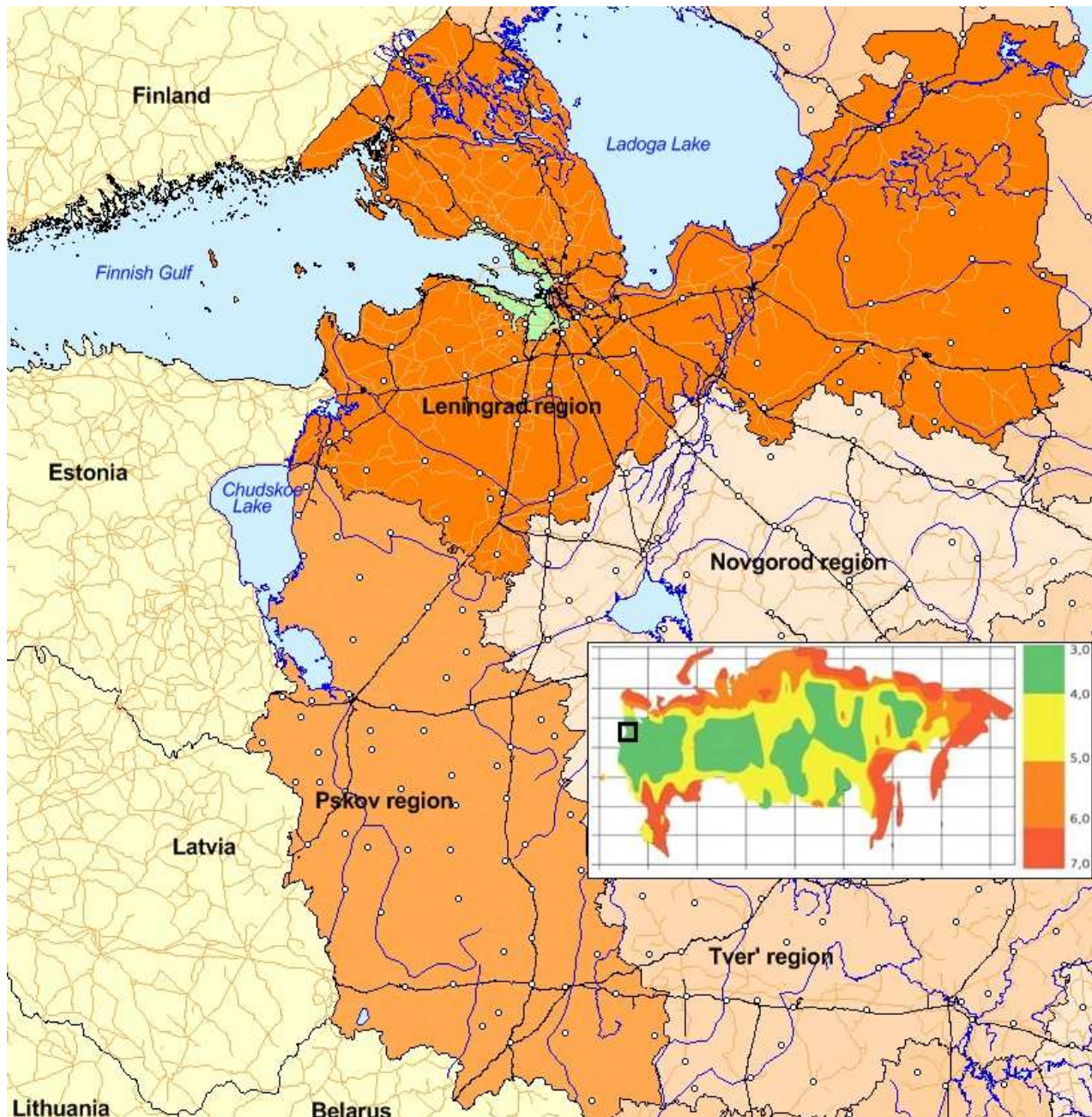


Fig. 1 North-Western part of Russia with Leningrad and Pskov regions

As shown in small map of Russia in Fig. 1 the considered regions belong to low wind energy potential regions with average annual wind speed about 3-4 m/sec. Therefore the opportunities for creating of wind farms are not very large. In this regard, the IAS developed have opportunity to create a complex estimation of future sites of wind park, taking into account technological (wind speed, infrastructure, etc.), ecological (stability, ecological state, bird migration path, etc.), economical (real energy requirements, local costs of other energy sources, etc.) and social (how peoples from the site support new energy source, how they support all kind of innovation, etc.) criteria. For estimation of these very different criteria appropriate models are included in the IAS. These models with GUI interface are integrated in GIS environment. For Pskov and Leningrad regions the IAS have the same capabilities. But local authorities of these regions the same version of IAS with separate database are used because of local law. Further in the text opportunities of the IAS are presented with the database for Leningrad region.

As we pointed out early the siting of wind farm is a multi-criteria task. At first it was solved the problem for identifying sites with the highest average annual wind speeds (technical criterion). For both regions it has been developed a spatial distributions of average annual wind speed on the base of information from regional weather stations (see Fig. 2). It is evident that it has been discovered that the main wind resources are located close to water bodies and over water bodies. For Leningrad region those bodies are the Finnish Gulf and the Ladoga Lake. For Pskov region those bodies are the Chudskoe Lake and the Pskovskoe Lake. It is well agreed with the results of other authors [12].

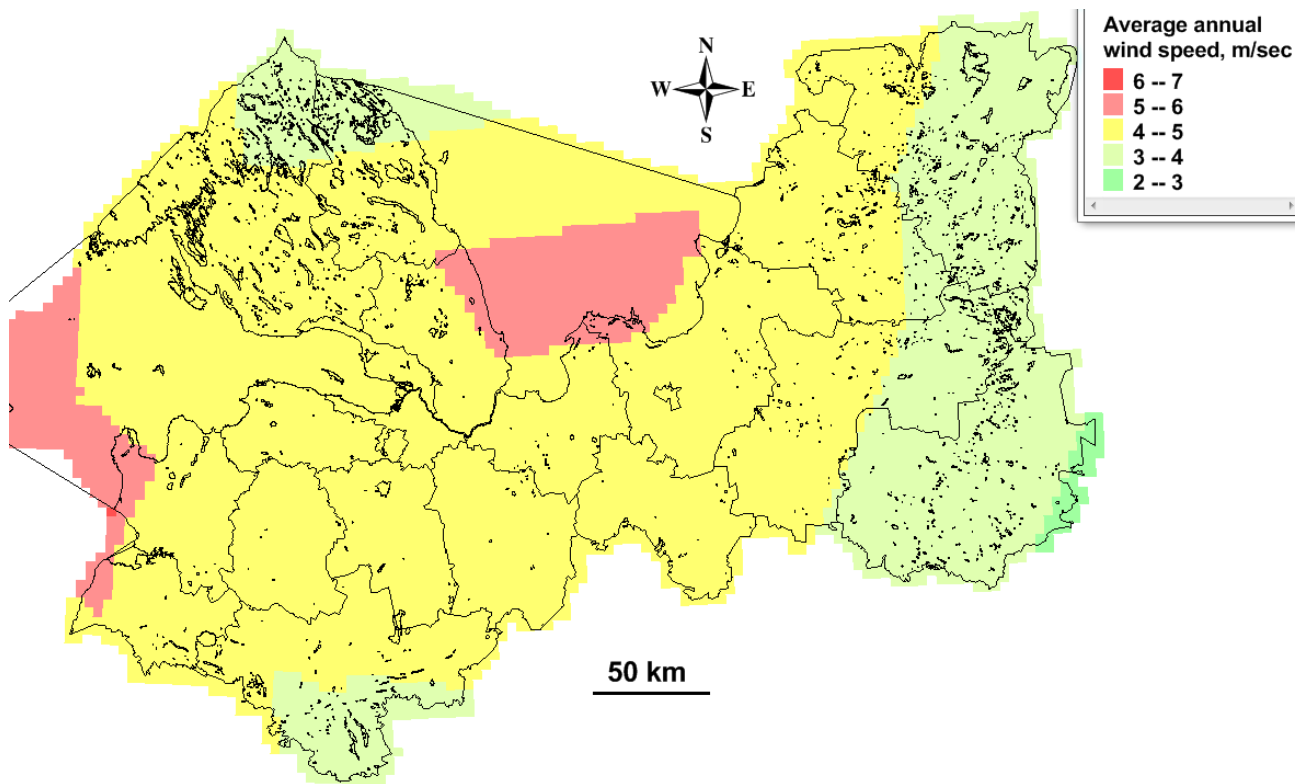


Fig. 2 Average annual wind speed for Leningrad region, m/sec

On the base of information about wind speed from regional weather stations, which had been collected on the standard height of 10 meters, and landcover data we can calculate technical wind energy potential for different height of wind equipment. For these calculations we used standard algorithms (see, for example [13]). The appropriate software has been designed and integrated into the GIS. Also designed GIS database have for key attributes a special characteristics – a measure of mistrust [14] for estimation of data quality. Here and in some other algorithms we used general approach based on fuzzy logic [15].

Result and Discussion

The main users for the IAS developed belong to different departments of the regional local authorities. For reach balance between sometimes different interests of the departments we had been proposed to use basin-landscape approach [16]. This approach allows for local authorities to support sustainable socio-economic-ecological development of the region.

For example, according wind energy potential estimation sites near Finnish Gulf are the best for wind parks. But for taking into account ecological factor we must have information about stability and ecological state of chosen landscapes. According our approach we must choose for wind farm landscapes with low ecological state and great stability. Fragment of dialog in IAS is presented in Fig. 3. Users have opportunities to combine these two features (ecological stability and state) automatically or directly use maps, presented in Fig. 3, during discussion and decision making.

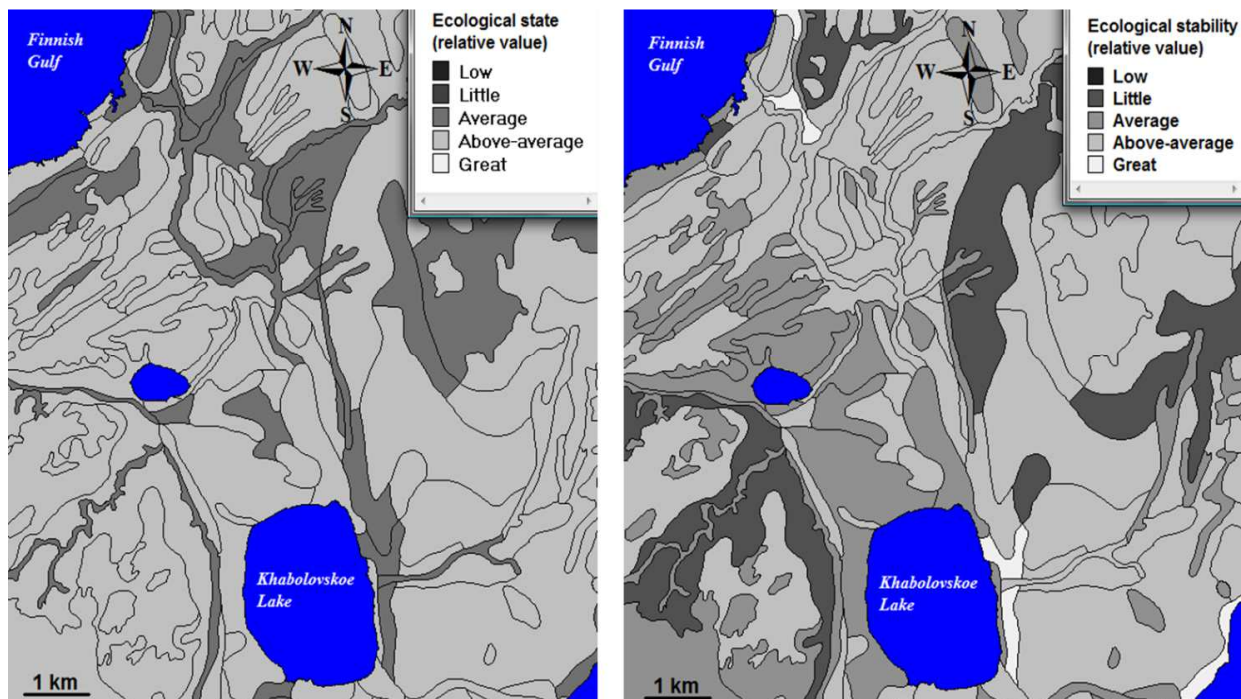


Fig. 3 Estimation of ecological state and ecological stability of landscapes

Summary

The Information-analytical system, based on GIS technologies has been developed for estimation of wind farm siting capabilities for two regions of North-West of Russia. But in real Russian economic situation wind energy have low potential for introduction on the reason of relativity low prices for tradition sources of energy like natural gas and oil. But local authorities have been understood, that situation can change very quickly, and they must have information about best places for wind farms. GIS environment provides opportunities for overlapping information from different sources and from different local authorities department. These features allow you to take into account all criteria during decision making on regional planning-technological, ecological, economic and social.

References

- [1] S. Grassi, N. Chokani, R.S. Abhari, Large scale technical and economical assessment of wind energy potential with a GIS tool: Case study Iowa, *Energy Policy*. 45 (2012) 73-85.
- [2] R. Van Haaren, V. Fthenakis, GIS-based wind farm site selection using spatial multi-criteria analysis (SMCA): Evaluating the case for New York State, *Renewable and Sustainable Energy Reviews*. 15 (2011) 3332-3340.
- [3] B. Sliz-Szkliniarz, J. Vogt, GIS-based approach for the evaluation of wind energy potential: A case study for the Kujawsko-Pomorskie Voivodeship, *Renewable and Sustainable Energy Reviews*. 15 (2011) 1696-1707.
- [4] S.M.J. Baban, T. Parry, Developing and applying a GIS-assisted approach to locating wind farms in the UK, *Renewable Energy*. 24 (2001) 59-71.
- [5] N.Y. Aydin, E. Kentel, S. Duzgun, GIS-based environmental assessment of wind energy systems for spatial planning: A case study from Western Turkey, *Renewable and Sustainable Energy Reviews*. 14 (2010) 364-373.
- [6] L.-I. Tegou, H. Polatidis, D.A. Haralambopoulos, Environmental management framework for wind farm siting: Methodology and case study, *Journal of Environmental Management*. 91 (2010) 2134-2147.
- [7] S. Grassi, N. Chokani, R.S. Abhari, Large scale technical and economical assessment of wind energy potential with a GIS tool: Case study Iowa, *Energy Policy*. 45 (2012) 73-85.
- [8] V. Gass, J. Schmidt, F. Strauss, E. Schmid, Assessing the economic wind power potential in Austria, *Energy Policy*. 53 (2013) 323-330.
- [9] W. Krewitt, J. Nitsch, The potential for electricity generation from on-shore wind energy under the constraints of nature conservation: A case study for two regions in Germany, *Renewable Energy*. 28 (2003) 1645-1655.
- [10] J. Malczewski, GIS-based land-use suitability analysis: a critical overview, *Progress in Planning*. 62 (2004) 3-65.
- [11] E.V. Ivanova, D.V. Smirnov Estimation methodology of wind energy potential in Russian Federation, *Transactions of the Main Geophysical (A.I. Voeikov) Observatory*. 559 (2009) 113-120.
- [12] A.K. Monzikova, V.N. Kudryavtsev, E.S. Larsen, B. Chapron, Estimation wind power potential of the Gulf of Finland, *Proceedings of the Russian State Hydrometeorological University*. 30 (2013) 116-133.
- [13] O. Probst, D. Cárdenas, State of the Art and Trends in Wind Resource Assessment, *Energies*. 3 (2010) 1087-1141.
- [14] D. Kurtener, V. Badenko, GIS fuzzy algorithm for estimating the quality of soil parameter Evaluation of attribute data quality, *Geomatics Info Magazine*. 15 (2001) 76-79.
- [15] D. Kurtener, V. Badenko, A GIS methodological framework based on fuzzy sets theory for land use management, *Journal of the Brazilian Computer Society*. 6 (2000) 26-32.
- [16] N.V. Aref'ev, V.L. Badenko, G.K. Osipov, Basin-landscape approach to the organization of environmental monitoring of hydropower complexes on the basis of geographical information technologies, *Power Technology and Engineering*. 32 (1998) 660-663.

Wind Power Market Development Initiative

RAKOVA Xeniya Mikhailovna^{1, a*}

¹29 Polytechnicheskaya Str. 195251, Saint-Petersburg, Russia

^ap4uik@mail.ru

Keywords: wind loads, wind power plants, wind atlas, meteorological mast

Abstract. Structures as high-rise buildings, long highway bridges with cable structures besides other loads are subjected to significant wind pressure. Therefore, this constructions kind requires wind loads qualitative evaluation and accurate data obtaining, such as wind speed and strength derived from wind atlas data and due to wind potential field assessment with implementation of long-term meteorological mast measurements. General meteorological data is usually insufficient. Current report is devoted to the wind resources potential assessment methodology representation.

Introduction

Due to modern conditions of progressive development in construction high-rise buildings, long cable-stayed bridges and other unique structures that do not have any analogues in history become more popular in construction. Among other loads such structures kind carry significant wind pressure loads. Considering that, this construction has a sharp necessity in precise date on long-term seasonal wind loads, wind speed, strength, its height disaggregation. Wind loads impact is usually considered in the course of urban territories planning and design, during construction process and objects exploitation [1].

Wind characteristics are represented in specifications for construction and in operation rules for bridges and other structures. However, the level of necessary wind data, must meet the requirements of modern construction. As standard meteorological data is not sufficient, the current subject relevancy consists of necessity of wind potential new evaluation ways and obtained results implementation in the unique structures project designing. As an example, we can learn the experience of wind power plants (WPP) project design [2].

Current paper contains wind-potential evaluation method of WPP construction ground experience of UNDP/GEF “Kazakhstan – wind power market development initiative”. However, such method has multifold possibilities of implementation and may be applied in other related areas, such as construction of high-rise buildings and unique structures.

Wind Modeling Technology

One of the major documents containing wind data is the Wind Atlas (WA). Within the terms of UNDP/GEF “Kazakhstan – wind power market development initiative” project, such instrument was developed for determination of more perspective grounds for WPP installation. However, this document implementation does not lies in terms of such use. The WA Data is appropriate for application in the evaluation of buildings and constructions wind loads impact, during the exploitation [3].

As the result of the project, the complete Wind Atlas of Kazakhstan includes a set of country territory thematic maps and makes possible wind modelling over the Republic. The Atlas generally represents wind potential quantitative characteristics and disaggregation of wind resources [4].

The document provides clarifications and necessary information for the evaluation of regional wind sources and possible places for wind turbines installation. It also includes evaluation methods for various landscape elements such as seaside, forest, hills, buildings and others impact on the wind sources implementation [5,6].

The map wind source layer is 80 m above the ground. The wind map resolution is equal to 9 km. For the grounds explorations of wind potential were realized with the use of meteorological masts, the resolution is 100 meters [7].

All the map materials were prepared by the means of special software, which allows modeling of wind sources all over the world. Such modeling refers to the accumulated synoptic data of World Meteorological Organization. The data sets contain information on wind speed, direction, air temperature, moisture, pressure and other atmosphere parameters gathered all over the world and processed according to the physical laws of large-scale atmosphere dynamics. As a result of meteorological data analysis, wind flows regional models are assembled with consideration of wind flows depending on the surface impact [8-13], this flows acceleration over the various topographical objects (for example, mountains) taking into account small air circulations as sea breeze [9].

Wind Atlas has been developed gradually. At the first stage, Kazakhstan territory has been divided into large squares – about 9×9 km [10].

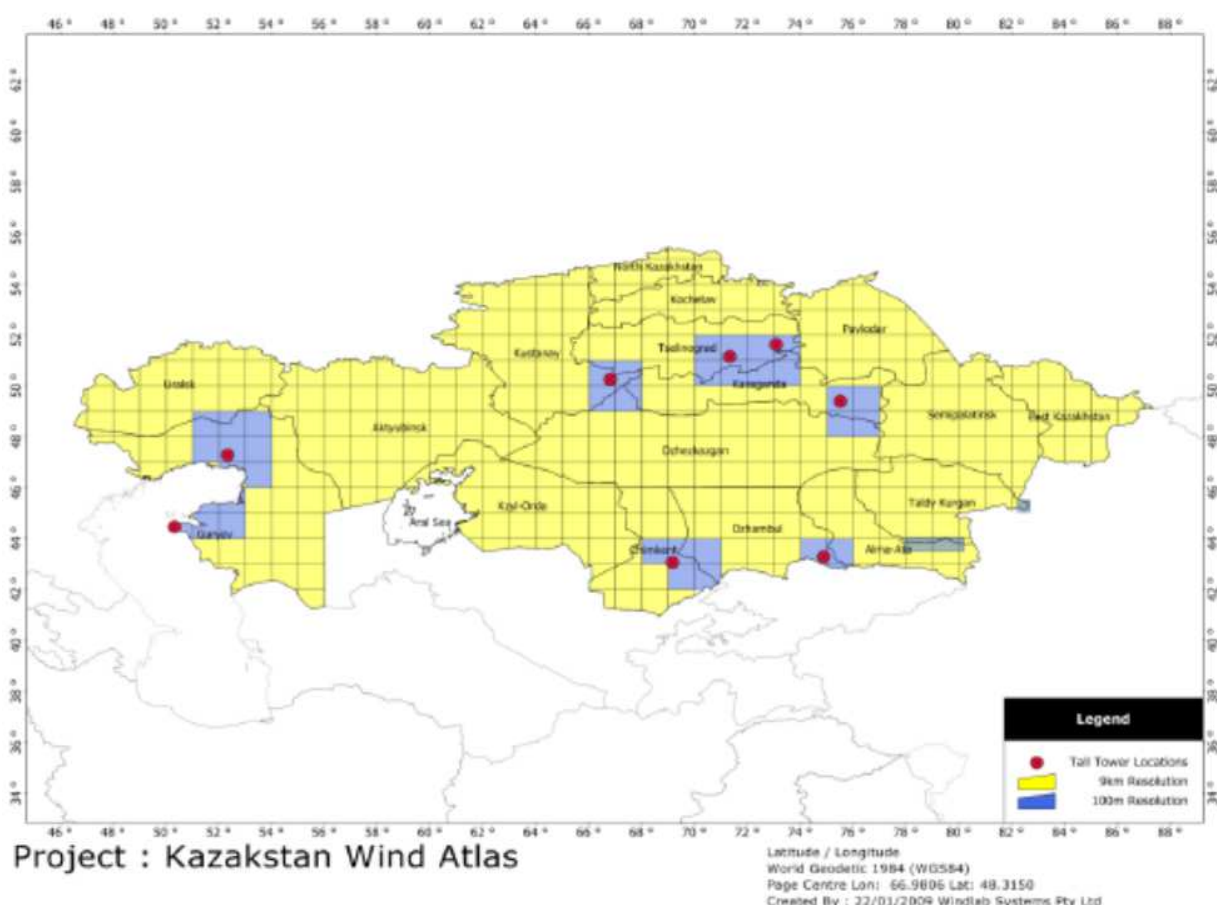


Fig. 1 Map with high resolution grounds marked

The Wind Atlas also contains maps of territories where the wind monitoring was held with the use of 50 meters meteorological masts [11].



Fig. 2 50 meters meteorological mast for wind potential assessment

The next stage became the detailed explorations of wind sources in 8 chosen regions and their qualitative analysis.

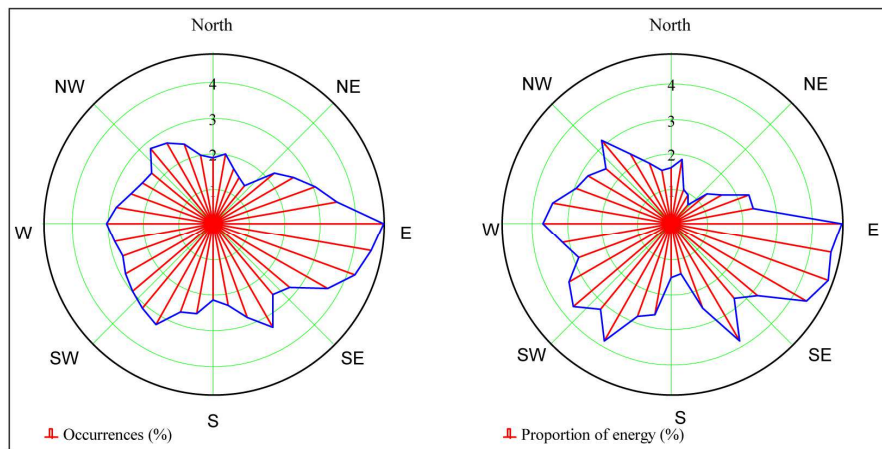


Fig. 3 Wind direction (left) and energy distributions (right) at 51 m for the Atyrau Karabatan) monitoring tower

Further work on the Wind Atlas detailization using annual wind monitoring data obtained from meteorological masts at the observed grounds made possible to incorporate maps with high resolution into the Atlas [12].

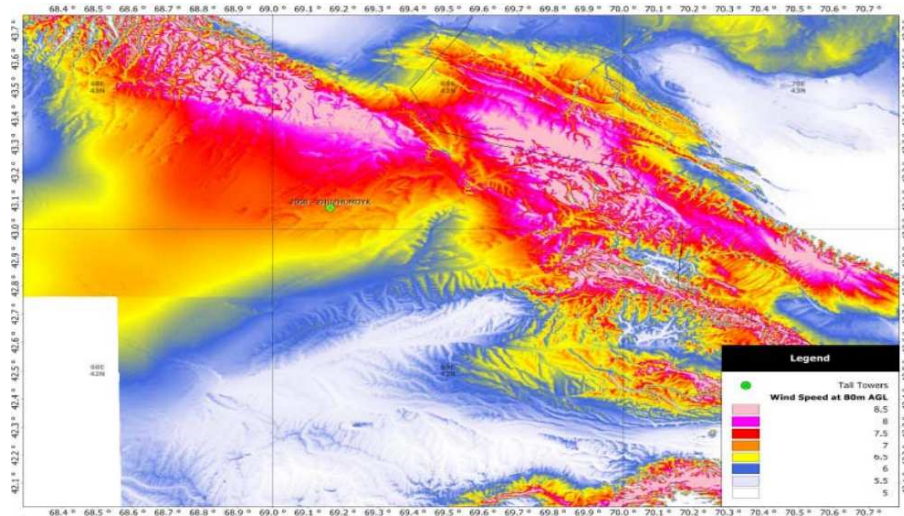


Fig. 4 Wind map of one of the studied areas with a resolution of 100 m

Such maps are very useful for project designing. Modern software allows visually represent long-term wind flows at certain heights [13]. Each monitoring site data was collected and verified monthly. The verification process included the following steps:

All the data was gathered carefully, any data loss was taken into account, in particular during the monitoring period, anemometers and wind vanes sensors over several Kazakhstan sites were affected by ice crust. Experts examined the data for this effect and removed any data believed to be recorded while the instruments were affected by ice [14].

Time traces for each anemometer were analyzed to show spurious or erroneous data. Direction traces and wind roses were analyzed to highlight faulty vanes [15].

Normalized wind speed plots were analyzed for evidence of any tower sheltering effects. It should be noted that many of the sites exhibited a degree of tower sheltering on the side-mounted anemometers which were corrected by specialists to closer reflect the 'free stream' wind speed [16].

Diurnal plots of wind shear and wind shear plots binned by direction were analyzed for occurrences of erroneous shear that may have been attributed to a malfunctioning anemometer [17].

Diurnal average plots of wind speed were analyzed to consider the profile of wind in the region of the monitoring mast [18].

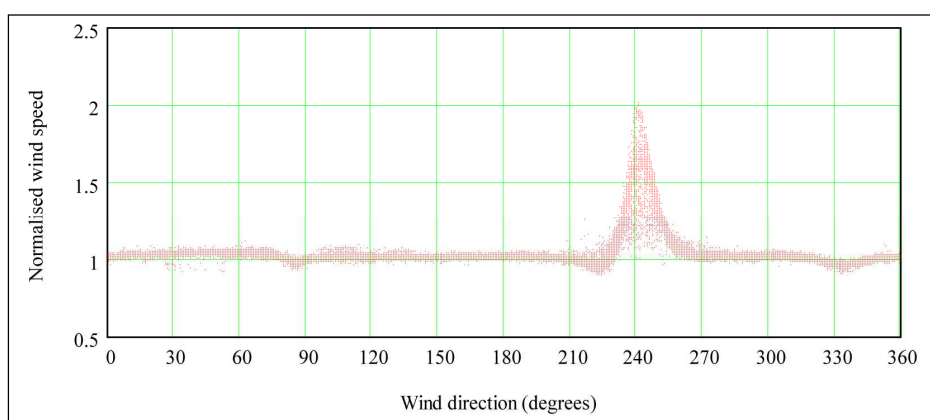


Fig. 5 Normalized wind speed plot for the 49 and 51 m anemometers at the Atyrau (Karabatan) monitoring tower

Wind speed and direction frequency table was analyzed to highlight any dominant wind regime at the site, and also helped to highlight spurious wind speed or directions being recorded.

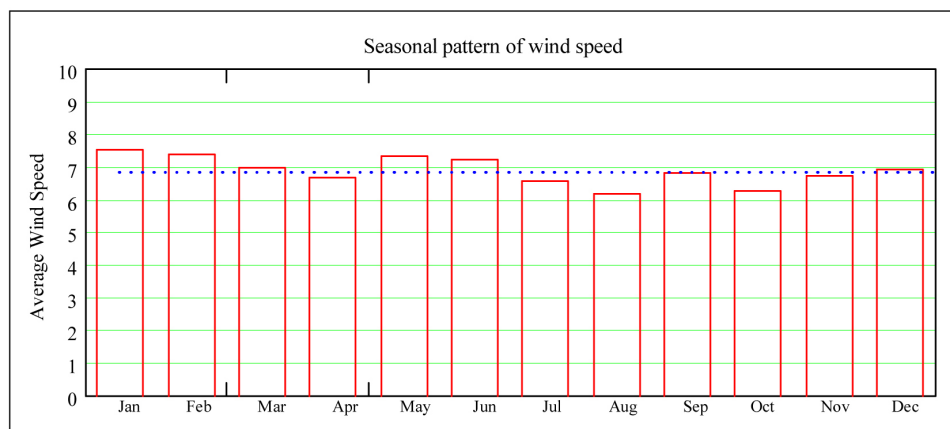


Fig. 6 Monthly average wind speeds for the 51 m level at the Atyrau (Karabatan) monitoring tower

Conclusions

Thus, in the result of the Wind Atlas development we have a number of positive results such as:

Implementation of a project map data set combining with the WA data may become the unique instrument not only for the WPP design and construction, but also may be implemented by design engineers and constructors for large- scale projects.

Implementation of the advanced software (GIS, MapInfo) allows visually represent wind flows on the specific height. Computer modelling of the wind layers at determined height of the explored ground makes the problem solution easier.

Today in the course of unique structures installation we meet new challenges but at the same time we find new possibilities that help us to achieve good results. This work provides such possibility. Development of the Wind Atlas is the innovation appeared at the related area – WPP construction. Its applied relevance for unique constructions creation will facilitate such projects design at new high quality level.

Besides, Wind Atlas provides calculation methods of various landscape elements impact on the wind sources implementation.

Acknowledgements

This contribution is the result of the research supported by “Kazakhstan – wind power market development initiative” UNDP/GEF project technical specialist Michail Pavlovich Rakov.

References

- [1] Research Institute of Building Physics: Building Climatology. Moscow, 2003.
- [2] M. Rakov, Wind Atlas of Kazakhstan, Astana, 2011.
- [3] A. Trethowan, A. Webb, T. Saba, UNDP Wind monitoring sites, Wind Resource and Energy Assessment. PB Power, 2008.
- [4] M. Rakov, Prospective of Wind Power Development in Kazakhstan. UNDP/GEF and Government of Kazakhstan project Kazakhstan - Wind Power Market Development Initiative. 2006.
- [5] L. Kieran, Effective regulatory framework to support wind energy in Kazakhstan. Almaty, 2010.
- [6] S.A. Isaev, N.I. Vatin, P.A. Baranov, A.G. Sudakov, A.Ye Usachev, V.V. Yegorov, Development and verification of multiblock computational technologies for solution of unsteady problems of high building aerodynamics in the framework of URANS approach, Magazine of Civil Engineering, №1(36) (2013) 103-109

- [7] Justification for the choice of perspective sites for further study for the construction of wind farms in the medium term until 2015. TOO Institute KazSEP, 2005.
- [8] S.A. Isaev, N.I. Vatin, V.A. Lebiga, V.N. Zinoviev, Keh-Chin Chang, Jiun-Jih Miau, Problems and methods of numerical and experimental investigation of high rise constructions' aerodynamics in the coastal region "sea-land", Magazine of Civil Engineering. 37 2 (2013) 54-61.
- [9] V.N. Bukhartsev, M.R. Petrichenko, Approximation of the depression curve of the inflow to an ideal trench, Power Technology and Engineering, №.44, 2011.
- [10] Information on <http://www.windlabsystems.com> [date of access: 10.03.2014].
- [11] V.N. Bukhartsev, M.R. Petrichenko, Condition of mechanical-energy balance of an integral flow with a variable rate, Power Technology and Engineering, 2001.
- [12] N.I. Vatin, K.I. Strelets, M.B. Kitain Determination of welding spark parameters for cyclone efficiency calculation, Magazine of Civil Engineering. 23 5 (2011) 5-9.
- [13] R.M. Petrichenko, A.B. Kanishchev, L.A. Zakharov, B. Kandakzhi, Some principles of combustion of homogeneous fuel-air mixtures in the cylinder of an internal combustion engine, Journal of Engineering Physics, №.59, 1990.
- [14] J.H. Ferziger, M.Peric, Computational methods for fluid dynamics, Berlin-Heidelberg: Springer Verlag, (1999) 389.
- [15] N.I. Vatin, T.N. Mikhailova, Computation of cross correlation function of induced potential for developed turbulent flow with axisymmetric mean velocity profile, Magnetohydrodynamics, New York, 1986.
- [16] D.N. Tseytin, D.V. Nemova, E.V. Kurasova, Avtonomnaya energoustanovka s kompleksnym energoeffektivnym elektroobespecheniem, Stroitelstvo unikalnyih zdaniy i sooruzheniy, №.5, 2013.
- [17] M.R. Petrichenko, N.S. Kharkov, Experimental study of the pumping action of helical flow, Technical Physics, №.54, 2009.
- [18] Information on <http://www.windenergy.kz> [date of access: 10.03.2014].

A			
Acoustic Emission (AE)	243	Computing Model	29
Aerodynamic	275	Concrete	96, 221, 239
Aerodynamic Model	175	Concrete Pavements	24
Aeroelastic Divergence	285	Concrete Slab	46
Aircraft	76	Concrete Slabs	100
Alkali Activation	243	Concrete Structure	152
Anchorage	233	Conductivity Losses	152
Anchored Sheet Pile Wall	70	Conductor	269
Angle of Failure	86	Conjugate Pairs of Strain	181
Anisotropic Prestress	130	Constructional Design	60
Annoyance	110	Cooling Towers	280
ANSYS	19, 171	Cornering Tire Stiffness	296
Approximation Relations	50	Crosswinds	296
Artificial Neural Network (ANN)	239	Cyclic Loading	221
Asphalt Pavement	29	Cylindrical Tank	66, 148
Assumption	86		
B		D	
Blast	263	Damage	3, 187
Blast Effect	86	Damage Detection	229
Blast Loading	92	Damage Mechanics	247
Blast Wave Dynamic Analysis	92	Degradation	142
BLWT Tunnel	257	Delamination	247
Bond	215	Destruction of Material	142
Bond of Reinforcement	225	Diagnostics	54
Boundary Layer Wind Tunnel	280	Dielectric Losses	152
Bridge	81	Double-K Fracture Model	239
Bridge Model	19	Drop-Weight Test	96
C		Dynamic Analysis	19, 40, 86
Cable-Membrane	124	Dynamic Approach to Study the Stability Problem	181
Calculation of Noise Levels	120	Dynamic Load	29
Calibration of Measuring Devices	257	Dynamic Relaxation	124
Cauchy Stress Tensor	130	Dynamic Response	175
Cement Dosage	239	Dynamic Stability	181
Cement Specimen	229	Dynamic Stability Criterion	181
CFD	275	Dynamic Tests	257
Complex Loading	187	Dynamics	60
Composite	233	Dynamics of Guyed Masts	175
Composite Material	104		
Composite Steel-Concrete Bridge	13	E	
Computational Fluid Dynamics (CFD)	291	Earthquake	66
Computer Model	40, 46	Eigenfrequencies	148
		Elastic Subgrade	40, 46
		Energy Productions	302
		Environmental Noise	110

Euler-Almansi Strain Tensor	130
Expansion Joints in Superstructures	197
Experiment	148
Experimental Measurements	162
Experimental Modal Analysis	3
Extreme Loads	81
F	
Factor of Seismicity	70
Failure	81
Fatigue	156, 221
Fatigue Damage Accumulation	197
Fatigue of Ship Structures	197
FEA Modeling of Structures	197
FEM Model	100
FETM-Technique	156
Fiber Reinforced Layers	247
Finite Element Analysis (FEA)	247
Finite Element Method (FEM)	66, 104, 148, 167, 171, 193
Fire-Resistance Rating	167
Fire Standard Temperature Conditions	167
Flat Winding	215
Flood	3
Fluid Structure Interaction (FSI)	66
Footbridge	3
Footbridge Aerodynamics	291
Forced Vibration	7
Form-Finding	130
Fourier Transform	34
Frequency Representation	34
FRP	221
FRP Materials	233
Functional of Variational Formulation	181
FWD Dynatest	40
G	
Gauss Distribution	193
Generalized Dynamic Factor	70
Geographic Information System (GIS)	302
Geometric Location of the Track	54
Glass Fiber Reinforced Polymer (GFRP)	215
Green Lagrange Strain Tensor	130
H	
Health Monitoring	229
Health Risk Assessment	110
Heat Field	162
Heat Flux	162
Heaviside Step Function	209
Heavy Vehicles	296
Hot Wire Anemometry	280
Human Induced Vibration	7
Human-Structure Interaction	7
I	
Identification	136, 187, 239
Impact	76
Impact Excitation Method	229
Impact Force	100
Impact Load Test	96
Impact Loading	100
Impact Mechanics	104
Impedance Spectroscopy	152
Insulator	269
Inverse Analysis Method	239
Isotropic Prestress	130
Iteration	124
K	
Kinetic Damping	124
L	
Large Displacements	181
Lateral Earth Pressure	70
Light Weight Building Structure	162
Limiting State	167
Long-Term Traffic Monitoring	13
Loss Factor	152
Low-Cycle Fatigue	187
Low Temperature	156
M	
Masonry	86
Mast	269
Mathematical Model	167
Mechanical Fracture Parameters	239
Mechanical Fracture Properties	243
Membrane Structure	130
Meshless Analysis	203

Meshless Local Petrov-Galerkin Method	209
Meshless Methods	209
Meshless Petrov-Galerkin Method	203
Meteorological Mast	307
Micro-Mechanical Modelling	156
Modal Analysis	136, 142
Mode Shape	229
Modeling	136, 142, 148, 253
Monte-Carlo Method	193
Monte Carlo Simulation	7
Moving Least Squares	209
Moving Load	24
Multibody Model	60
Multilayer	263
N	
Natural Frequency	3, 50, 229
Natural Modes	3
Navier-Stokes Equation	203
Noise Cloud	116
Noise Pollution	116
Nonlinear Aero-Elasticity	285
Nonlinear Analysis	76
Nonlinear Concrete Models	215
Nuclear Power Plant (NPP)	76, 81
Numerical Analysis	19
Numerical Methods	209
Numerical Modeling	171
Numerical Simulation	162
Numerical Solution	24, 29, 50
O	
Optimization	142
Optimization Process	130
Ordinary Pedestrian Traffic	7
P	
Plasticity	187
Plate	193, 263
Plate Element	247
Polarization Losses	152
Power Lines	269
Pressure Coefficient	253
Prestressed	233
Prestressed Girders	225
Probability	81, 193
Pull-Out Test	213, 225
R	
Railway Slabs	50
Railway Track	54
Random-Strength Model	247
Reinforced Concrete	76
Reliability	81
Response	86
Road Unevenness	29
Roadway Diameter	120
Rollover	296
Rotations	181
S	
Safety	76, 81
SDOF Model	92
Second Piola-Kirchhoff Stress Tensor	130
Seismic Lateral Earth Pressure	70
Sensitivity	193
Simulation	116
Site Selection	302
Slag	243
Soil Mechanics	70
Specimen	96
Speed Record	269
Stability	296
Stability Equations	181
Stabilization	130
Stabilizer Bar	60
Statics Analysis	193
Steel-Concrete Beam	167
Steel Fibres	96
Steel Specimen	156
Steel Structure	171
Stiffness	263
Stochastic Resonance	285
Strain-Life Format of Fatigue	197
Strengthening	233
Stress	263
Stress Analysis	46
Stress Vectors	181
Structure Fire Resistance	167
Swivelling of the Shaft	175
T	
Tall Building	253
Technical Diagnostics	136

Temperature Response	162
Thermal Stress	152
Thin-Walled Cold-Rolled Cross-Section	171
Three Point Bending Fracture Test	239
Three-Point Bending Test	243
Time Series	34
Tram Traffic Noise	120
Trapezoidal Sheet	171
Triangular Distribution	193
Trolleybus	60
Turbulence	285

U

UHPC	225
Ultimate Behaviour	156
Urban Area	110

V

Vandalism	7
Vegetation Growth	116
Vehicle	29
Vehicle Computing Models	24
Vehicle Model	19
Vibration	19, 263
Viscous Damping	124
Vortex Shedding	291

W

Wave Propagation	104
Wheel Squeal Noise	120
Wind Action	253
Wind Atlas	307
Wind Energy Projects	302
Wind Engineering	171
Wind Flow	257
Wind Induced Vibration	285
Wind Loads	307
Wind Power	302
Wind Power Plants	307
Wind Resources	302
Wind Tunnel	175
Wind Tunnel Contraction	275
Wind Tunnel Experiments	285
Winkler Foundation	50

Y

Young Healthy Individuals

A

- Arefiev, N. 302
Argalášová, L. 110

B

- Babjaková, J. 110
Badenko, V. 302
Baláž, L. 148
Benin, A.V. 215
Bogdanova, G. 215
Brožovský, J. 162, 275
Bvoc, M. 104

C

- Čavojcová, A. 221
Chobola, Z. 152
Čítek, D. 96, 225

D

- Daněk, P. 239
Daniel, L. 19

F

- Fajman, P. 124
Figuli, L. 92
Filová, A. 110
Fischer, O. 175
Flodr, J. 171

G

- Gnap, J. 296
Grajciar, I. 66

H

- Harabinová, S. 120
Havlíková, I. 239
Hirošová, K. 110
Hubová, O. 257
Huňka, P. 96, 225
Hüttner, M. 124

I

- Ižvolt, L. 54
Ižvoltová, J. 54

J

- Jendželovský, N. 100, 148, 253
Jurkovičová, J. 110

K

- Kánovicsová, A. 110
Keršner, Z. 239
Kolísko, J. 96, 225
Kolousek, M. 116
Konečná, L. 257
Kormaníková, E. 66, 247
Korovkin, V. 70
Kortiš, J. 40, 46
Kotrasová, K. 66, 247
Kovalov, M. 167
Král, J. 13
Králik, J. 76, 81, 81
Krejsa, M. 171
Kucharczyková, B. 239
Kuchárová, D. 50
Kusák, I. 152
Kushova, D.A. 181
Kuznětsov, S. 275

L

- Lajčáková, G. 24
Lalin, V.V. 181
Lang, R. 130
Lausová, L. 162
Lehký, D. 239
Lobotka, P. 257
Luňák, M. 152

M

- Máca, J. 3, 124
Makovička, D. 86, 86
Marková, J. 13
Marton, P. 263, 269
Mečer, J. 29

Melníkov, B.	187	Skrúcaný, T.	296
Melová, T.	116	Šoltýs, R.	291
Michalcová, V.	275	Stachová, D.	34
Michálek, P.	280	Štefániková, Z.	110
Mikolášek, D.	171	Sucharda, O.	171
Moravčík, M.	221		
Mužík, J.	203, 209	T	
		Tej, P.	13
N		Tejová, A.	13
Náprstek, J.	285	Tesár, A.	156
Němec, I.	130	Tesárek, P.	229
		Tomko, M.	291
O		Topolář, L.	243
Okénka, J.	229	Tvrďá, K.	193
Orel, Y.	167		
		U	
P		Urushadze, S.	175
Panulinová, E.	120		
Papán, D.	92	V	
Pelagić, Z.	104	Vatulia, G.	167
Petinov, S.	197	Vráblová, K.	100
Pirner, M.	175		
Plachý, T.	3, 229	Z	
Podolka, L.	233	Zacho, D.	280
Polach, P.	60	Zhdamirov, V.	70
Polák, M.	3, 7, 229	Žídek, L.	171
Pospíšil, S.	275, 285	Žmindák, M.	104
Priscak, T.	116	Žółtowski, B.	136
		Žółtowski, M.	136, 142
R			
Rakova, X.M.	307		
Rapanová, N.	40		
Řeháček, S.	96, 225		
Rovnaník, P.	243		
S			
Šána, V.	7		
Schmid, P.	243		
Sedlár, M.	156		
Semenov, A.	187		
Semenov, S.	215		
Šestáková, J.	54		
Ševčík, I.	130		
Ševčíková, L.	110		
Šimonová, H.	239, 243		
Šimůnek, I.	96		
Skotnicová, I.	162		